WRDC-TR-90-4096
VOLUME 3

DTIC
ELECTE
NOV 2 0 1991
S D
C

AD-A242 872

DETERMINATION OF THE TRIBOLOGICAL FUNDAMENTALS OF SOLID LUBRICATED CERAMICS VOLUME 3: APPENDICES P THROUGH II

M.N. Gardos
Hughes Aircraft Company
El Segundo, CA 90245

September 1991

Final Report for Period 09 September 1985 to 16 September 1989

Approved for public release, distribution is unlimited

91-15964

MATERIALS DIRECTORATE
WRIGHT RESEARCH AND DEVELOPMENT CENTER
AIR FORCE SYSTEMS COMMAND
WRIGHT-PATTERSON AIR FORCE BASE, OHIO 45433-6533

91 1119 091

NOTICE

When Government drawings, specifications, or other data are used for any purpose other than in connection with a definitely Government-related procurement, the United States Government incurs no responsibility nor any obligation whatsoever. The fact that the government may have formulated, or in any way supplied the said drawings, specifications, or other data, is not to be regarded by implication or otherwise in any manner construed, as licensing the holder or any other person or corporation, or as conveying any rights or permission to manufacture, use, or sell any patented invention that may in any way be related thereto.

This report is releasable to the National Technical Information Service (NTIS). At NTIS, it will be available to the general public, including foreign nations.

This technical report has been reviewed and is approved for publication.

Bobby D. McConnell, Chief
Nonstructural Materials Branch
Nonmetallic Materials Division

FOR THE COMMANDER

Merrill L. Minges, Director
Nonmetallic Materials Division

If your address has changed, if you wish to be removed from our mailing list, or if the addressee is no longer employed by your organization, please notify WL/____, Wright-Patterson AFB, OH 45433-____ to help us maintain a current mailing list.

Copies of this report should not be returned unless return is required by security considerations, contractual obligations, or notice on a specific document.

UNCLASSIFIED

SECURITY CLASSIFICATION OF THIS PAGE

REPORT DOCUMENT PAGE

Form Approved
OMB No. 0704-0188

1a. REPORT SECURITY CLASSIFICATION UNCLASSIFIED	1b. RESTRICTIVE MARKINGS
2a. SECURITY CLASSIFICATION AUTHORITY EDSG Document	3. DISTRIBUTION / AVAILABILITY OF REPORT Approved for public release; distribution is unlimited
2b. DECLASSIFICATION / DOWNGRADING SCHEDULE	
4. PERFORMING ORGANIZATION REPORT NUMBER(S)	5. MONITORING ORGANIZATION REPORT NUMBER(S) WRDC-TR-90-4096, Vol. 3
6a. NAME OF PERFORMING ORGANIZATION Hughes Aircraft Company Electro-Optical & Data Systems Group 6b. OFFICE SYMBOL (If applicable) EDSG	7a. NAME OF MONITORING ORGANIZATION Materials Directorate (WL/MLBT Wright Research and Development Center, AFSC
6c. ADDRESS (City, State, and ZIP Code) P.O. Box 902 El Segundo, CA 90245	7b. ADDRESS (City, State, and ZIP Code) Wright-Patterson AFB OH 45433-6533
8a. NAME OF FUNDING / SPONSORING ORGANIZATION 8b. OFFICE SYMBOL (If applicable)	9. PROCUREMENT INSTRUMENT IDENTIFICATION NUMBER F33615-85-C-5087
8c. ADDRESS (City, State, and ZIP Code)	10. SOURCE OF FUNDING NUMBERS PROGRAM ELEMENT NO. 61101E; PROJECT NO. 5177; TASK NO. 00; WORK UNIT ACCESSION NO. 01

11. TITLE (Include Security Classification)

Determination of the Tribological Fundamentals of Solid Lubricated Ceramics
Volume 3: Appendices P through II

12. PERSONAL AUTHOR(S)

Michael N. Gardos

13a. TYPE OF REPORT	13b. TIME COVERED	14. DATE OF REPORT (Year, Month, Day)	15. PAGE COUNT
Final Report	FROM 09-85 TO 09-89	September 1991	529

16. SUPPLEMENTARY NOTATION

17. COSATI CODES			18. SUBJECT TERMS (Continue on reverse if necessary and identify by block number)		
FIELD	GROUP	SUB-GROUP	Ceramics	Ab-initio	Solid Lubricants
			Diamond	Molecular Dynamics	Extreme Environments
			Tribology	Analytical Tribometry	Friction/Wear Testing

19. ABSTRACT (Continue on reverse if necessary and identify by block number)

The goals, structure and highlights of a recently completed multiyear/multinational research program are described. The main driving force behind this effort was the aim to advance the technology base so engineers can successfully and confidentially design, build and operate solid lubricated ceramic tribocomponents in extreme environments. Specially designed friction and wear testers were employed to perform well-defined model experiments on single crystal and polycrystalline ceramics and solid lubricants. The research led to discoveries such as (1) a lubricious oxide with the shear strength of MoS_2 in vacuum, (2) CVD diamond films with low friction and extraordinarily low wear, (3) intercalated graphites with high tribothermal resistance in vacuum and in air, and (4) a wear equation for Si_3N_4 ceramics. The fundamental nature of the research was exemplified by ab-initio predictions of the friction coefficient of single crystal (111) diamond sliding against its mating $(\bar{1}\bar{1}\bar{1})$ diamond plane, and molecular dynamics calculations on single crystal CaF_2 and BaF_2 (111) $[1\bar{1}0]$ interface shear forces. The test equipment developed for completing the model experiments included an Auger/ESCA tribometer capable of unidirectional and oscillatory sliding at room temperature, a SEM tribometer designed for oscillatory sliding to 1000°C in vacuum and in partial pressures of reactive gases, an 850°C + dual-rubshoe friction and wear tester employing a rolling contact fatigue rod as one of the sliding specimens, and 850°C + friction/traction apparatus capable of operating to extraordinarily high PV limits.

The fundamental nature of the research notwithstanding, the main goals were directed towards finding potential solutions and applications useful to practicing tribologists and lubrication engineers.

20. DISTRIBUTION / AVAILABILITY OF ABSTRACT	21. ABSTRACT SECURITY CLASSIFICATION
☒ UNCLASSIFIED/UNLIMITED ☐ SAME AS RPT. ☐ DTIC USERS	UNCLASSIFIED
22a. NAME OF RESPONSIBLE INDIVIDUAL KARL R. MECKLENBURG	22b. TELEPHONE (Include Area Code) (513) 255-2465
	22c. OFFICE SYMBOL WT, /MLBT

DD Form 1473, JUN 86 — Previous editions are obsolete. — SECURITY CLASSIFICATION OF THIS PAGE

UNCLASSIFIED

FOREWORD

The overall objective of this 48-month interdisciplinary program was to investigate fundamental microscopic, macroscopic and continuum phenomena which occur between bare and solid lubricated ceramic surfaces exposed to a variety of extreme, triboenvironmental conditions. The title of the program is "Determination of Tribological Fundamentals", DARPA Order No. 5177, WRDC Contract No. F33615-85-C-5087.

Key government personnel monitoring the program included: Lt. Col. Steven G. Wax, Dr. Kay Rhyne and Dr. Benjamin A. Wilcox as the DARPA Program Managers and Bobby D. McConnell as the WRDC/MLBT Project Engineer. Dr. Larry L. Fehrenbacher (TA&T, Inc., Annapolis, MD) was a consultant to DARPA, assisting in the programmatic oversight and guidance of the technical efforts.

Various aspects of research were performed within the Technology Support Division of the Electro-Optical and Data Systems Group (EDSG) of Hughes Aircraft Company, under the direction of Dr. Michael N. Gardos as the Principal Investigator. The Hughes Program Managers were Dr. Gardos, Robert W. Seibold, Dr. Arthur B. Naselow and Earl B. Holst in chronological order of service. The research activities were conducted by personnel at EDSG and other Hughes groups, ably assisted by expert subcontractors from academia and industry located in this country and Western Europe.

Hughes personnel performing various technical tasks included Bonnie L. Soriano, Bruce W. Buller, Patrick S. Davis, Gerald L. Meldrum and Phil M. Magallanes (tribotesting and data reduction), Leo Fiderer, Dr. Stuart S. Gassel, Larry Czichola, Hans D. Metzler and Jim J. Erickson (tribotester design), Crawford R. Meeks, Ahn A. Tran, John P. Harrell and Rick Williams (mechanical and thermal analyses by computer methods), Dr. Norman H. Harris, Dr. Daniel A. Demeo and Phyllis J. Kelleghan (ceramic science and chemical analysis), as well as Dr. Mort Robinson, Mr. Kevin W. Kirby and Dr. John A. Roth (CaF_2/BaF_2 single crystal growth, polishing and analysis). Special recognition is given to Dora A. Monteiro (technical publications).

The Hughes subcontractors and the DoD scientists which closely cooperated within the confines of the program are properly recognized in the INTRODUCTION AND EXECUTIVE SUMMARY section.

QUALITY INSPECTED 4

Accession For
NTIS GRA&I
DTIC Tab
Unannounced
Justification
By
Distribution/
Availability Codes
Dist | Avail and/or Special
A-1

CONTENTS

Page

VOLUME 3

APPENDIX P – N.H. Harris, "Phase Equilibria Relevant to the Tribological Fundamentals of Solid Lubricated Ceramics," Hughes Materials Science Dept. Report (Div. 76), Hughes Aircraft Co., El Segundo, CA, 13 March 1986 ..... P1-P28

APPENDIX Q – J.-M. Martin, Th. Le Mogne and M.N. Gardos, "Friction of Alpha Silicon Carbide Under Oxygen Partial Pressure: High Resolution Analysis of Interface Films," Proc. Jap. Int. Tribology Conf., Oct. 29 – Nov. 1, 1990, Nagoya, Japan Q1-Q6

APPENDIX R – J.-M. Martin, and Th. Le Mogne, selected Monthly Reports on α-SiC, ranging from Feb. 1988 to June 1988, Ecole Centrale de Lyon/SORETRIB, Lyon, France, Hughes P.O. S9-507874-SRW ... R1-R50

APPENDIX S – J.-M. Martin, "AES/XPS Analysis of Silicon Carbide Triboflats," Progress Report, Ecole Centrale de Lyon/SORETRIB, Lyon, France, 27 October 1989, Hughes P.O. S9-507874-SRW S1-S17

APPENDIX T – B. Wong, "Assessment of Sharp and Spherical Indentation Techniques," Hughes Avoid Verbal Orders (AVO) Memo, 25 July 1986 ..... T1-T

and

B. Wong, "Indentation for Tribocontact Fracture Characterization and Analysis," Hughes Interdepartmental Correspondence No. 7641.20/770, 06 January 1987 ..... T12-T35

APPENDIX U – B. Wong, "High-Speed Contact Failure and Microindentation," Hughes Interdepartmental Correspondence No. 7641.20/804, 27 February 1987 ..... U1-U26

APPENDIX V – G.D. Eisenbrand, "Status Report: Hertzian Cone Cracking Apparatus," Hughes Interdepartmental Correspondence No. 7621.13, 27 June 1986 ..... V1-V15

and

B. Billington, "Hertzian Stresses," Hughes Avoid Verbal Orders (AVO) Memo. 31 October 1986 ..... V16-V23

APPENDIX W – R.G. Hardistry, "Materials Removal Rate; Silicon Nitride Materials; Base-Data," Final Report, Spheric Special Products Report No. 1.015, Spheric, Inc., W. Sussex, England, 04 September 1989; Hughes P.O. M9-317643-KKD W1-W11

APPENDIX X – J.-M. Martin, and Th. Le Mogne, selected Monthly Reports on α-SiC, ranging from Dec. 1987 to March 1989, Ecole Centrale de Lyon/SORETRIB, Lyon, France, Hughes P.O. S9-317657-SKD ... X1-X43

CONTENTS (Continued)

Page

VOLUME 3

APPENDIX Y – H. Heshmat, "High Temperature Solid Lubricated Bearing Development - Dry Powder Lubricated Traction Testing," Proc. 26th Joint AIAA/SAE/ASME Propulsion Conf. Paper No. 90-2047, 16-18 July 1990, Orlando, FL Y1-Y8

APPENDIX Z – C. Schmutz, "Characterization of TiO_{2-x} Layers," CSEM Technical Report No. 232, Project No. 51.312, CSEM, Neuchatel Switzerland, Hughes P.O. S9-507875-SRW, Nov. 1988 ..... Z1-Z30

and

H. Boving, "Generation of TiO_2-Rutile Coatings and their Tribological Characterization," CSEM Technical Report No. 307, Project No. 51.207, CSEM, Neuchatel, Switzerland, Hughes P.O. S9-318804-SAC, November, 1988 ..... Z31-Z82

APPENDIX AA – B.G. Bovard, S. Chiao, and H. Angus Macleod, "Deposition of Titanium Oxide Films of Controlled Stoichiometries," Final Report, U. of Arizona Optical Sciences Center; Tucson, AZ, Hughes P.O. M9-315734-KKD AA1-AA18

APPENDIX BB – K.V. ravi, et al. "Thin Film Diamond Deposition on Silicon Wafers for Tribological Testing," Final Report (Phase I), Crystallume, Palo Alto, CA, 29 December 1987, Hughes P.O. P9-519308-SLX BB1-BB37

APPENDIX CC – L.S. Plano, S. Yokota, and K.V. Ravi, "Thin Film Diamond Deposition on Sapphire and Silicon Carbide for Tribological Testing," Crystallume, Menlo Park, CA, 30 June 1988, Hughes P.O. P9-519308-SLX CC1-CC16

APPENDIX DD – L.S. Plano, S. Yokota, and K.V. Ravi, "Thin Film Diamond Deposition on Silicon Carbide," Crystallume, Menlo Park, CA, 12 September 1988 ..... DD1-DD12

APPENDIX EE – R.W. Scibold, Hughes technical letter to Dr. K.V. Ravi of Crystallume, with data package on surface evaluation of HAC-GLAS disc prior to diamond coating, 8 August 1988 ..... EE1-EE26

APPENDIX FF – B.L. Soriano, and B. Buller, "HAC-GLAS 13-2 Optical Diamond Coating – Characterization and Polishing," Hughes Technical Internal Correspondence No. 7621.12/13, 21 February 1989 ..... FF1-FF30

APPENDIX GG – M.N. Gardos, "Graphite Fiber Reinforced Glass-Ceramic Composite Materials – Program Summary and Status Report" GG1-GG14*

and

* Pages GG2 through GG14 are deleted due to ITAR regulations.

CONTENTS (Concluded)

Page

VOLUME 3

B.L. Soriano, "HAC-GLAS 13-2 Substrate-Diamond Coating Characterization and Polishing"; viewgraph handouts of presentations given at the Diamond Initiative Planning Meeting, U. of A. Optical Sciences Center, Tucson, AZ, 23 February 1989..... GG1-GG29

APPENDIX HH – P.G. Magallanes, "Crystallume Diamond Films—Analysis by FTIR," Hughes Analytical Chemistry Laboratory Memo, Materials Science Dept. (Div. 76), Hughes Aircraft Co., El Segundo, CA, 18 December 1988..... HH1-HH5

and

P.G. Magallanes, "Wide Wavelength Spectrum of Diamond Film" Hughes Analytical Chemistry Laboratory Memo, Materials Science Dept. (Div. 76), Hughes Aircraft Co., El Segundo, CA 02 March 1989..... HH6-HH12

APPENDIX II – J.L. Margrave, R.H. Hauge, and R.B. Badachhape, "Oxidation and Fluorination Studies of Diamond," Program Report, Rice University, Houston, TX, 24 November 1987, Hughes P.O. S9-261816-Z7H..... ii1-il-4

APPENDIX P

N.H. Harris, "Phase Equilibria Relevant to the Tribological Fundamentals of Solid Lubricated Ceramics," Hughes Materials Science Dept. Report (Div. 76), Hughes Aircraft Co., El Segundo, CA, 13 March 1986

PHASE EQUILIBRIA RELEVANT TO THE TRIBOLOGICAL FUNDAMENTALS OF SOLID LUBRICATED CERAMICS

by

Norman H. Harris

March 13, 1986

Materials Science Department
Technology Support Division
Electro-Optical & Data Systems Group
Hughes Aircraft Company

Outline

		Page
1.0	Abstract	1
2.0	Introduction	2
3.0	Heterogeneous Ceramic/Solid Lubricant Reactions	3
4.0	SiC/Solid Lubricant Interactions	6
5.0	Si_3N_4/Solid Lubricant Interactions	8
6.0	Conclusions	11
7.0	References	13
8.0	Appendix	15

1.0 Abstract

The objective of this review was to survey the reported surface chemical interactions of silicon carbide, SiC, and silicon nitride, Si_3N_4, ceramic sliding interfaces with molybdenum sulfide, MoS_2, boron nitride, BN, and titanium nitride, TiN, solid lubricants from room temperature to 850°C (1500°F) in an oxidizing (air) environment. The SiC was considered both in its pure state and with Al_2O_3 additions. The Si_3N_4 was considered with the sintering aids, magnesium oxide, MgO, or yttrium oxide, Y_2O_3. Phase equilibrium diagrams were utilized to give the general relationships within each system. Relevant chemical studies were reviewed in the literature with the results being of interest to subsequent design of tribological experiments.

2.0 Introduction

The purpose of this review was to determine what the available literature would be able to provide in understanding the interactions of the materials to be studied in the M. Gardos research program entitled: "Determination of Tribological Fundamentals Governing Friction and Wear of Solid Lubricated Ceramics in Extreme Environments".[1] An important consideration is the phase equilibrium diagrams for the appropriate systems. While equilibrium will not likely be achieved under tribological conditions, a knowledge of the eutectic melting temperatures and phase relations will certainly be helpful in interpreting experimental results.

In addition, the relevant chemical literature was searched to determine whether prior research findings might be useful in understanding tribological fundamentals of the materials of interest.

The characteristics of surfaces and interfaces are of great interest to tribology. Surfaces and interfaces can be investigated from the approach of preparing solid surfaces of extreme purity and perfection. However such surfaces must be maintained in a very high vacuum.[2] The approach assumed in this review is that real surfaces will be investigated as well in the Gardos study but in a systematic way so that the results can be reproduced and interpreted by subsequent analysis.

3.0 Heterogeneous Ceramic/Lubricant Reactions

Even though the present review focus is simply on SiC and Si_3N_4 ceramic/solid lubricant interactions the chemistry becomes quite complex in the extreme environment of wear testing. The presence of sintering aids, Al_2O_3, MgO and Y_2O_3, as well as various impurities in contact with the BN, TiN and MoS_2 solid lubricants, in an oxidizing atmosphere at elevated temperatures and pressures, further complicates the present study.

In order to better understand the basic ceramic/solid lubricant interactions the variables investigated must be carefully controlled. Therefore a review of first the binary system phase equilibrium diagrams, then pertinent ternary systems, where available, will provide basic information on eutectics, intermediate compounds and solid solutions which may form.

Eutectic temperatures represent the lowest melting composition point between two or more compounds in a particular system. The significance of a eutectic in the tribological regime is that a viscous liquid phase will form above the eutectic temperature which may drastically increase the frictional forces involved. More importantly, though, the relatively slow diffusion controlled solid state reactions between contact surfaces at elevated temperatures can be greatly accelerated by the presence of a liquid phase. Above the eutectic temperature, liquid phases are formed. The presence of a liquid phase will greatly increase the reaction rates as the atomic mobility is increased and modify the reaction mechanisms as well.[3]

In the extreme tribological environment of the present study the SiC and Si_3N_4 substrates and the solid lubricants, BN, TiN, and MoS_2, would be expected to undergo surface oxidation to the respective oxides SiO_2, B_2O_3, TiO_2, and MoO_3. The presence of alkali or alkaline earth oxides can be expected to markedly decrease the silica liquidus temperatures (maximum temperatures at which equilibrium exists between the molten glass and its primary crystalline phases) as shown in Figure 3-1.[4] The liquidus temperatures in the SiO_2-RO, R_2O (R = metal alkali or alkaline earth ions) systems are drastically reduced in most cases accompanied by eutectics and the formation of intermediate compounds.

Boron oxide, B_2O_3, has a melting point of 460°C (860°F).[5] B_2O_3 is a strong melting point suppressant so that it is commonly used in ceramics (such as glazes, glasses, and enamels) to flux various oxides and more readily form liquid phases. Thus the presence of BN solid lubricants or boron impurities in the ceramics would be expected to form low temperature eutectics with the SiO_2 and other oxides present with attendant enhanced chemical reaction rates.

Silicon carbide is covalently bonded on the atomic level which makes sintering of pure SiC powders into a dense polycrystalline ceramic quite difficult. The use of sintering aids such as aluminum oxide, Al_2O_3, helps promote densification of the covalent SiC. Hot pressing or hot isostatic pressing in conjunction with the addition of sintering aids permits the attainment of commercial SiC densities of 3.25 g/cc or more. The theoretical density of SiC is 3.217 g/cc. The "higher" than theoretical" value of commercial hot pressed SiC can be attributed to the presence of impurities such as tungsten carbide, WC, which may be introduced through grinding of the SiC powders.

Grinding of SiC to a fine particulate powder prior to subsequent ceramic processing is difficult due to the extreme hardness of the SiC. WC grinding media and mill liners, although they reduce SiC to 1-5 microns, are themselves partially consumed in the process and become a major impurity in the SiC. With the use of sintering aids and careful control of temperature and time, the SiC can be hot-pressed to a near theoretical density with grain sizes limited to 3-5 microns.

The Norton Company produces a hot pressed SiC (Noralide NC-203) whose microstructure contains primarily 6H SiC with small amounts of 33R and 51R poly types. Trace quantities of β-SiC (3C) are likely to be present as well. Tungsten carbide, $W(SiAl)_2$ - 9H and tungsten silicides may also be present in the microstructure. The non-SiC elemental concentrations for NC-203 would not be expected to exceed the following*:

Element	Percent	Method
aluminium	2.5	atomic absorption spectroscopy
tungsten	3.5	atomic absorption spectroscopy
silicon (not in SiC)	1.0	hydrogen evolution
boron	0.1	emission spectroscopy
iron	0.3	emission spectroscopy
calcium	0.1	emission spectroscopy
magnesium	0.1	emission spectroscopy

*Technical Data Bulletin for Noralide High Performance Ceramics, Norton Company, Worcester, MA 01606

Silicon nitride is also difficult to sinter due to its covalent bonding. Even when high pressure is applied (ie. hot pressing or hot isostatic pressing), sintering aids are required to enhance densification.[6]

Yttrium oxide, Y_2O_3, is commonly used as a sintering aid to substantially improve the high temperature strength of Si_3N_4. Approximately 8% Y_2O_3 is added to the Norton Company NCX-34 hot pressed Si_3N_4. It also contains other elements per spectrographic analysis: 3.00 w/o tungsten, 0.75 w/o iron 0.50 w/o aluminum, 0.10 w/o magnesium, and 0.05 w/o calcium.

The microstructure of NCX-34 contains more than 80% β-Si_3N_4, with lesser amounts of yttrium silicate and tungsten silicide. Trace amounts of α-Si_3N_4, silicon oxynitride, tungsten-iron-silicide, and yttrium silicon oxynitride would be expected as well.

Another major sintering aid used is magnesium oxide, MgO, which provides more toughness to the silicon nitride ceramic. Norton NC-132 hot pressed silicon nitride contains the following elements by spectrographic analysis: 3.5 w/o tungsten, 1.00 w/o magnesium, 0.75 w/o iron, 0.5 w/o aluminum and 0.05 w/o calcium.

The primary crystalline form in NC-132 is at least 80% β- Si_3N_4 with the balance being principally α-Si_3N_4 and silicon oxynitride. Minor amounts of tungsten silicon and tungsten-iron-silicon phases are present as well.

The Norton hot isostatic pressed (HIP) version of NC-132 is NBD-100 and for the NCX-34 is designated NC-144. Slightly higher densities and strengths would be expected in the HIP processed material as well as more isotropic properties.

4.0 Silicon Carbide/Solid Lubricant Interactions

The wearing of two silicon carbide, SiC, ceramic rubshoes in contact would be expected to yield the surface oxidation product, silicon dioxide, SiO_2. The process of oxidation would not be complete but would be expected to proceed at a subsurface diffusion controlled oxidation reaction interface that would move inward into the SiC bulk ceramic. If intermediate states of oxidation were present then the Si - SiO_2 phase diagram shown in Figure 4-1 would be of interest.[7] Metastable SiO and the presence of two eutectics are indicated in the Si - SiO_2 system.

When the SiC rubshoes are lubricated with the solids BN, TiN, or MoS_2, surface oxidation would then be expected to result in the following binary oxide systems: SiO_2 - B_2O_3, SiO_2 - TiO_2, and SiO_2 - MoO_3. The SiO_2 - B_2O_3 system, shown in Figure 4-2, contains a eutectic melting point at 450°C and 95% B_2O_3.[8] Higher SiO_2 concentrations result in a higher glass viscosity while higher B_2O_3 yields a lower viscosity. The liquid phase which may form at the SiC surfaces lubricated with BN becomes an important tribological factor at temperatures above 450°C. Other important considerations in the SiO_2 - B_2O_3 system are the volatization of B_2O_3 and the rapid hydration of B_2O_3-rich glasses. The volatization of B_2O_3 becomes significant above 700°C (1300°F). The hydration of B_2O_3-SiO_2 glasses could further complicate interpretation of experimental results.

When SiC is lubricated with TiC or TiN the surface oxidation product system would be SiO_2 - TiO_2, illustrated in Figure 4-3.[9] The SiO_2 - TiO_2 eutectic temperatures are 1550°C and 1830°C with no intermediate compounds being reported. The eutectic temperatures are higher than the temperature range of interest.

Lubrication of SiC with MoS_2 would be expected to result in the SiO_2 - MoO_3 oxide system. Unfortunately the SiO_2 - MoO_3 system phase diagram is apparently not available in the oxide literature. However the MoO_3 would be expected to lower the liquidus temperatures of SiO_2 quite significantly. The melting point of MoO_3 itself is 795°C.[10]

If SiC contains Al_2O_3 the SiO_2-Al_2O_3 binary system would represent the surface oxidation products as given in Figure 4-4.[11] The SiO_2-Al_2O_3 system has been extensively investigated. There is still significant discrepancy in reported results for the SiO_2-Al_2O_3 system even though it is the single most important phase

diagram for ceramists (it contains the clay mineral, kaolinite, and the solid solution, mullite). The difficulty in studying the SiO_2-Al_2O_3 system arises from the enormous time required to reach equilibrium at elevated temperatures due to the extremely high viscosity of high SiO_2-rich melts.

The eutectics in the SiO_2-Al_2O_3 system occur at 9 w/o Al_2O_3 (1546°C) and 78 w/o Al_2O_3 (1912°C). The intermediate compound, mullite, $2SiO_2$-$3Al_2O_3$, melts congruently as reported by Staronka et al.[11] The work of MacDowell and Beall in Figure 4-5 indicates the complexity of the SiO_2 - Al_2O_3 system with mullite having a solid solution range and the possible presence of an immiscibility gap superimposed on the previous diagram of Aramaki and Roy.[12]

The SiO_2 - Al_2O_3 - TiO_2 ternary system is of interest when the solid lubricant TiN is considered as shown in Figure 4-6.[13] The primary phase fields are rutile, cristobalite, mullite, corundum and $TiO_2 \cdot Al_2O_3$.

The ternary SiO_2 - Al_2O_3 - B_2O_3, shown in Figure 4-7, would relate to the surface oxidation products of SiC and Al_2O_3 lubricated by the solid, BN. Again, the B_2O_3 causes liquidus temperatures in the SiO_2 - Al_2O_3 system to be significantly reduced.[14] Intermediate compounds, mullite, $2B_2O_3 \cdot 9Al_2O_3$ and $B_2O_3 \cdot 2Al_2O_3$ would be expected to crystallize out from the melt on cooling.

5.0 Si_3N_4/Solid Lubricant Interactions

The phase relations of interest to the Norton NC-132 silicon nitride (1% MgO/99% Si_3N_4) are incorporated in the binary system SiO_2 - MgO as shown in Figure 5-1.[15] The principal features of the diagrams shown are that the reaction of the sintering aid, MgO, combined with the surface oxidation product of Si_3N_4, SiO_2, will form the intermediate magnesium silicates, forsterite, 2 MgO•SiO_2, and enstatite, MgO•SiO_2.

Forsterite melts congruently, (directly to the liquid phase) at 1890°C, while enstatite melts incongruently to the forsterite plus liquid phases at 1559°C. There are three eutectics in the SiO_2 - MgO system, one at 1850°C, the second at 1543°C, and the third on the silica rich end at 1695°C.[15]

Of particular interest to the tribological considerations of the SiO_2 - MgO system are the complex phase relations as a function of pressure and temperature as illustrated in Figures 5-2, 5-3 and 5-4.[16,17,18] As the pressure is increased in the enstatite system, MgO•SiO_2, (Figure 5-3) the protoenstatite converts to the orthoenstatite form at 5 k bars pressure and 1400°C.[17] The conversion of enstatite to forsterite ($2MgO•SiO_2$) occurs at 1557°C at ambient pressure but this incongruent melting (and phase change) occurs at increasing temperatures with increasing pressure (~1600°C at 5 k bars pressure). Figure 5-1 also indicates that the melting temperature increases with increasing pressure (from 1557°C) at 0 k bars pressure to 1800°C at 28 k bars. Of even more interest is the complete suppression of the forsterite form above 8 k bars pressure.[18]

Figure 5-2 shows the schematic pressure/temperature relation of enstatite. As the pressure increases at 865°C, the vapor phase condenses to the solid enstatite, then to the metastable clinoenstatite. As the temperature increases at pressure, P, the metastable clinoenstatite converts to a metastable protoenstatite. At pressure, P, and temperature, 1042°C, the stable enstatite converts to the protoenstatite form.

More detail in the SiO_2 - MgO pressure/temperature relations can be obtained by looking at the forsterite-silica region (Mg_2SiO_4 - SiO_2) in Figure 5-5.[19]. Figure 5-5.A. indicates that the temperature of congruent melting of protoenstatite increases from 1560 to 1800°C as the pressure increases from 1 atmosphere to 25 k bars.

Figure 5-5.B. shows two orthoenstatite to protoenstatite curves for mixture B. The work of Chen and Presnall indicates that a curve intermediate between those shown in Figure 5-5.B. would be more appropriate.[19] Figure 5-5.C. shows the pressure-temperature phase diagram (isopleth) for mixture A while Figure 5-5.D. represents the isopleth for mixture B. The complexity of the pressure-temperature projection for the entire Mg_2SiO_4 - SiO_2 system is illustrated in Figure 5.5.E.

The introduction of the solid lubricants, BN, TiN, and MoS_2, to NC-132 causes further complications. In an oxidizing atmosphere, the BN, TiN and MoS_2 would be expected to form the respective oxides, B_2O_3, TiO_2 and MoO_3 which would be available to react with the SiO_2, MgO, WO_3 and other impurity oxides in the NC-132.

The effect of the interaction of MgO in NC-132 with B_2O_3 can be observed in tne MgO - B_2O phase diagram in Figure 5-6.[20] The MgO - B_2O_3 binary includes two eutectics, at 1146 and 1333°C, and intermediate compounds, MB_2, M_2B and M_3B (where M = MgO and B = B_2O_3). MB_2 and M_2B melt incongruently at 995 and 1312°C respectively while M_3B melts congruently to a liquid at 1412°C. Of particular significance to the present tribology study is the low melting temperature of B_2O_3, 460°C, and the coexistence of a liquid phase with solid MB_2 below 995°C, from 0 to 22 w/o MgO.[20]

The ternary phase equilibrium diagrams would be expected to be quite helpful in understanding the interactions of NC-132 in the presence of the solid lubricants. The system SiO_2-MgO-B_2O_3 ternary phase diagram is shown in Figure 5-7.[21] In addition to the previously mentioned binary eutectic points there are ternary eutectics at 1270 and 1186°C with peritectic points (incongruent melting) at 1327, 1203 and 1510°C.[21]

The SiO_2-MgO-TiO_2 pressure/temperature ternary diagrams, as shown in Figures 5-8, 5-9, 5-10 and 5-11 would be applicable to the solid lubrication of NC-132 with TiN. Figure 5-8 shows the subsolidus compatibility relations at 1480°C below and above 15 k bars and the pressure effect on the $MgSiO_3$ (enstatite) + $MgTi_2O_5$ reaction which forms Mg_2SiO_4 (forsterite) and TiO_2.[22]

Figure 5-9 shows the effect of pressure (1 atmosphere, 10, 15.5, 20 and 40 k bars) vs. temperature for the $MgSiO_3$ - TiO_2, Mg_2SiO_4 - TiO_2, and $MgSiO_3$-MgO-TiO_2 system.[22] The effect of increasing pressure generally was to shift the eutectic points toward the higher TiO_2 composition regions while raising the eutectic, liquidus, and subsolidus temperatures.

While the SiO_2-MgO-MoO_3 ternary is not reported in the literature the MgO-MoO_3 binary is shown in Figure 5-12.[23] The $MgMoO_4$-MoO_3 system includes a 745°C eutectic at 80.5 m/o MoO_3 and the formation of an intermediate compound $MgMo_3O_{11}$, which melts incongruently to $MgMoO_4$ and a liquid phase at 826°C.[23]

The Norton NCX-34 Si_3N_4 contains 8 w/o of the sintering aid, Y_2O_3, as well as previously mentioned impurities. The SiO_2-Y_2O_3 binary system is shown in Figure 5-13.[24] The SiO_2-Y_2O_3 system includes four eutectic points at 1700, 1660, 1900 and 1800°C. Intermediate compounds include congruently melting $SiO_2 \cdot Y_2O_3$, $3SiO_2 \cdot 2Y_2O_3$, and incongruently melting $2SiO_2 \cdot Y_2O_3$. The SiO_2-Y_2O_3 system also contains two immiscible liquids above 1700°C on the SiO_2-rich end of the binary. The melting temperature of Y_2O_3 is 2410°C and the eutectics in the SiO_2 - Y_2O_3 occur at temperatures above the range of interest for the tribological study. However, in conjunction with solid lubricants such as MoO_3 there may be ternary liquid phases well below those seen in the SiO_2-Y_2O_3 binary systems.

The Y_2O_3-MoO_3 binary system is shown in Figures 5-14 and 5-15. The full binary in Figure 5-14 is incomplete but shows a eutectic point at 740°C and five intermediate compounds, $Y_2Mo_4O_{15}$, $Y_2Mo_3O_{12}$, Y_2MoO_6, Y_4MoO_9, and Y_6MoO_{12}.[25]

The details of the MoO_4-rich end of the Y_2O_3-MoO_4 binary are shown in Figure 5-15.[25] The eutectic point is shown in Figure 5-15 at 8 m/o MoO_3 and 720°C with the compound $Y_2Mo_4O_{15}$ melting incongruently at 830°C. Clearly the interaction of MoO_3 with NCX-34 Si_3N_4 will introduce liquid phases within the temperature range of interest to the present tribological study.

6.0 Conclusions

The following conclusions can be made based on the review of the phase equilibria literature cited in the present study:

1. Minimizing experimental variables with single crystals and solid surfaces of extreme purity and perfection would facilitate determination of tribological fundamentals of these materials. However, commercial materials and real surfaces are of interest in the Gardos study as well.

2. The use of sintering aids, required to densify covalently bonded SiC and Si_3N_4, as well as the presence of impurities introduced in processing makes the prediction of chemical interactions more difficult.

3. The review of phase equilbria relations between the ceramics and solid lubricants has provided basic information concerning the conditions under which liquid phases and crystal phase transformations may occur.

4. The presence of liquid phases, above the eutectic points, will affect frictional forces as well as greatly accelerate chemical reaction rates at elevated temperatures.

5. Diffusion controlled surface oxidation would be expected to occur at elevated temperatures in air on both the ceramic solid lubricant surfaces to form layers of the oxides, SiO_2, B_2O_3, TiO_2, MoO_3, as well as oxides of the impurity and sintering aid compounds.

6. The presence of alkali or alkaline earth oxides can be expected to markedly suppress the silica liquidus and solidus temperatures, to form eutectic points and to yield numerous intermediate compounds.

7. The complex phase relations of the SiO_2-MgO system (applicable to the Si_3N_4 containing MgO) included reference to pressure-temperature studies. Higher pressures were reported to shift the eutectic points toward the higher TiO_2 composition regions while simultaneously increasing the eutectic, liquidus, and subsolidus temperatures.

8. The effect of MoO_3, Y_2O_3, and WO_3 on the phase relations of the ceramic/solid lubricant systems is much less well known. Additional investigation into their phase equilibria and chemical reactions with SiO_2 is needed.

9. The review of phase equilibria relations are of critical importance to the design of tribological experiments. However, the attainment of equilibrium conditions requires lengthy periods at temperature with high silica rich melts due to the high glass viscosities and low atomic mobilities of SiO_2.

10. The careful determination of experimental temperatures and pressures is extremely important in understanding and interpreting tribological fundmentals. Although experimental constraints make the measurement of temperature especially difficult, both accuracy and rapid scan speed are critical requirements.

11. It is apparent that much more information is needed to even begin to understand the surface chemical interactions of the ceramic substrates and solid lubricant systems of interest. Review of additional available relevant literature is recommended in order to provide information concerning the missing phase diagrams, and chemical interactions not covered in this survey.

7.0 References

1. M. N. Gardos, "Determination of Tribological Fundamentals - Detailed Study Plan", November 7, 1985, for AFWAL/MLBT and DARPA (Contract F33615-85-C-5087).

2. J. J. Burke, N. L. Reed, and V. Weiss, Surfaces and Interfaces I - Chemical and Physical Characteristics, Syracuse University Press (1967).

3. A. Packter, Silicates Industriels Vol. 49 (1), 3-11 (1984).

4. F. C. Kracek, Carnegie Inst. Wash., Year Book, Ann. Rep. Director Geophys. Lab., pp. 61-63 (1932-33); see also Kracek, J. Am. Chem. Soc., 52 [4] 1440 (1930). [#365]*

5. R. C. Weast, Handbook of Chemistry and Physics, Chemical Rubber Co., B-74 (1971).

6. G. E. Gazza, J. Am. Ceramic Soc. 56 (12) 662 (1973).

7. R. B. Sosman, Trans. Brit. Ceram. Soc., 54, 657 (1955). [#21]

8. T. J. Rockett and W. R. Foster, J. Am. Ceram. Soc., 48 [2] 78 (1965). [#2353]

9. R. C. DeVries, R. Roy and E. F. Osborn, Trans. Brit. Ceram. Soc., 53 [9] 531 (1954). [#113]

10. R. C. Weast, ibid., B-111 (1971).

11. A. Ataronka, H. Phan, and M. Rolin, Rev. Int. Hautes Temp. Refract., 5 [2] 112 (1968). [#4373]

12. R. F. Davis and J. A. Pask, J. Am. Ceram. Soc., 55 [101] 525 (1972). [#5190]

13. F. Ya. Galakhov, Invest. Akad. Nauk S.S.S.R. Otdel. Khim. Nauk, 533 (1958). [#/69]

14. P. J. Gielisse and W. R. Foster, Quart. Progr. Rept. 931-8, The Ohio State Univ. Res. Foundation, p.6, Oct. (1961). [#763]

15. N. L. Bowen and Olaf Andersen, Am. J. Sci. [4], 37, 488 (1914); modified by J. W. Grieg, ibid. [5] 13, 15, 133-54 (1927). [#266]

16. J. F. Sarver and F. A. Hummel, J. Am. Ceram., Soc., 45 [4] 156 (1962). [#268]

17. F. R. Boyd and J. L. England, Ann. Rept. Director Geophys. Lab. 1960-61; in Carnegie Inst. Washington Year Book, 60, 115 (1961). [#261]

18. F. R. Boyd and J. L. England, Ann. Rept. Director Geophys. Lab. 1964-65; in Carnegie Inst. Washington, Yearbook, 64, 118 (1965); F. R. Boyd, J. L. England, and B. T. C. Davis, J. Geophys. Res., 69 [10] 2104 (1964). [#2315]

*Figure Numbers in Phase Diagrams for Ceramists, Volumes I-V, published by The American Ceramic Society, 65 Ceramic Drive, Columbus, OH 43214.

19. C. H. Chen and D. C. Presnall, Am. Mineral., 60 [5-6] 398 (1975). [#5160]

20. T. Mutluer and M. Timucin, J. Am. Ceram. Soc., 58 [5-6] 196 (1975). [#5154]

21. Hans-Jurgen Kuzel, Neues Jahrb. Mineral., Abhandl., 100 [3] 326 (1963). [#2540]

22. I. D. MacGregor, Amer. J. Sci., 267A, 358 (1969). [#4576]

23. V. M. Zhukovskii and T. M. Yanushkevich, Fiz. Metal. Metalloved, 26 [5] 959 (1968); Phys. Metals Metallogr. (USSR), 26 [5] 199 (1968). [#4343]

24. N. A. Toropov, Trans. Intern. Ceram. Congr., 7th London, 1960, p. 438; N. A. Toropov and I. A. Bondar, Izv. Aka. Nauk SSSR, Otd. Khim. Nauk, 4, 547 (1961). [#2388]

25. J. P. Fournier, J. Fournier, and R. Kohlmuller, Bull. Soc. Chim. Fr., 1970, No. 12, p. 4280. [#4438]

26. S. S. Antonova, I. V. Shakhno, V. E. Plyushchev, Izv. Vyssh. Uchebn. Zaved., Khim. Tekhnol., 14 [1] 17 (1971). [#5254]

8.0 Appendix

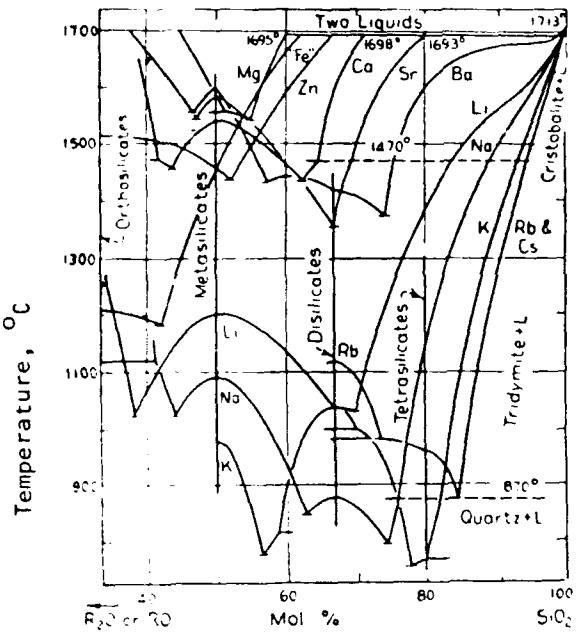

Figure 3-1. Liquidus relations in the alkali and alkaline earth-silicate systems.[4]

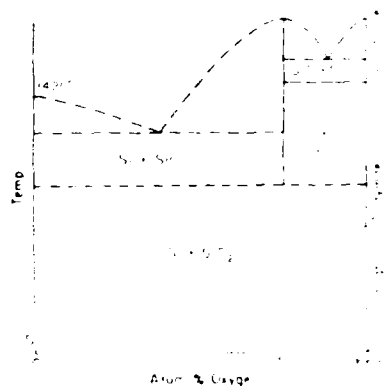

Figure 4-1.
Systems Si-SiO_2.[7]

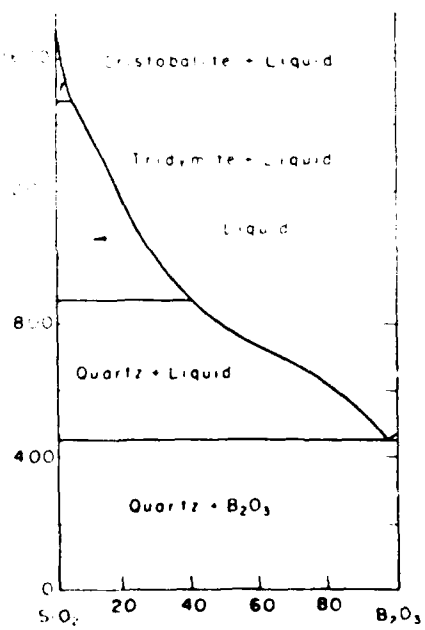

Figure 4-2.
System SiO_2-B_2O_3.[8]

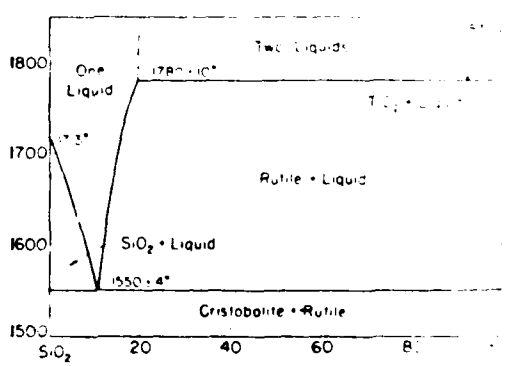

Figure 4-3.
System SiO_2-TiO_2.[9]

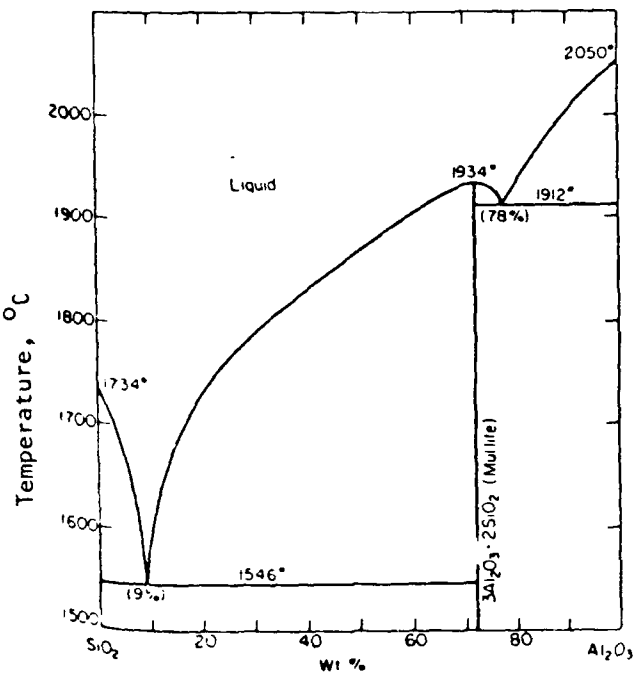

Figure 4-4.
System SiO_2-Al_2O_3.[11]

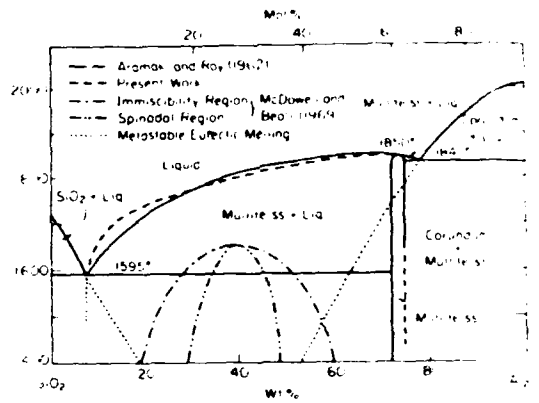

Figure 4-5.
System SiO_2-Al_2O_3.[12]

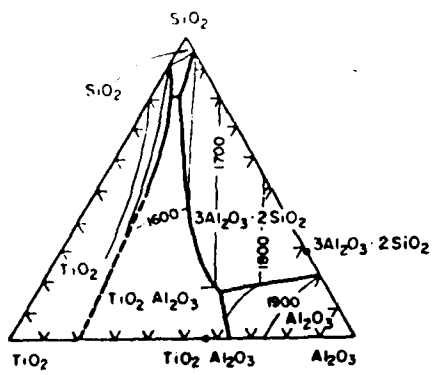

Figure 4-6.
System SiO_2- Al_2O_3-TiO_2.[13]

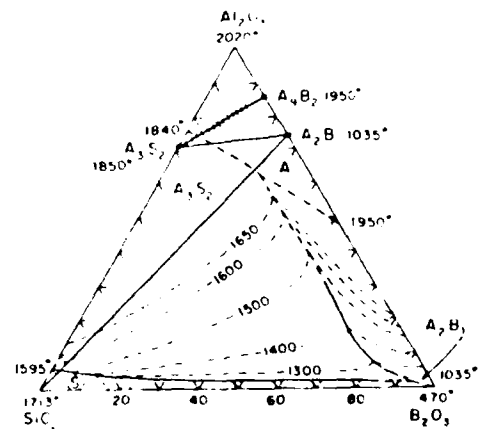

Figure 4-7.
System SiO_2-Al_2O_3-B_2O_3.[14]

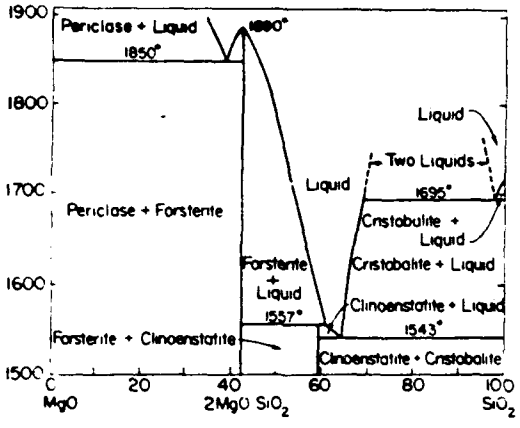

Figure 5-1.
System SiO_2-MgO.[15]

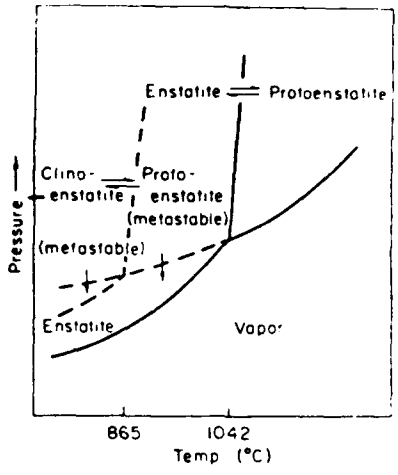

Figure 5-2.
System SiO_2-MgO,
Pressure Schematic.[16]

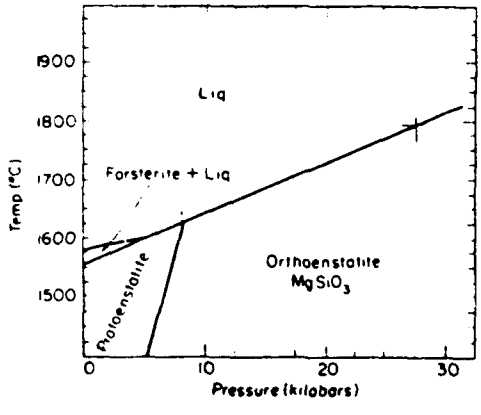

Figure 5-3.
System SiO_2-MgO,
Pressure to 30 k bars.[17]

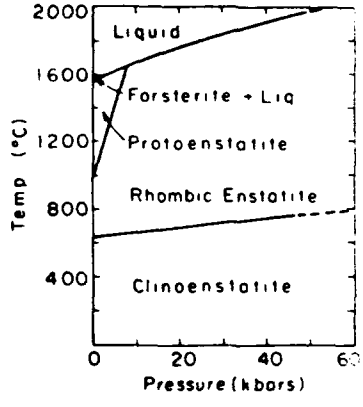

Figure 5-4.
System SiO_2-MgO,
Pressure to 60 k bars.[18]

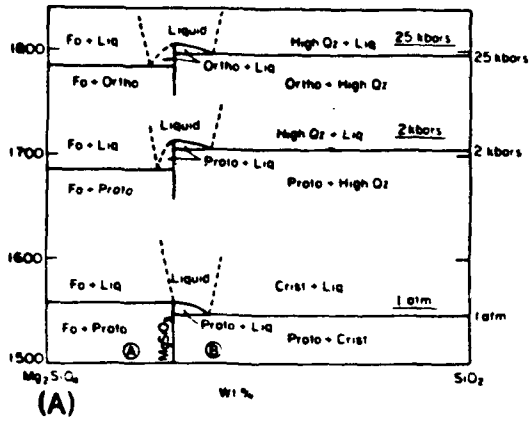

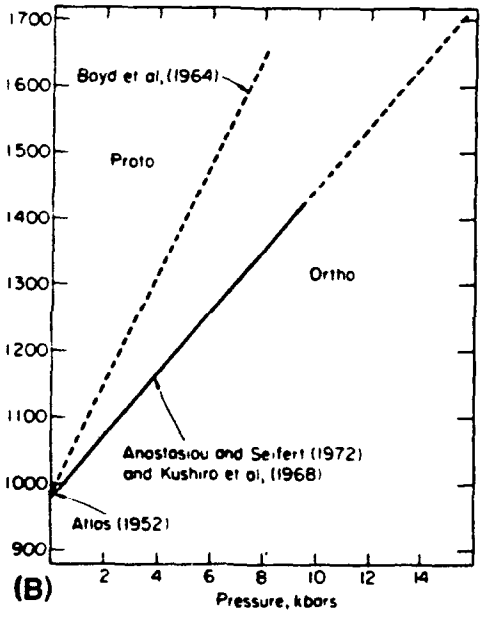

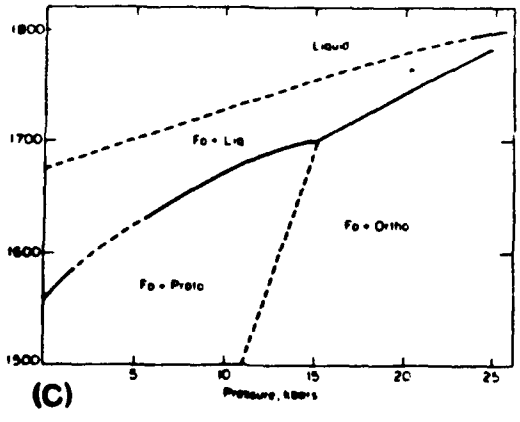

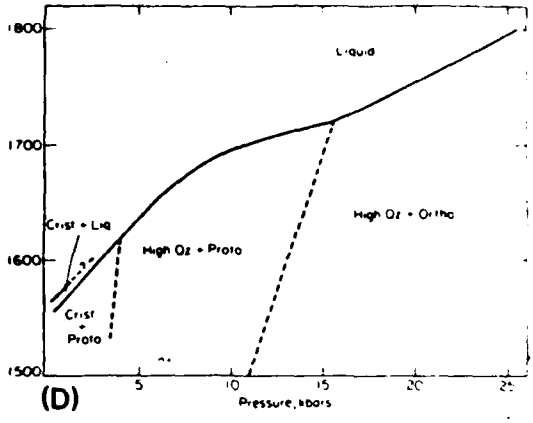

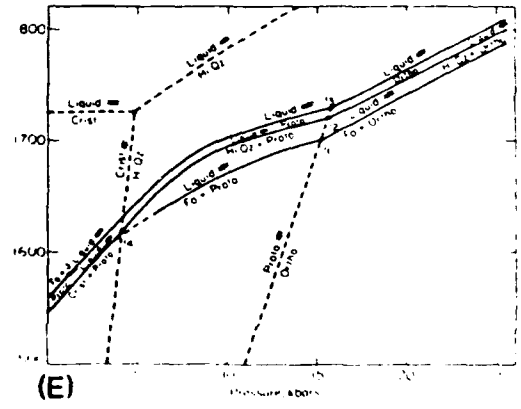

Figure 5-5.
System $MgSiO_4$-SiO_2. 19

A. Temperature/Composition
   1 bar, 2 k bars, and 25 k bars.
B. Subsolidus p-T for mixture B.
C. Subsolidus p-T for mixture A.
D. Subsolidus p-T for mixture B
   (1500 to 1800°C).
E. Pressure/temperature projection
   for the system.

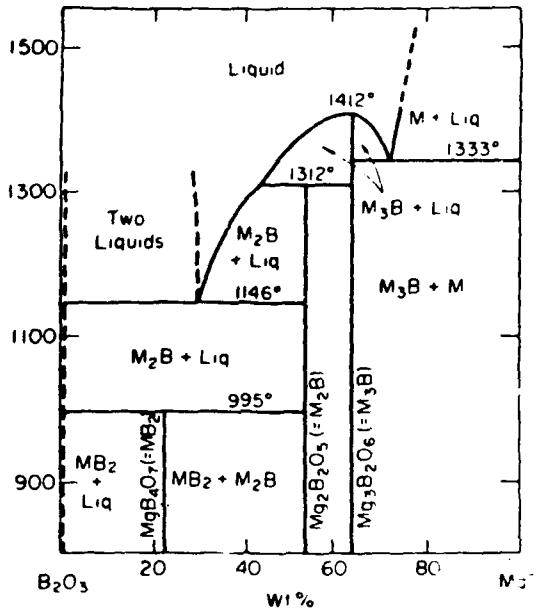

Figure 5-6.
System $MgO-B_2O_3$.[20]

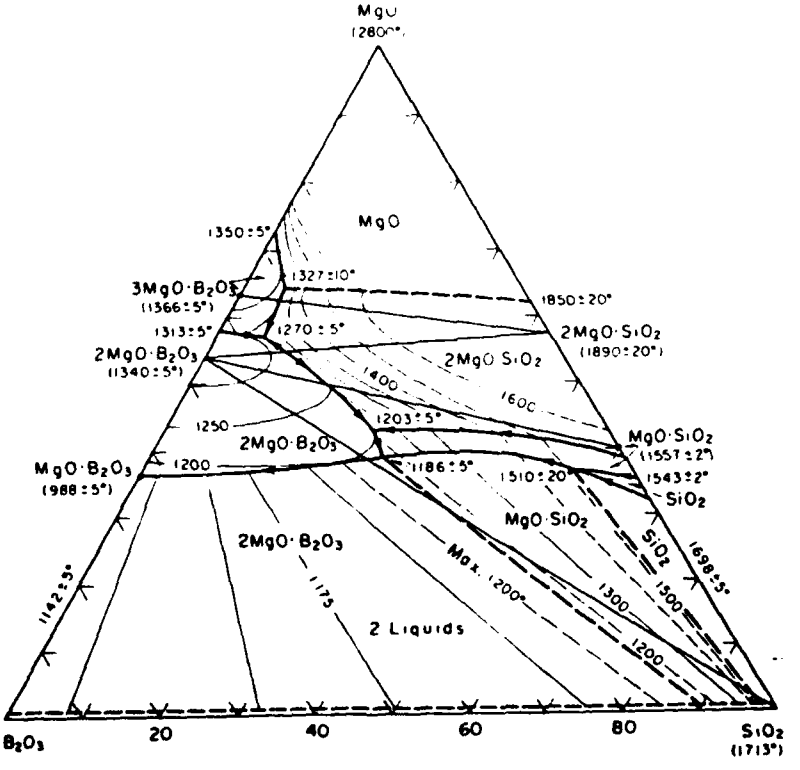

Figure 5-7.
System $SiO_2-MgO-B_2O_3$.[21]

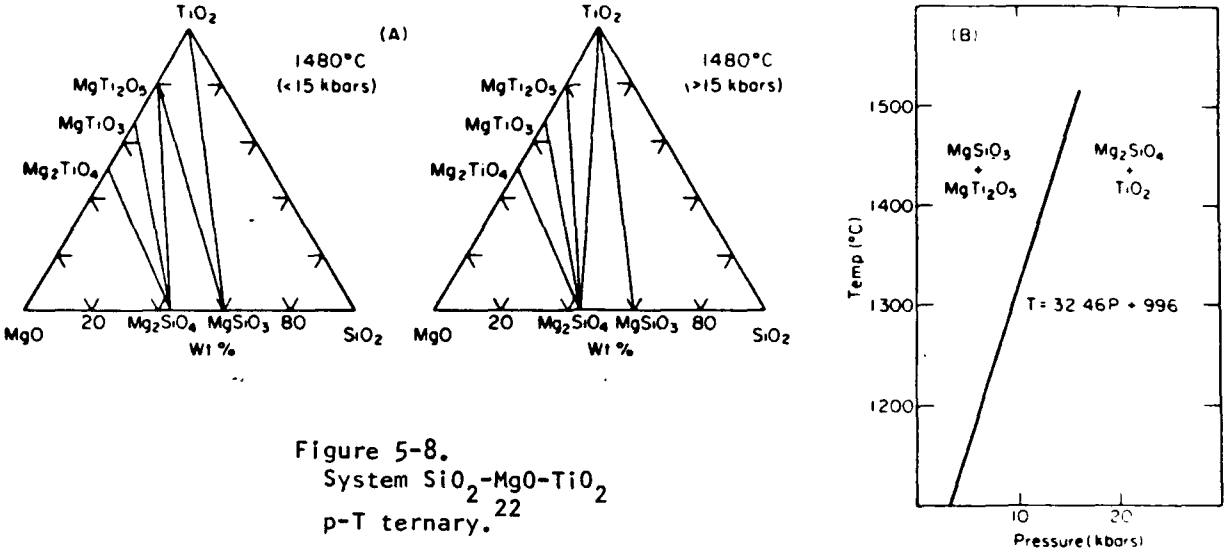

Figure 5-8.
System SiO_2-MgO-TiO_2
p-T ternary.[22]

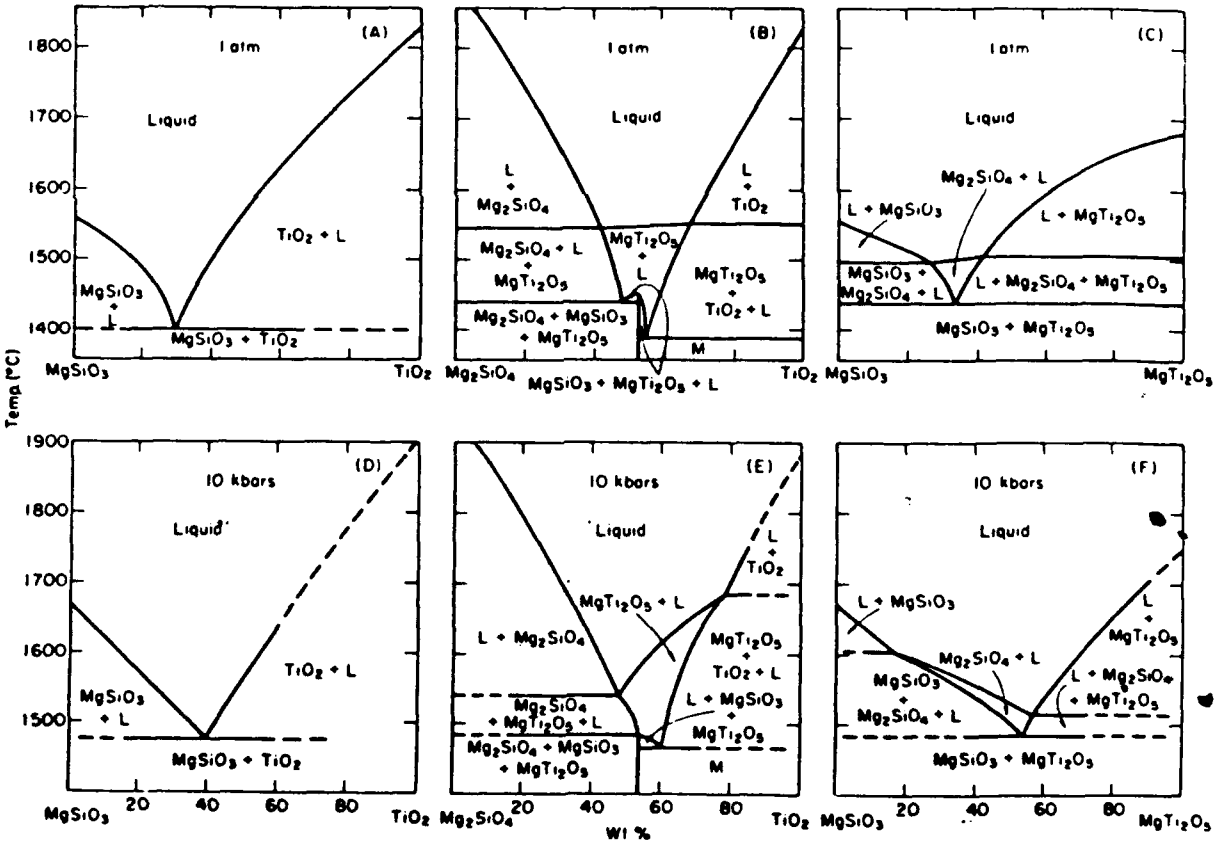

Figure 5-9.
System SiO_2-MgO-TiO_2 p-T binary sections.[22]

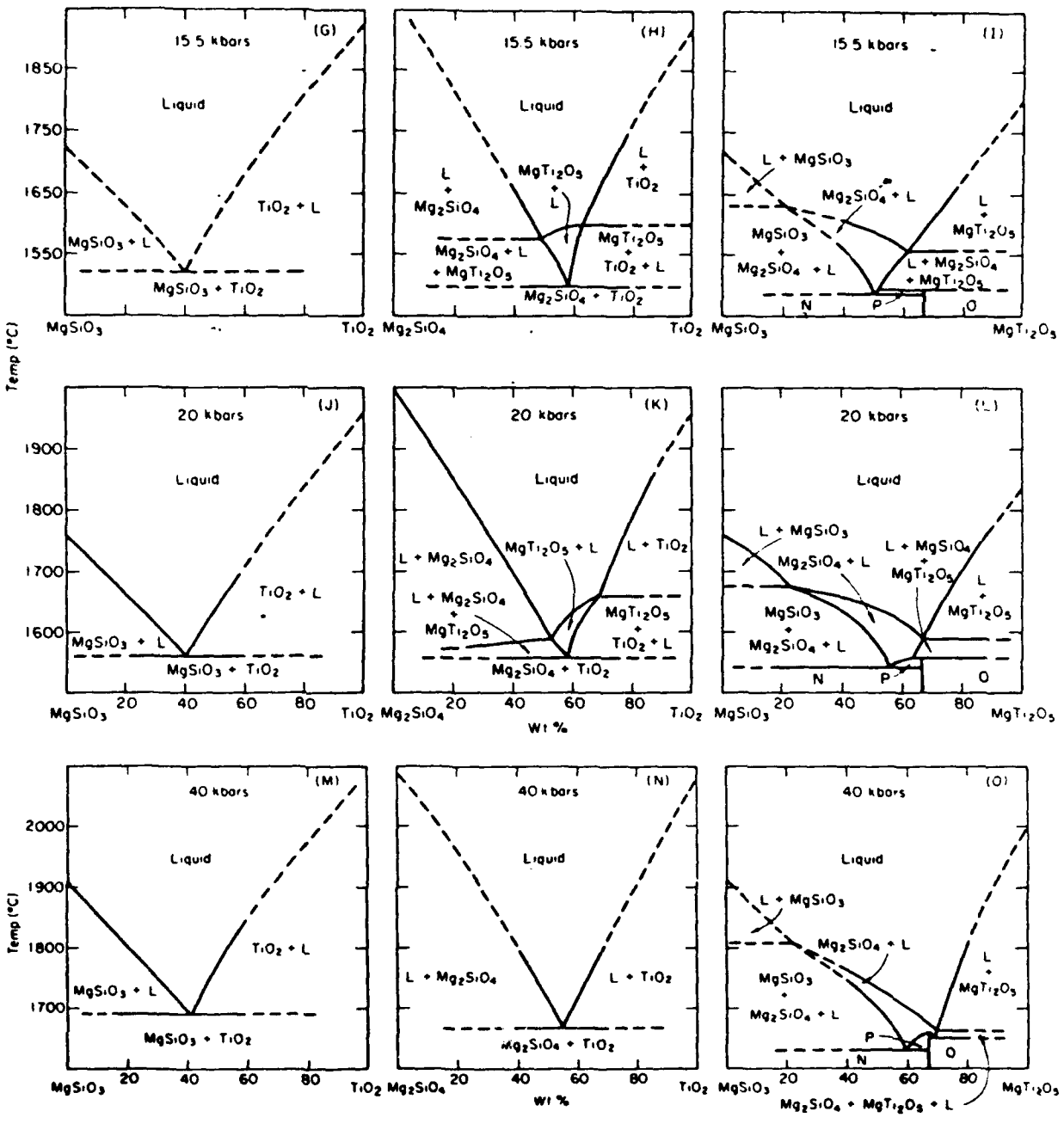

Figure 5-9.
(Continued)

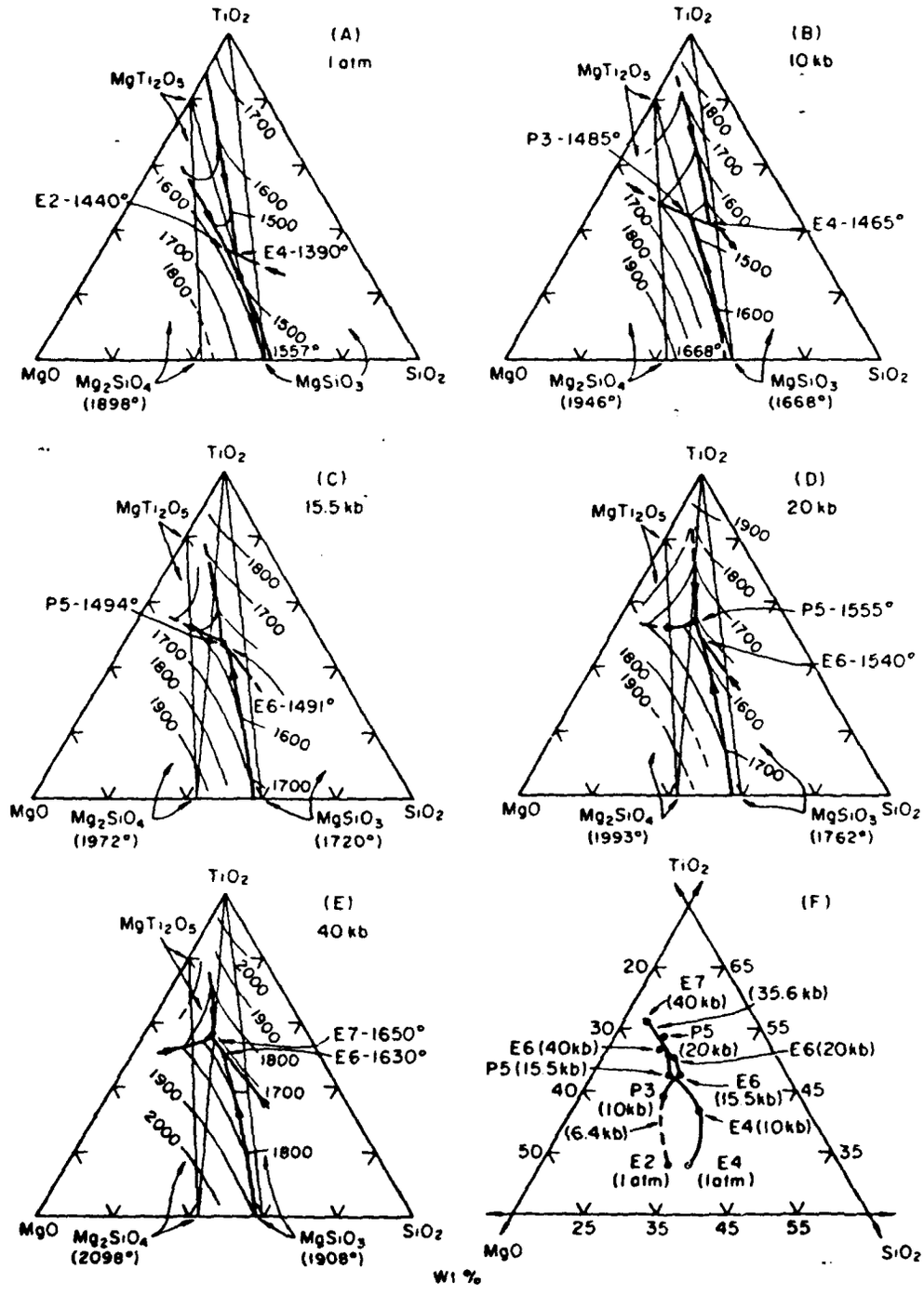

Figure 5-10.
System SiO_2-MgO
-TiO_2 p-T ternary
liquidus surfaces.[22]

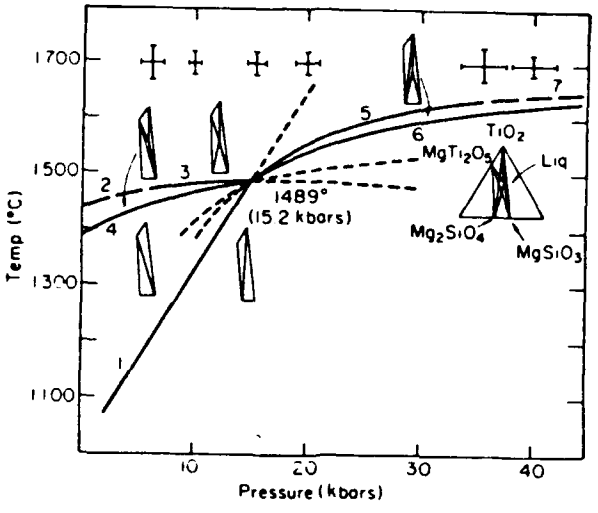

Figure 5-11.
System SiO_2-MgO-TiO_2
p-T univariant equilibria
for ternary reactions.[22]

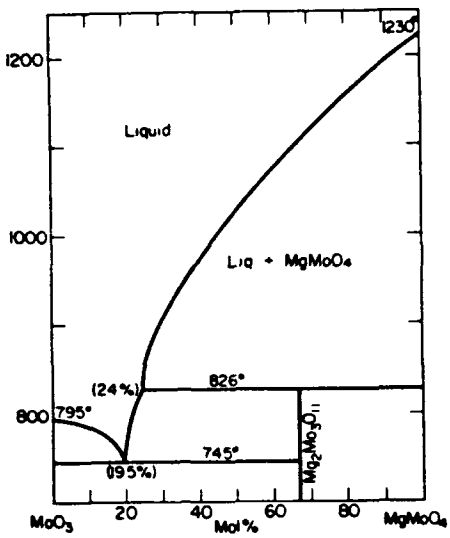

Figure 5-12.
System $MgMoO_4$-MoO_3.[23]

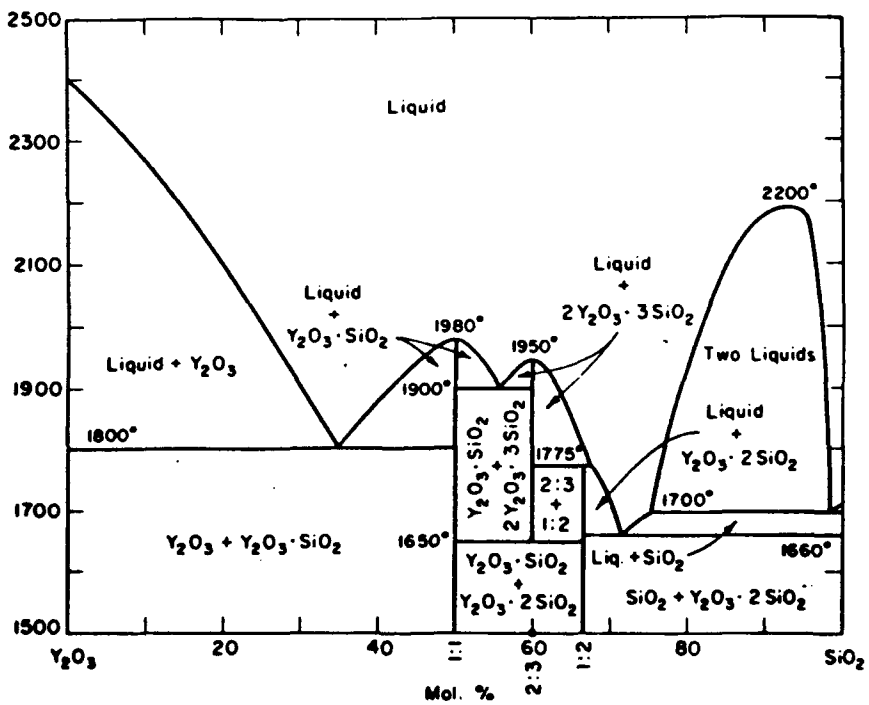

Figure 5-13.
System SiO_2-Y_2O_3.[24]

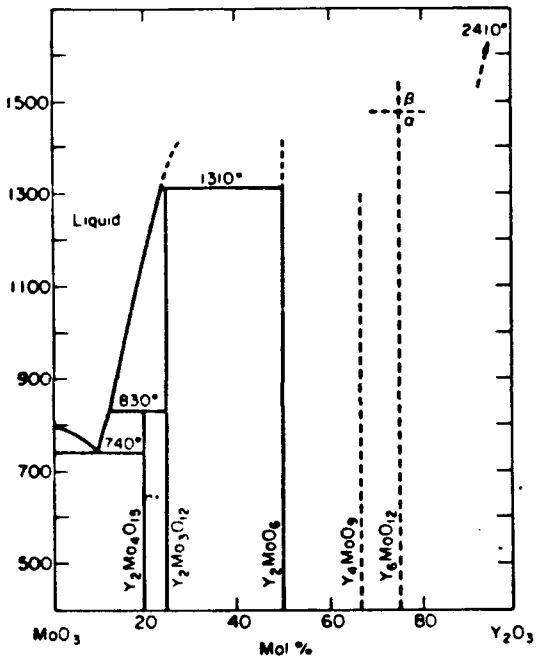

Figure 5-14.
System Y_2O_3-MoO_3.[25]

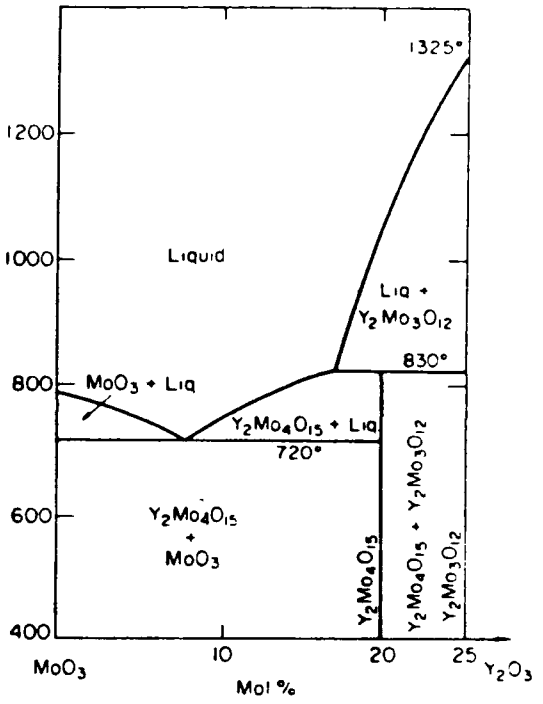

Figure 5-15.
System Y_2O_3-MoO_3.[26]

APPENDIX Q

J.-M. Martin, Th. Le Mogne and M.N. Gardos, "Friction of Alpha Silicon Carbide Under Oxygen Partial Pressure: High Resolution Analysis of Interface Films," Proc. Jap. Int. Tribilogy Conf., Oct. 29 – Nov. 1, 1990, Nagoya, Japan

Proceedings of Japan International Tribology Conference
Nagoya, 1990

FRICTION OF ALPHA SILICON CARBIDE UNDER OXYGEN PARTIAL PRESSURE : HIGH RESOLUTION ANALYSIS OF INTERFACE FILMS

Jean-Michel MARTIN*, Thierry. LE MOGNE*, Michael N. GARDOS**

Friction and wear of alpha silicon carbide against itself was experimentally investigated with a pin-on-flat machine installed in an Ultra High Vacuum (UHV) chamber equipped with surface analysis tools (XPS, AES). The influence of oxygen partial pressure was highlighted. Chnracterization of interface materials was carried out by surface analysis (AES) of wear scars and Energy Filtered Electron Microscopy (EFEM) on wear fragments. Friction under vacuum is dominated by grain attrition and partial amorphization of silicon carbide producing high friction values ($\mu \approx 0.8$). Friction under high partial pressure of oxygen is controlled by silicon oxide formation and some graphitization of wear products, which are mainly responsible for low friction values ($\mu < 0.1$). The data suggest that friction of alpha silicon carbide is tribochemically controlled and extremely dependent on reactive gases of the environment.

1. INTRODUCTION

The fundamentals of the surface chemistry-related tribological properties of alpha silicon carbide (α-SiC) are not clearly understood. The friction properties appear to depend strongly on the surface chemistry of silicon carbide and also, to a lesser extent, on the crystallographic orientation [1] [2]. The preferred crystallographic slip direction is the ⟨1120⟩ direction. The plastic deformation can occur by means of translational slip in the direction of closest atomic packing. The surface of α-SiC is further affected by temperature [3], because an increase in temperature under vacuum causes graphitization of the very top of surface and yields low friction values. The role of oxygen on α-SiC friction has been also studied [4] but as far as tribochemistry is concerned, there is no detailed analysis of the processes involved.

We have conducted experimental work at room temperature in order to emphasize the role of tribochemistry and therefore to minimize the role of any static interaction of the α-SiC surface with oxygen prior to friction. Surface tribochemistry of α-SiC was analyzed by scanning Auger Electron Spectroscopy (AES). High resolution analysis of third bodies, formed as wear fragments, was carried out in the Scanning Transmission Electron Microscope (STEM) equipped with Parallel Electron Energy Loss Spectroscopy (PEELS) and by High Resolution Transmission Electron Microscopy (HRTEM).

2. AES/XPS TRIBOMETER

We have developped an U.H.V. tribometer coupled with surface analysis instrumentation. The diagram of this apparatus is shown in figure 1.

In this tester a flat disc is rotated or a flat plate is oscillated against a hemispherical pin, in an ultrahigh vacuum (UHV) chamber. A vacuum environment of 10 nPa can be achieved. The test chamber can be filled (4) with different partial pressure of reactive gases for the tribo-tests and pumped down for surface analysis. The purity of the gas can be accurately controlled with a residual gas analyzer (11). XPS data acquisition and analysis are controlled by a microcomputer. An electron gun (16) with a probe of 200 nm diameter at 10 KV and 0.5 nA current permits both low magnification SEM, with the electron detector (15) during or after the friction test, (with video recording for image processing) and Auger electron spectroscopy (AES) with the use of the electron spectrometer (17). An important feature is that both the flat and the pin

* Ecole Centrale de Lyon, Laboratoire de Technologie des Surfaces, URA CNRS 855, 36 avenue Guy de Collongue, B.P. 163, 69131 Ecully Cedex, France.
** Hughes Aircraft Company, Electro Optical and Data Systems Group, PO Box 902, Bldg E1, MS F 150, El Segundo, Ca 90245, U.S.A.

FRICTION OF ALPHA SILICON CARBIDE UNDER OXYGEN PARTIAL PRESSURE : HIGH RESOLUTION ANALYSIS OF INTERFACE FILMS

J.M. MARTIN, T. LE MOGNE, M.N. GARDOS

can be imaged and analyzed, because the pin can be lifted off and turned around for periodic analysis of its wear scar.

The entire system (pin and disc) can be first translated into a preparatory chamber for vacuum evaporated layers (13, 14), ion etching, annealing or heating with a reactive gas. Before analysis and tribotesting, a specimen can be cleaned by ion etching (10) or annealed at a given temperature (12) and then back-transferred into the test chamber, analyzed by X-ray Photoelectron Spectroscopy (XPS) (19), tribo-tested and periodically analyzed in the wear scar with the scanning Auger spectrometer (SAM). The chamber is equipped with a fast entry lock (9) and a transfer mechanism, so that specimens can be changed without breaking UHV conditions in the main test chamber. Both pin and plate can be changed with this system. Another feature is the computerized data logging system, which permits the recording of the friction coefficient under different tribological conditions.

The test consisted of alternately oscillating the hemispherical pin (R = 4 mm) for 160 passes (length of the stroke = 3 mm), at an average sliding speed of 0.2 mm/s, under a normal load of 2 N. These conditions correspond to a maximum Hertzian contact pressure of 1 GPa and a contact flash temperature of 0.1 °C. Two friction tests are described and dicussed here in detail. The first experiment was carried out under UHV (10 nPa). AES analyses were performed at the end of this test, inside and outside of the wear scar. The second experiment was carried out with an oxygen partial pressure of 50 Pa in the chamber, with the same specimens (by slightly turning the pin and displacing the flat to present fresh surfaces). Thus the results can be compared.

3. MATERIALS AND SPECIMEN PREPARATION

The flat was a single crystal of α-SiC (SOHIO) grown by the Acheson process and the pin was sintered polycrystalline α-SiC (HEXOLOY SA) containing mainly boron carbide as a sintering aid. The aim of the preparation was mainly to eliminate oxygen and free carbon species from the surfaces. After polishing with diamond paste and cleaning, the specimens were placed in the UHV chamber and both pin and flat were subjected to alternate argon ion etching and annealing to obtain the silicon-carbon elemental composition before the friction test. Annealing at temperatures above 900 K is known to graphitize the very top of the surface [5]. Therefore the annealing temperature was held to 700 K. The AES spectrum (figure 2a) on the flat surface indicates a SiC composition with a carbon Auger lineshape characteristic of a carbide and only a slight oxygen peak ; the relative excess of carbon compared to silicon can be attributed to the existence of a carbon-rich surface [6]. The preparation of the pin was carried out in the same way, the secondary electron image shows black spots, the AES spectra indicates a boron and nitrogen composition, but the AES spectrum obtained in the scanning mode shows that stoichiometric silicon carbide is the main constituent of the surface. No attempt was made to check the crystallography of the surface, although it is known that argon sputtering may disorder the structure of silicon carbide but on a very low thickness scale. [5].

4. RESULTS

The evolution and magnitude of the friction coefficients are presented in figure 2. The SEM micrographs of the pin wear scars at the end of the tests are also shown in figure 2. The results mainly show :
- that friction under UHV is high ($\mu \approx 0.8$),
- that the presence of 50 Pa oxygen in the chamber rapidly leads to a drastic decrease of the friction coefficient to values below 0.1,
- that the wear volume on the SiC pin is higher in oxygen than in vacuum,
- that the worn surface is smoother under oxygen partial pressure than in vacuum,
- that under UHV, the SiC flat is severely damaged and fractured with possible material being transferred from the pin,
- that under O_2, an additional 0.1 µm thick layer is present , in the wear scar of the flat, with a lot of "rolling pins" lying perpendicularly to the direction of sliding.

From this set of data, it already appears that the wear behavior under oxygen is tribochemically controlled.

AES spectra obtained inside and outside of the wear scars at the end of the tests are presented in figure 3. It can be stated:
- that under UHV (figure 3b), the SiC stoichiometry is roughly preserved but there is a slight oxygen contamination on the worn surfaces. The disappearance of the argon AES peak indicates gross changes of the SiC surface under sliding. Unfortunately, the exact chemical form of carbon in the wear scar was difficult to determine using the carbon AES lineshape,
- that under 50 Pa oxygen (figure 3c, 3d), in the wear scar of the flat, silicon is preferentially bound to oxygen, but it is

FRICTION OF ALPHA SILICON CARBIDE UNDER OXYGEN PARTIAL PRESSURE : HIGH RESOLUTION ANALYSIS OF INTERFACE FILMS

J.M. MARTIN, T. LE MOGNE, M.N. GARDOS

interesting to note that the carbon signal has disappeared. Outside the track, the argon peak is always visible and only a slight oxidation takes place, in agreement with data from the literature [6].

The TEM examination of third bodies were carried out by Energy Filtered Transmission Electron Microscopy (EFEM). Wear fragments were collected at the end of the test, after breaking vacuum. Typical features are presented in figures 4, 5. It is shown :

- that under UHV, the wear debris are composed of collapsed and compacted spheroidal grains, with sizes lying in the 10 nm-100 nm range. From an electron diffraction study, we found that these grains had no preferential orientation. Each grain is found to be composed of a silicon carbide crystalline core surrounded by a complex shell and interface between grains. The fully amorphous character of silicon carbide in this shell can be demonstrated by electron diffraction and high resolution transmission electron imaging of (100) lattice fringes (figure 4a) and, even more accurately, by the damping of EXELFS modulations [7] (Extented Electron Energy Loss Fine Structures) in the carbon K edge spectrum, (figures 5b, 5c) obtained with the electron probe focused in the shell (STEM operating mode). The same EELS carbon K edge shows a very weak contribution of the $1s/\pi^*$ transition (anti-bonding π orbital) characteristic of the carbon sp_2 hybridization (double bonding) [8]. It appears that some free carbon species are mixed with disordered silicon carbide in the encapsulating shell. This is well demonstrated by the energy filtered image obtained on the π/π^* transition at 6 eV energy loss, showing the π orbital distribution around the crystalline SiC core. No oxygen peak was detected by the EELS technique (i.e., the concentration is less than 1 atomic percent),
- that under 50 Pa oxygen, bulk silicon oxide is formed as "rolling pins". Carbide is no longer detected, but pregraphitic organization of carbon seems to take place inside and at the periphery of amorphous silicon oxide wear debris. In fact, the fine structure of the 1s level excitation of carbon in EELS (figure 5d) shows the existence of a short range order in carbon planes ; the high resolution image of 002 lattice fringes of graphitic carbon (figure 4b) confirms this fact as well. Surprisingly, carbon was never detected by AES analysis in the wear scar. This is attributed to the fact that carbon is preferentially located in the wear fragments, as produced by the friction process. At the same time, the very unstable character of this silicon oxide under the electron beam suggests that oxygen might be non stoichiometric in the material.

5. DISCUSSION

5.1. Friction of SiC/SiC under UHV

The high value of the friction coefficient ($\mu \approx 0.8$) is not a surprise and is in agreement with previous data reported in the literature [1]. Actually, UHV-cleaned SiC surfaces produce high adhesion mainly because of the presence of dangling bonds at the very surface ; consequently and as is well known, the presence of a tangential force acting on a highly loaded contact area is a cause of fracturing in a Hertzian contact [9]. For example, in our case ($\mu \approx 0.8$), the corresponding maximum tensile strength has a calculated value of 800 MPa, which largely exceeds the fracture initiation threshold of the silicon carbide flat (approximately 500 MPa). Moreover the debris produced lead to the development of abrasive wear concomitant with heavy plastic deformation and transfer, so that a third body quickly takes place in the contact. In the steady state regime, the corresponding interface film shear strength has a value of 700 MPa (deduced from the measurement of the pin wear scar), thus continuing the undesirable action, viz tensile cracking, so that the wear of the SiC flat is unacceptably high in these conditions.

From the tribochemical point of view, the wear mechanism extends far beyond simple fracturing of the substrate. The third bodies formed are sheared, compacted at the interface and reduced to very small, sub-micronic grains. Because there is no preferential low energy shear planes in the α-SiC crystal structure, friction-induced attrition is accompanied by amorphization and also, to a lesser extent, by some transformation into substoichiometric silicon carbide and free carbon species. Our EXELFS data show that UHV friction-modified silicon carbide is fully amorphous on the atomic scale ; at the same time, free carbon itself does not exhibit long range order. So the interface material may be mainly described as an arrangment of distorted [SiC_4] tetrahedra bound to each other in a disordered structure. The existence of some oxycarbide chemical bonding between SiC and carbon is not completely excluded, even though the concentration of oxygen if very low.

It is believed that friction energy is mainly dissipated in the deformation of this high shear strength amorphous SiC structure, and that the absence of low energy crystallographic shear planes can explain the high value of the friction coefficient and the detrimental effect on the crystalline substratum.

5.2. Friction of SiC/SiC under oxygen

It is worthy to note that, at the beginning of SiC friction under 50 PaO_2, the friction coefficient has a high value, similar to the UHV conditions (μ = 0.8). Actually, the AES spectrum (figure 3c) obtained outside the wear scar, at the end of the test, confirms that molecular oxygen practically does not react with the cleaned SiC surface, at room temperature. Therefore it appears that physically adsorbed oxygen does not reduce the adhesion of silicon carbide ; moreover, in some cases, we noticed a slight friction increase due to the presence of oxygen. Perhaps an explanation is that adsorbed oxygen leads to an excitation of outer shell electrons levels of the SiC surface (transition of bonding to anti-bonding orbitals), so that the reactivity of the surface is increased. Anyway, after a few cycles the friction coefficient rapidly falls to a very low value (μ < 0.1). The calculated interface shear strength is as low as 3 MPa. The accompanying high wear of the pin immediately indicates that corrosive oxidative wear has occured. The analyses showed that carbon in the carbide form has disappeared and that the interface material consisted of a complex mixture of unstable silicon oxide species and pseudo graphitic carbon (sp_2 hybridization). As a result, the triboxidation of the SiC pin produce a lubricating film, the friction force and therefore fracturing of the SiC flat are reduced by virtue of the low shear strength of this film. The origin of the lubricating properties of the interface film is more questionnable.

When heated to 1500 K under vacuum, it is known had the SiC surface graphitizes by the collapse of the carbon planes lying perpendicular to the c-axis of the crystallographic unit cell. The friction on this heat-treated surface is low [3] due to weak Van der Waals energy interaction between carbon planes [10]. It is suggested that friction- induced oxidation of silicon carbide at such a low temperature also leads to a graphitic organization by a similar process, because carbon cannot escape as carbon oxide in the chamber at this low temperature. Although the presence of silicon oxide "rolling pins" may influence the friction process, the graphitic carbon, associated with these rolling pins structure, is thought to be mainly responsible for the very low friction value. The presence of excess oxygen can further enhance this trend either by physisorption on the carbon planes or by intercalation between them. Actually, the lubrication of graphite by oxygen has recently been recognized [11].

6. CONCLUSION

The tribochemistry of alpha silicon carbide was investigated with a pin-on-flat friction and wear tester installed in an UHV chamber equipped with surface analytical instrumentation. Special attention was paid to the role of a high oxygen partial pressure on the generation of interface products and their role on friction and wear.

The main results are :
- under high vacuum (10^{-8} Pa), α-SiC friction is dominated by high adhesion and by fracture, compaction and attrition of spheroidal grains in the interface region. No preferential shear planes appear to form but amorphization of silicon carbide takes place mainly at the edge of grains. Consequently, friction is high (μ = 0.8) and wear is predominant on the flat SiC surface.
- under 50 Pa O_2 partial pressure, silicon carbide quickly oxidizes at the interface only, producing silicon oxide as rolling pins and some graphitization of residual carbon from the carbide. Pre-graphitic components, having low energy shear planes in the presence of oxygen, are thought to be mainly responsible for the low shear strength of the interface film. Consequently friction is low (μ < 0.1) and corrosive wear is predominant on the SiC pin surface.

ACKNOWLEDGMENTS

This work was performed under a subcontract from Hughes Aircraft Company, P.O. n° S9-507874-SRW as a part of the "Determination of Tribological Fundamentals of Solid Lubricated Ceramics" program DARPA order n° 5177, AFWAL contract n° F33615-85-C-5087 with B.D. McConnell acting as the AFWAL Project Manager.

REFERENCES

[1] K. Miyoshi, and D. Buckley : ASLE/ASME Lubrication Conference, Kansas City, October 3-5, (1977).

FRICTION OF ALPHA SILICON CARBIDE UNDER OXYGEN PARTIAL PRESSURE : HIGH RESOLUTION ANALYSIS OF INTERFACE FILMS

J.M. MARTIN, T. LE MOGNE, M.N. GARDOS

[2] K. Miyoshi, and D. Buckley : 33rd ASLE Annual Meeting, Dearborn Michigan, April 17-20, (1978).
[3] K. Miyoshi, and D. Buckley : ASLE/ASME Lubrication Conference, New Orleans Louisiana, October 5-7, (1981).
[4] K. Miyoshi, and D. Buckley : NASA TP, (1978) 1265.
[5] J.J. Bellina and M.V. Zeller : Applied Surface Science, 25 (1986) 380-390.
[6] L. Muehlhoff and al : J. Appl. Phys. 60, (7), (1986) 2558-2563.
[7] J.L. Mansot, J.M. Martin and al. Physica B, 159 (1989), 560-561.
[8] R.D. Leapman, P.L. Fejes, J. Silcox :, Physical Review B, Vol 28, n° 5 (1983) 2361-2372.
[9] M.N. Gardos : Lubrication Engineering, May 1988 401-407
[10] F.P. Bowden, D. Tabor : Part 2, 11e edition, Oxford, (1964).
[11] E. Zaidi and al., Applied Surface Science, (1989), 40, 103-114.

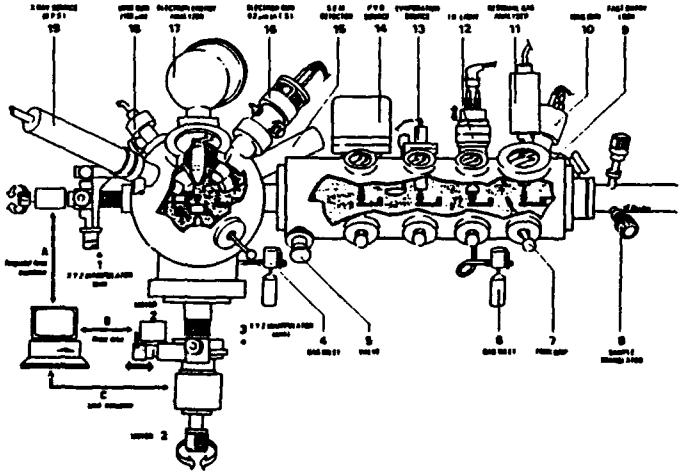

Fig.1 Diagram of the UHV analytical tribometer.

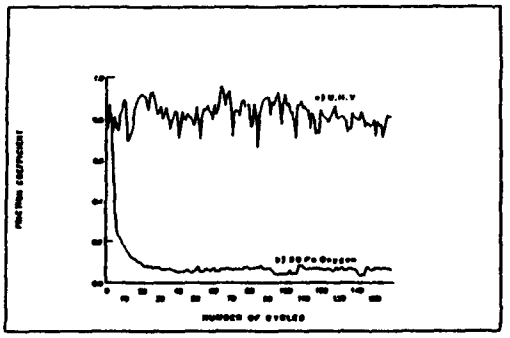

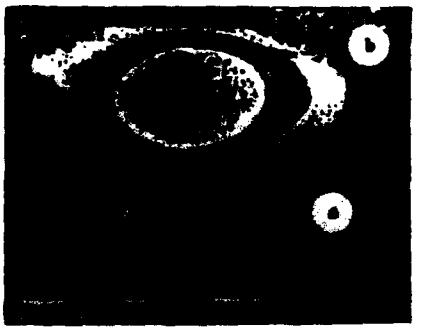

Fig.2 Evolution of the friction coefficient against the number of cycles and SEM micrographs of the pin wear scars.
a) Under UHV (10^{-8} Pa).
b) Under oxygen partial pressure (50 Pa).

FRICTION OF ALPHA SILICON CARBIDE UNDER OXYGEN PARTIAL PRESSURE :
HIGH RESOLUTION ANALYSIS OF INTERFACE FILMS

J.M. MARTIN, T. LE MOGNE, M.N. GARDOS

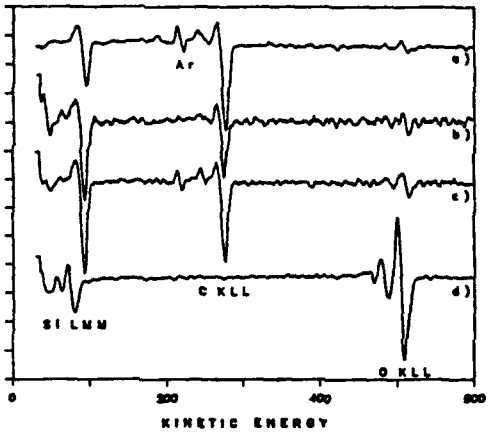

Fig.3 AES spectra obtained on the SiC flat surface.
a) Before the friction tests.
b) Inside the wear scar, (UHV).
c) Outside the wear scar (50 Pa O_2).
d) Inside the wear scar (50 Pa O_2).

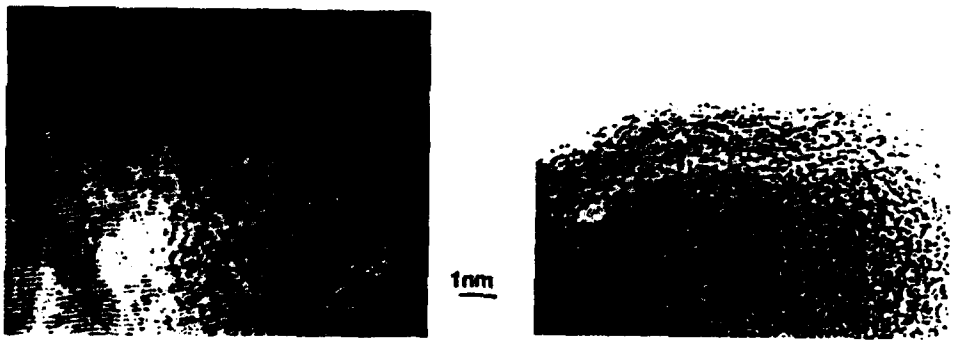

Fig.4 HRTEM micrographs of αSiC wear fragments.
a) (100) lattice fringes image of the interface zone between crystalline and amorphous SiC grain (UHV test).
b) Amorphous silicon oxide surrounded by pseudo-graphitic carbon (50 Pa O_2 test).

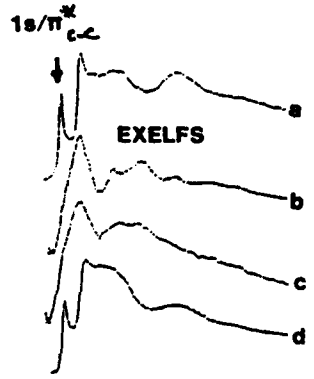

Fig.5 EELS carbon K edge at 284 eV loss for different chemical states :
a) Graphite.
b) α silicon carbide (note the well defined EXELFS modulations).
c) Friction-modified SiC under vacuum (note the damped modulations).
d) Friction-modified SiC under 50 Pa oxygen, the $1s/\pi^*$ C-C indicates the presence of free carbon species.

APPENDIX R

J.-M. Martin, and Th. Le Mogne, selected Monthly Reports on α-SiC, ranging from Feb. 1988 to June 1988, Ecole Centrale de Lyon/SORETRIB, Lyon, France, Hughes P.O. S9507874-SRW

SOCIÉTÉ DE RECHERCHE EN TRIBOLOGIE

SORETRIB

36, rue Guy de Collongue
69130 ÉCULLY
Tél. 78.33.02.17

Dr. Mike GARDOS
HUGHES AIRCRAFT CO
ELECTRO OPTICAL AND DATA SYSTEMS GROUP
2000 East El Segundo Boulevard
Po Box 902
El Segundo
U.S.A.

Écully, le February 16 th 1988

Dear Mike,

We have been very pleased to read your Jan. 22 letter. We had some understanding difficulties between our respective administrative departments but now every problem has been solved.

We are very interested in the information you give about the samples we received in October. When we started the work, we had not all these details, so we decided to begin by the ESCA characterization of the samples.

You must have already received our results about Boron Nitride, which includes a high quantity of Carbon in a chemical state near from graphite.

Before receiving your last letter, we continued the work with the analysis of the other samples : they are single crystal αSiC, SiC (ESK), Si_3N_4 Norton (NC 132), Si_3N_4 LSRH Ceralloy.

You will find below the results of these latest analysis.

Single crystal αSiC

We had two single crystal samples : ESK and Sohio. Both of them present an important layout of SiO_2 on the surface. We try to eliminate this layout by ionic etching. On ESK sample, we cannot remove the layout (Figure 1). On Sohio sample, we make an etching up to 1000 Å to make SiO_2 disappear (Figure 2).

After that, we have :

- Carbon binding energy : 282.9 eV
- Silicon binding energy : 99.8 eV
- Concentration ratio C/Si : 1.04

SiC ESK

On this sample, we detect Silicon, Carbon, and also Oxygen and Nitrogen, as well as Calcium and Sodium traces. After ionic etching up to about 500 Å (Figure 3), we detect the same elements :

	Binding energy	% at.	Nature
C1s	283.1 284.6	32.3 19.6	Carbide Graphite
O1s	532.3 534.5	12.7 1.6	
N1s	397.9	2.6	Nitride
Si 2p	100 101.8	26.3 5	Carbide Nitride

We do not performed precise measure on Calcium and Sodium traces, which may give the explanation of the important quantity of Oxygen (Oxygen presence can not be linked to any other element).

An observation on secondary electrons shows several zones with different aspects which sizes are about some micrometers. Auger analysis inside these zones shows that they are composed of carbon for the essential.

Si_3N_4 Norton (NC 132)

We detect on this sample Carbon, Nitrogen, Oxygen, Silicon. Sodium and Calcium traces are present on the surface. They will stay after ionic etching up to about 500 Å (Figure 4). For these analysis, we use $K\alpha_{1,2}$ X-Ray of Magnesium as excitation source. In these conditions, the most intense peak for Magnesium comes from Mg 2s and is near the Si 2p peak,

parasite due to $K\alpha_{3,4}$ X-Ray of Magnesium. For these sample, the use of the $K\alpha_{1,2}$ X-Ray of Aluminium would be more adapted.

After ionic etching, the following results are obtained for the most intense photoelectron peaks :

	Binding energy*	% at.	Nature
C1s	284.6	13	Graphite
O1s	532.8	13	
N1s	398.1	34.5	Nitride
Si 2p	102.0	37.5	Nitride

* after correction of charge effect

Si_3N_4 LSRH Ceralloy

On this sample, we observe the non polished face. After ionic etching up to about 500 Å (Figure 5), we obtain the following results for the most meaningful elements :

	Binding energy*	% at.	Nature
C1s	284.6 286.6	47.8 5.4	Graphite C-O
O1s	532.9	11.7	
N1s	398.5	17.2	Nitride
Si 2p	102.1	17.4	Nitride

* after correction of charge effect

We notice a high quantity of carbon in a chemical state near from graphite. The quantity of oxygen is still very important. We also detect the presence of Yttrium but the accuracy in the measure does not allow us to know its quantity and its chemical state.

All these experiments and measures permit us a deeper knowledge of most of the samples we received from you. We will continue the work by the tribotests in vacuum.

Best regards.

Th. LE MOGNE
H. MONTES
J.M. MARTIN

sic110.spc 4/12/1986 SiC ESK monocristal décapé 150 mn
Source Mg Mode CAE Energie d'analyse 50 Nombre de Cycle(s) 3

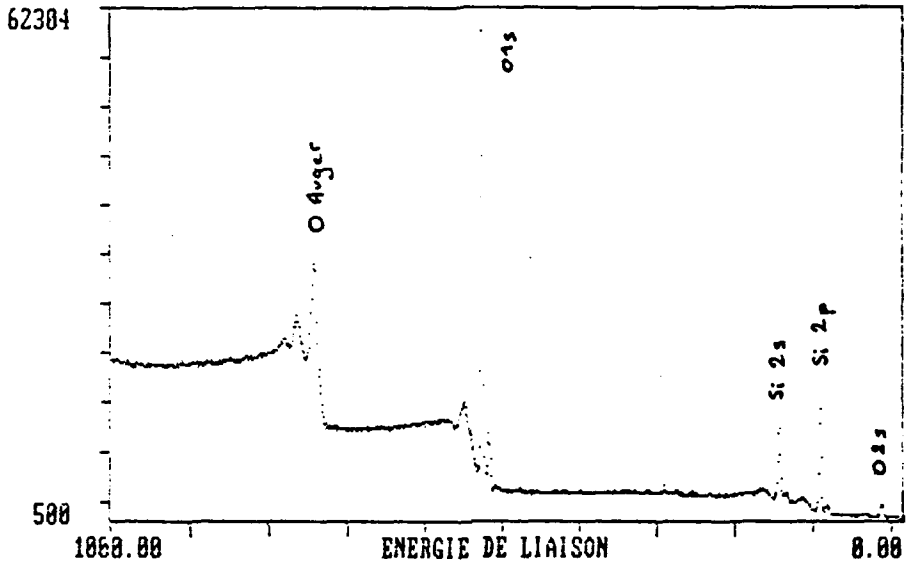

Résolution	:	1.00 eV
Nombre de points	:	1000
Vitesse de Balayage	:	3.00 eV/s
Energie de la source	:	10.00
Courant de la source	:	20
Tension Channeltron	:	3000
Fente	:	4.0
Nom du Fichier	:	sic110.spc

Figure 1

sic75.spc 2/12/1986 SiC Sohio 125 mn etching
Source Mg Mode CAE Energie d'analyse 50 Nombre de Cycle(s) 5

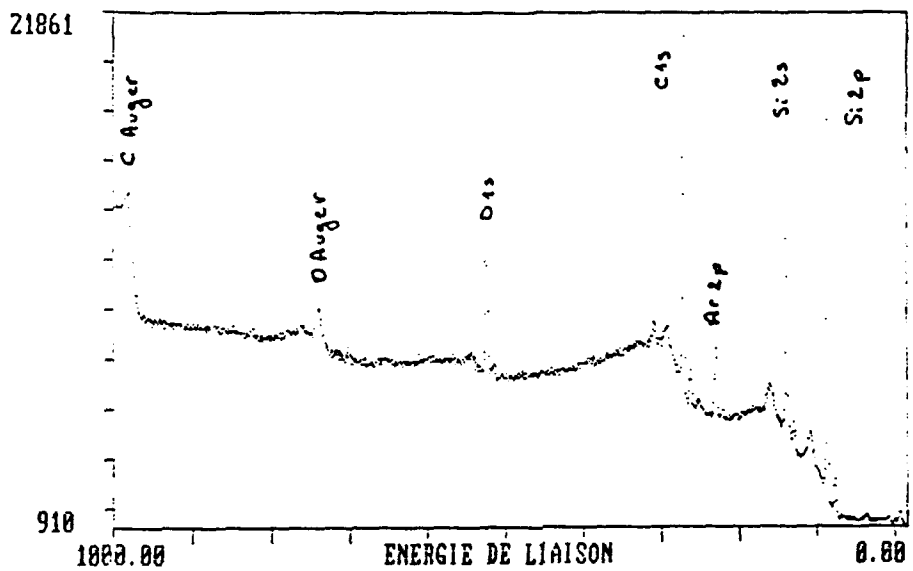

Résolution	:	1.00 eV
Nombre de points	:	1000
Vitesse de Balayage	:	3.00 eV/s
Energie de la source	:	10.00
Courant de la source	:	20
Tension Channeltron	:	3000
Fente	:	4.0
Nom du Fichier	:	sic75.spc

Figure 2

R-6

sic34.spc 25/11/1986 SiC ESK 68 mn etching
Source Mg Mode CAE Energie d'analyse 50 Nombre de Cycle(s) 2

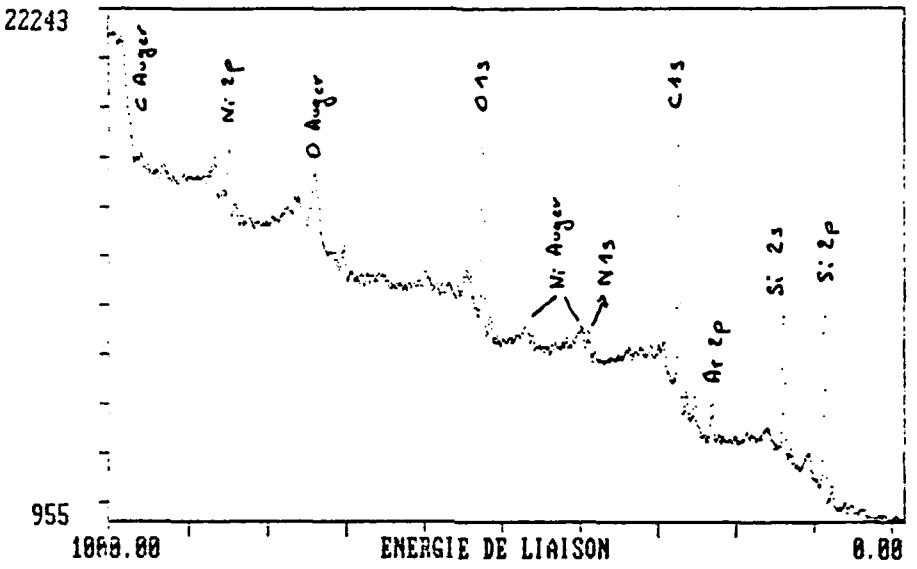

Résolution	:	1.00 eV
Nombre de points	:	1000
Vitesse de Balayage	:	3.00 eV/s
Energie de la source	:	10.00
Courant de la source	:	20
Tension Channeltron	:	3000
Fente	:	4.0
Nom du Fichier	:	sic34.spc

The presence of Nickel originates from the sample holder.

Figure 3

sic163.spc 14/12/1987 Si3N4 Norton 188 mn etching
Source Mg Mode CAE Energie d'analyse 50 Nombre de Cycle(s) 5

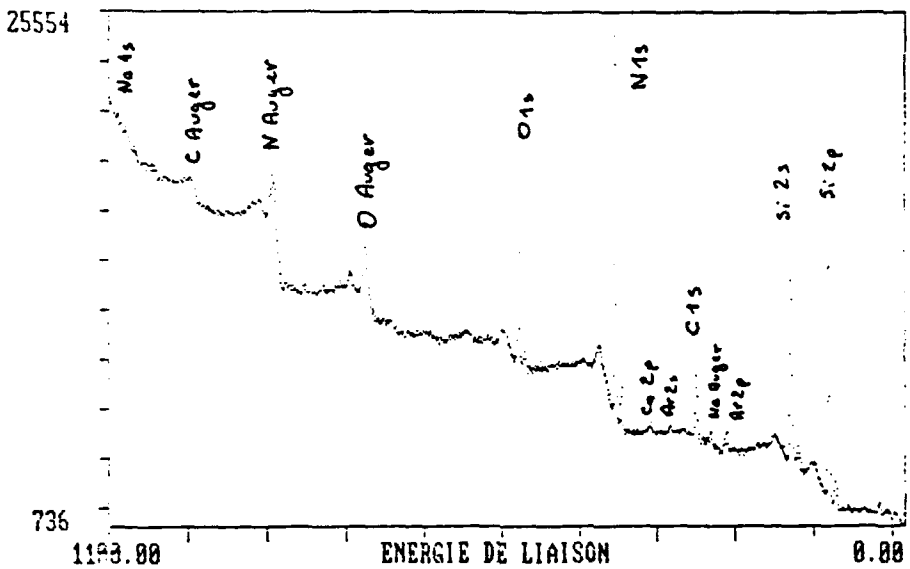

Résolution	:	1.00 eV
Nombre de points	:	1100
Vitesse de Balayage	:	3.00 eV/s
Energie de la source	:	10.00
Courant de la source	:	20
Tension Channeltron	:	3000
Fente	:	4.0
Nom du Fichier	:	sic163.spc

Figure 4

sic199.epc 16/12/1987 Si3N4 Caralloy 85 mn etching
Source Mg Mode CAE Energie d'analyse 50 Nombre de Cycle(s) 5

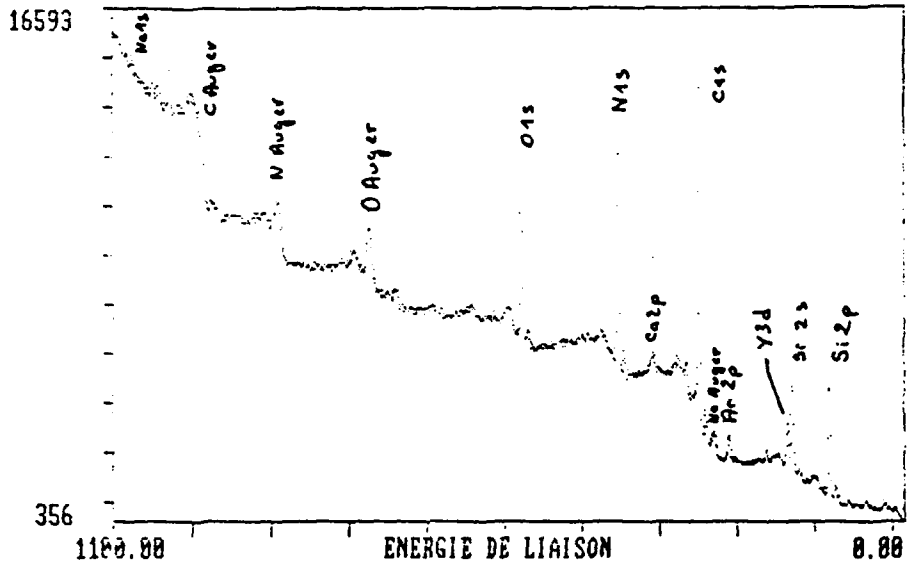

Résolution	:	1.00 eV
Nombre de points	:	1100
Vitesse de Balayage	:	3.00 eV/s
Energie de la source	:	10.00
Courant de la source	:	20
Tension Channeltron	:	3000
Fente	:	4.0
Nom du Fichier	:	sic199.spc

Figure 5

SOCIÉTÉ DE RECHERCHE EN TRIBOLOGIE

SORETRIB

36, rue Guy de Collongue
69130 ÉCULLY
Tél. 78.33.02.17

Dr. Mike GARDOS
HUGHES AIRCRAFT CO ELECTRO OPTICAL
AND DATA SYSTEMS GROUP
2000 East El Segundo Boulevard
Po Box 902 - El Segundo
U.S.A.

Écully, le March 21, 1988

Dear Mike

Below is our progress report for February 1988.

Introduction

The first friction experiment coupled with analytical data has been carried out on a SiC/SiC combination, with our UHV tribotester, but in ambiant air in order to check our methodology.

Tribological conditions

The specimen used were :

- pin : SiC - HEXOLOY SA
- plate : α SiC - SOHIO

Specimen were previously polished with diamond paste in order to remove thick oxide layers. The AES spectrum of figure 1 corresponds to the SiC plate after 10 minutes etching. The oxide thickness was therefore estimated to 5 nm before sliding.

The friction conditions were :

- normal load : 2 N
- sliding speed : $0{,}21.10^{-3}$ m/s
- length of the stroke : $2{,}40.10^{-3}$ m
- number of passages : 160
- temperature : 20°C

Friction results

First of all, there was no major problem associated with the use of our tribotester for the supplied specimen.

The evolution of the friction coefficient against the number of passages is presented in figure 2, and shows an average value of 0,3 all the test long. The optical micrograph of the wear scar on the plate is also shown in figure 2 : no severe damage is observed, no fracture has appeared in the α SiC cristal, but a glassy and transparent surface film is present in some areas, partially covering the original polishing grooves. Indoubtly the wear regime was tribochemicaly controlled in these conditions.

Analytical data

It was decided that the glassy surface film that was formed was of major interest to explain the situation, and some fragments of it were extracted from the worn surface by a scratching technique, under an optical microscope. The fragments were deposited on a holey carbon layer and examined in the analytical STEM with the EELS technique.

An electron image of the wear fragment film is shown in figure 3 with the corresponding electron diffraction pattern, the EELS analysis is shown in figure 4.

Clearly amorphous silicon oxide is formed, no SiC cristallites were observed. Therefore the wear mechanism is governed by the action of oxygen from air and the good shearing properties of triboreacted amorphous SiO_2 (or hydrated SiO_2).

Next investigations will include :
- friction under UHV,
- friction under nitrogen,
- friction under oxygen partial pressure.

T. LE MOGNE
H. MONTES
J.M. MARTIN

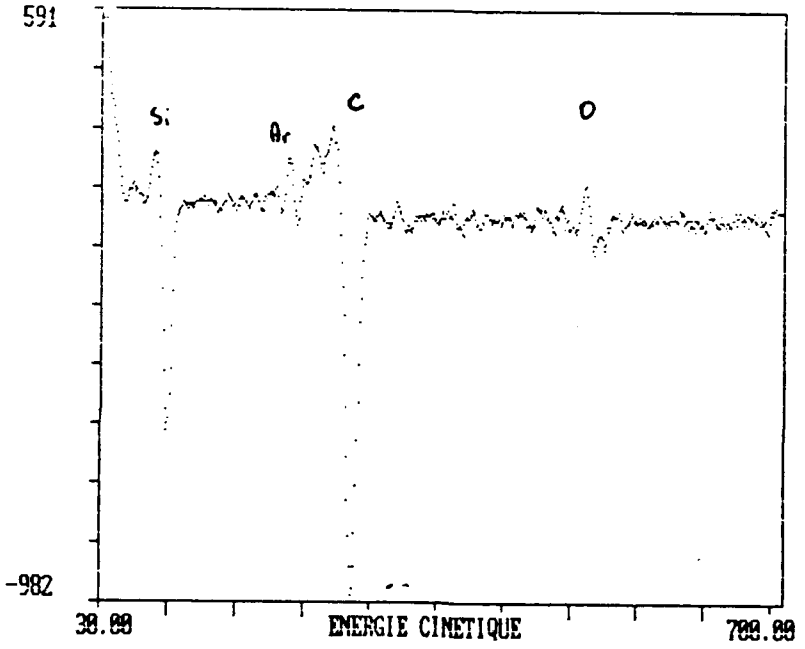

Figure 1 : AES spectrum of The α SiC plate, before sliding and after 10 minutes etching with argon ions. The shape of the carbon Auger peak indicates a carbide from.

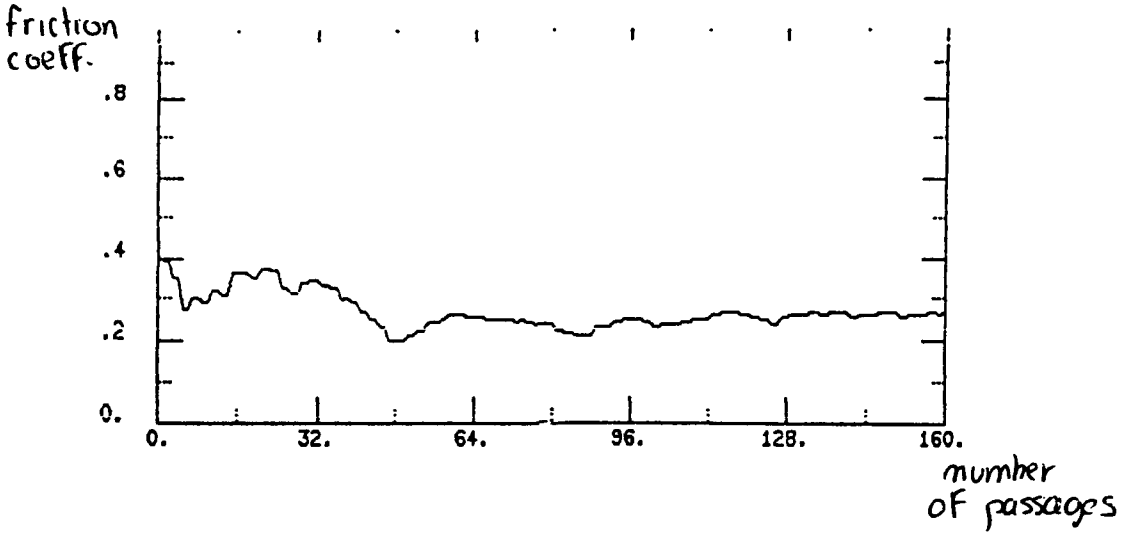

Figure 2 :

top : evolution of the friction coefficient versus the number of passages of the pin on the plate (SiC/SiC in air).

bottom : optical micrograph of the extremity of the wear scar. Note the glassy surface film covering the polishing scratches.

R-13

Figure 3 : TEM micrograph of a fragment of the glassy surface film as shown in the optical micrograph of figure 2.

R-4

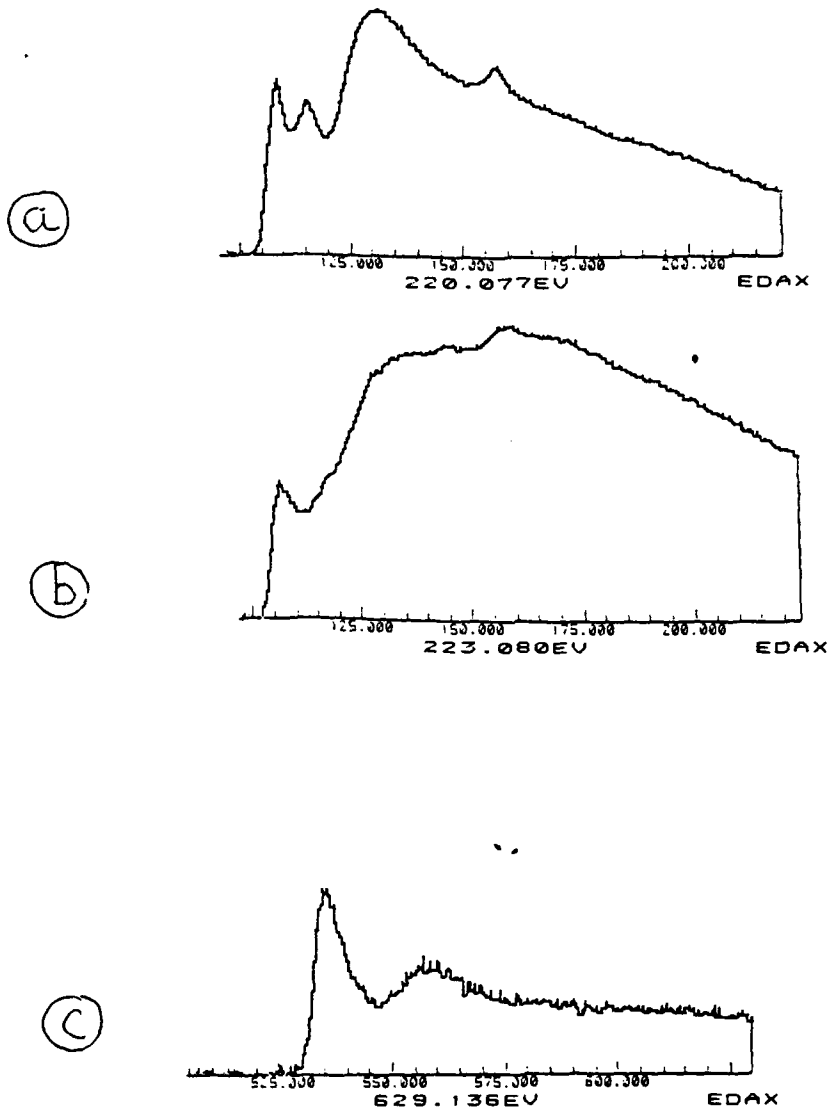

Figure 4 : SiL edges from EELS spectra of :
a) SiC/SiC in air (wear fragment)
b) α SiC monocristal (SOHIO)
The extra peak near 110 eV is characteristic of the Si-O bond.
c) O.K from EELS spectrum of SiC/SiC wear fragment, characteristic of SiO_2

SOCIÉTÉ DE RECHERCHE EN TRIBOLOGIE

SORETRIB

36, rue Guy de Collongue
69130 ÉCULLY
Tél. 78.33.02.17

Écully, le April 1988

Dr. Michael GARDOS
Senior Scientist
Materials Technology Laboratory
Technology Support Division
Electro-optical & Data Systems Group
Hughes Aircraft Company
P.O. Box 902
Bldg. E1, MS F150
El Segundo, CA 90245

Dear Mike,

FRICTION OF SiC/SiC SYSTEM UNDER UHV

Preparation of specimens

- αSiC(XTL SOHIO) plane

After polishing, specimens are introduced in the UHV chamber, and submitted to alternative ionic etching and annealing in order to recover a clean SiC surface before friction. The composition is checked by XPS (see spectra figure 1). The composition of the α SiC XTL surface is in this case (atomic %).

Si-C = 35 %
S-O = 2%
C-Si = 28%
C-C = 29%
C-O = 3%
O = 3%

The oxygen has not completely disappeared and the carbon is partly graphitic. This is due to the annealing at temperature superior to 900 K, as already noticed in the literature [1,2]. Therefore, before sliding, other ionic etching and annealing at a lower temperature are done and the AES spectra show that the carbon peak has decreased (see figure 2).

- Hexoloy SiC pin

The preparation of the pin is the same. The secondary electron image of the pin surface (see figure 3) shows black spots. The AES spectrum of these small areas shows the presence of nitrogen and boron, ingredients of the fabrication of the SiC specimen [3]. A spectrum of the whole area shows the presence of silicon carbide as the main constituent.

- Friction test

The tribological conditions are the same as for the friction test in the air (see report of february).

The evolution of the friction coefficient against the number of cycles (see figure 4) indicates a constant average value up to 0.8. The vacuum in the chamber is 2.10^{-9} mbar.

- Surface examination after UHV friction

The αSiC surface is severely scratched (see figure 5) and a lot of wear debris are produced. The AES spectrum (see figure 6) in the wear scar shows a Si enriched composition compared to the original one. A slight oxygen contamination is noticed on the worn surface.

An AES spectrum of the scar on the pin shows also the presence of oxygen. It is difficult to precise the chemical form of carbon . Unfortunately, XPS analysis in the wear scar are not possible, the X-ray source having a probe size of 8 mm diameter.

High resolution analysis of wear fragments

Wear debris are peaces of interphase material and their analysis give information on tribochemistry and related phenomena.

Classically, wear fragments are deposited on a holey carbon film, and investigated in the analytical transmission electron microscope (TEM) with Electron Energy Loss Spectroscopy (EELS).

First of all, the TEM bright field and dark field images in the low magnification mode show that wear debris are constituted of spheroïdal cristallites which diameters are found on the ten nanometers range (see figure 7). The corresponding electron diffraction is indexed as silicon

carbide but the rings are rather diffuse and this indicates some disorder in the material.

The EELS spectrum in the microprobe mode confirms the presence of SiC, practically no oxygen is visible, but the shoulder on the K-edge indicates that some carbon species are present (see figure 8).

At high magnification, (see figure 9) there is some evidence of a glassy interphase material between and around the SiC cristallites which seems interesting for analyse. Figure (8) shows the carbon K edges near 284 eV energy loss for αSiC (as a single crystal) and amorphous carbon (as evaporated film). The strong differences between the two spectra are attributed to :

(i) The difference in hybridization between the carbon atoms in the near edge structure (ELNES).

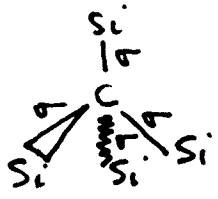

Tetragonal hybrid

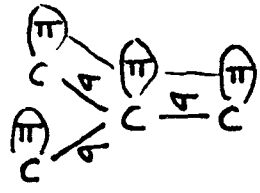

Trigonal hybrid

(ii) The difference in the local order in the extended electron energy loss fine structure (EXELFS). Strong interferences appear as sinusoidal modulations in the αSiC crystal.

By comparison with these standards, the shoulder in the carbon Kedge of wear debris is attributed to a $1s/\pi^*$ transition characteristic of the Sp^2 hybridization of carbon.

EELS analysis in the nanoprobe mode (probe size 4 nm) are performed in and between the two cristallites of figure (9), giving definitely evidence for a pre-graphitic organization between SiC cristallites. Another interesting feature in the carbon K-edge in the wear debris is the decrease of the EXELFS modulations suggesting a dissymmetry of the carbon site, (the reduction of EXELFS data is under investigation).

Discussion

As indicated in the litterature, SiC graphitizes at a temperature above 900K by the collapse of two Si-intercalated carbon layers [2]. Friction occurs at ambient temperature and calculated contact surtemperature is negligible. Therefore the result is very surprising and needs an explanation. It is suggested that C-Si bonds are broken by molecular shearing between two carbon layers and that Si atoms are either intercalated or migrate to the surface (see the AES spectrum with the Si enriched composition).

There is no evidence of anisotropy or preferential shearing planes in the interphase material, and the friction coefficient is elevated. Wear occurs first by fractures in the SiC plane and so develops an abrasive regime. As a conclusion, SiC is not a good candidate for UHV tribotesting at ambient temperature.

References

[1] Surface modification strategies for (100) 3 C-SiC. J.J. BELLINA Jr., J. FERRANTE, M.V. ZELLER, J. Vac. Sci. Technol., A4(3), Mai/Juin (1986).

[2] Tribological properties and surface chemistry of silicon carbide at temperatures to 1500°C, K. MIYOSHI, D.H. BUCKLEY, ASLE Trans., vol. 26, 1, 53-63.

[3] Multielement mapping al α-SiC by scanning Auger Microscopy, R.BROWNING, J.L. SMIALEK, N.S. JACOBSON, Adv. Ceram. Mat., vol. 2, n° 4 (1987).

Th. LE MOGNE H.MONTES J.M. MARTIN

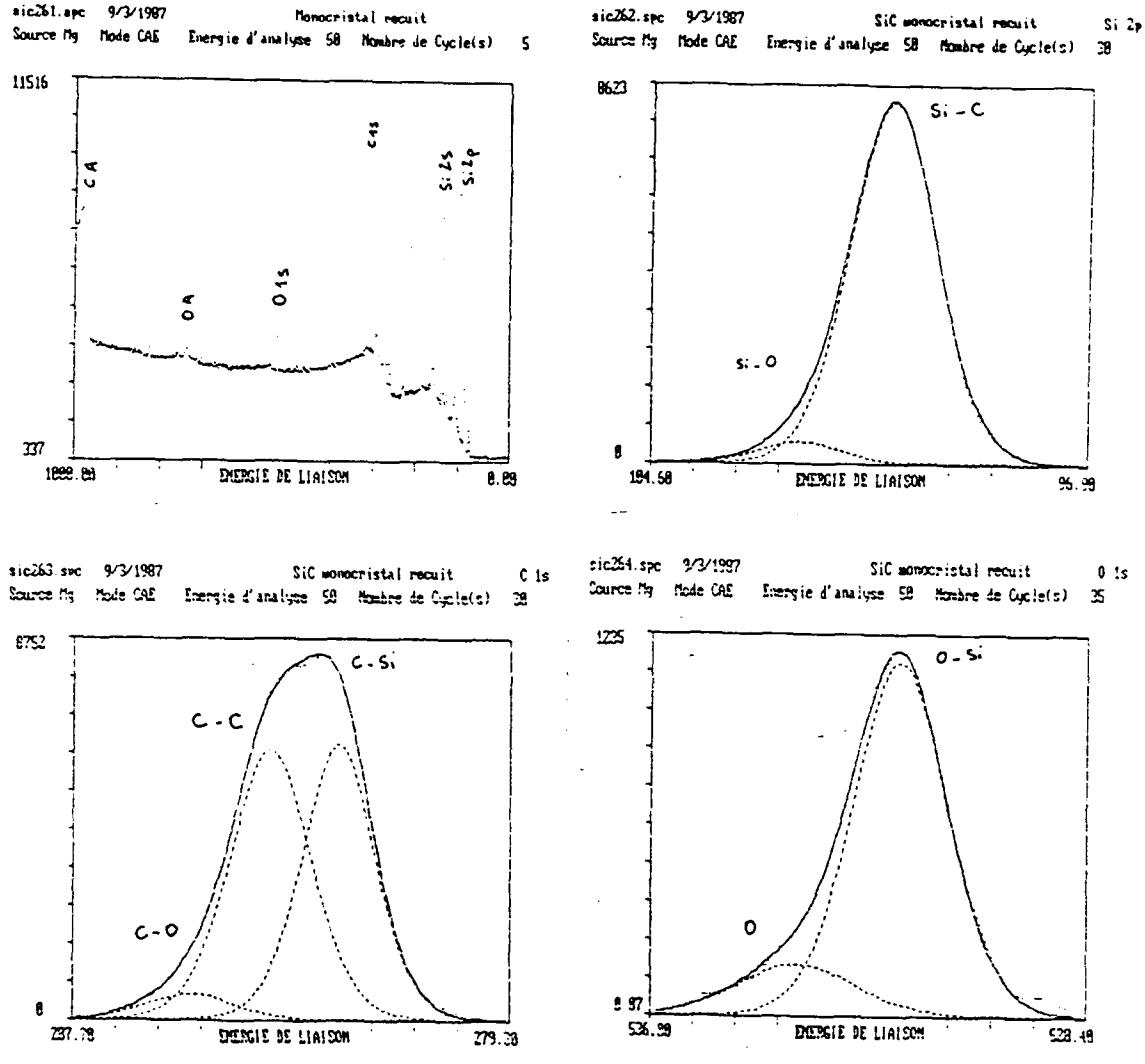

Figure 1 : XPS spectra of SiC single cristal after annealing at high temperature. Resolution in several Gaussian-Lorentzien components for the Si2p, C1s and O1s.

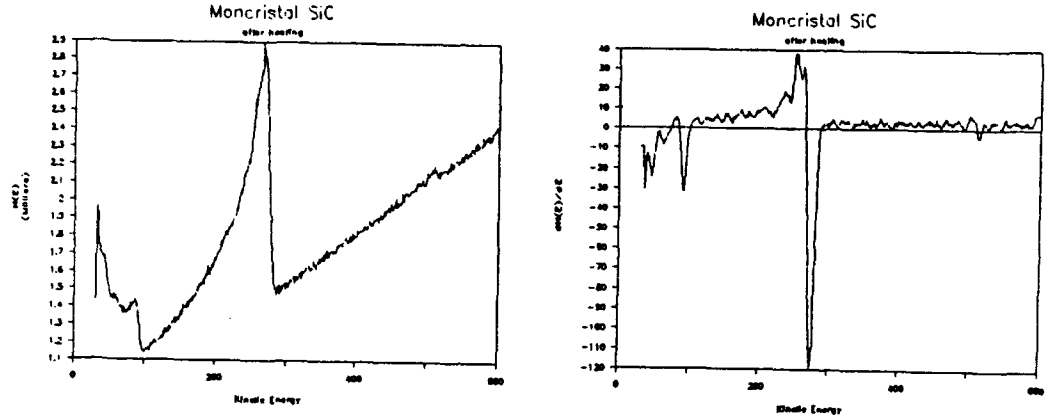

a)

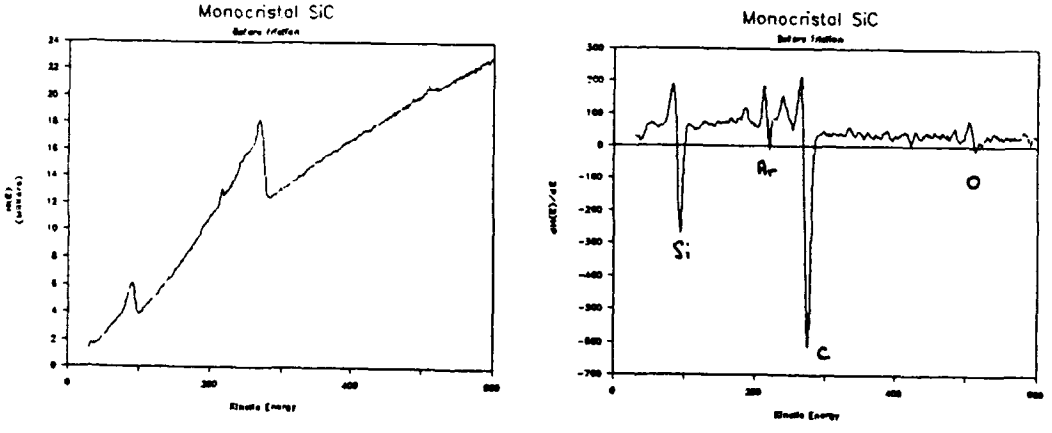

b)

Figure 2 : Direct and derivative AES spectra of SiC single cristal :
a) after annealing to ≈ 1100°K
b) after annealing to ≈ 700°K and before the friction test.

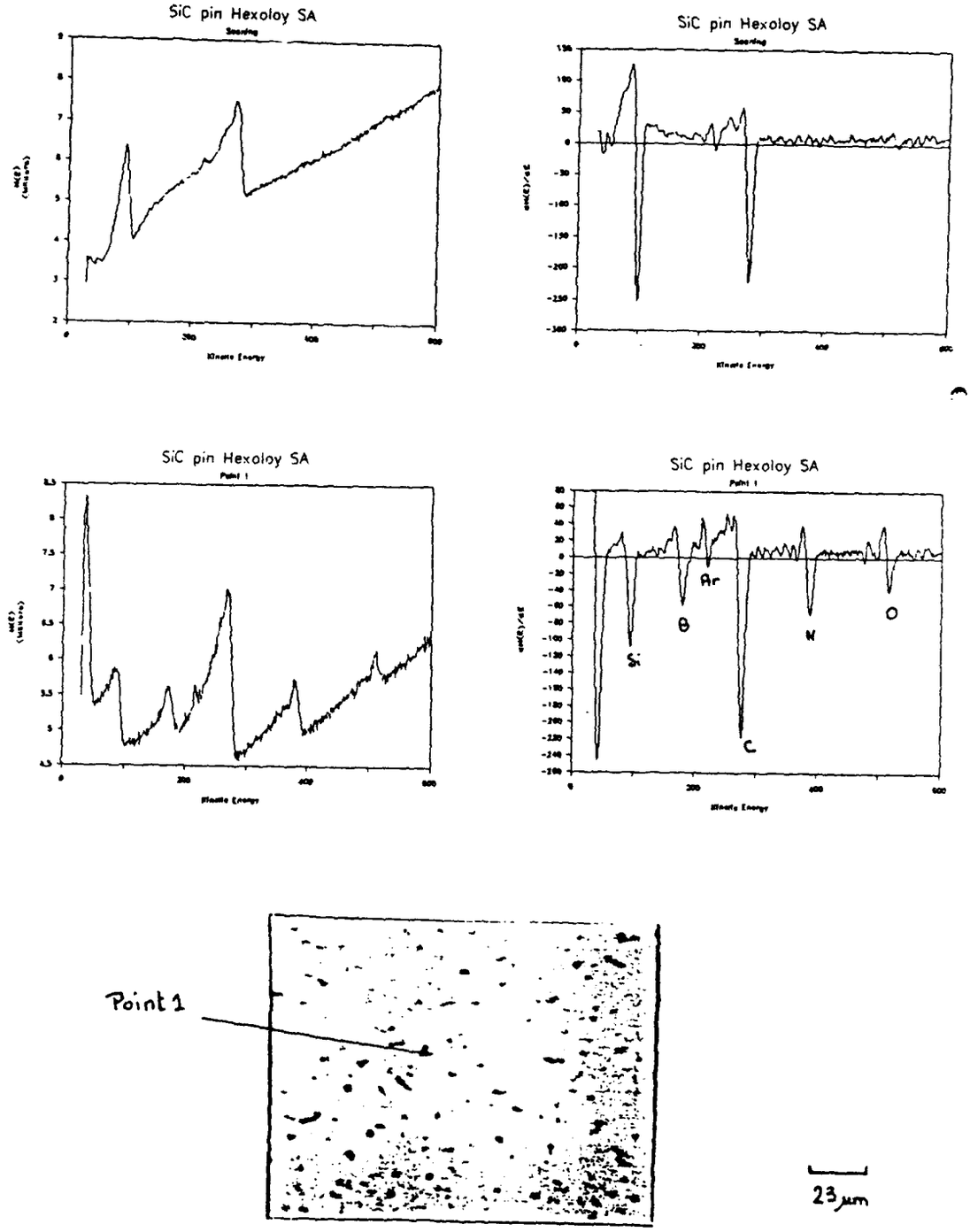

Figure 3 : Observation and AES analysis of SiC pin Hexoloy S.A.

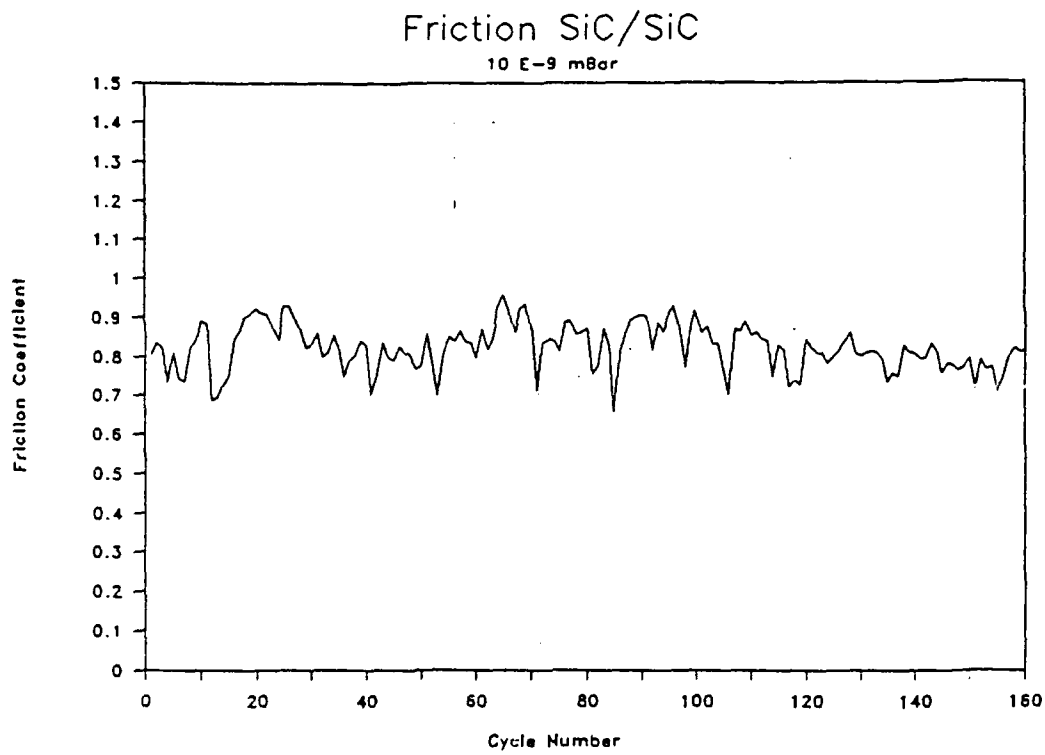

Figure 4 : Evolution of the friction coefficient under UHV.

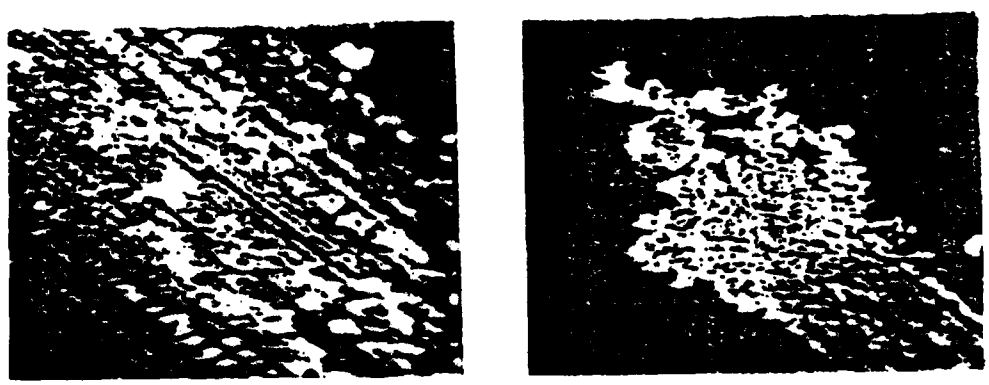

Figure 5 : Electron micrograph obtained in the track and the end of this track.

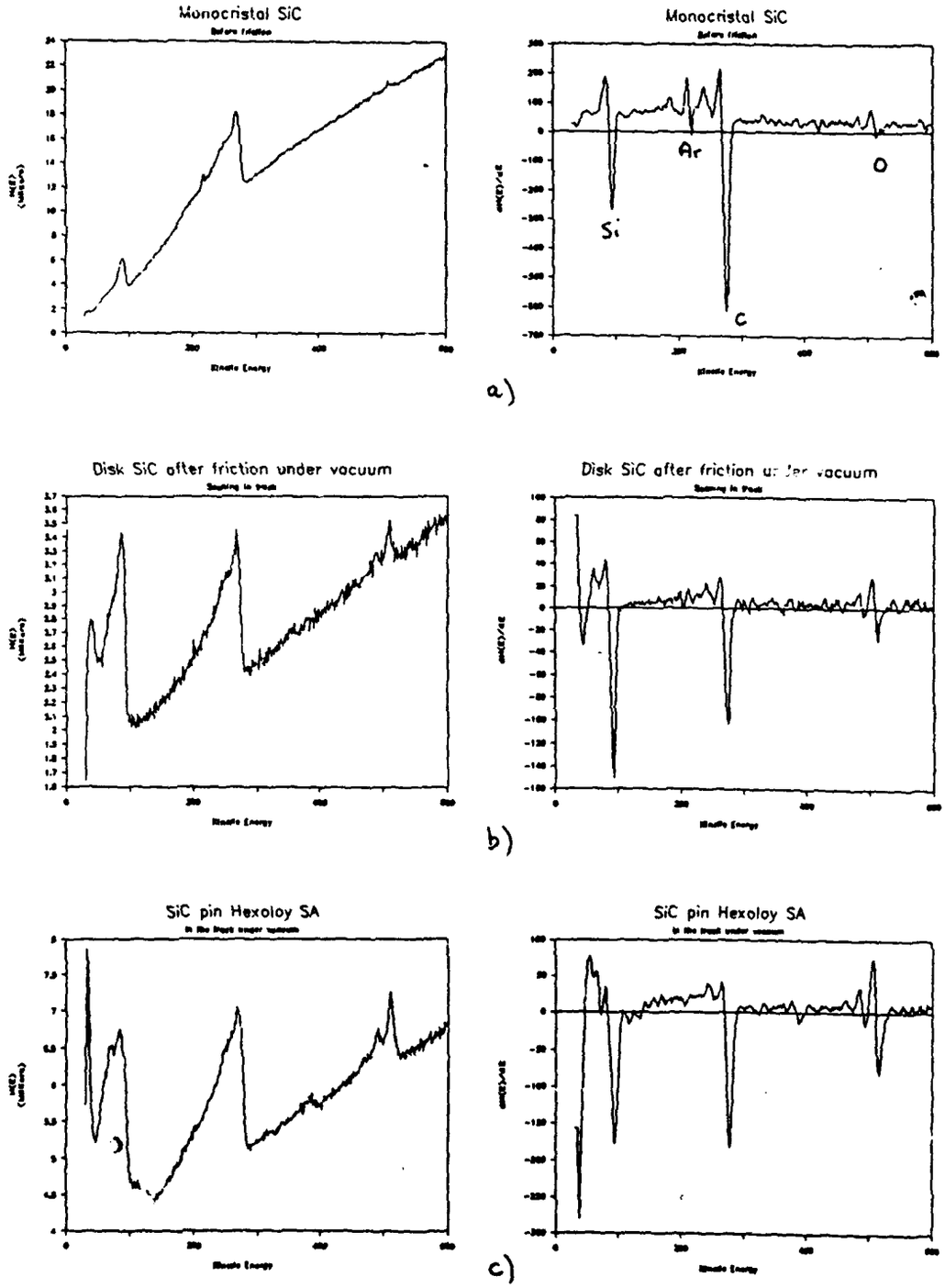

Figure 6 : Direct and derivative AES spectra obtained on :
a) the plate before friction,
b) in the track on the plate,
c) in the track on the pin.

0.1 μm

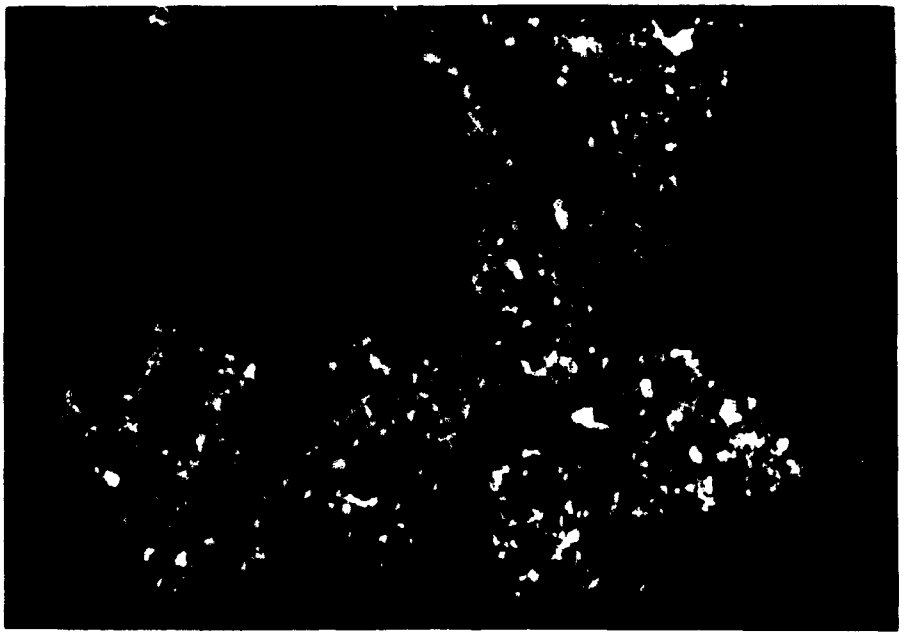

Figure 7 : Bright field and dark field TEM micrographs of wear debris of the SiC/SiC system.

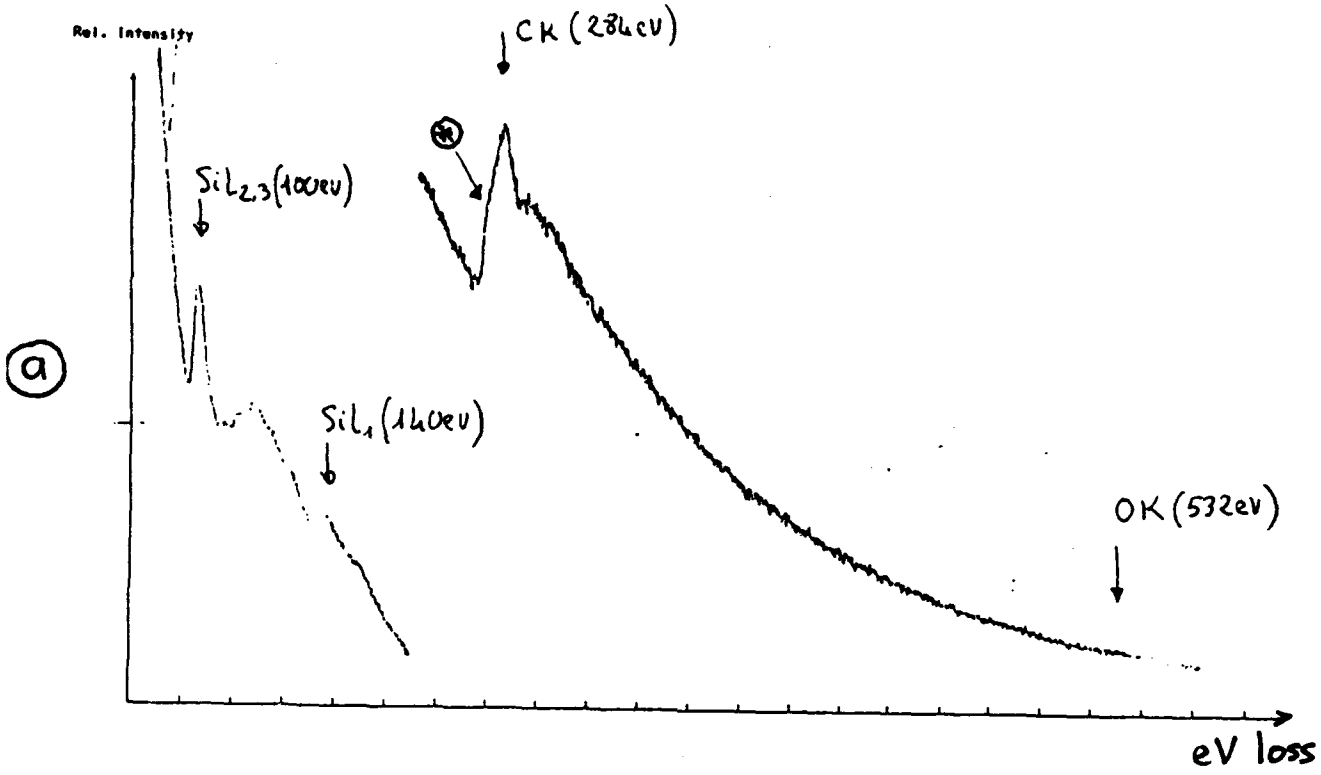

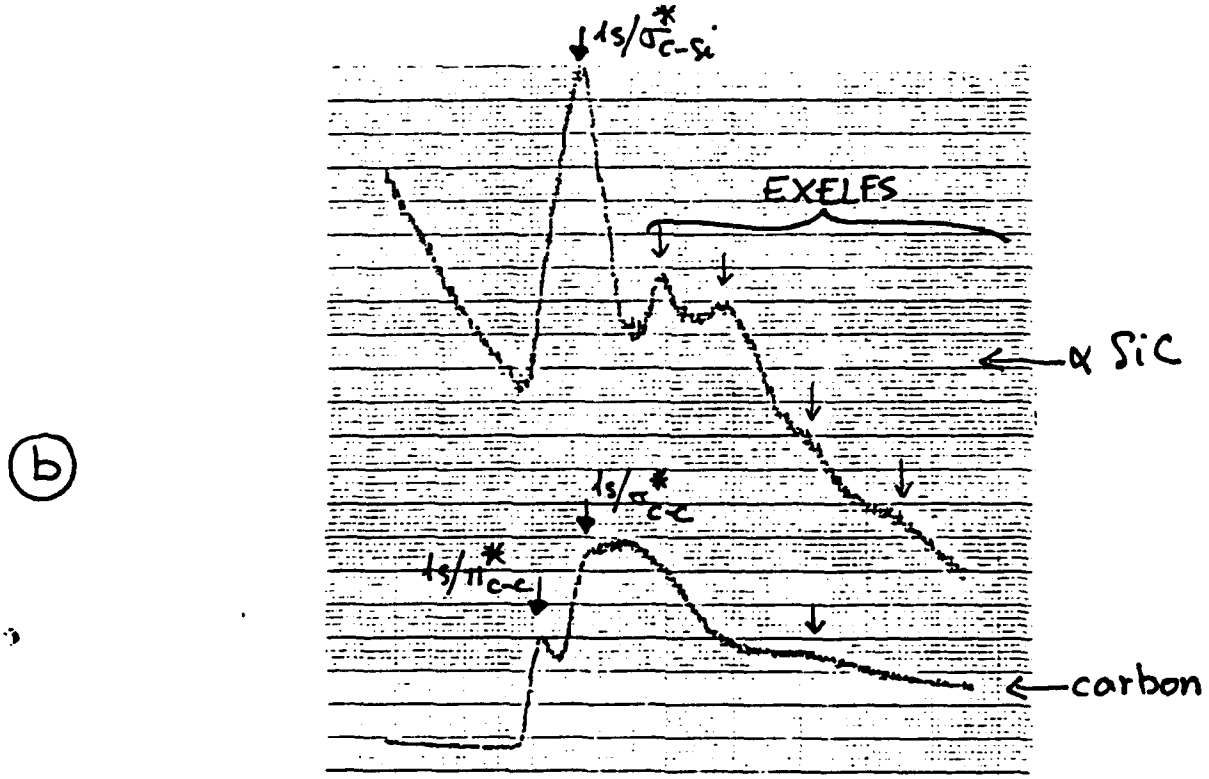

Figure 8 : a) EELS spectrum of wear debris.
b) Carbon K edge for a αSiC single cristal and for amorphous carbon.

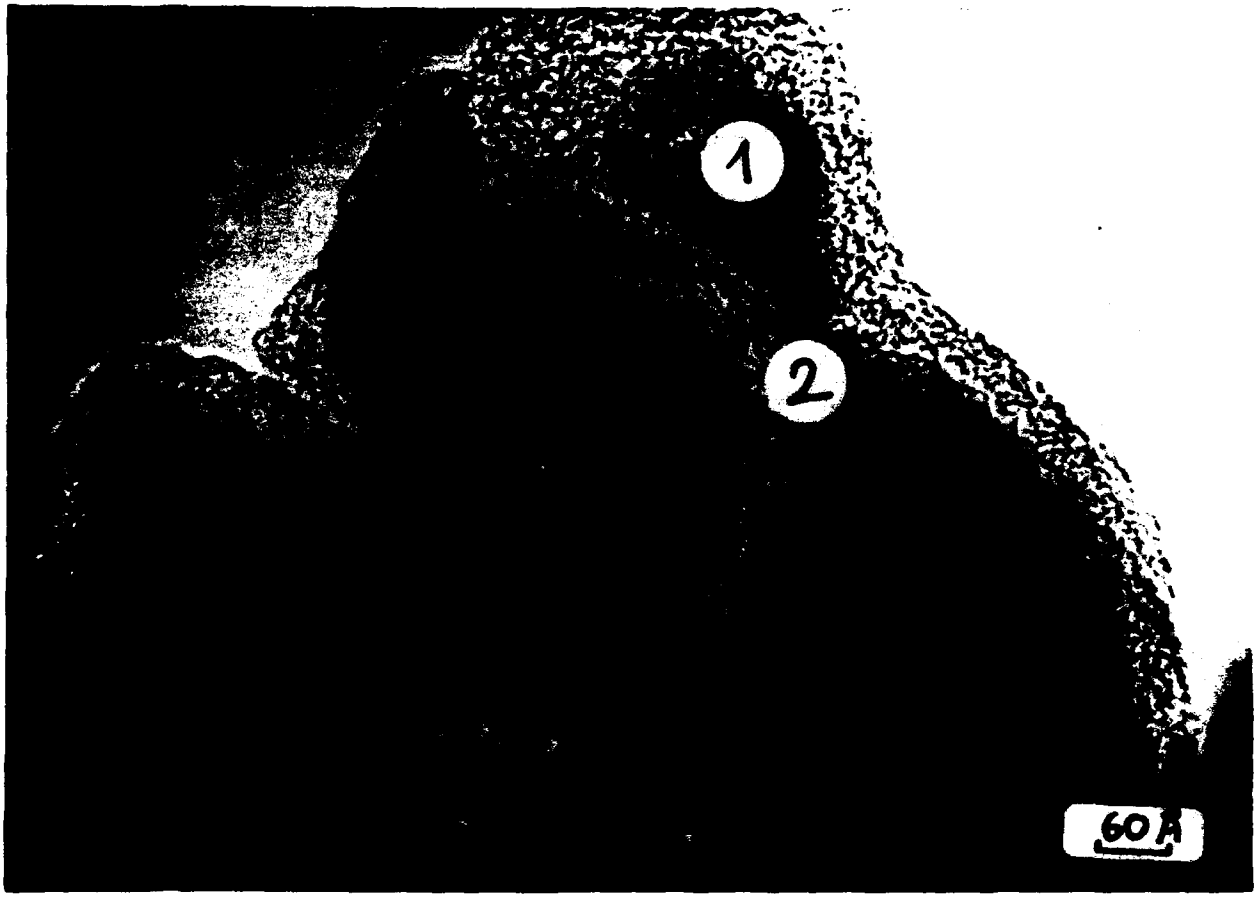

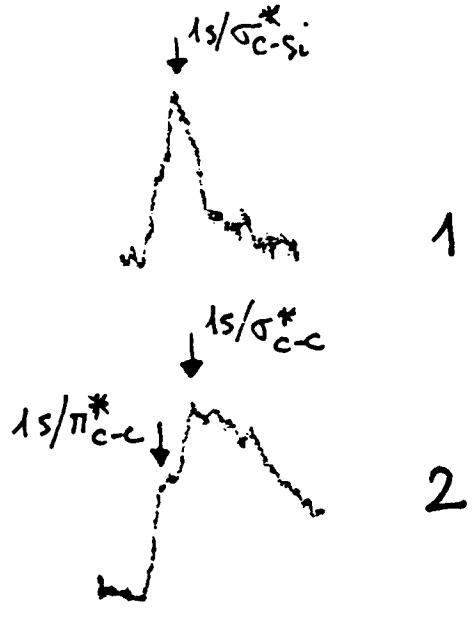

Figure 9 : High resolution TEM micrograph of SiC wear fragments. High resolution EELS analysis of the carbon K edge in and between SiC cristallites.

SORETRIB
36, Avenue Guy de Collongue
69130 ECULLY

ECOLE CENTRALE DE LYON
Laboratoire de Technologie
des Surfaces
UA CNRS 855
36 avenue Guy de Collongue
B.P. 163 - 69131 ECULLY Cédex

FRICTION OF SiC/SiC

OXYGEN EFFECT

Rapport partiel

11 Mai 1988

Contrat n° F 33615-85-C-5087
HUGHES AIRCRAFT CO
Mike GARDOS
El Segundo - USA

Th. LE MOGNE
J.M. MARTIN
H. MONTES

FRICTION OF SiC/SiC - OXYGEN EFFECT

Introduction

Previous work has shown some interesting and surprising features of the SiC/SiC combination when friction occurs under special environmental conditions, at ambient temperature, i.e. :

- A high value of the friction coefficient under UHV (f ≈ 0.8), associated with an amorphization process of silicon carbide in free carbon species (see March 88 report).
- A relatively low value of the friction coefficient in air (f ≈ 0.25) with triboreacted silicon oxide formation (see february 88 report).

In order to have a better understanding of the tribochemical reactions occurring with the SiC/SiC system, we investigated the effect of oxygen partial pressure on friction and wear.

Preparation of specimen and tribological conditions

The preparation of specimen has already been described in previous reports, and the friction tests have been performed out in the same conditions (except the nature of the environmental gas).

Friction tests - Results

Three experiments have been carried out :

Test 1 : Friction is started under UHV conditions and, after a few passages, a partial oxygen pressure of $0.5\ 10^{-3}$ Pa is admitted in the chamber.

Test 2 : The friction test is started with $0.5\ 10^{-3}$ Pa of oxygen (as in test 1) and, after a few passages of the pin, the pressure is allowed to increase to $0.5\ 10^{-2}$ Pa.

Test 3 : First a partial pressure of O_2 (50 Pa) is introduced in the chamber, and the friction is then started.

The evolutions of the corresponding friction coefficients are represented in figure 1.

Main results show :

1 - that a small O_2 pressure ($0.5\ 10^{-3}$ Pa) induces a slight increase of the UHV friction coefficient (from 0.8 to 0.9).

2 - That a pressure of 50 Pa induces a drastic decrease of the friction coefficient to a very low value (0.8 to 0.07).

3 - That these friction values are different from the one obtained in air ($f = 0.25$ with O_2 pressure of $\simeq$ 15,000 Pa).

To conclude, SiC/SiC behavior is very sensitive to oxygen partial pressure, and this was unexpected.

Surfaces observations and analysis

- AES analysis

Some AES spectra are presented (see figure 2 by 7), the ratio O/Si is different, depending ont the wear scar analysis (pin or plate) and on the O_2 pressure. As main results, it can be concluded :

1 - That under low pressure ($0.5\ 10^{-3}$ Pa) oxygen is partially reacted with the SiC worn surfaces (pin and plate).

2 - That under high pressure (50 Pa) oxygen is preferentially bound to silicon. No carbon is detected in the AES spectrum of αSiC worn face.

3 - That oxygen has reacted with the non rubbed surface (out of the wear scars), but to a less extend that in the wear scars. This latter result is in good agreement with literature data on SiC oxidation in the low temperature range.

Secondary electron images

As shown in figure (8), the very low value of the friction coefficient is associated with the presence of many rolling pins lying normally to the wear stroke.

Wear fragments analysis

The case of the high O_2 pressure has been particularly highlighted because of the occurrence of the very low friction value. Figure (9) shows a TEM micrograph of a rolling pin, and the EELS analysis which is corresponding. The interpretation of the EELS spectra indicates :

- The presence of Si-O bonding.
- The disappearance of the carbon as carbide.
- The presence of carbon in a graphitic organization as indicated by the strong peak at 284 eV energy loss (1s $\rightarrow \pi^*$ C-C) and the well defined peak at 290 eV (1s $\rightarrow \sigma^*$ C-C). It is to be noticed that the organization of carbon is not far from graphitized carbon black. This is well supported by high resolution TEM image showing the lattice of carbon planes (figure 10) but it is not well understood why carbon was not detected by Auger Electron Spectroscopy.

Discussions

O_2 pressure (Pa)	15,000	50	$0,5\ 10^{-3}$	UHV
f	0,25	0,07	0,8 - 0,9	0,8
Wear fragments morphology	thin foils	rolling pins	grains	grains
Tribochemistry	SiO_2	SiO_2 + graphitization	amorphization of SiC	amorphization of SiC

In the table, the different results are summarized. From the tribochemist eye view, three basic phenomena are shown :

- Amorphization process of SiC $\leftrightarrow$ high friction
- Graphitization of SiC $\leftrightarrow$ low friction
- Oxidation of SiC $\leftrightarrow$ medium friction

Next results will concern wear measurements.

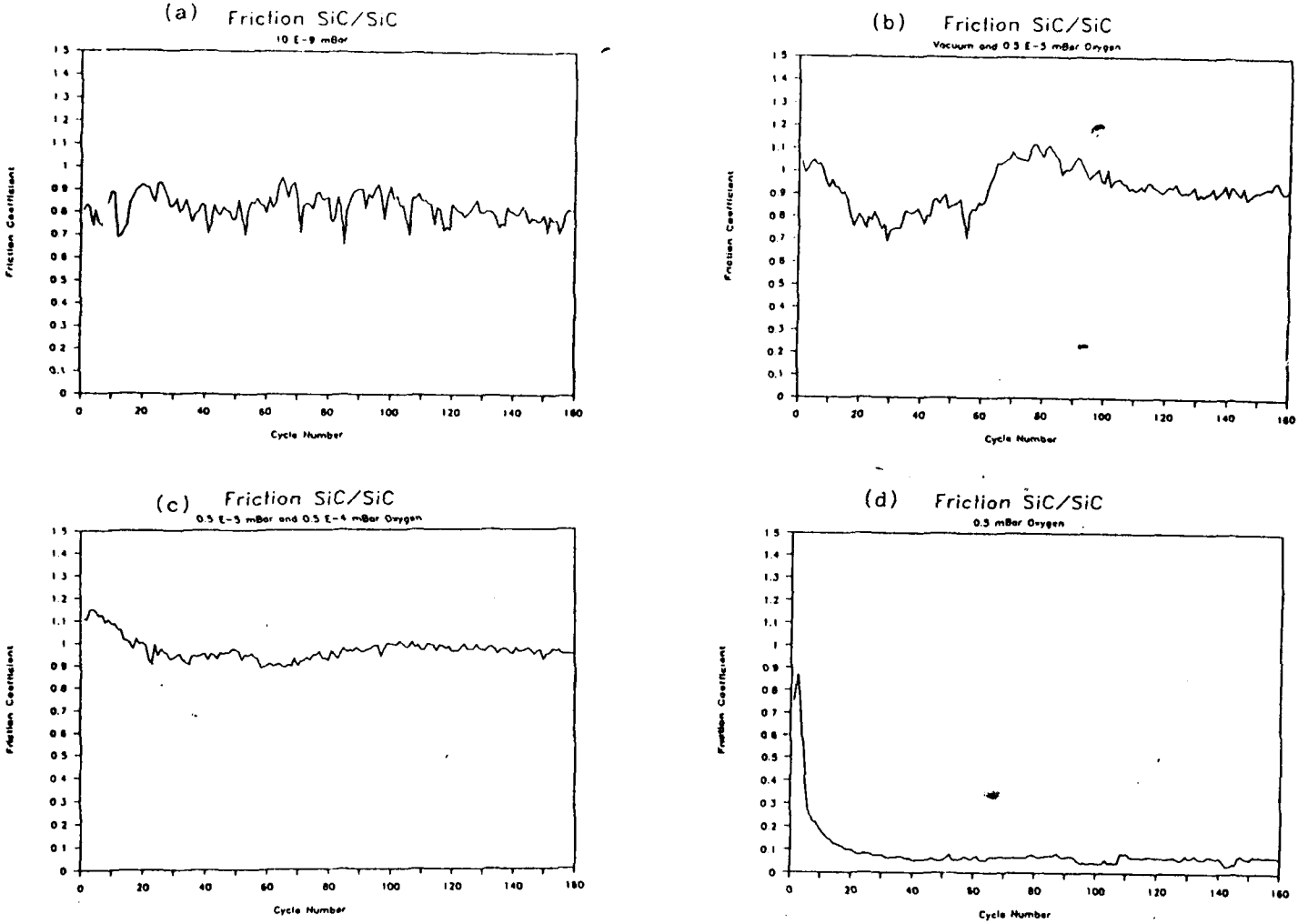

Figure 1 : Friction coefficient obtained under :
a) U.H.V.,
b) 0.5 10^{-3} Pa of oxygen,
c) 0.5 10^{-2} Pa of oxygen
d) 50 Pa of oxygen

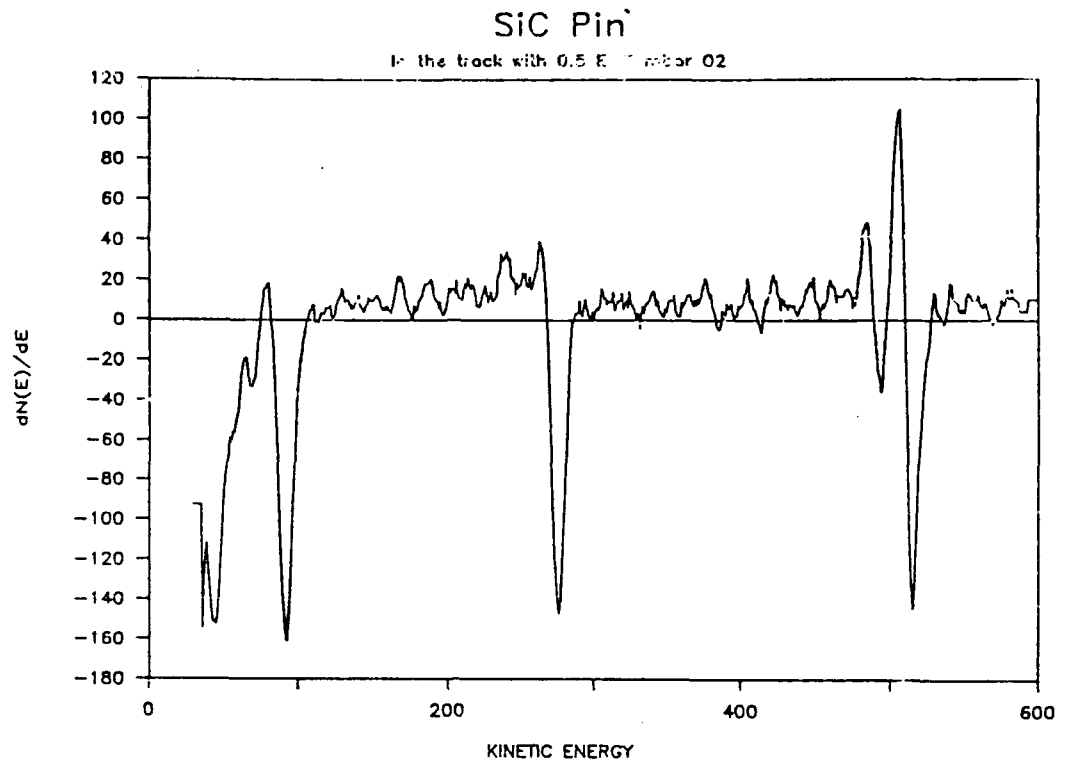

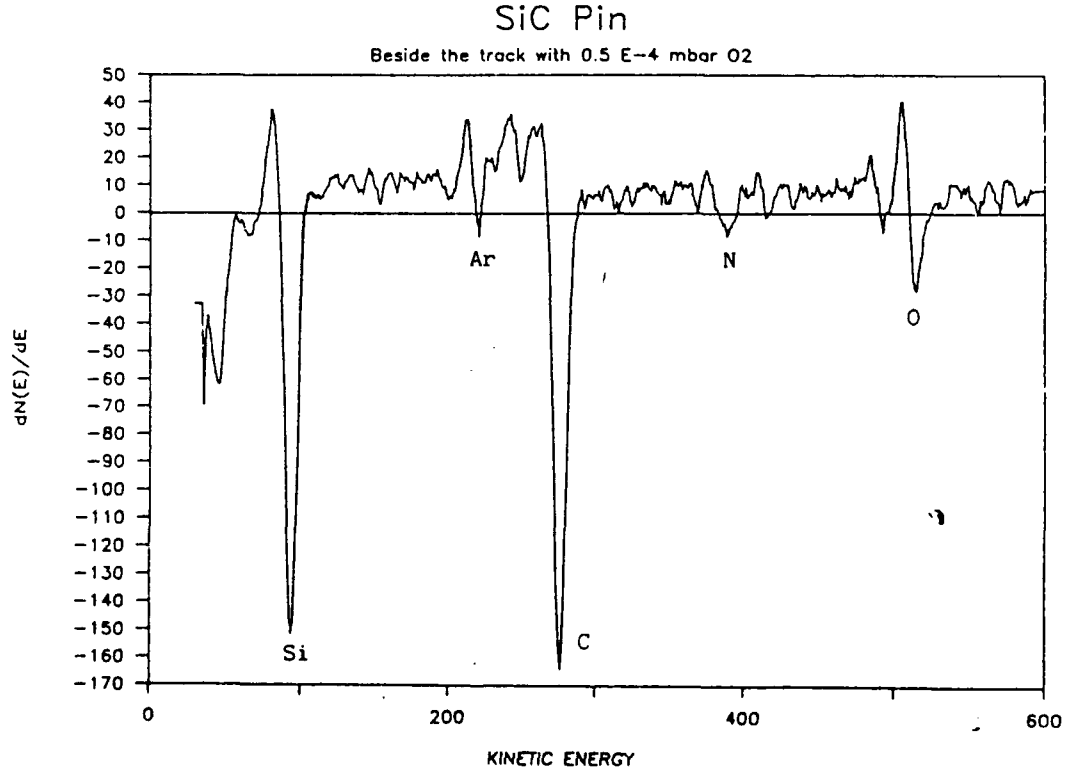

Figure 2 : AES spectra on the SiC pin obtained inside and beside the track with 0.5 10-3 Pa oxygen.

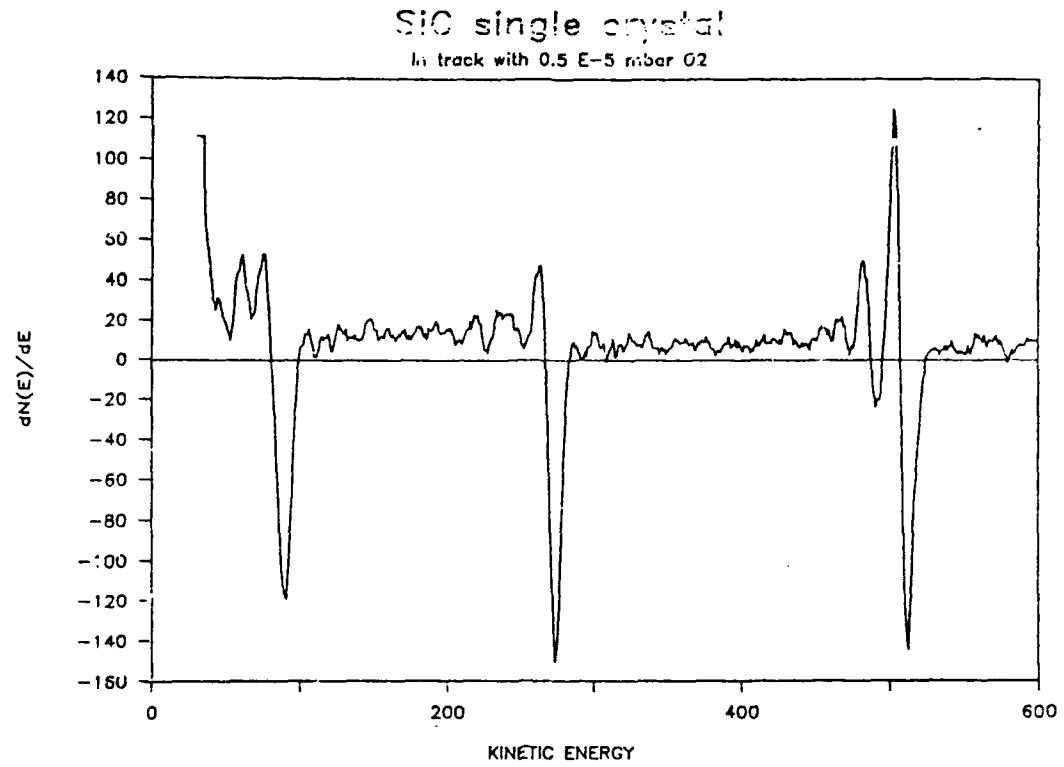

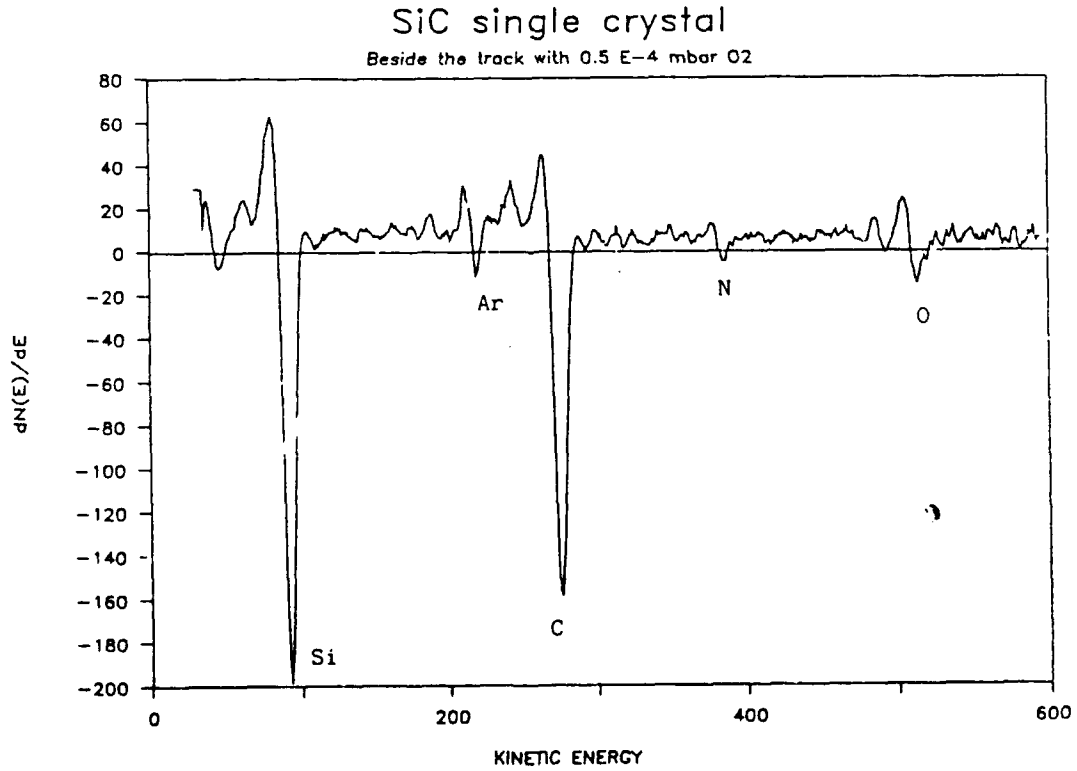

Figure 3 : AES spectra on the SiC plane obtained inside and beside the track with 0.5 10^{-3} Pa oxygen.

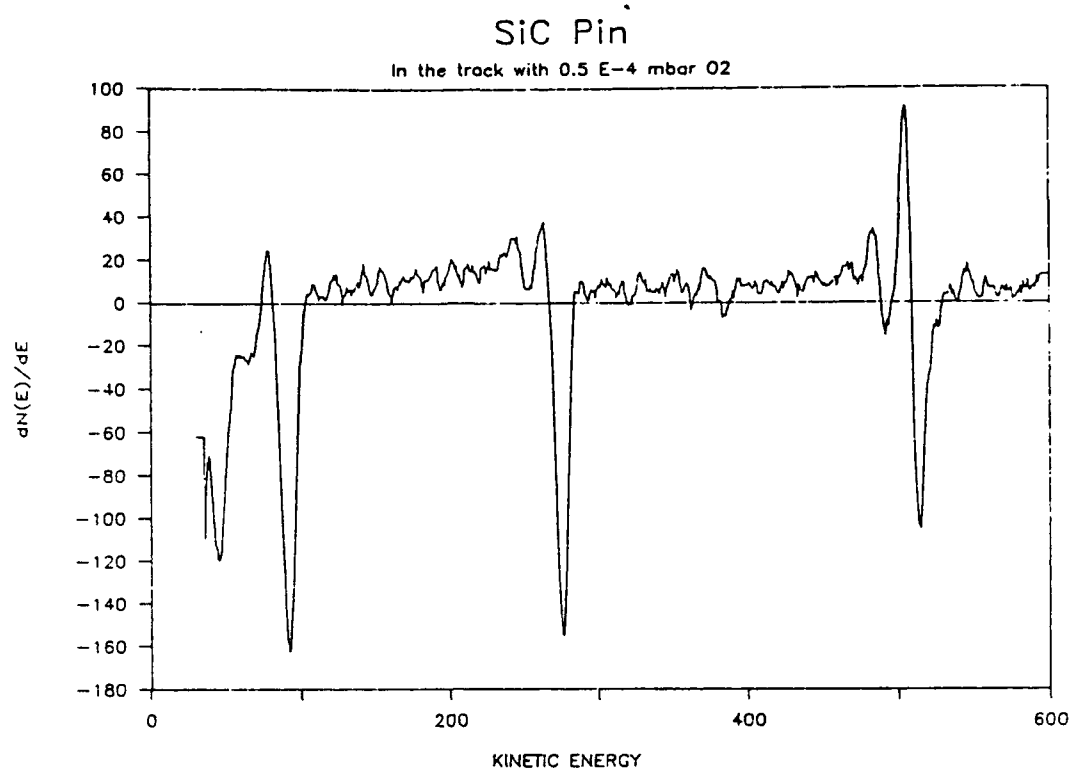

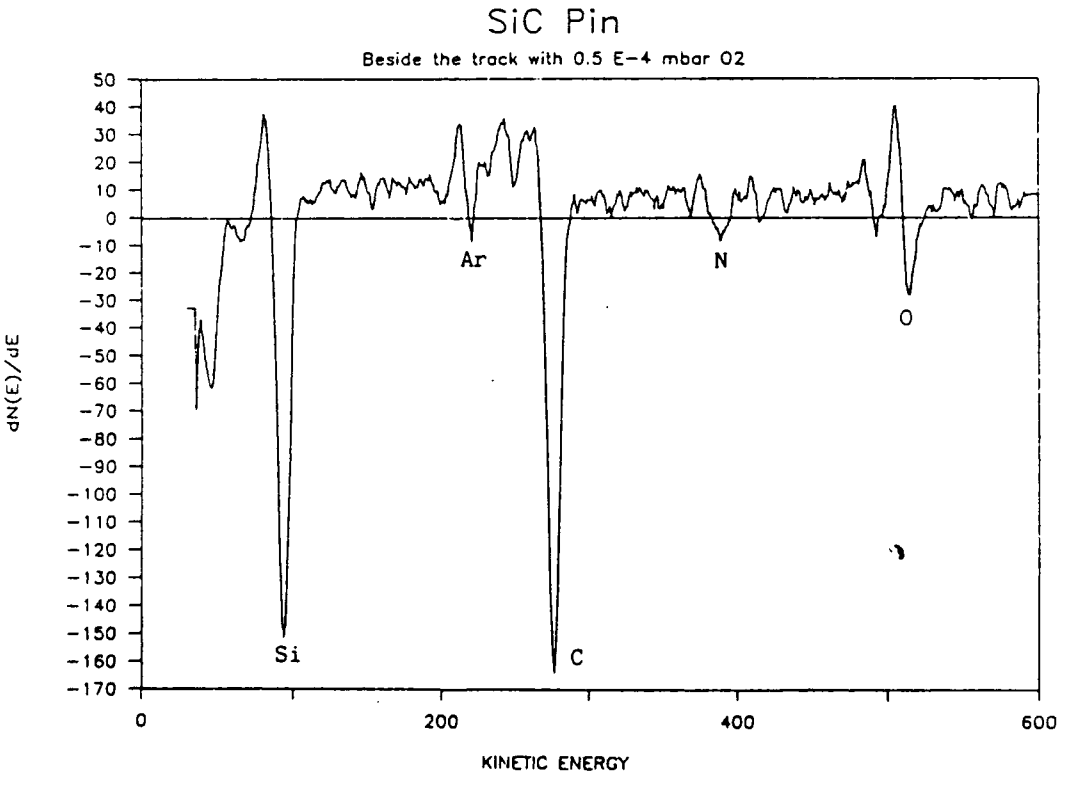

Figure 4 : AES spectra on the SiC pin obtained inside and beside the track with 0.5 10^{-2} Pa oxygen.

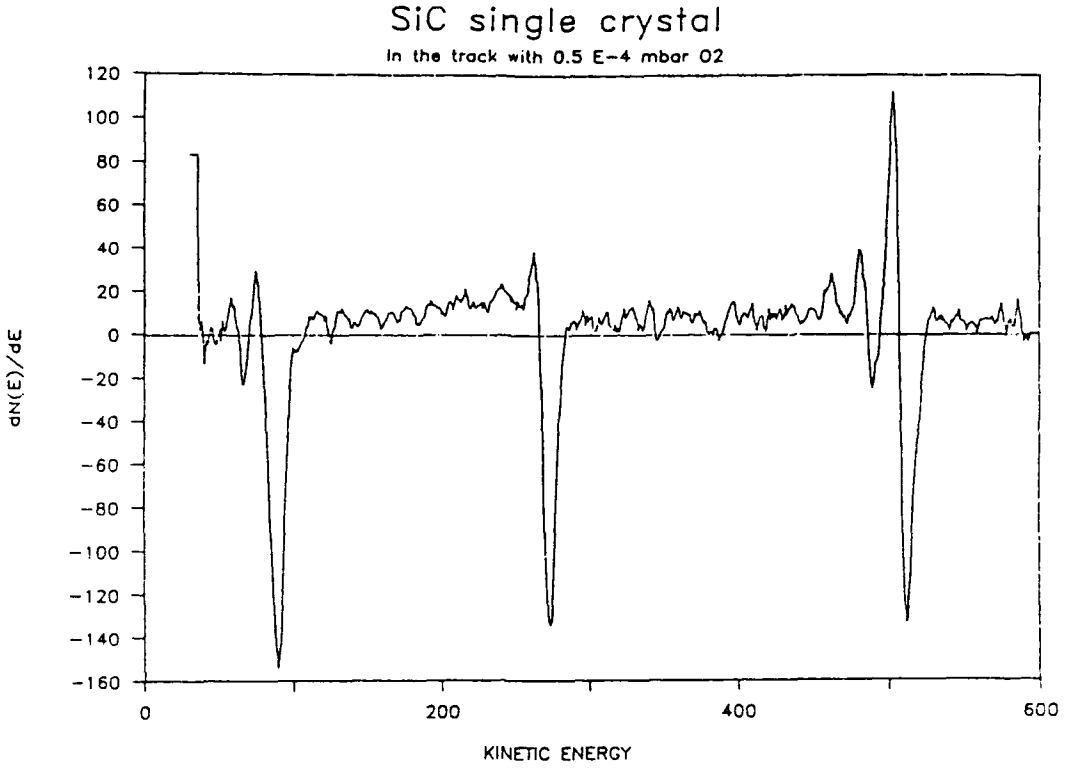

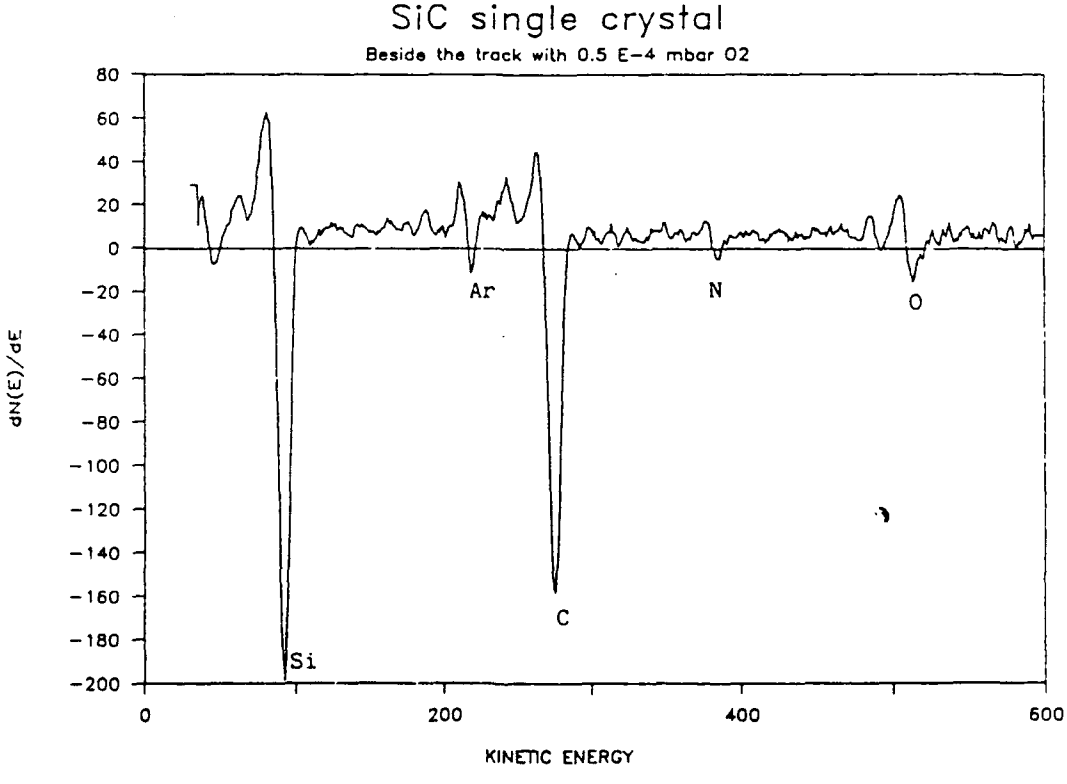

Figure 5 : AES spectra on the SiC plane obtained inside and beside the track with 0.5 10^{-2} Pa oxygen.

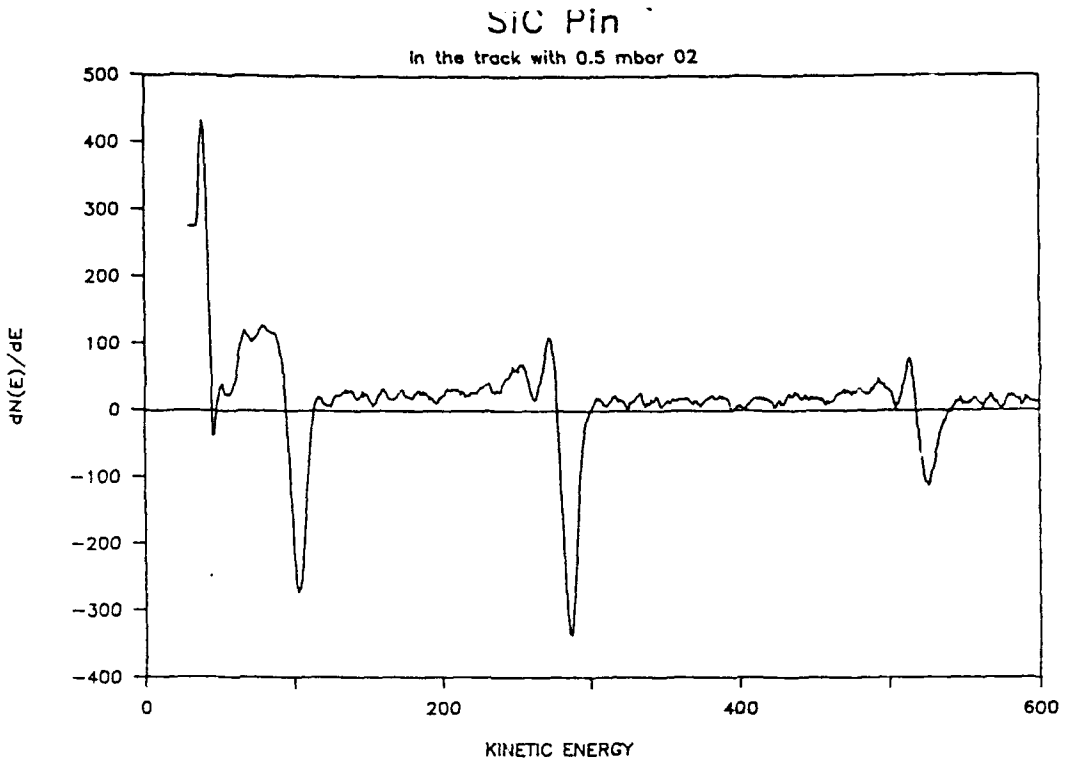

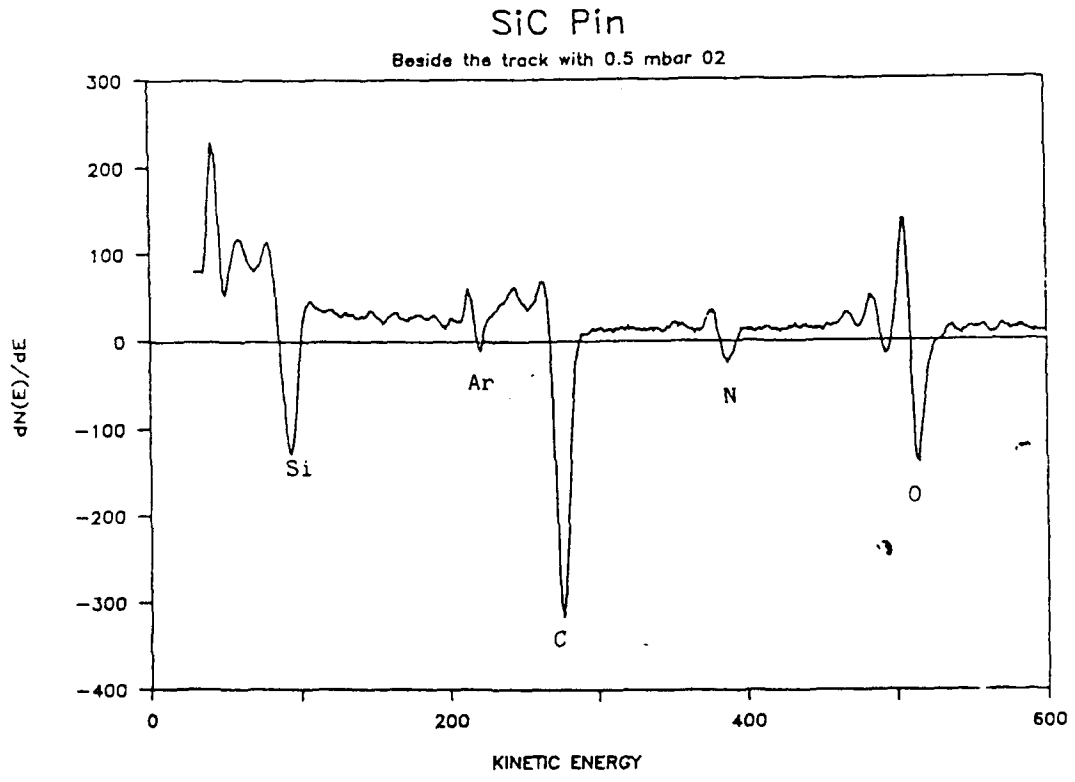

Figure 6 : AES spectra on the SiC pin obtained inside and outside the track with 50 Pa oxygen.

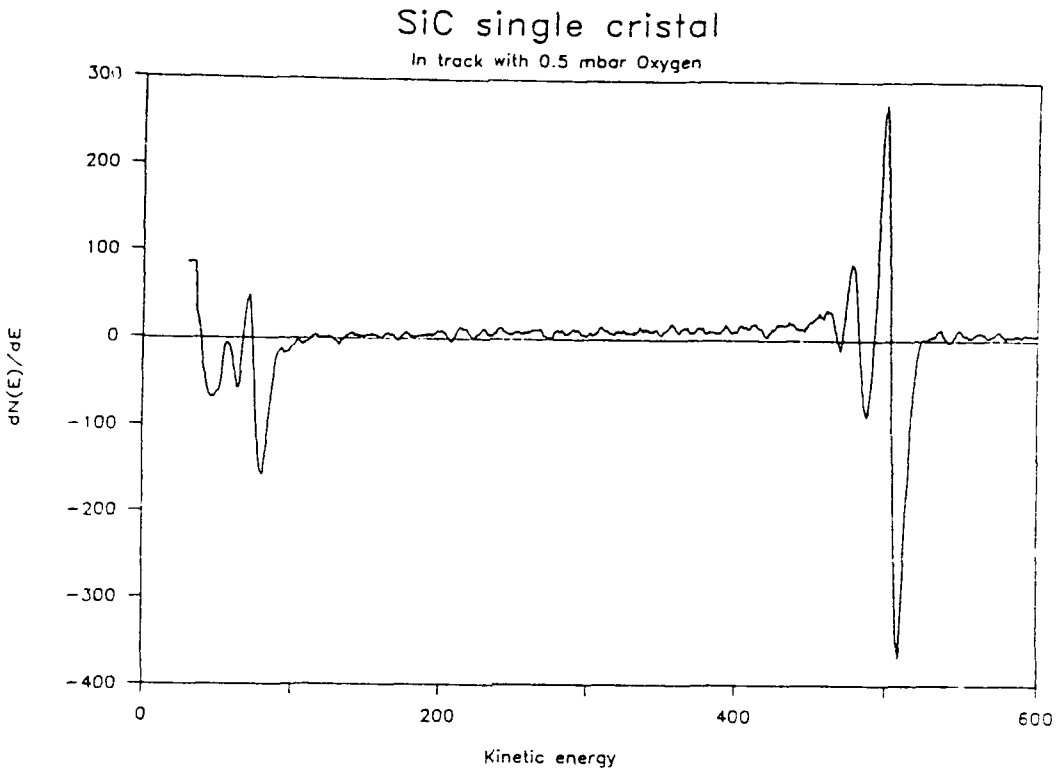

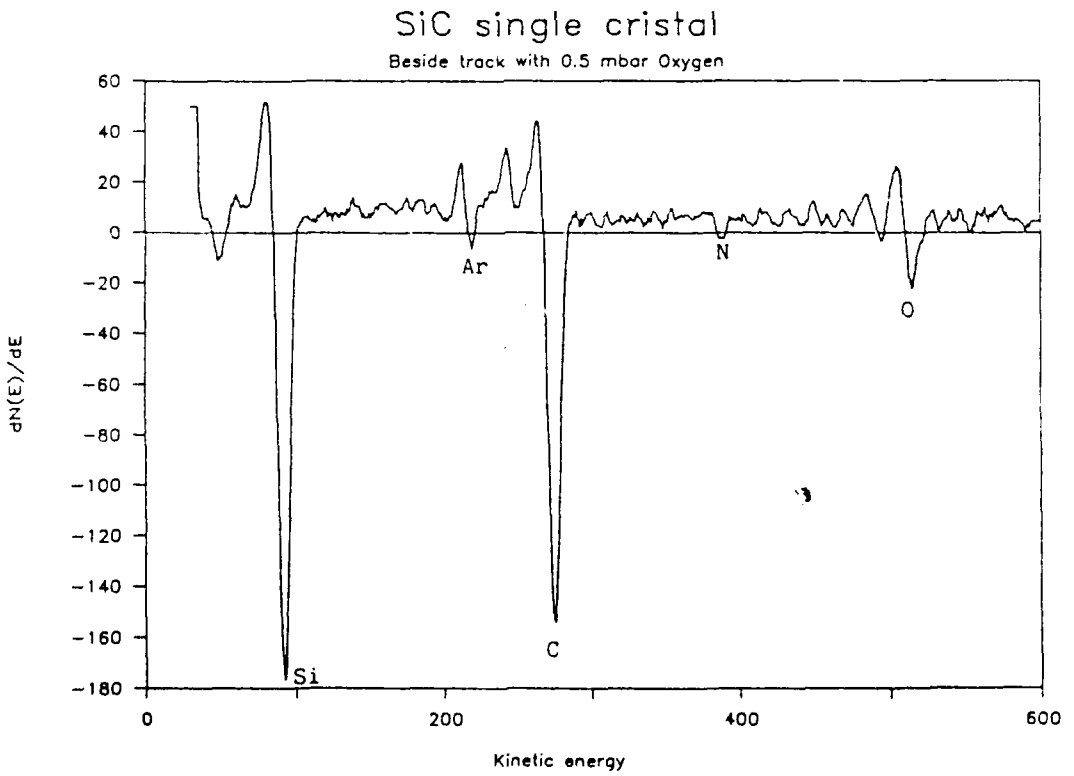

Figure 7 : AES spectra on the SiC plane obtained inside and beside the track with 50 Pa oxygen.

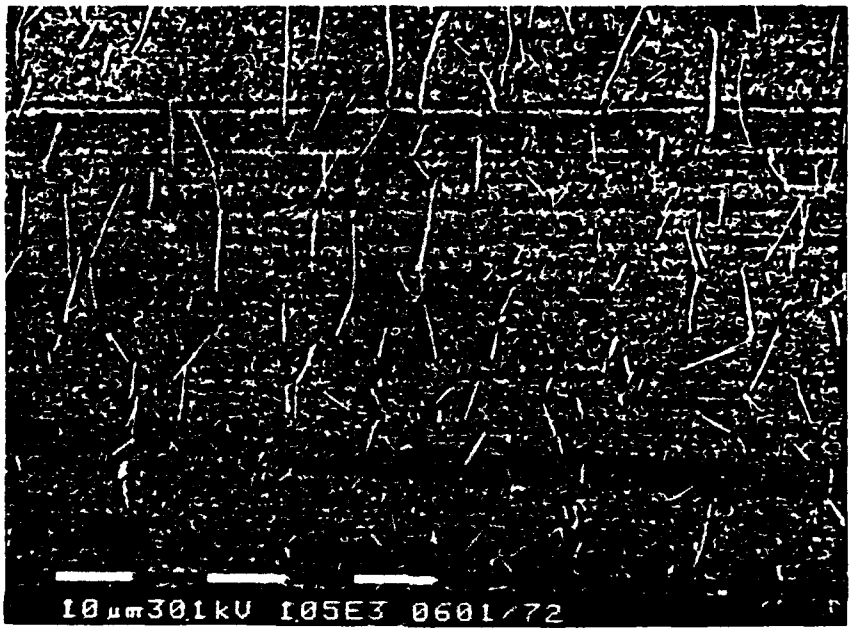

Figure 8 : Secondary electron image inside track on the plane obtained with 50 Pa O_2.

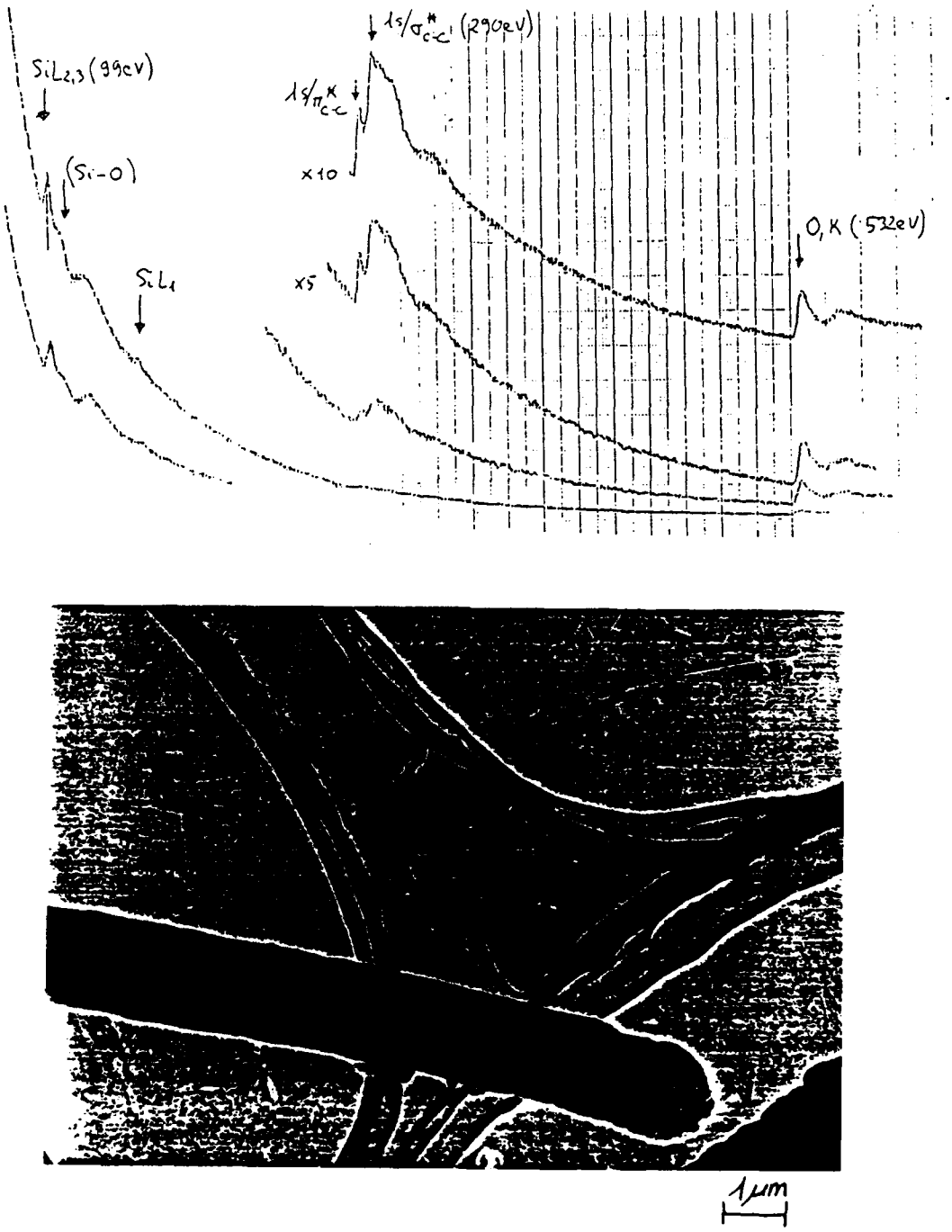

Figure (9) : TEM micrograph of a rolling pin (SiC/SiC 50 Pa O_2) and corresponding EELS analysis showing the presence of silicon oxide and free carbon species.

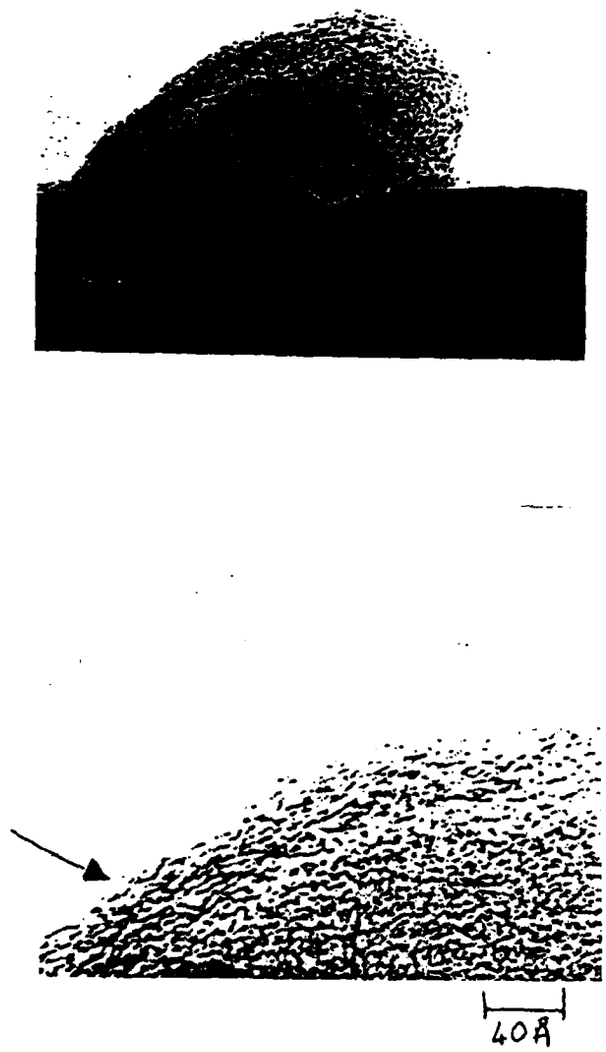

Figure (10) : High resolution TEM imaging of a wear fragment (SiC/SiC 50 Pa O_2) showing a pre-graphitic organization around a SiO_2 grain (see arrow).

SORETRIB
36, Avenue Guy de Collongue
69130 ECULLY

ECOLE CENTRALE DE LYON
Laboratoire de Technologie
des Surfaces
UA CNRS 855
36, avenue Guy de Collongue
B.P. 163 - 69131 ECULLY Cédex

FRICTION OF SiC/SiC

WEAR ASPECT

Rapport partiel

3 Juin 1988

Contrat n° F 33615-85-C-5087
HUGHES AIRCRAFT CO
Mike GARDOS
El Segundo - USA

Th. LEMOGNE
J.M. MARTIN
H. MONTES

Previous reports were concerned with friction of SiC/SiC combinations. The present report emphasizes wear measurements, including :

- degradation of worn surfaces by profilometry (presence of fractures)
- wear scar metrology in the SEM (wear scar diameter on the pin),
- morphology of wear fragments by SEM.

Two cases are considered :

- SiC/SiC under UHV (f = 0.08),
- SiC/SiC under 50 Pa O_2 (f = 0,07).

Profilometry

Figures (1) and (2) give the profilometric recording of wear scars respectively under vacuum and under O_2 partial pressure. It can be stated :

- that the wear volume on the pin is higher with 50 Pa O_2 than in vaccum (figure 2),
- that the worn surface on the pin is smoother under O_2 than under vaccum,
- that the flat is severely damaged under vaccum (fractures and possible transfers),
- that the flat is not worn under O_2, moreover à 0.1 µm thick layer is present.

SEM study of worn surfaces - SIMS profiling

Figure (3) shows SEM pictures of wear scars on the pin for different O_2 partial pressure. This confirms wear results obtained by profilometry.

Special attention has been paid to the case of the SiC flat with 50 Pa O_2 where a layer is present (see SEM pictures figures 4, 5).
SIMS profiling has been carried out in order to study the nature of this layer and the thickness of it (figure 6). As expected, the layer is oxygen rich (see evolution of O^- ions) probably silicon oxyde, and the thickness of the layer can be established by a calibration technique using profilometry in the crater. From this calculation, the silicon oxide layer

is estimated to 98 nm ; now if we compare this value to the thickness of the layer measured by profilometry (see figure 2) which is approximately 100 nm, we conclude that the α SiC flat has not been damaged, and that corrosive wear mainly occurs on the sintered pin.

Conclusion

We have compared wear of SiC/SiC system under vaccum and under 50 Pa O_2 partial pressure. Results are :

- under vaccum : due to high adhesion and friction (f = 0.8), fractures occurs both on the pin and on the flat,
- under 50 Pa O_2 : due to low value of friction (f = 0.08) no fractures are present, but corrosive wear brings on oxidation of the sintered pin leading to a protective silicon oxide layer on the flat (note that low friction is associated with the formation of graphite due to SiC oxidation, see previous report).

WEAR ON PIN

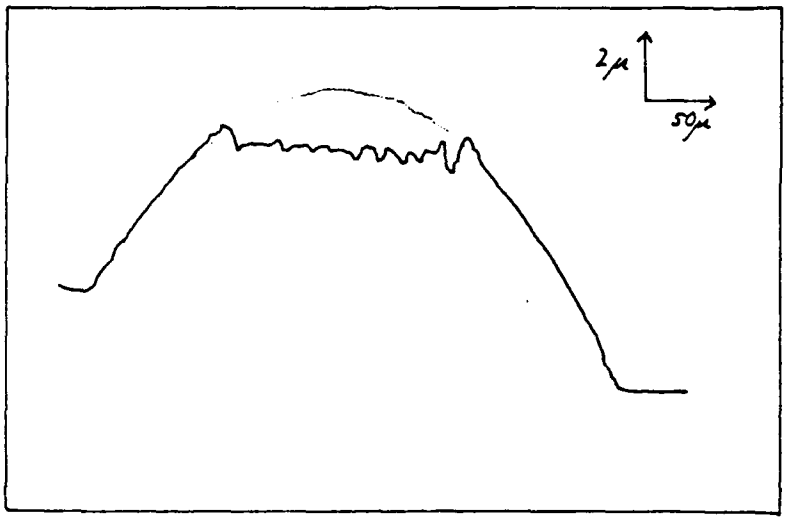

VACUUM

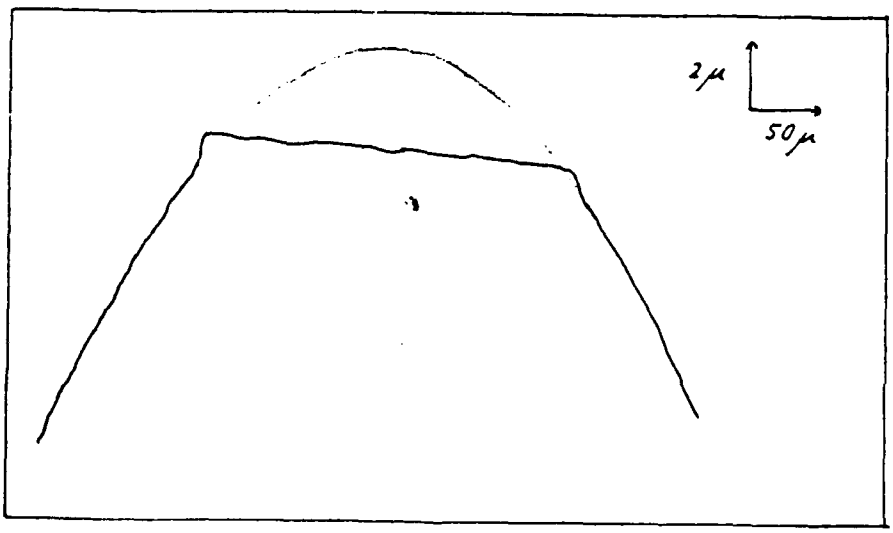

50 Pa Oxygen

R-15

Figure 2 : Cross surfaces profiles of wear tracks on pin.

WEAR ON FLAT

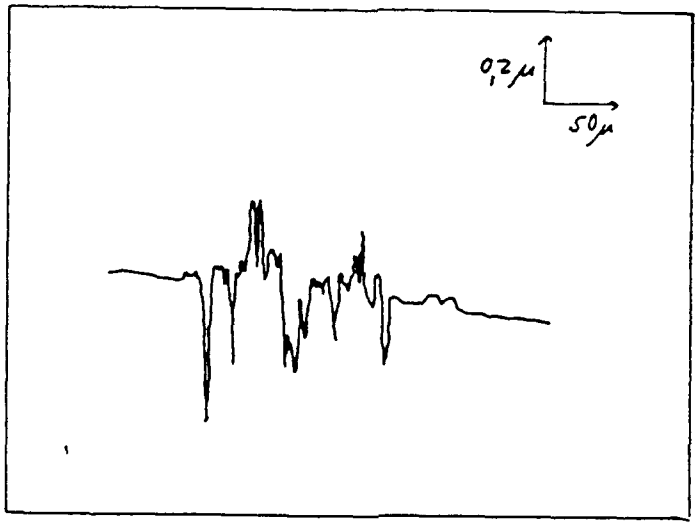

VACUUM

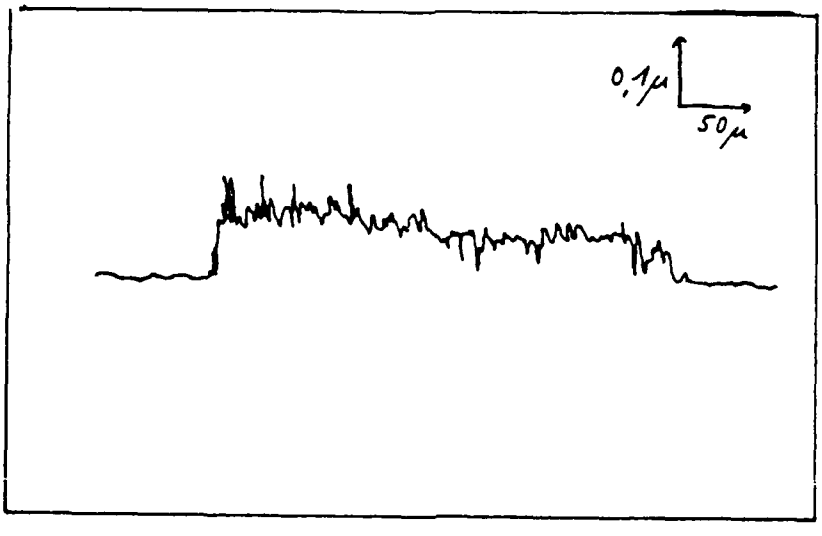

50 Pa Oxygen

R-46

Figure 1 : Cross surfaces profiles of wear tracks on flat.

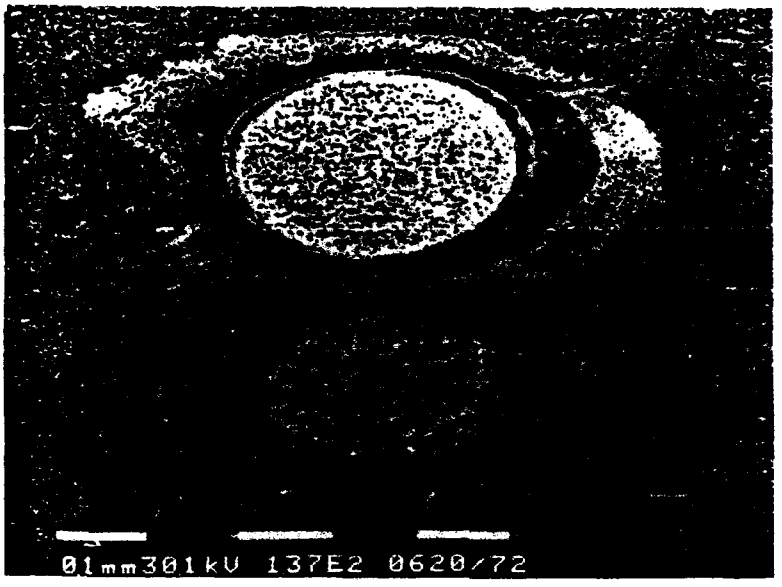

50Pa O_2

U.H.V.

Sintered SiC Pin - Tracks observation

5.10^{-4}Pa O_2

5.10^{-3}Pa O_2

Figure 3 : SEM pictures of the wear scar on the pin.

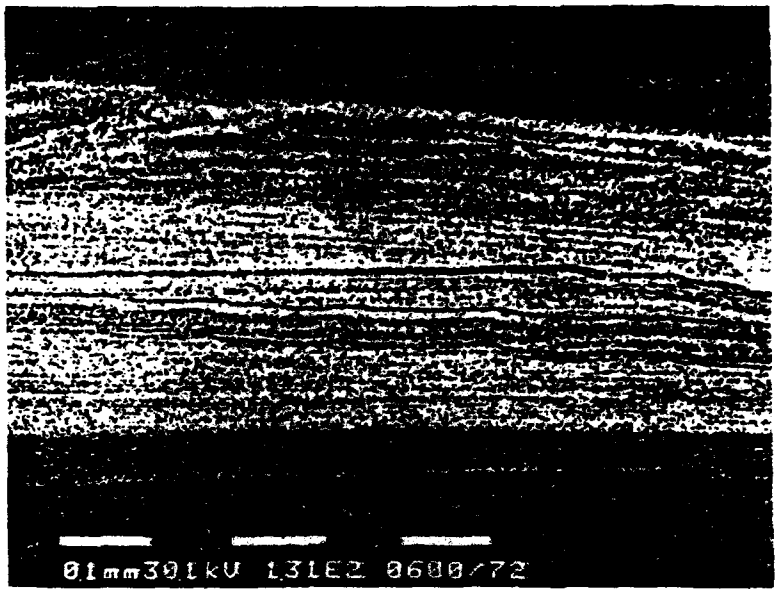

α SiC plate - 50 Pa O_2

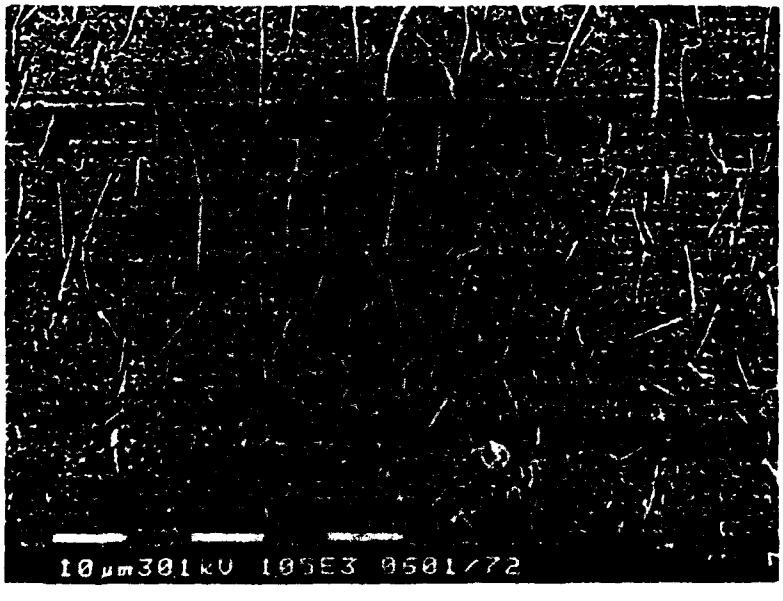

Figure 4 : SEM pictures of wear track on the flat with 50 Pa oxygen.

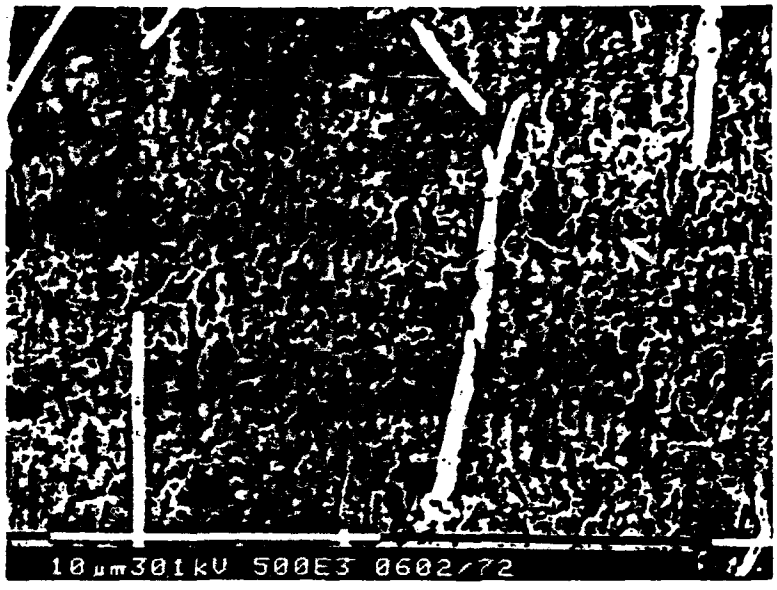

α SiC plate - 50 Pa O_2

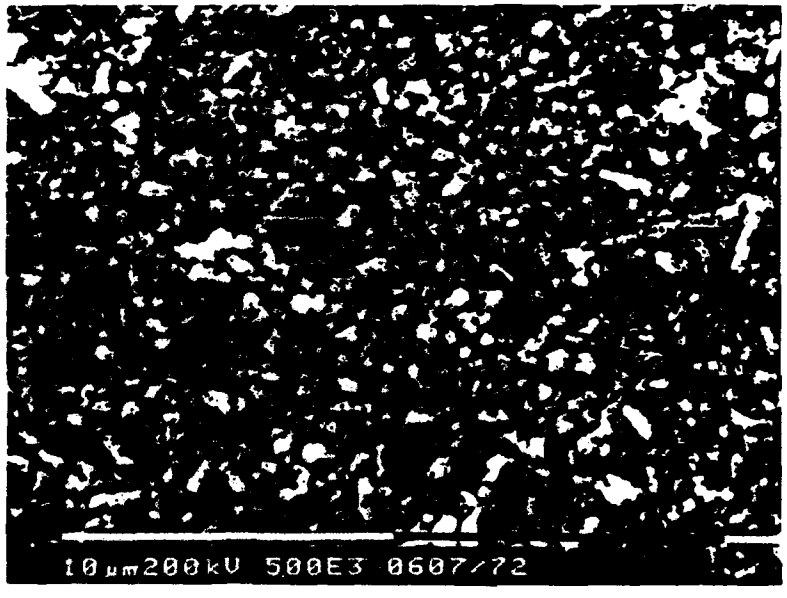

Figure 5 : SEM pictures details of wear fragments on the surface.

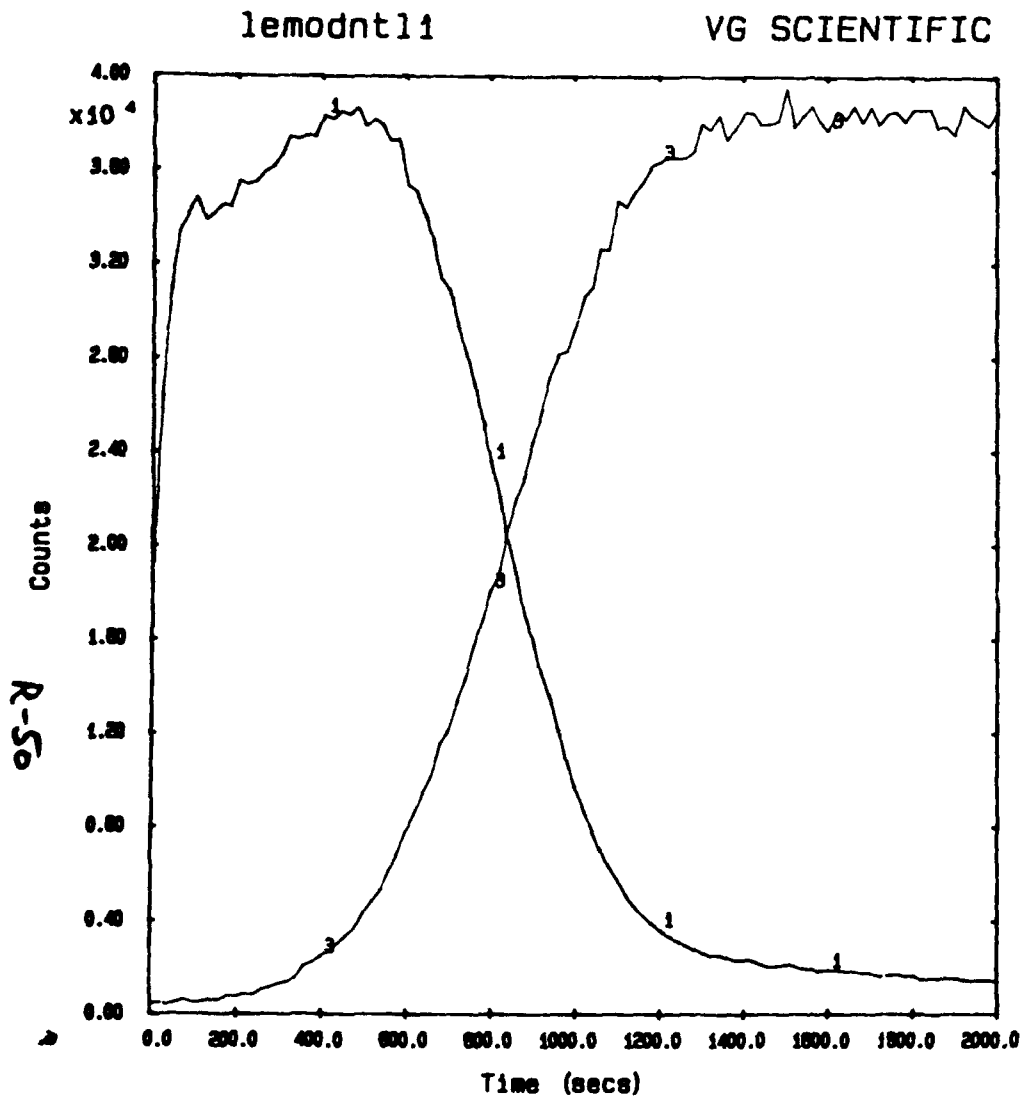

Negative SIMS Depth Profiles

No	Name	Mass	Target Bias (V)	Time (secs)	Scale factor
1	O-16	16.0	-12.0	2.000	1.00000
3	C2-24	24.0	-12.0	2.000	3.50000

* MONOCRISTAL SIC / SIC FRITTE *
- Profil de repartition en profondeur dans la trace de frottement (zone 1) -

Figure 6 : SIMS profile in the track with 50 Pa oxygen

APPENDIX S

J.-M. Martin, "AES/XPS Analysis of Silicon Carbide Triboflats," Progress Report, Ecole Centrale de Lyon/SORETRIB, Lyon, France, 27 October 1989, Hughes P.O. S9-507874-SRW

AES/XPS ANALYSIS OF SILICON-CARBIDE TRIBOFLATS

XPS analysis (see figures)

The whole surface of the flat was analyzed by XPS after ion etching to remove the contamination from environmental.

The carbon 1s photopeak displays two contributions, one for carbide and the other for oxycarbide.

The silicon 2p also shows evidence for the presence of silicon oxycarbide (not silicon oxide).

After ion etching with 3 KeV argon ions for 2 mn, in the same conditions, the oxycarbide contribution decreased, in good agreement with the presence of this compound.

The thickness of the oxycarbide layer is estimated between 1 and 3 nm.

Neverthless, the SiC stoichiometry is not obtained after etching. This may be attributed to the effect of ionic bombardment.

AES analysis

AES spectra were obtained from outside and inside the friction wear scars.

Generally, the dark areas (for example HSIC 18 inside track 4) displayed a lower oxygen AES peak than the light areas (HSiC 19).

Unfortunately, it was not possible to see differences in the carbon AES peak.

a:hsic11.spc 27/10/1989 SiC Scan géné
Source E Anal : 100 Nombre de Cycles 8
Al
39221

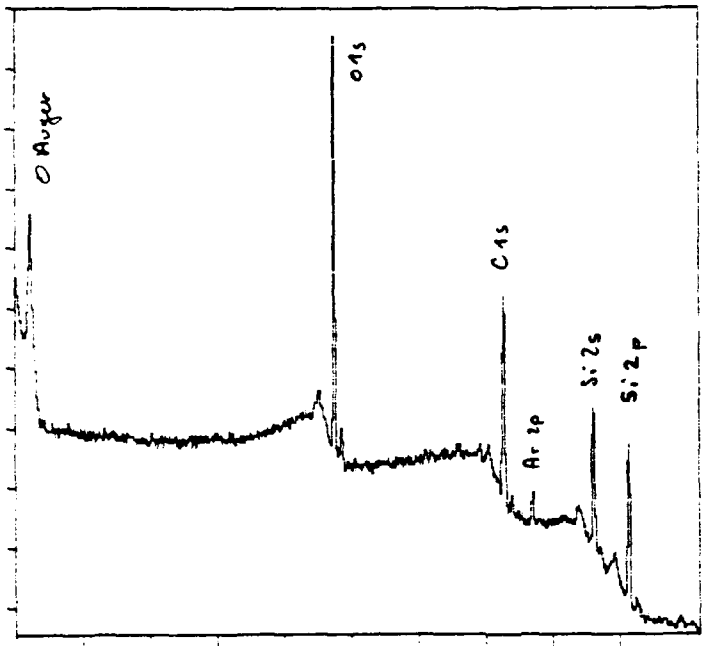

1484
1000.00 ENERGIE DE LIAISON 0.00

S-2

Forme : Assymetrique 0.45
aire : 8175
Intensité : 3124
Position : 533.10
Largeur : 2.35

a:hsic12.spc 27/10/1989 HsiC décapé 0 1s

Source Al E Anal : 50 Nombre de Cycles 50

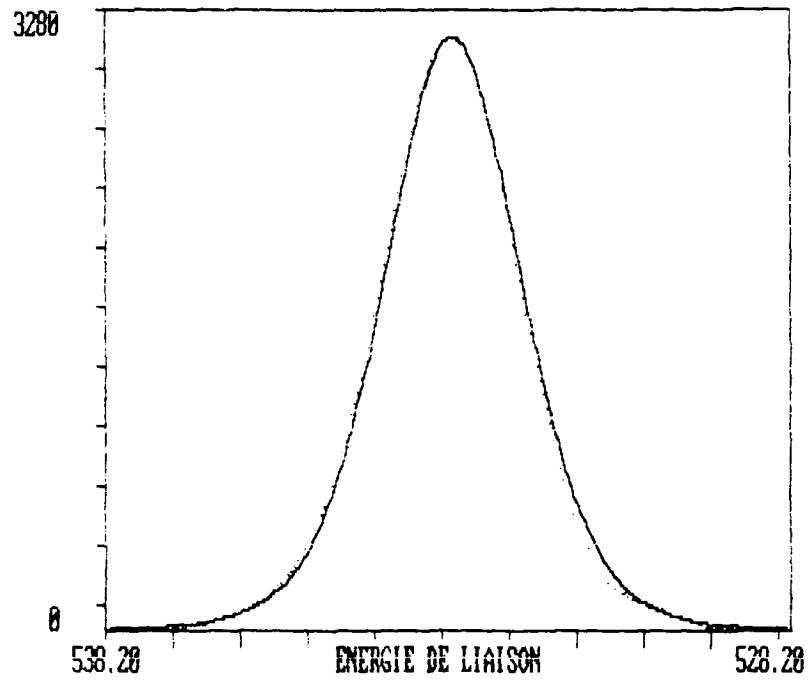

Borne 1 : 531.60 Borne 2 : 536.60 Aire brute = 410810

Raie : 1

Forme	:	Assymetrique	0.45
aire	:	3086	
Intensité	:	1074	
Position	:	284.08	
Largeur	:	2.17	

Raie : 2

Forme	:	Assymetrique	0.45
aire	:	2038	
Intensité	:	1015	
Position	:	285.89	
Largeur	:	2.17	

hsic13.spc 27/10/1989 HsiC décapé C 1s

Source Al E Anal : 50 Nombre de Cycles 50

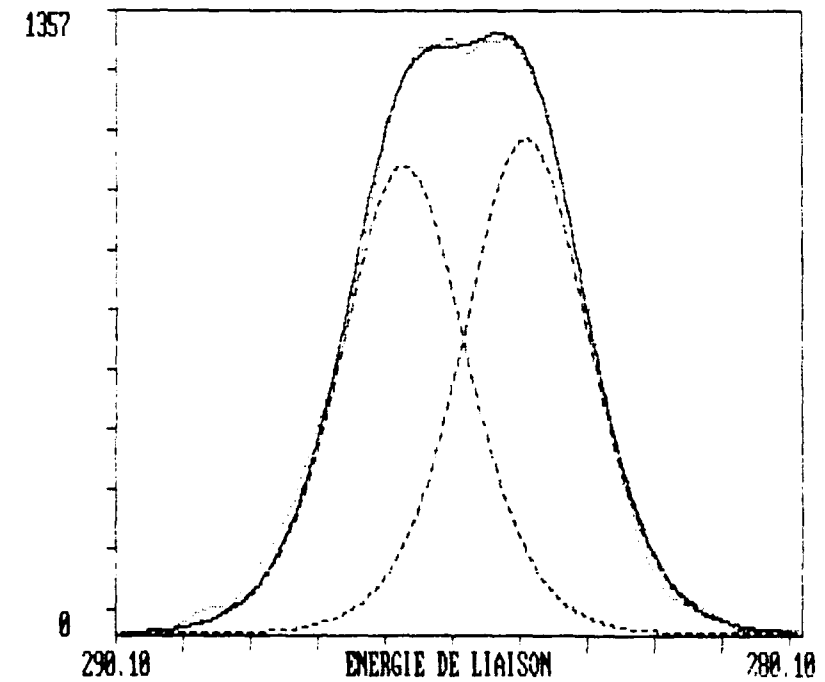

Borne 1 : 284.05 Borne 2 : 289.05 Aire brute = 102389

Raie : 1

Forme	:	Assymetrique	0.45
aire	:	2493	
Intensité	:	1116	
Position	:	101.30	
Largeur	:	2.00	

Raie : 2

Forme	:	Assymetrique	0.45
aire	:	1090	
Intensité	:	500	
Position	:	103.40	
Largeur	:	2.00	

hsic14.spc 27/10/1989 HsiC décapé Si 2p

Source Al E Anal : 50 Nombre de Cycles 50

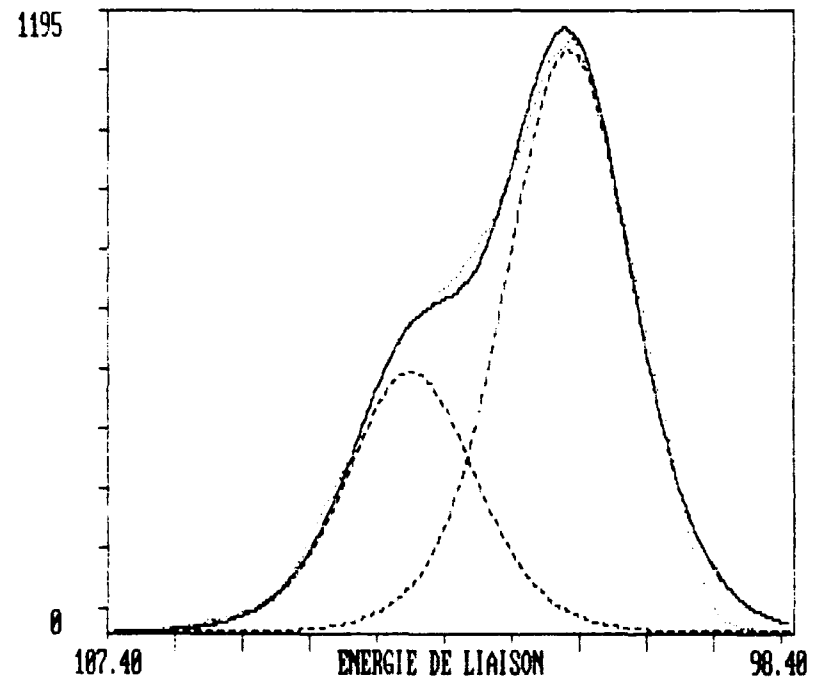

Borne 1 : 101.70 Borne 2 : 106.20 Aire brute = 54779

Raie : 1

Forme	:	Assymetrique	0.45
aire	:	6052	
Intensité	:	2513	
Position	:	532.42	
Largeur	:	2.10	

Raie : 2

Forme	:	Assymetrique	0.45
aire	:	930	
Intensité	:	397	
Position	:	533.80	
Largeur	:	2.10	

hsic15.spc 27/10/1989 HsiC 0 1s

Source Al E Anal : 50 Nombre de Cycles 50

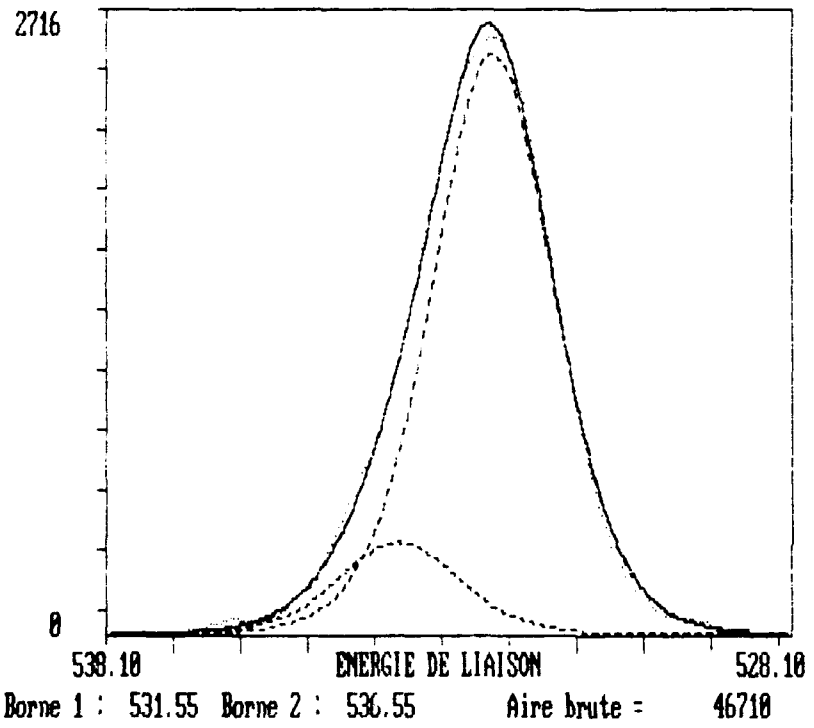

Borne 1 : 531.55 Borne 2 : 536.55 Aire brute = 46710

	Forme	:	Assymetrique 0.45
	aire	:	4312
	Intensité	:	1777
	Position	:	283.75
	Largeur	:	2.10
Raie : 2			
	Forme	:	Assymetrique 0.45
	aire	:	1450
	Intensité	:	604
	Position	:	285.44
	Largeur	:	2.10

hsic16.spc 27/10/1989 HsiC C 1s

Source Al E Anal : 50 Nombre de Cycles 50

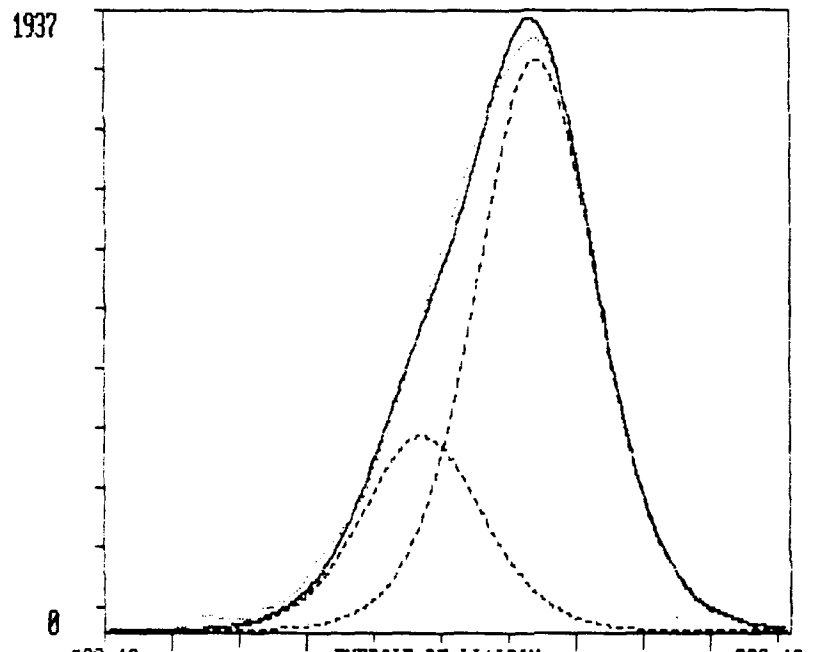

Borne 1 : 284.05 Borne 2 : 289.05 Aire brute = 72841

Raie : 1

Forme	:	Assymetrique	0.45
aire	:	3876	
Intensité	:	1659	
Position	:	100.91	
Largeur	:	2.10	

Raie : 2

Forme	:	Assymetrique	0.45
aire	:	845	
Intensité	:	343	
Position	:	102.99	
Largeur	:	2.10	

hsic17.spc 27/10/1989 HsiC Si 2p

Source Al E Anal : 50 Nombre de Cycles 50

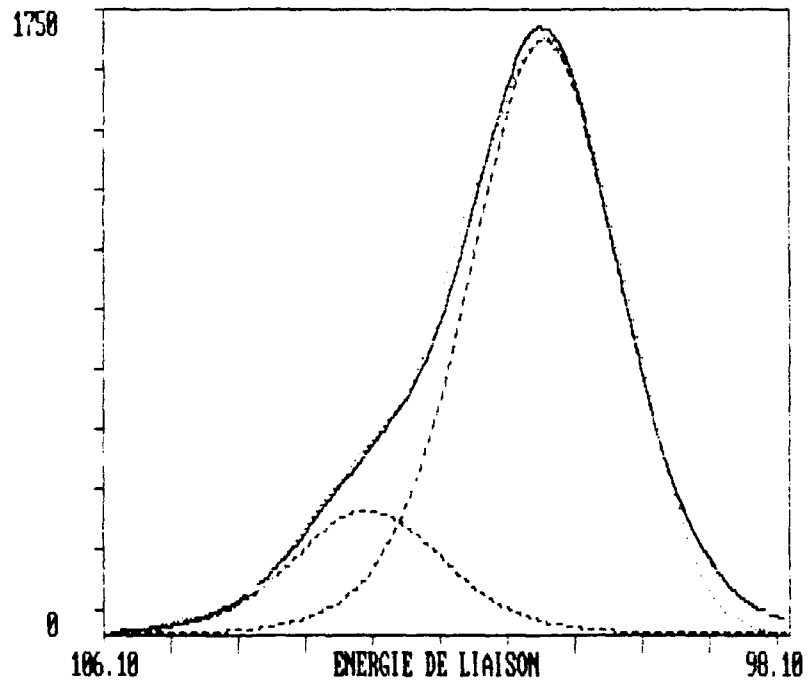

Borne 1 : 102.05 Borne 2 : 106.05 Aire brute = 42458

03-Nov-89 SiC Sintered GARDOS

élément	Position	Lmh	Aire	Sigma	Aire / Sigma	%	
	0	0	0		0.00	0.0%	
B 1s	0	0	0	0.13	0.00	0.0%	
	0	0	0		0.00	0.0%	
	282.6 284.08	2.17	3086		12344.00	29.8%	C-Si
C 1s	284.39 285.89 1.81	2.17	2038	0.25	8152.00	19.7%	C-O-Si ?
	0	0	0		0.00	0.0%	
	0	0	0		0.00	0.0%	
O 1s	531.6 533.1	2.35	8175	0.66	12386.36	29.9%	
	0	0	0		0.00	0.0%	
	0	0	0		0.00	0.0%	
N 1s	0	0	0	0.42	0.00	0.0%	
	0	0	0		0.00	0.0%	
	99.8 101.3	2	2493		5935.71	14.3%	Si C
Si 2p	101.9 103.4 2.1	2	1090	0.27	2595.24	6.3%	Si-O-C ?
	0	0	0		0.00	0.0%	
					41413.32	100.0%	

ΔeV = 1,5eV (calibration + effet de charge)

$\frac{C}{Si} = 2.08$.

la couche oxydé est faible. et en surface

↓

03-Nov-89 SiC Sintered GARDOS decape

element	Position	Lmh	Aire	Sigma	Aire / Sigma	%
	0	0	0		0.00	0.0%
B 1s	0	0	0	0.13	0.00	0.0%
	0	0	0		0.00	0.0%
	282.64 283.75	2.1	4312		17248.00	38.4%
C 1s	284.33 285.44 1.69	2.1	1450	0.25	5800.00	12.9%
	0	0	0		0.00	0.0%
	531.51 532.42	2.1	6052		9169.70	20.4%
O 1s	532.69 533.8	2.1	930	0.66	1409.09	3.1%
	0	0	0		0.00	0.0%
	0	0	0		0.00	0.0%
N 1s	0	0	0	0.42	0.00	0.0%
	0	0	0		0.00	0.0%
	99.8 100.91	2.1	3876		9228.57	20.6%
Si 2p	101.88 102.99 2.08	2.1	845	0.27	2011.90	4.5%
	0	0	0		0.00	0.0%
					44867.26	100.0%

ΔeV = 1.11.

$\frac{C-Si}{Si-C} = 1.86$.

a:hsic18.spc 27/10/1989 trace 4
Source CRR Rapport 4 Nombre de Cycles 16
ei

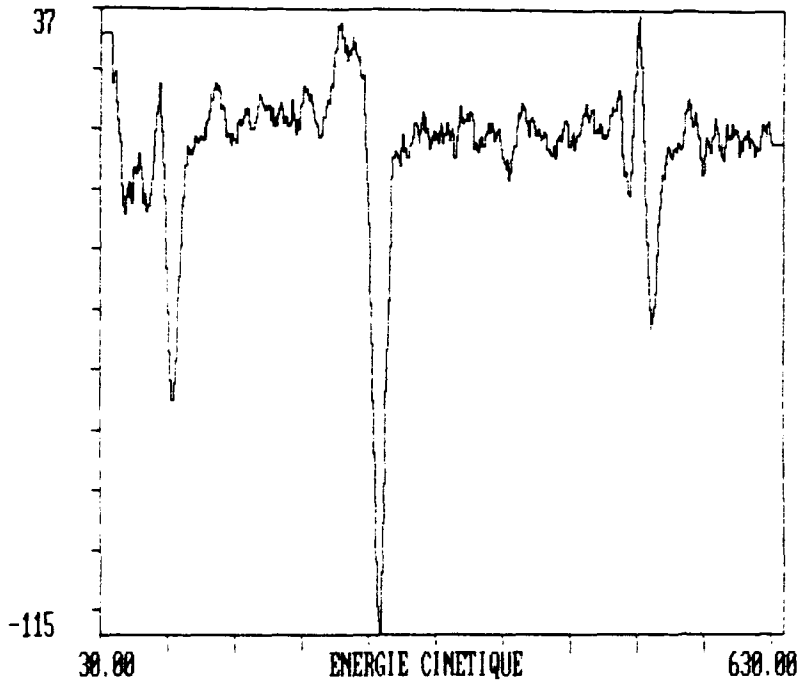

track 4.
black area.

a:hsic19.spc 27/10/1989 Hsic trace 4 zone sombr
Source CRR Rapport 4 Nombre de Cycles 18
ei

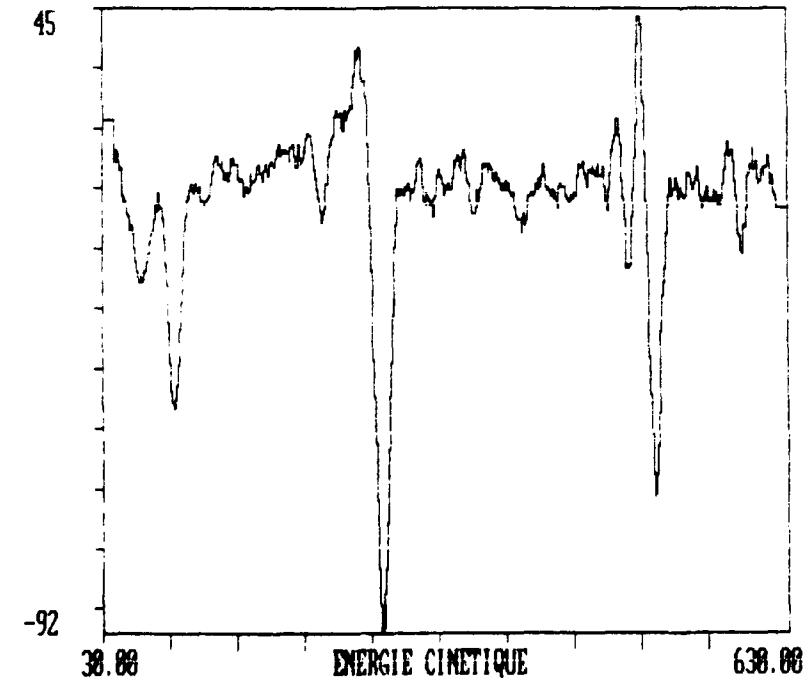

track 4
white area.

a:hsic20.spc 27/10/1989 Hsic G1000
Source CRR Rapport 4 Nombre de Cycles 11
el

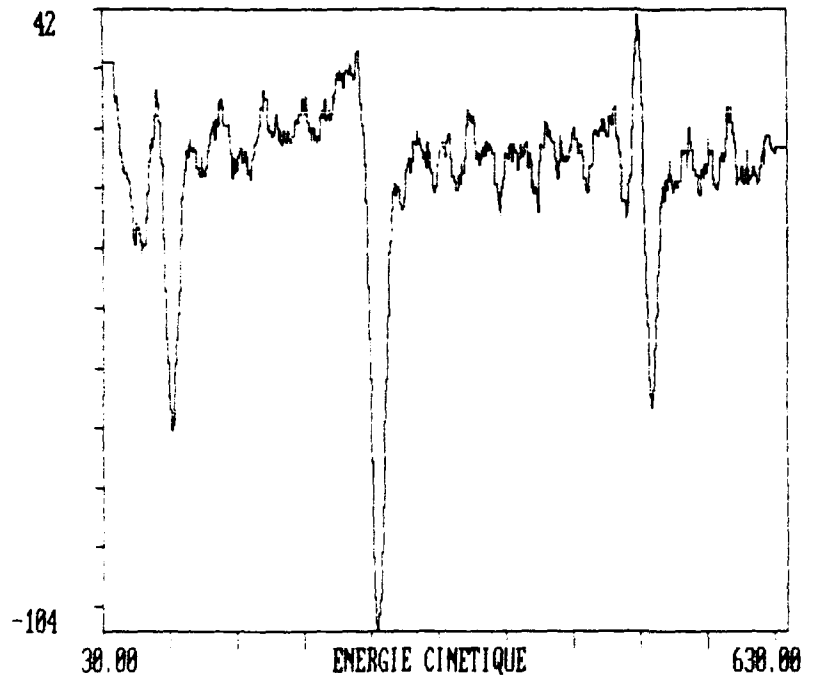

outside the track 4

a:hsic21.spc 27/10/1989 Trace 2 G2000
Source CRR Rapport 4 Nombre de Cycles 20
el

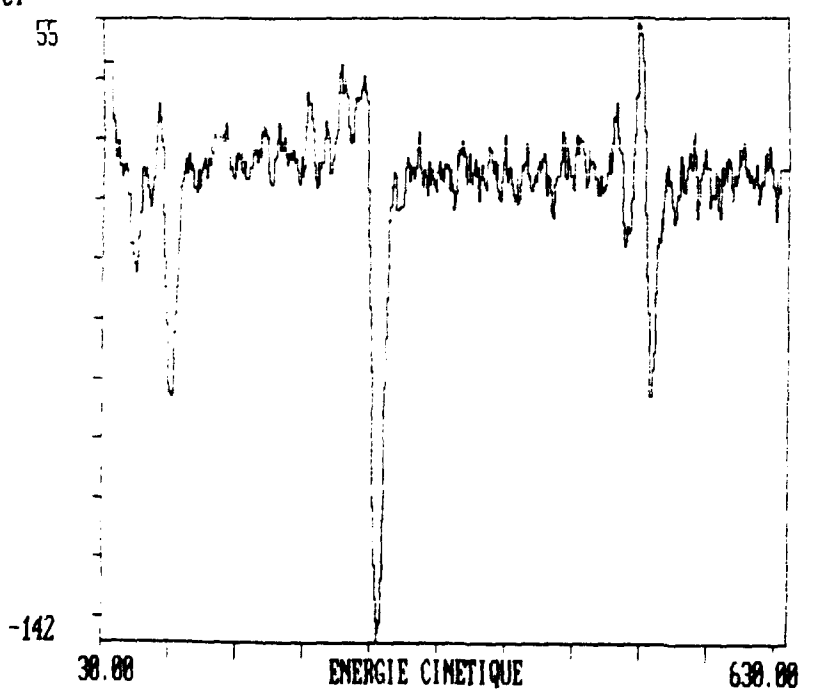

inside the track 2.

hsic6.spc 23/10/1989 SiC décapé 2 mn trace 1 G 200
Source CRR Rapport 4 Nombre de Cycles 6
el

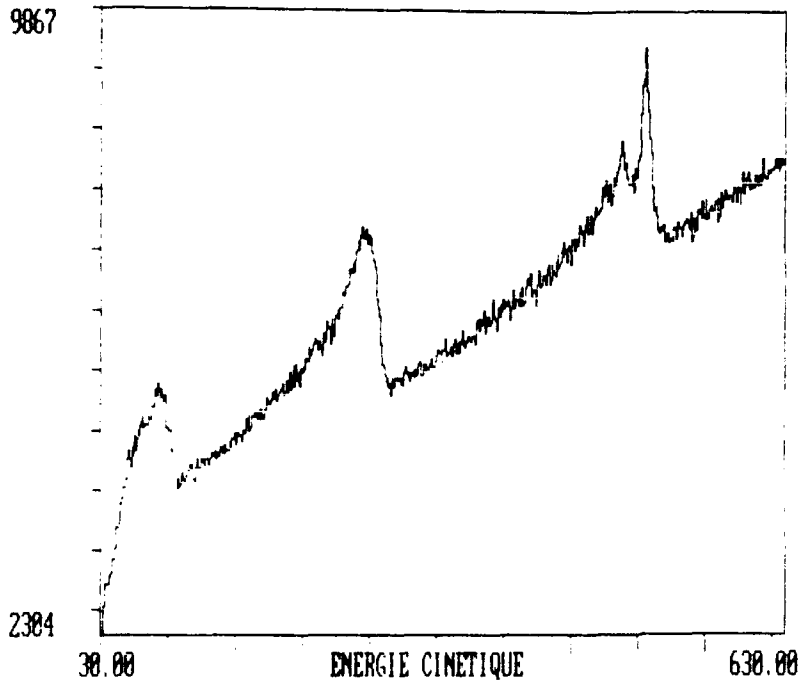

track 1.

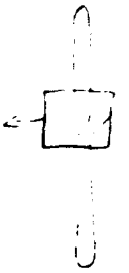

hsic6.spc 23/10/1989 SiC décapé 2 mn trace 1 G 200
Source CRR Rapport 4 Nombre de Cycles 6
el

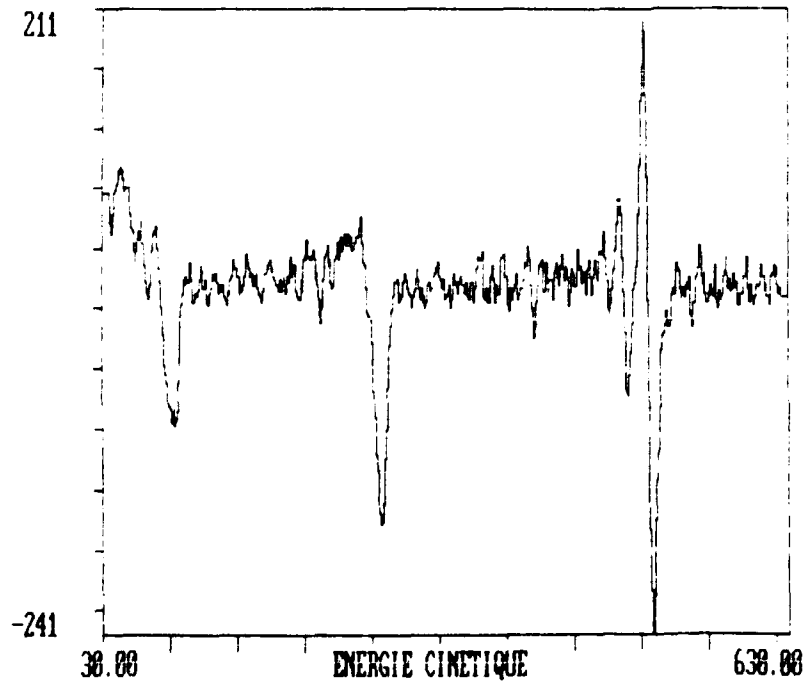

Silicium
lissé.

a:hsic9df.spc 23
Source CRR Rapport 4 Nombre de Cycles 1
Al

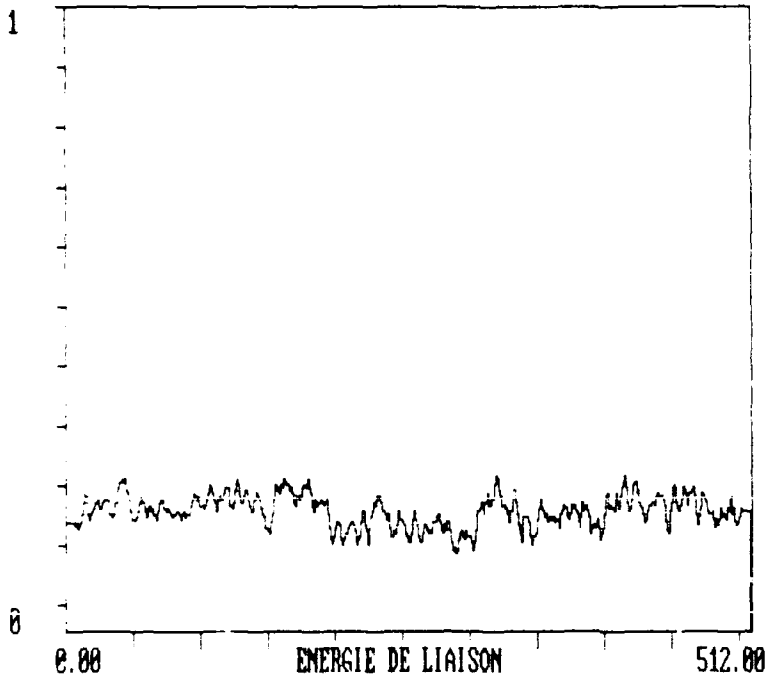

P_F
F
silicium.

Oxygène
Disse. 9pt/8cy.

sic7DL.spc 23
Source CRR Rapport 4 Nombre de Cycles 1
Al
3393

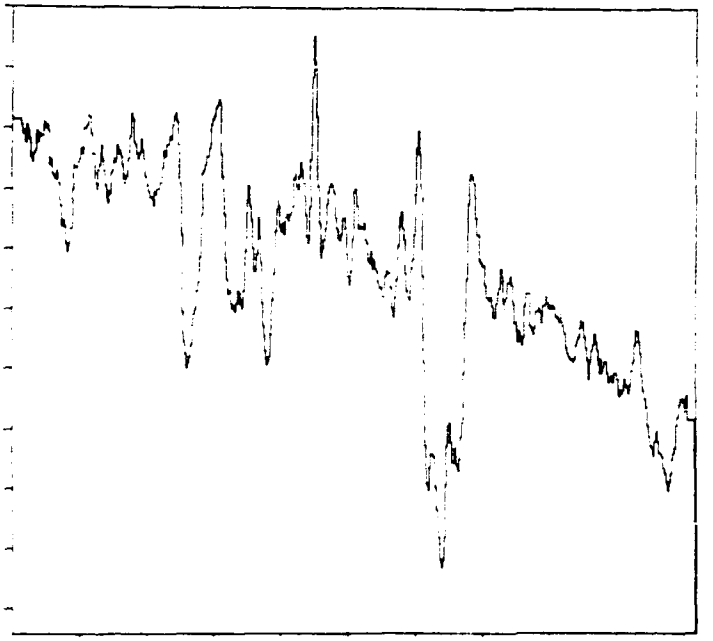

0
0.00 ENERGIE DE LIAISON 512.00

← P_F

hsic7dlf.spc 23
Source CRR Rapport 4 Nombre de Cycles 1
Al
1

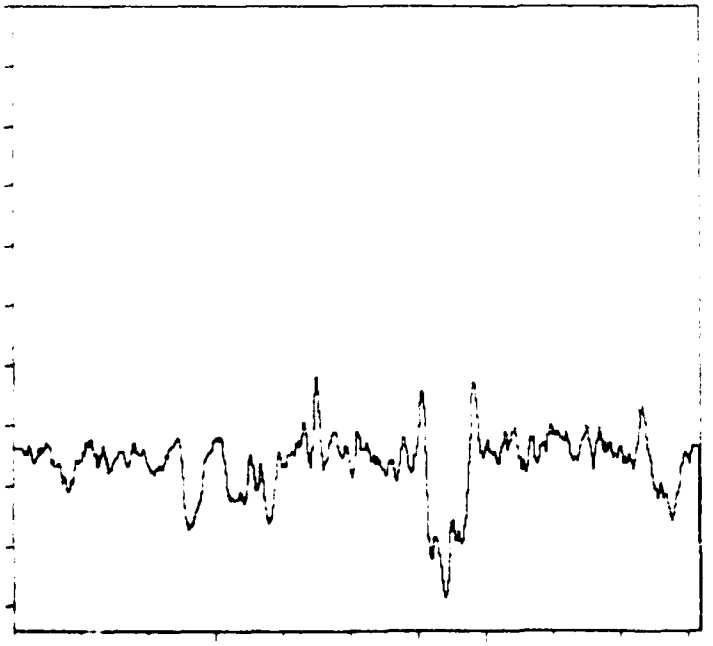

0

$\frac{P_F}{F}$ oxygen.

S-14

Carbone
lisse 9/2.

hsic8d.spc 23
Source CRR Rapport 4 Nombre de Cycles 1
Al

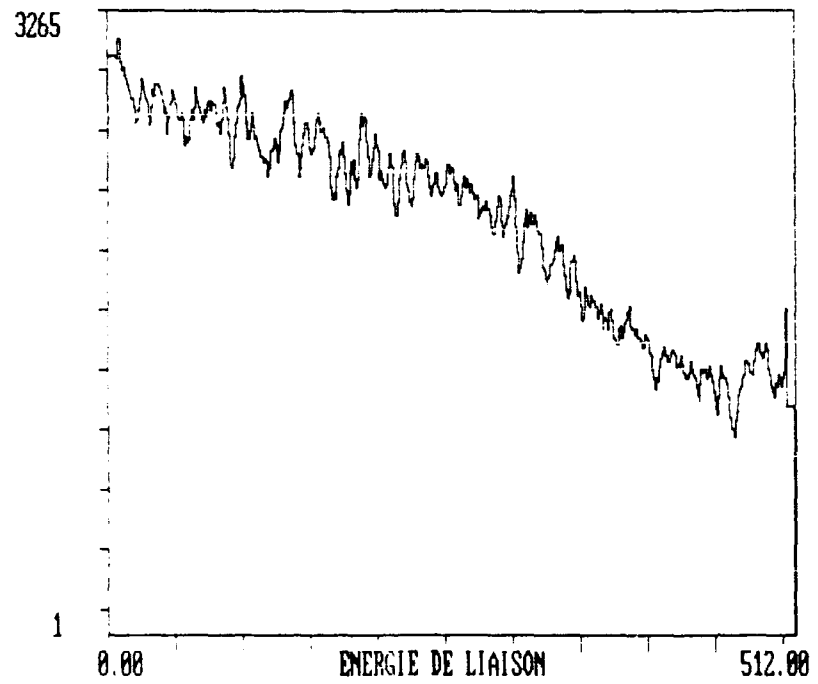

P - F

hsic8df.spc 23
Source CRR Rapport 4 Nombre de Cycles 1
Al

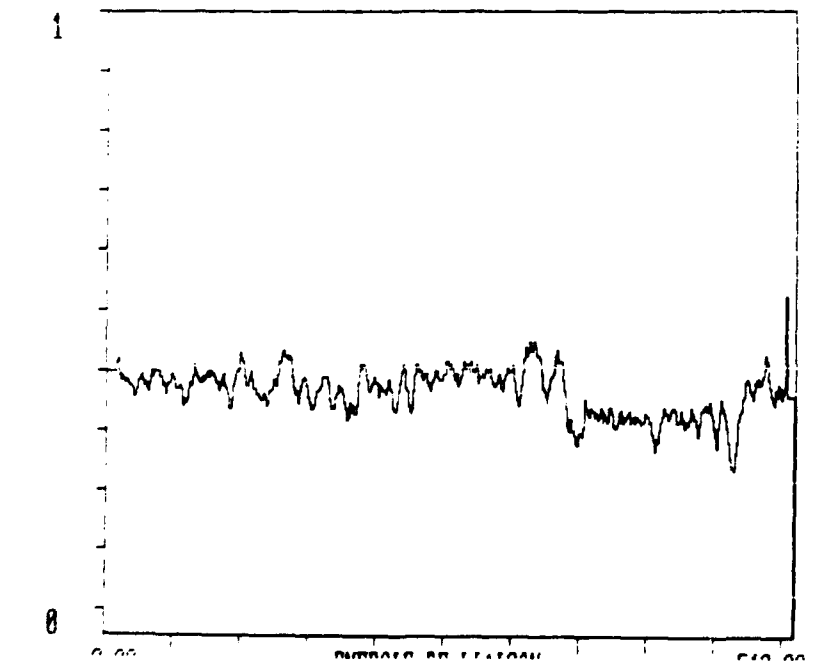

P_F
F

S-15

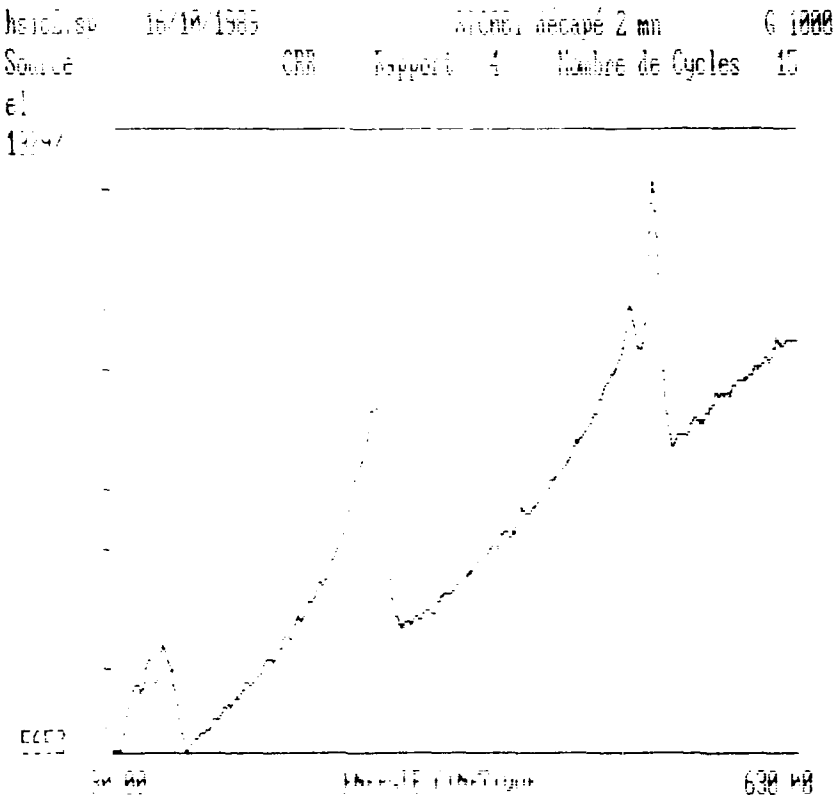

nside the track 1.

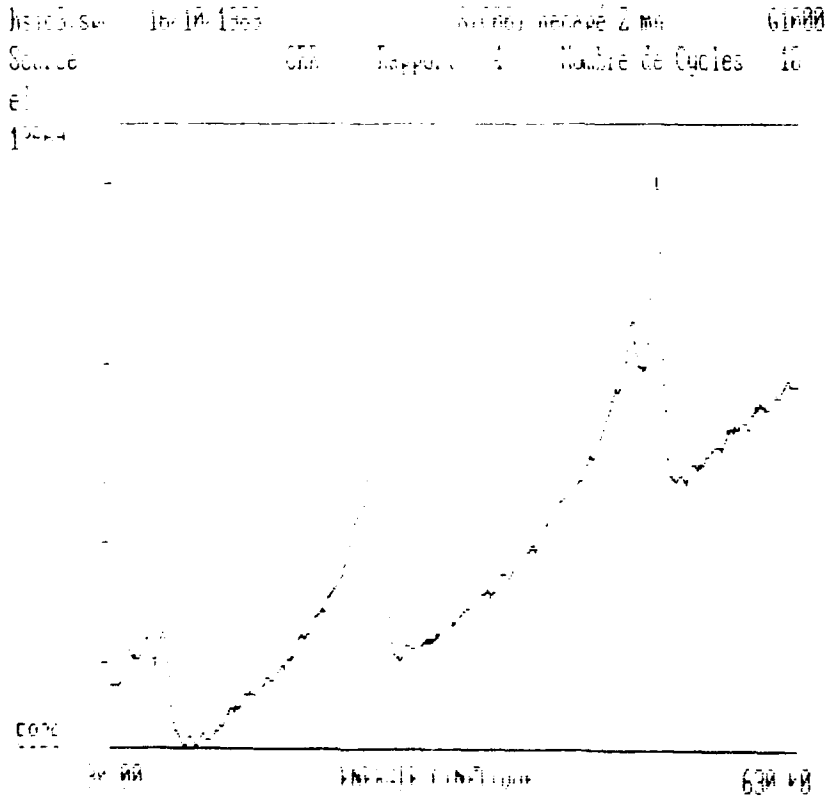

à côté de la

← track

outside the track 1

S-16

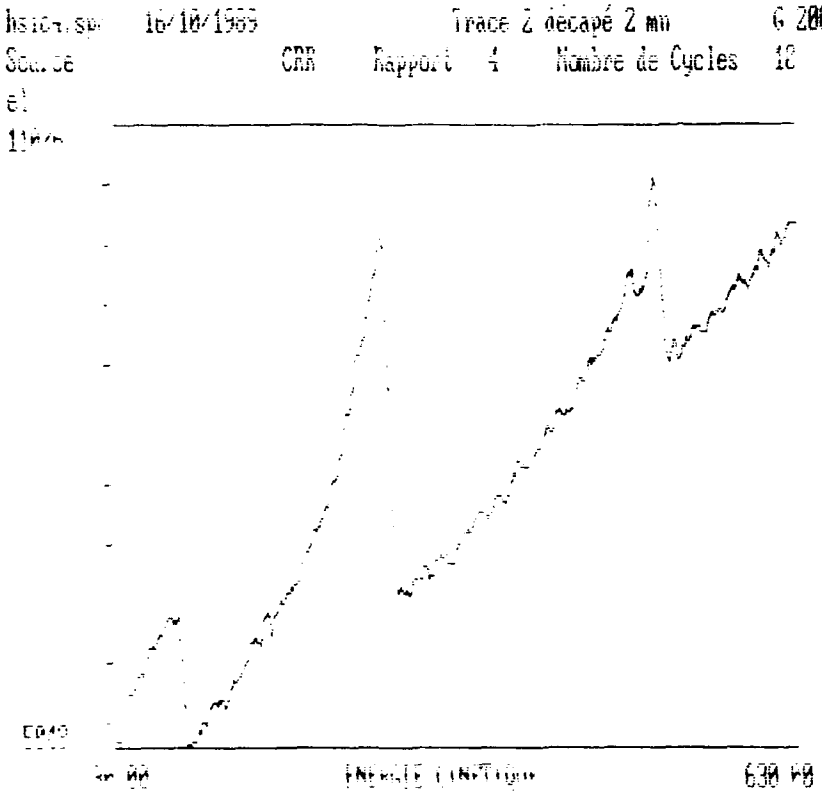

inside the track 2.

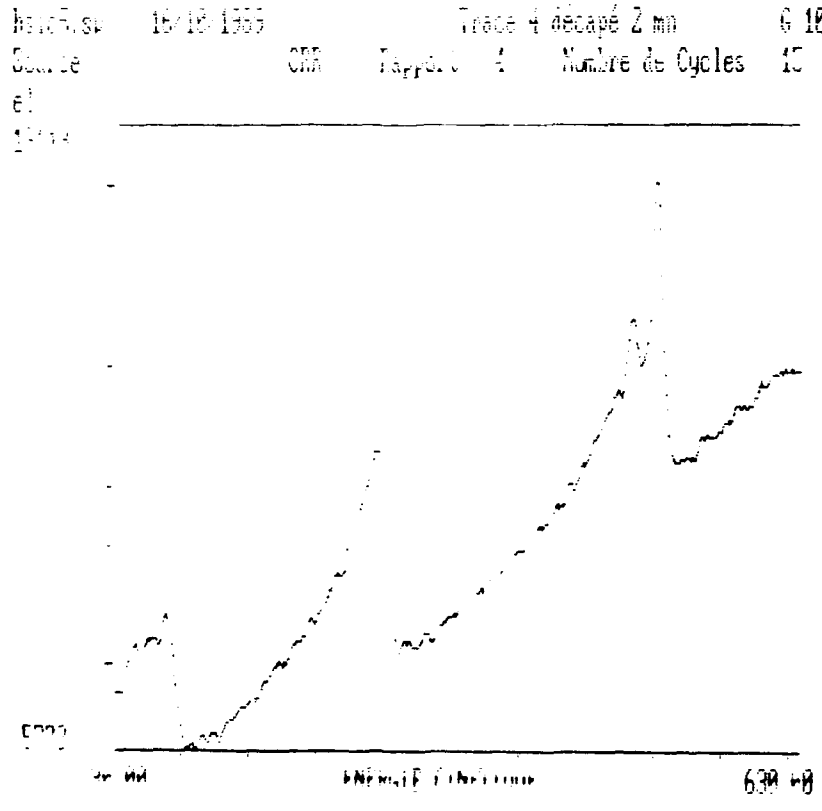

inside the track 4

S-17

APPENDIX T

B. Wong, "Assessment of Sharp and Spherical Indentation Techniques," Hughes Avoid Verbal Orders (AVO) Memo,25 July 1986

and

B. Wong, "Indentation for Tribocontact Fracture Characterization and Analysis," Hughes Interdepartmental Correspondence No. 7641.20/770, 06 January 1987

AVO

HUGHES

To: M. N. Gardos

From: B. Wong

Date: July 25, 1986

Subject: Assessment of Sharp and Spherical Indentation Techniques

cc: J. L. Cook

INTRODUCTION

Triboceramics like most of the high-strength materials may suffer considerable surface damage from even minute contact events. The cumulative effect of a large number of hard particle contacts that cause significant erosion and wear of their "brittle" surfaces usually results in a degradation of strength and reduction in their service lifetimes. Regardless of the complexity in "real" contact situations, relating to particle geometry, loading conditions, state of surfaces etc., this report reviews the mechanics fundamentals of Vickers(sharp) and Hertzian(spherical) contacts under static conditions and also presents their possible applications in evaluating materials properties relevant to tribological practice. The investigation of contact-induced fracture strength degradation under static and sliding conditions is deferred to a future study. Although real contact nature may lie anywhere between the extremes of ideally elastic and ideally plastic, the idealised spherical and sharp indentation fracture schemes set the boundaries to real contact behavior. The Hertzian(spherical) indentation is characterized by a perfectly elastic contact such that crack initiation is controlled by pre-existing surface flaws(cracks) whereas Vickers(sharp) indentation is characterized by elastic-plastic contact such that the subsurface flaws(cracks) are produced by the contact process itself. In general, the threshold load for crack initiation with a Vickers indenter is some orders of magnitude lower than that with a Hertzian indenter. However, once their indentation cracks have become well-developed, they all take the penny-like fracture geometry about a point-contact center.

VICKERS INDENTATION

The fracture-mechanics analysis[1] of Vickers indentation is based on the propagation of the mutually perpendicular penny-like median/radial cracks that form beneath the axisymmetric Vickers indenter as shown in Figure 1. P is the peak load and a and c are the characteristic dimensions of the plastically deformed impression and the median/radial crack, respectively. For an isotropic and homogeneous material, the elastic-plastic field created by the sharp indenter contributes two superposable components to the net driving force on the crack system, an elastic and a residual component. At the indentation surface, the elastic component is compressive whereas the residual component is tensile. The radial cracks, therefore, grow to their final dimensions as the indenter is unloaded; i.e., after the restraining compressive elastic field is removed. Accordingly, the residual field is the primary driving force for expanding the crack system into its final penny-like configuration. For a well-developed crack, $c \gtrsim 2a$, the penny-like crack may be considered to be center-point-loaded at the plastically deformed zone, the residual stress intensity factor may then be written

$$K_r = X_r (P/c^{3/2}) \qquad (1)$$

where X_r is a dimensionless indenter-material constant. It depends on the ratio of Young's modulus to hardness, E/H, to the one-half power,

$$X \approx 0.013 (E/H)^{0.5} \qquad (2)$$

Hardness H can be calculated from the deformed impression dimension a of the Vickers indentation whereas Young's modulus E may be evaluated by measuring elastic recovery of the in-surface dimensions of a Knoop indentation[2-5].

When the crack system is subject to mechanical equilibrium conditions both during and after the contact event, the radial cracks remain stable at $c = c_e$ as long as the residual stress intensity factor K_r is equal to the material facture toughness, K_{IC}.

$$K_{IC} = X_r (P/c_e^{3/2}) \approx 0.013 (E/H)^{0.5} (P/c_e^{3/2}) \qquad (3)$$

where c_e is the equilibrium crack dimension after indentation. Equation (3) is the equation for evaluating isotropic material fracture tonghness from the measurement of equilibrium crack dimension c_e after contact under the peak load P; its application to evaluate various brittle materials including polycrystalline ceramics, glasses and single crystal semiconductors have been

well documented[3,5-8]. Furthermore, an extension of the existing Vickers indentation mechanics, that allows internal stress anisotropy determinations and delayed failure predictions to be made upon a ceramic containing microelectronic system, has recently been developed[4]. The application of this new development to multilayer ceramic capacitors has been evaluated and verified[3,5,9].

HERTZIAN INDENTATION

Elastic Stress Field Distribution

When a spherical indenter of radius R is pressed into the flat surface of a sample, a complex and inhomogenious elastic stress field[10] is set up in the sample under and around the indenter (Figure 2). The load P is distributed over a circular region of radius a, the radius of contact, such that

$$a^3 = \frac{4kPR}{3E_s} \tag{4}$$

where E_s is the Young's modulus of the sample, R is the indenter radius and

$$k = \frac{9}{16}\left[(1-\nu_s^2) + (1-\nu_i^2)\frac{E_s}{E_i}\right] \tag{5}$$

where ν_s and ν_i are the Poisson's ratios of the sample and indenter, respectively and E_i is the Young's modulus of the indenter. During contact, the average contact pressure is $P/(\pi a^2)$. Directly below the indenter, the stresses are compressive while on the periphery and outside the contact circle in the sample surface plane, a radially-directed tensile stress σ_r which gradually diminishes away from the contact circle periphery is generated:

$$\sigma_r(r, z=0) = \frac{(1-2\nu_s)P}{2\pi r^2} \quad ; \quad r \geq a \tag{6}$$

where r is the radial distance from the center of the contact circle. Therefore the maximum tensile stress occurs on the contact circle periphery.

Below the sample surface outside the contact circle, the value of this tensile stress decreases rapidly with depth (z); i.e. a highly tensile "skin" in the sample surface outside the contact circle is created.

Fracture (Figure 3)

During contact between an elastic spherical indenter and an elastic-brittle flat sample, the indenter subjects pre-existing surface flaws to increasing tensile stress outside the expanding contact circle. Under a critical load P_c, initiation of a surface ring crack takes place at the most deleterious surfce flaw located outside the contact circle where the stress intensity factor K_I is the greatest; i.e. a critical Griffith configuration is established. Further loading results in continuous enlargement of the contact circle and rapid downward crack growth for the complete development of cone crack; outward deviation of the crack growth direction is to avoid the compressive zone directly underneath the contact circle. On still further loading, the contact circle eventually engulfs the surface ring crack and therefore closes the fracture surface. Applying the contact resistance technique initially developed by Grzybowski and Ruoff[11], the Hertzian cone cracking vs. load can be monitored and the critical load for crack initiation P_c may be determined (Figure 3).

Due to the extreme inhomogeneity of the Hertzian elastic field, by far there is no existing exact analytical solution to correlate the critical load, P_c, initial surface flaw size and fracture toughness. One can only apply expressions for limiting cases of small and large flaws[12] as shown in Figure 4:

1) Small flaw approach

When the initial flaw size $c_0^{\frac{1}{3}}$ is small compared with elastic field dimension a ($c_0^{\frac{1}{3}}/a \ll 0.01$), the inhomogeniety of the field along the crack trajectory is therefore negligibly small; i.e. the flaw is in a uniform field of tension. Crack initiates when Griffith conditions are fulfilled.

$$P_c = \alpha K_{Ic}^3 R^2 / (c_0^{\frac{1}{3}})^{3/2} = G R^2 \qquad (7)$$

where α is a constant of sample-indenter materials system, K_{Ic} is the fracture toughness, R and $c_0^{\frac{1}{3}}$ have their usual meanings,

$$G = \alpha K_{Ic}^3 / (c_0^{\frac{1}{3}})^{3/2}$$

is called Griffith's constant in this report. The dependence of the critical load on initial flaw size and indenter radius should be specially noted in Equation (7). For $c_0^{\frac{1}{3}}/a \ll$, this equation provides a pretty exact expression for fracture toughness or initial surface flaw size determination.

2) Large flaw approximation

When flaw size is sufficiently large such that the diminishing tensile stress gradient along the flaws becomes significant, i.e. $c_o^2/a \gtrsim 0.01$, the Griffith's configuration of uniform field does not hold. Various fracture-mechanics calculations yield the same general solution as follows[13,14] :

$$P_c = \beta K_{Ic}^2 R = AR \qquad (8)$$

where β is a constant of the sample-indenter materials system, this constant is sensitive to the reliability of individual fracture-mechanics model and knowledge of Poisson's ratio of the sample; also it can only be estimated to within an order of magnitude by numerical analysis, $A = \beta K_{Ic}^2$ is the Auerbach's constant. Equation (8) which suggests the linear dependence of P_c on R and the independence of P_c on c_o^2 , was first empirically discovered by Auerbach[15] and has been confirmed in a number of experimental studies[13,14,16] . This equation or sometimes called Auerbach's law breaks down in the limit of small surface flaws or large indenters. Although Auerbach's law has potential importance in that Auerbach's constant A contains the fracture toughness (fracture surface energy), the inability of predetermining the constant β in A to much better than an order of magnitude seems to be the drawback in applying the law alone to evaluate fracture parameters of materials.

SUMMARY

This report has reviewed some fundamentals of both sharp(Vickers) and spherical(Hertzian) indentation mechanics and their potential applications for fracture parameter determinations. From the mechanical testing point of view, sharp indentation is a better developed method and has been more widely applied as a test for mechanical assessment of high-strength materials[3-9] ; while spherical indentation, due to its involvement of a complex stress field, is therefore still debatable to be used for precise materials characterization without pre-calibration.

For interim experimental investigation on tribomaterials, I suggest:
1) apply sharp (Vickers and Knoop) indentation techniques to evaluate elastic, plastic, and fracture parameters as well as to determine possible internal stress anisotropies, crack velocities and delayed failure behavior;
2) in conjunction with the elastic and fracure properties measured in 1), within the Griffith's range, apply Hertzian fracture test to determine surface flaw statistics;
3) calibrate the Hertzian test with Vickers indentation results and extend it for high-temperature applications within its Auerbach's range.
On the other hand, for long-term indentation technique development for tribological studies, a "reliable and realistic" fracture-mechanics model for Hertzian cone cracking is called for; microstructural and mechanical nature of contact-induced strength degradation under static and sliding conditions should also be carefully investigated.

REFERENCES

1. B. R. Lawn, A. G. Evans, and D. B. Marshall, "Elastic/Plastic Indentation Damage in Ceramics: The Median/Radial Crack System", J. Am. Ceram. Soc., 63 [9-10] 574-81 (1980).

2. D. B. Marshall, Tatsuo Noma, and A. G. Evans, "A Simple Method for Determining Elastic-Modulus-to-Hardness Ratios Using Knoop Indentation Measurements", J. Am. Ceram. Soc., 65 [10] c175-76 (1982).

3. B. Wong, R. J. Holbrook, C. A. Megerle, and L. E. Medina, "Microindentation for Mechanical Assessment of Microelectronic Components", to be published, ISHM Proceedings, October 1986.

4. B. Wong, R. J. Holbrook, and C. A. Megerle, "Microindentation for Mechanical Integrity Assessment of Microelectronic Components I. Background and Technique development", to be published.

5. B. Wong, R. J. Holbrook, C. A. Megerle, and L. E. Medina, "Microindentation II. Assessment of the Strength and Fracture of Multilayer Ceramic Capacitors", to be published.

6. A. G. Evans and E. A. Charles, "Fracture Toughness Determinations by Indentation", J. Am. Ceram. Soc., 59 [7-8] 371-72 (1976).

7. G. R. Anstis, P. Chantikul, B. R. Lawn, and D. B. Marshall, "A Critical Evaluation of Indentation Techniques for Measuring Fractire Toughness:I. Direct Crack Measurements", J. Am. Ceram. Soc., 64 [9] 533-38 (1981).

8. B. R. Lawn, D. B. Marshall, and P. Chantikul, "Mechanics of Strength-Degrading Contact Flaws in Silicon", J. Mater. Sci., 16 [7] 1769-75 (1981).

9. B. Wong, R. J. Holbrook, C. A. Megerle, and L. E. Medina, "Microindentation III. Delayed Failure Predictions for Multilayer Ceramic Capacitors", to be published.

10. T. R. Wilshaw, "Hertzian Fracture Test", J. Phys. D, 4 [10] 1567-81 (1971).

11. T. A. Grzybowski and A. L. Ruoff, "New Method of Determining the Onset of Ring Cracking", Rev. Sci. Instrum., 54 [3] 357-60 (1983).

12. B. R. Lawn and T. R. Wilshaw, "Indentation Fracture: Principles and Applications", J. Mater. Sci., 10 [6] 1049-81 (1975).

13. I. B. Langitan and B. R. Lawn, "Hertzian Fracture Experiments on Abraded Glass Surfaces as Definitive Evidence for an Energy Balance Explanation of Auerbach's Law", J. Appl. Phys., 40 [10] 4009-17 (1969).

14. R. Warren, "Measurement of the Fracture Properties of Brittle Solids by Hertzian Indentation", Acta Met., 26 1759-69 (1978).

15. F. Auerbach, "Measurement of Hardness", Ann. Phys. Chem. 43, 61-100 (1891).

16. B. R. Lawn, "Hertzian Fracture in Single Crystals with the Diamond Structure", J. Appl. Phys. 39 [10] 4828-36 (1968).

FIGURE CAPTIONS

Figure 1. Schematic of a Vickers-produced indentation-fracture system under a peak load P showing penny-like median/radial cracks and hardness impression; lateral cracks parallel to the surface included for reference.
(a) a section normal to the indented surface.
(b) the indented surface.

Figure 2. Elastic stress distributions during contact between a spherical indenter and a flat specimen.

Figure 3. Evolution of Hertzian crack pattern during loading monitored by contact resistance measurement.

Figure 4. Critical load for Hertzian cone fracture P_c as a function of indenter radius R.

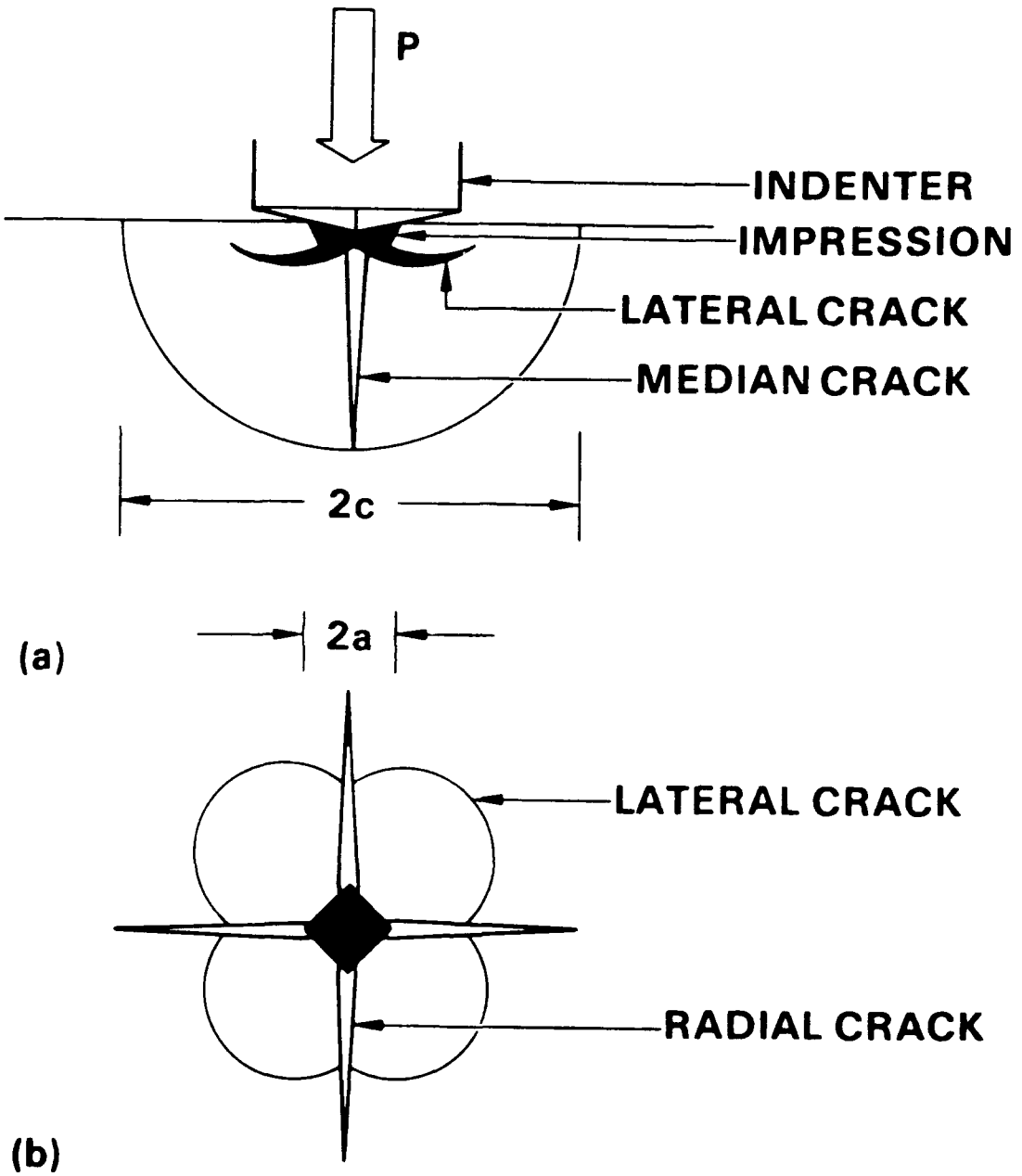
P
INDENTER
IMPRESSION
LATERAL CRACK
MEDIAN CRACK
2c
(a)
2a
LATERAL CRACK
RADIAL CRACK
(b)

FIG. 1

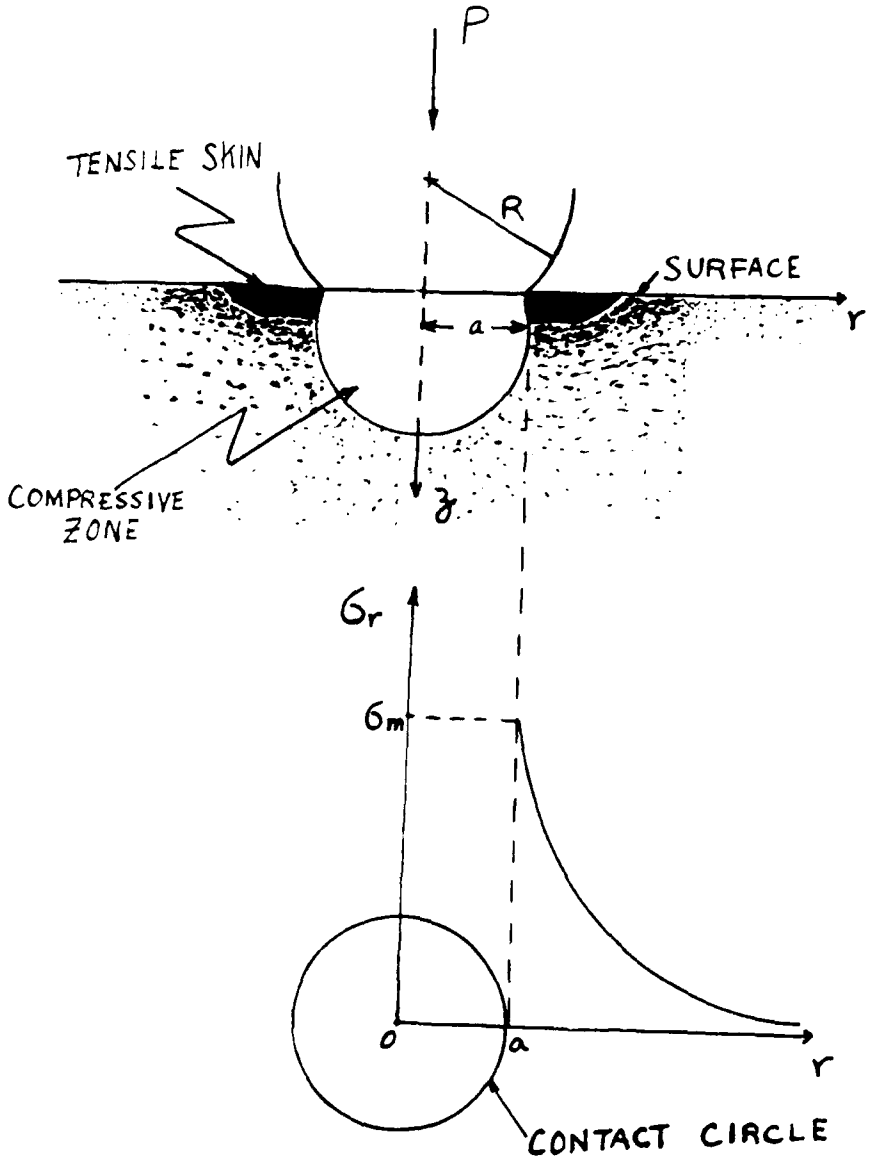
P
TENSILE SKIN
R
SURFACE
r
a
COMPRESSIVE ZONE
z
σ_r
σ_m
0
a
r
CONTACT CIRCLE

FIG. 2

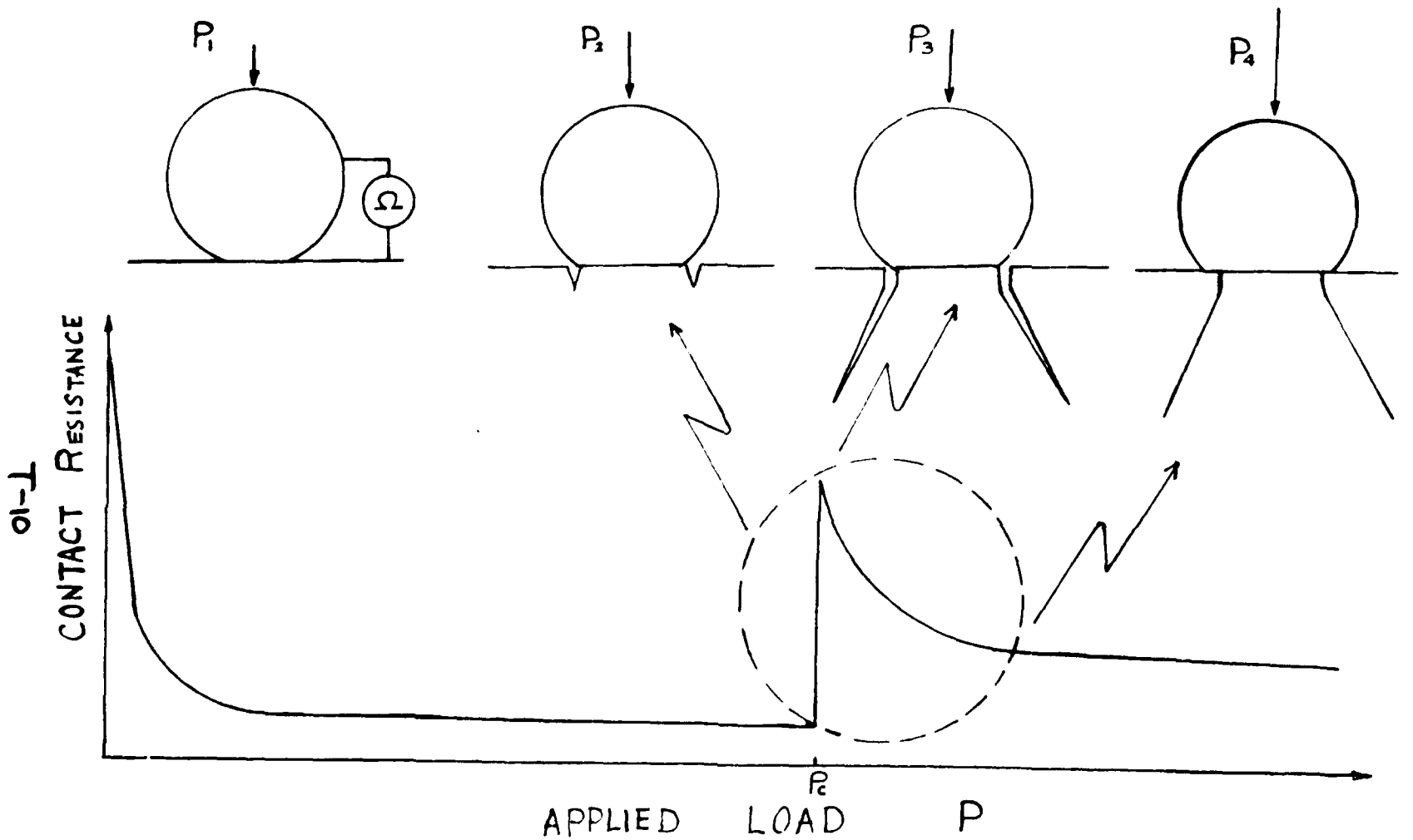

FIG. 3

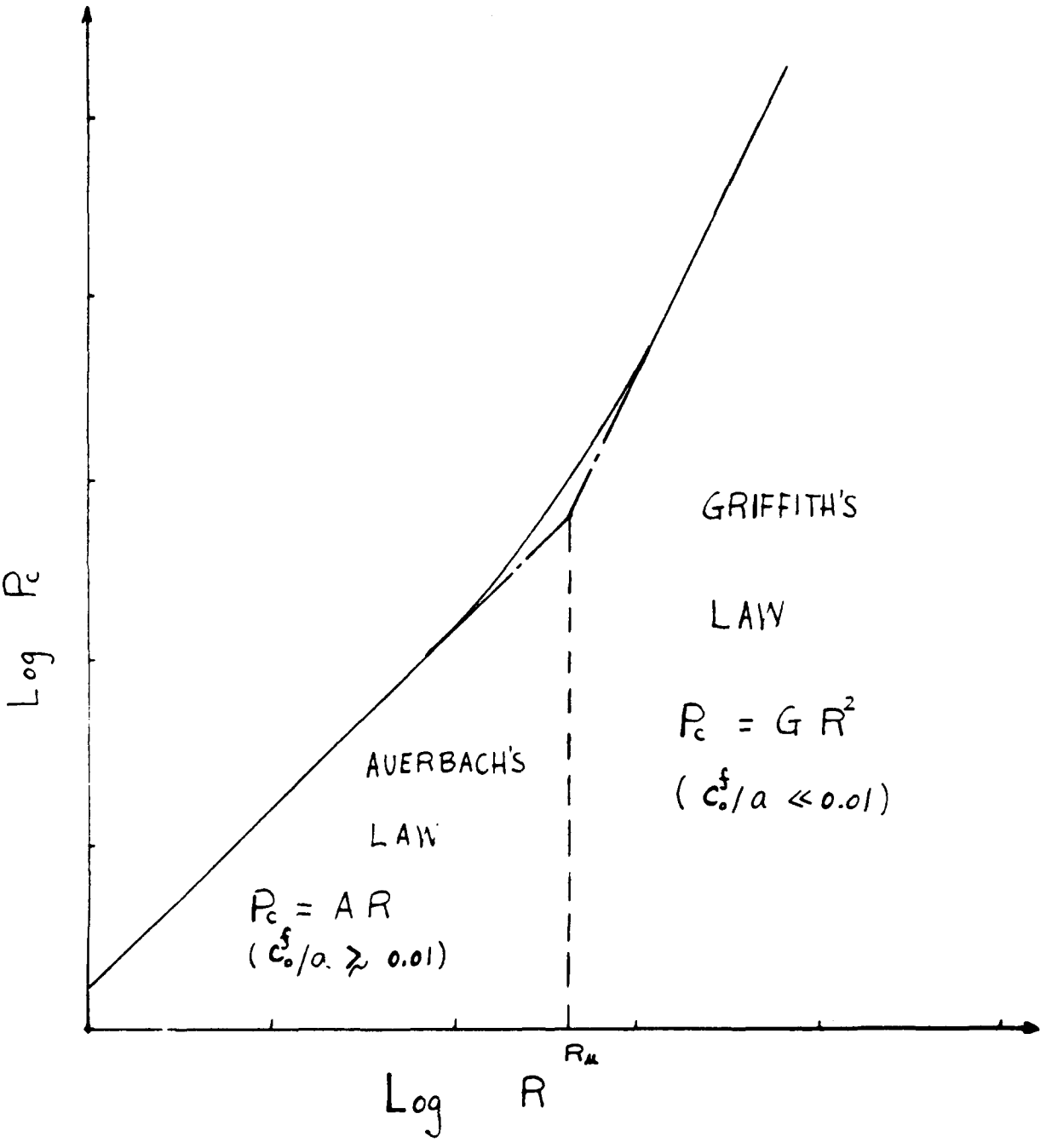
Log P_c
GRIFFITH'S
LAW
$P_c = G R^2$
$(c_o^f/a \ll 0.01)$
AUERBACH'S
LAW
$P_c = A R$
$(c_o^f/a \gtrsim 0.01)$
R_m
Log R

FIG. 4

HUGHES

INTERDEPARTMENTAL CORRESPONDENCE

TO: M.N. Gardos
ORG: 76-21-10

CC: D.H. Buettner, J.L. Cook, S.S. Gassel, E.B. Holst, A.B. Naselow, R.Y. Scapple, R.W. Seibold, J.A. Zelik

DATE: 06 January 1987
REF. 7641.20/770

SUBJECT: Indentation for Tribo-Contact Fracture Characterization and Analysis

FROM: B. Wong
ORG. 76-41-20

BLDG. E1 MAIL STA. C132
LOC. E0 PHONE 60656

I. INTRODUCTION AND SUMMARY

The purpose of this IDC is to report the relevance of some important fracture parameters to tribocontact lifetime predictions under high-speed contact motion conditions. We were asked by the Darpa/Hughes Tribology Program to evalute the applications of Hertzian (spherical) and Vickers (sharp) indentation techniques for the determinations of some of these parameters for triboceramics having various contact surface conditions.

The importance of both fracture toughness K_{IC} and hardness H upon fracture domiated wear rate of a tribocontact has been recognized (1-3). It is believed that an optimum combination of these two fundamental tribological parameters usually gives materials of superior wear resistance. Hardness studies as a means of assessing general mechanical properties have been a predominant theme since last century; the techniques involved in hardness measurements have been established and well-documented (4). In contrast, fracture toughess studies did not evolve until early 1960's; the techniques evaluating fracture toughness of engineering materials/components, having a complex stress-strain behavior and geometry, are still needed to be developed. In addition to the thermomechanical stress $\sigma_T + \sigma_A$, the subcritical crack growth characteristics, the fracture toughness, the initial

surface flaw size, and the surface residual stress are all important and necessary to an accurate time-to-failure prediction for a contact under high-speed motions. Indentation techniques in conjunction with pertinent fracture-mechanics methods are justified and applicable for the measurement of these important parameters.

II. PARAMETERS RELEVANT TO HIGH-SPEED TRIBOCONTACT FAILURE

Under high-speed motion conditions, the most probable failure mechanism of a triboceramic contact is believed to be thermal fatigue. This is a fatigue resulting from subcritical crack growth at stress levels below those required for rapid fracture induced by repeated thermal shock. The crack growth rate or crack growth per cycle during thermal fatigue could be expressed by

$$\frac{d\tilde{c}}{dN} \propto \frac{d\tilde{c}}{dt} = AY^n \tilde{c}^{n/2} \left(\sum_{j=1} \sigma_j\right)^n \exp\left(\frac{-Q}{RT}\right) \qquad [1]$$

where

$d\tilde{c}/dN$ is the crack growth per cycle

$d\tilde{c}/dt$ is the crack growth rate

$\tilde{c}$ is the crack size

$\sum\sigma_j$ is the algebraic sum of the stresses; i.e., the sum of thermal σ_T, applied σ_A and residual σ_R stresses

T is the temperature at maxium $\sum\sigma_j$

Y is a geometrical factor, A, n and Q are all empirical terms obtained from subcritical crack growth studies (5). The prediction of time-to-failure (cycles-to-failure) for a triboceramic may then be made by solving the differential equation, i.e., Equation [1] using the following initial and boundary conditions:

I.C.: $\tilde{c} = \tilde{c}_i > \tilde{c}_{th}$, $t = o$

B.C.: $\tilde{c} = \tilde{c}_f = \left(\frac{K_{IC}}{Y \sum \sigma_j}\right)^2$, $t = t_f$

where $\tilde{c}_i$, $\tilde{c}_{th}$ and $\tilde{c}_f$ are initial, threshold and failure crack sizes, respectively. K_{IC} is the fracture toughness at temperature T. Therefore,

$$N_f \propto t_f = \left(\frac{2}{2-n}\right) Y^{-n} A^{-1} \left(\sum_{j=1} \sigma_j\right)^{-n} \exp\left(\frac{Q}{RT}\right) \left[\left(\frac{K_{IC}}{Y \sum_{j=1} \sigma_j}\right)^{2-n} - \tilde{c}_i^{(2-n)/2}\right] \qquad [2]$$

N_f or t_f of a tribocontact under high-speed motion conditions can be calculated only if K_{IC}, $\tilde{c}_i$ and $\sum_{j=1} \sigma_j$ are pre-determined as well as subcritical crack growth in the ceramic material is well characterized. Only mode I fracture, K_{IC}, is considered here for the thermal fatigue (Equation [1]) because crack propagation in ceramics has almost exclusively been confined to the opening mode (6).

III. INDENTATION FOR TRIBOCONTACT CHARACTERIZATION

The reasons for the choice of indentation approach for fracture parameter evaluations for triboceramic contacts against other techniques (double-cantilever beam, four-point bending, etc.) are threefold. First, the sample preparation and data collection procedures needed with this approach are simple. Second, actual materials/components, even irregular in shape and small in size, can be used as samples. Third, because of their high spatial resolution of about 100 micrometers, applications of these techniques yield comprehensive and precise point-by-point, mechanical characterization within the microstructurally complex tribomaterials/components, while using minimal amount of sample material, and causing minimal damage to irreplaceable samples.

Our indentation studies in silicon nitride triboceramics are proposed to be performed at room-temperature; the data and results obtained, however, will well apply to predictions of mechanical failures of contacts at elevated temperatures due to the little temperature dependence of the pertinent physical properties of

silicon nitride below 1000°C (7). Some applications of indentation techniques for various triboceramic measurements are summarized in Table 1. Details of the analyses and justifications for the techniques are attached in this report as appendices. Figures 1 and 2 are plots showing different deformation modes for various materials during Hertzian and Vickers indentations, respectively. These plots are generated based on rigid-elastic, elastic-plastic and rigid-plastic theories (Appendix A). Hertzian analysis (Appendix B), orginated from the theory of elasticity, applicable for initial surface flaw (crack) size determination (small-flaw approximation), fails to apply to "soft" materials either in a bulk or layer form having $(E^{2/3}/Y) \gtrsim 0.015$ (Figure 1). On the other hand, Vickers indentation, whose analysis (8) is based on elastic-plastic deformation concept and far-field approximation, remains valid for K_{IC} measurements for most materials (Figure 2), including ceramics having a thin, rigid-plastic surface layer (Appendix C). In addition, fracture-mechanics analysis (Appendix D) has also successfully extended the application of Vickers indentation for the measurement of surface residual stress σ_R caused by a strain mismatch between a hard surface layer and the ceramic as shown in Figure 3.

IV. FUTURE WORK

Since predictions of lifetimes for tribocontacts under high-speed motions require accurate knowledge of those fracture parameters mentioned earlier in this report, I therefore propose that the future work in the Tribology Program must include:

1. subcritical cracking characterization of the contacts at elevated temperatures;
2. Hertzian and Vickers indentations on the contacts for the evaluations of K_{IC}, $\tilde{c}_i$, and σ_R;

3. thermomechanical stress analyses under anticipated high-speed contacting motion conditions (9) for $\sigma_T + \sigma_A$ determinations within elastic, elastic-plastic and rigid-plastic regimes.

Let me once again emphasize that these three listed research items are all necessary for a fundamental understanding of the high-speed tribocontact performance.

ACKNOWLEDGEMENT

Helpful discussions with Mr. J.L. Cook in preparation of this report are gratefully acknowledged.

Boon Wong

B. Wong

BW/ik

References

1. Omar, M.K., Atkins, A.G., and Lancaster, J.K., "The Role of Crack Resistance Parameters in Polymer Wear", J. Phys. D: Appl. Phys., 19, 177-95 (1986).

2. Baldoni, J.G., Wayne, S.F., Buljan, S.T., "Cutting Tool Materials: Mechanical Properties - Wear Resistance Relationships", ASLE Trans., 29[3], 347-52 (1986).

3. Gardos, M.N., "Determination of Tribological Fundamentals of Solid Lubricated Ceramics", Contract F33615-85-C-5087, Second Semiannual Report, 1 May 1986 through 31 October 1986, Hughes Aircraft Company, El Segundo, CA, 15 November 1986.

4. Tabor, D., "The Hardness of Metals", Clarendon Press, Oxford (1951).

5. Evans, A.G., Russell, L.R., and Richerson, D.W., "Slow Crack Growth in Ceramic Materials at Elevated Temperatures", Metall, Trans. A, 6[4], 707-16 (1975).

6. Evans, A.G. and Langdon, T.G., "Structural Ceramics", Progress in Materials Science, 21 [3-4] (1976).

7. Evans, A.G. and Wiederhorn, S.M., "Crack Propagation and Failure Prediction in Silicon Nitride at Elevated Temperatures", J. Mater. Sci., 9, 270-78 (1974).

8. Lawn, B.R., Evans, A.G., and Marshall, D.B., "Elastic/Plastic Indentation Damage in Ceramics: The Median/Radial Crack System", J. Am. Ceram. Soc., 63[9-10], 574-81 (1980).

9. a) Ju, F.D. and Chen, T.Y., "Thermomechanical Cracking in Layered Media from Moving Friction Load", J. Tribology, 106[10], 513-18 (1984).

   b) Gassel, S.S., to be proposed.

Table 1. Applications and Limitations of Various Indentation Techniques for Triboceramic Measurements.

INDENTATION / MATERIAL	HERTZIAN		VICKERS	
	CONDITION	A/NA*	CONDITION	A/NA*
CERAMICS	$R > a \gg \bar{\varepsilon}_i$	A ($\bar{\varepsilon}_i$)	$c_o \gg a$	A (K_{IC})
	$\bar{\varepsilon}_i \gtrsim 0.01\,a$	NA		
CERAMICS COATED WITH A "HARD" LAYER	$R > a \gg \bar{\varepsilon}_i$ AND $\delta > \bar{\varepsilon}_i$	A ($\bar{\varepsilon}_i$)	$c_o \gg a$	A(K_{IC}, σ_R)
	$\bar{\varepsilon}_i > \delta$ OR $\bar{\varepsilon}_i \gtrsim 0.01\,a$	NA		
CERAMICS COATED WITH A "SOFT" LAYER	INELASTIC REGIME	NA	$c_o \gg a \gg \delta$	A (K_{IC})
		NA	$c_o \lesssim a$ OR $\delta \gtrsim a$	NA

* A FOR "APPLICABLE"; NA FOR "NOT APPLICABLE"

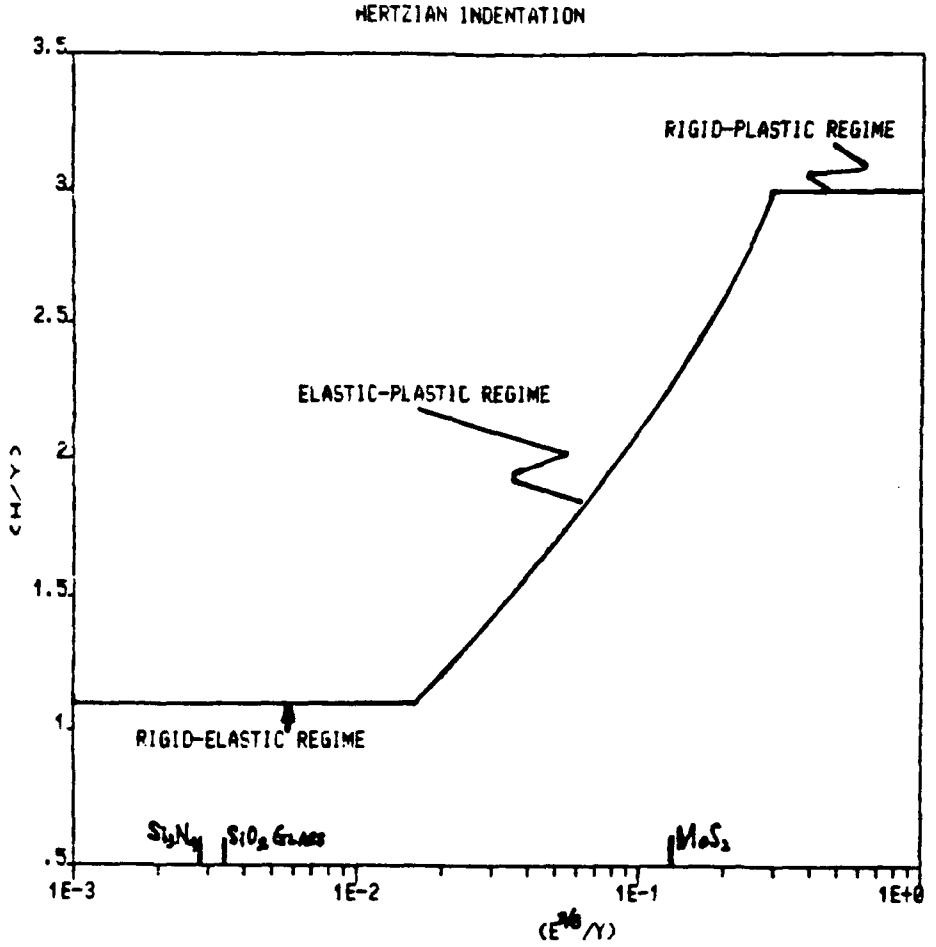

Figure 1. Different deformation modes for various materials at the proposed maximum experimental load during Hertzian indentation.

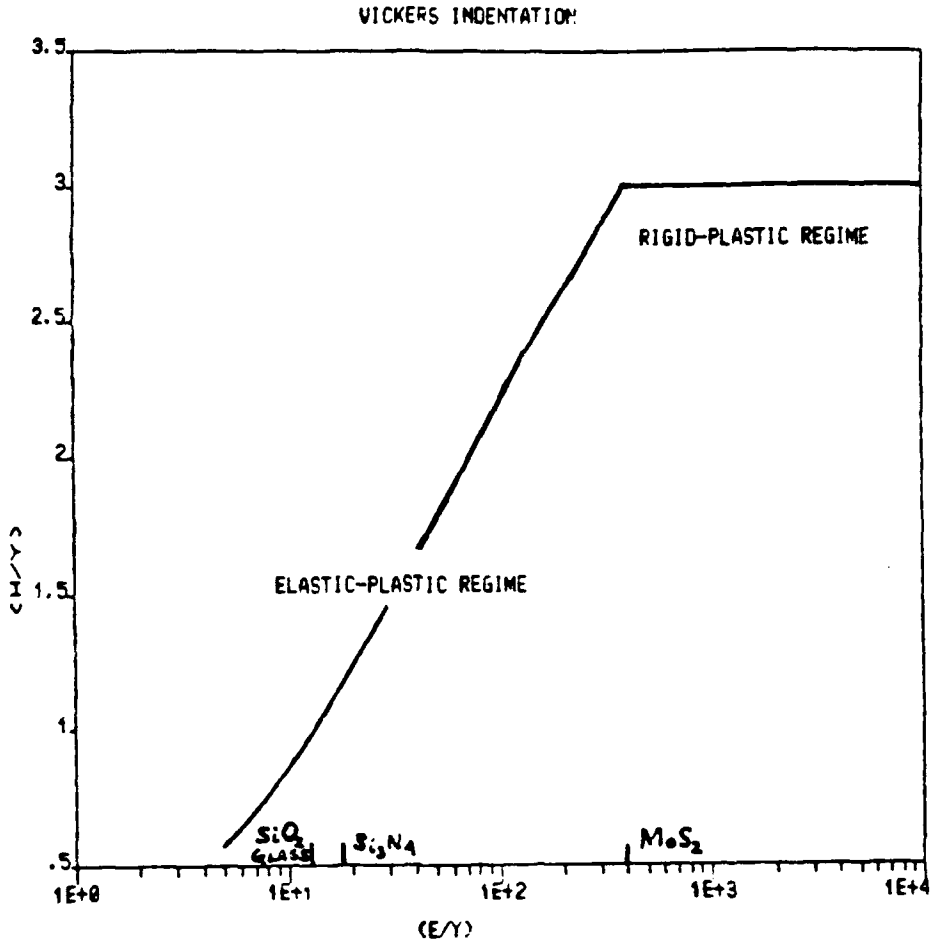

Figure 2. Different deformation modes for various materials during Vickers indentation.

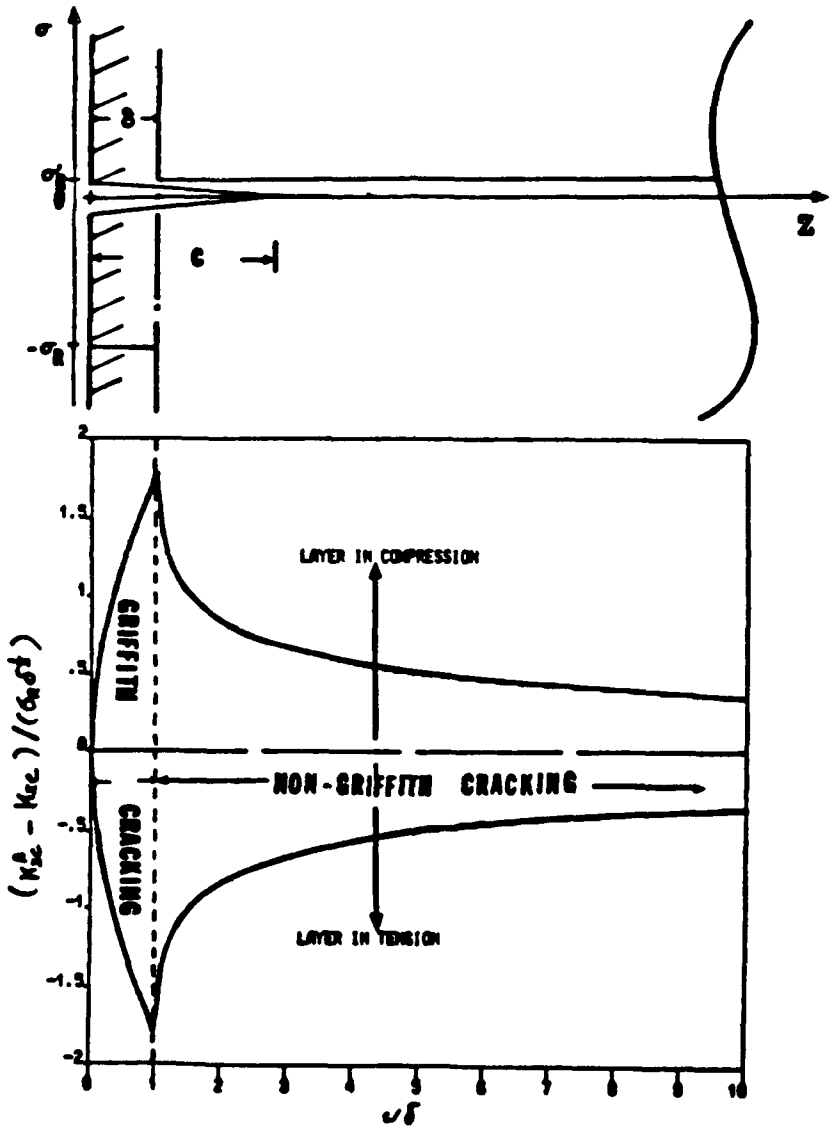

Figure 3. A Vickers indentation fracture-mechanics solution to the "hard" surface layer problem.

Appendix A

Deformation Mode for Various Materials During Vickers and Hertzian Indentations

According to rigid-plastic theory, the hardness-to-yield ratio (H/Y) is a constant and approximately equal to 3 regardless of indenter geometry; whereas the theory of elasticity predicts that (H/Y) is a constant only if the indenter geometry is fixed, e.g., (H/Y) = 1.1 for spherical indenter, (H/Y) = 1.5 for cylindrical indenter etc. For deformation within the elastic-plastic regime, (H/Y), depending on elastic and plastic strain contributions, varies between the values predicted by the theories of elasticity and plasticity. Based on Johnson's analysis*, for Vickers indentation, (H/Y) can be expressed by

$$(H/Y) = \frac{2}{3}\left\{1 + \ln\left[0.096\,(E/Y) + 0.381\right]\right\} \qquad [A1]$$

For Hertzian indentation, the expression becomes

$$(H/Y) \approx \frac{2}{3}\left\{1 + \ln\left[0.209\,(E^{2/3}/Y)\,(P^{1/3}/R^{2/3}) + 0.381\right]\right\} \qquad [A2]$$

where E is the Young's modulus of the indented material, P is the load, R is the radius of the Hertzian (spherical) indenter.

Equation [A1] is graphically expressed in Figure 2 for various materials; Equation [A2] is illustrated in Figures 1 and A. MoS_2 (Figure A) during Hertzian indentation ($0.0012m \leq R \leq 0.0127m$), deforms inelastically even under a low load P.

---

* Johnson, K.L., J. Mech. Phys. Solids, 18, 115-26 (1970).

Figure A. Deformation mode for MoS_2 vs. applied load under Hertzian indenters of various sizes.

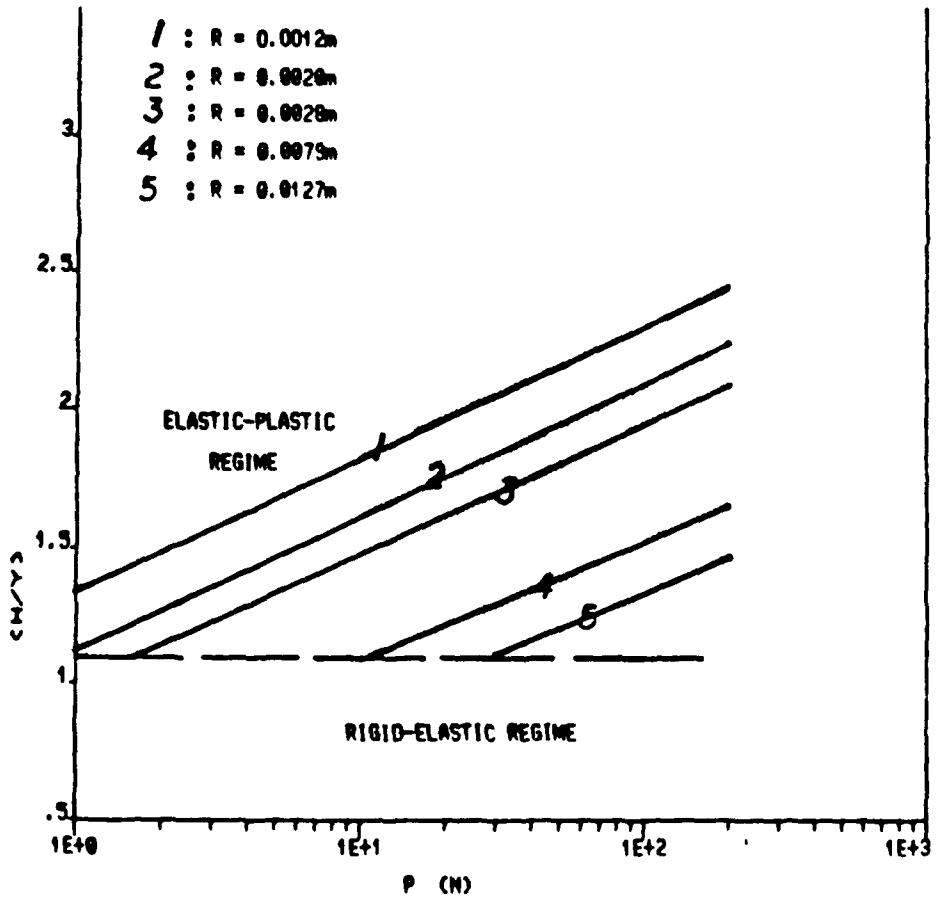

Appendix B

Hertzian (Spherical) Indentation on Ceramics Having Various Surface Conditions

Thus far, only Hertzian-type analysis which is based on the theory of elasticity has been sucessfully applied to analyze data obtained from Hertzian (spherical) indentation on elastic solids. Hertzian indentation on "virgin" ceramics was discussed in one of my earlier reports*. Applying small-flaw approximation, i.e., $\tilde{c}_i \ll a$, in the Griffith regime, initial surface flaw size in ceramics can be estimated by Hertzian indentation if we premeasure the K_{IC} value from Vickers indentation. On the other hand, no exact analytical solution for Hertzian fracture parameter evaluations can be achieved using large-flaw approach ($\tilde{c}_i \gg$) due to the complex stress-strain relations within Auerback regime. My intent here is to extend the application of the small-flaw approximation to evaluate surface flaw size in ceramics coated with a "hard" layer.

With all the configurations in Figure B and assuming $R > a > \delta > \tilde{c}_i$

$$K_I = K_A + K_R \qquad [B1]$$

or

$$K_I = Y \sigma_A \sqrt{\tilde{c}_i} + Y \sigma_R \sqrt{\tilde{c}_i} \qquad [B2]$$

Since

$$\sigma_A = 1/2 \ (1 - 2\nu) \left(\frac{P}{\pi a^2} \right) \qquad [B3]$$

---

* Wong, B., "Assessment of Sharp and Spherical Indentation Techniques", A Report to Gardos, M.N., Hughes Aircraft Company, July 25 (1986).

and

$$a^2 = \left(\frac{4}{3}\right)^{2/3} \left(\frac{k}{E}\right)^{2/3} P^{2/3} R^{2/3} \qquad [B4]$$

Therefore,

$$K_I = \sqrt{\tilde{c}_i} \left[\alpha_1 P^{1/3} R^{-2/3} + Y \sigma_R\right] \qquad [B5]$$

where

$$\alpha_1 = \left[Y/2(1-2\nu)\right] \Big/ \left[\pi (4/3)^{2/3} \left(\frac{k}{E}\right)^{2/3}\right]$$

At fracture,

$$K_{IC} = \left[\alpha_1 P_c^{1/3} R^{-2/3} + Y \sigma_R\right] \sqrt{\tilde{c}_i} \qquad [B6]$$

or

$$P_c = \left[\left(K_{IC} - Y \sigma_R \tilde{c}_i^{1/2}\right)^3 R^2\right] \Big/ \left[\alpha_1^3 \tilde{c}_i^{3/2}\right] = G_1 R^2 \qquad [B7]$$

when $\sigma_R = 0$

$$P_c = \left(K_{IC}^3 R^2\right) / \left(\alpha_1^3 \tilde{c}_i^{3/2}\right) = G_0 R^2 \qquad [B8]$$

Where G_0 and G_1 are the Griffith's coefficients of the zeroth and first kinds, respectively.

Notice that Equation [B8] is the equation for the case of "virgin" ceramics.+

Hertzian theory become irrelevant to the analysis of Hertzian indentation data obtained from either "soft" ceramics or ceramics coated with a "soft" layer

---

+ Footnote on p. B1

whose deformations near the surface/subsurface regions during indentation are dominated by the elastic-plastic or even rigid-plastic behavior (Appendix A). New analysis based on the elastic-plastic theory has to be developed for Hertzian indentation fracture characterization of these materials.

Figure B. Schematic of Hertzian indentation on a ceramic coated with a "hard" layer.

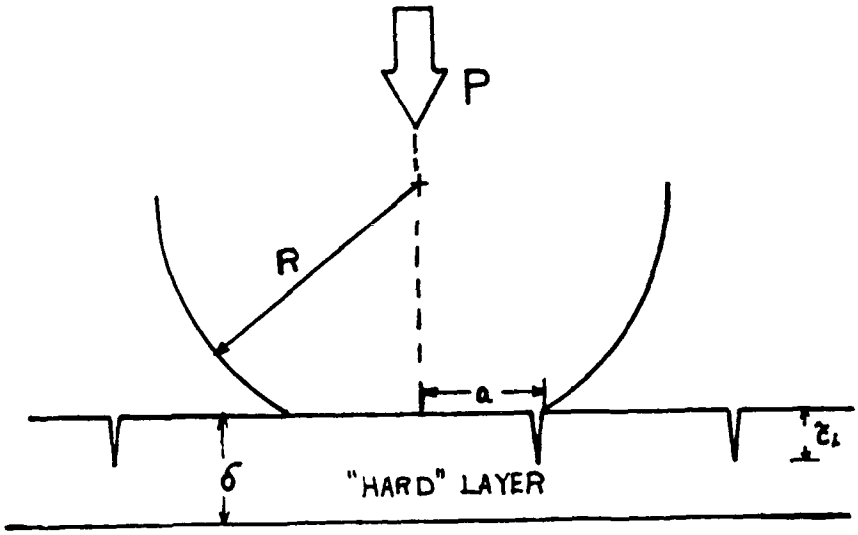

Appendix C

Vickers Indentation for K_{IC} Measurements on Layered Ceramics

The original Lawn-Evans-Marshall (L-E-M) elastic-plastics analysis of Vickers indentation fracture is based on the assumptions of (with configurations in Figure C1):

1. a well-developed half penny-like crack configuration under a center-point-load (far-field approximation);
2. the existence of a residual field arose from the mismatch tractions exerted on the surrounding matrix by the permanently deformed material;
3. the insignificance of frictional force between the faces of the indenter and the sample.

$$K_I \propto P_r / c^{3/2} \propto (\delta V/V) / c^{3/2} \qquad [C1]$$

where K_I is the residual stress intensity factor, P_r is the outward residual force on the crack, $(\delta V/V)$ is the irreversible strain induced by the indentation.

Since

$$(\delta V/V) \propto (a/b)^3 \cos 68^\circ \qquad [C2]$$

where a and b are the characteristic dimensions of the impression and plastically deformed zones, respectively.

Therefore, the application of L-E-M concept and analysis to ceramics coated with a "hard" layer (Figure C2) is still appropriate. However, the analysis has restrictions for its application to ceramics coated wtih a "soft" layer (Figure C3).

Under such circumstances,

$$(\delta V/V) \propto (a^3 \cos 68^\circ - a^2 \delta) / b^3 \qquad [C3]$$

Only if $\delta \ll a$, P_r and subsequently K_I (K_{IC}) will be correctly calculated by L-E-M analysis.

Figure C1. Schematic of a Vickers-produced indentation-fracture system.

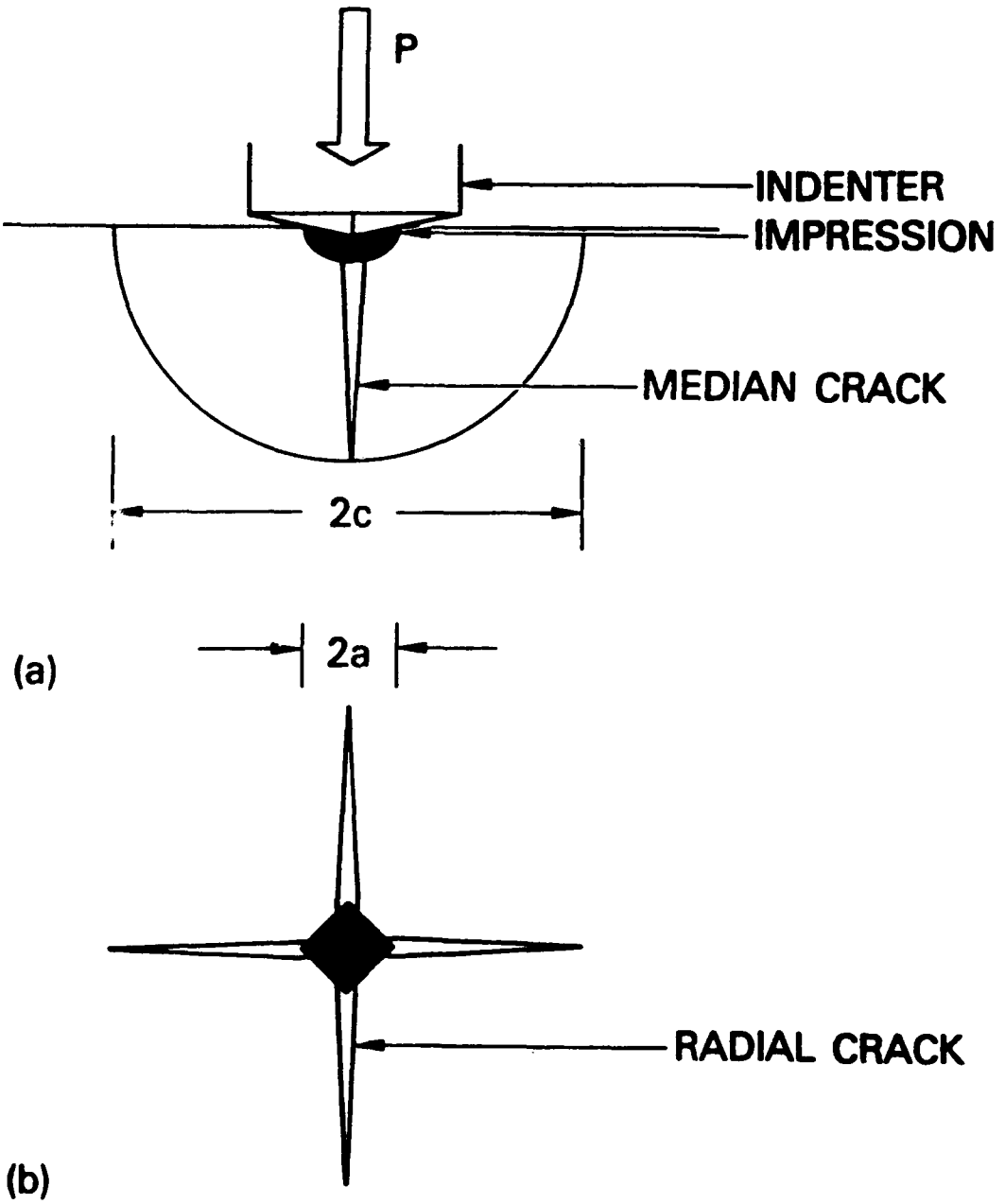

Figure C2. A model for Vickers indentation on ceramics coated with a "hard" layer.

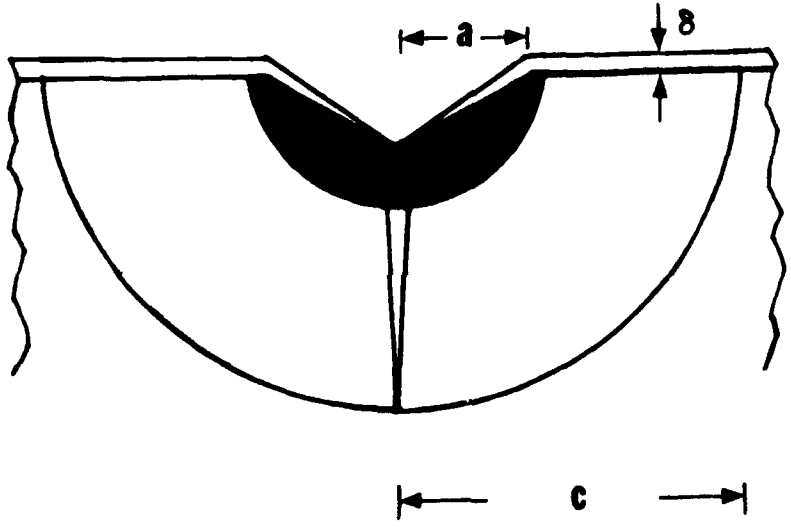

ASSUMPTION: $f_\mu \approx 0$

Figure C3. A model for Vickers indentation on ceramics coated with a "soft" layer.

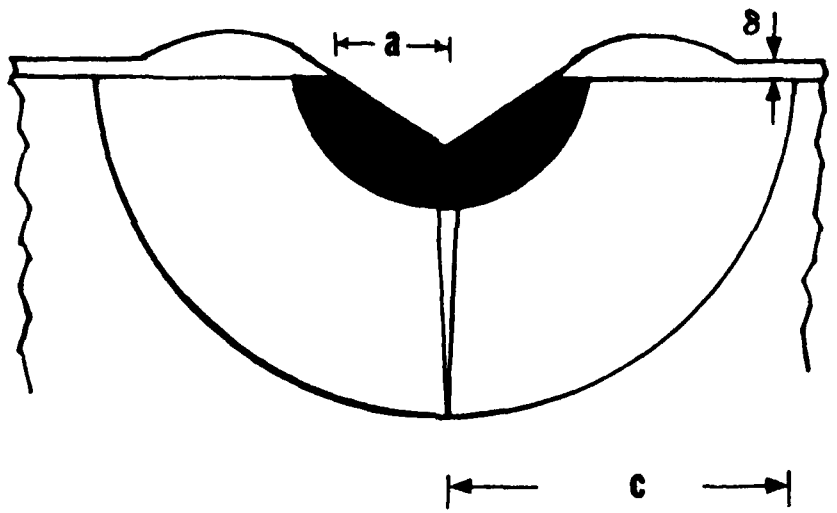

ASSUMPTION : $f_\mu \approx 0$

Appendix D

Fracture-Mechanics Analysis of Vickers Indentation on Ceramics Coated with a "Hard" Layer

Assuming that the model shown in Figure 3 (top drawing) holds, the surface residual stress intensity factor can be expressed by

$$K_R = 2\,(c/\pi)^{1/2} \int_0^c \frac{-\sigma_R\, dz}{\sqrt{c^2 - z^2}} \quad , \qquad 0 \le c/\delta \le 1 \qquad [D1]$$

and

$$K_R = 2\,(c/\pi)^{1/2} \left\{ -\int_0^{\delta} \frac{\sigma_R\, dz}{\sqrt{c^2 - z^2}} + \int_{\delta}^{c} \frac{\sigma_R \delta}{d} \left(\frac{dz}{\sqrt{c^2 - z^2}} \right) \right\} , \qquad 1 \le c/\delta \le d/\delta \qquad [D2]$$

Equations [D1] and [D2] can be simplified into Equations [D3] and [D4], respectively.

$$K_R = -1.77\, \sigma_R\, c^{1/2} \quad , \qquad 0 \le c/\delta \le 1 \qquad [D3]$$

and

$$K_R = -1.13\, \sin^{-1}(\delta/c)\, \sigma_R\, c^{1/2}, \qquad 1 \le c/\delta \le d/\delta \qquad [D4]$$

where d is the half-thickness of the sample.

Since

$$(K_{IC}^{A} - K_{IC}) = -K_R \qquad [D5]$$

where K_{IC}^{A} and K_{IC} are the "apparent" and "real" fracture toughness values of the ceramic under stressed and stress-free conditions, respectively. They are the outputs of Vickers Indentation measurements.

Therefore,

$$\left(\frac{K_{IC}^{A} - K_{IC}}{\sigma_R \, \delta^{1/2}}\right) = 1.77\,(c/\delta)^{1/2}, \quad 0 \leq c/\delta \leq 1 \qquad [D6]$$

and

$$\left(\frac{K_{IC}^{A} - K_{IC}}{\sigma_R \, \delta^{1/2}}\right) = \left[1.13 \sin^{-1}(\delta/c)\right]\left[c/\delta\right]^{1/2}, \quad 1 \leq c/\delta \leq d/\delta \qquad [D7]$$

Equations [D6] and [D7] are graphically expressed in Figure 3 (bottom drawing).

Application of this fracture-mechanics analysis to an experimental problem is illustrated in Attachment D. The surface glass layer of the oxidized (816°C, 4h) NC-132 HPSN* was accordingly found to be under tension because the measured "apparent" fracture toughness increased with increasing indentation crack dimension (load) within $1 \leq c/\delta \leq d/\delta$ as predicted by the proposed fracture-mechanics solution. This finding fully supports the theory that an internal strain (stress) is induced by the molar volume mismatch between the SiO_2 glass and Si_3N_4. Knowing the thickness of the glass layer eventually allows determination on the surface residual stress.

---

* The mechanical properties of "virgin" NC-132 HPSN measured by the indentation techniques in this study are: E = 321 ± 44 GPa, H = 18.02 ± 0.92 GPa and K_{IC} = 4.14 ± 0.11 MPa $m^{1/2}$.

Attachment D. Experimental evidence supporting the fracture-mechanics solution to the "hard" coating problem.

- EXPERIMENTAL:

  VICKERS INDENTATION ON OXIDIZED (816 ℃, 4H) NC-132

- RESULTS

P (N)	c (M)	A K_{IC} (M-PA $M^{1/2}$)	A $K_{IC} - K_{IC}$ (M-PA $M^{1/2}$)
34.01	64.1	2.55	-1.59
39.05	69.2	2.63	-1.51
44.64	75.8	2.77	-1.37

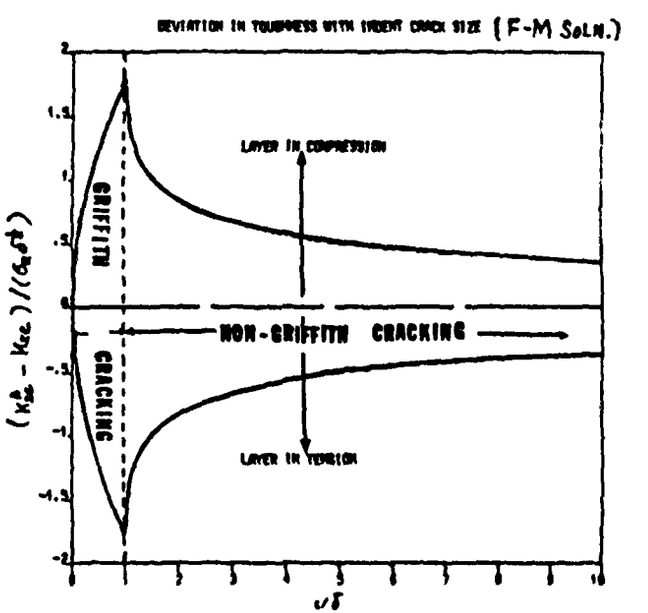

- IMPLICATIONS:

  (1) SURFACE GLASS LAYER IN TENSION SUPPORTING THE MOLAR VOLUME MISMATCH THEORY

  (2) KNOWING GLASS LAYER THICKNESS, SURFACE RESIDUAL STRESS DETERMINABLE

T-32

APPENDIX U

B. Wong, "High-Speed Contact Failure and Microindentation," Hughes Interdepartmental Correspondence No. 7641.20/804, 27 February 1987

HUGHES

INTERDEPARTMENTAL CORRESPONDENCE

TO	M.N. Gardos	CC	D.H. Buettner
ORG	76-21-10		J.L. Cook
			S.S. Gassel
SUBJECT	High-Speed Contact Failure and Micro-indentation		E.B. Holst
			A.B. Naselow
			R.Y. Scapple
			R.W. Seibold
			J.A. Zelik

DATE 27 February 1987
REF. 7641.20/804

FROM B. Wong
ORG. 76-41-20

BLDG. E1 MAIL STA. C132
LOC. E0 PHONE 60656

I. INTRODUCTION

The first objective of this IDC is to present an evaluation of our proposed failure mechanistic mode for high-speed triboceramic contacts. Predicted lifetimes of HPSN contacts calculated based on some pre-determined failure parameters are found to be in good agreement with the published fatigue life data of ball bearings made of the same material obtained under high-speed motions.

The second objective of this IDC is to provide comments on IBM and NBS experimental work on microindentation.

II. TIME-TO-FAILURE FOR HIGH-SPEED TRIBOCONTACTS

It has been recently proposed that the most probable failure mode of a tribo-contact under high-speed motion conditions is the thermal fatigue and its time-to-failure can be calculated if certain failure-related parameters are pre-determined (1).

$$t_f = \left(\frac{2}{2-n}\right) \gamma^{-n} A^{-1} \left(\sum_{j=1} \sigma_j\right)^{-n} \exp\left(\frac{Q}{RT}\right) \left[\left(\frac{K_{IC}}{\gamma \sum_{j=1} \sigma_j}\right)^{2-n} - \varepsilon_i^{(2-n)/2}\right] \qquad [1]$$

where

t_f is the time-to-failure

$\sum \sigma_j$ is the total stress

$\tilde{c}_j$ is the initial surface crack (flaw) depth

K_{IC} is the fracture toughness

T is the absolute temperature at maximum $\sum \sigma_j$

R is the gas constant

Y is a geometrical factor

A, n and Q are all empirical terms obtained from subcritical crack growth studies.

For HPSN, obtaining the slow crack growth behavior from the study by Evans et al. (2), i.e., $A \approx 10^{-7}$ m/s, n = 5.5, Q = 170 K-cal/mol, also using K_{IC} = 4.14 MPa $m^{1/2}$ according to (1) and assuming T = 617°C*, time-to-failure vs. total stress plots at various initial surface crack depths are shown in Figure 1. As expected under high speed motion conditions, i.e., under a high total stress and elevated temperature, time-to-failure of the HPSN tribocontact is particularly sensitive to the depth of its initial surface cracks (flaws) caused by fabrication and surface finish procedures. Based on the comparison of initial crack depth, the good agreement of the predicted lifetimes with the 90% confidence experimental data (3) obtained from the NC-132 HPSN under a shaft speed of 9400 rpm therefore fully supports the failure mechanistic mode for high-speed tribocontacts previously proposed (1).

III. Technique Review

The indentation debonding test for polymer coated substrates proposed by IBM (4) demonstrates that quantitative adhesive strength can be evaluated by simply

* Due to high-speed motions (> 10,000 rpm), local temperature rise at ceramic contact surfaces >600°C are very possible.

measuring the characteristic debond strain, which is a constant for a given film-substrate configuration regardless of load and indenter geometry. However, this test seems applicable only to interface characterization for plastic films whose adhesive strengths are weak. For evaluation of interface and contact-induced damage of rigid oxide coated substrates, Marshall-Evans analysis (5) appears to be more appropriate. On the other hand, the NBS dynamic microindentation testing (6,7) that characterize materials in terms of continuous measurements of applied load and penetration depth seems to be a comprehensive technique for mechanical property determinations. It allows the determination of the unrecovered impression area under load and also a comparison between the indentation impressions under load and after unload; therefore, deformation energy in terms of elastic, plastic, and anelastic components can be measured. This technique has been thus far applied to unworn and worn metallic alloys for differentiation of wear behavior; its validity to wear characterization for ceramic containing systems however, has to be justified.

IV. CONCLUSION

Thermal fatigue has been illustrated to be at least one of the major modes for high-speed triboceramic failure. Microindentation techniques which can provide accurate measurements of some important parameters for thermal fatigue such as fracture toughness, initial flaw depth, residual stress, adhesion behavior, etc. are therefore required in materials characterization to predict high-speed tribo-contact reliability. IBM and NBS methods, after thoroughly tested, are suggested to be included in our triboceramic characterization program.

Bon Wong

B. Wong

BW:ii

REFERENCES

1. Wong, B., Interdepartmental Correspondence to M.N. Gardos, 7641.20/770, Hughes Aircraft Company, 6 January (1987).

2. Evans, A.G., Russel, L.R., and Richerson, D.W., Metall. Trans. A., 6[4], 707-16 (1975).

3. Parker, R.J. and Zaretsky, E.V., Journal of Lubrication Technology, ASME Trans., 350-57 (1975).

4. Engel, P.A., Int. J. Adhesion and Adhesives, 5[3], 129-32 (1985).

5. Marshall, D.B. and Evans, A.G., J. Appl. Phys., 56[10], 2632-38 (1984).

6. Polvani, R.S., Ruff, A.W., and Whitenton, E.P., J. Testing and Evaluation, to be published.

7. Ruff, A.W. and Polvani, R.S., Proc. 3rd International Conference on Surface Technology, J3, 1-8, Berlin (1985).

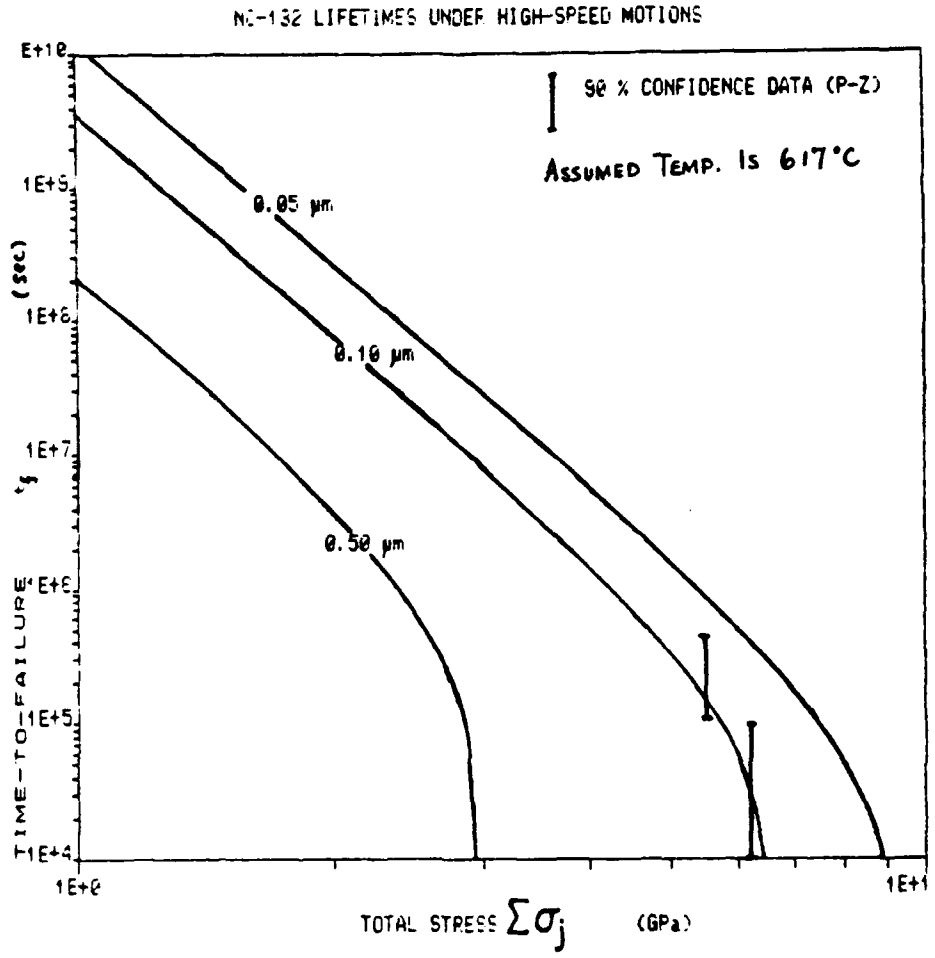

FIGURE 1. TIME-TO-FAILURE PREDICTIONS OF Si_3N_4 TRIBOCONTACTS CONTAINING VARIOUS INITIAL SURFACE CRACKS UNDER HIGH-SPEED MOTIONS.

HUGHES

INDENTATION FOR TRIBOCONTACT FRACTURE CHARACTERIZATION AND ANALYSIS

BOON WONG

U-6

ATTACHMENT

OUTLINE

HUGHES

I. WHY INDENTATION FOR MECHANICAL CHARACTERIZATION

II. HERTIZIAN INDENTATION

(1) CONCEPT

(2) APPLICATIONS AND LIMITATIONS TO TRIBOCERAMIC FRACTURE CHARACTERIZATION

A) "VIRGIN" CERAMICS

B) CERAMICS COATED WITH A "HARD" LAYER

C) CERAMICS COATED WITH A "SOFT" LAYER

III. VICKERS INDENTATION

(1) CONCEPT

(2) SAME OUTLINE AS II (2)

IV. RELEVANCE OF THE INDENTATION MEASUREMENTS FOR LIFETIME PREDICTIONS OF A TRIBOCONTACT UNDER HIGH-SPEED CONTACT MOTION CONDITIONS

WHY INDENTATION FOR MECHANICAL CHARACTERIZATION

HUGHES

- SAMPLE PREPARATION AND DATA COLLECTION PROCEDURES ARE SIMPLE
- ACTUAL ELECTRONIC COMPONENTS CAN BE USED AS SAMPLES
- COMPREHENSIVE AND PRECISE POINT-BY-POINT MECHANICAL CHARACTERIZATION WITHIN THE MATERIALS/COMPONENTS IS POSSIBLE; SPATIAL RESOLUTION IS APPROXIMATELY 100 MICROMETERS

HUGHES

SCHEMATIC OF A VICKERS-PRODUCED INDENTATION-FRACTURE SYSTEM

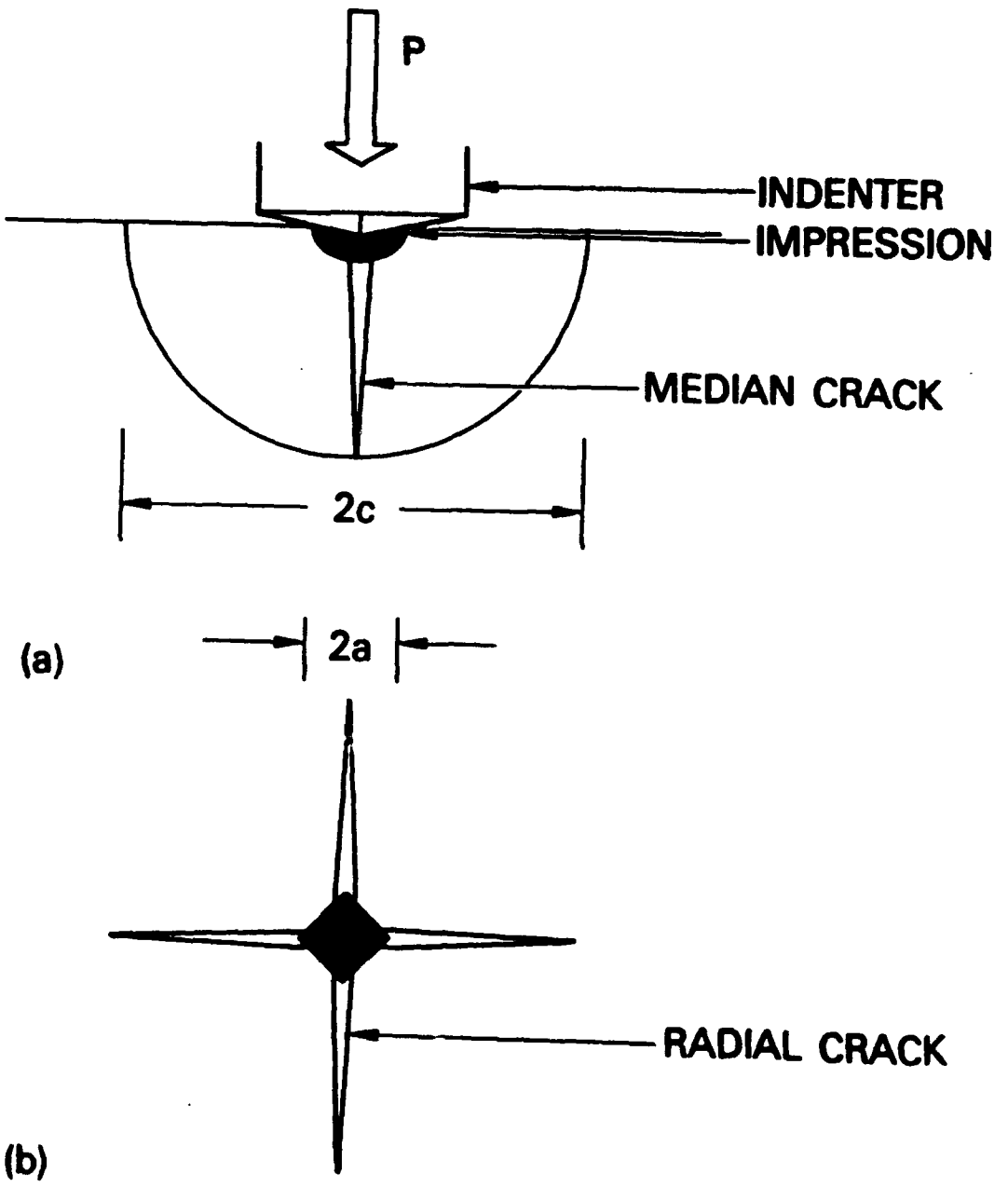

CRACKING UNDER THE ELASTIC-PLASTIC FIELD CREATED BY VICKERS MICROINDENTATION

HUGHES

- BASIC ASSUMPTIONS: ISOTROPIC AND HOMOGENEOUS SOLIDS; $c >> a$
- STRESS INTENSITY FACTOR:

$$K_r = X_r \, (P/c^{3/2})$$

- FRACTURE TOUGHNESS:

$$K_{IC} = X_r \, (P/c_o^{3/2})$$

50 μm

(H/Y) VS. LN (E/Y) FOR VARIOUS MATERIALS GENERATED BY VICKERS INDENTATION

HUGHES

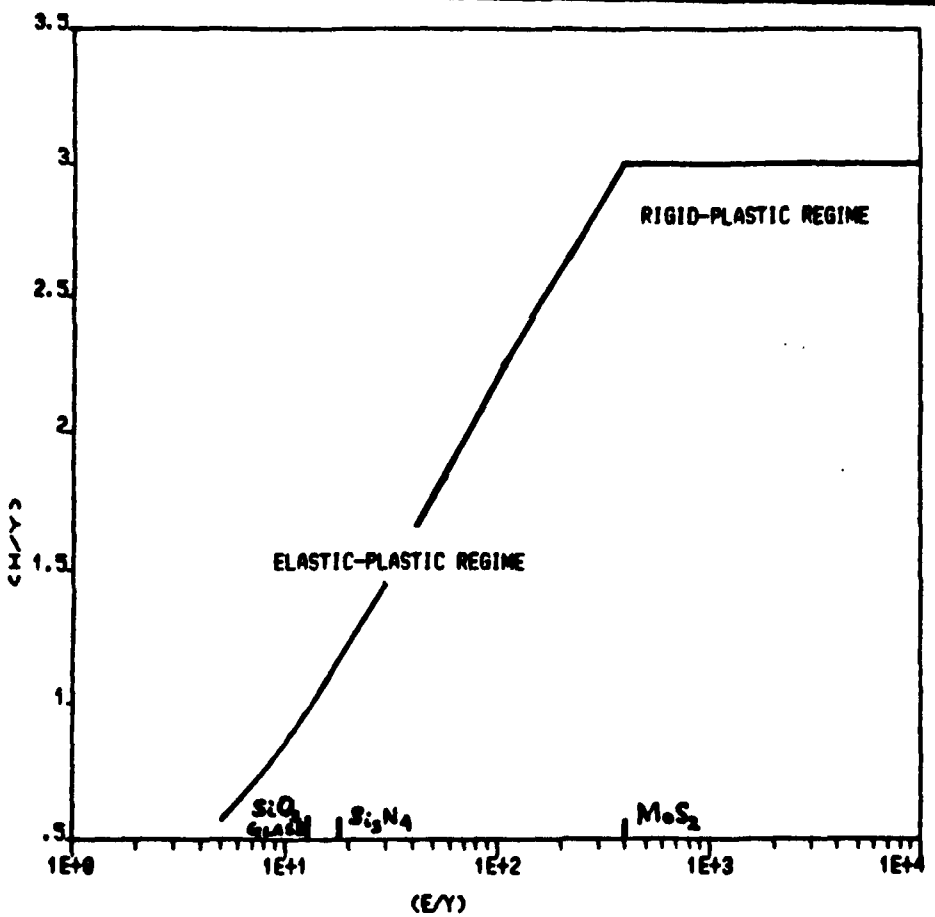

MECHANICAL PROPERTIES OF HPSN (NC-132)

HUGHES

PROPERTY / TECHNIQUE	E (GPA)	H (GPA)	K_{IC} (MPA $m^{1/2}$)
CONVENTIONAL (LITERATURE)	310	17.64 - 19.60	4 - 6
INDENTATION* (THIS STUDY)	321 ± 44	18.02 ± 0.92	4.14 ± 0.11

* INDENTATION LOAD USED RANGED FROM 29N TO 45N

MODEL FOR VICKERS INDENTATION ON
CERAMICS COATED WITH A "HARD" LAYER

HUGHES

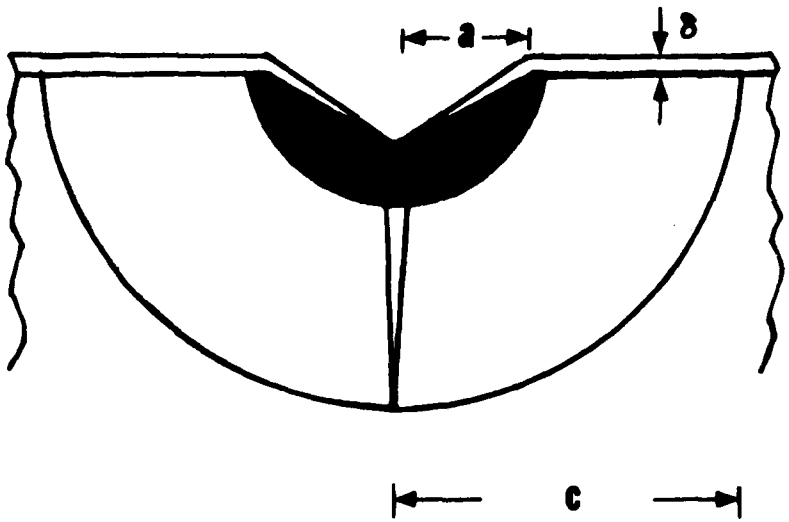

ASSUMPTION: $f_\mu \approx 0$

A FRACTURE-MECHANICS SOLUTION
TO THE TANDEM-FIELD PROBLEM

HUGHES

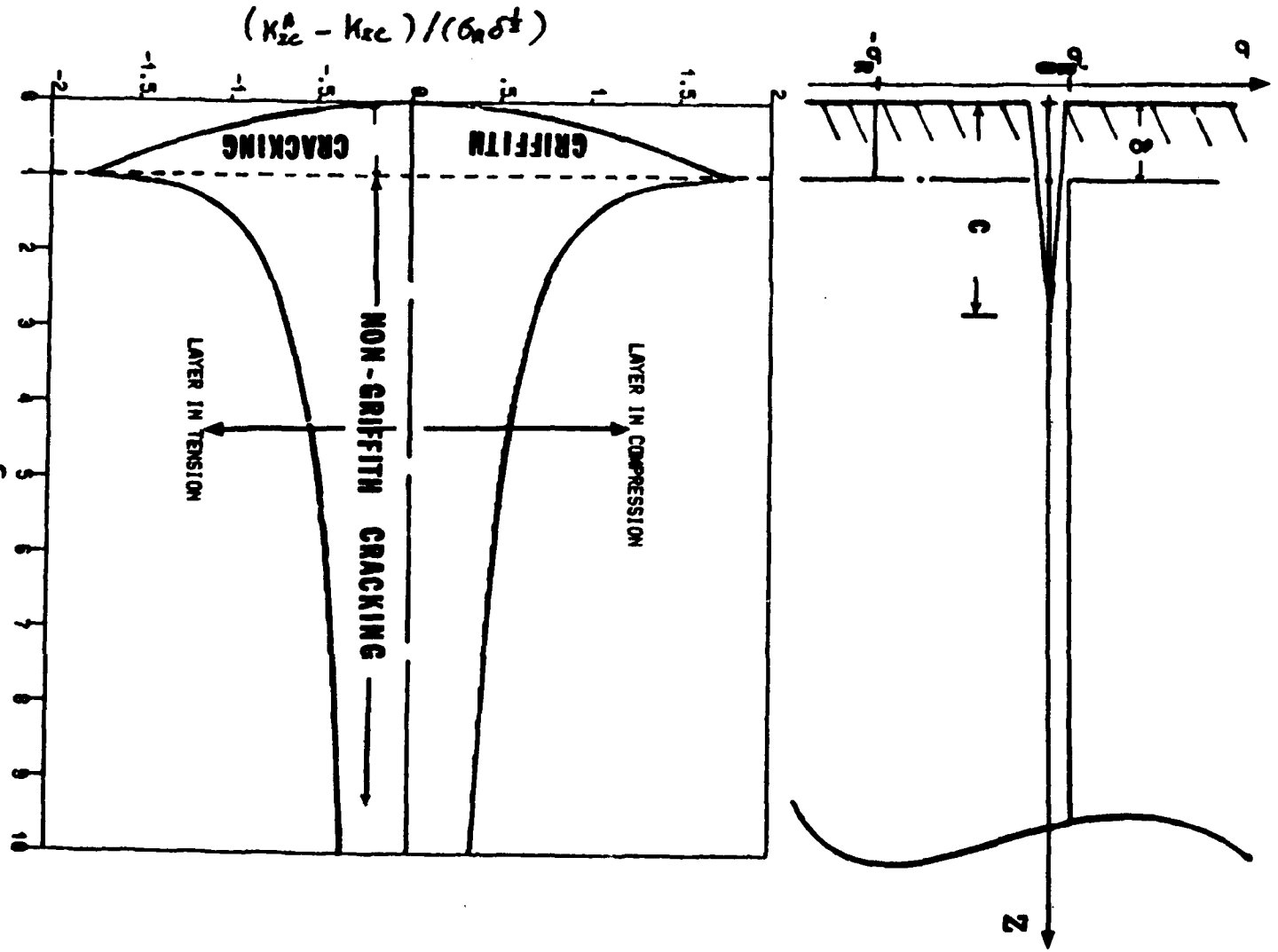

EXPERIMENTAL EVIDENCE SUPPORTING THE FRACTURE-MECHANICS SOLUTION TO THE TANDEM-FIELD PROBLEM

HUGHES

- EXPERIMENTAL:

  VICKERS INDENTATION ON OXIDIZED (816 ℃, 4H) NC-132

- RESULTS

P (N)	c (M)	A K_{IC} (M-PA $M^{1/2}$)	A $K_{IC} - K_{IC}$ (M-PA $M^{1/2}$)
34.01	64.1	2.55	-1.59
39.05	69.2	2.63	-1.51
44.64	75.8	2.77	-1.37

- IMPLICATIONS:

  (1) SURFACE GLASS LAYER IN TENSION SUPPORTING THE MOLAR VOLUME MISMATCH THEORY

  (2) KNOWING GLASS LAYER THICKNESS, SURFACE RESIDUAL STRESS DETERMINABLE

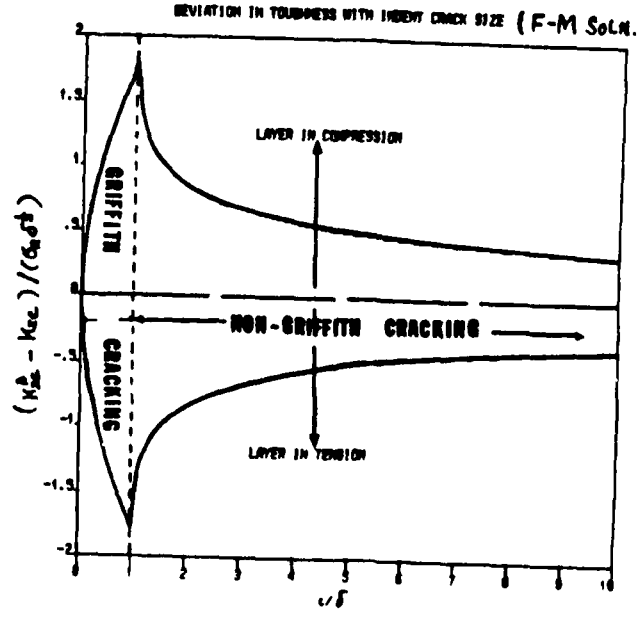

MODEL FOR VICKERS INDENTATION ON
CERAMICS COATED WITH A "SOFT" LAYER

HUGHES

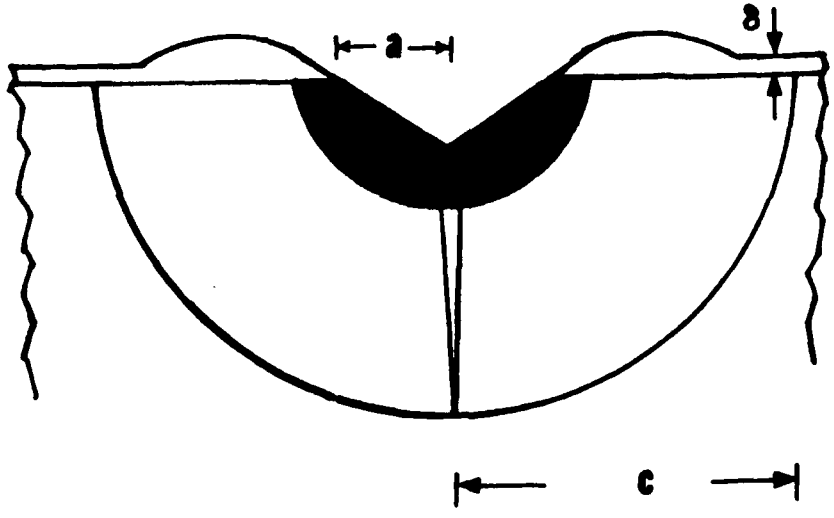

ASSUMPTION: $f_\mu \approx 0$

HUGHES

ELASTIC STRESS DISTRIBUTIONS
DURING HERTZIAN INDENTATION

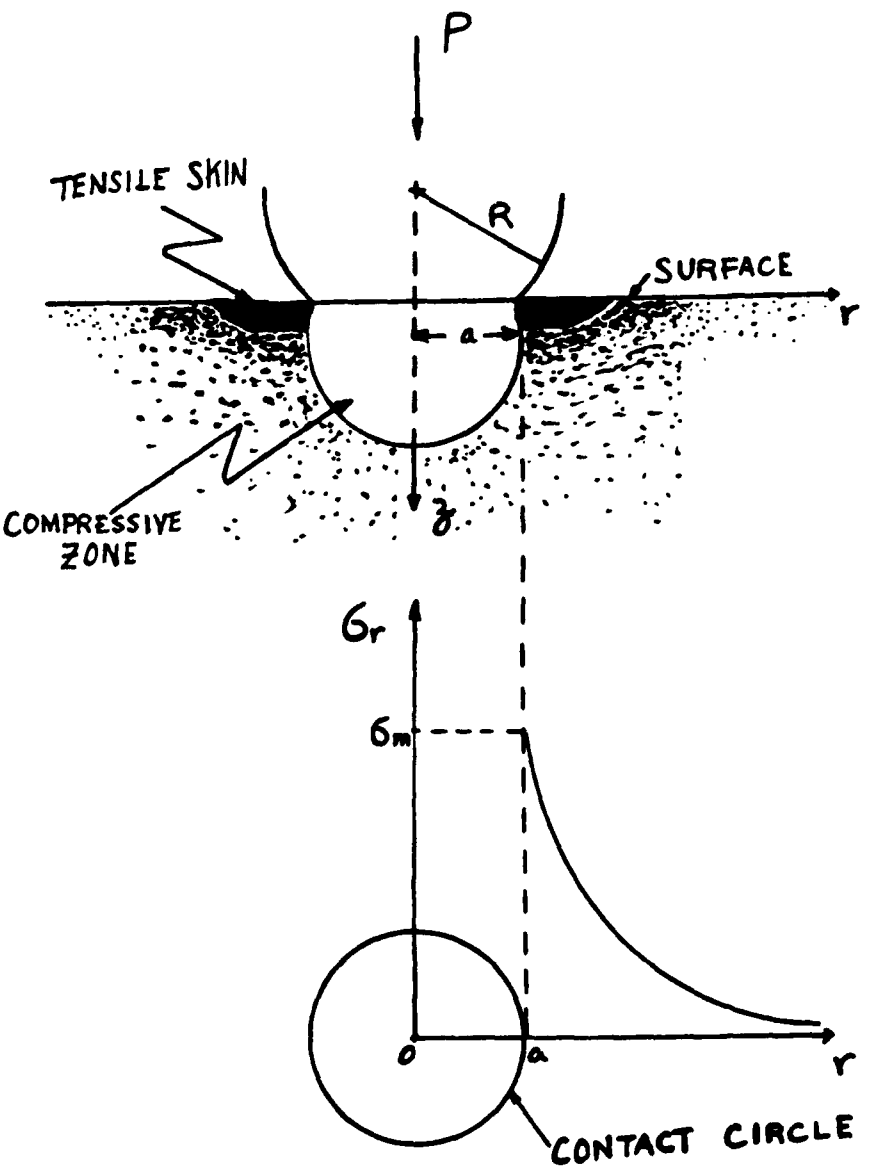

CRACKING UNDER THE PERFECTLY ELASTIC FIELD CREATED BY HERTZIAN INDENTATION

HUGHES

I. SMALL-FLAW APPROXIMATION ($\tilde{c}_i \ll a$)

- $P_c = GR^2$ (GRIFFITH REGIME)
- $K_{IC} = a_1 P_c^{1/3} \tilde{c}_i^{1/2} / R^{2/3}$

II. LARGE-FLAW APPROACH ($\tilde{c}_i \gtrsim a$)

- $P_c = AR$ (AUERBACH REGIME)
- NO EXACT ANALYTICAL SOLUTION FOR K_{IC} EVALUATION

HUGHES

P_c VS. R FOR HERTZIAN INDENTATION

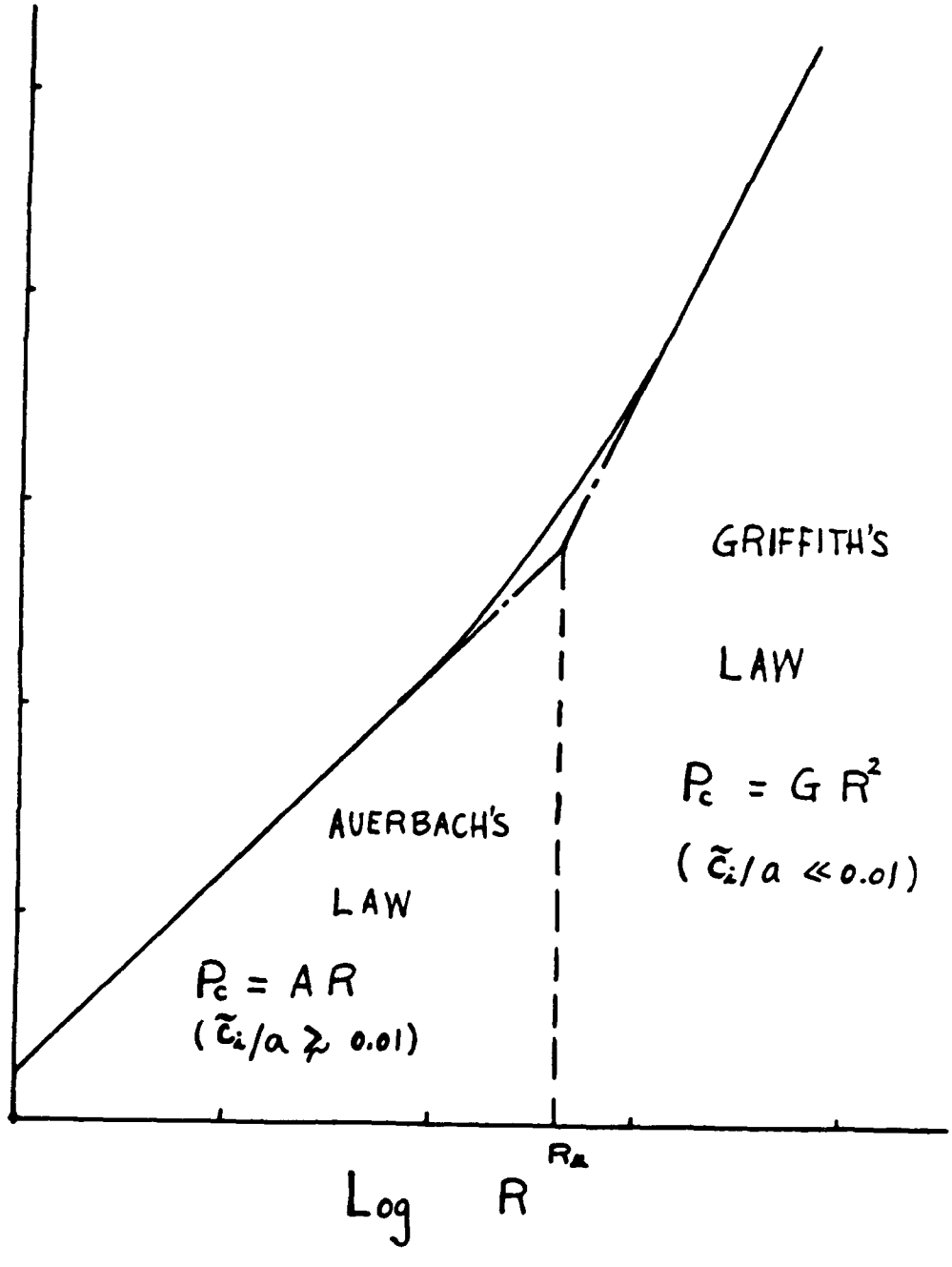

DETERMINATION OF HERTZIAN
CRITICAL LOAD FOR FRACTURE

HUGHES

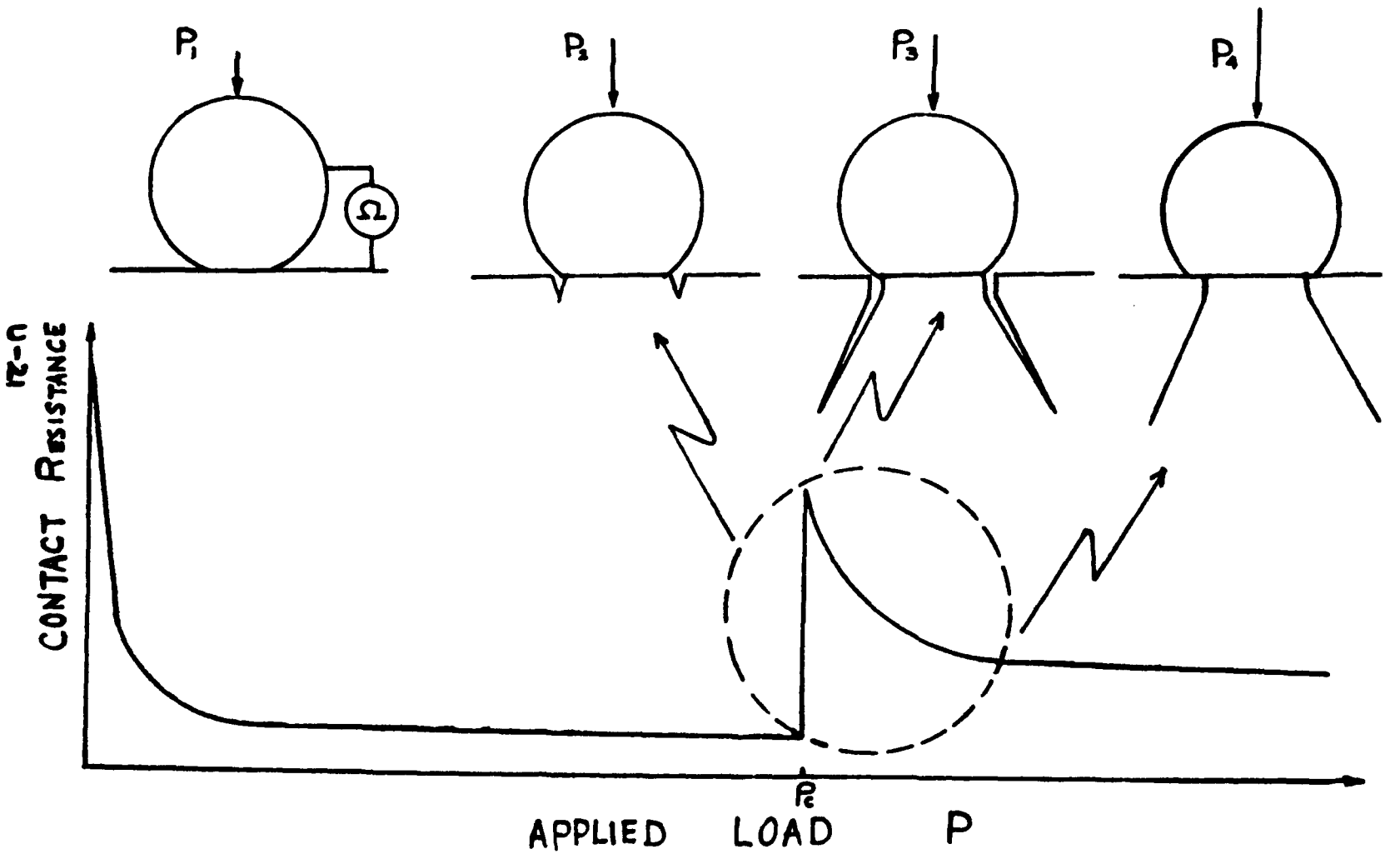

(H/Y) VS. LN $\left(\frac{E^{2/3}}{Y}\right)$ FOR VARIOUS MATERIALS GENERATED BY HERTZIAN INDENTATION

HUGHES

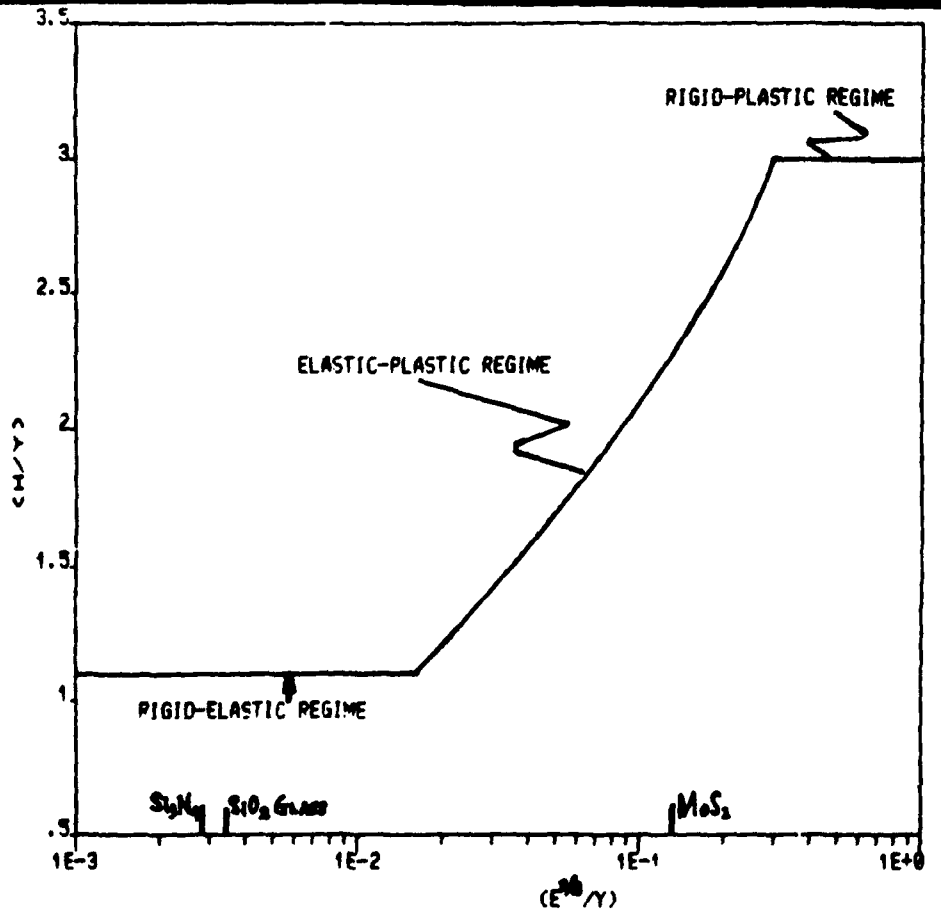

(H/Y) VS. LNP FOR M_oS_2 USING
DIFFERENT SIZES OF HERTZIAN IDENTER

HUGHES

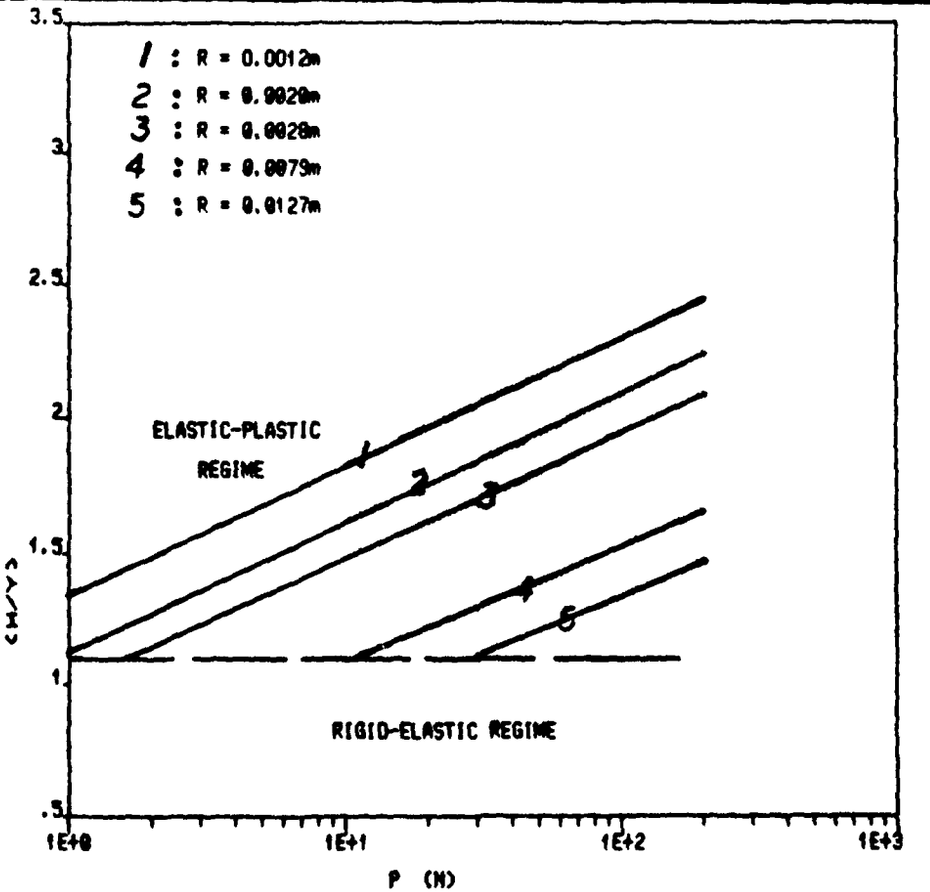

APPLICATIONS AND LIMITATIONS OF VARIOUS INDENTATION TECHNIQUES FOR TRIBOCERAMIC MEASUREMENTS

HUGHES

MATERIAL \ INDENTATION	HERTZIAN		VICKERS	
	CONDITION	A/NA*	CONDITION	A/NA*
CERAMICS	$R > a \gg \tilde{c}_i$	A ($\tilde{c}_i$)	$c_o \gg a$	A (K_{IC})
	$\tilde{c}_i \gtrsim 0.01\,a$	NA		
CERAMICS COATED WITH A "HARD" LAYER	$R > a \gg \tilde{c}_i$ AND $\delta > \tilde{c}_i$	A ($\tilde{c}_i$)	$c_o \gg a$	A(K_{IC}, σ_R)
	$\tilde{c}_i > \delta$ OR $\tilde{c}_i \gtrsim 0.01\,a$	NA		
CERAMICS COATED WITH A "SOFT" LAYER	INELASTIC REGIME	NA	$c_o \gg a \gg \delta$	A (K_{IC})
		NA	$c_o \lesssim a$ OR $\delta \gtrsim a$	NA

* A FOR "APPLICABLE"; NA FOR "NOT APPLICABLE"

THERMAL FATIGUE CRACKING - A FAILURE MODE
OF A TRIBOCONTACT UNDER HIGH-SPEED MOTION CONDITIONS

HUGHES

- $\frac{d\tilde{c}}{dN} \propto \frac{d\tilde{c}}{dt} = AY^n \tilde{c}^{n/2} \left(\sum_{j=1} \sigma_j\right)^n \exp\left(\frac{-Q}{RT}\right)$

- I.C. $\tilde{c} = \tilde{c}_i > \tilde{c}_{th}$, $t = o$

- B.C. $\tilde{c} = \tilde{c}_f = \left(\frac{K_{IC}}{Y \sum_{j=1} \sigma_j}\right)^2$, $t = t_f$

SOLUTION TO THE THERMAL FATIGUE EQUATION LIFETIME PREDICTIONS

HUGHES

- $N_f \propto t_f = \left(\frac{2}{2-n}\right) \gamma^{-n} A^{-1} \left(\sum_{j=1} \sigma_j\right)^{-n} \exp\left(\frac{Q}{RT}\right) \left[\left(\frac{K_{IC}}{\gamma \sum_{j=1} \sigma_j}\right)^{2-n} - \tilde{\varepsilon}_i^{(2-n)/2}\right]$

  WHERE $\sum_{j=1} \sigma_j = \sigma_R + \sigma_T + \sigma_A$

- DETERMINATIONS OF SOME IMPORTANT FEATURES

  K_{IC}: VICKERS INDENTATION

  $\tilde{\varepsilon}_i$: HERTZIAN INDENTATION

  σ_R : VICKERS INDENTATION

  σ_T, σ_A: THERMOMECHANICAL STRESS ANALYSIS (E.G., JU AND CHEN APPROACH)

APPENDIX V

G.D. Eisenbrand, "Status Report: Hertzian Cone Cracking Apparatus," Hughes Interdepartmental Correspondence No. 7621.13, 27 June 1986

and

B. Billington, "Hertzian Stresses," Hughes Avoid Verbal Orders (AVO) Memo. 31 October 1986

INTERDEPARTMENTAL CORRESPONDENCE

HUGHES

TO:	M.N. Gardos	CC:	R.C. Davis	DATE:	27 June 1986
ORG	76-21-13		E.B. Holst	REF:	7621-13/38
			L.C. Lipp		
SUBJECT	Status Report: Hertzian Cone-Cracking Apparatus		B. Wong	FROM: ORG:	G.D. Eisenbrand 76-21-13
				BLDG. LOC	E1 MAIL STA F150 E0 PHONE 66038

Introduction

Ring cracks are usually detected by optical inspection of the flat after unloading and removal of the specimen. However, the initiation of a ring crack can be observed directly by optical means if the flat is optically transparent and if the radius of the ring crack is large enough. Since this is not always possible or convenient for ceramic materials, it is highly desirable to have a technique which determines the onset of these ring cracks.

As reported in the DARPA First Semiannual Report, initial model experiments will be performed on a semiautomatic, Hertzian cone-cracking apparatus adapted from that reported by Grzybowski and Ruoff[1]. The apparatus is shown schematically in Figure 1. Ceramic flats will be indented by new, high modulus Co-WC cermet and TiN-coated, Ni-Mo-TiC cermet balls to determine the microstructural effects of static load-carrying capacity. A thin film of gold (optimally 1000 Å thick) will be deposited on the ceramic flat and, upon being cracked by the ball, will interrupt a circuit between the gold metal layer and the electrically conductive ball indenter (i.e., the ball is sufficiently conductive in its own right). In this way, the load can be increased in a controlled manner until, at a critical load, Hertzian cone-cracking is indicated by a marked increase or interruption in contact resistance.

I. Theory

The state of stress within a brittle flat being indented by a spherical indenter, both made of an isotropically elastic material, can be determined by the application of the elastic contact solution (Hertz contact problem)[2]. The resulting stress field is axially symmetric about the indenters and yields a maximum pressure at the center of contact given by:

$$Po = \frac{3}{2\Pi} \left[\left(\frac{4}{3\Pi}\right)^2 (K_f + K_I)^2 R^2 / F \right]^{-1/3}$$

and a contact radius given by

$$a = \left[\frac{3\Pi}{4} (K_f + K_I) RF \right]^{1/3}$$

where Po is the maximum pressure, R is the tip radius, F is the applied force, and K_f and K_I are defined in the following equations

$$K_f = (1 - \nu_f^2) / \Pi E_f$$

$$K_I = (1 - \nu_I^2 / \Pi E_I$$

where E_f and E_I are Young's moduli, and ν_f and ν_I are Poisson's ratios[2]. The subscripts f and I refer to the flat and to the indenter, respectively.

An indenter pressed against a flat made of a different material produces additional frictional forces within the contact region not dealt with in the aforementioned Hertz theory. However, observations by Tolansky[3] have shown that in glass flats, ring cracks follow the contour of the maximum tensile stress producing a circular geometry. Due to the tensile nature of the radial stress outside the contact region, a surface step and fissure are produced during ring crack formation.

The height of the generated surface step cannot be calculated, in general, due to the flow and stress distributions present. However, if we assume that the surface outside the contact perimeter returns to its initial unloaded position upon crack formation at r = a, then the elastic contact solution yields a minimum surface displacement perpendicular to the flat surface at the contact perimeter given by

$$W_1 = \frac{a^2}{2R} \left(\frac{K_f}{R_f + R_I}\right)$$

The topography of the cracked surfaces conducted in tests to be in this study will be measured with precise optical interferometric methods to verify (or refute) the assumption.

Ruoff's (et al) technique requires a thin metal film (200-1000 Å) on the electrically insulating flat and the indenters if it is also insulating. The electrical contact resistance between the flat and the indenter is continually monitored during loading. This resistance decreases continually due to the growth of the area of contact with increasing applied force. For a spherical indenter pressed against the center of a circular flat, the contact resistance is then given by:

$$\Omega = \frac{\rho_f}{2\pi t_f} \ln(D/a) + \frac{\rho_f}{2\pi t_I} \ln\left(\frac{\pi R}{4a}\right) + \Omega_0$$

$$\text{for } \frac{a}{r} < 1$$

where $\rho_{f,I}$ and $t_{f,I}$ are the resistivities and thicknesses of the metal film, D is the radius of a circular flat, and Ω_0 is the sum of the constant lead resistances[4]. For a gold film approximately 1000 Å thick, the contact resistance is calculated to be at least 0.46 ohm.

If we ignore the effects produced by the thin films on stress distributions[4], then the electrical contact resistance should follow the above equation until a ring crack is formed. The production of the ring crack with its associated surface step and fissure act to severely deform the metal film, and causes it to tear along the step. The tear blocks the normally conductive path, and hence, increases the contact resistance.

Initially, these tests will be run at room temperature. Table 1 shows the theoretical Hertzian stresses which would be imparted to an α- SiC ceramic flat by Co-WC balls with three different diameters and at two different loads. Inasmuch as Lucek[5] demonstrated that new and oxidized Nc-132 HPSN flats are cracked by comparably-sized (approximately 3/32 - 7/32 inch diamter) Co-WC balls at around 9 GPa, the range of our experimental variables is more than adequate.

II. Experimental Equipment

A. Loading

A special loading device is being constructed from an existing Hertzian cone-cracking apparatus (see Figure 2)[6]. The loading mechanism consists of a ball-bearing guided, vertical steel shaft with an in-line force transducer and a ball-holder on the bottom end, and a dead-weight loading platform on the top end.

The ball holder, which houses an adhesively-bonded ball (silver-filled EC 56C per HP 16-95) can rest on any given contact point of the flat coupon positioned underneath it (see Figure 3). The position can be precisely adjusted with an X-Y stage (Newport Research Model 460-XY).

The load is sensed by a force transducer (Sensotec Model 34) installed in-line with a dead-weighted loading rod. Progressively increased dead weights will be applied by pouring fine lead shot into a weighting pan through an orifice of controlled size. Changing the ball indenter diameter and the lead shot orifice size of the loading funnel will permit measurements of the critical normal load-to-fracture of the ceramic flat as a function of indenter radius and loading rate.

Note that a load-retarding spring (Century Springs, Inc.) prevents contact between the ball and flat when the system is not loaded. The idea is to prevent shock-loading of the system with careful experimental technique and use of the compensating spring.

B. Electrical

An electrical wiring schematic diagram for the apparatus is shown in Figure 4. The force transducer (Sensotec Model 34) has a 20 mV full-scale output (2 mV/lb) and requires a 10 volt stable power supply. (Sensotec sells a suitable power supply (Sensotec 10-240) for $160 if we cannot locate one in the equipment pool). The output lines (positive and negative) from the transducer will connect to the "Type 4" input terminals (x-axis) of the X-Y Recorder (Houston Instruments 2000 Recorder).

The change in the electrical contact resistance with applied force will be monitored continuously using a digital multimeter with analog output (Hewlett Packard Model 412A DC Vacuum Tube Voltmeter). The leads from the balls and flat will be connected to the DC Voltmeter which, in turn, will have leads connected to the "Type 3" input terminals (y-axis) of the X-Y Recorder. The X-Y Recorder will indicate changes in electrical resistance with changes in applied load.

C. RF Sputtered Parts

Six ceramic flats have been sputtered with an "adhesive layer" of chromium approximately 200 Angstroms thick followed by a layer of gold approximately 1500 Angstroms thick (see Figure 5). These six (three α- SiC and three HPSN substrates) will be used for preliminary calibration and check-out of the Hertzian cone-cracking apparatus. The chromium/gold sputtered films demonstrates excellent adhesion (passes the tape test to the ceramic substrates and exhibits excellent electrical conductivity).

D. Items Yet to be Done

Essentially there are four items yet to be done to complete assembly/fabrication of the apparatus' component parts. Frist, a constant power supply for the force transducer must be purchased or appropriated here at Hughes (as discussed in section B). Second, the hard-coated balls must be bonded to the aluminum ball-holders, as discussed in section A. Third, the moveable stage from the old Brinell indentation apparatus must be modified as shown in Figure 6. By countersinking four thru-holes as shown in Figure 5, the stage can be mounted properly to the precision X-Y stage. Fourth, the baseplate from the Brinell indentation apparatus must be modified as shown in Figure 7. The four new thru-holes will enable the precision X-Y stage to be mounted to the baseplate.

III. Conclusions

The existing Hughes Brinell apparatus will be refurbished in accordance with the new design. The necessary drawings are complete, and the necessary equipment has been ordered. The model experiments should begin as soon as the force transducer (the pacing item) is received.

for G.D.E. Mielgaard
G.D. Eisenbrand

Approved by: R.E. Kelchner
R.E. Kelchner, Head
Materials Physics Section

jsb:

TABLE 1

Maximum Hertzian Stress of an ESK -SiC

Ceramic Flat Contacted by Co-WC Balls

Ball Diameter, m. (in.)	Load, Ig (lbs.)	Max. Stress, GPa (psi)
2.381×10^{-3} (3/32)	0.454 (1)	10.9 (1.575×10^6)
2.381×10^{-3} (3/32)	4.54 (10)	23.4 (3.394×10^6)
3.968×10^{-3} (5/32)	0.454 (1)	7.8 (1.120×10^6)
5.556×10^{-3} (7/32)	0.454 (1)	6.2 (0.895×10^6)

SP 410438

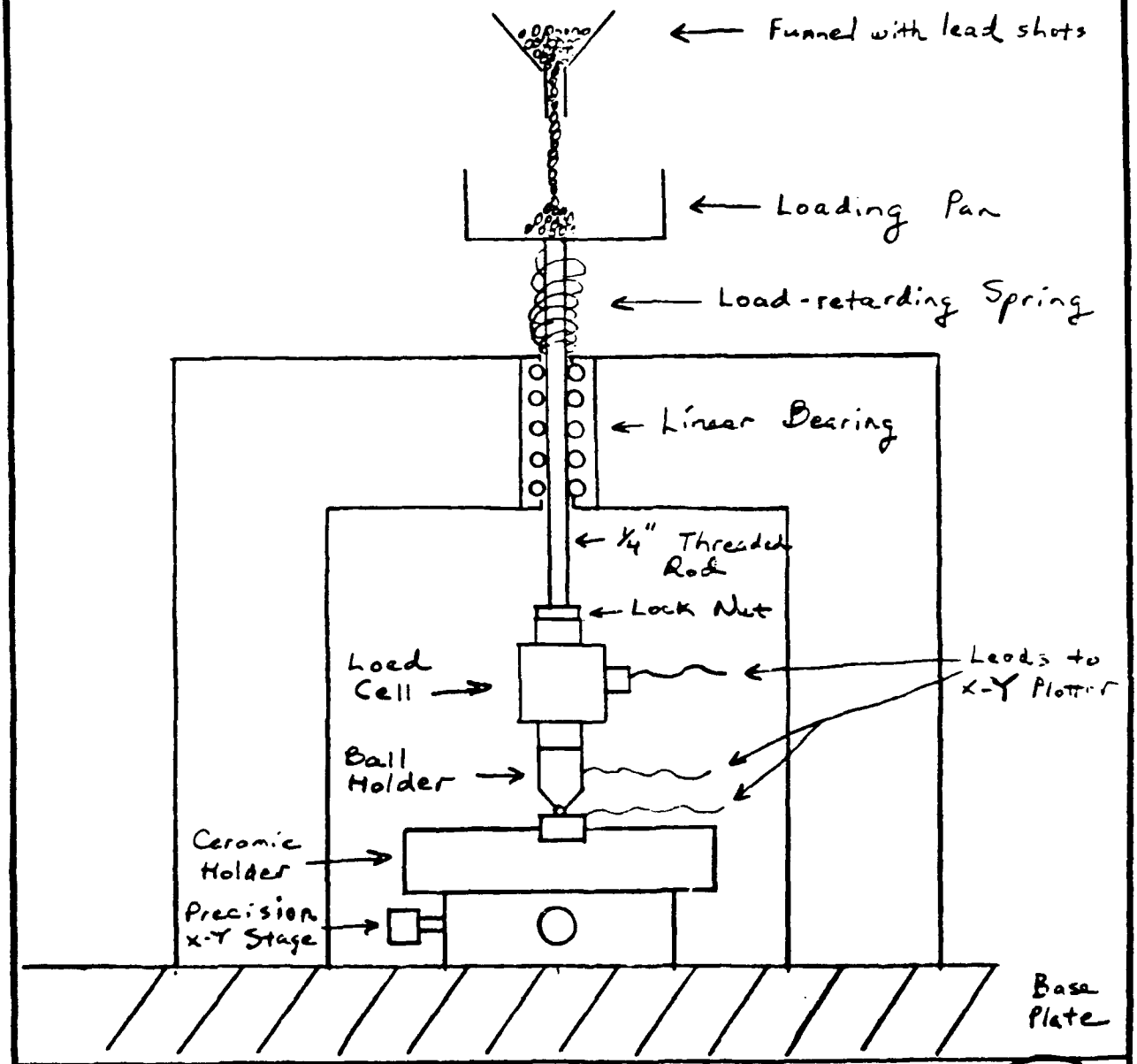

PURPOSE: TO MEASURE ONSET OF "RING CRACKING"					TITLE: CONE-CRACKER			V-7
MAT'L & SPEC.					SCALE: 1:2	TOLERANCES: ANGULAR ±	LINEAR ±	SKETCH PAD
ORIGINATOR: GDE	APPR.	DATE	BLDG.: E1	ROOM (STA.): C1331	PHONE: x66078	HUGHES		SP 410438

437 CC MAR 65

FIGURE 1

SP 410437

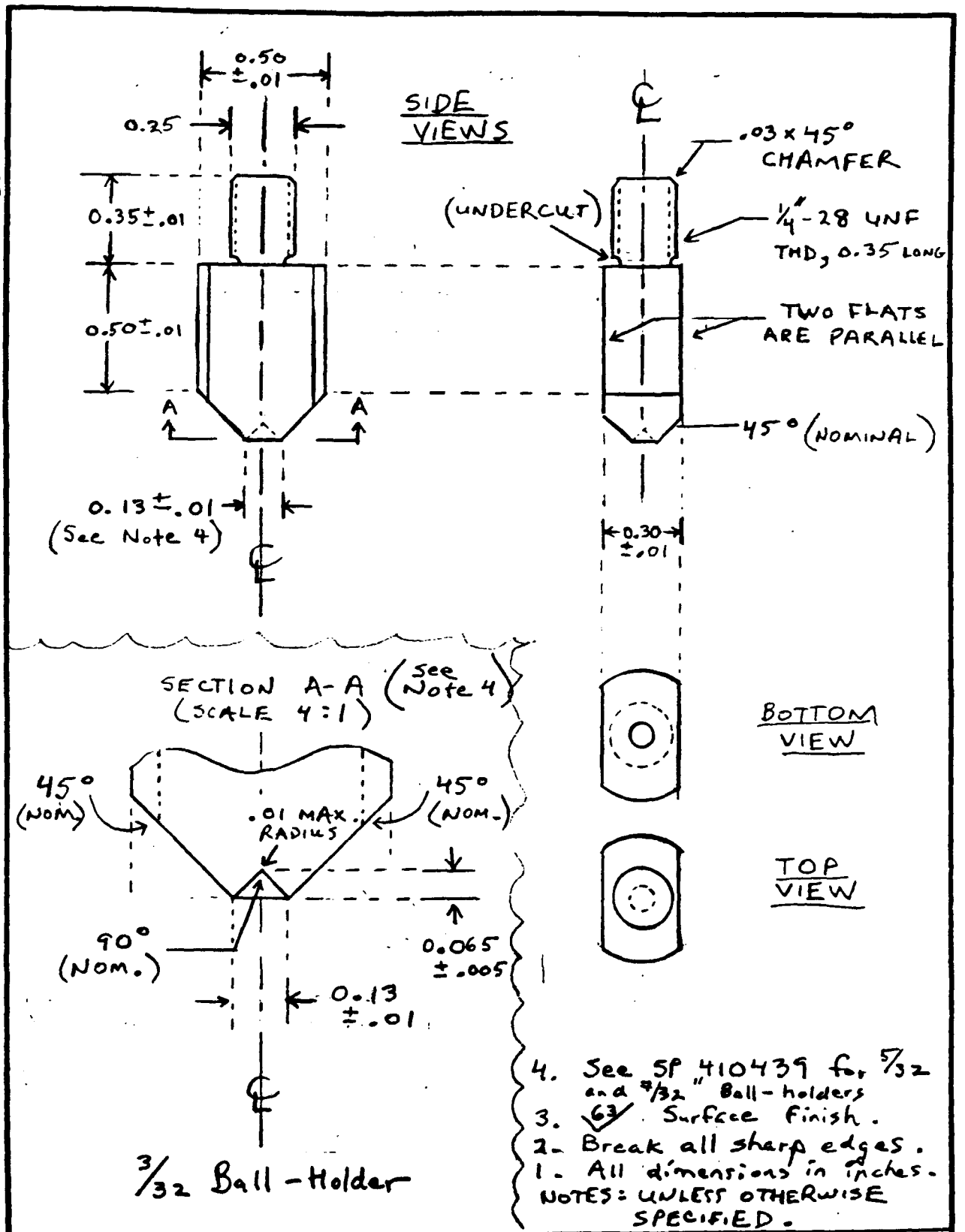

4. See SP 410439 for 5/32 and 7/32" Ball-holders
3. 63 Surface Finish.
2. Break all sharp edges.
1. All dimensions in inches.

NOTES: UNLESS OTHERWISE SPECIFIED.

PURPOSE: CONE-CRACKER (V-8)					TITLE: BALL-HOLDER FOR 3/32" BALL		
MATL & SPEC: ALUMINUM					SCALE: 2:1	TOLERANCES: ANGULAR ± 1.0° / LINEAR ± 0.01	SKETCH PAD
ORIGINATOR: GDE	APPR.	DATE: 06/22/86	BLDG: E1	ROOM (STA): C1331	PHONE: 66038	HUGHES	SP 410437

SP 410439

Reference :
SP 410437

SECTION A-A

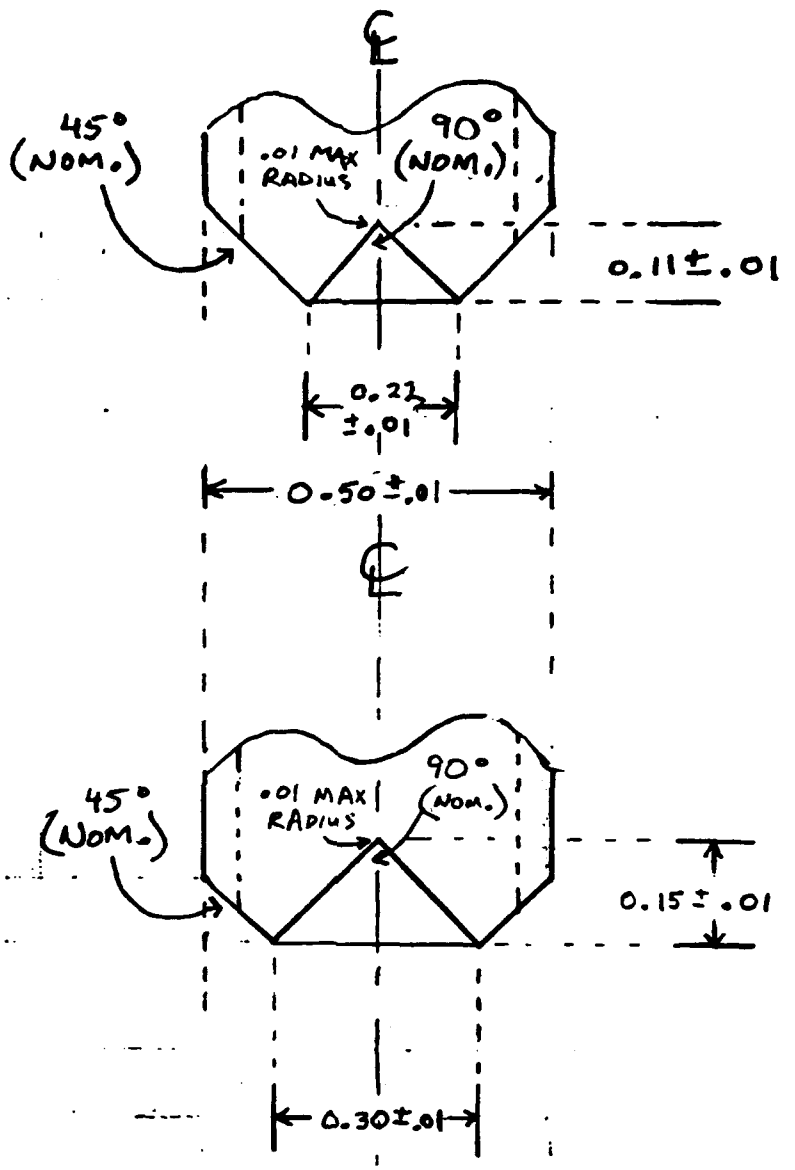

NOTES: UNLESS OTHERWISE SPECIFIED
1. All Dimensions in inches
2. Break all sharp edges

PURPOSE: CONE-CRACKER (V-9)					TITLE: BALL-HOLDER FOR 5/32, 7/32" BALLS			
MATL & SPEC: ALUMINUM T4 or T6; Anodize per MIL-A-8625, Type II, No dye					SCALE: 4:1	TOLERANCES: ANGULAR ±1.0	LINEAR ±.01	SKETCH PAD
ORIGINATOR: GDE	APPR.	DATE: 06/04/86	BLDG. E1	ROOM (DIV.) C1331	PHONE: x66038	HUGHES		SP 410439

437 CC MAR 86

FIGURE 2 (CONTINUED)

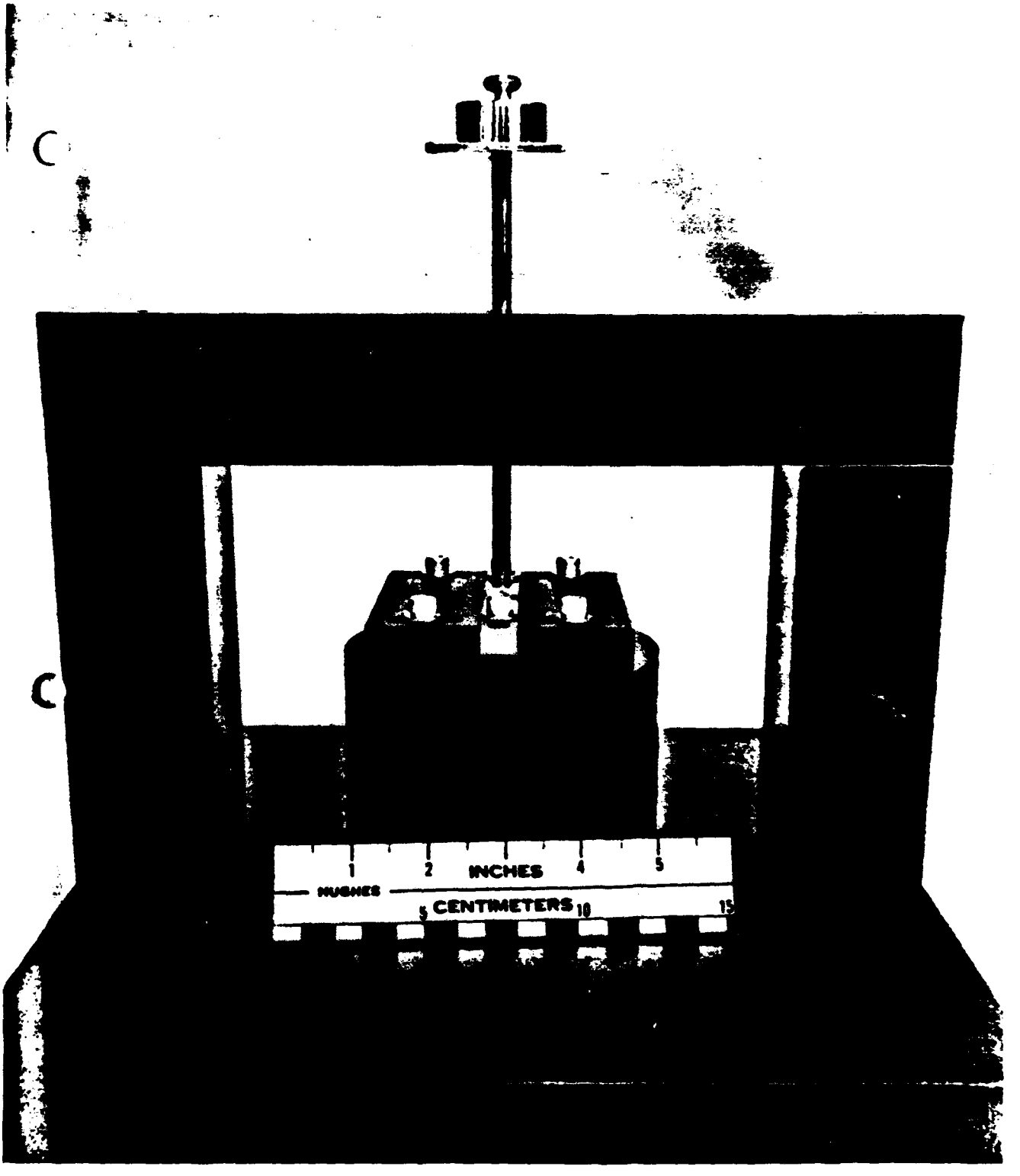

Figure 3. The Brinell indentation apparatus.

FIGURE 4

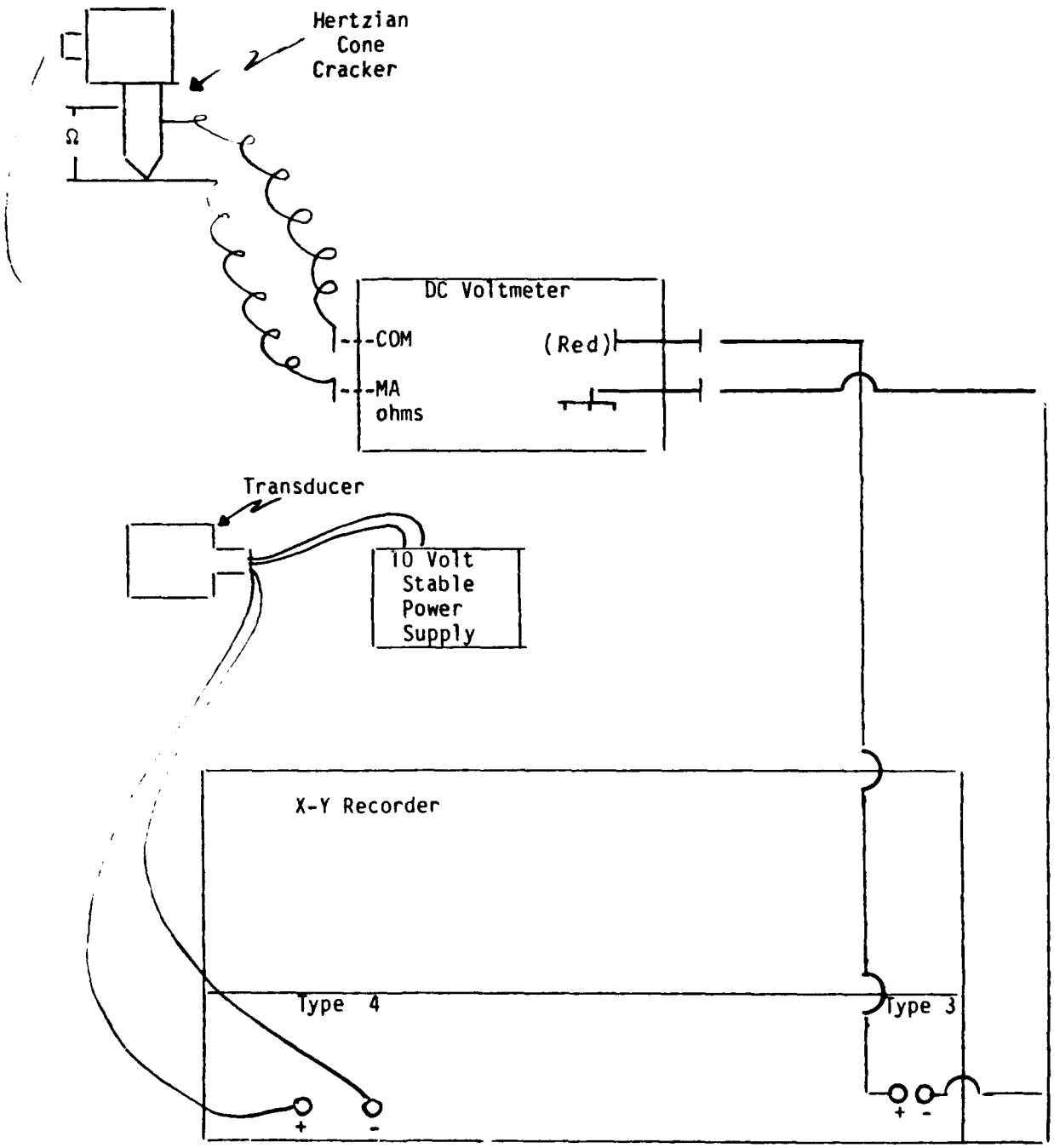
Hertzian
Cone
Cracker
Ω
DC Voltmeter
COM
(Red)
MA
ohms
Transducer
10 Volt
Stable
Power
Supply
X-Y Recorder
Type 4
Type 3
+
-
+
-

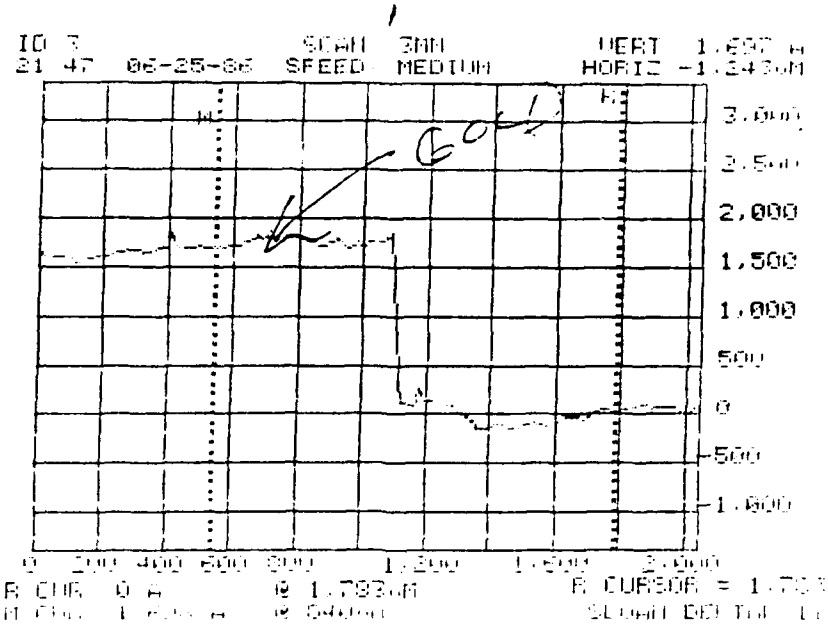

FIGURE 5

Surface profilometer trace of a glass microscope slide which was RF sputtered with chromium and gold simultaneously with six ceramic flats. The total thickness of the chromium/gold film is between 1500 and 2000 Angstroms.

SP 410441

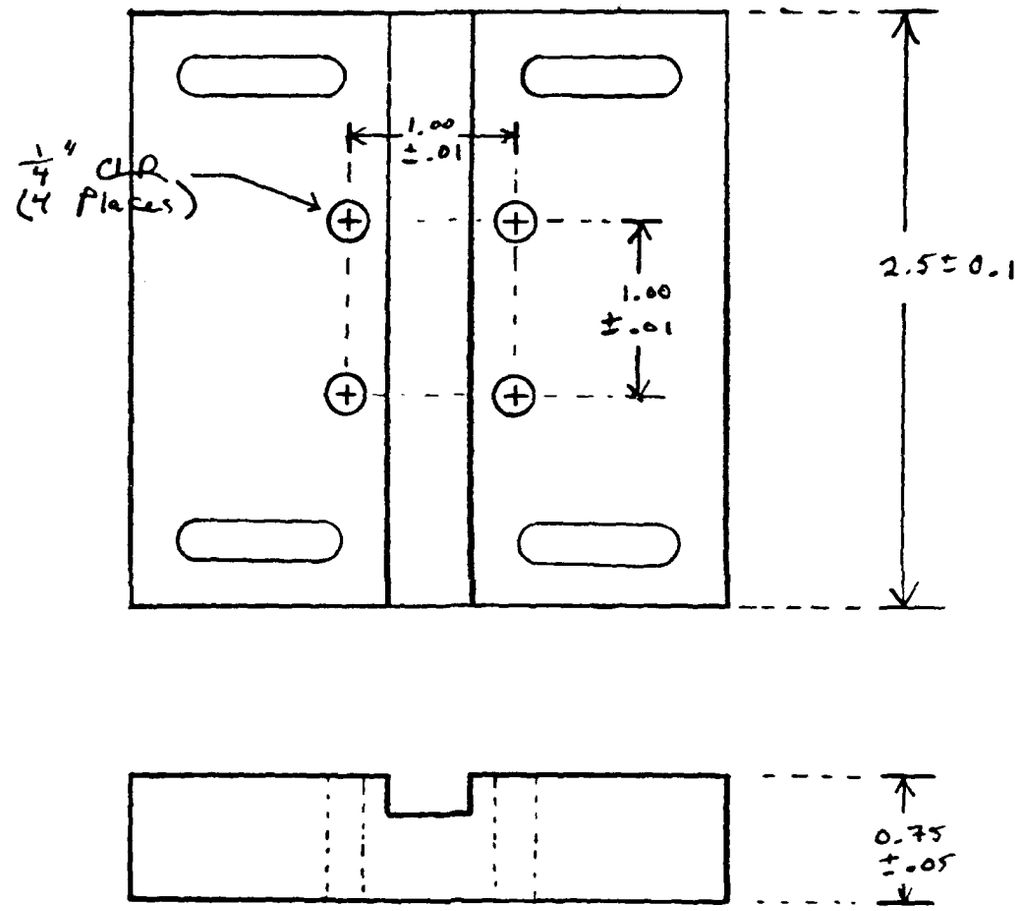

PURPOSE					TITLE		
CONE - CRACKER (V-13)					MOVABLE STAGE		
MATL & SPEC.					SCALE	TOLERANCES ANGULAR ± / LINEAR ±	SKETCH PAD
ALUMINUM					1 : 1		
ORIGINATOR	APPR.	DATE	BLDG.	ROOM (STA.)	PHONE	HUGHES	SP 410441
GDE		04/19/96	E1	C1331	6038		

437 CC MAR 55

FIGURE 6

SP 410440

TOP VIEW

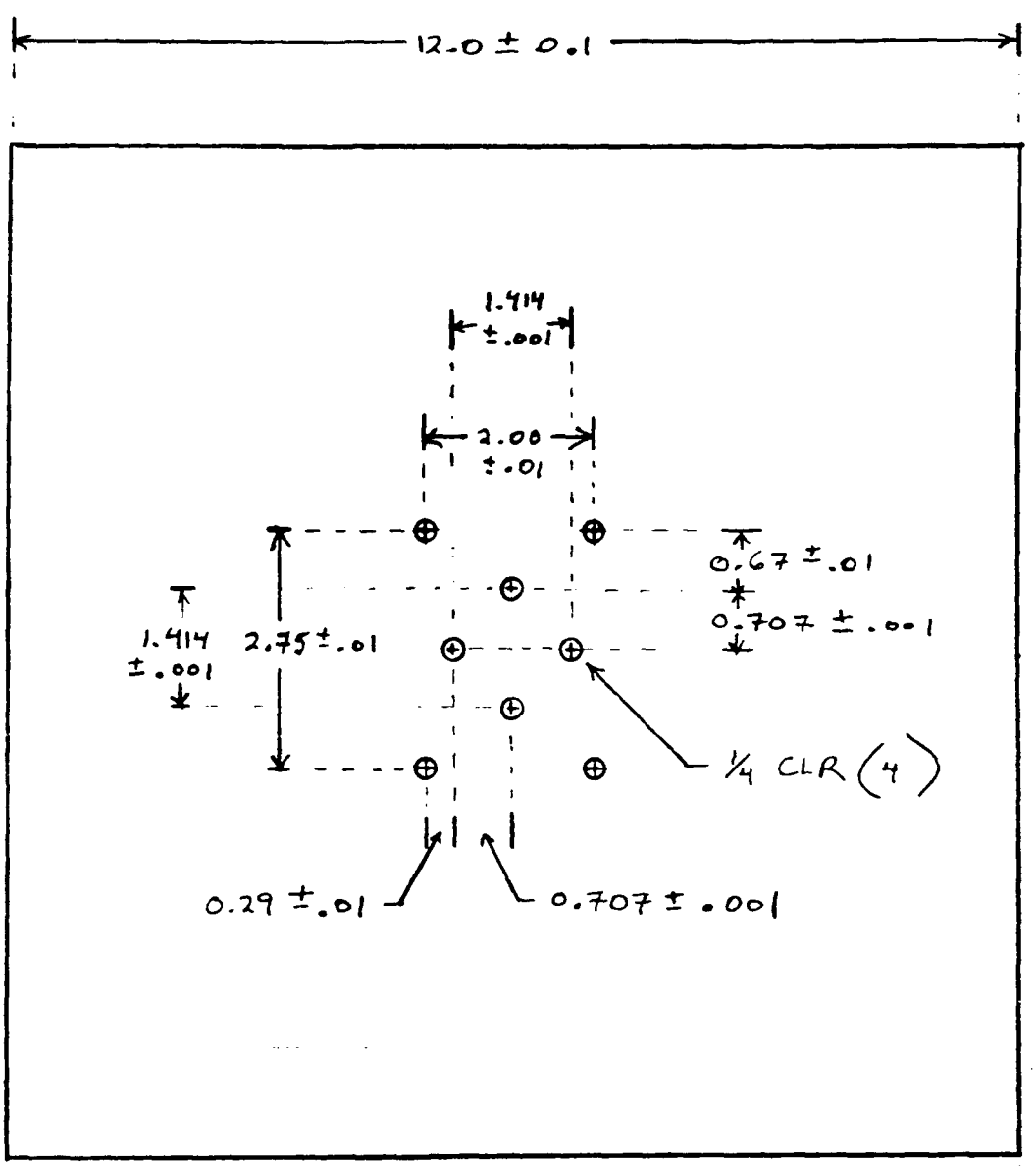

SIDE VIEW

1. All dimensions in inches.

PURPOSE: SUPPORT, STABILITY OF APPARATUS					TITLE: CONE CRACKER BASE-PLATE			
MATL & SPEC: ALUMINUM (V-14)					SCALE: 1:2	TOLERANCES: ANGULAR ±	LINEAR ± .001	SKETCH PAD
ORIGINATOR: GDE	APPR.	DATE: 06/13/86	BLDG: E1	ROOM (STA): C1331	PHONE: 66038	HUGHES		SP 410440

NOTES

(1) Grzybowski, T.A. and Ruoff, A.L., "New Method of Determining the Onset of Ring Cracking", Rev. Sci., Instrum. 54 (3), March 1983, pp. 357 - 360.

(2) Ibid, p. 357.

(3) Tolanski, S. and Halperin, A., Proc. R. Soc. 67, p. 473 (1954).

(4) Grzybowski, T.A. and Ruoff, A.L., op. cit.

(5) Gardos, M.N., et al, IDC #7621.10/106, "Static Load of Beryllium Copper as a Rolling Element Bearing Material (C-rite), November 27, 1985.

(6) Gardos, M.N., et al, op. cit.

AVOID VERBAL ORDERS

HUGHES AIRCRAFT COMPANY

To: M N Gardos 76 21 Loc:E1/F150
From: B L Billington 76 21 Loc:E1/F150
Subject: Hertzian Stresses 10/31/86

A detailed review of Grzybowski and Ruoff's article uncovered that their equation describing the Hertzian stresses between a ball and a flat is incorrect. This equation, as used by Greg Eisenbrand in his June status report, describes the maximum contact stress as follows:

$$P_o = \frac{3}{2\pi}\left[\left(\frac{4}{3\pi}\right)^2 (K_f + K_I)^2 R^2/F\right]^{-1/3} \quad (1)$$

The correct equation:

$$P_o = \frac{3}{2\pi}\left[\left(\frac{3\pi}{4}\right)^2 (K_f + K_I)^2 R^2/F\right]^{-1/3} \quad (2)$$

yields much different loads than originally believed for a tungsten carbide ball in contact with a HPSN test flat (table 1). Note the inverted $4/3\pi$ and $3\pi/4$ ratios in the respective equations.

By replacing high load sensitive components, the current test set up can be modified to provide the necessary loads. This test set up is limited by the 10 lb. load cell and the x-y stage which has a maximum load capacity of 25 lbs. The test frame can be replaced with an available, more massive Tinius Olsen frame and loading rod in which an available 300 lb. load cell can be easily mounted. Adaptors have been machined so that the indentor tip can be attached to the new load cell. The current 15 lb. loading system will have to be replaced with one that will provide loads to 150 lbs. I am currently in the process of locating a loading device that will suit our needs.

Because this test method has not been explored fully, I would like to continue with the above mentioned modifications which will enable me to determine if this is a viable method to detect the onset of cracking in our test samples. If not, I would like to suggest using acoustic emission as a measure of cracking. It is estimated that the cost of such a system will not exceed $3500.

V-16

For your review I have included the tabulated and graphical result generated for the Hertzian contact problem using the following load, material and geometrical constraints:

Max stress	9.0 Gpa
E (indentor)	94×10^6 psi
E (flat)	40×10^6 psi
Poisson's(ind.)	.28
Poisson's(flat)	.27
Ball dia	3/32 in
	5/32 in
	7/32 in

These data were generated by eq.(2).

B L Bubley Jr

V-17

Hertzian Stresses

Ball Dia.(in.)	Max Load (lb)	Max. Stress (GPa)
3/32	27.47	9.00
5/32	76.27	9.00
7/32	149.80	9.00

Table 1

HPSN flat, Co/WC indentor

Tungsten Carbide Ball on SiN Flat

Input Params.	Intermediate Calculations	Contact Load (Lbs.)	Contact Load (Newton)	Contact Radius (inch)	Mean Stress (psi)	Max.Stress (psi)	Mean Stress (GPa)	Max.Stress (GPa)
Young s Mod 1	Mtlf.1	0.000000E+00	0.000000E+00	0.000000E+00	ERR	ERR	ERR	ERR
9.400000E+07	3.921702E-08	4.000000E+00	1.779289E+01	1.977250E-03	3.256767E+05	4.885151E+05	2.245462E+00	3.368193E+00
Young s Mod 2	Mtlf.2	8.000000E+00	3.558577E+01	2.491179E-03	4.103270E+05	6.154905E+05	2.829105E+00	4.243657E+00
4.000000E+07	9.271000E-08	1.200000E+01	5.337866E+01	2.851689E-03	4.697071E+05	7.045607E+05	3.238517E+00	4.857775E+00
Pois.Ratio 1	Summation 1/R	1.600000E+01	7.117155E+01	3.138689E-03	5.169796E+05	7.754694E+05	3.564449E+00	5.346673E+00
2.800000E-01	2.560000E+01	2.000000E+01	8.896443E+01	3.381051E-03	5.568994E+05	8.353491E+05	3.839686E+00	5.759529E+00
Pois.Ratio 2		2.400000E+01	1.067573E+02	3.592903E-03	5.917939E+05	8.876909E+05	4.080275E+00	6.120413E+00
2.700000E-01		2.800000E+01	1.245502E+02	3.782344E-03	6.229972E+05	9.344958E+05	4.295414E+00	6.443122E+00
Ball Diameter		3.200000E+01	1.423431E+02	3.954501E-03	6.513538E+05	9.770302E+05	4.490924E+00	6.736386E+00
1.562500E-01		3.600000E+01	1.601360E+02	4.112847E-03	6.774349E+05	1.016152E+06	4.670749E+00	7.006124E+00
		4.000000E+01	1.779289E+02	4.259857E-03	7.016493E+05	1.052474E+06	4.837701E+00	7.256552E+00
		4.400000E+01	1.957218E+02	4.397366E-03	7.242986E+05	1.086448E+06	4.993863E+00	7.490794E+00
		4.800000E+01	2.135146E+02	4.526774E-03	7.456136E+05	1.118420E+06	5.140825E+00	7.711237E+00
		5.200000E+01	2.313075E+02	4.649178E-03	7.657750E+05	1.148663E+06	5.279833E+00	7.919749E+00
		5.600000E+01	2.491004E+02	4.765455E-03	7.849273E+05	1.177391E+06	5.411883E+00	8.117824E+00
		6.000000E+01	2.668933E+02	4.876319E-03	8.031879E+05	1.204782E+06	5.537786E+00	8.306670E+00
		6.400000E+01	2.846862E+02	4.982359E-03	8.206540E+05	1.230981E+06	5.658210E+00	8.487315E+00
		6.800000E+01	3.024791E+02	5.084068E-03	8.374066E+05	1.256110E+06	5.773715E+00	8.660572E+00
		7.200000E+01	3.202720E+02	5.181862E-03	8.538145E+05	1.280272E+06	5.884778E+00	8.827163E+00
		7.600000E+01	3.380648E+02	5.276098E-03	8.699364E+05	1.303555E+06	5.991795E+00	8.987692E+00
		8.000000E+01	3.558577E+02	5.367083E-03	8.857227E+05	1.326034E+06	6.095127E+00	9.142603E+00
		8.400000E+01	3.736506E+02	5.455084E-03	9.985175E+05	1.347776E+06	6.195059E+00	9.292589E+00
		8.800000E+01	3.914435E+02	5.540334E-03	9.125591E+05	1.368839E+06	6.291873E+00	9.437809E+00

$d = \frac{5}{32}$

Input Params.	Intermediate Calculations	Contact Load (Lbs.)	Contact Load (Newton)	Contact Radius (inch)	Mean Stress (psi)	Max.Stress (psi)	Mean Stress (GPa)	Max.Stress (GPa)
Young s Mod 1	Mtlf.1	0.000000E+00	0.000000E+00	0.000000E+00	ERR	ERR	ERR	ERR
9.400000E+07	3.921702E-08	3.000000E+00	1.334466E+01	1.515186E-03	4.159486E+05	6.239229E+05	2.867865E+00	4.301797E+00
Young s Mod 2	Mtlf.2	6.000000E+00	2.668933E+01	1.909014E-03	5.240624E+05	7.860936E+05	3.613283E+00	5.419924E+00
4.000000E+07	9.271000E-08	9.000000E+00	4.003399E+01	2.185276E-03	5.999017E+05	8.998525E+05	4.136176E+00	6.204265E+00
Pois.Ratio 1	Summation 1/R	1.200000E+01	5.337866E+01	2.405207E-03	6.602773E+05	9.904159E+05	4.552451E+00	6.828677E+00
2.800000E-01	4.266667E+01	1.500000E+01	6.672332E+01	2.590931E-03	7.112621E+05	1.066893E+06	4.903979E+00	7.355969E+00
Pois.Ratio 2		1.800000E+01	8.006799E+01	2.753275E-03	7.558288E+05	1.133743E+06	5.211256E+00	7.816884E+00
2.700000E-01		2.100000E+01	9.341265E+01	2.898446E-03	7.956811E+05	1.193522E+06	5.486028E+00	8.229041E+00
Ball Diameter		2.400000E+01	1.067573E+02	3.030371E-03	8.318972E+05	1.247846E+06	5.735729E+00	8.603594E+00
9.375000E-02		2.700000E+01	1.201020E+02	3.151713E-03	8.652080E+05	1.297812E+06	5.965399E+00	8.948098E+00
		3.000000E+01	1.334466E+02	3.264369E-03	8.961341E+05	1.344201E+06	6.178627E+00	9.267940E+00
		3.300000E+01	1.467913E+02	3.369743E-03	9.250614E+05	1.387592E+06	6.378074E+00	9.567111E+00
		3.600000E+01	1.601360E+02	3.468909E-03	9.522846E+05	1.428427E+06	6.565771E+00	9.848656E+00
		3.900000E+01	1.734876E+02	3.562709E-03	9.780344E+05	1.467052E+06	6.743309E+00	1.011496E+01
		4.200000E+01	1.868253E+02	3.651813E-03	1.002495E+06	1.503743E+06	6.911962E+00	1.036794E+01
		4.500000E+01	2.001700E+02	3.736769E-03	1.025817E+06	1.538726E+06	7.072762E+00	1.060914E+01
		4.800000E+01	2.135146E+02	3.818029E-03	1.048125E+06	1.572187E+06	7.226566E+00	1.083985E+01
		5.100000E+01	2.268593E+02	3.895969E-03	1.069521E+06	1.604281E+06	7.374087E+00	1.106113E+01
		5.400000E+01	2.402040E+02	3.970910E-03	1.090094E+06	1.635141E+06	7.515931E+00	1.127390E+01
		5.700000E+01	2.535486E+02	4.043124E-03	1.109918E+06	1.664877E+06	7.652615E+00	1.147892E+01
		6.000000E+01	2.668933E+02	4.112847E-03	1.129058E+06	1.693587E+06	7.784582E+00	1.167687E+01
		6.300000E+01	2.802380E+02	4.180282E-03	1.147571E+06	1.721356E+06	7.912221E+00	1.186833E+01
		6.600000E+01	2.935826E+02	4.245610E-03	1.165504E+06	1.748257E+06	8.035869E+00	1.205380E+01

$\frac{1}{2} = \frac{3}{32}$

Hertzian Stress Spread Sheet
Tungsten Carbide Ball on a Silicon Nitride Flat
Ball Diameter 0.31 inch

Input Params.	Intermediate Calculations	Contact Load (Lbs.)	Contact Load (Newton)	Contact Radius (inch)	Mean Stress (psi)	Max. Stress (psi)	Mean Stress (GPa)	Max. Stress (GPa)
Young's Mod. 1	Mdif.1	0.000000E+00	0.000000E+00	0.000000E+00	ERR	ERR	ERR	ERR
9.400000E+07	3.921702E-08	7.000000E+00	3.113755E+01	2.665501E-03	3.126434E+05	4.704451E+05	2.162219E+00	3.249
Young's Mod 2	Mdif.2	1.400000E+01	6.227510E+01	3.356755E-03	3.951155E+05	5.926733E+05	2.724125E+00	4.086
4.000000E+07	9.271000E-08	2.100000E+01	9.341265E+01	3.844361E-03	4.522943E+05	6.784415E+05	3.1184eaE+00	4.677e
Pois.Ratio 1	Summation 1/R	2.800000E+01	1.245502E+02	4.231266E-03	4.976143E+05	7.464215E+05	3.421e+00	5.13
2.800000E-01	1.612571E+01	3.500000E+01	1.556878E+02	4.557994E-03	5.362542E+05	8.043814E+05	3.697147E+00	5.54
Pois.Ratio 2		4.200000E+01	1.868253E+02	4.843541E-03	5.698552E+05	8.547828E+05	3.929103E+00	5.89
2.700000E-01		4.900000E+01	2.179629E+02	5.098977E-03	5.999017E+05	8.998525E+05	4.13e176E+00	6.204
Ball Diameter		5.600000E+01	2.491004E+02	5.331062E-03	6.272066E+05	9.408102E+05	4.324476E+00	6.48
3.100000E-01		6.300000E+01	2.802380E+02	5.544528E-03	6.522213E+05	9.78482E+05	4.497547E+00	6.74
		7.000000E+01	3.113755E+02	5.742713E-03	6.756380E+05	1.013457E+06	4.656e+00	6.98
		7.700000E+01	3.425131E+02	5.928059E-03	6.974477E+05	1.046172E+06	4.81E77E+00	7.21
		8.400000E+01	3.736506E+02	6.102542E-03	7.179725E+05	1.07695E+06	4.95e24eE+00	7.42
		9.100000E+01	4.047882E+02	6.2e7555E-03	7.373e65E+05	1.106e1.E+06	5.08e11E+00	7.62
		9.800000E+01	4.359257E+02	6.424309E-03	7.558288E+05	1.133743E+06	5.211e5eE+00	7.81
		1.050000E+02	4.670633E+02	6.5777e4E-03	7.734125E+05	1.16e119E+06	5.332491E+00	7.99
		1.120000E+02	4.982008E+02	6.716717E-03	7.902310E+05	1.185347E+06	5.446451E+00	8.17
		1.190000E+02	5.293384E+02	6.850e3eE-03	8.063e26E+05	1.209544E+06	5.55e74E+00	8.33
		1.260000E+02	5.604759E+02	6.9656e7E-03	8.218734E+05	1.232810E+06	5.666e17E+00	8.49
		1.330000E+02	5.916135E+02	7.112707E-03	8.368198E+05	1.255234E+06	5.769e6E+00	8.65
		1.400000E+02	6.227510E+02	7.253e64E-03	8.512e0eE+05	1.276e75E+06	5.869ebeE+00	8.80
		1.470000E+02	6.538886E+02	7.3e7497E-03	8.652e30E+05	1.297812E+06	5.96E79E+00	8.94
		1.540000E+02	6.850262E+02	7.4e6503E-03	8.7e1e3eE+05	1.318e44E+06	6.05ee2eE+00	9.08

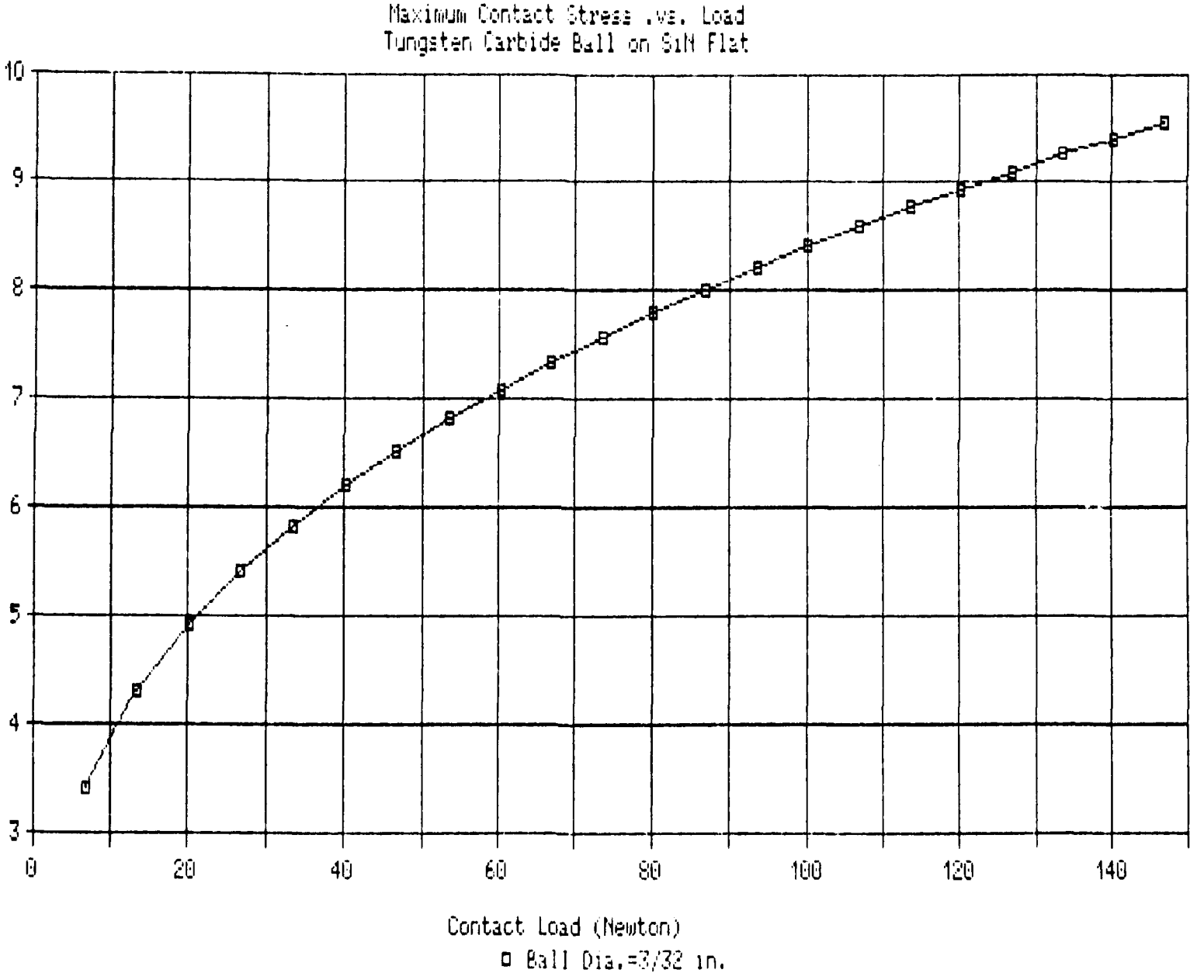
Maximum Contact Stress .vs. Load
Tungsten Carbide Ball on SiN Flat
Max. Stress (GPa)
10
9
8
7
6
5
4
3
0
20
40
60
80
100
120
140
Contact Load (Newton)
Ball Dia.=3/32 in.

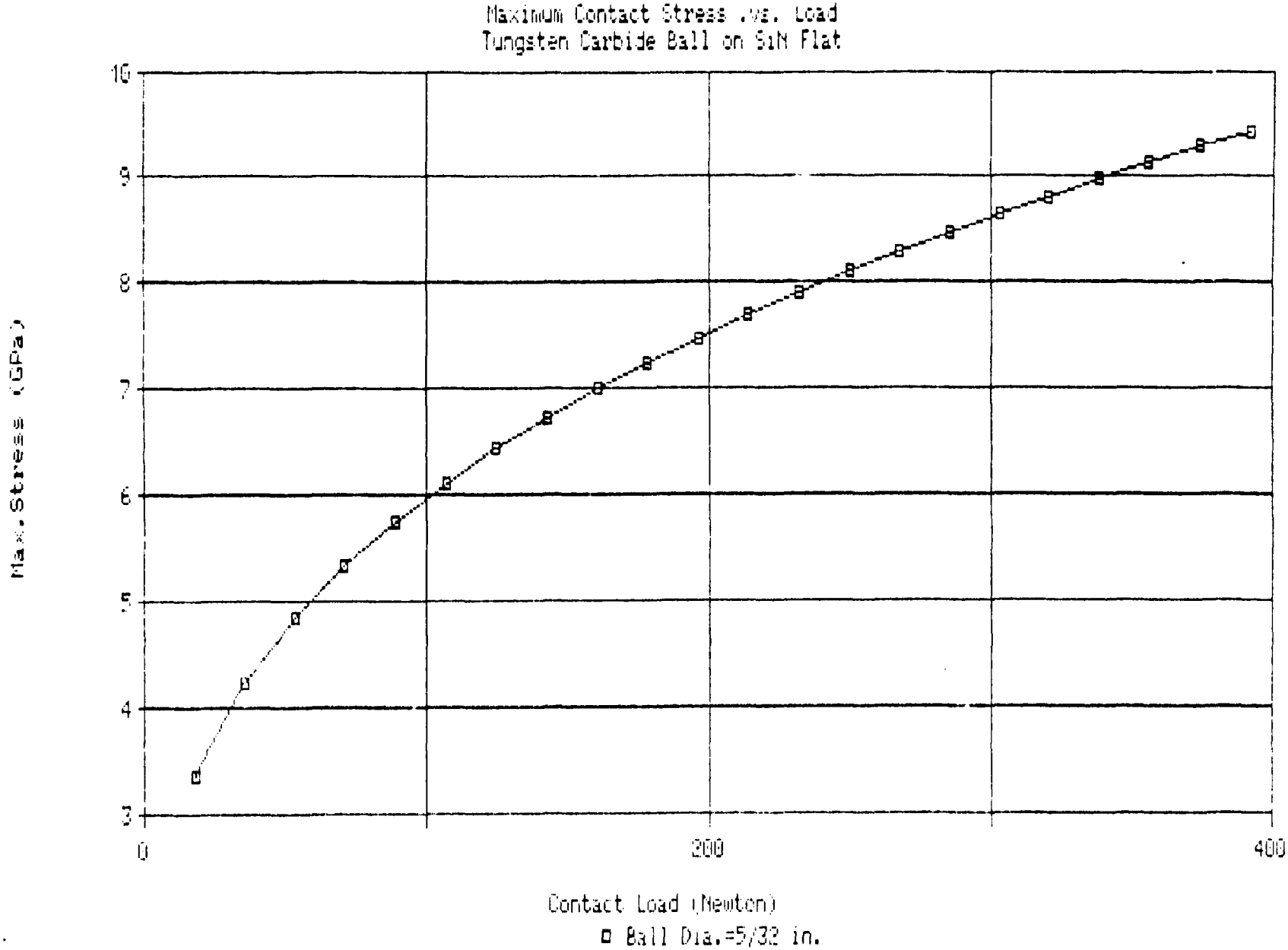
Maximum Contact Stress .vs. Load
Tungsten Carbide Ball on SiN Flat
Max. Stress (GPa)
10
9
8
7
6
5
4
3
0
200
400
Contact Load (Newton)
Ball Dia.=5/32 in.

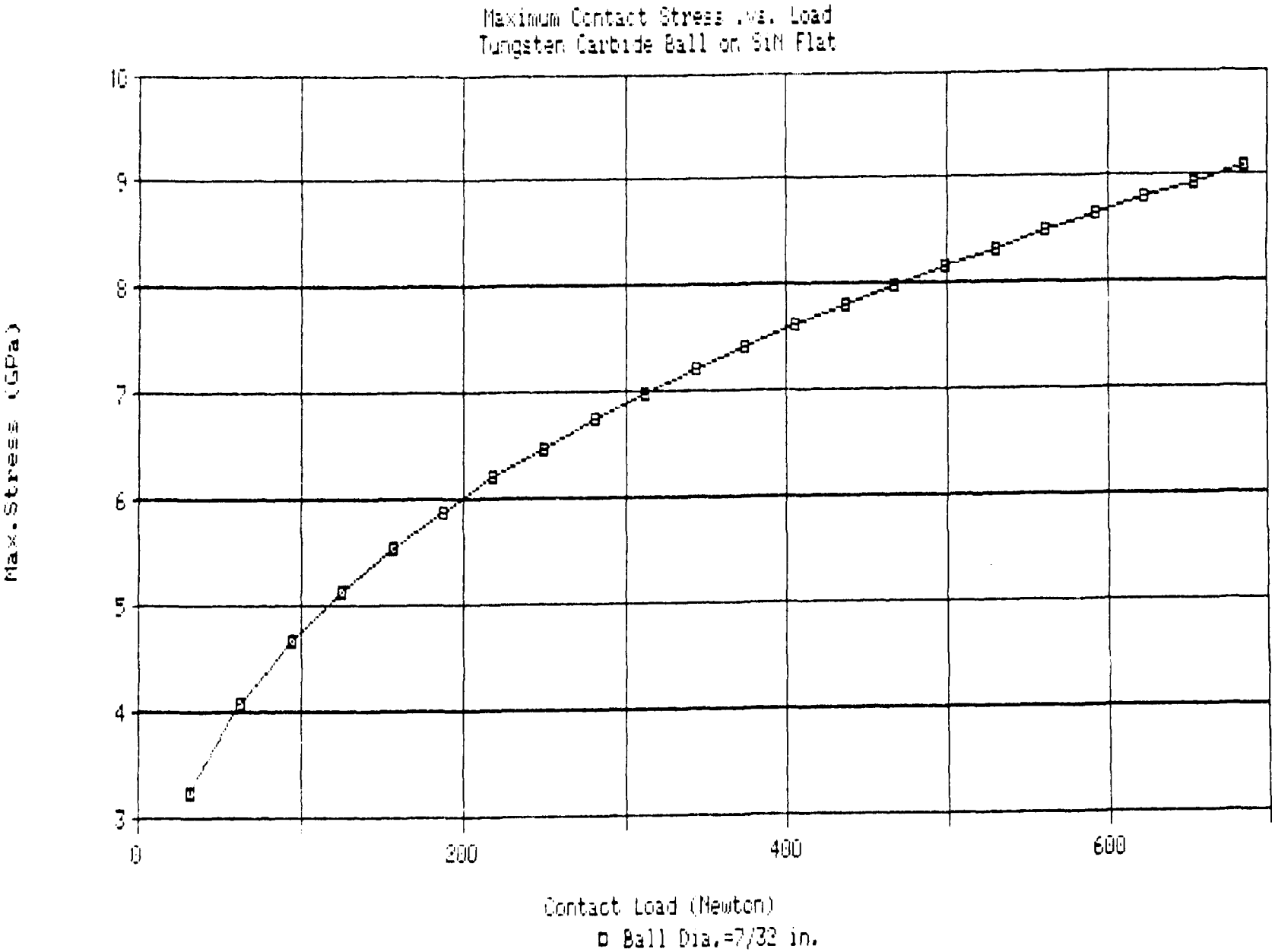
Maximum Contact Stress vs. Load
Tungsten Carbide Ball on SiN Flat
Max. Stress (GPa)
10
9
8
7
6
5
4
3
0
200
400
600
Contact Load (Newton)
Ball Dia.=7/32 in.

APPENDIX W

R.G. Hardistry, "Materials Removal Rate; Silicon Nitride Materials; Base-Date," Final Report, Spheric Special Products Report No. 1.015, Spheric, Inc., W. Sussex, England, 04 September 1989; Hughes P.O. M9-317643-KKD

Material Removal Rate Silicon Nitride Materials Base - Data

W-1

1 Introduction

We have reviewed all of the data collected in processing 6 types of material under controlled conditions and have produced a summary of the measurements made during the grinding process.

The process data is contained in section 2, and summarised in section 3.

Previously when analysing this data to produce diametric and volumetric grind rates we have used the change in size between the end of the rounding stage and the end of the grinding process. This approach does therefore consider the whole grinding process but as the applied load is changed during the process may distort the results, and provide unrelated values for grind rate.

In carrying out this review it we have therefore, considered only that part of the grinding process during which the applied load is constant at 1kgf per ball. Because of this change the grind rates are different from those previously stated, and are i believe more accurate.

2 Basic Data From Grinding Process

The data listed below shows the mean diameter, and applied load at various times within the grinding process, for each lot of balls covering the 6 material processed under controlled conditions.

The load is shown as load per ball, and is that which was applied from the elapsed time shown.

The time starts at the completion of the rounding process, although in some cases, the balls may not have been fully round at this time.

2.1 Babcock & Wilcox

time (hours)	load (kgf)	diameter (inches)
0	2.5	0.525512
4	1	0.519500
8	1	0.515510
10	1	0.510170
11	1	0.508390
12	1	0.506510
13	1	0.504510
14	1	0.502730
15	0.4	0.501530
16	0.4	0.500772
17	0.4	0.500374
mean grind rate		0.001479

2.2 Cercom - Hot Pressed

time (hours)	load (kgf)	dia (inches)
0	0.625	0.519094
4	2.5	0.513650
8	1	0.508350
10	1	0.503150
11	1	0.501550
12	1	0.501150
13	1	0.500950
14	1	0.500800
15	1	0.500720
16	1	0.500500
17	1	0.500450
mean grind rate		0.000878

2.3 Cercom - HIP

time (hours)	load (kgf)	dia (inches)
0	0.65	0.513701
4	2.5	0.512002
6	1	0.510500
8	1	0.505500
10	1	0.503400
11	1	0.502100
12	0.4	0.500900
13	0.4	0.500400
mean grind rate		0.001023

2.4 Toshiba

time (hours)	load (kgf)	dia (inches)
0	0.65	0.524055
4	2.5	0.523622
8	1	0.522047
16	1	0.519685
24	1	0.516535
32	1	0.512992
40	1	0.509843
48	1	0.507480
56	1	0.504331
60	1	0.502756
64	1	0.501575
66	1	0.501181
68	1	0.499409
mean grind rate		0.000362

2.5 UBE

time (hours)	load (kgf)	dia (inches)
0	0.65	0.518504
4	2.5	0.518110
8	1	0.517717
16	1	0.515354
24	1	0.512205
32	1	0.509449
40	1	0.506299
48	1	0.504331
56	1	0.502756
64	1	0.501181
68	1	0.500591
70	1	0.500315
71	1	0.500236
mean grind rate		0.0003

2.6 Norton

time (hours)	load (kgf)	dia (inches)
0	1	0.512260
4	1	0.508620
6	1	0.506730
7	1	0.505900
8	1	0.504500
10	1	0.503200
11	1	0.502100
12	0.4	0.500900
mean grind rate		0.000947

3 Summary of Data

The data shown in section 1 is summarised below.

The start and finish sizes used in this summary are the end points of the process during which a constant load of 1kgf per ball was applied, and as a result the grind rates are different from those previously stated.

The hardness and toughness values are those previously stated, and were all measured under the same controlled conditions.

	Cercom HIP	Babcock & Wilcox	Cercom HP	Norton	Toshiba	UBE
Start Size[1]	0.510500	0.519500	0.50835	0.512260	0.522047	0.517717
End Size[2]	0.500900	0.501530	0.50045	0.500900	0.499409	0.500236
Time[3]	6	11	9	12	60	63
Hardness $Hv_{(5kgf)}$	1655	1390	1570	1820	1545	1610
Toughness	4.70	5.60	5.82	5.00	6.93	6.97
diameter reduction rate	0.0016	0.001633	0.000877	0.000946	0.000377	0.000277
Product of hardness and toughness	7778.5	7784	9137.4	9100	10706.85	11221.7
volume change rate	0.000642	0.000668	0.000350	0.000381	0.000154	0.000112
$\frac{1}{hardness^{\frac{1}{2}}}$	0.024581	0.026822	0.025237	0.023440	0.025441	0.024922
$\frac{1}{toughness^{\frac{2}{3}}}$	0.313275	0.274700	0.266874	0.299069	0.234126	0.233117
$\frac{1}{toughness^{\frac{1}{2}}} \times \frac{1}{hardness^{\frac{1}{2}}}$	0.007700	0.007368	0.006735	0.007010	0.005956	0.005809

1 The size when the pressure was reduced to 1kgf per ball, and not the true start size.

2 The size when the load was reduced below 1kgf

3 The running time between the start and end size

4 Rate of Material Removal

4.1 Diameter Change Rate

Previously in analysing the results we have suggested the possible relationship between the diameter change rate and the product of hardness and toughness.

Figure 1 shows the relationship of diameter change rate to the product of hardness and toughness. As before the Cercom HP material is not included as the degree of size variation present in the batch appeared to provide a significant potential error. However, having re-examiner the original grind rate data it appears reasonable to include this material.

fig. 1

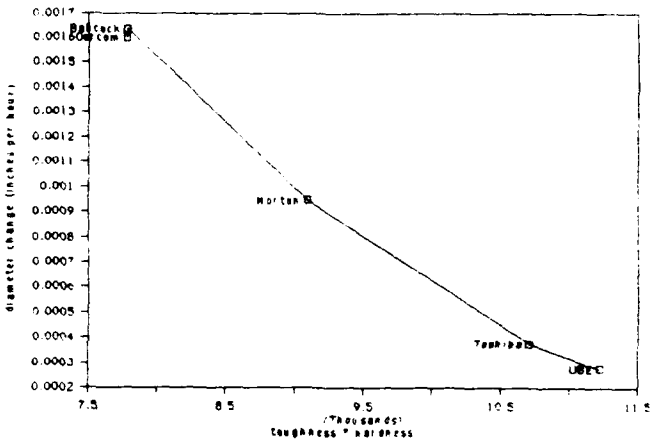

Figure 2 shows the same values but *includes the Circom HP* material and it is clear that this also fits the general pattern. Overall these results, based that part of the grinding process where a constant 1kgf load was applied reinforce the view that the product of hardness and toughness provides a good indication of the resistance of the material to the process and by extension to wear in use.

fig. 2

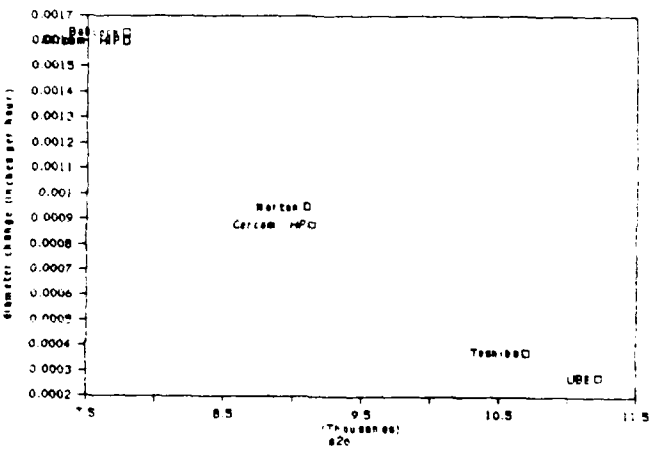

4.2 Volumetric Change Rate

Considering the relationship

$$\frac{1}{volume\ \ reduction} \propto \frac{1}{fracture\ \ toughness^{\frac{3}{4}}} \times \frac{1}{hardness^{\frac{1}{2}}}$$

Figure 3 shows the volumetric change rate against

$$\frac{1}{fracture\ \ toughness^{\frac{3}{4}}} \times \frac{1}{hardness^{\frac{1}{2}}}$$

excluding the Circom HP material as previously. With the exception of the Babcock & Wilcox material the relationship appears to be good.

fig. 3

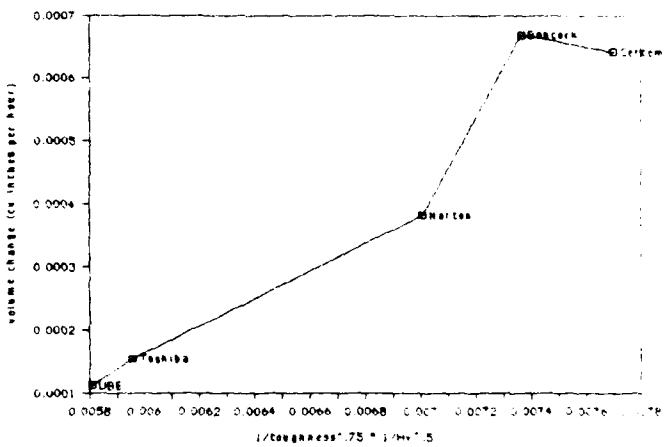

Figure 4 shows the same values but includes the Cercom HP material which again seems to fit the relationship. The higher material removal rate shown for the Babcock & Wilcox material may be related to the Boron Carbide Inclusions providing a "soft" spot for entry of the abrasive particles, thereby increasing the rate of cutting.

fig. 4

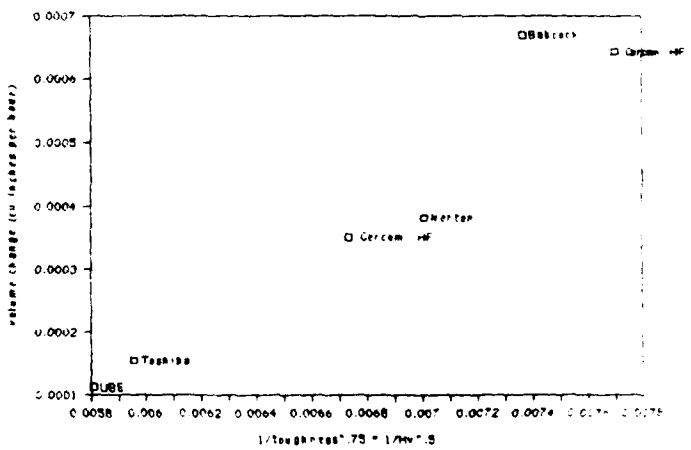

5 Discussion

It is clear from the data and figures above that a relationship exists between the grind rate and a combination of hardness and toughness, and that for balls there is a considerable similarity between the values for change in diameter and change in volume.

The relationship is certainly more clearly demonstrated using the change under the constant 1kgf as in this analysis as opposed to the change through the whole process as used previously.

It may be that in comparing wear rate of balls with wear rate on flat specimens, the swept surface area is more relevant than either volume or diameter change. Certainly we have found that in trying to predict the cutting rate in our normal process, that it is difficult to produce a simple relation ship between size and time using either change in diameter or change in volume.

However, if we consider the process at the micro level, it is clear that we achieve very little real depth of cut. The cutting process may therefore be characterised as a repeated scratching of the surface, probably to a depth of a of 2 to 5 micro inches[4], the size being reduced as these scratches join to cover the whole surface.

Effectively, the process repeatedly removes very thin layers from the ball which can be described as a series of the form

$$volume = 4\pi r_s^3 - (4\pi(r_s - d)^2 d) - (4\pi(r_s - 2d)^2 d) - (4\pi(r_s - 3d)^2 d) - (4\pi(r_s - 4d)^2 d) \ \ldots\ldots\ etc$$

where r_s is the start radius and **d** is the depth of cut.

If the surface area is the controlling factor the time taken to remove each layer would be less than the time for the preceding layer, such that the time taken to remove any layer **(n+1) would be**

$$t_{n+1} = \frac{r_{n+1}^2}{r_n^2} t_n = \frac{(r_n - d)^2)}{r_n^2} t_n$$

This would apply in the same way to a flat surface, but in that case the surface area would be constant and the time for each layer constant.

---

4 Measurements of the surface finish of balls during the grinding process give values in the range 1 to 4 µinches Ra.

It may be that by taking this approach, and measuring the time taken to produce a very small change in diameter, that we can accurately predict the time for a given diameter change.

Figure 5 shows the rate of change in surface area against the product of hardness and toughness.

fig. 5

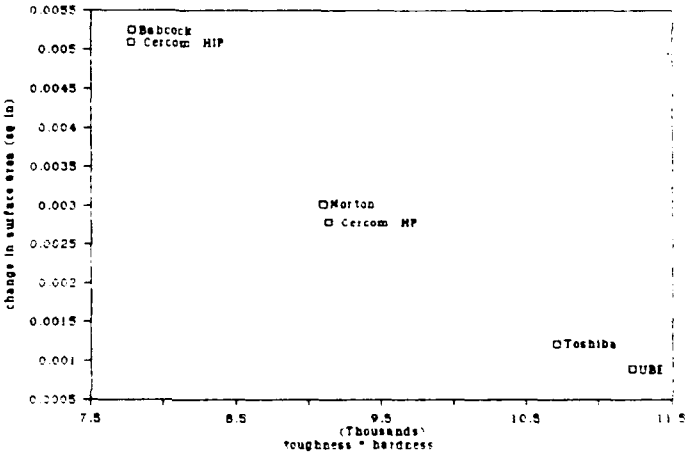

Figure 6 shows the rate of change in surface area

$$\frac{1}{\text{fracture toughness}^{\frac{3}{4}}} \times \frac{1}{\text{hardness}^{\frac{1}{2}}}$$

fig. 6

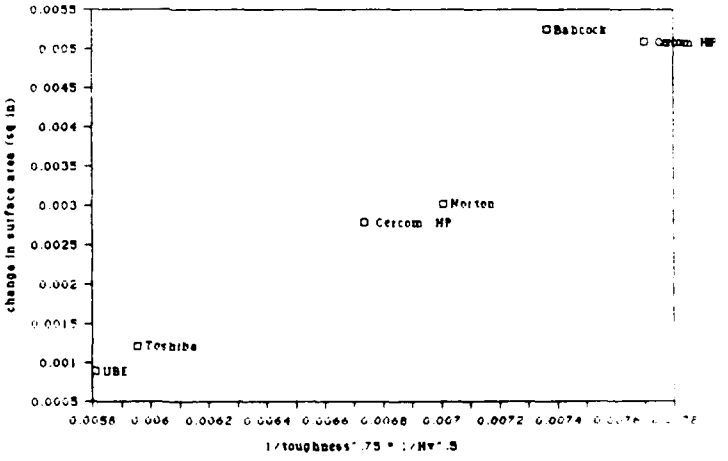

Both fig 5 and fig 6 show slightly better relationships than the previous figures, and tend to suggest that the grind rate may be more accurately predicted as being related to the change in surface area. Effectively the time taken is related to **change in diameter²** rather than **change in diameter³**

APPENDIX X

J.-M. Martin, and Th. Le Mogne, selected Monthly Reports on α-SiC, ranging from Dec. 1987 to March 1989, Ecole Centrale de Lyon/SORETRIB, Lyon, France, Hughes P.O. S9-317657-SKD

SOCIÉTÉ DE RECHERCHE EN TRIBOLOGIE

SORETRIB

36, rue Guy de Collongue
69130 ÉCULLY
Tél. 78.33.02.17

Dr. Mike GARDOS
Materials Technology Laboratory
Technology Support Division
Electro Optical & Data Systems Group
Hughes Aircraft Company
P.O. Box 902
Bldg E1? MS F150
El Segundo CA 90245

Écully, le December 18 th 1987

Dear Mike,

Below is our progress report for November 1987

INTRODUCTION

The first step of our proceeding is the characterization of the samples as received.

EXPERIMENTATION CONDITIONS

The X-Ray source is Magnesium Kα (1253.6 eV). Vacuum in analysis chamber is 10^{-9} Torr. Ionic etching is done with Ar ions (3 kV). The samples are cleaned up with Hexane in ultrasonic bath.

I - BN Pyrolytic analysis (hexagonal)

Before etching, we find out carbon, oxygen, nitrogen and boron. We also notice light traces of calcium : the binding energy of carbon and oxygen shows that these traces are the result of a surface contamination. The Nitrogen 1s peak shape presents an asymmetry. After a two gaussian resolution, the new peak energy might correspond to N_2O_2 or NH_3. The ratio B/N amounts to 1,03 before etching.

After etching, an high quantity of carbon and oxygen remains. The binding energy of carbon shows that these are carbon free atoms (maybe graphite). The binding energy of carbon and oxygen does not allow to attribute it to a defined molecule. The ratio B/N amounts to 1,3. This result teaches us that the sample should be baked after etching.

Considering the samples technical preparation, this analysis has been performed on the two faces. The same results have been obtained.

II - BN Combat analysis

The same analysis were performed on this sample. We detected silicon presence under the oxide form. Boron peak presents two componants. After resolution, we characterize Boron BN and Boron Oxide. The ratio Boron (BN)/N amounts to 0,96. After fifteen minutes etching, the remaining quantity of carbon and oxygen is still very high. The binding energy of carbon 1s shows that these are carbon free atoms. Silicon quantity has increased. The Nitrogen 1s peak presents two gaussian with energy of BN and NH_3 or N_2O_2. The ratio Boron(BN)/N amounts to 1.27.

CONCLUSIONS

These analysis shows that the samples surfaces present high quantities of impurities. These are essentially carbon which binding energy has the character of carbon free atoms, and oxygen which cannot be associated to any existing element.

The results are described in annex 1 for BN pyrolytic and in annex 2 for BN Combat.

Next report will present SIC analysis results.

You will receive the December report in two weeks. Excuse our late due to specimen problems.

Best regards.

J.M. MARTIN T. LE MOGNE

ANNEX 1

Results for BN Pyrolytic

1I - Before etching

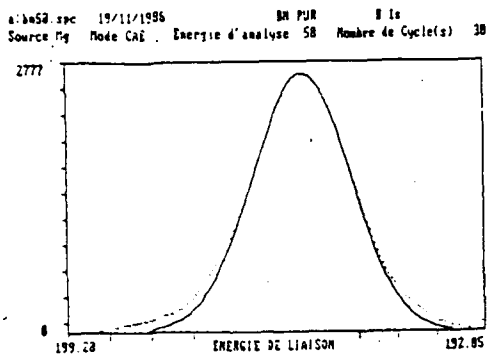

B_{1S}

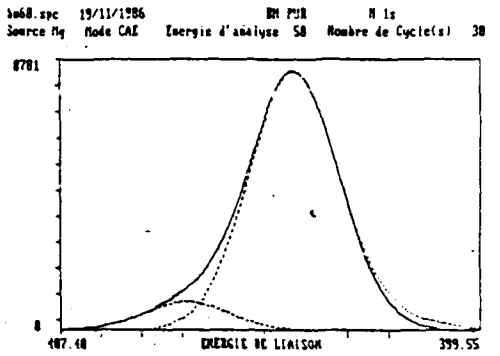

N_{1S}

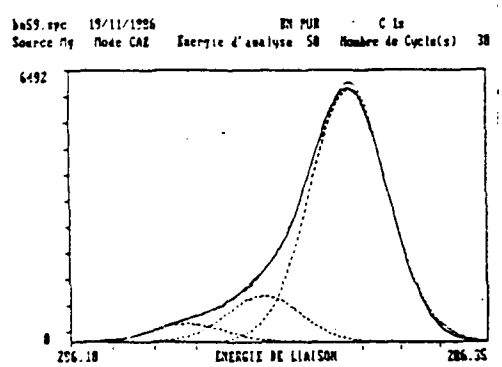

C_{1S}

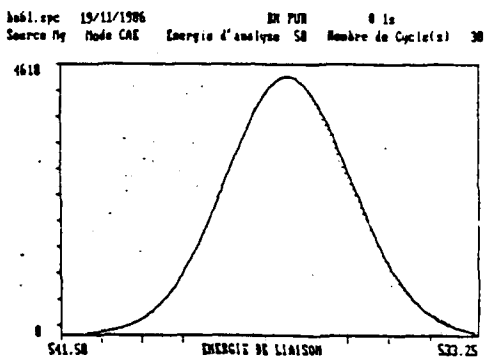

O_{1S}

element	Binding* energy	FWHM	% at.
B_{1S}	190,3	2	24,3
C_{1S}	284,4 286,75 288,5	2,2 2 2	31,2 5,2 2
O_{1S}	532,05	2,95	11,6
N_{1S}	398,05 400,1	2 1,85	23,5 2,3

* Charge effect : 4,9 eV

II - After etching

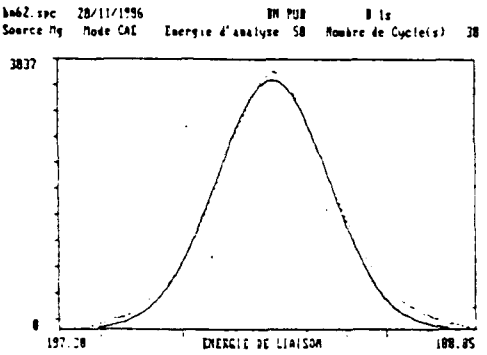

B_{1S}

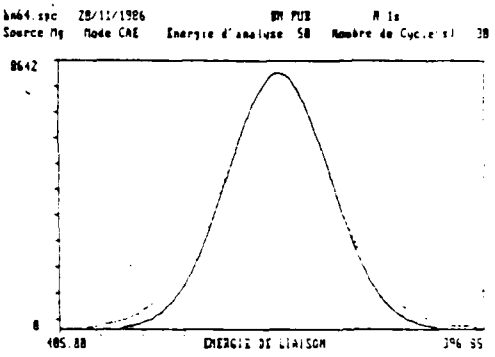

N_{1S}

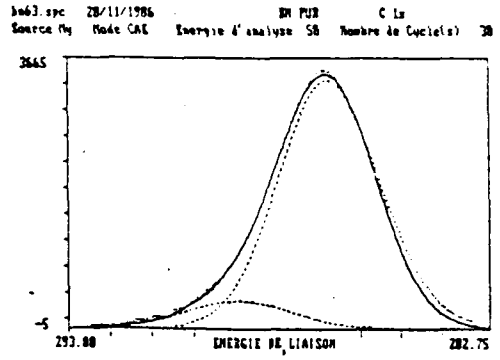

C_{1S}

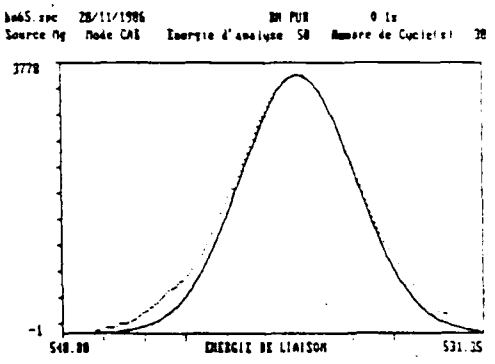

O_{1S}

element	Binding* energy	FWHM	% at.
B_{1S}	190,3	2,7	36,1
C_{1S}	284,05 286,25	2,85 3	23,7 2,7
O_{1S}	532,35	2,8	9,5
N_{1S}	398,1	2,3	28,0

* Charge effect : 2,65 eV

ANNEX 2

Results for BN COMBAT

I - Before etching

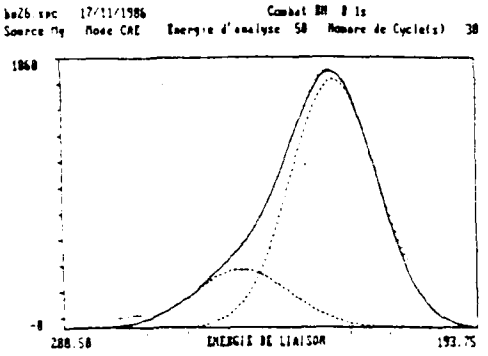

B_{1S}

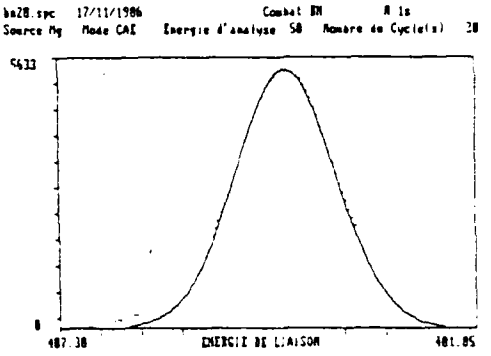

N_{1S}

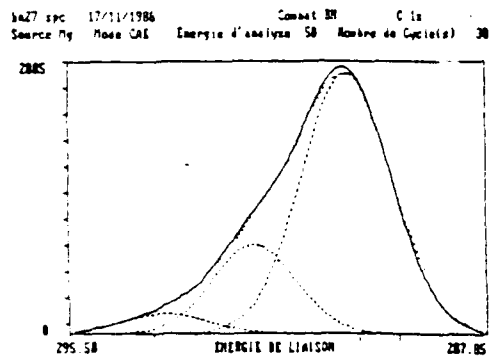

C_{1S}

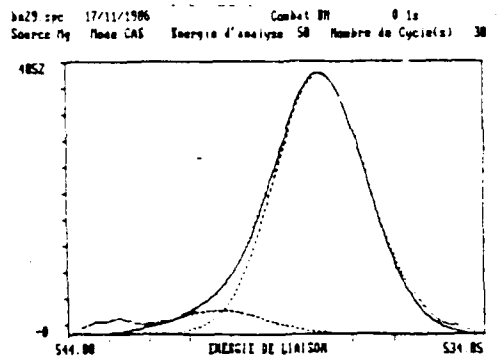

O_{1S}

element	Binding* energy	FWHM	% at.
B_{1S}	190,3 191,85	1,7 1,85	24,7 6,2
C_{1S}	284,65 286,4 288,05	2 1,8 1,8	17,6 5,4 1,2
O_{1S}	532,1 534,6	2,6 2,6	16,8 1,5
N_{1S}	398,1	1,8	25,7
Si 2p	102,35	2,6	0,9

* Charge effect : 5,75 eV

II - <u>After etching</u>

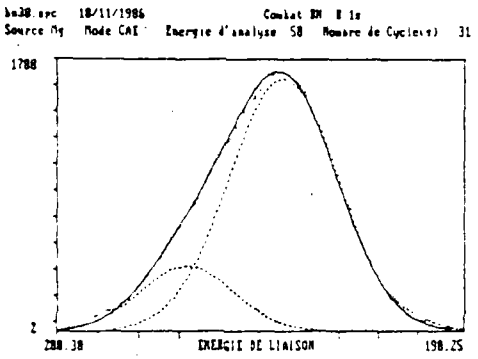

B_{1S}

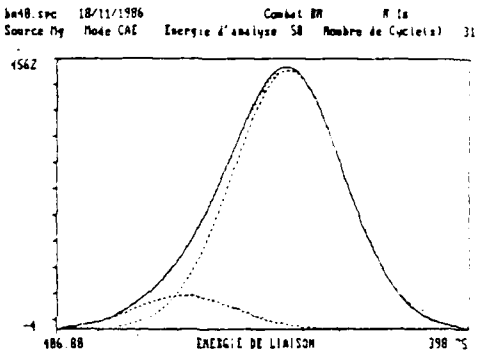

N_{1S}

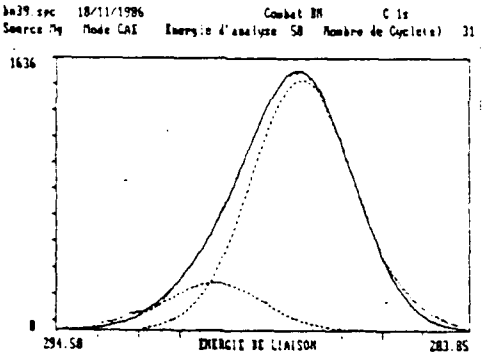

C_{1S}

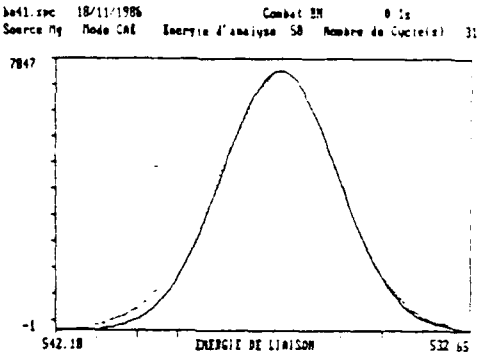

O_{1S}

element	Binding* energy	FWHM	% at.
B_{1S}	190,3 192,7	3,2 2,7	29,1 6,3
C_{1S}	283,7 286,0	3,15 2,95	13,5 2,4
O_{1S}	532,5	3,1	25,1
N_{1S}	397,8 399,95	2,6 2,35	19,3 2,2
Si 2p	102,95	3,5	2,1

* charge effect : 4,45 eV

SOCIÉTÉ DE RECHERCHE EN TRIBOLOGIE

SORETRIB

36, rue Guy de Collongue
69130 ÉCULLY
Tél. 78.33.02.17

Dr. Mike GARDOS
Materials Technology Laboratory
Electro-Optical & Data Systems Group
Hughes Aircraft Company
P.O. Box 902
Bldg E1, MS F150
El Segundo, CA 90245

Écully, le January 11 th 1988

INTRODUCTION

In the near future, Electron Energy Loss Spectroscopy (EELS) will provide chemical, structural and electronic parameters on interface materials formed under tribotesting which are needed for fundamental understanding of wear processes. The technique will be complementary to surface analysis (XPS, AES etc...). In addition EELS analysis is very well spatially resolved (probe size diameter 2 nm possible) and can be coupled to electron microdiffraction and high resolution electron microscopy (HRTEM).

The letter reports the performance of EELS applied to hexagonal boron nitride and some elements of interpretation of data recorded. Future works with EELS will be devoted to αSiC B_2O_3 and wear fragments from VHV tribotests.

K EDGES FINE STRUCTURES FROM h BN

We shall consider mainly on the boron K edge (192 eV) rather than the nitrogen K edge whose signal is appreciably weaker. Figure (1) shows the boron K edge recorded with serial detection from a monocrystal oriented with the C axis parallel to the incident beam. The size of the detector aperture averages the signal over different scattering angle centered around (θ = 0).

As already mentionned in the litterature, the core edge fine structure can be related to density of states [1]. A resemblance is expected between peaks in the energy loss spectrum and the density of inoccupied conduction states in the solid. Neverthless the following factors should be considered : Firstly for 1s electron excitation, only transitions to states of p

BORON EXELFS

Steps in data reduction

In the analysis of the data, following procedures are needed [5] :

- 1 - Subtraction of the background intensity preceding the edge by at least squares fits to an inverse power law $I \alpha E^{-r}$ where E is the energy loss and r is a constant around 3 or 4 found empirically.
- 2 - Deconvolution of the plasmon excitations by Fourier Transform method to eliminate plural scattering effects. Extra peaks above threshold are produced and may cause inaccuracies in EXELFS analysis especially as for as short atomic distances are concerned.
- 3 - Removal of the background after the edge by fitting the intensity to a low order polynomial, either third or fifth order.
- 4 - Change the energy of the final state above threshold to a wavenumber scale.
- 5 - Multiply by K^3 to take account of attenuation by the backscattering amplitude function.
- 6 - Truncate the intensity modulations at $k_{min.}$ and $k_{max.}$ The limited range of k available is one ot he main problem associated with electron absorption, limiting the resolution and accuracy in the radial distribution function.
- 7 - Calculate the magnitude of the Fourier Transform to give the RDF (radial distribution function).
- 8 - Add the phase shift on to the peak of the RDF (estimated from the data of Teo and Lee).

RESULTS ON BORON K EDGE

Results presented in figure (3) have been obtained in following the procedures described above except that the phase shifts have not been estimated and added. Two major contributions are seen in the RDF obtained, namely a peak at 1.12 Å and a peak at 3,06 Å. The first peak is attributed to nitrogen neighbors in plane (3 neighbors at 1,45 Å) the second peak is

attributed to inter plane atoms in the C-axis direction (8 atoms at average distance of 3.56 Å).

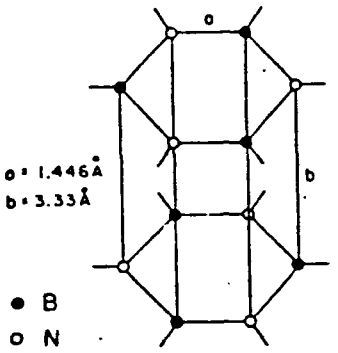

In the two cases, the values of phase shifts to add have reasonable values (near 0,3 Å), and in a first approximation the data reduction of boron EXELFS seems acceptable. A complete analysis of the spectrum is precluded because of the difficulty of removing the unwanted carbon peak (near 284 eV), the small discontinuity in the background substrated spectrum gives additionnal noise in the Fourier Transform.

CONCLUSION

The application of EELS on h BN is very encouraging, the technique gives valuable information on the electronic structure of specific atoms (B and N), and on the local cristallography by EXELFS analysis.

REFERENCES

[1] R.D. LEAPMAN, P.L. FEJES and J. SILCOX, Physical Review, B vol. 28, n° 5, pp. 2361-2373 (1983).

[2] A. ZUNGER and al, "Phys. Rev., B vol. 13, p. 5560 (1976).

[3] E. DONI and al, Nuovo Cimento, B 63, p. 117 (1969).

[4] D.J. JOYNER and D. HERCULES, J. Chem. Phys., 72, (2), Janv. 1980.

[5] R.D. LEAPMAN, L.A. GRUNES, "EXAFS spectroscopy", Edited by B.K. TEO and D.C. JOY, Plenum Press (1980).

Figure 1 : EELS on h BN Boron K edge (energy resolution 0.6 eV).

Figure 2 : EELS on h BN Boron and Nitrogen K edges. Differences in peak intensities are attrributed to electronegativity.

Figure 3 : EXELFS treatment of Boron K edge.

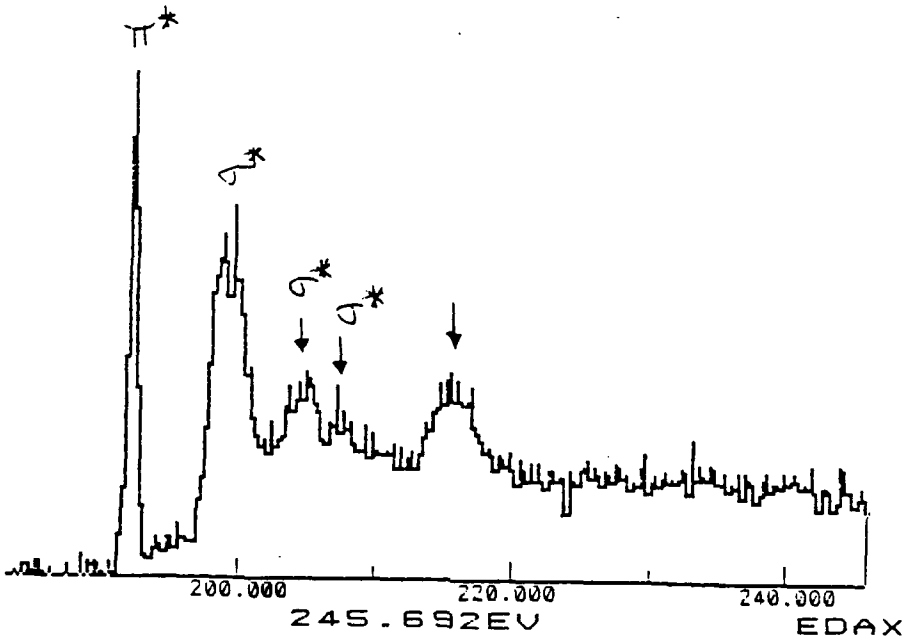

Figure 1 : EELS on h-BN Boron K edge (energy resolution 0.6 eV).

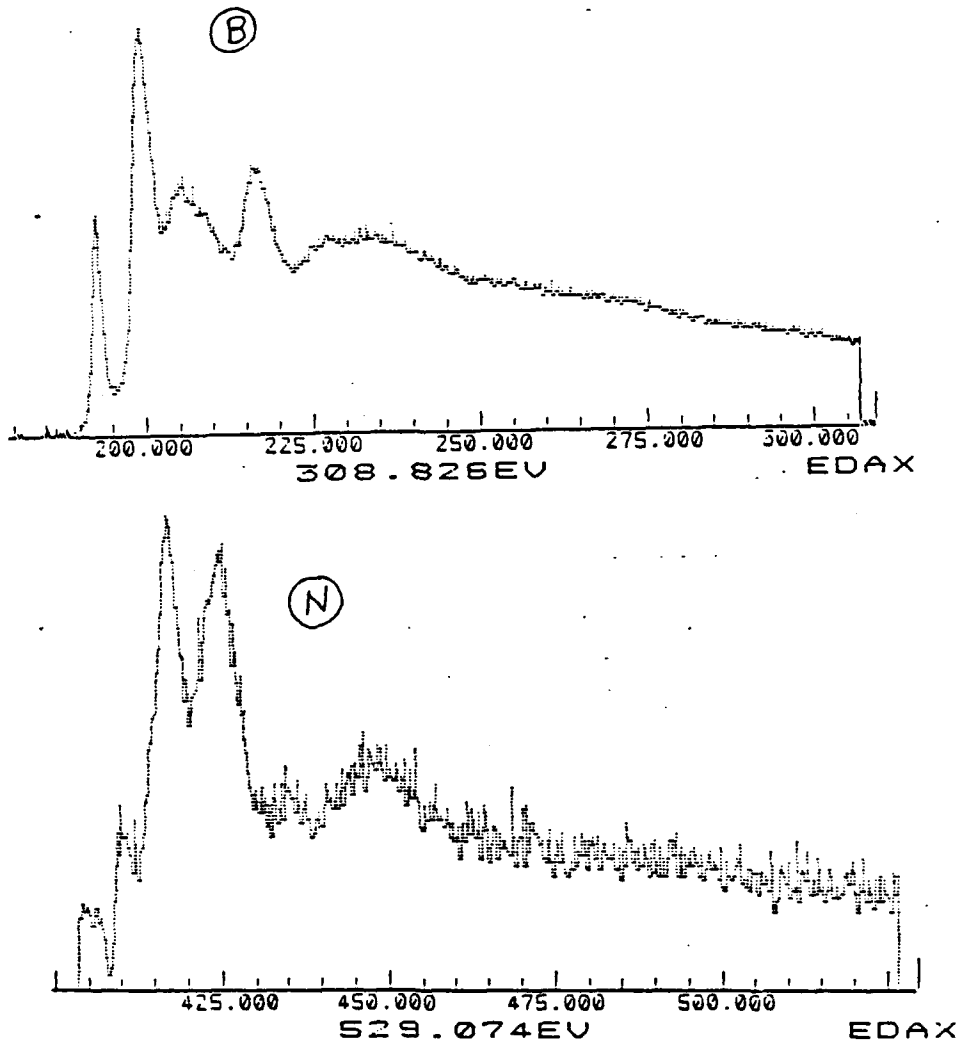

Figure 2 : EELS on h BN Boron and Nitrogen K edges. Differences in peak intensities are att ributed to electronegativity.

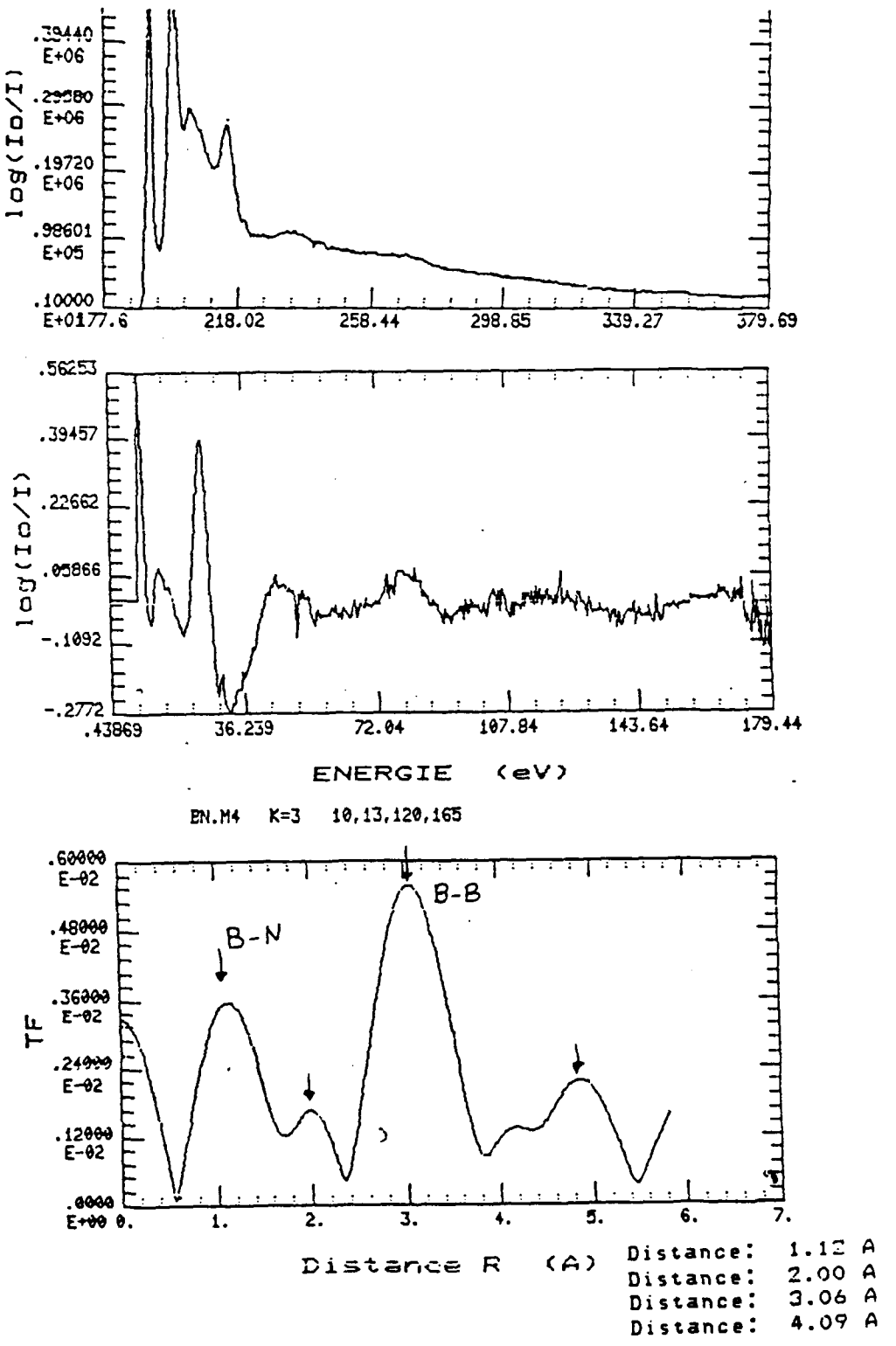

Figure 3 : EXELFS treatment of Boron K edge.

SORETRIB
36, avenue Guy de Collongue
69130 ECULLY

ECOLE CENTRALE DE LYON
Laboratoire de Technologie des Surfaces
UA CNRS 855
36, avenue Guy de Collongue
B.P. 163 - 69131 ECULLY Cedex

FRICTION OF SiC/SiC

WEAR ASPECT

Rapport intermédiaire

4 Novembre 1988

Contrat n° F 33615-85-C-5087
HUGUES AIRCRAFT CO
Mike Gardos
El Segundo - USA

J.M. MARTIN
Th. LE MOGNE

SOCIÉTÉ DE RECHERCHE EN TRIBOLOGIE

SORETRIB

36, rue Guy de Collongue
69130 ÉCULLY
Tél. 78.33.02.17

Dr. Mike GARDOS
HUGHES AIRCRAFT CO
ELECTRO OPTICAL AND DATA
SYSTEMS GROUP
2000 East El Segundo Boulevard
Po Box 902
EL SEGUNDO
U.S.A.

Écully, le November 4th 1988

Dear Mike,

I have well received your interesting comments on the finding of carbon in CVD hBN plate and the problem of orientation of BN basal plane. Indeed we enjoy that you get involved in our own research and to answer your questions, we have made additionnal experiments on the characterization of BN plate (ESCA and AEM).

First, remember that in our first report we have detected the presence of nitrogen in NH_3 form by XPS and this can be due to the precursor B_2H_6 NH_3 for example.

ESCA analysis of both faces have already been carried out (see report 1) and show the presence of carbon and oxygen. For confirmation ESCA (SSX) has been performed with a 150 µm diameter probe. Results are summarized in table 1 and confirms previous data.

We have observed by TEM some flakes coming from inside the 1 mm plate (as you suggested we peeled the millefeuille). EELS spectra obtained from thin areas figure (1) shows that free carbon is undoubtly present and presumably inserted in the BN structure. The concentration might be approximately 10 % atomic. Energy filtered images were then obtained respectively before and part the carbon K-edge (ΔE = 284 eV). Results show that additionnal carbon layers are included in the millefeuille and can be visualized by EFEM (Energy Filtered Electron Microscopy) on the carbon K-edge at 284 eV (figure 2).

	See report 1	ESCA (SSX)	ESCA (VG) peeled BN plate
B 1S %	36	38	40
C 1S %	25	22	18
O 1S %	10	7	6
N 1S %	28	33	33

Table 1

X-16

With respect to preferential basal plane orientation the electron diffraction with the electron beam normal to the millefeuille is show figure (3) with the corresponding bright field image. Results suggest that the microstructure of figure 9 (b) Appendix III is possible with cristallites oriented in any direction but as you mentionned at the macroscopic scale the BN layers of each cristallite might have parallel C axis.

Indoubtly there is porosity between BN grains and XPS results on oxygen suggest that water is present in the structure (7 % atomic is presumed).

So BN plates have a complex structure and are far from pure BN single crystal that was expected. Neverthless friction work will be done with the inner layers.

Very best regards

J.M. MARTIN

P.S. : Abstract accepted at EUROTRIB 1989

03-NOV-88 12:28:10 EELS DECON
LBL:
LBL:BORON NITRIDE PLATE
CNT: 2659 CNT: 2498
FS: 25684 MEM:B/A FS: 25684

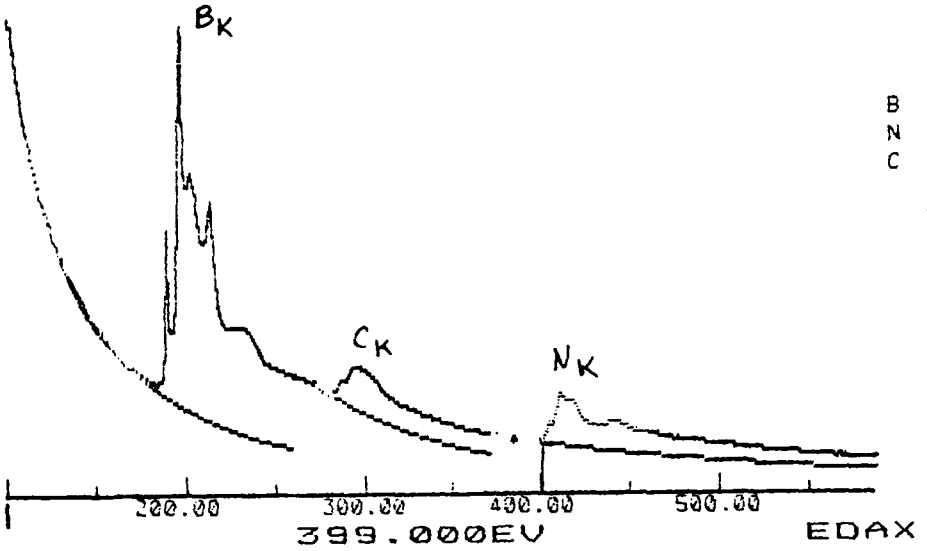

EELS QUANTITATIVE ANALYSIS

03-NOV-88 12:03:03
Auto Data Input
Composition from Intensity

Accelerating voltage	120.0 KV
Incidence angle	2.0 MR
Scattering angle	13.0 MR
Integration window	60.0 EV

ELEM	AT %	SIGMA	INTENSITY
B K	49.73	1.235E-20	1.327E+06
N K	34.79	2.326E-21	1.748E+05
C K	15.48	5.150E-21	1.722E+05

ΔE = 272 eV 60nm ΔE = 300 eV

Figure 2 X-19

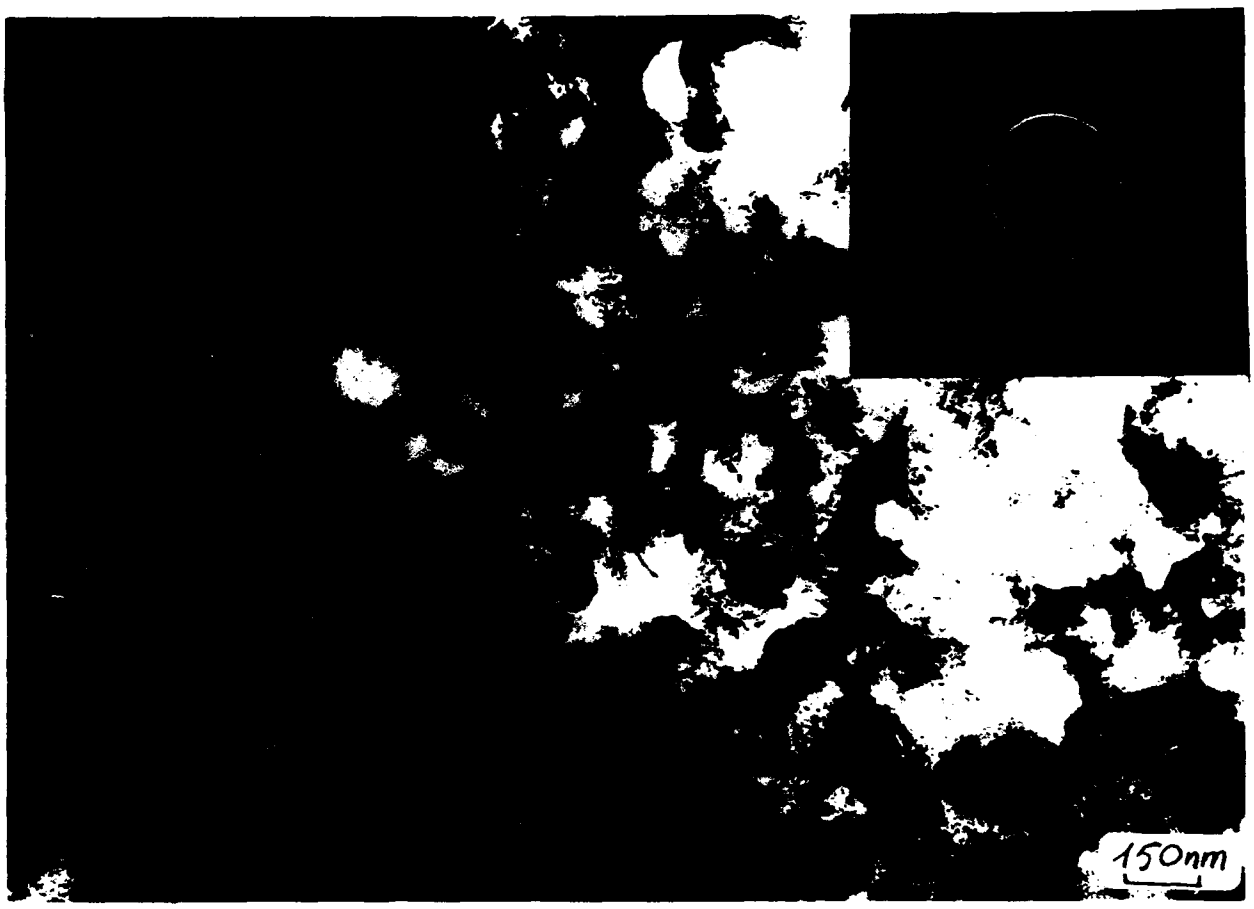

Figure 3 X-20

TRIBOCHEMISTRY OF SILICON CARBIDE UNDER OXYGEN PARTIAL PRESSURE

J.M. MARTIN *, Th. LE MOGNE *, H. MONTES *, M.N. GARDOS **

* *Ecole Centrale de Lyon, Laboratoire de Technologie des Surfaces, URA CNRS 246, 36 avenue Guy de Collongue, B.P. 163, 69131 ECULLY Cédex, France.*

** *Hugues Aircraft Co, Electro Optical and Data Systems Group, 2000 East, El Segundo Boulevard, P.O. Box 902, El Segundo, CA 90245, U.S.A.*

Friction and wear of silicon carbide on itself have been studied in different environmental conditions including vacuum and oxygen partial pressures. We have built an U.H.V. tribotester with a pin on disk configuration, installed in an analytical chamber with X.P.S. and A.E.S. facilities. A unique feature is the possibility to clean and analyse both pin and disk wear scars at the end of the test, without breaking vacuum. Wear debris microstructure is studied in the T.E.M. by Electron Energy Loss Spectroscopy and high resolution imaging. Results show that friction and wear of SiC under vacuum (2.10-10 mbar) is very severe (f = 0,8), and associated with SiC attrition and amorphization in the contact. Friction is very sensitive to oxygen partial pressure, a drastic decrease of the friction coefficient down 0.08 has been recorded, and this is due to graphitization in the contact area, associated with the formation of silicon oxide in low temperature range. Tribochemistry of SiC at ambient temperature of SiC under oxygen is discussed.

Dr Kenneth Holmberg
Technical Research Centre, VTT/KOT
Metallimiehenkuja 6
SF-02150, ESPOO, FINLAND
tel. 358-0-4561 telex: 122 972 vtlha sf

Mr. Th. Le Mogne
Ecole Centrale de Lyon
Technologie des Surfaces
36 av. Guy de Collongue
B.P. 163, 69131 Ecully Cédex
France

ABSTRACT NO.: 110
RE: TRIBOCHEMISTRY OF SILICON CARBIDE UNDER OXYGEN PARTIAL PRESSURE

Authors: J M Martin, T Le Mogne, H Montes and M N Gardos

Dear Sir,

Thank you for submitting your abstract for consideration to the international Congress on Tribology EURTOTRIB 89.

The Scientific Board of EUROTRIB 89 has found your paper most interesting and has accepted it for oral presentation at the congress. The time available for your presentation is 15-20 minutes. The paper will be published in the Congress Proceedings and special sheets for camera-ready copies with detailed instructions will be sent you later this year. Because of the great number of accepted abstracts the length of the paper is limited to 6 pages (suggested 4 pages of text and 2 pages for pictures).

Looking forward to welcoming you to EUROTRIB 89 next June.

Yours sincerely,

Kenneth Holmberg
EUROTRIB 89 Manager

X-22

SORETRIB
36 avenue Guy de Collongue
B.P. 163
69131 ECULLY Cedex

Ecole Centrale de Lyon
Laboratoire de Technologie des Surfaces
26 avenue Guy de Collongue
B.P. 163 - 69131 ECULLY Cedex
fax : 78.43.39.62

DETERMINATION OF TRIBOLOGICAL FUNDAMENTALS OF SOLID LUBRICATED CERAMICS

Contract F 33615-85-C-5087

Monthly report from December 1st to December 31th 1988

Report n° 3

CHARACTERIZATION OF hBN SPECIMENS PRIOR TO UHV FRICTION

RFQ 520765

Prepared for :

HUGUES AIRCRAFT COMPANY
Electro-Optical & Data Systems Group
Mike GARDOS, Senior Scientist

Prepared by : - J.M. MARTIN

- Th. LE MOGNE

Adm. Div. :

I - Survey of h BN friction

Classically, h-BN friction is associated and compared with graphite friction, because there are some basic similarities in the crystallographic structure. Both compounds contain low energy shear planes in the (002) direction (van der Waals interactions). Neverthless, their electronic structures are quite different as far as valence and conductions bands are concerned. The mechanisms of h-BN friction are reviewed by TABOR [1], and are closely related to those of graphite. The main features are the following :

- friction depends on the orientation of basal planes of the crystallites in the sliding direction,
- friction depends on the chemical state of the edges of individual crystallites (dangling bonds, oxides etc...),
- friction depends on the energy of the surface of crystallites (adsorption of gases...),
- friction depends on the presence of intercalated compounds in the graphite structure (presence of water, mineral species...).

But the respective role of each phenomenon is not clearly understood when testing a manufactured specimen.

II - Caracterization of h-BN specimens

h-BN specimens were previously analyzed by XPS and EELS (see reports Dec. 1987 and Jan. 1988). The results showed that carbon was present in great quantities in both specimens. Before the friction test, and taking into account the role of impurities and the microstructure in the mechanisms of h-BN friction, we decided to explore in more detail the two specimens that we have at the moment, namely :

- the CVD h-BN plate
- the COMBAT sintered h-BN.

The detection of water was carried out by SIMS and the microstructure of the CVD sample was investigated by high resolution TEM.

The results are the following :

- *Concerning the CVD h-BN sample*

BN is not really oriented with the c axis perpendicular to the external face, the high resolution image (figure 1) shows that (002) lattice fringes can be easily imaged (c axis parallel to the surface) (when sampling a flake inside the 2 mm plate). On the other hand, carbon is a main constituent of the CVD h-BN, and EELS and XPS agree that the atomic concentration is 20% (see table below).

	XPS(1)	XPS(2)	EELS
B	36*	38*	50
N	28	33	35
C	26**	22**	15**
O	10	7	not analyzed
Total	100	100	100

(1) XPS (VG CLAM 100) after etching Ar^+ 3KeV
(2) XPS (SSL) after etching Ar^+ 0,5 KeV
* Boron is not found in the oxide chemical state
** Carbon is predominantly graphitic

Moreover, EELS spectra (figure 2) show that carbon is in an amorphous form with the sp_2 hybridation.

SIMS spectra are presented in figures 3-4.
The presence of carbon is confirmed by peaks C^- and C^-_2, and the ratio C^-/C^-_2 indicates that carbon is graphitic. Oxygen is also detected (O^-) and also hydrogen (H^+) but the OH^- peak representing water is very weak, so that the quantity of water can be neglected in our experiment. From these analytical data, it can be concluded that oxygen (≈ 10% atomic) is neither water, nor boron oxide, nor carbon oxide, nor nitrogen oxide. Therefore, we suggest that gas (oxygen) may be intercalated in the graphitic structure. When analyzing thin flakes in the TEM, oxygen can escape into the vacuum and is not detected . Moreover, as the excess of boron is not oxide, it is also possible that some carbon lies in the graphitic planes close to boron and nitrogen [2].

SIMS is a very sensitive technique to study impurities and traces. The main elements that are found are :

- Ca (Mg and Si are also present) (< 1%)
- Na, K, Li, Cl as traces (< 0.1 %).

- *Concerning the COMBAT hBN specimens*

BN is oriented with the c-axis perpendicular to the external face. Carbon is present in the chemical composition (22 % atomic in XPS, 1 cm^2 probed) but it is segregated, because EELS on individual flakes does not indicate the presence of carbon, but stoechiometric BN. SIMS spectra (figures 5-6) do not show the presence of water, but show oxygen and carbon (confirming XPS data) and impurities with Mg and Si are more important than in CVD hBN.

	XPS	EELS
B	37	51
N	31	49
C	22	/
O	9	/

Note : Due to argon or gallium bombardment, the surface of hBN specimens turns to a black colour (figure 7) which is more accentuated for the COMBAT hBN. At the moment, we have no explanation of this.

III - Conclusion

The h-BN specimen that we have at the moment is of an extremely complex nature. Neverthless, the situation can be summarized as follows :

- *CVD - hBN*

* no preferential orientation of crystallites,
* carbon in the graphitic structure (≈ 20 % atomic),
* oxygen may be intercalated in the structure,
* some impurities at a low level (< 1 %).

- *COMBAT hBN*

* BN crystallites are oriented parallel to the surface,
* carbon is segregated in the microstructure (≈ 20 % atomic),
* oxygen as borate (?),
* impurities at a low level (< 1 %).

The next report will concern friction of BN/BN under vacuum.

References

[1] F.P. BOWDEN and D. TABOR, "The friction of lamellar solids" Part II, Oxford at the Clarendon Press, (1964).

[2] Amy Y. LIU and al, "Atomic arrangement and electronic structure of BC_2N", Applications of intercalation compounds, pp. 136-144, (1988).

LIST OF FIGURES

Figure 1 : High resolution TEM micrograph of a CVD hBN flake showing (002) lattice fringes lying perpendicular to the external face.

Figure 2 : EELS spectrum of a CVD hBN flake showing boron and carbon K edges. Note that carbon is sp_2 hibridated in an amorphous form.

Figure 3 : SIMS spectra of CVD hBN (positive ions).

Figure 4 : SIMS spectra of CVD hBN (negative ions).

Figure 5 : SIMS spectra of COMBAT hBN (positive ions).

Figure 6 : SIMS spectra of COMBAT hBN (negative ions).

Figure 7 : Optical micrographs of the hBN specimens after ion etching (SIMS).
a) CVD hBN
b) COMBAT hBN

20Å

Figure 1

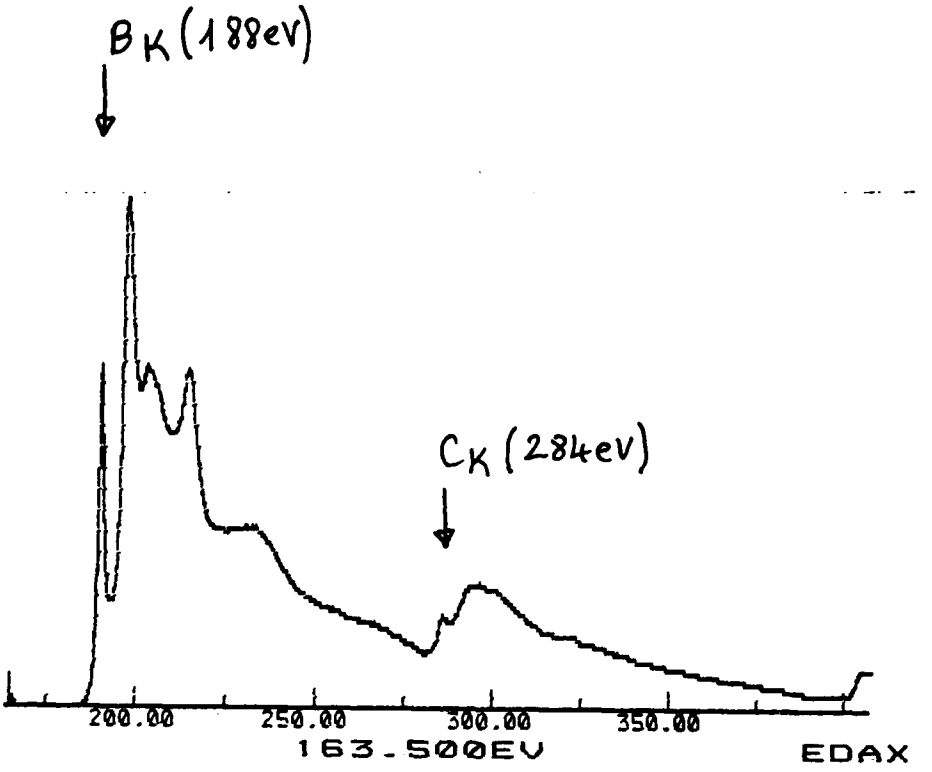

Figure 2

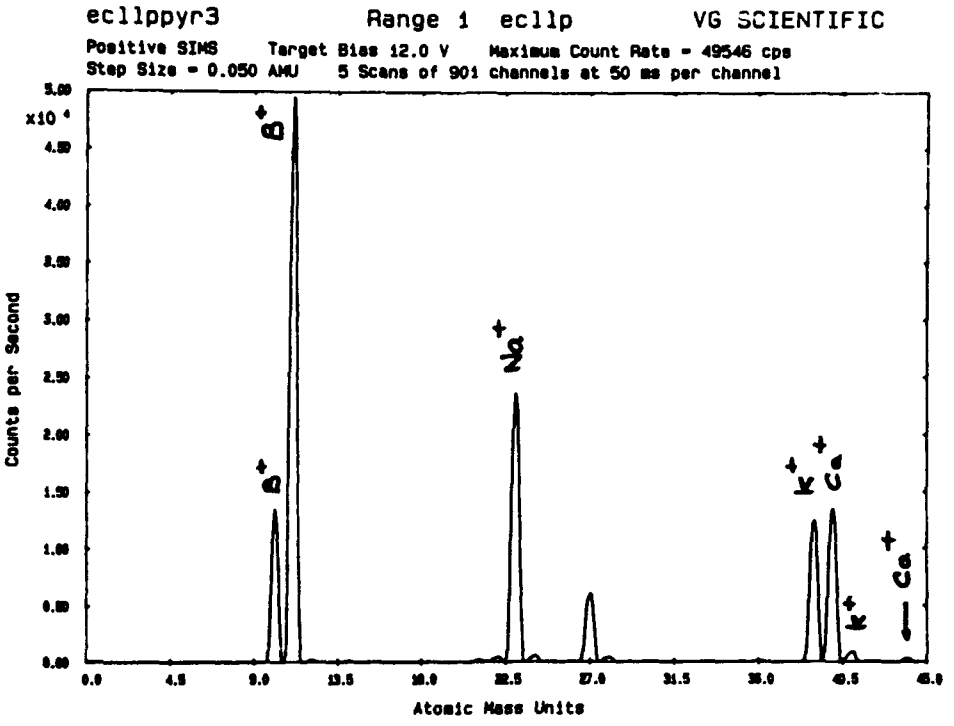

BN PYROLYTIQUE
- Analyse elementaire en ions positifs
  ' a coeur ' -

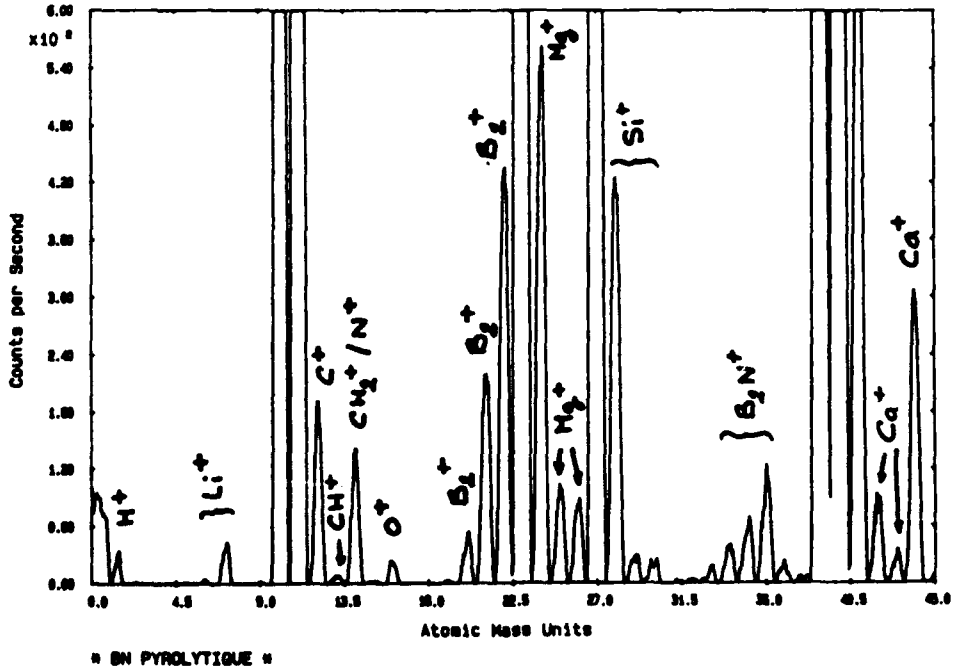

BN PYROLYTIQUE
- Analyse elementaire en ions positifs
  ' a coeur ' -

X-30

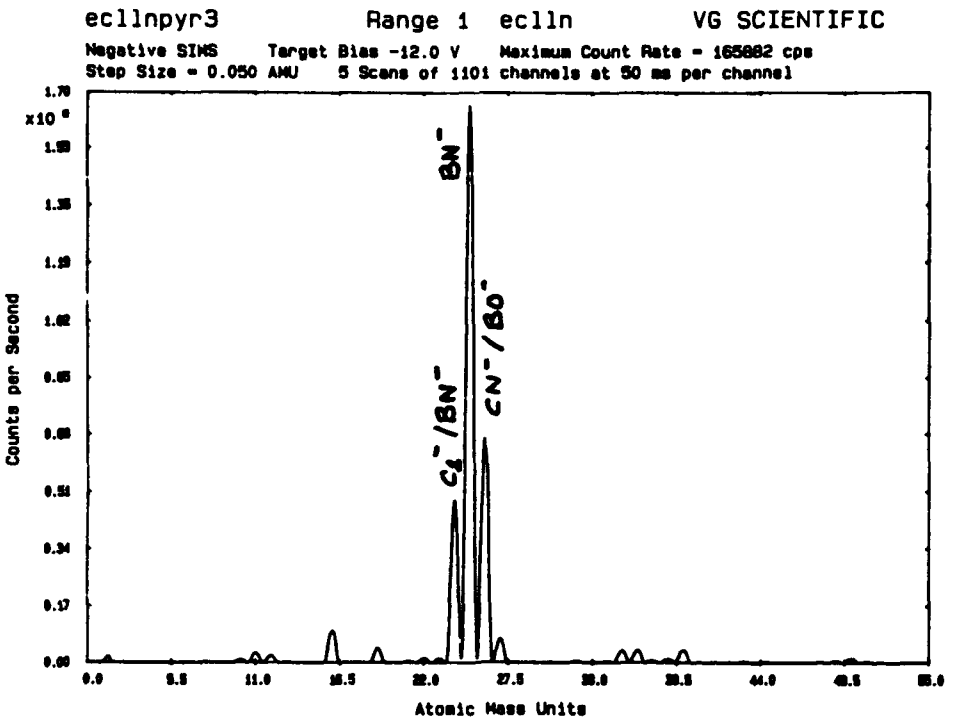
ecllnpyr3 Range 1 eclln VG SCIENTIFIC
Negative SIMS Target Bias -12.0 V Maximum Count Rate = 165882 cps
Step Size = 0.050 AMU 5 Scans of 1101 channels at 50 ms per channel
x10 6
Counts per Second
BN⁻
C₂⁻/BN⁻
CN⁻/BO⁻
Atomic Mass Units
* BN PYROLYTIQUE *
- Analyse elementaire en ions negatifs
' a coeur ' -

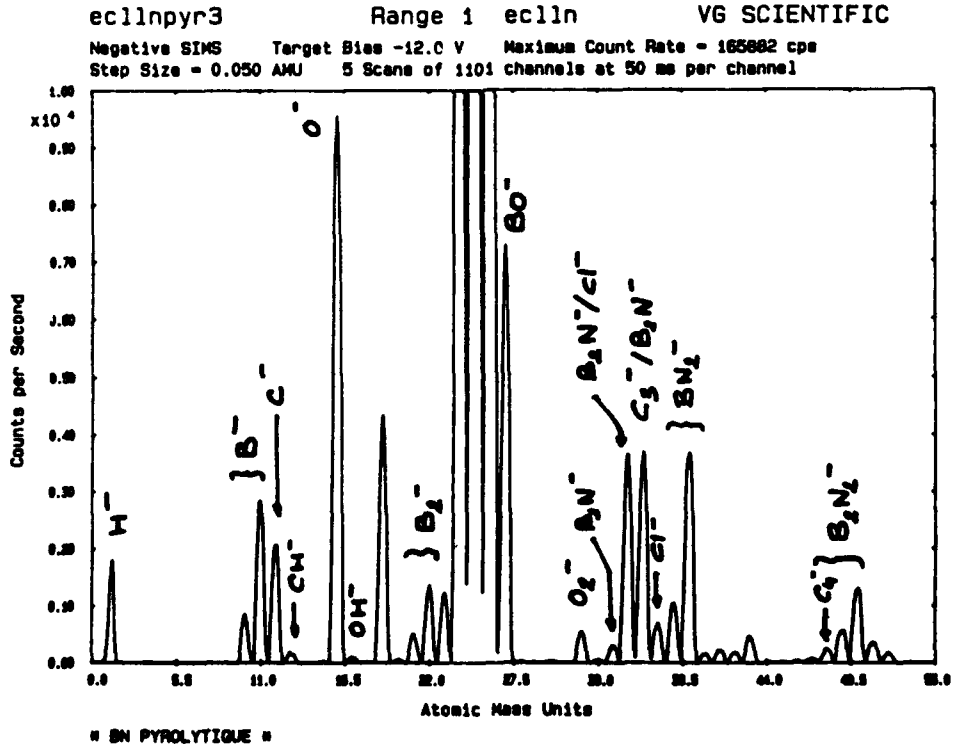
ecllnpyr3 Range 1 eclln VG SCIENTIFIC
Negative SIMS Target Bias -12.0 V Maximum Count Rate = 165882 cps
Step Size = 0.050 AMU 5 Scans of 1101 channels at 50 ms per channel
x10 4
Counts per Second
H⁻
B⁻
C⁻
CH⁻
O⁻
OH⁻
B₂⁻
BO⁻
O₂⁻
B₂N⁻
B₂N⁻/Cl⁻
C₃⁻/B₂N⁻
Cl⁻
BN₂⁻
C₄⁻
B₂N₂⁻
Atomic Mass Units
* BN PYROLYTIQUE *
- Analyse elementaire en ions negatifs
' a coeur ' -

X-31

Figure 4

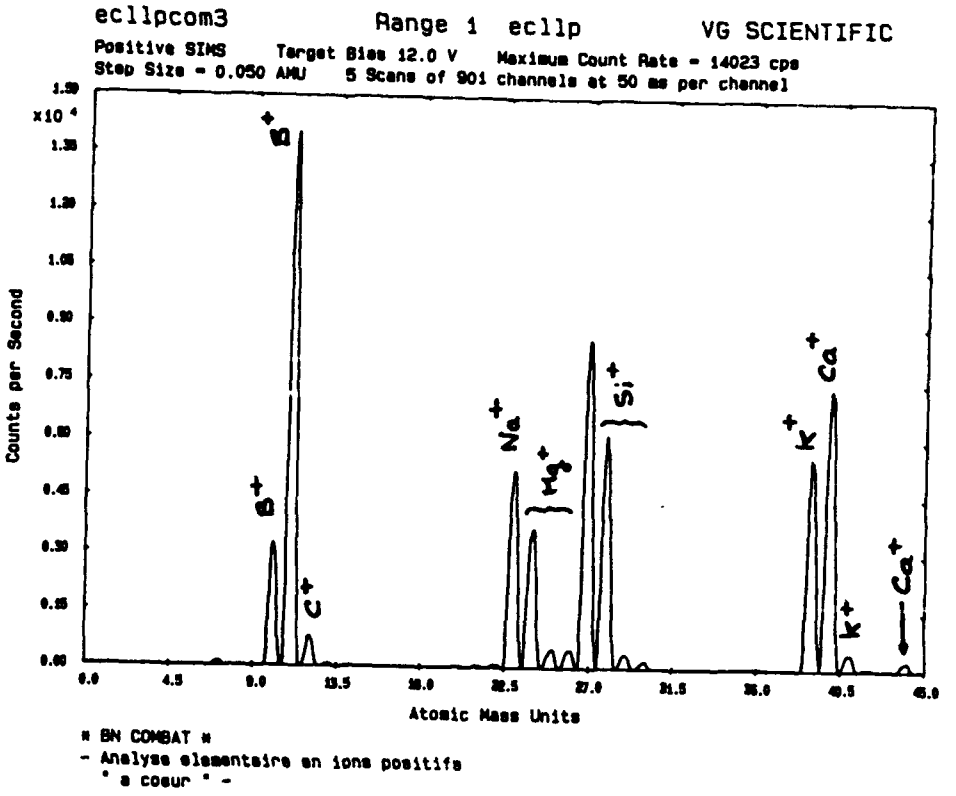
ecllpcom3
Range 1 ecllp
VG SCIENTIFIC
Positive SIMS
Target Bias 12.0 V
Maximum Count Rate = 14023 cps
Step Size = 0.050 AMU
5 Scans of 901 channels at 50 ms per channel
Counts per Second
Atomic Mass Units
B+
C+
Na+
Mg+
Si+
K+
Ca+
k+
Ca+
* BN COMBAT *
- Analyse elementaire en ions positifs
* a coeur * -

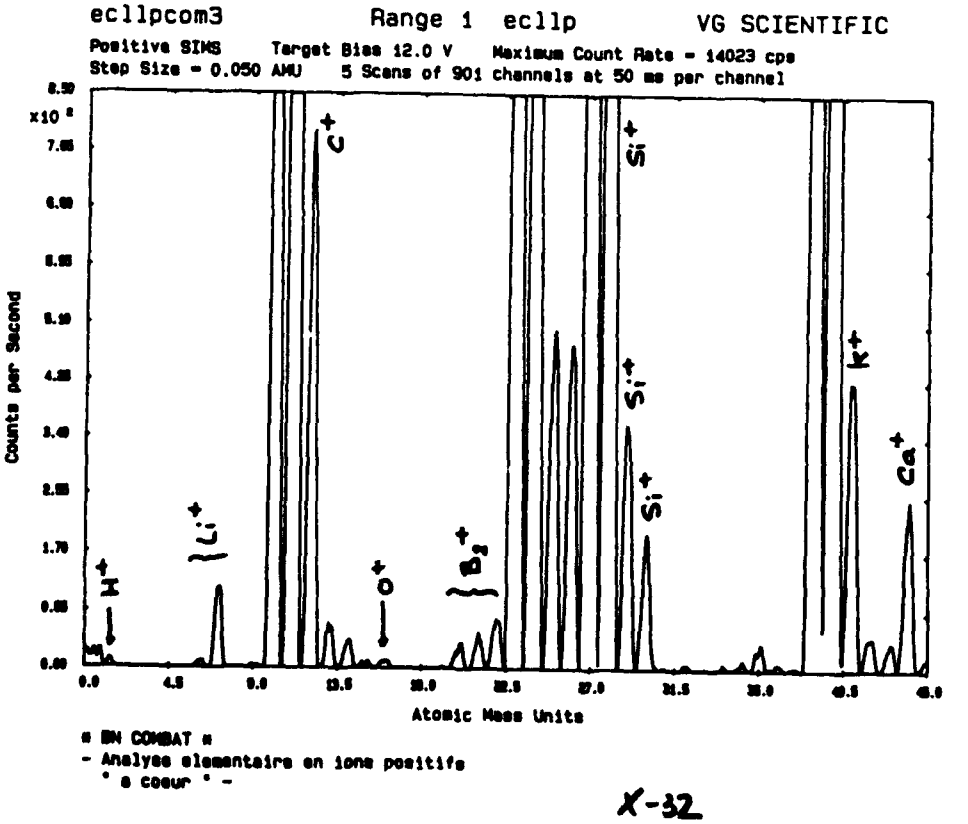
ecllpcom3
Range 1 ecllp
VG SCIENTIFIC
Positive SIMS
Target Bias 12.0 V
Maximum Count Rate = 14023 cps
Step Size = 0.050 AMU
5 Scans of 901 channels at 50 ms per channel
Counts per Second
Atomic Mass Units
H+
Li+
C+
O+
Ba+
Si+
Si+
Si+
k+
Ca+
* BN COMBAT *
- Analyse elementaire en ions positifs
* a coeur * -

X-32

Figure 5

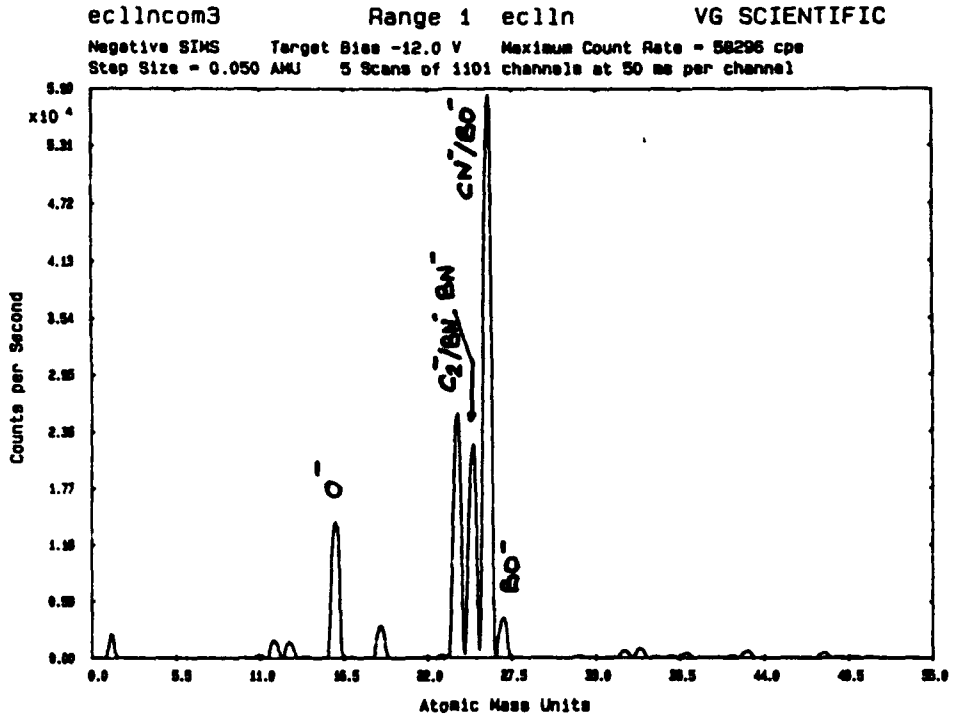

« BN COMBAT »
- Analyse elementaire en ions negatifs
' a coeur ' -

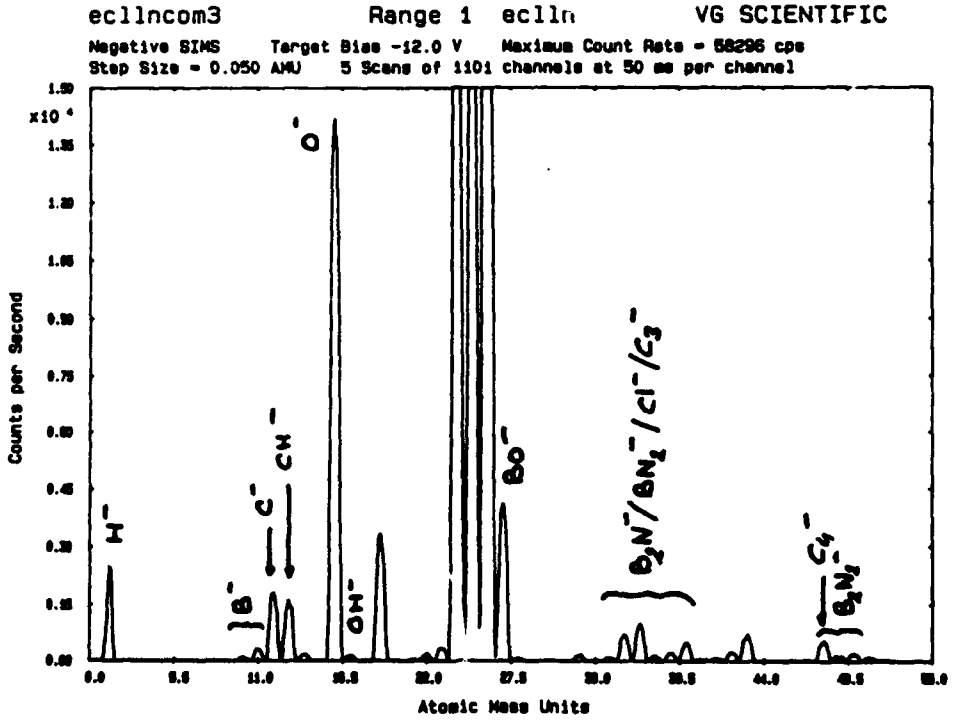

« BN COMBAT »
- Analyse elementaire en ions negatifs
' a coeur ' -

Figure 6

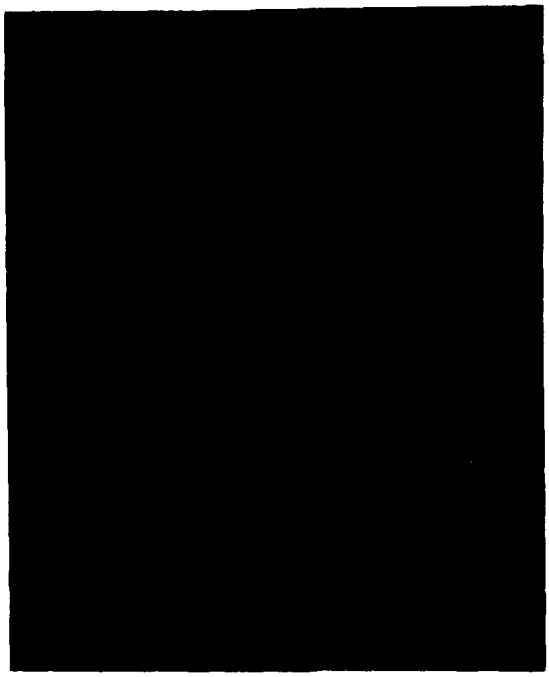

a) CVD h BN

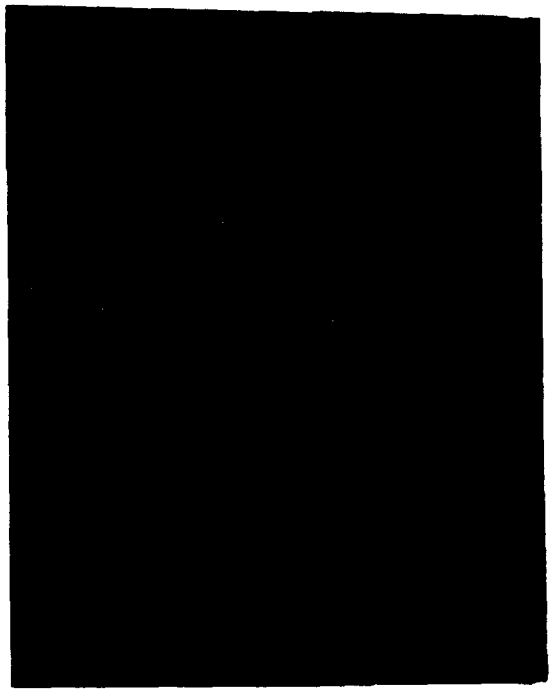

b) Combat h BN

Figure 7

SORETRIB
36 avenue Guy de Collongue
B.P. 163
69131 ECULLY Cedex
FRANCE

Ecole Centrale de Lyon
Laboratoire de Technologie des Surfaces
36 avenue Guy de Collongue
B.P. 163 - 69131 ECULLY Cedex
FRANCE

DETERMINATION OF TRIBOLOGICAL FUNDAMENTALS OF SOLID LUBRICATED CERAMICS

Contract F 33615-85-C-5087

Monthly report from March 1st to March 31th 1989

Report n° 6

THE OBTENTION OF CONTAMINATION FREE AND STOECHIOMETRIC BN SURFACES FROM COMBAT SPECIMEN

RFG 520765

Prepared for :

HUGUES AIRCRAFT COMPANY
Electro-Optical & Data systems Group
Mike GARDOS, Senior Scientist

Prepared by : - J.M. MARTIN

- Th. LE MOGNE

Adm. Div. :

Etude Soretrib n° D50

Tél : 78.33.81.27 *Fax : 78.43.39.62* *Télex : ECE LY 310856F*

CONTENTS

INTRODUCTION ..... p 1

I - ANALYZING STANDARDS BY XPS ..... p 1

II - OPTIMIZING THE COMBAT h-BN SURFACE CHEMISTRY ..... p 3

CONCLUSION ..... p 6

BIBLIOGRAPHIE ..... p 7

THE OBTENTION OF CONTAMINATION FREE AND STOECHIOMETRIC BN SURFACES FROM COMBAT SPECIMEN

INTRODUCTION

Now, we have received the COMBAT h-BN specimens from SAPHIRWERK (namely "flat and edge" configurations). To continue our work, we decided to carry out some preliminary friction tests under UHV, with these new specimens, and with the same procedure that previously described for the h-BN/h-BN combination (see report III). Surprisingly, we found lower friction values, for both configurations, generally inferior to 0.15. Although very interesting, this result is in disagreement with the friction value previously obtained under UHV in the same conditions (0.3-0.4) (see report III). Moreover, we already reported some difficulties to prepare and characterize COMBAT h-BN surfaces, as far as carbon contamination, presence of oxygen and boron/nitrogen stoechiometry are concerned. Consequently, we decided to study in more details the surface of h-BN specimens, depending on the cleaning procedure. The reason is that the initial friction value of the prepared surface is thought to play a key role in the wear process of the h-BN system and that basically it is necessary to know what is beginning to slide on what, to have a good interpretation of the data obtained.

I - ANALYZING STANDARDS BY XPS

Pure h-BN powder, pure boron trioxids (B_2O_3) and boron carbide (B_4C) (from Fluka AG) were analyzed by XPS, with the purpose to obtain standard values for quantitative analysis of boron, nitrogen and oxygen and to measure chemical shifts of B1s, N1s, C1, and O1s in their respective chemical bonding. Our results are given in table 1, where available literature data are also shown. Generally it appears that standards are of good quality because XPS peaks (B1s, N1s and O1s) have only one contribution. At the same time, our data are in excellent agreement with values already published. Concerning B1s, the binding energy shifts from 186.3 eV for boron carbide to 187.8 eV for elemental boron to 190.3 eV for boron nitride and to 193.4 eV for boron oxide, so that these different contributions can be easily distinguished in the XPS spectra. Concerning C1s, the binding energy shifts from 284.2 eV for graphitic carbon [1] to 283 eV for boron carbide and to 284.8 eV for environment contamination (hydrocarbon) ; here it is more difficult to separate the different contributions with the equipment at hand.

BN	[1]	[2]	[3]	[6]	[4]	our results
B1s	190.3	190.3	190.6	190.2	190.6	190.3
N1s	397.9	398.0	398.3	397.6	398.3	397.9
δ(N - B)	207.6	207.5	207.7	207.4	207.7	207.6

B_2O_3	[5]	[4]	[1]	our results
B1s	192.4	193.4	193.1	193.4
O1s	532.6	533	/	533
δ(O - B)	340.2	339.6	/	339.6

B metal	[5]	[6]
B1s	187,8	187,7

H_3BO_3	[5]
B1s	192,8

B_4C	[6]	our results
B1s	186,3	186,3
C1s	283,0	283,0
δ(O - B)	96,7	96,7

Table 1 : B1s, N1s and O1s binding energy (eV) obtained by XPS for different standards (available data from the literature are also shown).

II - OPTIMIZING THE COMBAT h-BN SURFACE CHEMISTRY

II.a) The effect of ion etching

COMBAT h-BN, grade A, is a polycrystalline material containing boron trioxide (B_2O_3) as a sintering aid (6 % by weight). Table 2 shows the effect of argon etching at 3 KeV, on the composition of the h-BN surface of as received specimens (the first supply of COMBAT specimens). It is shown :

- a BN stoechiometry deviation, the B/N ration being of 1.5 after etching, surprisingly, the selective sputtering of nitrogen does not shift the binding energy of B1s,
- Argon implantation, as shown by the X-ray analysis of the surface fragments,
- a change in the colour of the h-BN surface, from white opalescent to tarnished and brown,
- a modification in the carbon chemical form. Sputtering cleaning does not eliminate carbon from the h-BN surface (13 % atomic), moreover a change in the C1s binding energy indicates that carbon is graphitized and/or carbide,
- the oxygen content is roughly preserved, under a boron oxide chemical bonding, but the stoechiometry deviates from B_2O_3.

	as received		after etching	
	B.E.	% atomic	B.E.	% atomic
B1s	190.3 191.9	24.7 6.2	190.3 192.7	29.1 6.3
N1s	398.1	25.7	397.8	19.5
C1s	284.65 286.4 288.1	17.6 5.4 1.2	283.7	13.5
O1s	532.1 534.6	16.8 1.5	532.5	25.1
B/N	/	1	/	1.49

Table 2 : Etching effect on the COMBAT BN surface : binding energy (B.E.) and atomic concentration.

II.b) The effect of annealing

We decided to modify our specimen preparation procedure before tribotesting the whole set of new COMBAT specimens, with three purposes in mind :

- eliminate carbon from h-BN surfaces,
- preserve the BN stoechiometry,
- characterize the residual boron oxide from the sintering aid.

The table 3 illustrates the effect of three cleaning sequences on the characterization of h-BN flat surfaces by XPS :

- annealing at 450°C under UHV,
- sputter cleaning with Argon (3 KeV),
- annealing at 450°C under UHV.

After annealing at 450°C, it appears that the carbon content has disappeared, that the BN stoechiometry is preserved (B/N = 0.9) and that, in these conditions, the h-BN surface is easily cleaned. When the heat treated BN surface is sputter cleaned, the carbon appears again, but under carbide and/or graphitic organization, it seems that boron carbide is also detected with the B1s XPS peak. Annealing of these sputter cleaned BN surface does not remove carbon. It is wondering what is the effect of this treatment on friction ?

The same procedure can be applied to the h-BN pin (flat or edge configuration) see table 4. The conclusions are the same as far as B, N and C are concerned.

The characterization of oxygen is another problem.

	Annealed at 450°C in UHV	
	B.E.	% atomic
B1s	190.3	42.4
N1s	397.9	44.2
C1s	/	/
O1s	532.8	13.4
B/N	/	0.86

Table 4 : Analyze of h-BN pin after annealed at 450°C

	Step 1 : cleaned with propanol 2		Step 2 : annealed at 450°C in UHV		Step 3 : argon etching		Step 4 : Annealed at 450°C in UHV	
	B.E.	% atomic	B.E.	% atomic	B.E.	% atomic	B.E.	% atomic
B1s	/ 190.3 192.5	/ 35.3 1.6	/ 190.3 192.8	/ 41.9 3.0	188.3 190.3 /	3.3 45.6 /	188.4 190.3 193.5	1.5 41.9 1.5
N1s	397.9	39.2	397.9	45	397.8	36.2	397.8	35.1
C1s	/ 284.5	/ 16.2	/ /	/ /	282.4 284.2	4.1 3	282.4 283.9	5.5 4.4
O1s	532.2	7.7	532.6	10.1	532.4	7.7	532.7	8.9
δ	N - B : 207.6 eV O - B : 339.7 eV		N - B : 207.6 eV O - B : 339.8 eV		N - B : 207.5 eV B - C : 94.1 eV		N - B : 207.5 eV O - B : 339.2 eV B - C : 94.0 eV	
B/N ratio	/	0.90	/	0.93	/	1.26	/	1.19

Table 3 : Annealed and etching effect on the h-BN surface : binding energy and atomic concentration.

II.c) XPS analysis of oxygen on the h-BN surface

As we earlier mentionned the O1s XPS signal peaks at 532.3 eV, is very near from the binding energy of oxygen in pure boron trioxide and shows only one contribution. Surprisingly, the B1s peak corresponding to B-O (E_B = 192.4 eV) is practically absent in the XPS spectra, so that the B_2O_3 stoechiometry is never obtained. In the propanol cleaned specimens O/B ratio is 5.7 and O/B is even more after annealing (the O/B ratio is 1.5 in B_2O_3). At the same time, the literature indicates that annealing at 450°C has no chemical effect on boron trioxide composition [5].

As we checked by SIMS that water was not present in the h-BN structure (see report IV), the excess of oxygen was attributed to gas entrapped in the BN microstructure, but this is in disagreement with the O1s XPS peak, the binding energy of which corresponding to O-B bonding. We can observe twice more oxygen with the old specimens than with the new ones (see table 5).

	as received			
	November 1987		April 1989	
	B.E.	% atomic	B.E.	% atomic
B1s (B-N) (B-O)	190.3 191.9	24.7 6.2	190.3 192.5	35.3 1.6
O1s	532.1	16.8	532.2	7.7
B oxided/O	/	0.37	/	0.2

Table 5 : Oxygen quantities analyzed in the old and new h-BN COMBAT.

CONCLUSION

The COMBAT h-BN specimen have a complex nature due to the presence of boron oxide from the sintering aid. It has been observed :

- that the first supply of specimens contain twice more oxygen than the second one,
- that the boron oxide species do not have the B_2O_3 stoechiometry (oxygen is largely surstoechiometric),
- that the cleaning procedure does not remove oxygen from the surface.

It is thought that oxidized species play a key role in the friction process of BN under vacuum.

Analyzing several cleaning procedure, it has been shown :

- that ion etching modifies the BN stoechiometry and changes the chemical form of carbon contaminant,
- that annealing at 450°C preserves the BN stoechiometry and eliminates carbon from the surface,
- that etching a heat treated BN surfaces makes carbon to appear as a bulk contaminant.

BIBLIOGRAPHY

[1] C.D. Wagner, W.M. Riggs, L.E. Davis, J.F. Moulder and G.E. Merilenberg (Eds) Handbook of X-Ray Photoelectron Spectroscopy, Perkin Elmer Corp., Minesota, 1979.

[2] Shigeni Kohiki, Takuhi Ohmura and Kenji Kusao, J. Electron Spectroscopy Relat. Phenom, 31 (1983) 85-90.

[3] K. Hamrin, G. Johansson, U. Gelius, C. Nordling and K. Siegbahn, Phys. Scr, 1 (1970) 277.

[4] D.J. Joyner and D.M. Hercules, J. Chem. Phys. 72 (1980) 1095.

[5] J. Kiss, K. Revesz and F. Solymosi, Applied Surface Science 37 (1989) 95-110.

[6] Results obtained by Science and Surface Company with an SSX 100 apparatus. Ecully, FRANCE.

APPENDIX Y

H. Heshmat, "High Temperature Solid Lubricated Bearing Development - Dry Powder Lubricated Traction Testing," Proc. 26th Joint AIAASAE/ASME Propulsion Conf. Paper No. 90-2047, 16-18 July 1990, Orlando, FL

26th JOINT PROPULSION CONFERENCE
16th-18th July 1990
Paper No. 90-2047

HIGH TEMPERATURE SOLID LUBRICATED BEARING DEVELOPMENT - DRY POWDER LUBRICATED TRACTION TESTING

Dr. Hooshang Heshmat
Sr. Program Manager/Sr. Scientist
Mechanical Technology Incorporated
968 Albany-Shaker Road
Latham, New York 12110

ABSTRACT

As part of a high temperature, dry lubricated bearing technology and lubricant system development program, a high-speed and high-temperature disk-on-disk tribometer was utilized and a matrix of traction data covering a range of load, speed and temperature was obtained. An experimental investigation of powder-lubricated rolling and sliding contacts for three types of triboparticulates (NiO, TiO_2 and $ZnMoO_2S_2$) was undertaken. The influence of dry triboparticulates on the traction coefficients between two ceramic materials (Si_3N_4 against itself) was investigated. The most important results of this investigation are characteristic curves for the traction coefficient versus the slide/roll ratio with dry powders which are reminiscent of fluids, and the observation that dry powder lubricants lower traction coefficients and wear. Measured tractions are found to be a strong function of powder lubricant type and values decrease with slide-to-roll ratio and load. The data show a weak sensitivity to temperature.

NOMENCLATURE

F_x	Tractive force in rolling direction
W_n	Normal load
P_{HZ}	Hertz maximum pressure
N_A	Rotational speed of lower disk (disk 1)
N_B	Rotational speed of upper disk (disk 2)
E_1, E_2	Modules of elasticity of disk 1 and disk 2
R_1, R_2	Outer radius of disk 1 and disk 2
R_{c1}, R_{c2}	Crown radius of disk 1 and disk 2
$\nu_{1,2}$	Poisson's Ratio of disk 1 and disk 2
U_1, U_2	Surface velocity of disk 1 and disk 2
ZΔU	$(U_2-U_1)/U_1)x100$ = percent slip ratio
η_T	(F_x/W_n) = Traction coefficient
Ta	Ambient temperature
RT	Room temperature = 25°C
Kyo	Si_3N_4, Kyocera
NBD	Si_3N_4, NBD-100
CER	Si_3N_4, Cercom "pad" improved
K162B	TiC cermet with Mo and Ni as a binder
τ_o	Coefficient of yield shear stress (threshold)
τ_L	Coefficient of limiting shear stress
τ_T	Coefficient of thermal limiting shear stress
α_1	Angle of slope at maximum traction (deg.)
α_2	Angle of slope at stable portion of traction curve

Held at Orlando, Florida, USA
sponsored by AIAA, SAE, and ASME
Organized and chaired by Mr. J.R. Miner of Pratt & Whitney and Mr. P.W. Center of WRDC/POSL

1.0 INTRODUCTION

The need for solid lubricated bearing technology has become increasingly evident with the recent advanced turbine engine initiatives which are aimed at achieving a revolutionary improvement by doubling propulsion capacity. Attaining this performance improvement goal will require the engine bearings to be subjected to increased temperatures, loads, and speeds -- a severe operating environment for bearings of the future. The severity of this environment precludes the use of current liquid lubricants, since bearing temperatures are expected to exceed 1000°F and may reach levels as high as 1500°F.

It naturally goes without saying that such an extreme environment precludes the use of liquid lubricant and the most common materials such as VIM-VAR M50 used for aeroengine bearings since their practical operating temperatures are limited to 700-800°F. In Fig. 1, the most important

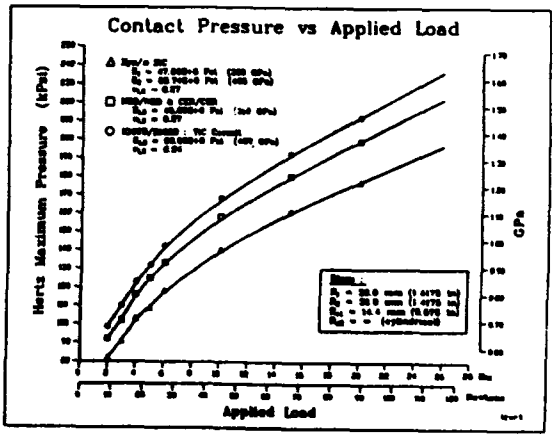

Fig. 1 Contact pressure vs applied load for various materials combinations o Si_3N_4/α-SiC, □ Si_3N_4/Si_3N_4, Δ TiC/TiC

characteristics of some potential high temperature cermet and ceramic materials for rolling element bearings are compared. As can be seen from the plots of Fig. 1, under constant applied loads the computed

maximum Hertzian stress varies substantially for a given material combination. A group of materials which appears promising for high temperature bearings is high performance ceramics. Prominent among them is the hot pressed silicon nitride series (known by their tradenames: Kyocera, NBD-100, Cercom "PAD"), which have been developed during this decade for high speed and high temperature rolling element bearings. Despite their many advantages, there are drawbacks with Si_3N_4, including high coefficient of friction, low tensile strength, low thermal coefficient of expansion and moderate wear properties in the absence of lubricant. Thus, considerable development effort is needed for the fabrication and application of bearings from these ceramics.

One potential solution to the temperature problem is to use dry triboparticulates (powder lubricants) to minimize bearing friction and wear and to maximize heat dissipation in the bearing's mating surfaces[1-3]. The tribology of powder lubrication's central proposition is that provided the particles are small enough the mechanism and rheodynamics of dry powders acting as lubricants are in many ways similar to the hydrodynamic action of non-Newtonian fluids[1-4]. Thus, an important aspect in the application of dry triboparticulate lubrication is the understanding of frictional force developed in shearing a powder film in a Hertzian contact. Most of the experimental data to date have been obtained from pin-on-disk machines in which the friction forces are measured in pure sliding. Although these data are far from complete, they show that in general the frictional force increases with the sliding speed, up to a peak value and beyond this point an increase in sliding speed causes a decrease in friction.

This paper describes an advanced rolling/sliding tribometer designed to obtain traction data under high speed, loads and temperatures for both powdered and non-powdered (dry) conditions. Data are presented for hot pressed, silicon nitride (Si_3N_4) disks (manufactured by Kyocera) The powder lubricants used include nickel oxide, NiO; titanium dioxide (TiO_2, rutile form); and zinc oxythiomolybdate, $ZnMoO_2S_2$. Surface speeds up to 68 m/s (13,386 ft/min), temperatures from 70 to 1200°F, and slip ratios up to 100% were investigated. Baseline data were obtained for unlubricated conditions and using a synthetic liquid lubricant. The results of baseline data correlated well with other available data for the conditions and reported here and elsewhere[5-7].

The powder-lubricated data are analyzed in various ways, however, the lack of previously published data in the literature did not allow for comparison. Although the experimental observations presented in this paper are an extension of considerations and theory developed in an earlier paper by Heshmat, Pinkus, Godet[1] and Heshmat[2], the traction data is presented here to provide a data base and guidelines for designers to arrive at reasonable estimates of powder lubricant properties under severe conditions of operation.

2.0 EXPERIMENTAL SETUP

A schematic of the disk-on-disk tribometer used for conducting tests is presented in Fig. 2. The lower disk, #1, mounted on spindle A, has a plain cylindrical form with a radius of 36 mm. The upper crowned disk #2 on spindle B has a major radius of 36

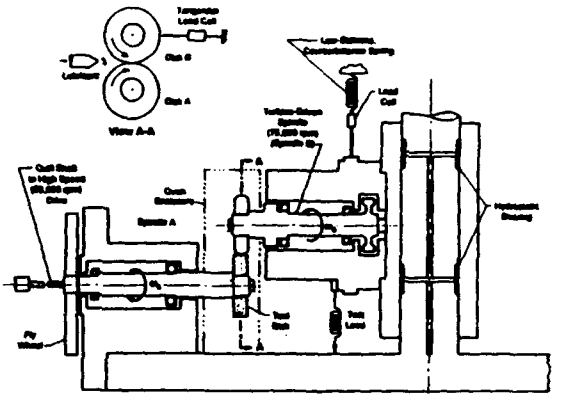

Fig. 2 Extreme environment rolling/sliding traction simulator

mm and a crown radius of 14.4 mm. The contact surfaces of the disks were lapped to achieve 0.51 nm or better finish. For the tests, the disks were made from hot pressed Si_3N_4 (from Kyocera). The design methodology and dynamic analysis of this apparatus is given in Ref. 8.

As shown in Fig. 2, spindle A is rigidly mounted on the base and is driven by a variable-speed electric motor through a quill shaft and flywheel. Spindle B is driven by an integral air turbine. The spindle unit is suspended on a soft spring, but is restrained by hydrostatic bearings. These bearings operate against a vertical member which is integral with the base. The hydrostatic bearings keep the axes of the two spindles parallel but present virtually no resistance to the vertical and small rotational motion of spindle B. In operation, the disks are loaded by a pneumatic cylinder that pulls down on spindle B through a load cell. The traction force is measured by a tangential load cell, as shown in Figure 2, view A-A. An insulated oven enclosure surrounds the two disks to control the environment for high-temperature testing. During the tests, temperatures were monitored by three thermocouples located close to the disks and contact area.

The system for delivering powder lubricants to the inlet zone of the contact is based on a conventional air brush. A tube from the airbrush nozzle penetrates the oven wall and discharges the dry air/powder mixture approximately 25 mm from the contact zone.

Prior to operation, the suspension spring for spindle B is adjusted so that the disks are separated from each other by a distance of 90 to 100 μm with no pressure in the loading cylinder. Spindle A (disk #1) is then accelerated to a preselected speed that is maintained throughout the test. Spindle B (disk #2) is then accelerated to a speed higher than that of spindle A. The traction test is started by applying the load, which brings the disks into contact, and then shutting off the air to the drive turbine. Spindle B subsequently coasts down to a speed lower than that of spindle A. The sequence of events for each test is carried out automatically by a rig control and data acquisition system based on a PC/AT computer. During coastdown, the speed and traction force are continuously

monitored and data are stored for subsequent analysis. During a typical 5- to 6-sec coastdown, 1.5 to 2 megabytes of data are recorded and 250 to 300 data points are subsequently extracted from this raw data to produce a traction curve. Some tests were repeated up to eight times in order to verify the repeatability of the traction data.

The triboparticulate size ranged from 0.1 to 10 μm with 99.99% purity for all lubricants. Powder lubricants including NiO with a light green color (particles having spheroid shape), TiO_2 with a tan color in rutile form, and zinc oxythiomolybdate with a dark orange color (particles of TiO_2 and $ZnMoO_2S_2$ having irregular shapes with many facets and sharp edges) were tested.

The test load, speed conditions and temperatures were as follows:

W_n:	5 to 15 lbs.
Speeds:	N_A = 150 cps; N_B: 150-300 cps
Ta:	22°C-650°C (RT to 1200°F)

For the disk material and geometries, the maximum Hertzian stress as a function of normal load is given in Fig. 1 (NBD/NBD curve).

3.0 TRACTION DATA

Traction coefficients η_τ are defined here as the measured tractice force divided by applied normal load W_n and slip rates are defined as the difference between the surface velocities (U_2-U_1). The traction data are presented in the form of η_τ vs. percent slip ratio, %ΔU.

For comparison of relative performance, the traction curves were fit. Data relevant to the characteristics of a particular traction curve such as τ_o, τ_ℓ, τ_T and others were boxed in and given with the subsequent plots. Where τ_o, coefficient of yield shear stress--a powder is not likely to flow until the shear exceeds the yield strength of the powder film. In addition to τ_o a powder film has a limiting shear strength τ_ℓ which is related to the bulk powder property, characteristics, and physical boundary conditions of the tribosurfaces.

As can be seen from Fig. 3, the traction increases with a moderate slip until the traction coefficient increases up to a value of limiting shear, τ_ℓ, then gradually decreases as slip rate increases. The decrease in traction coefficient beyond τ_ℓ, up to a limiting value of τ_T is believed to be due to the temperature rise and other tribological phenomena as is evident from traction behavior of liquid lubricants at a higher slip/roll region[5,6].

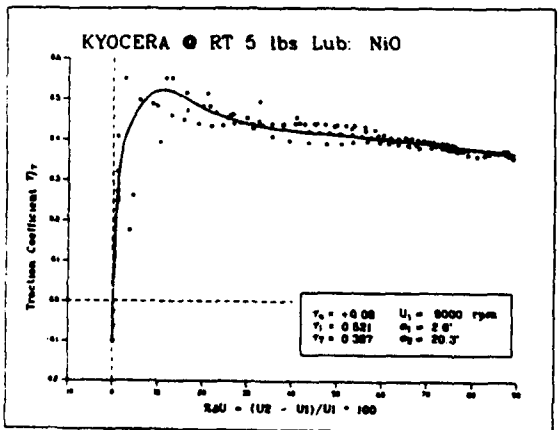

Fig. 3 η_τ vs %ΔU for NiO powder at RT, Wn = 22.23N

The angle of slope at maximum traction, and the angle of slope of the stable portion of traction are designated by α_1 and α_2, respectively. For instance, the smaller the magnitude of α_1, the higher the stable region of the traction curve is and vice versa, the greater the α_2, the higher the ratio of traction force over slip velocities. The traction data are presented here in the following parametric manner:

- For each powder lubricant the traction data of constant W_n at RT and at maximum test temperature are presented individually.
- Traction curves are combined for each constant test temperature as a function of the applied load.

For the latter case test data points were omitted from the plots while smooth fitted curves are shown for clarity and comparison.

3.1 Tests with NiO

The traction coefficients generated using dry NiO powder as a lubricant are presented in Figures 3 through 8. The values of τ_o and τ_ℓ decreased as applied normal loads increased for all temperatures except 600°F. However, approximate values of τ_ℓ remained almost insensitive to the temperature variation. Also, at higher temperatures the traction curve approached its peak at a lower value of slip ratio.

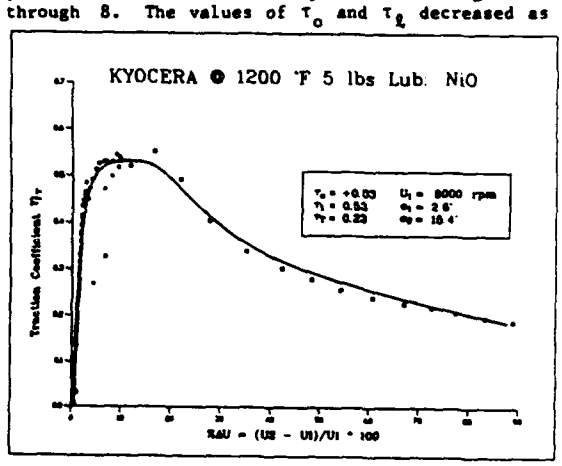

Fig. 4 η_τ vs %ΔU for NiO powder at 650°C, Wn = 22.23N

The traction curve beyond τ_ℓ decreases as ΔU increases. The decrease in traction coefficient beyond τ_ℓ up to a limiting value of τ_T was observed (temperature effect is noted). As seen from the plots of Fig. 3 and 4, τ_T dropped from 0.387 to 0.23 at %ΔU equal to 90%.

3.2 Tests with TiO_2

The traction coefficients generated using dry TiO_2 powder as a lubricant are presented in Figures 9 through 14. At room temperature τ_o and τ_ℓ were lower than those at higher temperatures. However, at 1200°F the traction curve approaches its peak at a higher value of slip (%ΔU = 15% and α_1 = 1.77 deg)

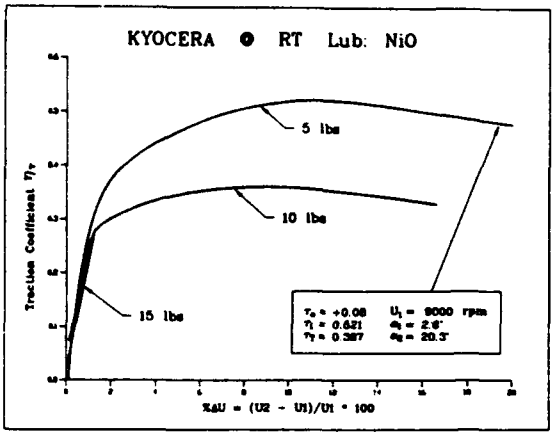

Fig. 5 Traction data for NiO powder at RT; Wn = 22.23, 44.48 and 66.72N

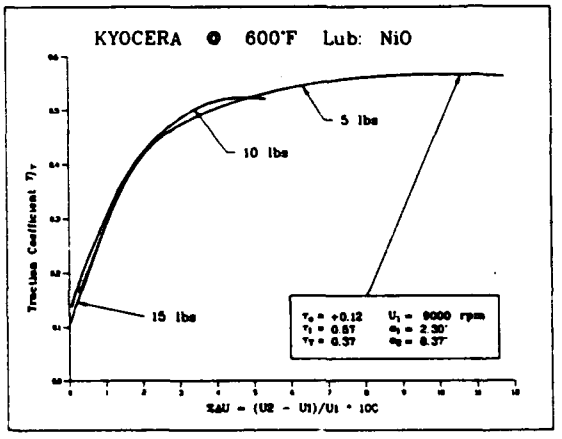

Fig. 6 Traction data for NiO powder at 316°C; Wn = 22.23, 44.48 and 66.72N

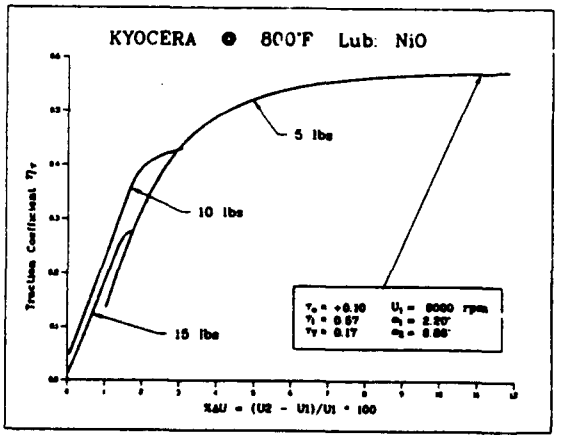

Fig. 7 Traction data for NiO powder at 427°C; Wn = 22.23, 44.48 and 66.72N

while at room temperature the corresponding slip values were 10% and its α_1 = 3.5 deg. (Figs. 9 and 10).

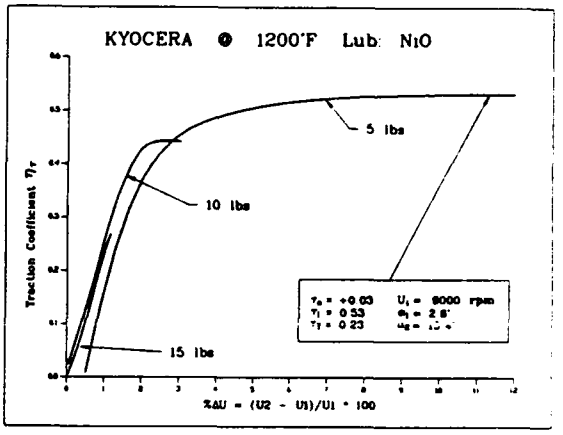

Fig. 8 Traction data for NiO powder at 650°C; Wn = 22.23, 44.48 and 66.72N

The depth of the wear track generated on the test disks was insignificant and immeasurable, although the surface finish was changed about fourfold over the original one. The track width was about 47 mils, 1.7 times that of the calculated Hertz half width, the center portion of the track appeared smooth and glassy while the edges were discolored and showed deposition and transferred or adhered powder film. This film of powder which was strongly bonded onto the surface faded outwardly, suggesting a plowing action akin to the side flow in liquid lubrication.

3.3 Tests with $ZnMoO_2S_2$

The traction data using $ZnMoO_2S_2$ powder at room temperature is given in Fig. 15 and at 1050°F is given in Fig. 16 for a constant load of 5 lbs. At room temperature τ_0 was higher than that at a high temperature of 1050°F, although τ_g and τ_T were lower than those at higher temperatures. However, at RT the traction curve approaches its peak at a lower value of slip (%ΔU = 10% and α_1 = 1.46°), while at 1050°F the corresponding slip value was 12% and its α_1 = 1.2 deg.

The traction data at RT is given in Fig. 17 for various contact loads. Figure 17 shows a progressive decrease in the τ_g with an increase in

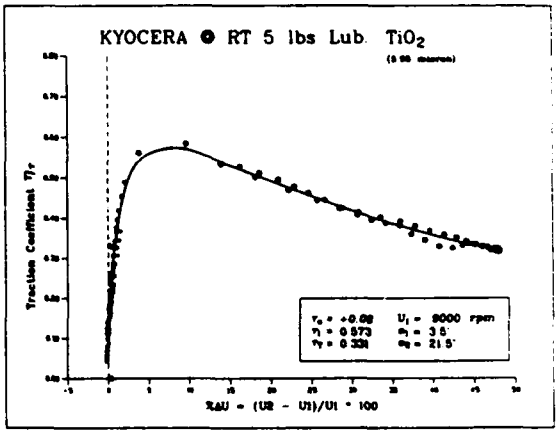

Fig. 9 η_T vs %ΔU for TiO_2 powder at RT, Wn = 22.23N

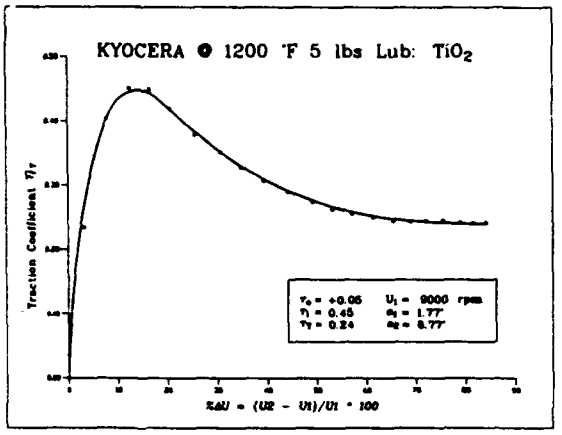

Fig. 10 η_T vs %ΔU for TiO_2 powder at 650°C, Wn = 22.23N

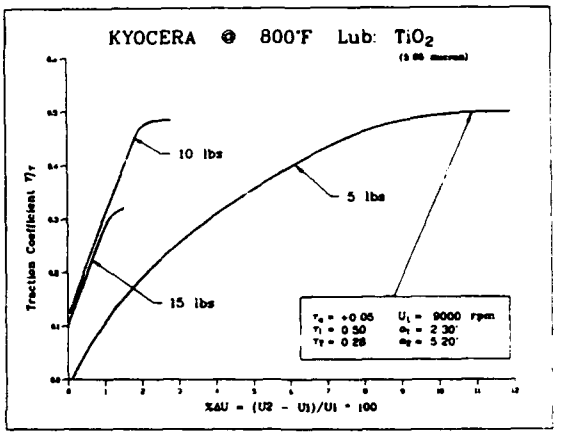

Fig. 13 Traction data for TiO_2 powder at 427°C; Wn = 22.23, 44.48 and 66.72N

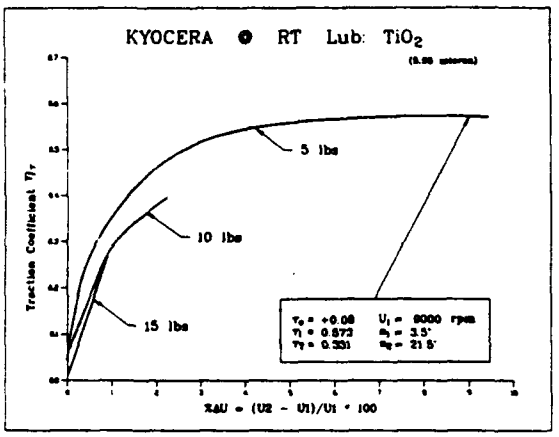

Fig. 11 Traction data for TiO_2 powder at RT; Wn = 22.23, 44.48 and 66.72N

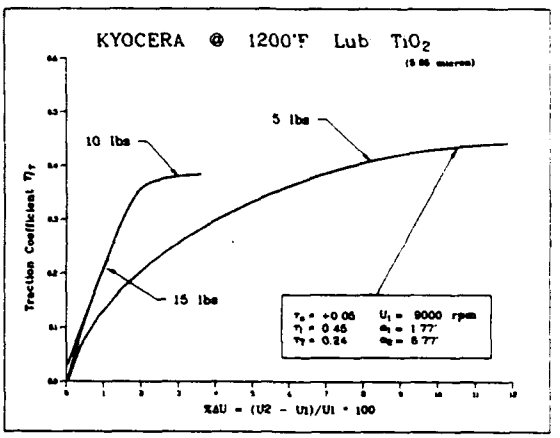

Fig. 14 Traction data for TiO_2 powder at 650°C; Wn = 22.23, 44.48 and 66.72N

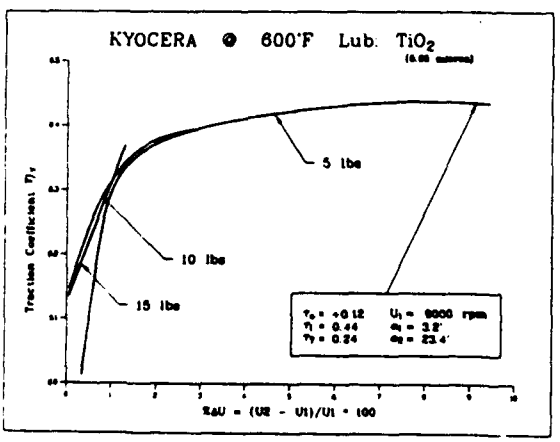

Fig. 12 Traction data for TiO_2 powder at 316°C; Wn = 22.23, 44.48 and 66.72N

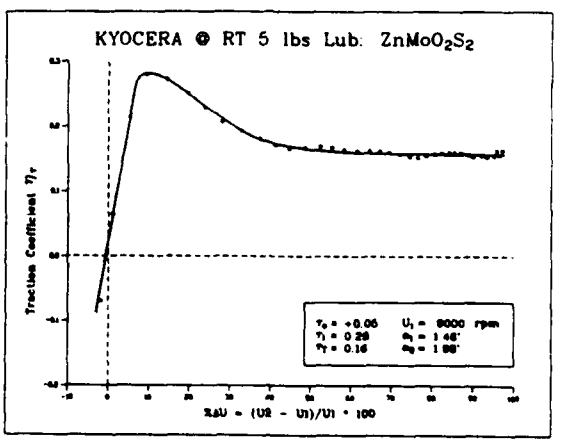

Fig. 15 η_T vs %ΔU for $ZnMoO_2S_2$ powder at RT, Wn = 22.23N

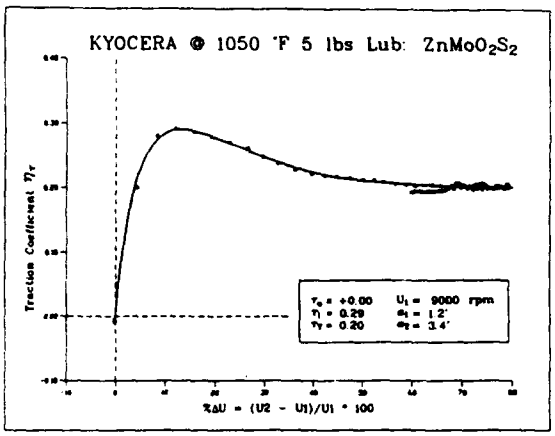

Fig. 16 η_T vs $\%\Delta U$ for $ZnMoO_2S_2$ powder at 566°C; Wn = 22.23N

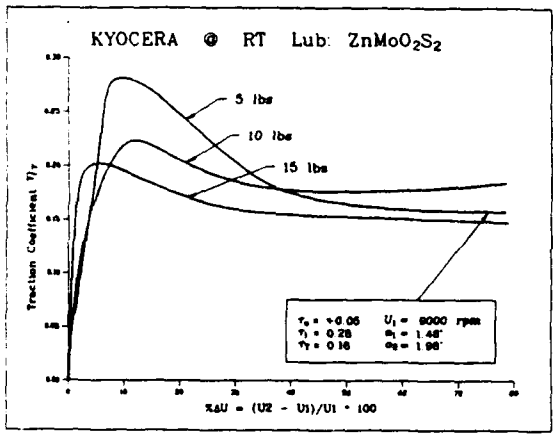

Fig. 17 Traction data for $ZnMoO_2S_2$ powder at RT; Wn = 22.23, 44.48 and 66.72N

load. The same holds for the traction data at 800°F and 1050°F given in Figs. 18 and 19, with the exception at 800°F τ_g for 10 lbs, which has about the same value as τ_g at 5 lbs. Worthy of note, overall traction coefficients show a decrease at 800°F relative to RT and 1050°F data. In almost all cases the τ_o was about zero within the tolerances of the experimental data, which is reminiscent of a liquid lubricant's behavior. The limiting stresses τ_g were also about 50% less than those measured with NiO and TiO_2. At higher temperature, 1050°F and contact stresses beyond 125 ksi, the traction curves began to flatten or rise as slip was increased. This phenomena is analagous to that of film rupture in liquid lubricants. The appearance of the contact surfaces was similar to that from the TiO_2 tests.

Overall the traction curves with dry $ZnMoO_2S_2$ are reminiscent of liquid lubricants. However, the review of literature[566] on liquid lubricant traction curves shows a decrease in η_T beyond the slip ratio of 20%, which is mainly due to thermal effects, while the traction curve for $ZnMoO_2S_2$ begins to flatten or slightly raise rather than drop off.

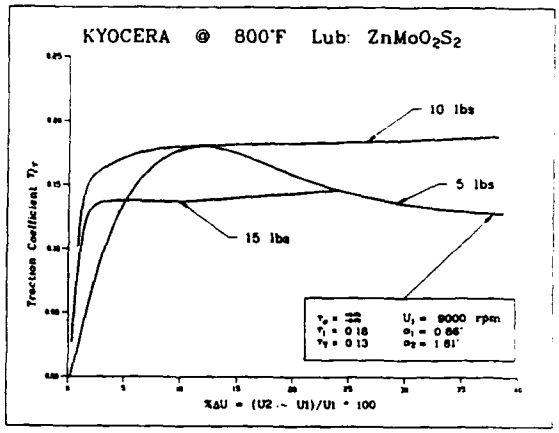

Fig. 18 Traction data for $ZnMoO_2S_2$ powder at 427°C; Wn = 22.23, 44.48 and 66.72N

3.4 Unlubricated (Dry) Tests

To provide a baseline for assessing the advantages of powder lubricants, tests were carried out with no insertion of lubricant into the contact. This test was conducted with three different types of Si_3N_4 materials. A sample result at 1200°F is shown in Fig. 20. The dry traction curves showed no change in traction performance with load or temperatures. The traction curves closely resemble friction curves that one might expect from a pin-on-disk apparatus.

As can be seen from the plots of Fig. 20, traction data with TiO_2 were also plotted for comparison. With the contact load of 160 ksi the traction coefficient approached a value of approximately 0.9 at $\%\Delta U \sim 10\%$, and the η_T has risen to approximately .93 at 60% slip ratio as shown in Fig. 20. These values of maximum traction coefficients (about 0.9) correlate well with the static coefficient of

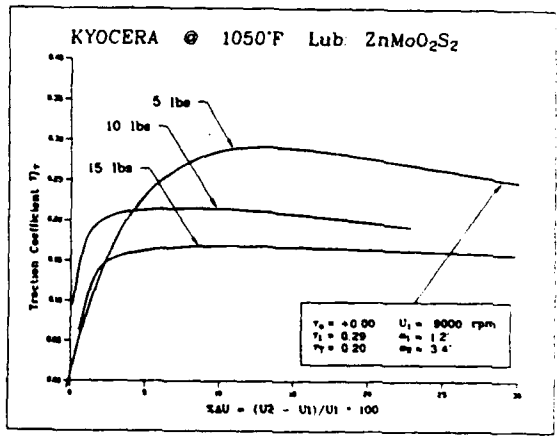

Fig. 19 Traction data for $ZnMoO_2S_2$ powder at 566°C; Wn = 22.23, 44.48 and 66.72N

friction reported elsewhere for Si_3N_4 materials. In comparison with powder lubricated tests the results of the dry condition showed the highest values of τ_o, τ_g, and α_2 and wear depth.

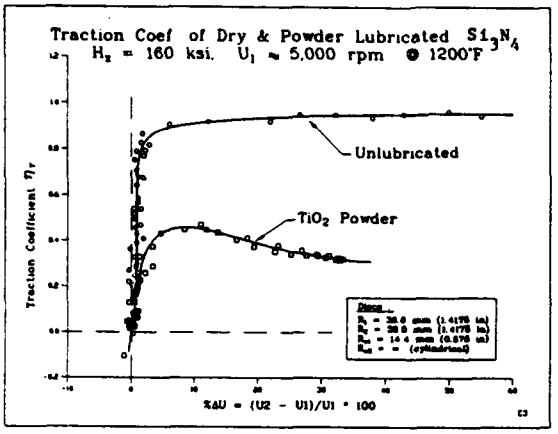

Fig. 20 Traction data for unlubricated and powder TiO_2 lubricated Si_3N_4 materials at 650°C, Wn = 44.48N

4.0 QUASI-HYDRODYNAMIC MODEL

The results of all powder lubricated series of experiments indicate that the mechanism of powder flow seems to follow some of the basic features of hydrodynamic lubrication by exhibiting a layer-like shear, reminiscent of fluids. This shear is deemed responsible for the reduction in traction coefficients and wear that accompanies the presence of debris between interacting surfaces. The nature of the sheared flow causes the least possible discontinuity between the various laminae of the powder bed. Thus, the basic feature of the quasi-hydrodynamic model is a layered flow of the powder bed, as portrayed in Fig. 21. While powder lubricants are similar to fluids, they do have some unique features, as discussed below.

4.1 Intermediate Film

It has been postulated and is so shown in the model of Fig. 21 that an intermediate film, a form of boundary layer, is created between the interacting surfaces and the lubricant film under powder lubrication conditions. An accommodation of velocities occurs across the intermediate film, between the velocities of the two surfaces (V_1 and V_2) and the edge velocities of the lubricant film (U_1 and U_2). The thickness of the intermediate films correspond to the surface roughness (δ_1 and δ_2) of the respective mating material.

The tests conducted under this program clarifies and amplifies the mechanism of formation of these intermediate films. The result of prolonged exposure to powder lubrication is the formation of this adhesive film, which consists of the powder lubricant or of one of its components, either in pure form or in some chemically altered state, very likely an oxide. Thus, the tribological film formed in powder lubrication resembles the form portrayed schematically in Fig. 21. The intermediate layer, made up of the adhered powder, has the flexibility of behaving either as a solid or as a semi-powder in which considerable creep occurs. This creep makes the accommodation of flow velocities from V_1 and V_2 to U_1 and U_2 possible.

5.0 CONCLUSIONS

- The NiO and TiO_2 triboparticulates changed the shapes of the traction curves. Compared with the unlubricated data, the powder reduces the traction coefficients over a wide span of slip ratios. Its effect on lowering the effective contact shear stress, τ_e was about 50% relative to the unlubricated case.
- The traction characteristics of the $ZnMoO_2S_2$ powder were quite different compared to the NiO and TiO_2 powders. The $ZnMoO_2S_2$ powder gave zero threshold shear stress and low traction coefficients under all test conditions. Overall the behavior of this powder and the magnitude of the traction coefficients were very similar to those seen with liquid lubricants.
- The persistent presence of powder buildup on the outsides of the contact region suggests the occurrence of side leakage of the power lubricant, analogous to the sideflow in liquid EHD.
- Due to the short duration of each test, the amount of wear that took place on the disks was too small to measure accurately. Therefore, the data reported should only be used to compare the traction characteristics of the powder lubricants with the chosen combination of disk materials.

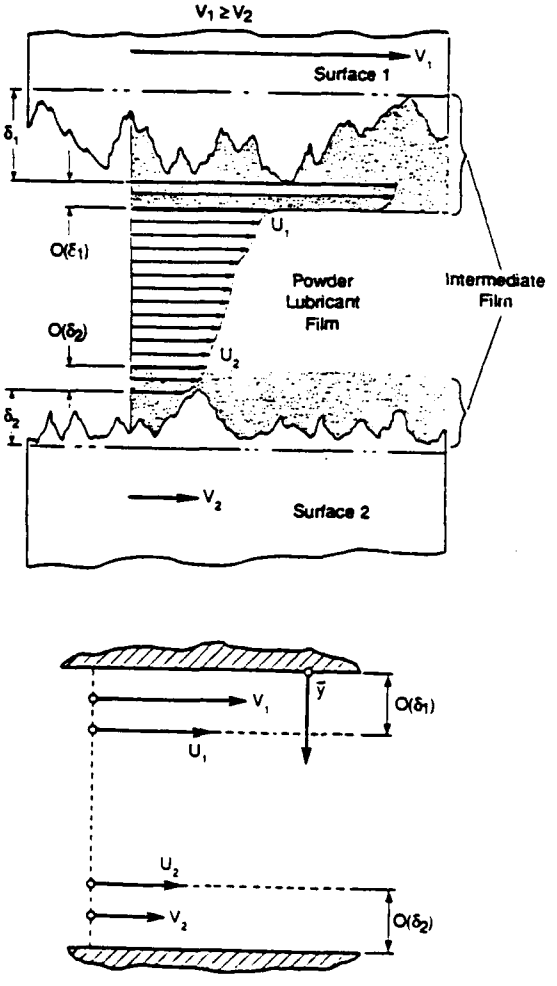

Fig. 21 Quasi-Hydrodynamic model for powder lubrication

- Since the traction in solid lubrication is most likely a function of both the disk materials and the powder lubricant, care must be taken about generalizing these data to predicting the behavior of the same lubricants with other disc materials.

6.0 ACKNOWLEDGEMENTS

Acknowledgement is due the United States Air Force Wright Aeronautical Laboratories for its sponsorship of this investigation and in particular to R. Dayton of AFWAL/POSL for his sustained interest in and support of this work. The author gratefully acknowledges Messrs. D. Hosterman, J. Walton, and A. Soltesz of MTI for their support given at various stages of this effort.

7.0 REFERENCES

1. Heshmat, H. and O. Pinkus, "Performance of Starved Journal Bearing With Oil Ring Lubrication," JOT, ASME Trans., 107, no. 1 (1985): 23-32.

2. Heshmat, H. "The Rheology and Hydrodynamics of Dry Powder Lubrication", submitted for publication by STLE and presentation at the 1990 ASME-STLE Tribology Conference, Ontario, Canada.

3. Heshmat, H. "Wear Reduction Systems: Powder Lubricated Piston Rings for Coal Fired Diesel Engines," Proceedings DOE-METC Contractors' Review Meeting, October 1989.

4. Heshmat, H. "Diesel Wear: Powder-Lubricated Piston Rigns for Coal-Fired Diesel Engines", Proceedings DOE-METC Contractors' Review Meeting, March 1990.

5. Walowit, J.A. and Anno, J.N. Modern Development in Lubrication Mechanics, Applied Science Publishers, Ltd., London, 1975.

6. Gupta, P.K. "Traction Modeling of Military Oils", Technical Report C-104-86-TR, prepared for AFAPL/AFWAL, January 1986.

7. Heshmat, H. and Dill, J., "Traction Characteristics of High Temperature Powder Lubricated Ceramics ($Si_3N_4/\alpha SiC$)", submitted for publication by STLE and presentation at the 1990 ASME-STLE Tribology Conference, Ontario, Canada.

8. Heshmat, H. "The Effect of Dynamic Loads in Tribometers--Analysis and Experiments", Proceedings of the 16th Leeds-Lyon Symposium on Tribology, Elsevier Science Publishers, Tribology Series 14, 1989.

APPENDIX Z

C. Schmutz, "Characterization of TiO_{2-x} Layers," CSEM Technical Report No. 232, Project No. 51.312, CSEM, Neuchatel, Switzerland, Hughes P.O. S9-507875-SRW, Nov, 1988

and

H. Boving, "Generation of TiO_2-Rutile Coatings and their Tribological Characterization," CSEM Technical Report No. 307, Project No. 51.207, CSEM, Neuchatel, Switzerland, Hughes P.O. S9-318804-SAC, November, 1988

CENTRE SUISSE D'ELECTRONIQUE ET DE MICROTECHNIQUE S.A.
– Recherche et Développement –

CSEM MALADIERE 71 CH-2007 NEUCHATEL (SWITZERLAND)
TEL. 038/24 01 61 TELEX 952 664 (CSEM) TELEFAX 038/25 40 78

CSEM TECHNICAL REPORT No. 232

(for the exclusive use of *HUGHES AIRCRAFT Comp.*)

TITLE : Characterization of TiO_{2-x} layers

by: C. Schmutz

PROJECT: N° 51.312 TiO_{2-x} depositions and characterizations

DATE : November 1988 **Class : A**

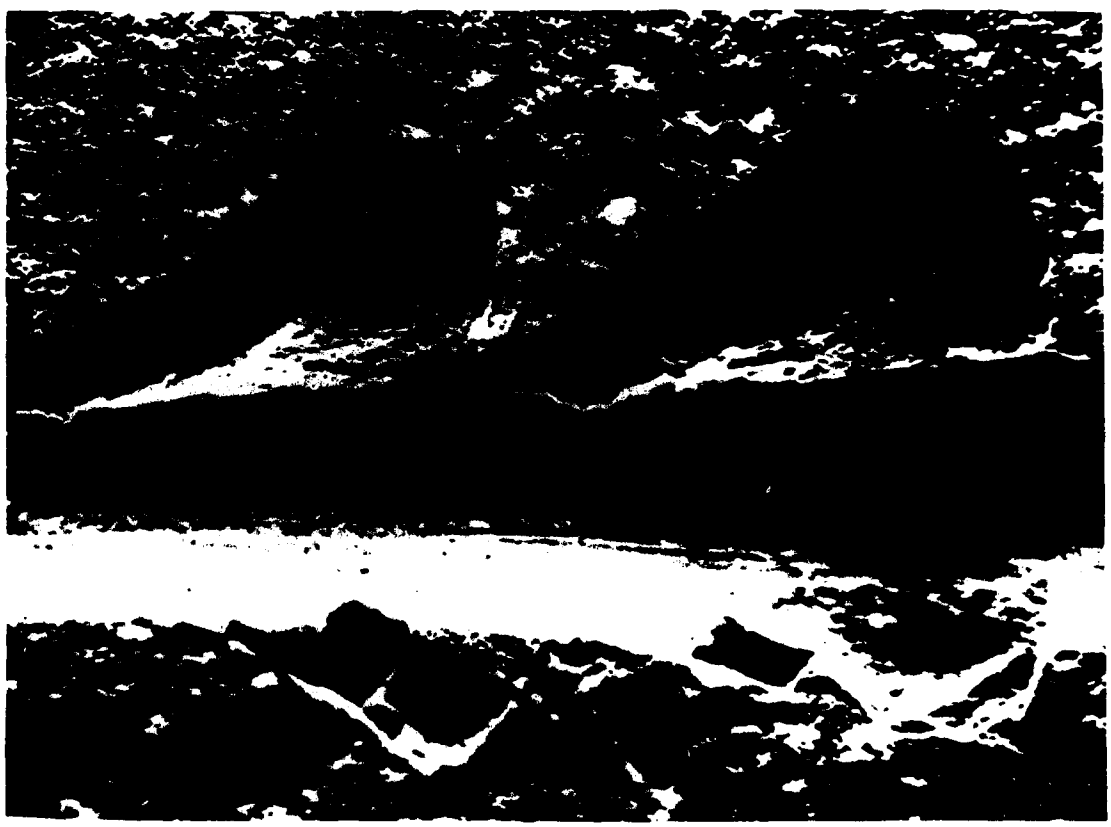

CENTRE SUISSE D'ELECTRONIQUE ET DE MICROTECHNIQUE S.A.
– Recherche et Développement –

CSEM MALADIERE 71 CH-2007 NEUCHATEL (SWITZERLAND)
TEL. 038/24 01 61 TELEX 952 664 (CSEM) TELEFAX 038/25 40 78

CSEM TECHNICAL REPORT No. 232

(for the exclusive use of HUGHES AIRCRAFT Comp.)

TITLE : Characterization of TiO_{2-x} layers

by: C. Schmutz

PROJECT : No. 51.312 TiO_{2-x} depositions and characterizations

DATE : November 1988 **Class: A**

Abstract:

The purpose of this investigation was to produce and characterize 3 different types of TiO_{2-x} coatings produced by CVD related techniques. The substrate consisted of CVD-TiC coated AISI 440C stainless steel discs. The characterization comprised X-ray diffraction (microstructure, internal stresses), metallography (coating thickness, microhardness) and the tribological properties.

The analysed oxide surface layer consists mainly of rutile. Friction and wear measurements were made on a pin-on-disk tester under both dry and humid air environments at room temperature.

The tribological properties are better in humid air environment than in dry air; however, in general it can be said that the analysed coatings cannot be qualified as having good self-lubricant properties. The oxide layers reduce the wear rates of the coated parts.

Contresigné:

Material and Tribology Dept:

TABLE OF CONTENTS

	PAGE
1. INTRODUCTION	1
2. WORK STATEMENT	1
2.1. Task 1: "Specimen Preparation"	1
2.2. Task 2: "Coating of samples with TiO_{2-x} layers"	1
2.3. Task 3: "Characterization of TiO_{2-x} coating"	1
3. FIRST SERIES OF SAMPLES: LOTS 1, 2 AND 3	2
3.1. Crystal structure (XRD)	2
3.2. Metallographic examination	2
3.3. Tribometry with the CSEM pin-on-disc TRIBOMETER	4
3.4. Adhesion control by Scratch-testing	4
3.5. Conclusions	5
4. SECOND SERIES OF SAMPLES: LOTS 4, 5 AND 6	5
4.1. Specimen preparation	5
4.2. Coating of samples with TiO_{2-x} layers	5
4.3. Physical characterizations	6
4.3.1. Crystal structure (XRD)	6
4.3.2. Internal stresses	7
4.4. Chemical characterization	9
4.5. Tribometry with the CSEM pin-on-disc TRIBOMETER	15
4.6. Metallographic examination	16
4.7. Adhesion Control by scratch testing	18
4.8. Microhardness	23
4.8.1. Substrate	23
4.8.2. Coatings and interfaces (cross section)	23
4.8.3. Coatings (surface)	26
5. CONCLUSION	27

1. INTRODUCTION

In the scope of Hughes Aircraft Company's Purchase Order Nr S 9-507875-SRW of 19 November 1987, CSEM has deposited, then chemically and microstructurally characterized, and finally friction-tested TiO_{2-x} coatings. The oxide coatings were deposited on CVD-TiC coated AISI 440C steel substrates, by various techniques, detailed under 2.2.

Two series of samples have been prepared :

- for the first series (lots 1, 2 and 3), some of the AISI 440C discs were NOT CVD-TiC coated, prior to the TiO_{2-x} treatments;
- for the second series (lots 3, 4 and 5), CVD-TiC coated AISI 440C discs were used as planned.

This report contains the "partial characterization" of lots 1-3 and the "complete characterization", according to the Work Statement, of lots 4-6.

2. WORK STATEMENT

Hereafter is the Work Statement as mentioned in the P.O.

2.1 TASK 1 : "Specimen Preparation"

Preparation of 20 ea., 20 mm diam., 5 mm thick, approx. 5 µm CVD-TiC coated AISI 440C steel discs; one side of the CVD-TiC coated discs is to be polished to 0.1 µm cla.

These polished CVD-TiC coated discs will serve as substrates for the subsequent TiO_{2-x} layers prepared in various ways described in TASK 2.

2.2 TASK 2 : "Coating of samples with TiO_{2-x} layers"

Production of adherent TiO_{2-x} layers of different chemistry and crystal structure, in three different ways :

- H_2O vapor oxidation of the TiC substrate at elevated temperatures to produce a thick "native oxide" on the TiC surface (treatment 1),
- conventional CVD - TiO_{2-x} (treatment 2),
- conventional CVD - TiO_{2-x} and a high temperature oxidation of the TiO_{2-x} coating (treatment 3).

The TiO_{2-x} coatings shall be between 1 and 3 µm thick, depending on the process.

2.3 TASK 3 : "Characterization of the TiO_{2-x} coating"

The following physical, chemical and tribological properties will be determined:

- crystal structure, texture and internal stresses by X-ray diffraction,
- morphology and microstructure by SEM,

- chemical composition by microprobe,
- microhardness by Vickers indentation,
- coating adhesion by scratch-testing,
- friction and wear characterization by pin-on-disc tribometry performed in both dry and humid air test-environments, at room temperature, and
- thickness.

3. FIRST SERIES OF SAMPLES : LOTS 1, 2 AND 3

The AISI 440C discs were NOT all CVD-TiC coated prior to the TiO_{2-x} treatments. Due to the poor quality of some of these "TiO_{2-x}" coatings, these samples were only partially characterized. Hereafter follows a summary of the work performed on samples originating from lots 1, 2 and 3.

The three different sample lots are defined as follows :

Lot 1 : H_2O-vapor oxidation of CVD-TiC coated AISI 440C discs at 900° C during 1 hour;

Lot 2 : Conventional CVD - TiO_{2-x} process, on AISI 440C discs with NO CVD-TiC coating prior to the TiO_{2-x} treatment;

Lot 3 : The same treatment as Lot 2 with an additional high temperature (800° C during 1 hour) IPO (ISOPROPANOL) oxidation of the CVD-TiO_{2-x} coating.

3.1 Crystal structure (XRD)

Lot 1 : rutile structure with weak TiC-peaks

Lot 2 : anatase structure

Lot 3 : rutile structure with weak steel-peaks

3.2 Metallographic examination

Lot 1 :
- coating thickness : approx. 13 µm,
- poor adhesion as shown by coating spalling,
- Figure 1 : micrographs.

Lot 2 :
- coating thickness : 3 to 6 µm,
- dense, apparently well adherent coating
- Figure 2 : micrograph.

Lot 3 :
- coating thickness : 3 to 5 µm,
- apparently "double" layer, created during the high temperature oxidation perhaps by C-diffusion from the substrate and partial reduction of the oxide layer,
- Figure 3 : micrograph

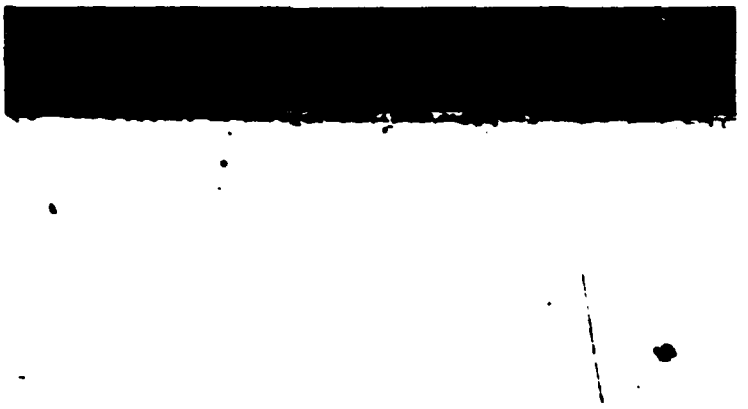

26611 500 x

Fig. 1 : Metallographic view of the H_2O-vapor oxidized CVD-TiC coated AISI 440C steel discs (Lot 1).

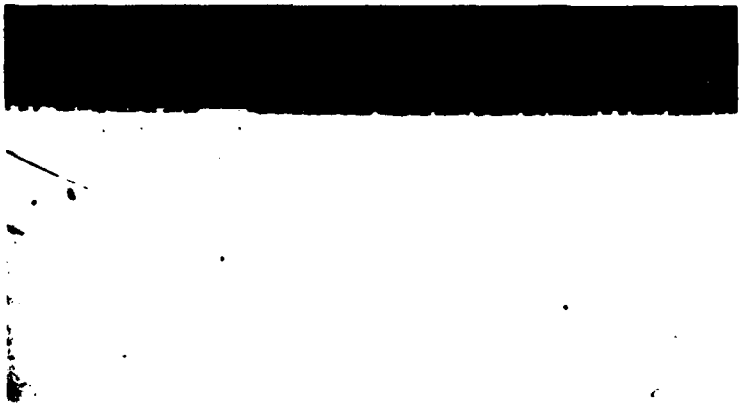

26613 500 x

Fig. 2 : Metallographic view of the conventional CVD-TiO_{2-x} coating (Lot 2)

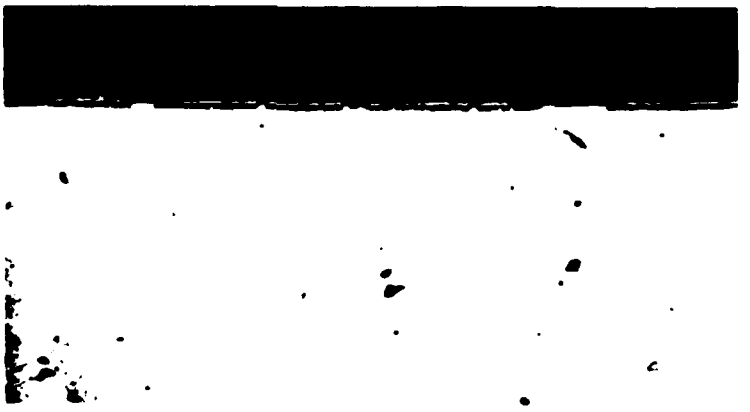

26617 500 x

Fig. 3 : Metallographic view of the high temperature oxidized CVD-TiO_{2-x} coating (Lot 3)

3.3 Tribometry with the C.S.E.M. pin-on-disc TRIBOMETER

The test conditions were as follows :

pin : 6 mm diam. AISI 52100 steel GRADE 3ball (non rotating)
load : 5 N
sliding speed : 0.1 m/s
relative humidity : 99% or less than 1%

The data are presented as :

- the coefficient of friction (μ) as a function of time; this gives the lifetime of the lubricant, in revolutions up to a friction coefficient of 0.3,

- the wear rate of the contacting partners.

A summary of the tribology results is presented in Table 1. The friction coefficients are relatively high, especially in dry air. The different TiO_{2-x} types have different wear resistances : Lots 1 and 3 have a high wear rate in dry air, while Lot 2 does not wear in dry air, because materiel transfer from the ball to the disc occurs. In all cases transfer from the ball to the disc occurs in humid air; this produces a "lubrication" by the oxidation of the steel transfered on the disc.

TABLE 1 : Friction and wear data obtained on samples from Lots 1, 2 and 3 in both humid and dry-air environments at room temperature.

RH %	Lot #	Frict. start	Coeff. (μ) average	Revs μ <0.3	Disc wear rate 10^{-15} m^2/N	Ball wear rate 10^{-15} m^2/N
99	1	0.17	0.50	1600	dep.*	7.2
99	2	0.16	0.46	1400	dep.*	5.3
99	3	0.17	0.47	1300	dep.*	6.1
<1	1	0.31	0.80	3	2270	26
<1	2	0.32	1.05	13	dep.*	62
<1	3	0.39	0.90	14	284	33

* dep. = material transfer from the ball to the disc's surface.

3.4 Adhesion control by Scratch-testing

A CSEM Automatic-Scratch tester with a 200 µm radius diamond indenter (type Rockwell C) was used. The following scratching conditions were applied :

- loading rate : dL/dt = 100 N/min

- sliding speed: dx/dt = 10 mm/min

The coating adhesion is evaluated by the critical load (L_c), which is the lowest load at which the coating is damaged by either adhesive or cohesive failure.

The following values for the critical load "L_c" were obtained :

Lot 1 : $L_c \leq 6$ N

Lot 2 : Lc ~ 20-22 N

Lot 3 : $L_c \leq 6$ N

The adhesion data, by the scratch test, are in agreement with the metallographical observation, i.e. a poor adhesion of the TiO_{2-x} layer for Lots 1 and 3, and a better adhesion for Lot 2.

3.5 Conclusions

The characterization (adhesion, tribology, metallography, XRD crystal structure) shows that a rutile layer has a different mechanical behaviour as compared to a anatase layer; the rutile layer has a poorer adhesion and a larger wear rate in dry air.

Because of wrong sample preparation, as mentioned under 3, the characterization of these TiO_{2-x} layers (Lots 1, 2 and 3) were stopped at this point.

4. SECOND SERIES OF SAMPLES : LOTS 4, 5 AND 6

4.1 Specimen preparation

Twenty AISI 440C steel discs were "one-side" mechanically polished on paper with diamond paste. These discs were then coated with a 5 µm thick CVD-TiC layer. After repolishing, the average surface roughness of the TiC layer is 0.16 µm cla.

4.2 Coating of samples with TiO_{2-x} layers

TiO_{2-x} layers were deposited on the CVD-TiC coated steel substrates by three different techniques, presented in Figure 4, and detailed below.

The 3 different techniques are as follows :

- a H_2O vapor oxidation of TiC to TiO_{2-x} at 850°C during 30 minutes (Lot 4)
- CVD-TiO_{2-x} (Lot 5)
- a IPO (isopropanol) oxidation of the CVD-TiO_{2-x} coating, at 800° C during one hour (Lot 6).

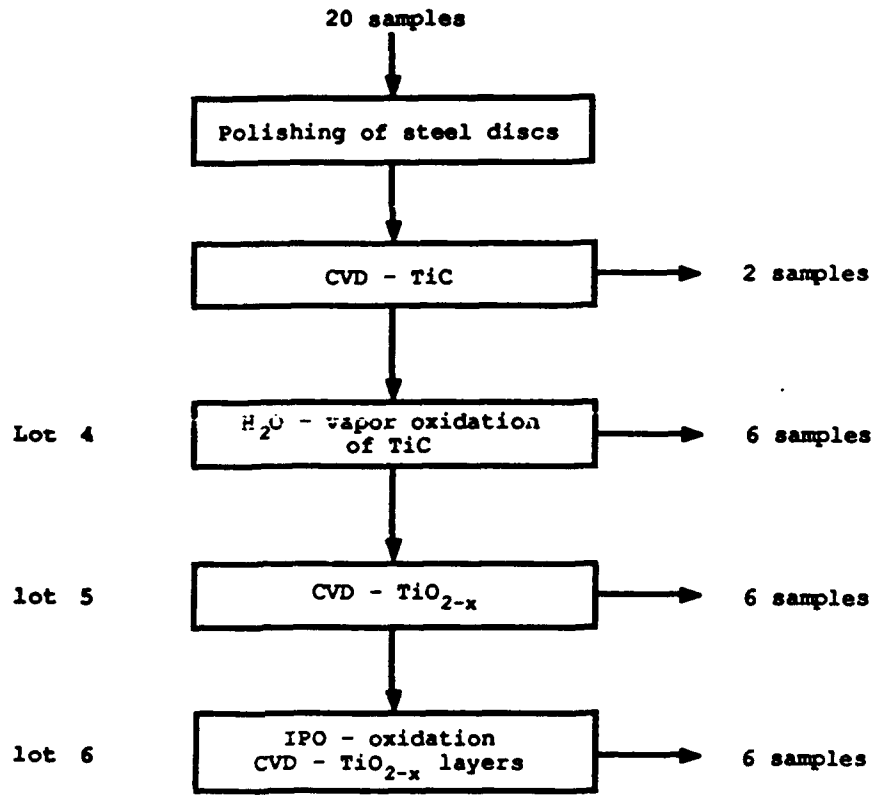

Fig. 4 : Schematic view of the production of TiO_{2-x} layers, and the number of samples used for each technique.

4.3 Physical characterizations

4.3.1 Crystal structure (XRD)

The X-ray diffraction patterns of the three sample types presented peaks of TiO, rutile. There vere, however, important differences between them:

- the relative intensities of the peaks are different,
- the angular positions and the reticular distances vary little, slow recording of the important peaks gave more precise information.

Lot 4 :

Many peaks of lov intensity could not be identified, others could be attributed to the steel substrate (very veak Ti_2O_3 peaks). A strong preferential orientation of (002) type vas observed.

Lot 5 :

The rutile peaks here all of lower intensity than for Lot 4. The two most intense peaks are not of rutile; they correspond to anatase and are of average intensity in an isotropic sample (data JCPDS). A few other peaks of anatase are present with lower intensity; other weak peaks correspond to the steel substrate. The samples of Lot 5 consist of a mixture of rutile and anatase :

- rutile has a (002)-type texture,
- anatase has a (220)-type texture.

Lot 6 :

The diffraction patterns for these samples are more defined than the previous ones. They show essentialy rutile peaks, and some very lov intensitiy peaks and which can be attributed to the steel substrate. The texture is a mixture of the (002)- and (110)- types.

4.3.2 Internal stresses

Difficulties were encountered for the internal stress measurements due to the low intensities of the peaks at high diffraction angles. Figures 5 a), b) and c) show, for respectively lot 4, 5 and 6 the lattice parameter "a" versus $\sin^2\phi$. The stresses which were deduced, are :

Lot 4 : σ = - 916 MPa (compression)

Lot 5 : σ = + 1786 MPa (traction)

Lot 6 : σ = - 2889 MPa (compression)

The internal stress values obtained with Lot 5 are questionable due to the discontinuity of the lattice parameter plot in Figure 5b); nearby anatase peaks might disturb the measurement.

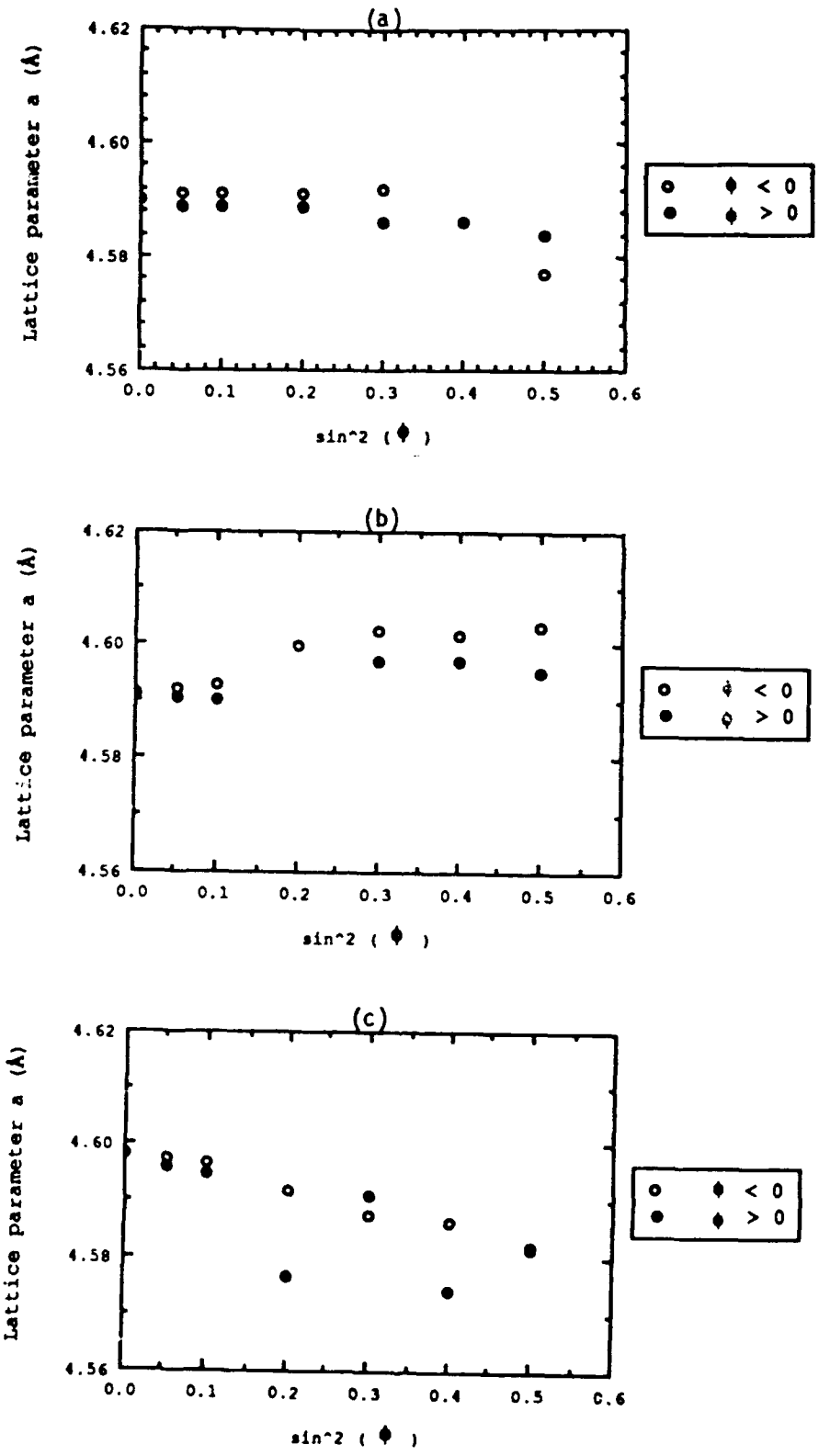

Fig. 5 : Presentation of the lattice parameter as a function of $\sin^2\phi$ for (a) Lot 4, (b) Lot 5 and (c) Lot 6.

4.4 Chemical characterization

Figures 6 and 7 show the O, Ti, C and Fe concentration profiles for respectively the original CVD-TiC coated substrate and Lots 4, 5 and 6, a first diagram shows the O, Ti, C and Fe profiles; a second one, gives the O and C profiles again, but on another scale. For all the analysed samples, the added concentrations are lower than 100% in both the substrate and the coating :

- in the substrate, the Cr content (17 %) could explain this difference.

- on the contrary, in the TiO_{2-x} layers or in the TiC substrate is lover than in the Cr-content the steel substrate, as shows fig. 8. Even if, we include the chromium content for the layers, in the concentration profil, the total content does not reach 100%.

The quantitative analysis data can be used to express the atomic O/Ti ratio; for the stoechiometric composition the ratio is 2.

Lot 4: O/Ti $\simeq$ 2

According to the TiO_2-Ti phase diagram, there should be TiO_2-rutile (water-vapor deposition at 850°C). The x-ray diffraction analysis shows rutile and very weak Ti_2O_3 peaks. It is not understood why; the presence of C must be at least one reason.

Lot 5: O/Ti $\simeq$ 1,8

According to the TiO_2-Ti diagram, there should be mainly TiO_2-anatase (CVD-TiO_{2-x} at 380°C). The x-ray diffraction shows TiO_{2-x} (mainly rutile, little anatase and traces of Ti_2O_3). Again, it is believed that C in the coating influences its microstructure.

Lot 6: O/Ti $\simeq$ 1.8

According to the TiO_2-Ti diagram, these should be TiO_2-rutile and anatase (TiO_{2-x} oxidation at 800°C). The X-ray diffraction shows TiO_{2-x} only rutile.

(a)

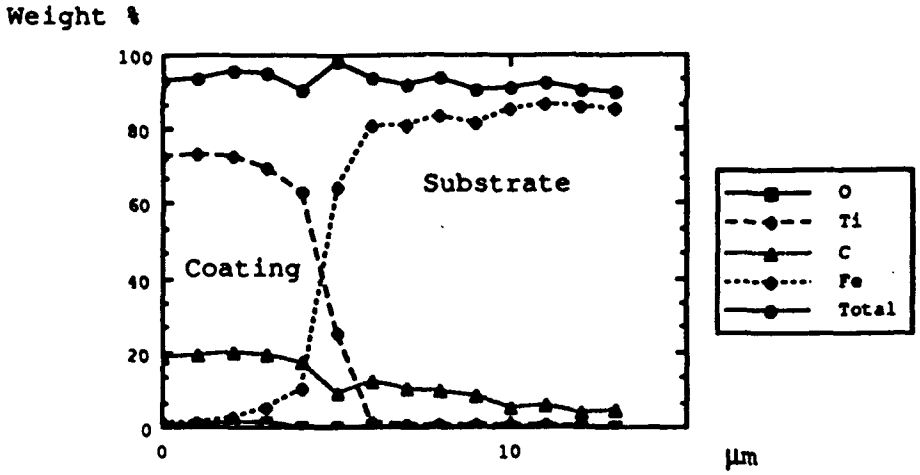

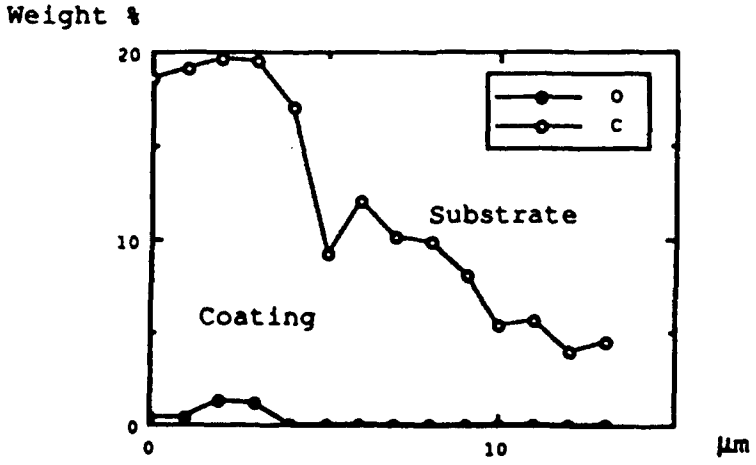

Fig. 6 : The O, Ti, Fe and C concentration profiles, through the interface for (a) the original CVD-TiC coated sample, Lot 4.

(b)

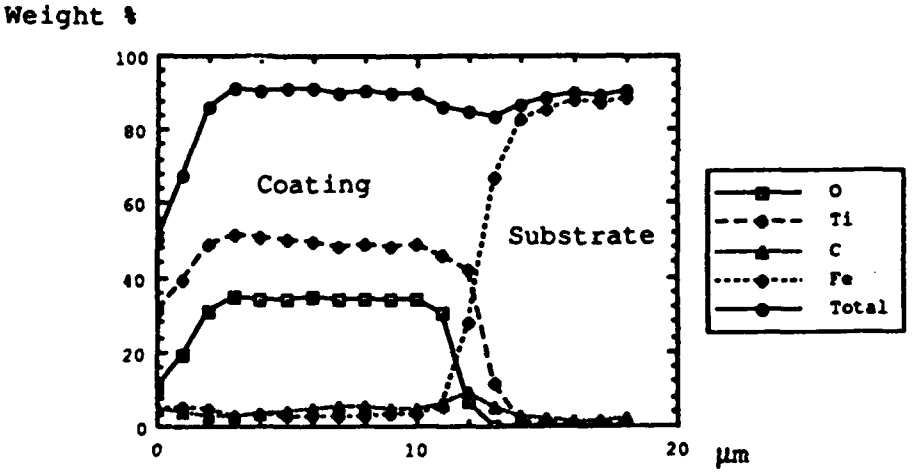

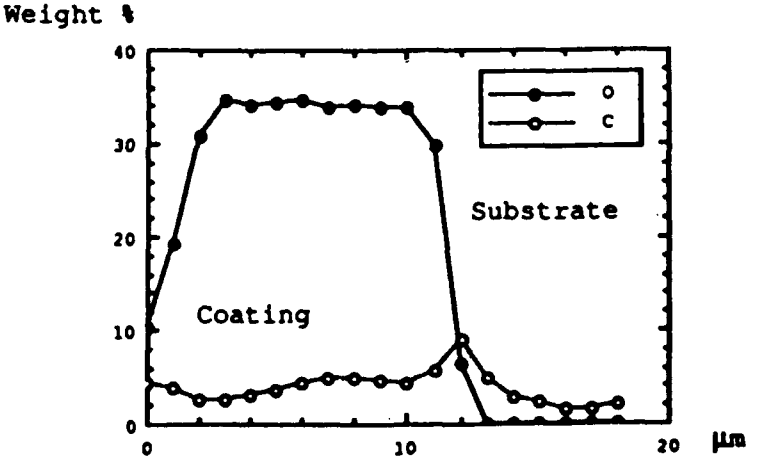

Fig. 6 : The O, Ti, Fe and C concentration profiles, through the interface for (b) the original CVD-TiC coated sample, Lot 4.

(a)

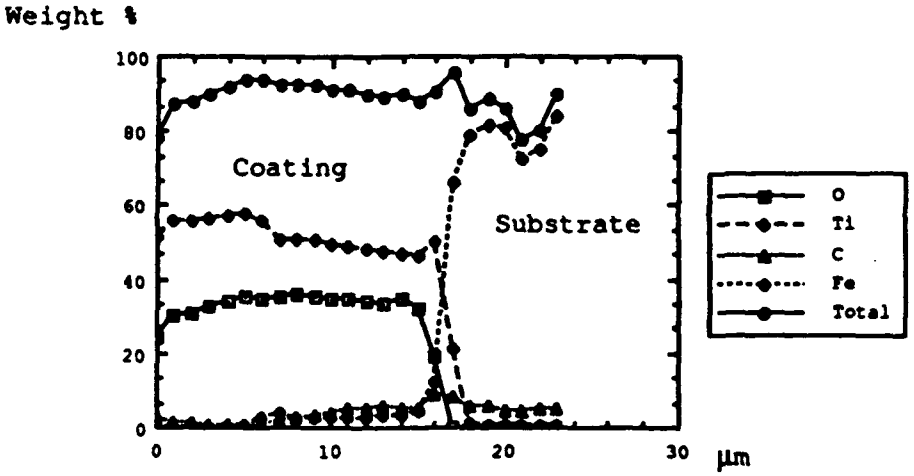

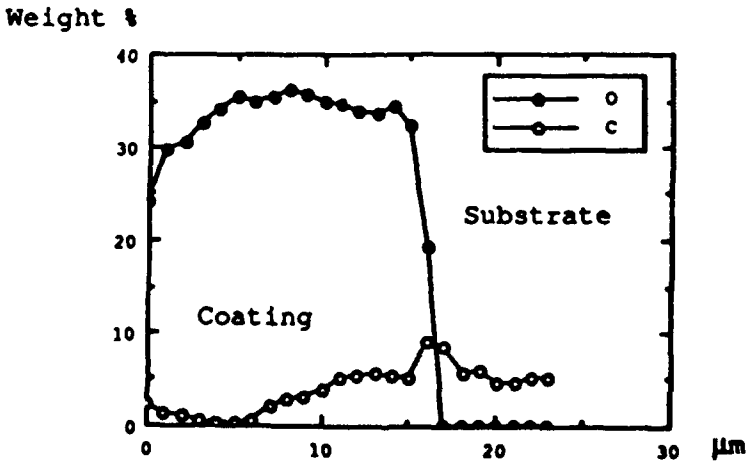

Fig. 7 : The O, Ti, Fe and C concentration profiles, through the interface for (a) Lot 5.

(b)

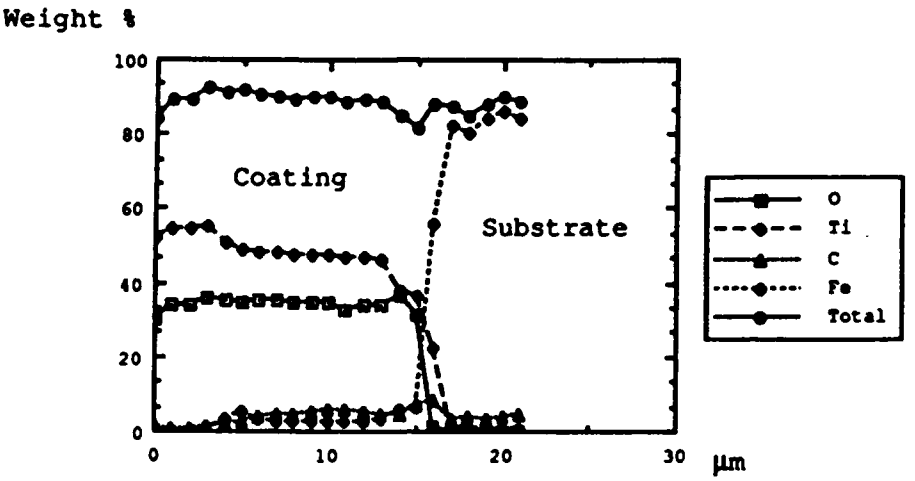

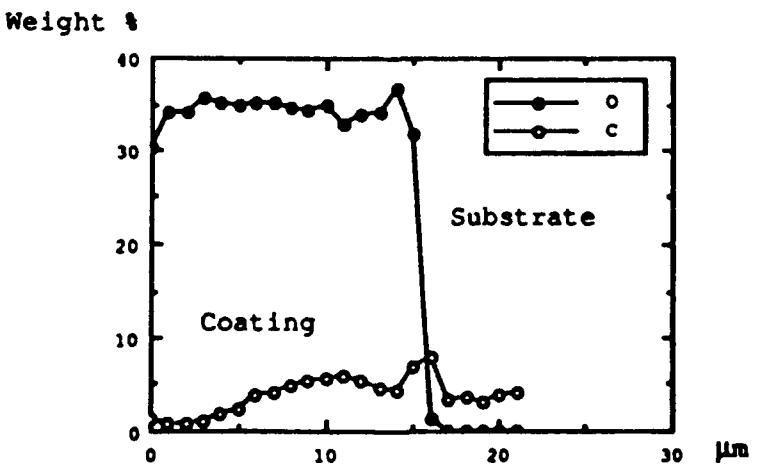

Fig. 7 : The O, Ti, Fe and C concentration profiles, through the interface for (b) Lot 6.

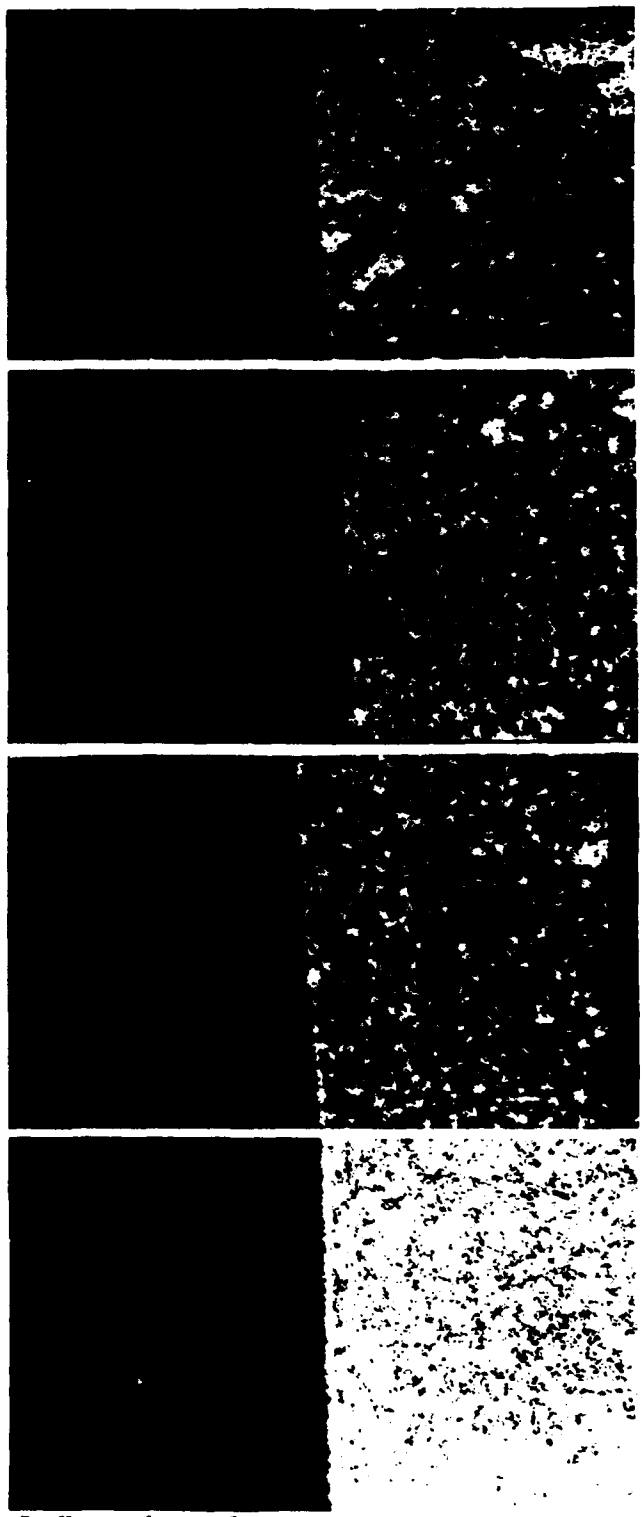

B 27907
(a)
800 x

B 27908
(b)
800 x

B 27909
(c)
800 x

B 27906
(d)
800 x

Fig. 8 : Cr-X-ray image for sections through respectively (a) the original CVD-TiC coated sample, (b) Lot 4, (c) Lot 5 and (d) Lot 6.

4.5 Tribometry with the CSEM pin-on-disc TRIBOMETER

The test conditions are as follows :

pin : 6 mm diam. AISI 52100 steel GRADE 3 ball (non rotating)
load : 5 N
sliding speed : 0.1 m/s
relative humidity : 99% or less than 1%

The data are presented as :

- the friction coefficient (μ)as a function of time; this gives the lifetime of the lubricant, in revolutions up to a friction coefficient of 0.3.

- the wear rate of the contacting partners.

Two friction tests were performed on each sample under one set of conditions.

The obtained data are summarized in Table 2 and compared in Figures 9a) and 9b). These results show that :
- the friction coefficients are relatively high, especially in dry air (up to 0.5)
- the number of revolutions until μ reaches 0.3 is rather small (typically < 700)
- in humid air, oxidized ball-wear debris "lubricates" the contact without adhesive wear; therefore the total wear rate is very similar from one coating to another : ~ 6.1 * 10^{-15} m^2/N (see fig. 9a)
- in dry air, the TiO_{2-x} top layer for Lots 5 and 6, show a lower wear rate than the oxidized TiC alone (Lot 4) (see fig. 9b)

TABLE 2 : Friction and wear data obtained on samples from lots 4, 5 and 6 in both humid and dry air environments at room temperature (average of two tests)

RH %	Lot	Frict. start	Coeff. (μ) average	Revs μ <0.3	Disc wear rate 10^{-15} m^2/N	Ball wear rate 10^{-15} m^2/N
99	4	0.35	0.42	250	dep.*	6.4
99	5	0.27	0.45	490	dep.*	6.1
99	6	0.27	0.43	700	dep.*	6.1
<1	4	0.27	0.50	18	162	63
<1	5	0.23	0.52	40	dep.*	60
<1	6	0.25	0.52	166	dep.*	55

*dep. = material transfer from the ball to the disc.

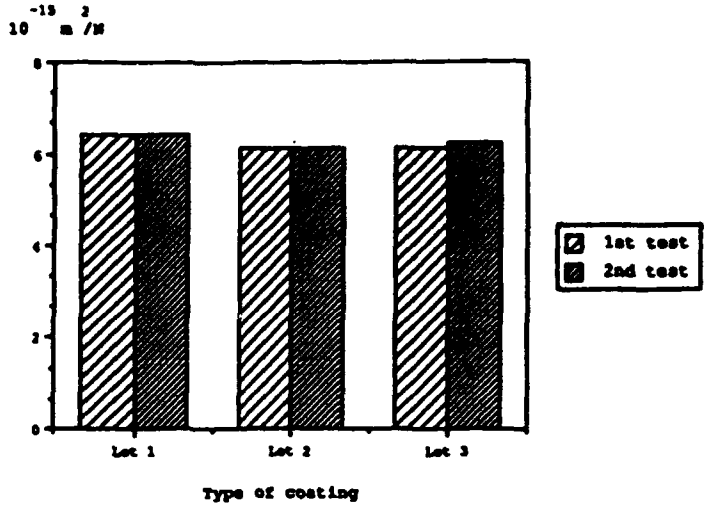

a)

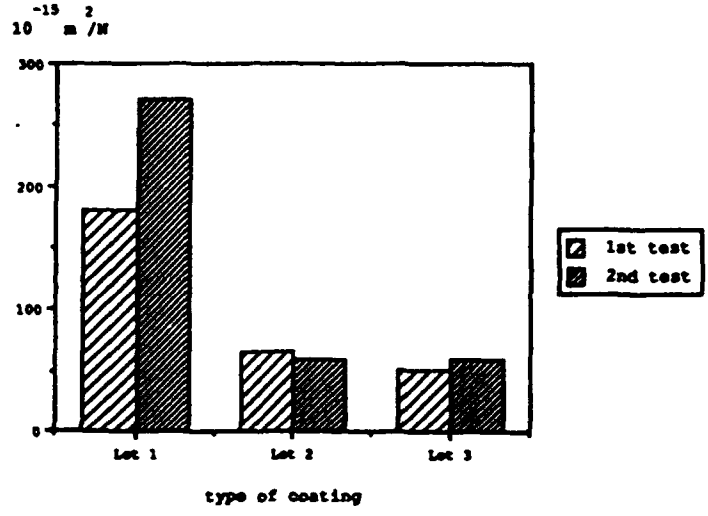

b)

Fig. 9 : Total wear rate in (a) humid and (b) dry air for pin-on-disc tests with a AISI 52100 steel ball on the 3 different TiO_{2-x} coating types.

4.6 Metallographic examination

The metallographical sections through the coated samples provide information on the coating thicknesses and general aspects.

- CVD-TiC coated AISI 440C discs :
  - coating thickness : 5 µm
  - adhesion : apparently good
  - figure 10a : micrographs
- Lot 4 :
  - during the H_2O-vapor oxidation the coating-volume increased
  - coating thickness : oxidized CVD-TiC 10-11 µm
  - dense and apparently well adherent coating
  - figure 10b : micrographs

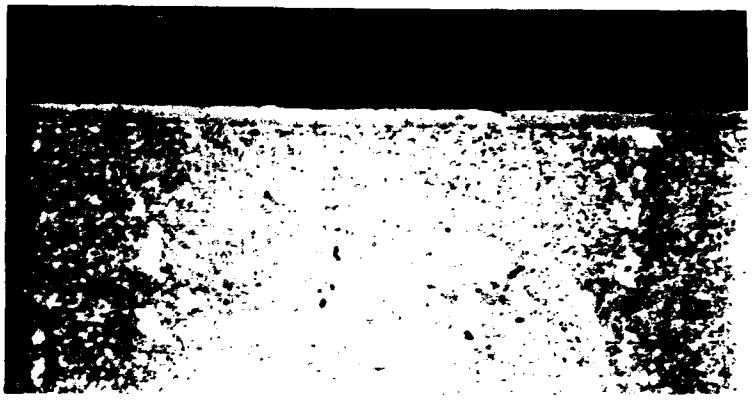

26690 (a) 500 x

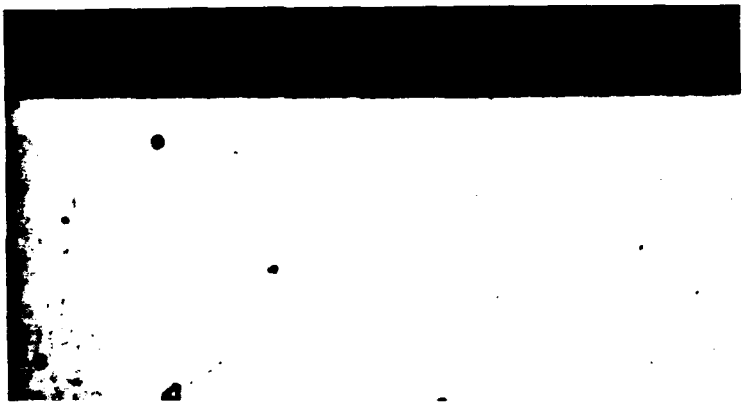

26715 (b) 500 x

Fig. 10 : Metallographic views of respectively
(a) a CVD-TiC coated AISI 440C steel disc and
(b) after H_2O-vapor oxidation (Lot 4)

- Lot 5 :
  - coating thickness : - oxidized CVD-TiC ~ 10 µm
    - CVD-TiO_{2-x} ~ 5 µm
  - dense and apparently well adherent coating
  - appears more compact than layer of Lot 4
  - figure 11a : micrographs

- Lot 6 :
  - coating thickness : - oxidized TiC ~ 10 µm
    - CVD-TiO_2 ~ 5 µm
  - coating has same general aspect as that of Lot 5
  - regularly there are cracks perpendicular to the surface through the coatings
  - figure 11b : micrographs

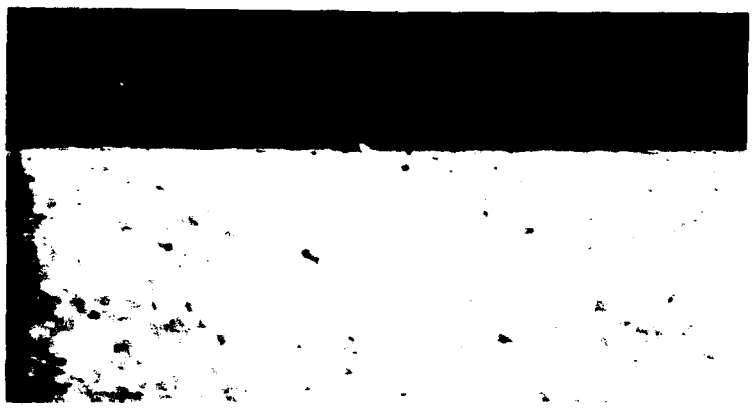

26697 (a) 500 x

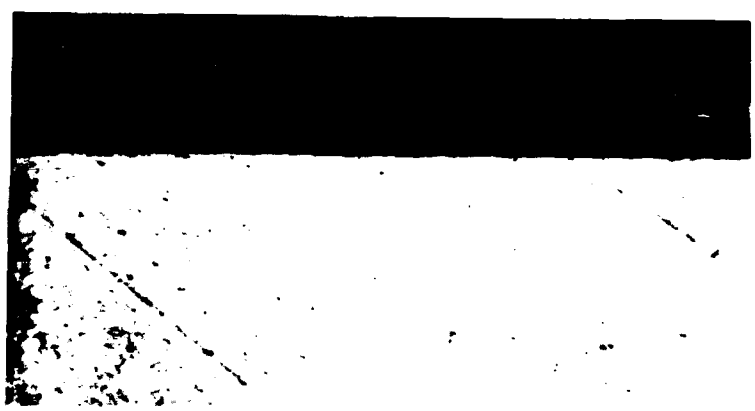

26698 (b) 500 x

Fig. 11 : Metallographic views of respectively
(a) a CVD-TiO_{2-x} sample (Lot 5) and
(b) an IPO-oxidized CVD-TiO_{2-x} sample (Lot 6)

4.7 Adhesion Control by scratch testing

A CSEM Automatic Scratch Tester with a 200 µm radius diamond indenter (type Rockwell C) was used. The following scratching conditions were applied :
- loading rate dL/dt = 100 N/min
- sliding speed dx/dt = 10 mm/min

The coating adhesion is evaluated by its critical load (L_c), which is the lowest load at which the coating is damaged by either adhesive or cohesive failure.

The critical-load data are given in Table 3.

Additional adhesion information can be obtained by electron- and optical microscopy and by X-ray imaging of damaged areas. Figures 12, 13, 14 and 15 show electron micrograph and X-ray image of damaged zones at the critical load, for respectively the CVD-TiC coated AISI 440C sample, and samples of Lots 4, 5 and 6.

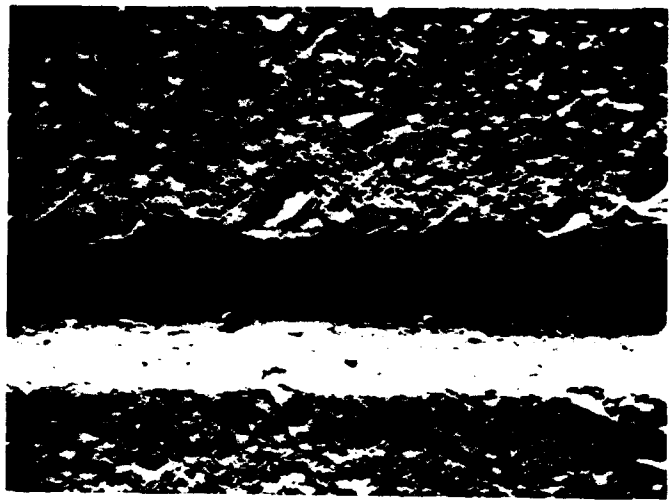

B 27830 (a) SEM 200 x

B 27831 (b) X-ray Image "Fe" 200 x

Fig. 12 : SEM and X-ray (Fe) images of scratch-tested CVD-TiC coated AISI 440C steel disc; the SEM view shows the coating damage at L_c and the Fe X-ray image shows the underlying substrate.

TABLE 3 : Critical loads "L_c" obtained on the CVD-TiC coated discs and on samples of Lots 4, 5 and 6.

	Lc [N]		
Sample type	test 1	test 2	test 3
CVD-TiC	17	16	17
Lot 4	15	18	16
Lot 5	8	10	10
Lot 6	16	16	15

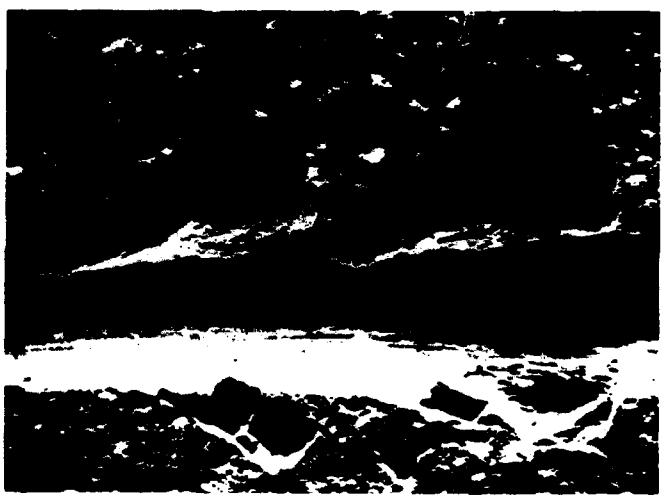

B 27828 SEM 200 x

Fig. 13 : SEM image of scratch-tested oxidized CVD-TiC sample (Lot 4); the SEM view shows the coating damage at L_c.

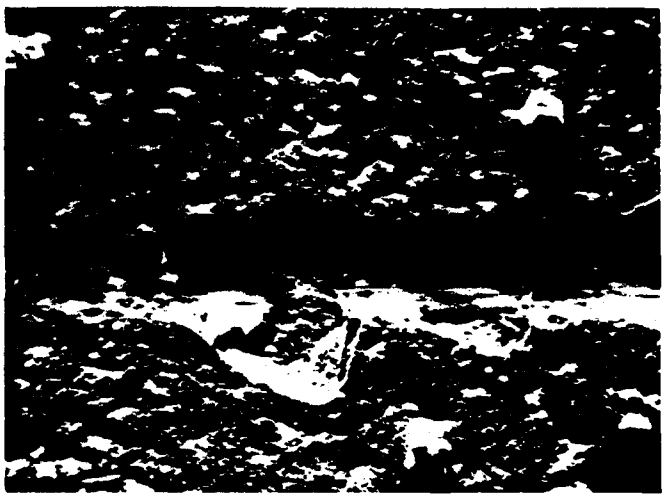

B 27824 (a) SEM 200 x

B 27825 (b) X-ray Image "Fe" 200 x

Fig. 14 : SEM and X-ray image (Fe) of Scratch-tested CVD-TiO_{2-x} sample (Lot 5); the SEM view shows the coating damage at L_c and the Fe X-ray image shows the underlying substrate.

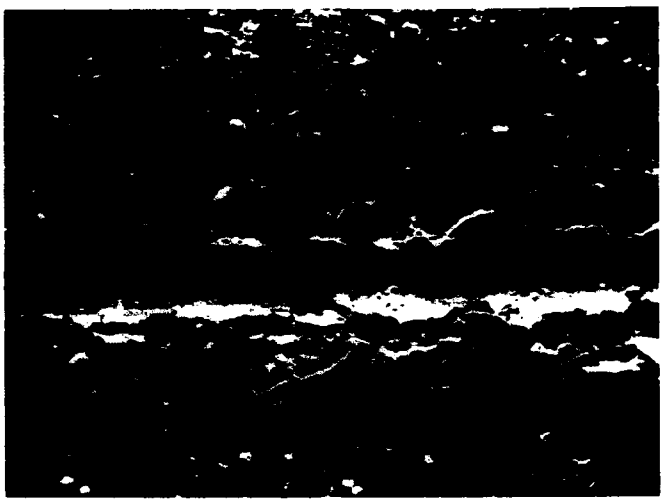

B 27821 (a) SEM 200 x

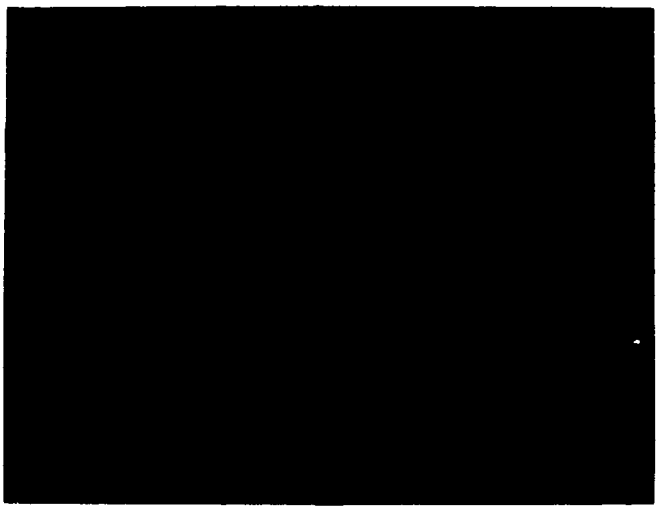

B 27820 (b) X-ray Image "Fe" 200 x

Fig. 15 : SEM and X-ray (Fe) image of scratch-tested oxidized CVD-TiO_{2-x} sample (Lot 6); the SEM view shows the coating damage at L_c and the Fe X-ray image shows the underlying steel substrate.

Lot 5

The of adhesion data and the different illustrations previously mentioned confirm the poor adhesion of the CVD-TiO_{2-x} coating (Lot 5) which leads to "flaking" (adhesive failure). In the other cases (Lots 4 and 6) mixed adhesive-cohesive failures are observed.

4.8 Microhardness

4.8.1 Substrate

The AISI 440C steel substrate of all tested samples had a Vickers hardness of 2300 MPa (under 1 kg).

4.8.2 Coatings and interfaces (cross section)

The CSEM Ultra microhardness tester was used to produce "force-penetration depth", graphs with a maximum load of 1 g (Vickers diamond). Figures 16 a, b and c present graphically the "under-load" hardnesses of the TiO_{2-x} coatings against distance across the interface region.

For comparison purposes the coating-interface was chosen at 10 µm on all graphs of figure 16.

On each of the three graphs shown in figure 16, there is a peak value (between 12'000 and 16'000 MPa) in the "under-load" hardness at approxim. 10 µm. This value is believed to correspond to the Cr-carbide layer which is present at the CVD-TiC layer and the substrate. This Cr-carbide layer comes from the TiC-CVD process in which a "flash" of Cr is deposited before TiC. The Cr transforms into carbide with carbon from the substrate and this carbide contributes favorably to the coating adhesion and toughness.

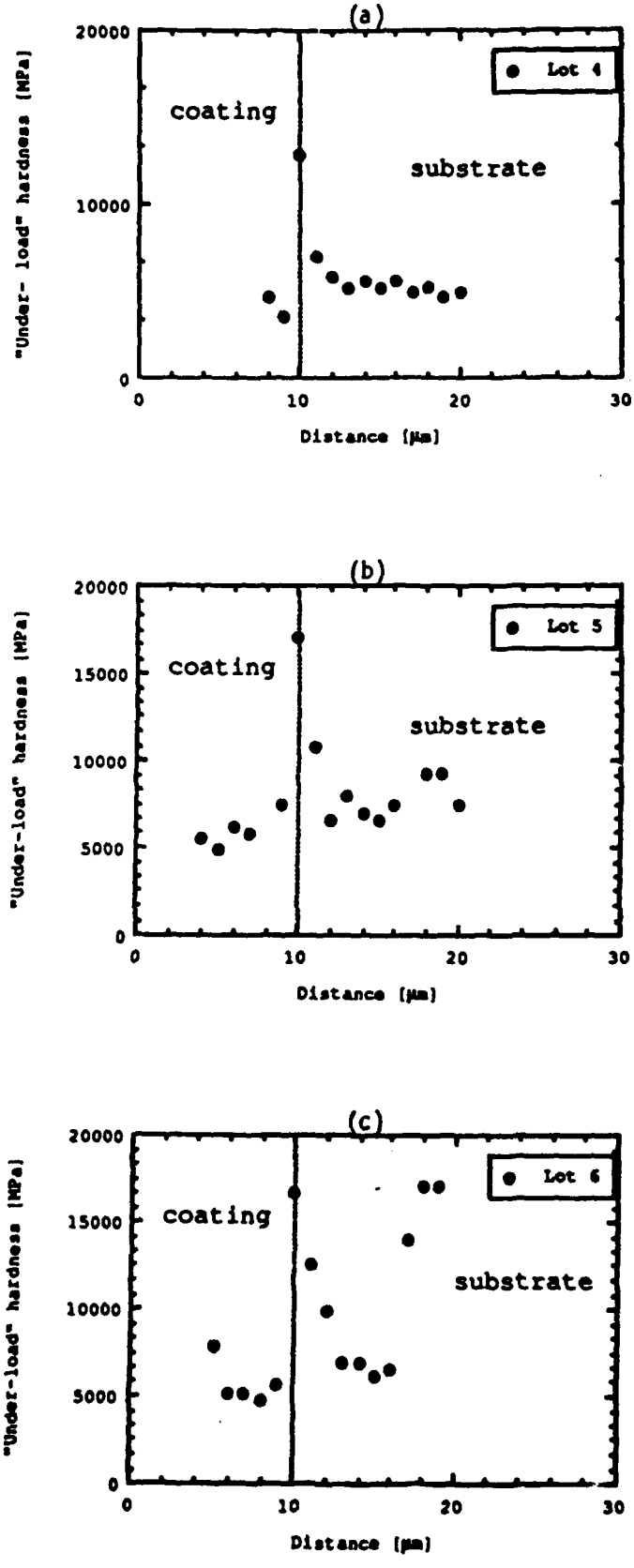

Fig. 16 : "Under-load" hardness profiles under a maximal load of 1 g through the interface for (a) Lot 4, (b) Lot 5 and (c) Lot 6

Z-27

Lot 4 :

The "under-load" hardness seems to be homogeneous throughout the approx. 10 µm of the coating (see figure 16 a).

Lot 5 :

The average "under-load" hardness is slightly higher here than that of sample from Lot 4. The data are also less homogeneous (see figure 16 b).

Lot 6 :

The "under-load" hardness of the top coating-layer (oxidized CVD TiO_{2-x}), is definitely higher than the underlying TiO_{2-x} coating (see figure 16 c).

The "under-load" hardness data of the three TiO_{2-x} coating types are summarized in Table 4.

TABLE 4 : Summary of the average "under-load" hardness values (under a maximum load of 1 g) for the three different TiO_{2-x} coating types.

Lot number	"Under-load" hardness [MPa]		
	oxidized CVD-TiC	CVD-TiO2-x	oxidized CVD-TiO2-x
Lot 4	5170	--	--
Lot 5	6985	9250	--
Lot 6	6860	--	17020

A SEM-micrograph of the sample used to produce the "under-load" hardness diagram against distance given in figure 16 c, is shown in figure 17. The indentations are clearly visible in the steel substrate but become difficult to distinguish in the Cr-carbide region and in the TiO_{2-x} top layers.

B 27911-12 2500 x

Fig. 17 : SEM view of "under-load" hardness indentations (Vickers diamond under 1g) on the sample of Lot 6 (corresponding to graph of Figure 16 c)

4.8.3 Coatings (surface)

Microhardness measurements were made, using both a conventional Leitz microhardness tester and the CSEM Ultramicrohardness tester. Vickers diamonds were used for both types of hardness determinations. For the "Leitz" hardness tester, the indentations were made on the coated surface; and for the "CSEM" one, they were performed on a perpendicular section to the surface on the TiO_{2-x} top coating (see figure 18).

The data obtained on the three TiO_{2-x} coating types are presented in Table 5.

with the "LEITZ" Hardness tester	with the "CSEM" Ultramicrohardness tester

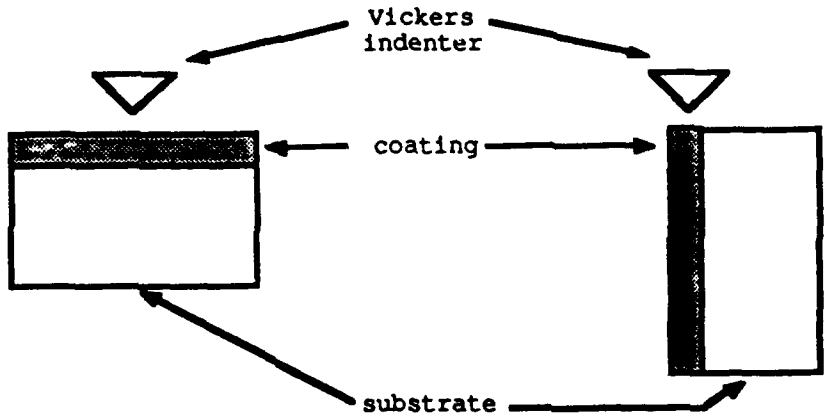

Fig. 18 : Schematic view of how the microhardness indentations were were made.

TABLE 5 : Vickers microhardness data obtained with the "Leitz" microhardness tester and the "CSEM" ultrahardness tester, on the three different TiO_{2-x} coating types.

Lot #	"Leitz" microhardness [MPa] under 10 g	"CSEM" microhardness [MPa] under 1 g
4	4000	6300
5	4200	7900
6	6050	20150

The conventional "Leitz" microhardness values are certainly influenced by the "soft" steel substrate. The data are in between the hardness values of the substrate (HV = 2300 MPa) and of the coatings (~ HV > 6000 MPa)

The "CSEM" ultramicrohardness values are in agreement with the values given in Table 4. The influence of the "soft" substrate is no longer felt.

5. CONCLUSION

The following table gives a summmary of the physical, chemical and mechanical characterizations of the 3 TiO_{2-x} layer types (Lots 4 to 6).

	Crystal structure	σ [MPa]	Lc [N]	HV [MPa]
Lot 4	rutile (002) ±	-916	16	6300
Lot 5	rutile (002) - anatase(220) +	+1786	9	7900
Lot 6	rutile + (002)+(110)	-2889	16	20150

The sign in the crysal structure column indicates the relative intensity of the rutile or anatase peak.

The tribological properties of the tested coatings are such that, at least at room temperature, these coatings cannot be qualified as "self lubricating", especially in dry-air environment. However, the TiO_{2-x} layers do increase the wear-resistance of the coated components.

CENTRE SUISSE D'ELECTRONIQUE ET DE MICROTECHNIQUE S.A.
– Recherche et Développement –

CSEM MALADIERE 71 CH-2007 NEUCHATEL (SWITZERLAND)
TEL. 038/24 01 61 TELEX 952 664 (CSEM) TELEFAX 038/25 40 78

CSEM TECHNICAL REPORT N° 307

TITLE : Generation of TiO_2 - Rutile Coatings and their Tribological characterisation

by H. Boving

PROJECT : H.A.C. P.O. No 89-318804-SAC
CSEM No 51.207

DATE : 21st November 1989 **Class : A**

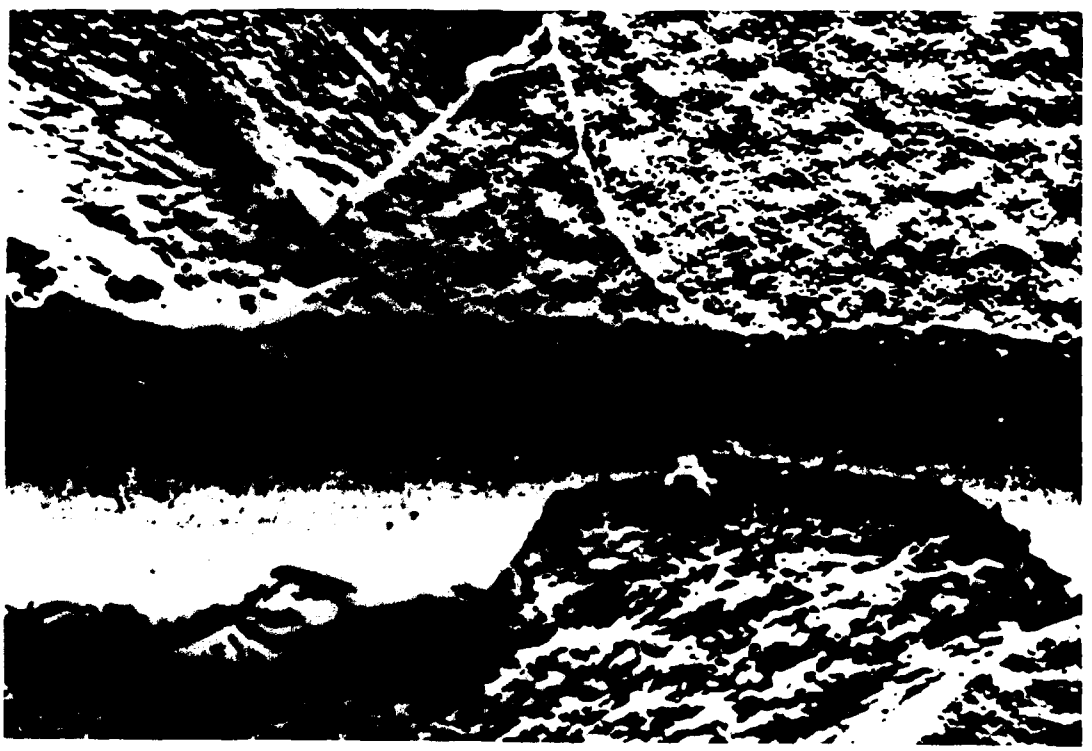

CENTRE SUISSE D'ELECTRONIQUE ET DE MICROTECHNIQUE S.A.
– Recherche et Développement –

CSEM MALADIERE 71 CH-2007 NEUCHATEL (SWITZERLAND)
TEL. 038/24 01 61 TELEX 952 664 (CSEM) TELEFAX 038/25 40 78

TECHNICAL REPORT CSEM NO 307

TITLE : Generation of TiO_2 - Rutile Coatings and their Tribological characterisation

by H. Boving

PROJECT : H.A.C. P.O. 59-318804-SAC
CSEM No 51.207

DATE : 21st November 1989 **CLASS** : A

ABSTRACT

Seven different types of TiO_2 coated samples were produced by oxidising, under different conditions, TiC-coated AISI 440C steel discs. The TiO_2 - rutile coatings were characterised for coating thickness, stoechiometry, adhesion and tribological properties. It was found that the friction and wear properties of the TiO_2 coatings against steel are very dependent on the surface roughness and that these coatings do not have self-lubricating properties. During the work covered in this study it was attempted to produce TiO_2 coatings with both stoechiometric, and O_2-deficient compositions; this attempt was only partially successful and no influence of the stoechiometry on the tribological properties could be observed.

Countersigned:

Materials and
Micromechanics
Division

H.E. Hintermann
(Head of division)

Composite Materials
and Tribology

H. Boving
(Project leader)

TABLE OF CONTENTS

	Page
1. INTRODUCTION	1
2. SAMPLE PREPARATION	1
3. TiC-OXIDATION TREATMENT	1
4. CHARACTERISATION	4
4.1 Visual aspect	4
4.2 Surface morphology	4
4.3 Coating thicknesses	4
4.4 X-Ray diffraction	9
4.5 Stoechiometry	9
4.6 Coating adhesion	12
4.7 Tribological properties	20
4.7.1 Tribological properties of As-coated TiO_2 surfaces	20
4.7.2 Tribological properties of polished TiO_2-coated discs	21
5. CONCLUSIONS	26
6. AKNOWLEDGMENTS	26
ANNEX	

1. INTRODUCTION

In the scope of the Hughes Aircraft Comp. (HAC) Purchase Order No S9-318804-SAC, CSEM is to generate in-situ TiO_{2-x} rutile layers on CVD-TiC-coated AISI 440C steel specimens by a technique established under a previous HAC Purchase Order No S9-507875-SRW. The rutile layers are formed under conditions with different oxidation potentials to produce partially reduced rutile coatings.
Seven different oxidation surface treatments have been performed. The obtained coatings were characterised for thickness, microstructure, stoechiometry, adhesion and tribological properties.

2. SAMPLE PREPARATION

- The AISI 440C steel samples were disk shaped : Ø 25 mm, h 5 mm. The surface was ground and polished prior to the TiC CVD coating (Ra = 0.09 µm).

- The CVD TiC treatment was performed in an equipment as shown in figure 1; the approximately 8 µm thick coating was obtained at 1000°C during a 4 to 5 hour treatment. Figure 2 shows a metallographic section of a TiC coated AISI 440C sample.

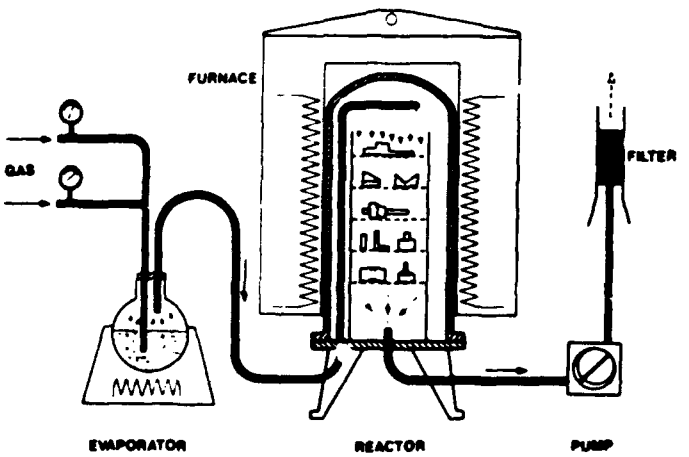

Figure 1 : Schematic of the CVD equipment used for the TiC coating of the AISI 440C steel samples

3. TiC-OXIDATION TREATMENT

Seven different oxidation treatments were used, to produce Ti-oxide coatings of different stoechiometries.
All 7 treatments were performed in the same equipment; the apparatus is presented schematically in figure 3. The different oxidation treatments were as follows :

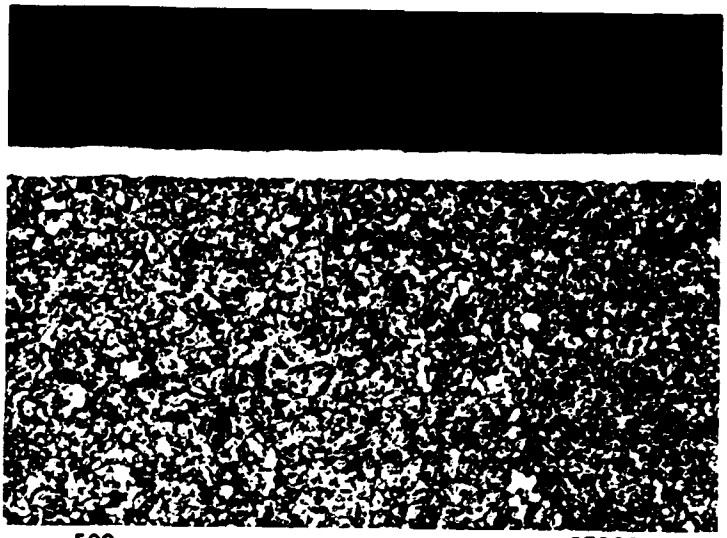

Figure 2 : Micrograph of TiC coated AISI 440C steel sample

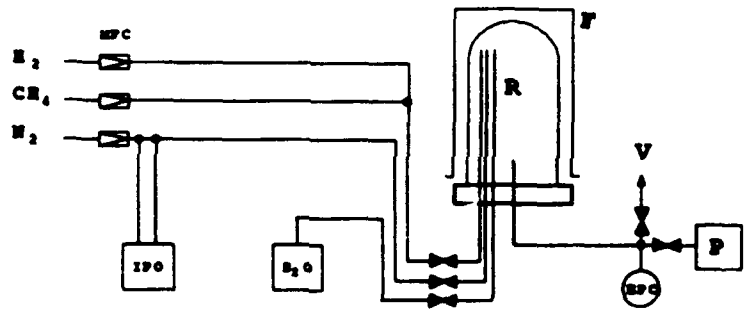

MFC	: Mass-Flow-Control	IPO	: Isopropanol
P	: Vacuumpump	H_2O	: Water-Vapor Generator
F	: Furnace		
EPC	: Electronic Pressure Control		
V	: Ventilation		
R	: Reactor		

Figure 3 : Schematic of TiC-oxidation equipment

T 101 :	atmoshpere	:	H_2O-Vapor
	concentration	:	100 %
	temperature	:	800°C
	pressure	:	normal
	duration	:	30'

T 102	atmoshpere	:	H_2O-Vapor
	concentration	:	100 %
	temperature	:	800°C
	pressure	:	normal
	duration	:	60'
T 103	atmoshpere	:	IPO (IPO = ISOPROPANOL)
	carrier gas for IPO	:	N_2 (8% IPO)
	temperature	:	800°C
	pressure	:	50 Torr
	duration	:	60'
T 104	atmoshpere	:	IPO + H_2
	carrier gas for IPO	:	N_2 (8% IPO)
	concentration H_2	:	33%
	temperature	:	800°C
	pressure	:	50 Torr
	duration	:	60'
T 105	atmoshpere	:	IPO + H_2 + CH_4
	carrier gas for IPO	:	N_2 (8% IPO)
	concentration H_2+CH_4	:	33%
	Ratio H_2/CH_4	:	100/1
	temperature	:	800°C
	pressure	:	50 Torr
	duration	:	60'
T 106	atmoshpere	:	IPO + H_2 + CH_4
	carrier gas for IPO	:	N_2 (8% IPO)
	concentration H_2+CH_4	:	33%
	Ratio H_2/CH_4	:	10/1
	temperature	:	800°C
	pressure	:	50 Torr
	duration	:	60'
T 107	atmoshpere	:	H_2O-Vapor + H_2
	concentration H_2	:	10%
	temperature	:	800°C
	pressure	:	normal
	duration	:	60'

4. CHARACTERISATION

4.1 Visual aspect

- TiC coating : grey-brown
- T 101 : grey
- T 102 : grey
- T 103 : grey, slightly blueish
- T 104 : grey, slightly blueish
- T 105 : grey, slightly blueish
- T 106 : grey, slightly blueish
- T 107 : grey

4.2 Surface morphology

SEM views of the surface of the oxidised samples are shown in figures 5-12; the initial TiC coating surface, before oxidation is shown in figure 4. These micrographes indicate that the surface roughness is relatively elevated. Figure 12, in addition makes us believe that the coating porosity is high.

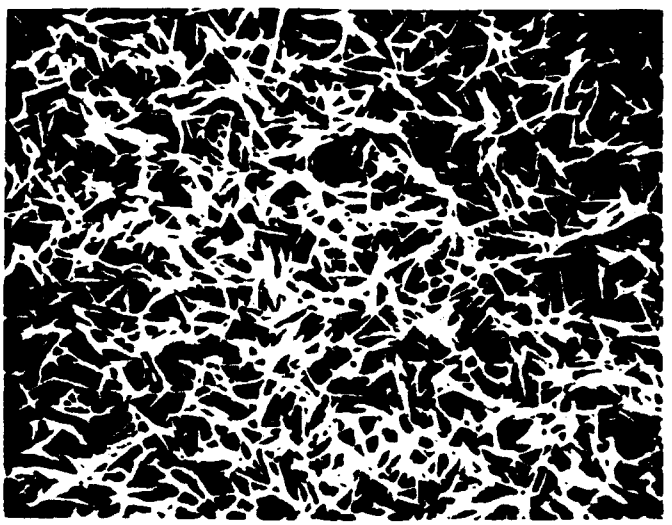

5000x B 30135

Figure 4 : SEM view of the surface of an unoxidised TiC coated sample

4.3 Coating thicknesses

Metallographical sections were made through oxidised samples; one for each type of oxidation treatment was mounted, ground, polished and examined by optical microscopy. The following coating thicknesses were measured :

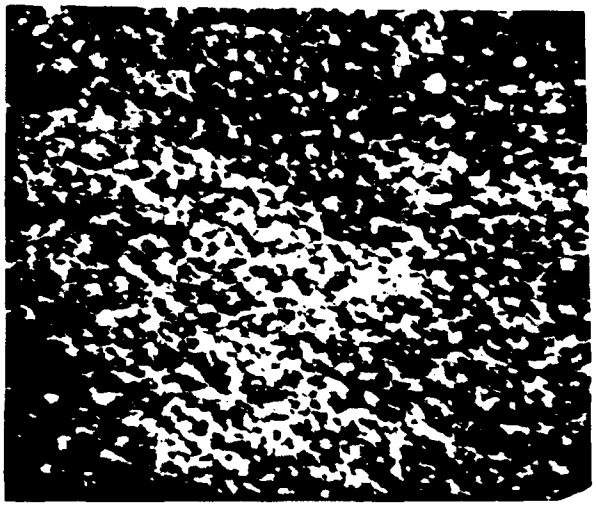

5000x B 30002

Figure 5 : SEM view of the T 101 sample surface

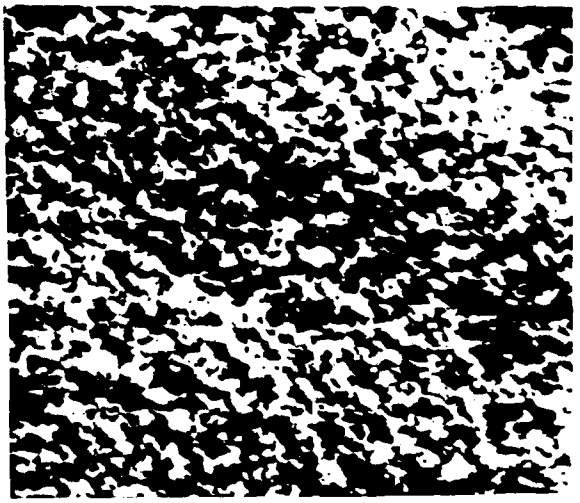

5000x B 30006

Figure 6 : SEM view of the T 102 sample surface

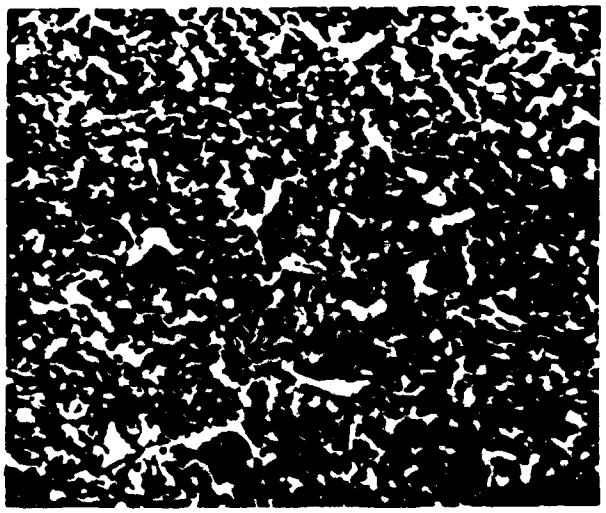

5000x B 30008

Figure 7 : SEM view of the T 103 sample surface

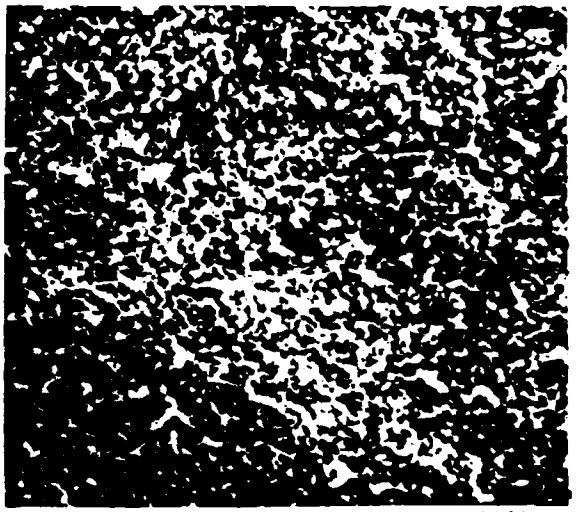

5000x B 30010

Figure 8 : SEM view of the T 104 sample surface

5000x B 30009

Figure 9 : SEM view of the T 105 sample surface

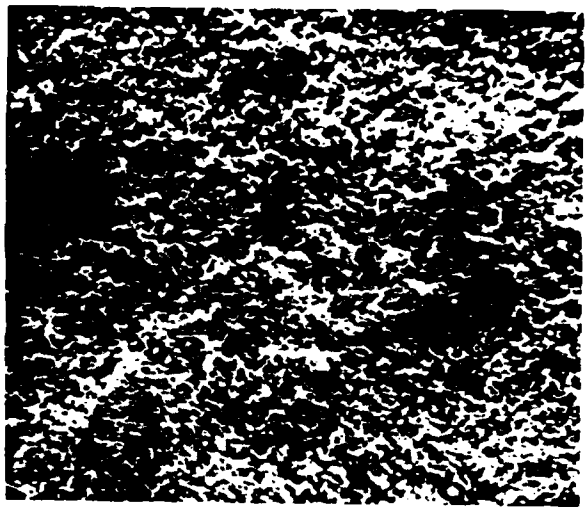

5000x B 30007

Figure 10 : SEM view of the T 106 sample surface

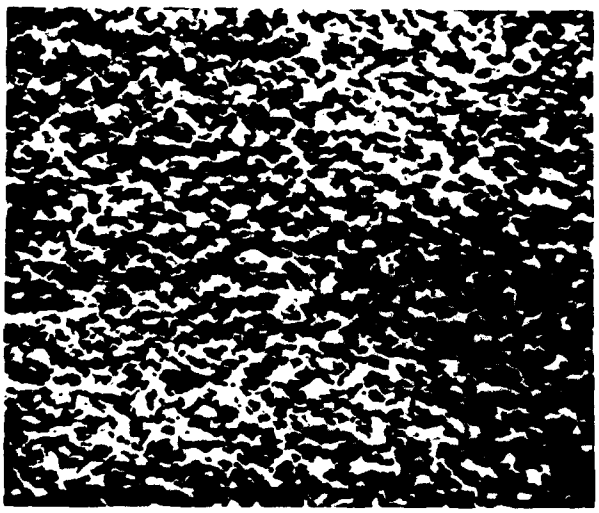

5000x B 30003

Figure 11 : SEM view of the T 107 sample surface

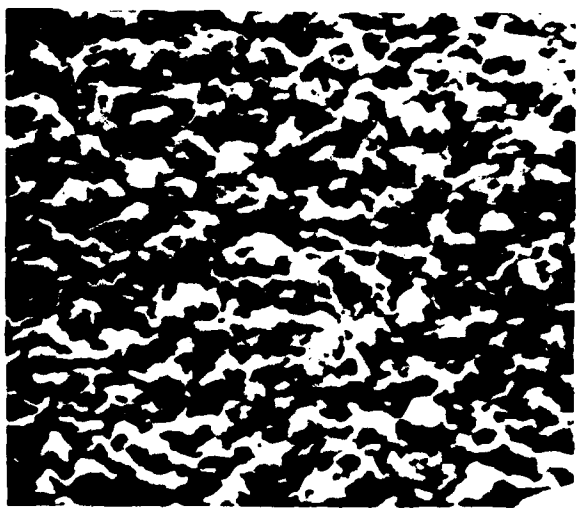

10000x B 30004

Figure 12 : idem as figure 11, but at 10000x

Treatment	Thickness (µm) TiC	Oxide	Figure
TiC	8	--	2
T 101	4	7	13
T 102	-	14	14
T 103	7	~ 1	--
T 104	7	~ 1	--
T 105	7	$\leq$ 1	--
T 106	7	$\leq$ 1	--
T 107	-	14	15

T 101 : only half of the TiC coating has been transformed in Ti-oxide. Approximately 4 µm TiC formed roughly 7 µm Ti-oxide. As the X-rays diffraction shows the Ti-oxide consists of RUTILE.
The specific densities of TiC and TiO_2-rutile are not very different (TiC = 4.93 g/cm³; TiO_2= 4 g/cm³); it can be deduced that the porosity of the TiO_2 layer is important (at least 20%).

T 102 : this treatment is in pinciple identical to T 101, except that the duration is 60' instead of 30'. The result is that practically the whole TiC coating is transformed into Ti-oxide. The volume of the TiO_2 is almost double of the TiC; this leads again to the reflection that the TiO_2 has an important porosity.

T 103/104/105/106 :

no micrographes were made of these samples since the sections did not allow to measure the thickness of Ti-oxide layer. This oxide layer is smaller than 1 µm and cannot be determined by optical microscopy. The metallographical sections have the same aspect as the one of fig. 2; e.g. the unoxidised TiC coating.

T 107 : the morphology of this coating is very similar to that of T 102; most of the TiC is transformed in TiO_2.

To obtain the coating thickness values with more precision, spherical cap erosions were made on the surface of 1 sample of each series, using the CSEM CALOTEST (see annexe 1). The folloving values were obtained :

Sample #	Coating thickness (µm) TiC	TiO_2
TiC	9.3	--
T 101	5.0	7.1
T 102	1.6	12.0
T 103	7.1	$\leq$ 1.0
T 104	9.0	$\leq$ 1.0
T 105	7.8	$\leq$ 1.0
T 106	7.9	$\leq$ 1.0
T 107	2.2	14.5

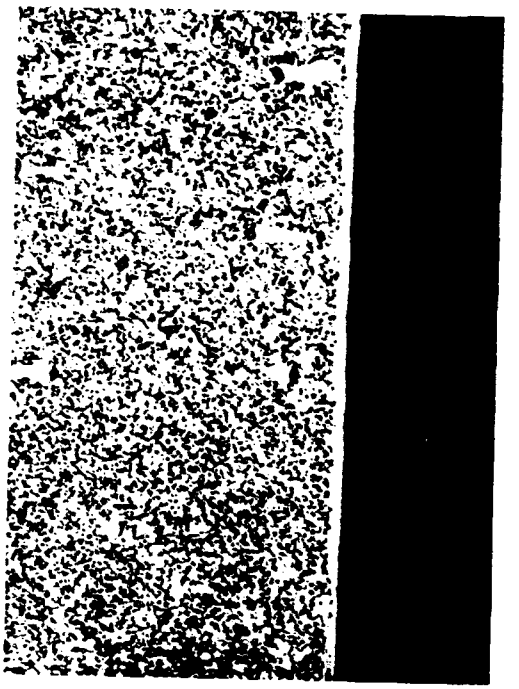

500x 27304

Figure 13 : Micrograph of sectioned T 101 sample; half of the TiC-coating is transformed in Ti-oxide

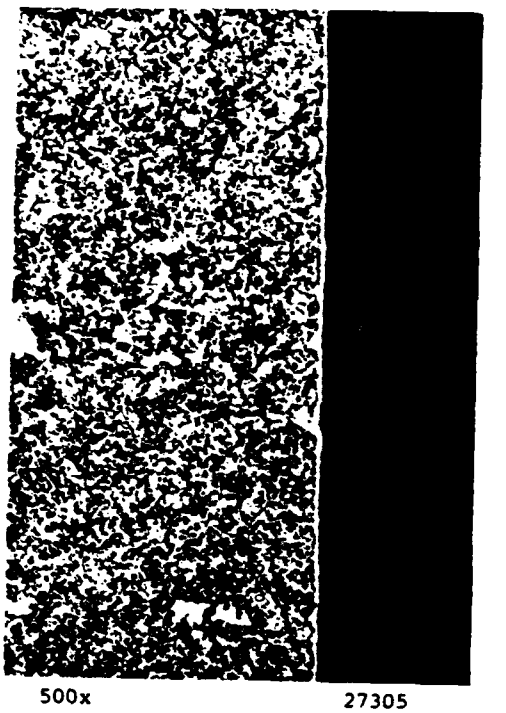

500x 27305

Figure 14 : Micrograph of sectioned T 102 sample; the whole TiC-coating is transformed in Ti-oxide

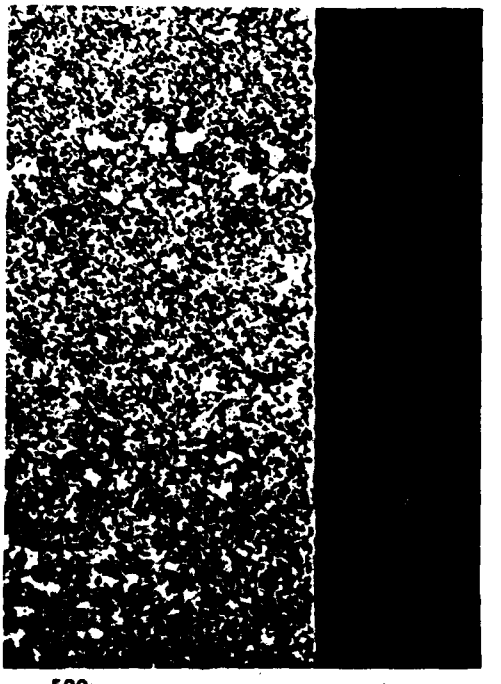

500x 27310

Figure 15 : Micrograph of sectioned T 107 sample; the whole TiC-coating is transformed in Ti-oxide

Figures 16, 17 and 18 show micrographes of the spherical cap erosions, using a 30 mm ball, of samples T 101, T 102 and T 107 respectively; the different interface regions appear clearly. The spherical caps formed on the other samples are not presented since they show mainly the TiC coating.

4.4 X-Ray diffraction

- The X-Ray diffraction diagrams were recorded at relatively high speed (2° 2θ/min), using a CoK_α (Fe-filter) radiation with 36 kV and 20 mA.

- There were no major problems with the recording of the X-ray diffraction patterns; the different samples show important different diffraction patterns. Hereafter the results :

  T 101 : rutile peaks
  weak peaks of TiC

  T 102 : rutile peaks
  weak, unidentified peaks

  T 103 : rutile peaks appear weakly
  TiC peaks appear strong
  some peaks corresponding to the substrate steel

  T 104 : rutile peaks appear very weak
  TiC peaks appear strong
  steel peaks appear weak

  T 105 : TiC peaks appear strong
  steel peaks appear very weak

  T 106 : TiC peaks appear strong
  steel peaks appear very weak

  T 107 : rutile peaks
  weak, unidentified peaks.

· These results are in agreement with the data indicated under 4.3.

· T 105 and T 106 do not have enough Ti-oxide on their surface to show up in the X-ray diffraction.
Some oxidation must however have taken place, since the visual examination showed similar surface for T 103, T 104, T 105 and T 106, and since the electron microprobe analysis showed the presence of Ti and O.

4.5 Stoechiometry

· The stoechiometry of the Ti-oxide caotings was determined by electron microprobe analysis. Since there was no TiO_2-standard available at the moment of these analyses, a TiO-standard was used.

· The analyses gave the following results, presented as atomic percents, with reference to 100% for Ti+O.

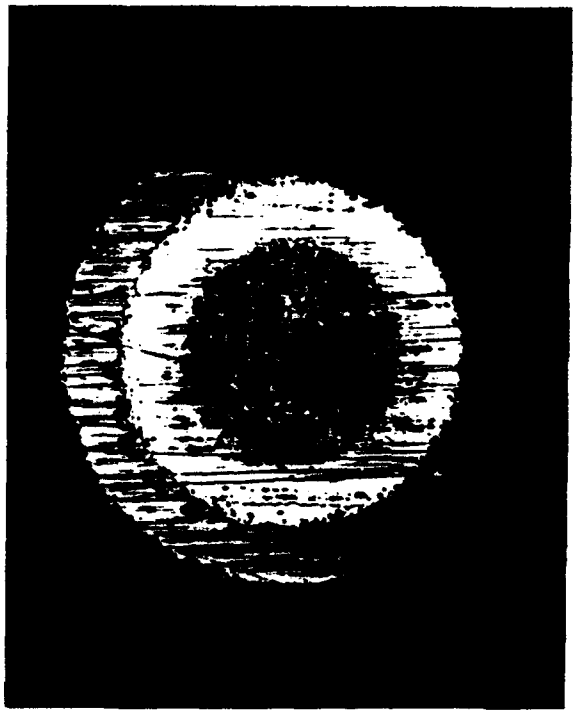

50x 27328

Figure 16 : Micrograph showing the eroded spherical cap on sample T 101

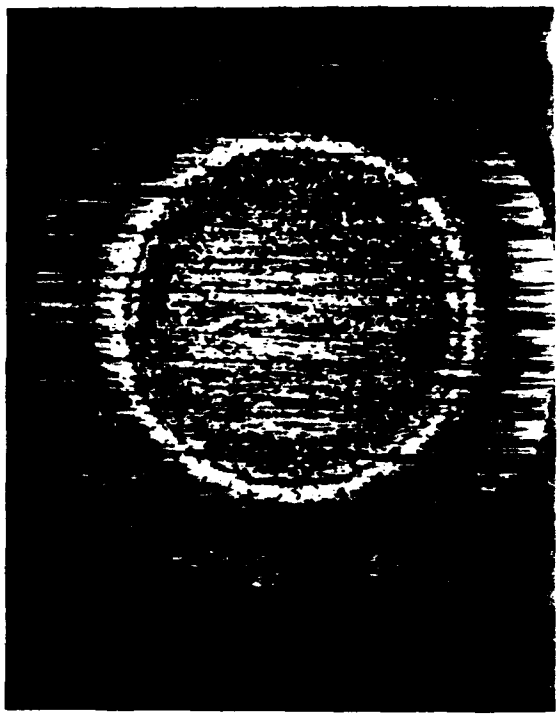

50x 27329

Figure 17 : Micrograph showing the eroded spherical cap on sample T 102

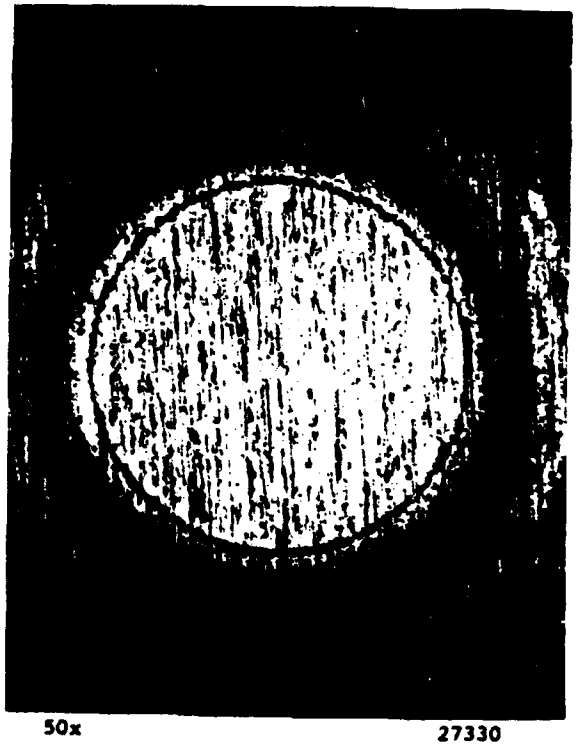

50x 27330

Figure 18 : Micrograph showing the eroded spherical cap on sample T 107

Z-43

Sample	At. % Ti	At. % O	Chemical Formula
T 101	31.5	68.5	$TiO_{2.17}$
T 102	30.2	69.8	$TiO_{2.31}$
T 103	32.1	67.9	$TiO_{2.12}$
T 104	33.7	66.3	$TiO_{1.97}$
T 105	34.9	65.1	$TiO_{1.87}$
T 106	35.6	64.4	$TiO_{1.81}$
T 107	32.0	68.0	$TiO_{2.13}$

- The electron microprobe analysis results show that the Ti-oxide compositions are close to that of TiO_2. There are samples with excess oxygen, and others, which are deficient in oxygen.

- For T 105 and T 106, the X-ray diffraction shows no TiO_2; the micrograph analysis however indicated the presence of Ti-oxide.
The Ti-oxide layer here must be well below 1 µm and appears amorphous in the X-ray diffraction analysis.

- A microprobe analysis has been made for C.
The following results were obtained :

Sample	Wt % C
T 101	0.7
T 102	0.2
T 103	3.2
T 104	3.7
T 105	4.9
T 106	4.9
T 107	0.8

Samples T 101, T 102 and T 107 with important TiO_2 layers, show a very small C content, which, most probably is left over of the original TiC-coating.
Samples T 103 to T 106 show important C contents in the coatings; because the Ti-oxide coatings are very thin, these C-content values must be strongly influenced by the underlying TiC.

- The stoechiometries, as indicated in the Ti-TiO_2 phase diagram (TiO_2-$TiO_{1.9}$) are not found in this investigation. The important fact however for the purpose of this project is that oxides of different stoechiometries were found : saturated with oxygen and oxygen deficient.

- The TiO_2 lattice constants were determined by recording slowly diffraction patterns of the main peaks, on the samples which showed the presence of rutile. The rutile structure is tetragonal, and is therefore determined by constants a and c. The following table indicates the obtained values :

Sample	a (Å)	c (Å)
T 101	4.599	2.960
T 102	4.599	2.960
T 103	4.600	2.973
T 107	4.596	2.960

The a and c values on sample T 103 are larger than the other ones; this must be due to the fact that the rutile peaks obtained on this sample were weak.
The a and c parameters given in the literature (JCPDS file) are a = 4,5933 Å and c = 2,9592 Å.

4.6 Coating adhesion

- The CSEM REVETEST Automatic Scratch Tester has been used to evaluate the adhesion characteristics of the different coating systems. A description of the instrument and related technical data are given in Annexe 2.

- The operating conditions were as follows :

  - diamond tip radius : 200 µm
  - loading rate : $\frac{dL}{dt}$ = 100 N/min
  - scratching speed : $\frac{dx}{dt}$ = 10 mm/min
  - 3 scratches/sample

- The results are summerised in Table 1.

- The following remarks can be made :

  - TiC-coating : the first cracks in the coating appear near 25 N; the damages caused here are mainly of the cohesive type since the Fe of the substrate does not show up on the X-ray image (see figures 19 and 20); at a load of 28 N delamination of TiC starts in the scratch itself (see figures 21 and 22).

  - T 101 : figures 23 and 24 show clearly that the critical load of 17 N corresponds to spalling, by lack of adhesion, of the TiO_2 coating; the TiC present on this sample remains undamaged. Figures 25 and 26 show that the TiC caoting is damaged once the load reaches 22 N.

  - T 102 : the TiC layer is practically totally transformed in TiO_2; the critical load of 12.5 N corresponds therefore to the adhesion of TiO_2 to steel. The important damages seen on figure 27 are mainly of the cohesive type since no Fe shows up on figure 28.
  The TiO_2 damage on sample T 101 was mainly of the "adhesive" type, while on sample T 102, the damage is mainly of the "cohesive" type. The oxidation duration, and therefore the TiO_2 thickness, are very different in these two samples.

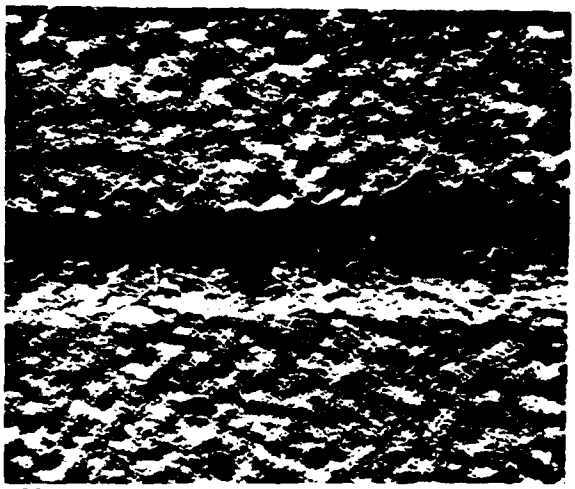

200x B 30109

Figure 19 : Micrograph of scratch under 25 N load on TiC-coated sample

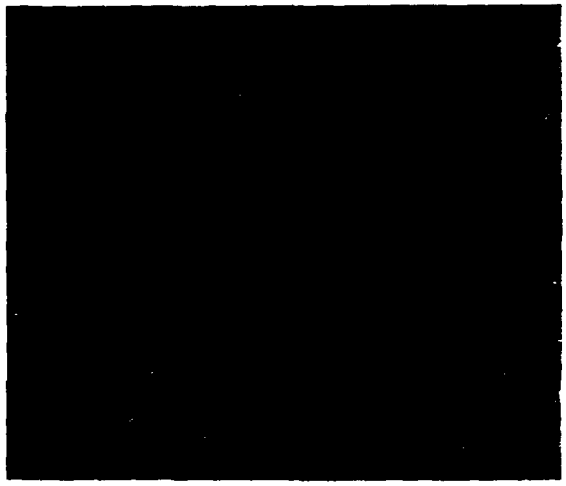

200x B 30110

Figure 20 : Fe X-ray image of same area as on figure 19

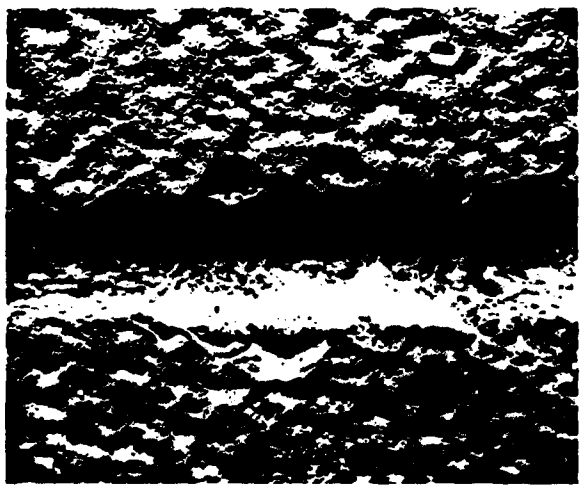

200x B 30111

Figure 21 : Micrograph of scratch under 28 N load on TiC-coated sample

200x B 30112

Figure 22 : Fe X-ray image of same area as on figure 21

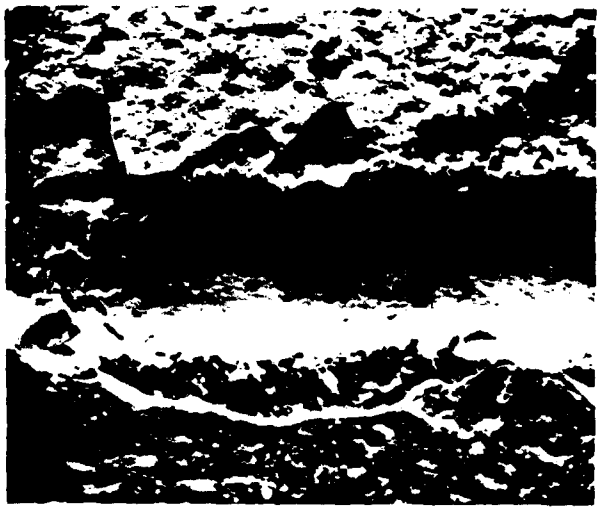

200x B 30113

Figure 23 : Micrograph of scratch under 18 N load on sample T 101

200x B 30114

Figure 24 : Pe X-ray image of same area as on figure 23

200x B 30115

Figure 25 : Micrograph of scratch under 22 N load on sample T 101

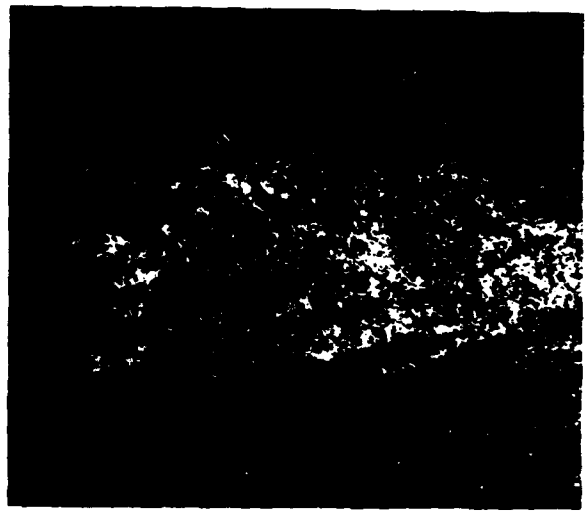

200x B 30116

Figure 26 : Pe X-ray image of same area as on figure 25

- T 103 : the spalling of the oxide layer is accompanied by small damages where Fe of the substrate can be observed (see figures 29 and 30). The critical load of 23 N seems to correspond to the adhesion of the TiO_2/TiC composite coating; the damage type being more cohesive.
  In zone A of figures 31 and 32, it appers that 3 different surfaces can be seen : the steel, the TiC and the TiO_2. These micrographes indicate that the failure of TiO_2 on TiC is of the adhesive type.

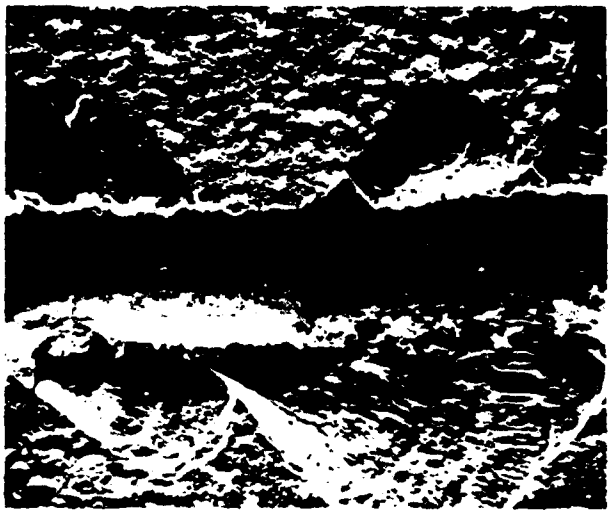

200x 30117

Figure 27 : Micrograph of scratch under 13 N load on sample T 102

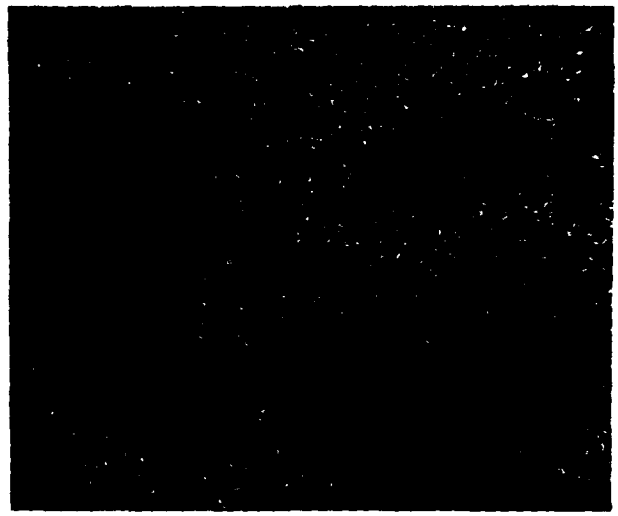

200x 30118

Figure 28 : Fe X-ray image of same area as on figure 27

- T 104 : the delamination of the coating appears simultaneously as the "cohesive" type damages (see figures 33 and 34).
  In zone A of figures 35 and 36, two different surfaces are observed; since Fe of the substrate does not come through, it must be assumed that the 2 surfaces belong to TiC and TiO_2 respectively.

- T 105 : same remarks as for T 104; see figures 37 and 38.

- T 106 : same remarks as for T 104; see figures 39 and 40.

- T 107 : the first critical load at 16.5 N corresponds to damages of the TiO_2 coating (see figures 41 and 42). Long flakes of TiO_2 are removed by a cohesive damage type, as can be seen on figure 43. The X-ray image shows that practically no substrate is exposed (see figure 44); therefore it must be assumed that the damages take mainly place in the TiO_2 caoting.

200x B 30119

Figure 29 : Micrograph of scratch under 23 N load on sample T 103

200x B 30120

Figure 30 : Fe X-ray image of same area as on figure 29

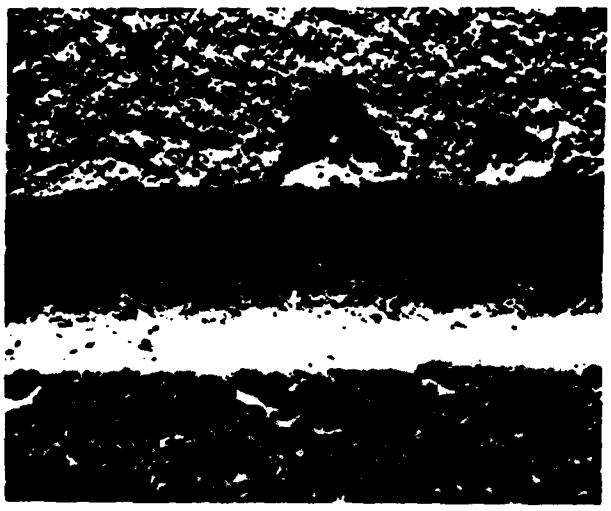

200x B 30121

Figure 31 : Micrograph of scratch under 26 N load on sample T 103

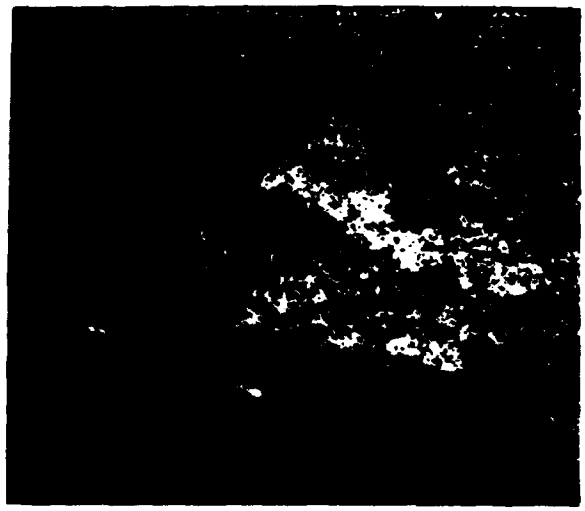

200x B 30122

Figure 32 : Fe X-ray image of same area as on figure 31

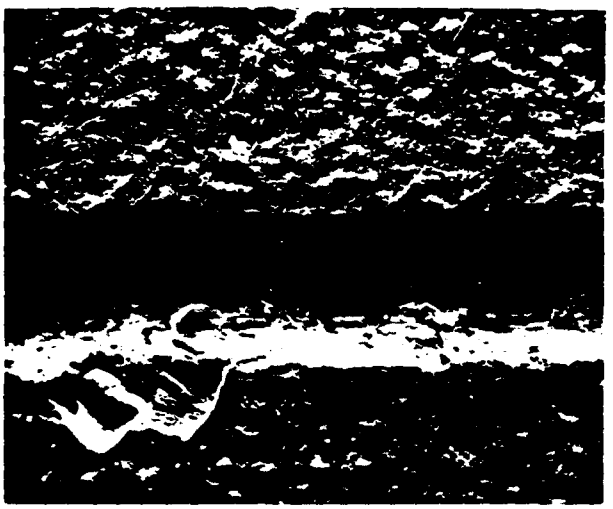

200 x B 30123

Figure 33 : Micrograph of scratch under 23 N load on sample T 104

200x B 30124

Figure 34 : Fe X-ray image of same area as on figure 33

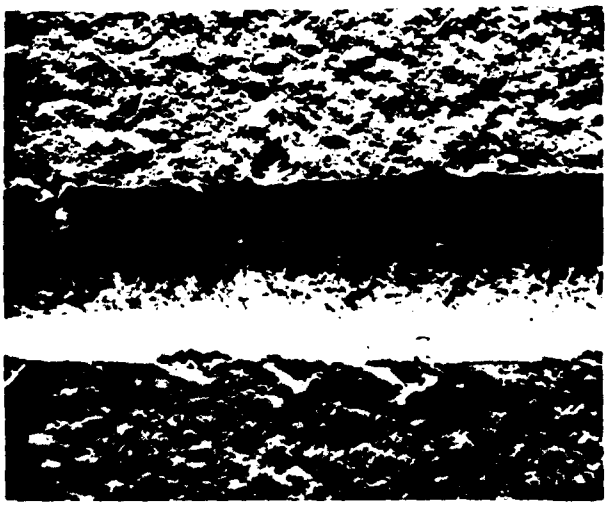

200 x B 30125

Figure 35 : Micrograph of scratch under 24 N load on sample T 104

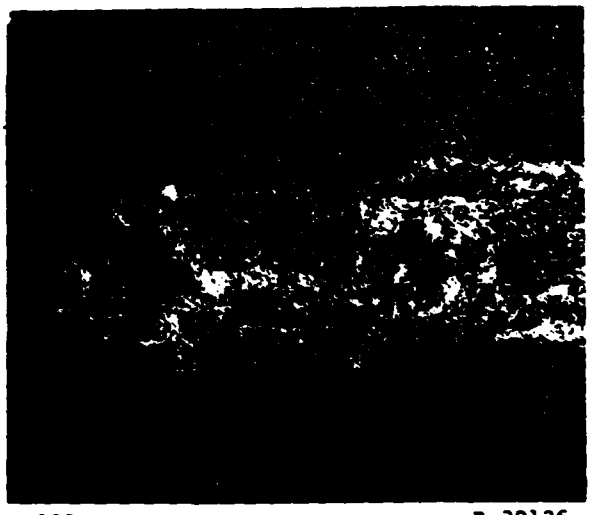

200x B 30126

Figure 36 : Fe X-ray image of same area as on figure 35

200x B 30127

Figure 37 : Micrograph of scratch under 23 N load on sample T 105

200x B 30128

Figure 38 : Fe X-ray image of same area as on figure 37

200 x B 30129

Figure 39 : Micrograph of scratch under 23 N load on sample T 106

200x B 30130

Figure 40 : Fe X-ray image of same area as on figure 39

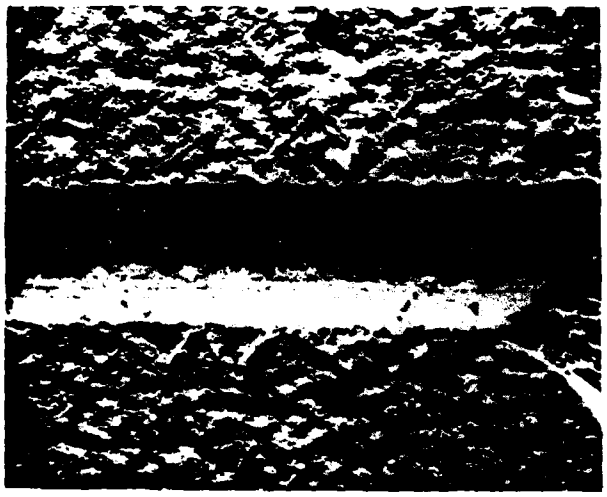

200x B 30131

Figure 41 : Micrograph of scratch under 17 N load on sample T 107

200x B 30132

Figure 42 : Fe X-ray image of same area as on figure 41

200x B 30133

Figure 43 : Micrograph of scratch under 21 N load on sample T 107

200x B 30134

Figure 44 : Fe X-ray image of same area as on figure 43

4.7 Tribological properties

4.7.1 Tribological properties of As-coated TiO_2 surfaces

- The Pin on Disk type CSEM Tribometer has been used for the determination of the TiO_2 coated samples (see Annex 3).

- The disks were the TiO_2 coated AISI 440C steel discs; the pin was an AISI 52100 steel ball of 6 mm diameter. The load on the pin was in all tests 5 N. The wear track radius was between 4 and 7 mm; the rotating speed was in each case adjusted so that the linear speed was 10 cm/s.

- Basically 2 series of measurements were made : one serie at 600°C under air environment and one series at room temperature under Ar environment.

- The individual data sheets that go with the pin-on-disk tests at 600°C are given in Annex 4-1 to 4-7. The individual data sheets that go with the pin-on-disk tests at room temperature under Ar are given in Annex 5-1 to 5-7.

- These results are presented graphically in figure 44, which shows the coefficient of friction values, for the 7 different TiO_2-coating systems, obtained under the 2 different environments; the corresponding wear-values are shown in figure 45.

- For the friction values determined at room temperature under Ar, the following remarks can be made :
  - the number of revolutions is between 2000 and 20'000; the exact values are given in Annex 5;
  - the friction coefficients are high and have a wide scattering;
  - for the 3 samples where a substantial TiO_2 coating is present, the coefficient goes well over 1;
  - steel is smeared to the TiO_2 surface; the absence of O_2 keeps the metal from oxidising, which leads to important adhesive wear;
  - for samples T 103, T 105 and T 106, where the TiO_2 coating is $\leq$ 1 µm the coefficient of friction remains relatively low; this is probably due to the fact that some friction between steel and TiC is taking place;
  - in all cases no wear was observed on the disc; steel was transferred from the pin to the disc surface. Therefore the wear values given in figure 46 relate to the pin-wear.

- For the friction values determined at 600°C under air, the following remarks can be made :
  - the number of revolutions was 1000 for each test;
  - the friction coefficients are lower and less scattered. In practically each case there is an average value, which shows that there is a more stable behaviour of the friciton;

- here also there is a transfer of steel from the pin to the TiO_2-surface; however the 600°C-air environment causes a rapid oxidation of the transfered metal, resulting in less adhesive type friction;
- the pin wear is very important here; the reason can be that the pin steel softens consideratly at 600°C, and flattens out on the TiO_2 surface.

4.7.2 Tribological properties of polished TiO_2-coated discs

- The tribological pin on disc tests performed on the "as coated" TiO_2 covered discs, resulted in an important material transfer from the pin to the disc. This material transfer was certainly due to the roughness of the TiO_2 surface as compared to that of the polished steel pins. Therefore tribological pin on disc tests were run on polished TiO_2-coated discs belonging to series T 101, T 102 and T 107. The other series did not have enough TiO_2 coating to enable a polishing without partial or total removal of the oxide. Unfortunately it was not possible to run tests under 600°C/Air. These comparative tests were made under the RT/Ar-environmental conditions only.

- Figure 47 shows the friction results obtained on the polished discs, and compares them to those obtained on the unpolished ones. The detailed data sheets for these tests are given in Annex 6-1 to 6-3. The wear data of both pins and discs are shown graphically in figure 48.

- It can be seen that the friction coefficient values obtained on the polished TiO_2 surfaces were definitely lower than those on the unpolished surfaces.
  The transfer of pin-material to the disc surface does not start immediately and is much more reduced when the disc surface is polished.
  Before the transfer starts wear of the TiO_2 can be observed; this was not the case when unpolished discs were tested.

- As mentioned earlier it was not possible due to technical reasons to perform the tribological pin on disc tests at 600°C/Air on the polished TiO_2 surfaces. Since in the unpolished state, the friction was better in the 600°C/Air environment than in the RT/Ar, most probably the same tendency would be observed with the polished TiO_2 surfaces.

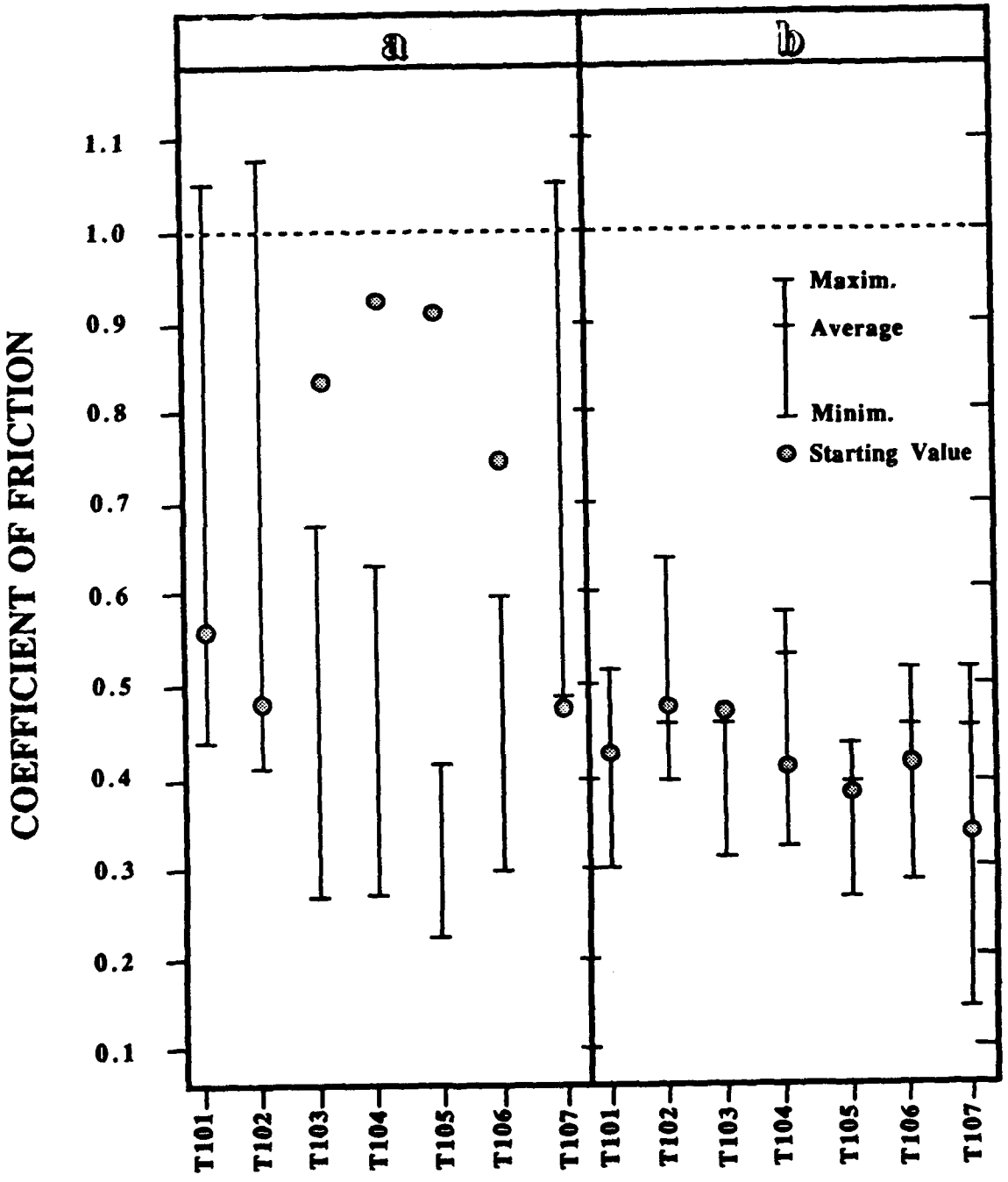

FIGURE 45 : Coefficient of friction between AISI 52100 steel and TiO_2 ; the test conditions are in chapter 4.7;
a : Room Temperature, Ar - Environment
b : 600°C, Air Environment

2-55

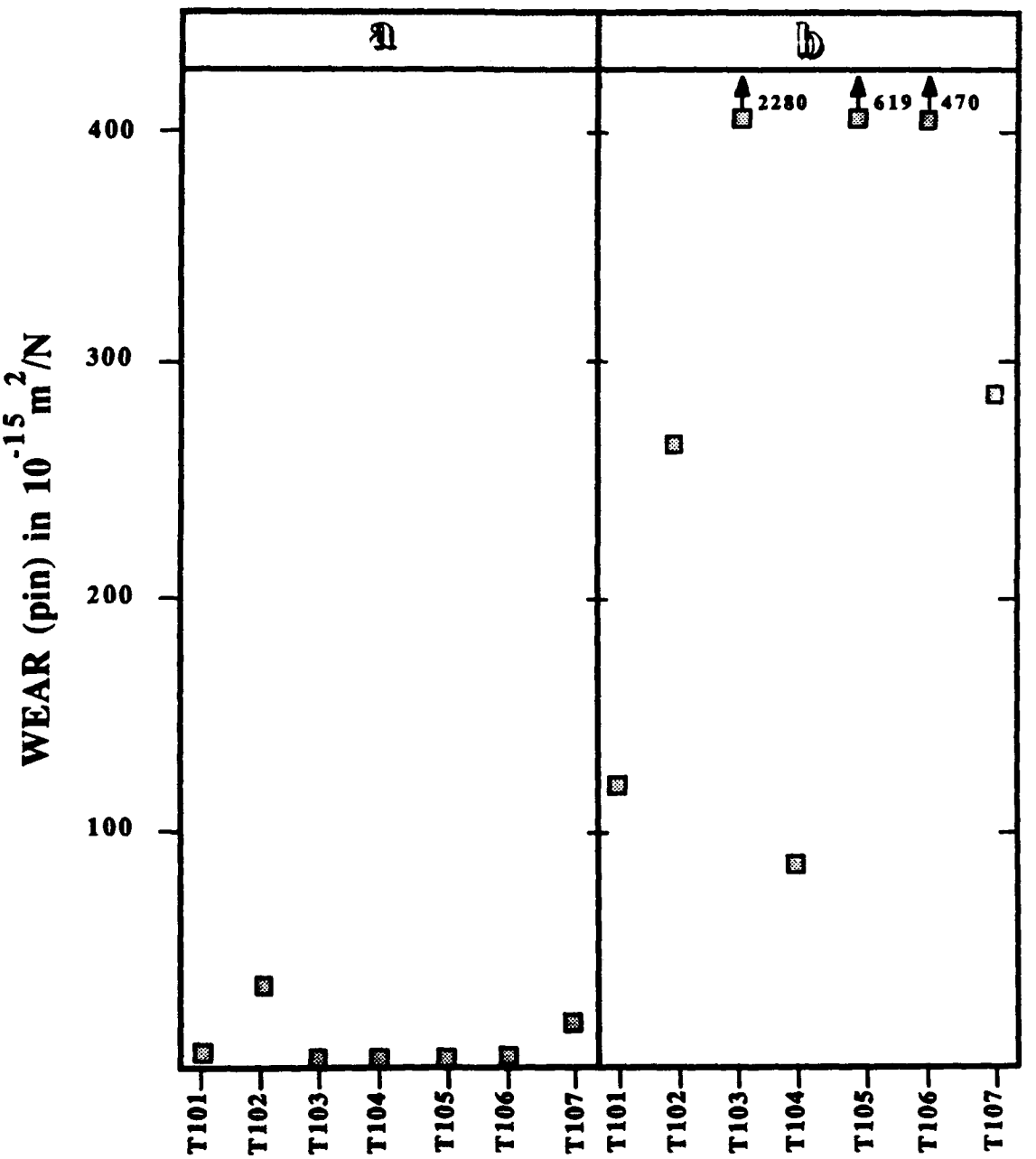

FIGURE 46 : Wear values for friction between a steel pin and a TiO_2 coated disk, obtained with the CSEM Pin on Disk TRIBOMETER; the indicated wear values relate to the pin.
a : Room Temperature, Ar - Environment
b : 600°C, Air Environment

2-56

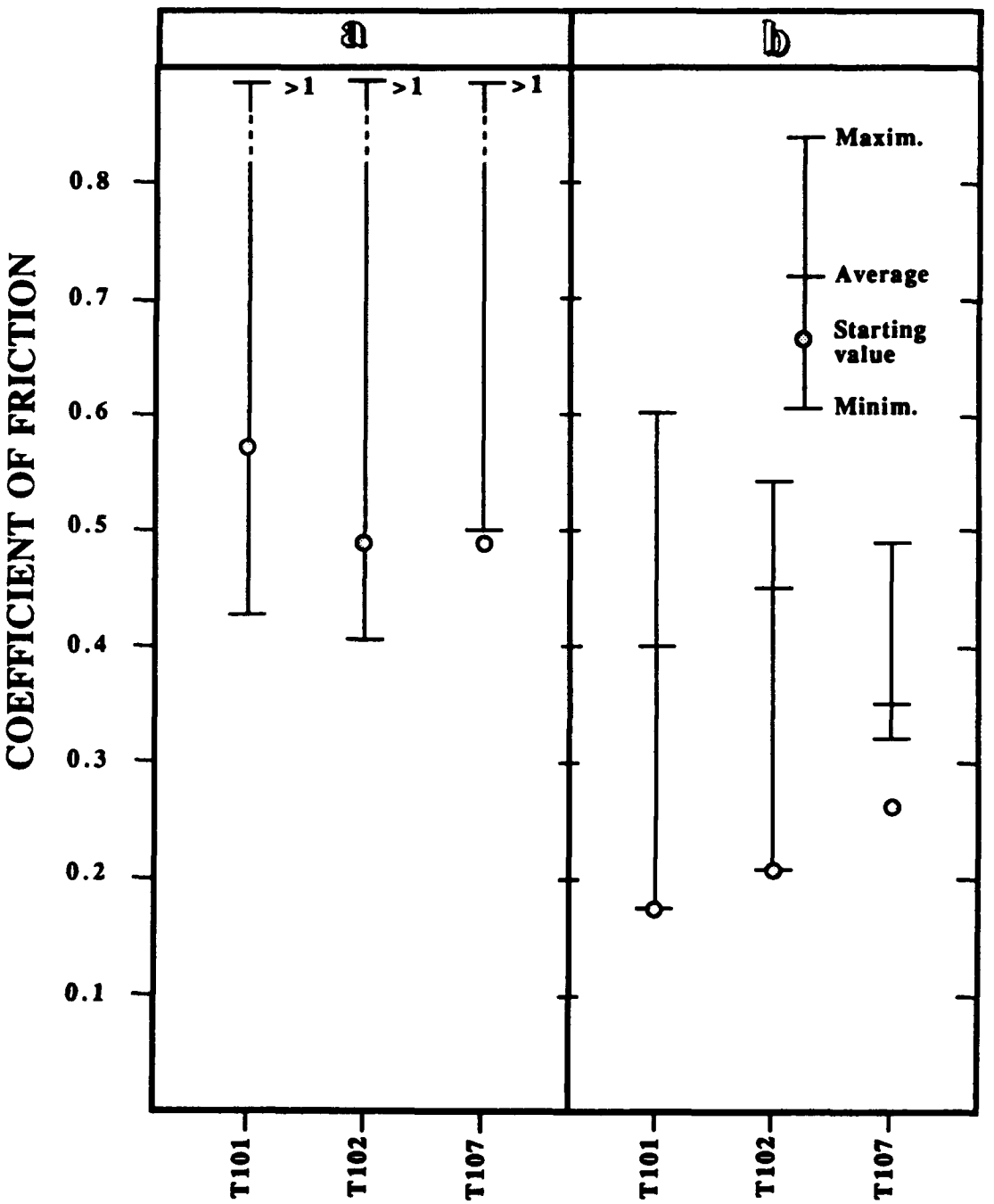

FIGURE 47 : Coefficient of friction between AISI 52100 steel and TiO_2 ; the test conditions are in chapter 4.7; Room Temperature, Ar - Environment
a : TiO_2 -surface is UNPOLISHED
b : TiO_2 -surface is POLISHED

2-57

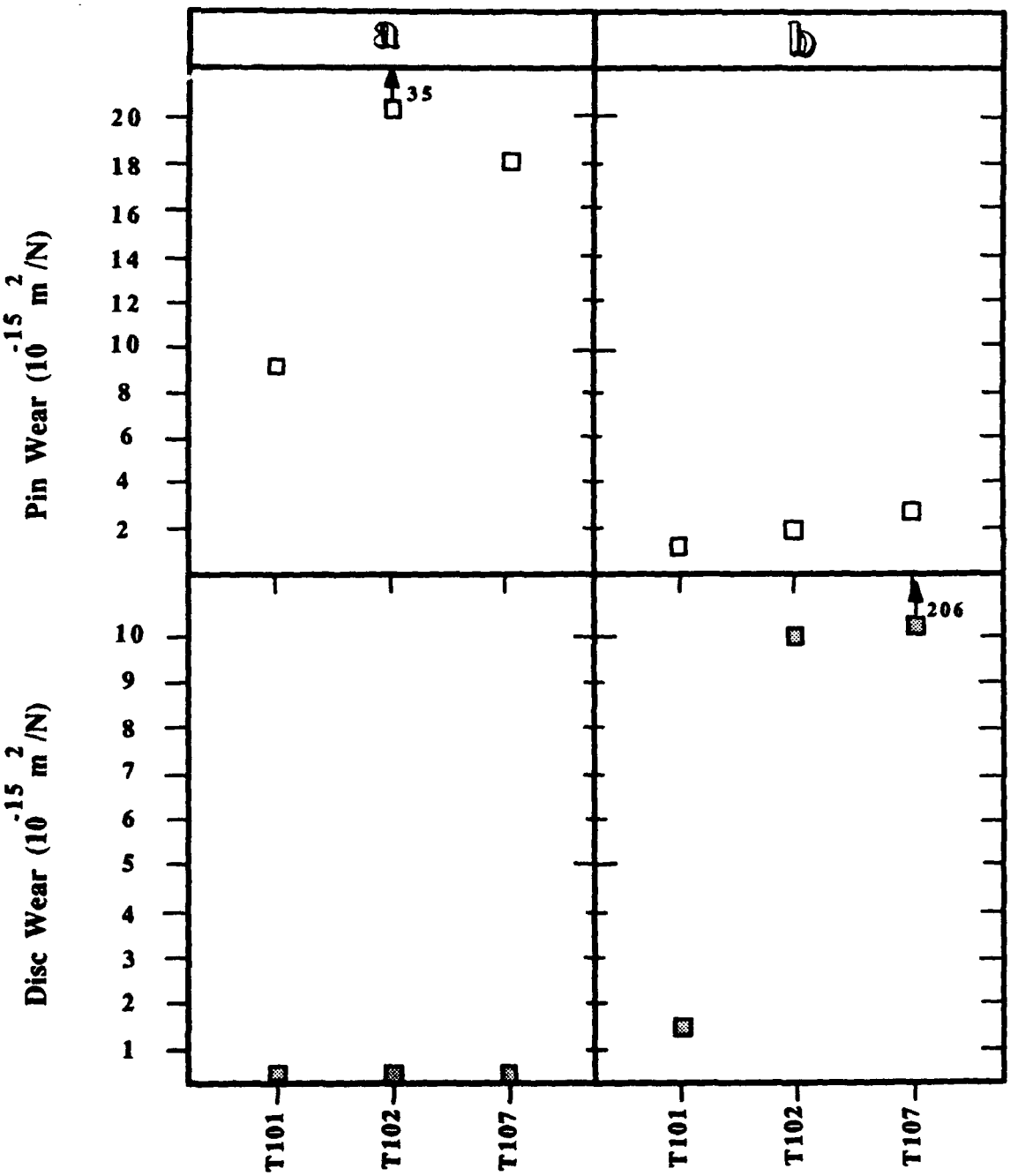

FIGURE 48 : Wear values for friction between a steel pin and a TiO_2 coated disk, obtained with the CSEM Pin on Disk TRIBOMETER; Room Temperature, Ar - Environment
a : TiO_2 -surface is UNPOLISHED
b : TiO_2 -surface is POLISHED

Z-58

TABLE 1 : Results of the adhesion characterisation by the scratch test method

Sample #	Scratch #	COATING DAMAGE* (N) VISUAL CRACK	VISUAL SPALL.	AE	FF
TiC	1	8.0	23.5	28	28
	2	6.5	25.5	26	28
	3	8.5	25.0	25	24
	aver.	7.5	24.5		
T 101	1	7.5	17.0	18	18
	2	6.5	17.0	20	19
	3	6.5	17.5	18	18
	aver.	7.0	17.0		
T 102	1	7.0	12	16	16
	2	8.5	11.5	16	14
	3	7.5	13.5	14	15
	aver.	7.5	12.5		
T 103	1	10.5	24.5	20	25
	2	10	24.0	24	24
	3	10	24.0	21	21
	aver.	10.0	23.0		
T 104	1	8.0	25.5	22	23
	2	10.0	21.0	18	21
	3	11.0	22.5	22	23
	aver.	9.5	22.0		
T 105	1	8.5	22.0	22	22
	2	9.0	24.0	23	24
	3	7.0	20.5	21	20
	aver.	8.0	23.0		
T 106	1	7.5	23.0	22	23
	2	9.0	23.5	23	24
	3	9.0	23.0	22	24
	aver.	8.5	23.0		
T 107	1	3.0	17.5/21.5	22	22
	2	3.0	15.5/21.0	24	22
	3	4.5	17.0/20.5	23	18
	aver.	3.5	16.5/21.0		

* Coating damage : the values indicated in these columns are in N; they correspond to the load at which a coating damage is observed by :

- visual examination (optical microscope under ~ 200 x); two types of damage can be recognised a) cracking of the coating; b) spalling
- acoustic emission (AE)
- frictional force (FF)

ANNEX 1

CENTRE SUISSE D'ELECTRONIQUE ET DE MICROTECHNIQUE S.A.
– Recherche et Développement –

CSEM MALADIERE 71 CH-2007 NEUCHATEL (SWITZERLAND)
TEL. 038/24 01 61 TELEX 952 664 (CSEM) TELEFAX 038/25 40 78

CALOTEST

Apparatus for the rapid measurement of the thickness of thin coatings and for the preparation of specimens for depth profiling analyses.

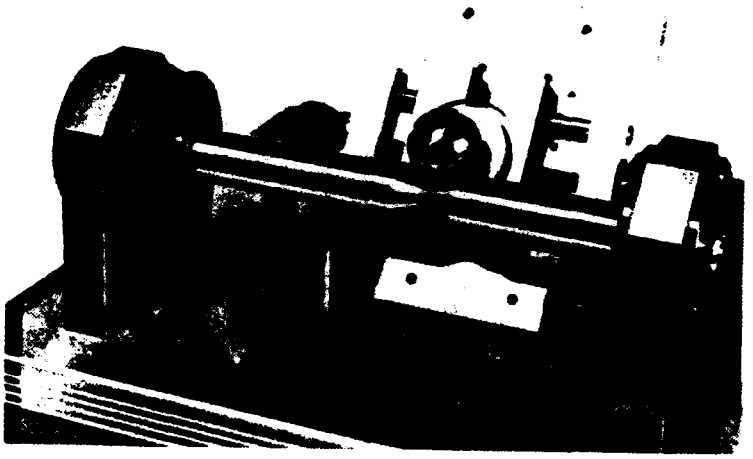

PROCEDURE

A ball coated with an abrasive paste is kept in rotation on the specimen by a shaft with a V-groove.
A depression with the form of a spherical cap is abraded in to the specimen. X and Y are measured with the aid of an optical microscope and the thickness of the coating may be determined by the following relation :

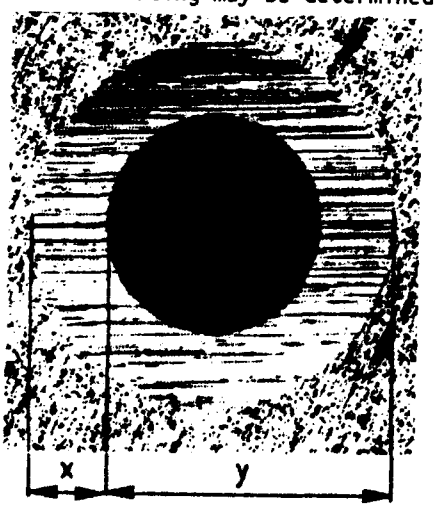

$$E = \frac{X \cdot Y}{\varnothing_{ball}}$$

Z-60

NEWS RELEASE

APPLICATIONS

The method is applicable in the following fields to coatings having thicknesses from 0,5 to 50 µm :

- Surface treatment by CVD
- Sputtering, ion plating
- Evaporation in vacuum
- Anodic oxidation
- Galvanized coatings
- Chemical coatings

  etc.

PRINCIPAL FEATURES OF THE APPARATUS

Working table	: tilttable, 80 x 80 mm of usable surface, mounting by two clamping devices. Optional universal working table
Rotational speed of the shaft	: 60 to 1200 rev/min, continually adjustable by a potentiometer
Diameters of the balls	: The apparatus is supplied with two sets of balls : Ø 10, 20 and 30 mm
Abrasion time	: Electronic timer incorporated. Selection of the abrasion time : 1 to 9 min.
Dimensions	: 230 x 250 x 180 mm
Weight	: 4,5 kg
Power supply	: 220 V ∿, optional 110 V ∿

ACCESSORIES

- universal working table with interchangeable clamps for mounting rods, washers, rings, slabs and plates
- on request, gliding working table or special mountings

JFC
July 1986

CENTRE SUISSE D'ELECTRONIQUE ET DE MICROTECHNIQUE S.A.
– Recherche et Développement –

CSEM MALADIERE 71 CH-2007 NEUCHATEL (SWITZERLAND)
TEL 038/24 01 61 TELEX 952 664 (CSEM) TELEFAX 038/25 40 78

REVETEST

AUTOMATIC SCRATCH TESTER

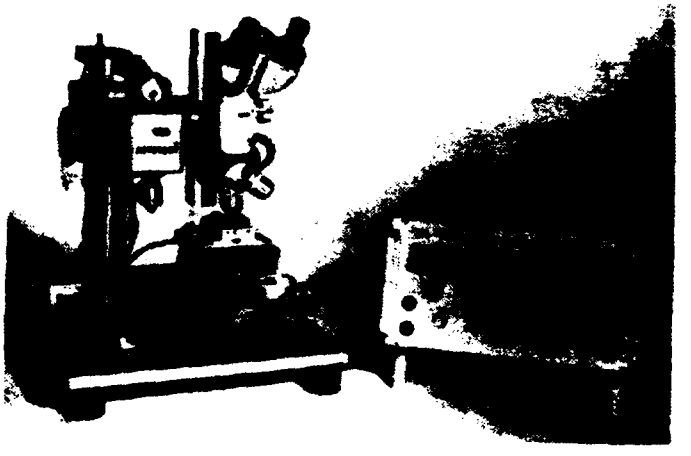

The REVETEST developed by CSEM is an automatic device which enables the measurement of the mechanical strengh - adhesion and intrinsic cohesion- of hard and brittle coatings obtained by chemical vapor deposition (CVD) or physical vapor deposition (PVD) on softer and tougher substrates.

The test consists in scratching the surface of a coated substrate with a rounded diamond point. The load applied on the point increases continuously as it scratches along the surface and a piezoelectric accelerometer detects the acoustic emission produced as the coating is being damaged. The apparatus also enables the scratching test under constant load.

The intensity of the acoustic emission depends on the nature of the damage : levelling of asperities, cracking, flaking of the coating, etc. The acoustic emission signal recorded as a function of the load applied on the diamond point is a characteristic of the tested sample. The analysis of the obtained graph provides qualitative and quantitative information on the mechanical strength of the coating.

NEWS RELEASE

TECHNICAL DATA

Mechanical

Dimensions of double cross motion table	:	60 x 75 mm
Maximum scratch length	:	25 mm
Maximum perpendicular displacement	:	25 mm
Scratching speed (adjustable)	:	4 to 40 mm/min.
Load (adjustable low and high limits)	:	1 to 200 N
Loading rate (adjustable)	:	40 to 400 N/min.
Diamond point	:	Rockwell C diamond (R = 0.2 mm)

Electronic

Actual load display

Acoustic emission signal display

Chart recorder electrical output of main signals

Dimensions

Scratch tester	:	250 x 430 x 360 mm
Control unit	:	330 x 470 x 190 mm
Total weight	:	50 kg

Options

Rotating table and specimen holder

Measurement microscope

Chart recorder

ADVANTAGES

o Simple to use	:	push-button operation, once adjusted
o Time saving	:	complete test in approx. one minute
o Objective	:	results are operator-independant

o Subsequent sample investigation possible

JFC/cbr
June 1986

ANNEX 3

CENTRE SUISSE D'ELECTRONIQUE ET DE MICROTECHNIQUE S.A.
– Recherche et Développement –

CSEM MALADIERE 71 CH-2007 NEUCHATEL (SWITZERLAND)
TEL. ++41(0)38 24 01 61 TELEX 952 064 FAX ++41(0)38 25 40 78

TRIBOMETER

The TRIBOMETER developed by CSEM is a high quality, easy to use pin-on-disc type machine for the precise measurement of the friction and wear properties of materials and the functional sliding life of tribological coatings.

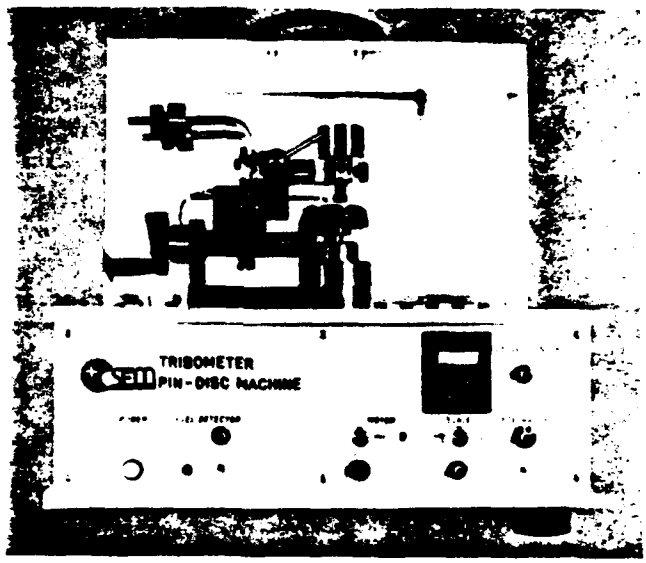

Technical description

- Disc dimensions	: diameter up to 60 mm thickness up to 15 mm
- Radius of fixed pin or ball	: 3 mm (standard)
- Lubrication	: with or without
- Standard loads	: 1 to 10 N
- Friction track radius	: 0 to 40 mm
- Rotation speed range	: 0.03 rpm to 500 rpm
- Dimensions (l,w,h)	: 500 x 350 x 480 mm
- weight	: 32 kg

NEWS RELEASE

The CSEM TRIBOMETER also includes the following standard features:

- Direct friction coefficient output
- Automatic switch-off when either:
  - the required number of revolutions is reached (1 to 10^7 revs), or
  - a preselected friction coefficient is reached.
- Adjustable time constant to smoothen out friction fluctuations

Standard accessories

- Plexiglas cover for testing in various atmospheres (moist or dry air, gases)
- Rotating container for tests with liquids
- Pin holders, ball holders
- Special holder for testing flat on flat.

Applications

- **Sliding life determination of self-lubricating coatings**

  The instrument enables the number of revolutions up to break-through to be determined, as characterized by an increase in the friction coefficient. Typical parameters in this application are coating thickness, structure and other deposition and interface conditions, environment, load and speed, lubrication or cleaning, running-in conditions, etc.

- **Determination of friction and wear data of bulk materials or hard coatings**

  By comparing the wear and friction coefficient data, materials can be classified and selected for practical use.

  Important parameters include: material combinations, roughness, speed, geometry, humidity, lubrication, contamination or cleaning, etc.

  The friction coefficient recording allows such characteristic data as minimum, average and maximum values during and after running-in to be determined.

  At the end of the test, microscope measurements on the ball flat spherical cup and profilometric readings on the disc enable the wear rate to be evaluated (wear volume per applied load and sliding length).

JFC/MMa/cbr
August 1989

CENTRE SUISSE D'ELECTRONIQUE ET DE MICROTECHNIQUE S.A. - Recherche et Développement -

DATA SHEET Nr. T 101 (600°C-air) October 11, 1989

FRICTION TYPE

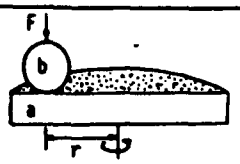

X

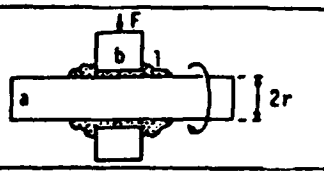

TRIBOLOGICAL SYSTEM

Lubrication ☒ without ☐ with

Load : F = 5 N

Test duration : 1000 revolutions
0.038 km

Radius : r = 6 mm

Speed : 10 cm/s

Environment ☐ vacuum : 10^{-} Torr
☒ gas : air Humidity: Temperature: 600°C

TiO_2 (a) / Steel (b)

Cleaning a : alcohol
b : "

RESULTS

Friction coefficient				Wear in $10^{-15}m^2/N$		Lifetime ~~after running-in~~ (for layers) in 10^3 revolutions			
start	~~after running-in~~								
	mini	mean	maxi	a	b	μ< 0.1	μ< 0.2	μ< 0.3	μ<0.5
0.43	0.30	→	0.51	deposit	139	0	0	0	0.08

Characteristic diagram

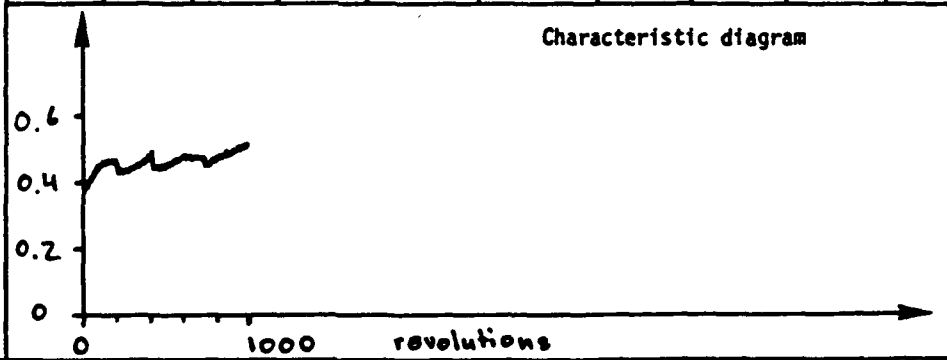

CHARACTERISTICS OF PARTNERS

	Geometry	Substrat	Layer (s)	Surface
a	disc 101	AISI 440/TiC/ TiO_2 unpolished		as coated
b	ball	AISI 52.100	-	polished

FURTHER INFORMATIONS

for a ☐ b ☐

For the other partner see data sheet Nr.

Supplier: Running-in: revolutions

CENTRE SUISSE D'ELECTRONIQUE ET DE MICROTECHNIQUE S.A. - Recherche et Développement -

DATA SHEET Nr. T 102 (600°C-air) October 16, 1989

FRICTION TYPE

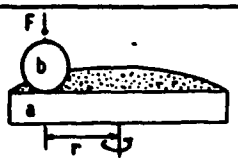

X

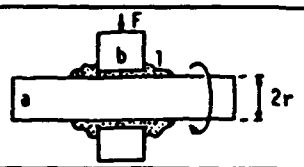

TRIBOLOGICAL SYSTEM

Lubrication ☒ without ☐ with

$\frac{TiO_2}{a} / \frac{Steel}{b}$

Load : F = 5 N

Test duration : 1000 revolutions

0.036 km

Cleaning a : alcohol

b : "

Radius : r = 6 mm

Speed : 10 cm/s

Environment ☐ vacuum : 10^{-} Torr

☒ gas : air Humidity: Temperature: 600°C

RESULTS

Friction coefficient				Wear in $10^{-15} m^2/N$		Lifetime ~~after running-in~~ (for layers) in 10^3 revolutions			
start	~~after running-in~~								
	mini	mean	maxi	a	b	μ< 0.1	μ< 0.2	μ< 0.3	μ<0.5
0.47	0.40	~0.45	0.63	deposit	265	0	0	0	0.8

Characteristic diagram

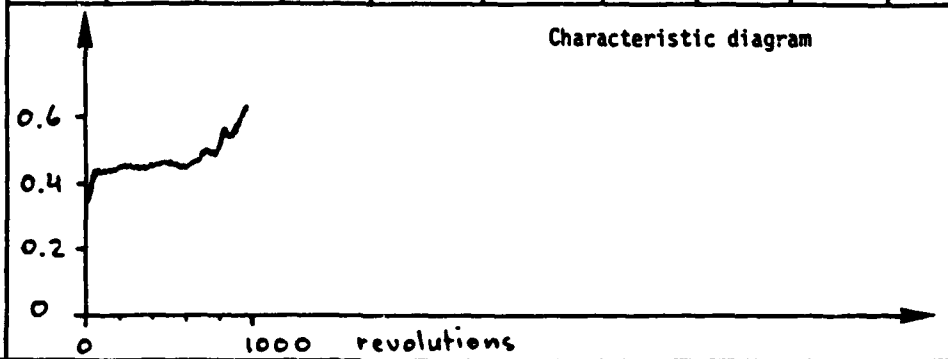

CHARACTERISTICS OF PARTNERS

	Geometry	Substrat	Layer (s)	Surface
a	disc 102	AISI 440/TiC/ TiO2 unpolished		as coated
b	ball	AISI 52.100	-	polished

FURTHER INFORMATIONS

for a ☐ b ☐

For the other partner see data sheet Nr.

Supplier: Running-in: revolutions

CENTRE SUISSE D'ELECTRONIQUE ET DE MICROTECHNIQUE S.A. - *Recherche et Développement* -

DATA SHEET Nr. T 103 (600°C-air) October 16, 1989

FRICTION TYPE

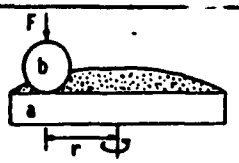

X

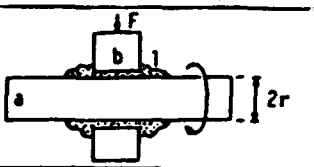

TRIBOLOGICAL SYSTEM

Lubrication ☒ without ☐ with

TiO_2 (a) / Steel (b)

Load : F = 5 N

Test duration : 718 revolutions

0.032 km

Cleaning a : alcohol

Radius : r = 7 mm

b : "

Speed : 10 cm/s

Environment ☐ vacuum : 10^{-} Torr

☒ gas : air Humidity: Temperature: 600°C

RESULTS

Friction coefficient				Wear in $10^{-15} m^2/N$		Lifetime ~~after running in~~ (for layers) in 10^3 revolutions			
start	~~after running in~~								
	mini	mean	maxi	a	b	μ< 0.1	μ< 0.2	μ< 0.3	μ<0.5
0.46	0.31	~ 0.4	0.45	deposit	2280	0	0	0	> 0.7

Characteristic diagram

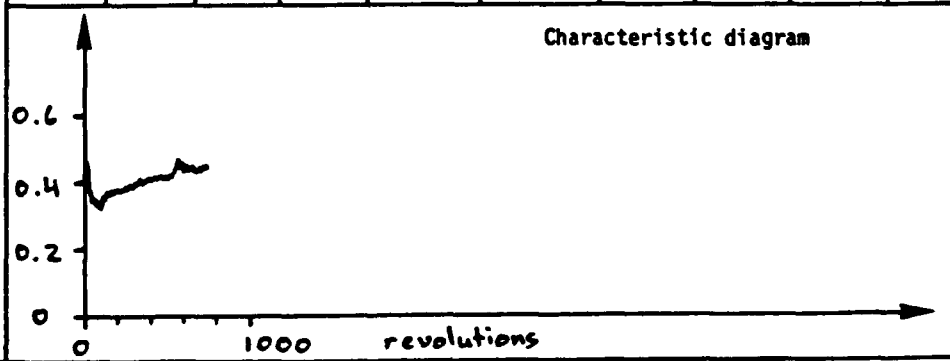

CHARACTERISTICS OF PARTNERS

	Geometry	Substrat	Layer (s)	Surface
a	disc 103	AISI 440/TiC/ TiO_2 unpolished		as coated
b	ball	AISI 52.100	-	polished

FURTHER INFORMATIONS

for a ☐ b ☐

For the other partner see data sheet Nr.

Supplier: Running-in: revolutions

CENTRE SUISSE D'ELECTRONIQUE ET DE MICROTECHNIQUE S.A. - Recherche et Développement -

DATA SHEET Nr. T 104 (600°C-air) October 17, 1989

FRICTION TYPE

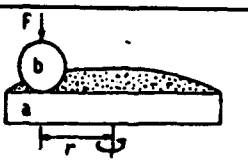

X

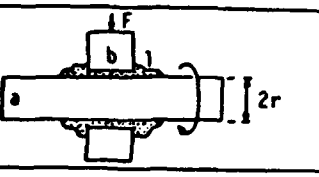

TRIBOLOGICAL SYSTEM

Lubrication ☒ without ☐ with

Load : F = 5 N

Test duration : 1000 revolutions

0.044 km

Radius : r = 7 mm

Speed : 10 cm/s

Environment ☐ vacuum : 10^{-} Torr

☒ gas : air Humidity: Temperature: 600°C

TiO_2 (a) / Steel (b)

Cleaning a : alcohol

b : "

RESULTS

Friction coefficient				Wear in $10^{-15} m^2/N$		Lifetime ~~after running-in~~ (for layers) in 10^3 revolutions			
start	~~after running-in~~								
	mini	mean	maxi	a	b	μ< 0.1	μ< 0.2	μ< 0.3	μ<0.5
0.41	0.32	~0.53	0.57	deposit	85	0	0	0	0.25

Characteristic diagram

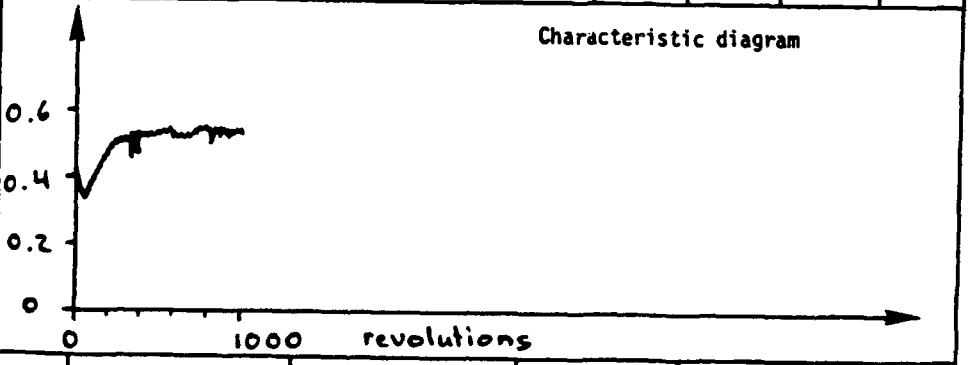

CHARACTERISTICS OF PARTNERS

	Geometry	Substrat	Layer (s)	Surface
a	disc 104	AISI 440/TiC/ TiO_2 unpolished		as coated
b	ball	AISI 52.100	-	polished

FURTHER INFORMATIONS

for a ☐ b ☐

For the other partner see data sheet Nr.

Supplier:

Running-in: revolutions

CENTRE SUISSE D'ELECTRONIQUE ET DE MICROTECHNIQUE S.A. - Recherche et Développement -

DATA SHEET Nr. T 105 (600°C-air) October 17, 1989

FRICTION TYPE

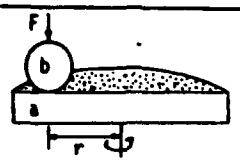

X

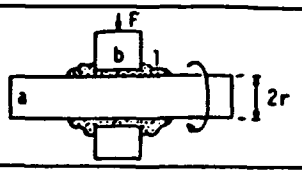

TRIBOLOGICAL SYSTEM

Lubrication ☒ without ☐ with

TiO_2 (a) / Steel (b)

Load : F = 5 N

Test duration : 1000 revolutions

0.038 km

Cleaning a : alcohol

b : "

Radius : r = 6 mm

Speed : 10 cm/s

Environment ☐ vacuum : 10^{-} Torr

☒ gas : air Humidity: Temperature: 600°C

RESULTS

Friction coefficient				Wear in $10^{-15} m^2/N$		Lifetime ~~after running-in~~ (for layers) in 10^3 revolutions			
start	~~after running-in~~								
	mini	mean	maxi	a	b	μ< 0.1	μ< 0.2	μ< 0.3	μ<0.5
0.39	0.28	~0.4	0.42	deposit	619	0	0	0.02	> 1

Characteristic diagram

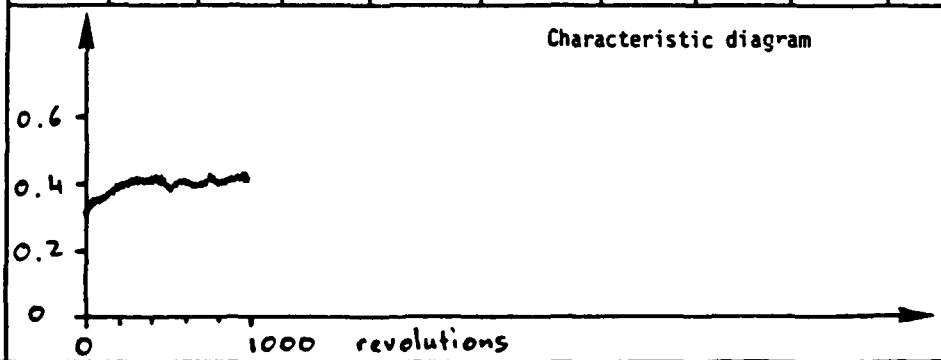

CHARACTERISTICS OF PARTNERS

	Geometry	Substrat	Layer (s)	Surface
a	disc 105	AISI 440/TiC/ TiO_2 unpolished		as coated
b	ball	AISI 52.100	-	polished

FURTHER INFORMATIONS

for a ☐ b ☐

For the other partner see data sheet Nr.

Supplier: Running-in: revolutions

Z-70

CENTRE SUISSE D'ELECTRONIQUE ET DE MICROTECHNIQUE S.A. - Recherche et Développement -

DATA SHEET Nr. T 106 (600°C-air) October 17, 1989

FRICTION TYPE

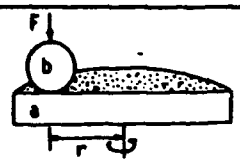

X

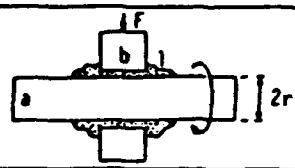

TRIBOLOGICAL SYSTEM

Lubrication ☒ without ☐ with

Load : F = 5 N

Test duration : 1000 revolutions
0.038 km

Radius : r = 6 mm

Speed : 10 cm/s

Environment ☐ vacuum : 10^{-} Torr
☒ gas : air Humidity: Temperature: 600°C

$\frac{TiO_2}{a} / \frac{Steel}{b}$

Cleaning a : alcohol
b : "

RESULTS

Friction coefficient				Wear in $10^{-15} m^2/N$		Lifetime ~~after running-in~~ (for layers) in 10^3 revolutions			
start	~~after running-in~~								
	min.	mean	maxi	a	b	μ< 0.1	μ< 0.2	μ< 0.3	μ<0.5
0.42	0.29	~0.45	0.51	deposit	471	0	0	0.02	0.9

Characteristic diagram

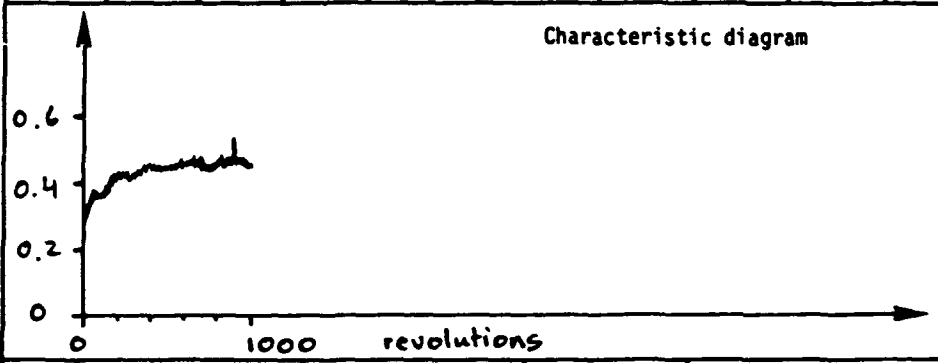

CHARACTERISTICS OF PARTNERS

	Geometry	Substrat	Layer (s)	Surface
a	disc 106	AISI 440/TiC/ TiO_2 unpolished		as coated
b	ball	AISI 52.100	-	polished

FURTHER INFORMATIONS

for a ☐ b ☐

For the other partner see data sheet Nr.

Supplier: Running-in: revolutions

CENTRE SUISSE D'ELECTRONIQUE ET DE MICROTECHNIQUE S.A. - Recherche et Développement -

DATA SHEET Nr. T 107 (600°C-air) October 17, 1989

FRICTION TYPE

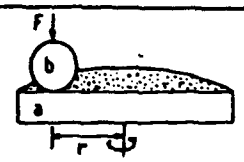

X

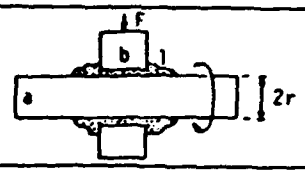

TRIBOLOGICAL SYSTEM

Lubrication ☒ without ☐ with

Load : F = 5 N

Test duration : 1000 revolutions
0.038 km

Radius : r = 6 mm

Speed : 10 cm/s

Environment ☐ vacuum : 10^{-} Torr
☒ gas : air Humidity: Temperature: 600°C

$\frac{TiO_2}{a} / \frac{Steel}{b}$

Cleaning a : alcohol
b : "

RESULTS

Friction coefficient				Wear in $10^{-15} m^2/N$		Lifetime ~~after running in~~ (for layers) in 10^3 revolutions			
start	~~after running in~~								
	mini	mean	maxi	a	b	μ< 0.1	μ< 0.2	μ< 0.3	μ<0.5
0.34	0.14	~0.45	0.51	deposit	282	0	0	0.06	0.5

Characteristic diagram

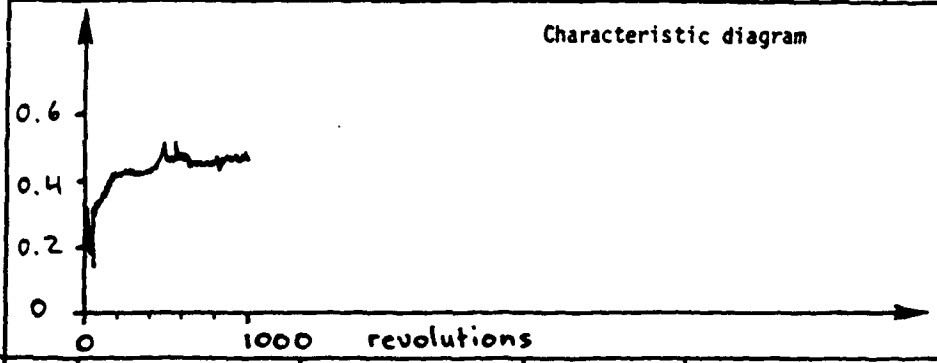

CHARACTERISTICS OF PARTNERS

	Geometry	Substrat	Layer (s)	Surface
a	disc 107	AISI 440/TiC/ TiO_2 unpolished		as coated
b	ball	AISI 52.100	-	polished

FURTHER INFORMATIONS

for a ☐ b ☐

For the other partner see data sheet Nr.

Supplier: Running-in: revolutions

CENTRE SUISSE D'ELECTRONIQUE ET DE MICROTECHNIQUE S.A. - Recherche et Développement -

DATA SHEET Nr. T 101 (RT - Ar) November 7, 1989

FRICTION TYPE

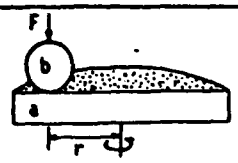

X

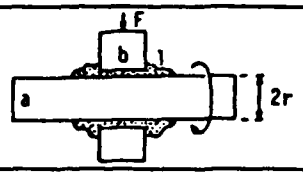

TRIBOLOGICAL SYSTEM

Lubrication ☒ without ☐ with

Load : F = 5 N

Test duration : 5000 revolutions
0.13 km

Radius : r = 4 mm

Speed : 10 cm/s

Environment ☐ vacuum : 10^{-} Torr
☐ gas : Ar Humidity: < 2% RH Temperature: 24 °C

TiO_2 (a) / Steel (b)

Cleaning a : compressed dry air
b : alcohol

RESULTS

Friction coefficient				Wear in $10^{-15}m^2/N$		Lifetime ~~after running-in~~ (for layers) in 10^3 revolutions			
start	~~after running-in~~								
	mini	mean	maxi	a	b	μ< 0.1	μ< 0.2	μ< 0.3	μ<0.5
0.56	0.43	<—>	> 1	deposit	9.4	0	0	0	0

Characteristic diagram

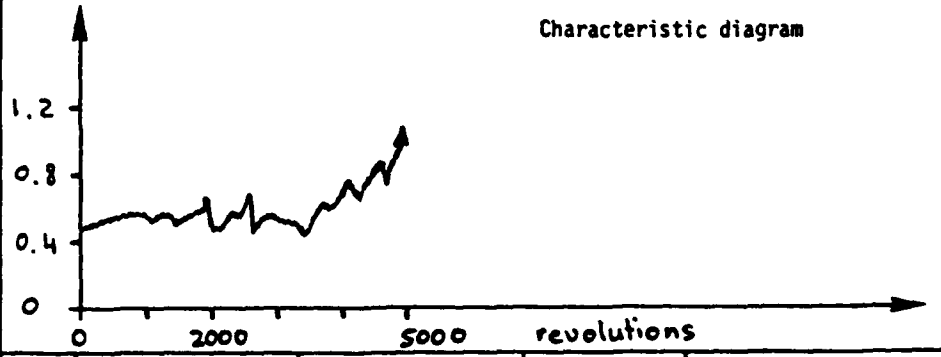

CHARACTERISTICS OF PARTNERS

	Geometry	Substrat	Layer (s)	Surface
a	disc 101	AISI 440/TiC/ TiO_2 unpolished		as coated
b	ball	AISI 52.100	-	polished

FURTHER INFORMATIONS

for a ☐ b ☐

For the other partner see data sheet Nr.

Supplier: Running-in: revolutions

Z-73

CENTRE SUISSE D'ELECTRONIQUE ET DE MICROTECHNIQUE S.A. - Recherche et Développement -

DATA SHEET Nr. T 102 (RT - Ar) November 7, 1989

FRICTION TYPE

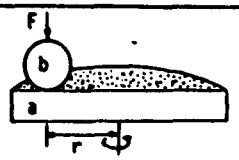

X

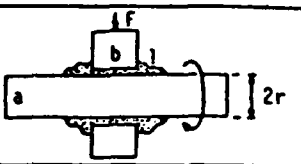

TRIBOLOGICAL SYSTEM

Lubrication ☒ without ☐ with

Load : F = 5 N

Test duration : 2375 revolutions
0.06 km

Radius : r = 4 mm

Speed : 10 cm/s

Environment ☐ vacuum : 10^{-} Torr
☒ gas : Ar Humidity: < 2% RH Temperature: 24 °C

$\frac{TiO_2}{a} / \frac{Steel}{b}$

Cleaning a : compressed dry air
b : alcohol

RESULTS

Friction coefficient				Wear in $10^{-15} m^2/N$		Lifetime ~~after running in~~ (for layers) in 10^3 revolutions			
start	~~after running in~~								
	mini	mean	maxi	a	b	μ< 0.1	μ< 0.2	μ< 0.3	μ<0.5
0.47	0.41	→	1.07	deposit	35	0	0	0	0.07

Characteristic diagram

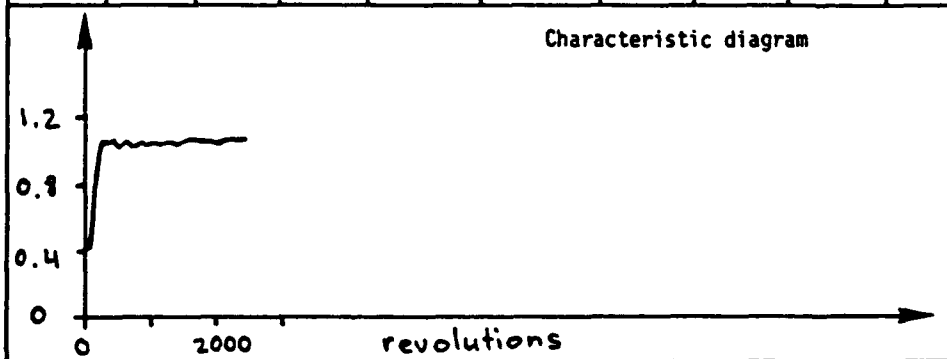

CHARACTERISTICS OF PARTNERS

	Geometry	Substrat	Layer (s)	Surface
a	disc 102	AISI 440/TiC/ TiO2 unpolished		as coated
b	ball	AISI 52100	-	polished

FURTHER INFORMATIONS

for a ☐ b ☐

For the other partner see data sheet Nr.

Supplier: Running-in: revolutions

Z-74

CENTRE SUISSE D'ELECTRONIQUE ET DE MICROTECHNIQUE S.A. - Recherche et Développement -

DATA SHEET Nr. T 103 (RT - Ar) November 7, 1989

FRICTION TYPE

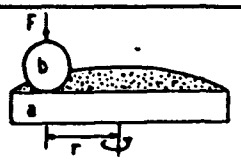

X

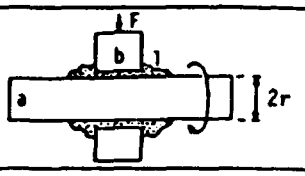

TRIBOLOGICAL SYSTEM

Lubrication ☒ without ☐ with

Load : F = 5 N

Test duration : 20'000 revolutions
0.50 km

Radius : r = 4 mm

Speed : 10 cm/s

Environment ☐ vacuum : 10^{-} Torr
☒ gas : Ar Humidity: < 2% RH Temperature: 24 °C

TiO_2 (a) / Steel (b)

Cleaning a : compressed dry air
b : alcohol

RESULTS

Friction coefficient start	Friction coefficient after running-in mini	mean	maxi	Wear in $10^{-15}m^2/N$ a	b	Lifetime after running-in (for layers) in 10^3 revolutions $\mu < 0.1$	$\mu < 0.2$	$\mu < 0.3$	$\mu < 0.5$
0.82	0.27	-->	0.68	deposit	1.5	0	0	0.8	11

Characteristic diagram

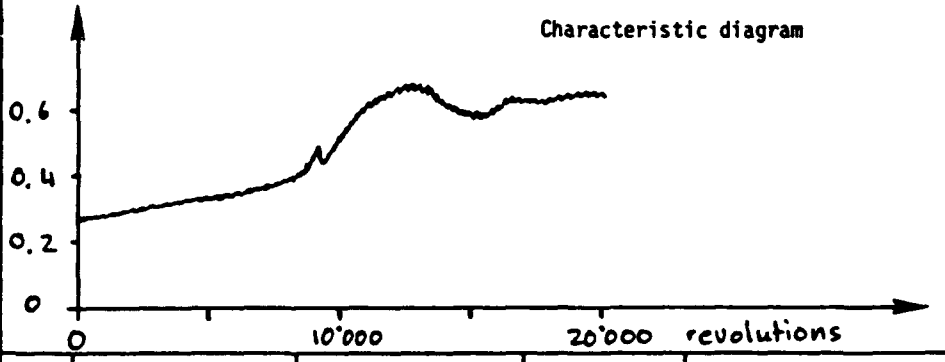

CHARACTERISTICS OF PARTNERS

	Geometry	Substrat	Layer (s)	Surface
a	disc 103	AISI 440/TiC/TiO_2 unpolished		as coated
b	ball	AISI 52.100	-	polished

FURTHER INFORMATIONS

for a ☐ b ☐

For the other partner see data sheet Nr.

Supplier: Running-in: revolutions

2-75

DATA SHEET Nr. T 104 (RT - Ar) November 7, 1989

FRICTION TYPE

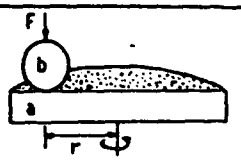

X

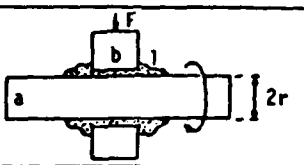

TRIBOLOGICAL SYSTEM

Lubrication ☒ without ☐ with

Load : F = 5 N

Test duration : 5000 revolutions 0.13 km

Radius : r = 4 mm

Speed : 10 cm/s

Environment ☐ vacuum : 10^{-} Torr ☒ gas : Ar Humidity: < 2% RH Temperature: 24 °C

TiO_2 (a) / Steel (b)

Cleaning a : compressed dry air
b : alcohol

RESULTS

Friction coefficient start	Friction coefficient after running-in mini	mean	maxi	Wear in $10^{-15}m^2/N$ a	b	Lifetime after running-in (for layers) in 10^3 revolutions $\mu < 0.1$	$\mu < 0.2$	$\mu < 0.3$	$\mu < 0.5$
0.92	0.27	→	0.63	deposit	2.4	0	0	0.16	2.9

Characteristic diagram

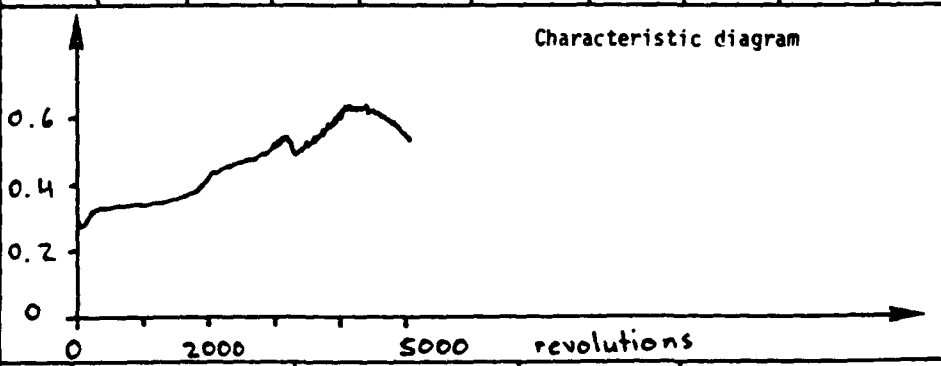

CHARACTERISTICS OF PARTNERS

	Geometry	Substrat	Layer (s)	Surface
a	disc 104	AISI 440/TiC/TiO_2 unpolished		as coated
b	ball	AISI 52.100	-	polished

FURTHER INFORMATIONS for a ☐ b ☐

For the other partner see data sheet Nr.

Supplier: Running-in: revolutions

Z-76

CENTRE SUISSE D'ELECTRONIQUE ET DE MICROTECHNIQUE S.A. - Recherche et Développement -

DATA SHEET Nr. T 105 (RT - Ar) November 7, 1989

FRICTION TYPE

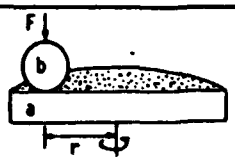

X

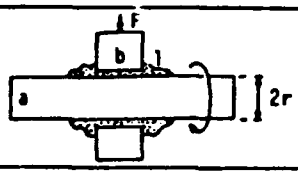

TRIBOLOGICAL SYSTEM

Lubrication ☒ without ☐ with

Load : F = 5 N

Test duration : 5000 revolutions

0.13 km

Radius : r = 4 mm

Speed : 10 cm/s

Environment ☐ vacuum : 10^{-} Torr

☒ gas : Ar Humidity: < 2% RH Temperature: 24 °C

TiO_2 (a) / Steel (b)

Cleaning a : compressed dry air

b : alcohol

RESULTS

Friction coefficient				Wear in $10^{-15}m^2/N$		Lifetime ~~after running in~~ (for layers) in 10^3 revolutions			
start	~~after running in~~								
	mini	mean	maxi	a	b	μ< 0.1	μ< 0.2	μ< 0.3	μ<0.5
0.91	0.23	→	0.41	deposit	1.1	0	0	0.05	>5

Characteristic diagram

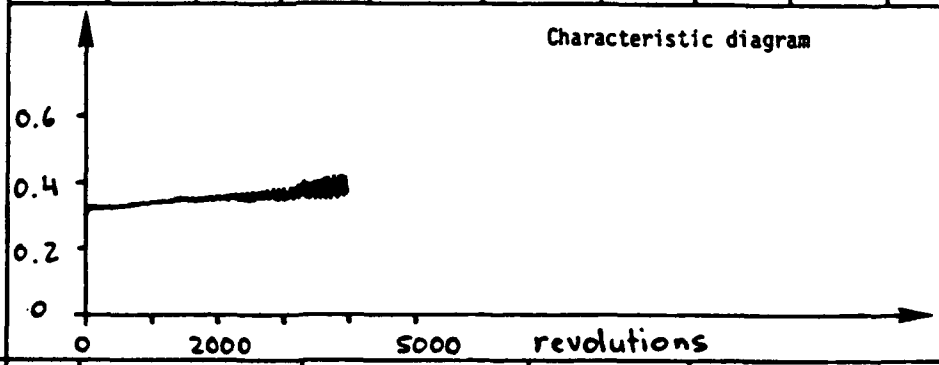

CHARACTERISTICS OF PARTNERS

	Geometry	Substrat	Layer (s)	Surface
a	disc 105	AISI 440/TiC/TiO_2 unpolished		as coated
b	ball	AISI 52.100	-	polished

FURTHER INFORMATIONS

for a ☐ b ☐

For the other partner see data sheet Nr.

Supplier: Running-in: revolutions

Z-77

CENTRE SUISSE D'ELECTRONIQUE ET DE MICROTECHNIQUE S.A. - Recherche et Développement -

DATA SHEET Nr. T 106 (RT - Ar) November 7, 1989

FRICTION TYPE

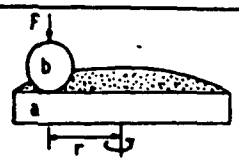

X

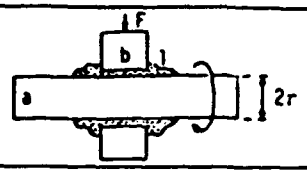

TRIBOLOGICAL SYSTEM

Lubrication ☒ without ☐ with

Load : F = 5 N

Test duration : 9420 revolutions

0.24 km

Radius : r = 4 mm

Speed : 10 cm/s

Environment ☐ vacuum : 10^{-} Torr

☒ gas : Ar Humidity: < 2% RH Temperature: 24 °C

TiO_2 (a) / Steel (b)

Cleaning a : compressed dry air

b : alcohol

RESULTS

Friction coefficient				Wear in $10^{-15} m^2/N$		Lifetime ~~after running-in~~ (for layers) in 10^3 revolutions			
start	~~after running-in~~								
	mini	mean	maxi	a	b	μ< 0.1	μ< 0.2	μ< 0.3	μ<0.5
0.74	0.30	→	0.60	deposit	2.2	0	0	0	7.6

Characteristic diagram

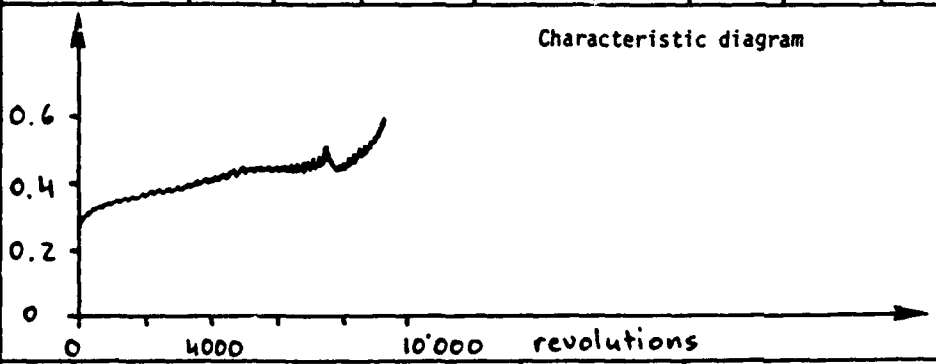

CHARACTERISTICS OF PARTNERS

	Geometry	Substrat	Layer (s)	Surface
a	disc 106	AISI 440/TiC/ TiO_2 unpolished		as coated
b	ball	AISI 52.100	-	polished

FURTHER INFORMATIONS

for a ☐ b ☐

For the other partner see data sheet Nr.

Supplier: Running-in: revolutions

Z-78

CENTRE SUISSE D'ELECTRONIQUE ET DE MICROTECHNIQUE S.A. - Recherche et Développement -

DATA SHEET Nr. T 107 (RT - Ar) November 8, 1989

FRICTION TYPE

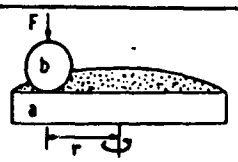

X

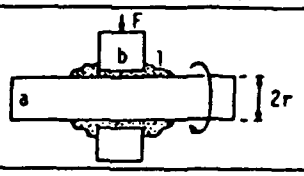

TRIBOLOGICAL SYSTEM

Lubrication ☒ without ☐ with

Load : F = 5 N

Test duration : 2960 revolutions
0.074 km

Radius : r = 4 mm

Speed : 10 cm/s

Environment ☐ vacuum : 10^{-} Torr
☒ gas : Ar Humidity: < 2% RH Temperature: 22 °C

TiO_2 (a) / Steel (b)

Cleaning a : compressed dry air
b : alcohol

RESULTS

Friction coefficient				Wear in $10^{-15} m^2/N$		Lifetime ~~after running-in~~ (for layers) in 10^3 revolutions			
start	~~after running-in~~								
	mini	mean	maxi	a	b	μ< 0.1	μ< 0.2	μ< 0.3	μ<0.5
0.47	0.47	→	→	deposit	18	0	0	0	0.05

Characteristic diagram

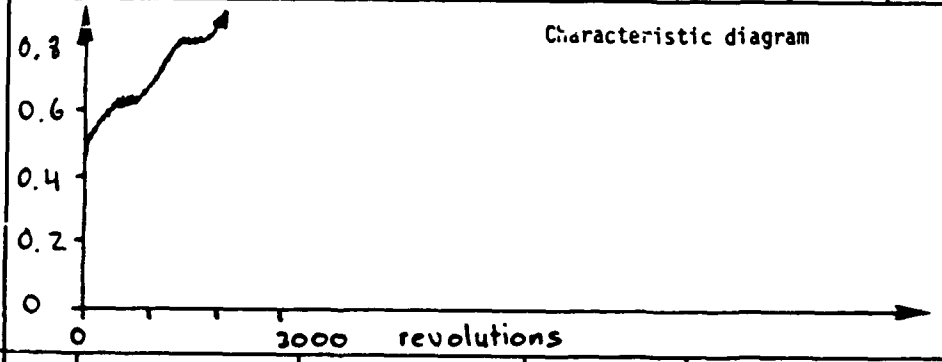

CHARACTERISTICS OF PARTNERS

	Geometry	Substrat	Layer (s)	Surface
a	disc 107	AISI 440/TiC/ TiC_2 unpolished		as coated
b	ball	AISI 52.100	-	polished

FURTHER INFORMATIONS

for a ☐ b ☐

For the other partner see data sheet Nr.

Supplier:

Running-in: revolutions

Z-79

DATA SHEET Nr. T 101 (RT - Ar) November 13, 1989

FRICTION TYPE

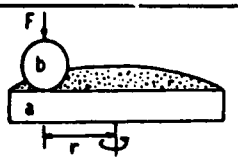

X

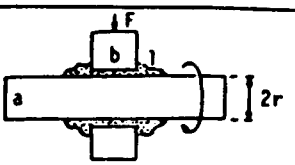

TRIBOLOGICAL SYSTEM

Lubrication ☒ without ☐ with

Load : F = 5 N

Test duration : 5000 revolutions
0.20 km

Radius : r = 6.5 mm

Speed : 10 cm/s

Environment ☐ vacuum : 10^{-} Torr
☒ gas : Ar Humidity: < 2% RH Temperature: 22 °C

$\frac{TiO_2}{a} / \frac{Steel}{b}$

Cleaning a : alcohol
b : "

RESULTS

Friction coefficient				Wear in $10^{-15}m^2/N$		Lifetime ~~after running in~~ (for layers) in 10^3 revolutions			
start	~~after running in~~								
	mini	mean	maxi	a	b	μ< 0.1	μ< 0.2	μ< 0.3	μ<0.5
0.18	0.18	↔	0.60	1.6	1.2	0	0.005	0.08	1.6

Characteristic diagram

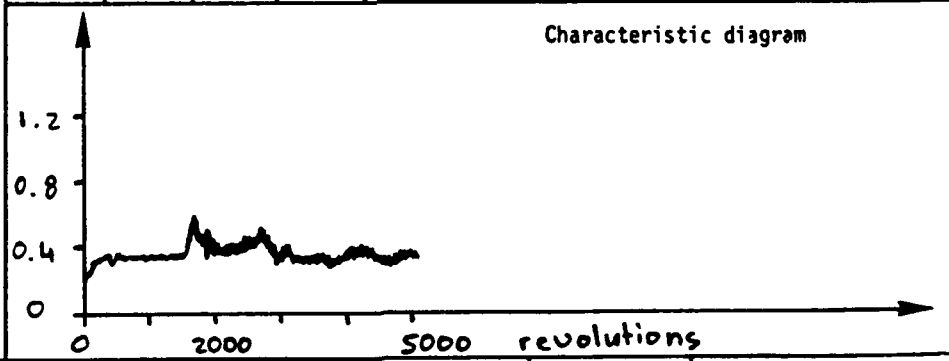

CHARACTERISTICS OF PARTNERS

	Geometry	Substrat	Layer (s)	Surface
a	disc 101	AISI 440C/TiO_2 polished		polished
b	ball	AISI 52.100	-	polished

FURTHER INFORMATIONS

for a ☐ b ☐

For the other partner see data sheet Nr.

Supplier: Running-in: revolutions

Z-80

CENTRE SUISSE D'ELECTRONIQUE ET DE MICROTECHNIQUE S.A. - Recherche et Développement -

DATA SHEET Nr. T 102 (RT - Ar) November 13, 1989

FRICTION TYPE

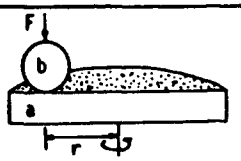

X

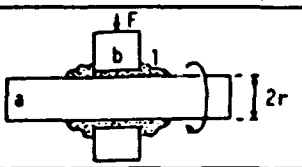

TRIBOLOGICAL SYSTEM

Lubrication ☒ without ☐ with

Load : F = 5 N

Test duration : 2375 revolutions
0.097 km

Radius : r = 6.5 mm

Speed : 10 cm/s

Environment ☐ vacuum : 10^{-} Torr
☒ gas : Ar Humidity: < 2% RH Temperature: 22 °C

$\frac{TiO_2}{a} / \frac{Acier}{b}$

Cleaning a : alcohol
b : "

RESULTS

Friction coefficient				Wear in $10^{-15} m^2/N$		Lifetime ~~after running-in~~ (for layers) in 10^3 revolutions			
start	~~after running-in~~								
	mini	mean	maxi	a	b	μ< 0.1	μ< 0.2	μ< 0.3	μ<0.5
0.21	0.21	→	0.54	10	1.5	0	0	0.05	0.8

Characteristic diagram

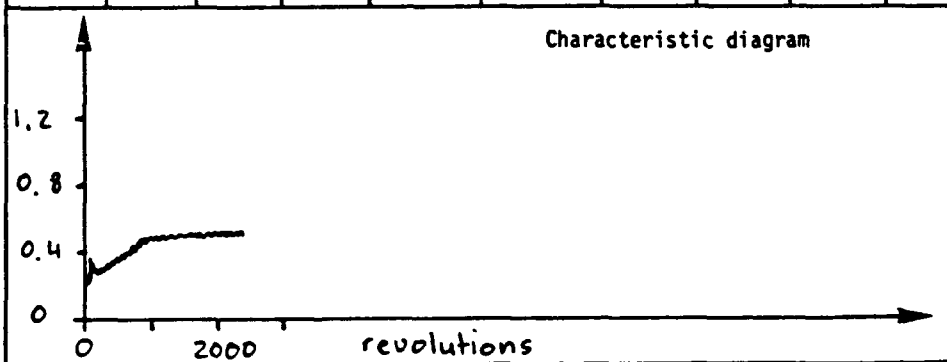

CHARACTERISTICS OF PARTNERS

	Geometry	Substrat	Layer (s)	Surface
a	disc 102	AISI 440C/TiO_2 polished		polished
b	ball	AISI 52.100	-	polished

FURTHER INFORMATIONS

for a ☐ b ☐

For the other partner see data sheet Nr.

Supplier: Running-in: revolutions

DATA SHEET Nr. T 107 (RT - Ar)

November 13, 1989

FRICTION TYPE

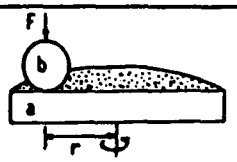

X

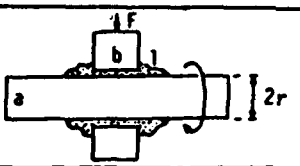

TRIBOLOGICAL SYSTEM

Lubrication ☒ without ☐ with

TiO_2 (a) / Steel (b)

Load : F = 5 N

Test duration : 2960 revolutions

0.12 km

Cleaning a : alcohol

b : "

Radius : r = 6.5 mm

Speed : 10 cm/s

Environment ☐ vacuum : 10^{-} Torr

☒ gas : Ar Humidity: < 2% RH Temperature: 22 °C

RESULTS

Friction coefficient				Wear in $10^{-15} m^2/N$		Lifetime ~~after running-in~~ (for layers) in 10^3 revolutions			
start	~~after running-in~~								
	mini	mean	maxi	a	b	μ< 0.1	μ< 0.2	μ< 0.3	μ<0.5
0.26	0.33	0.35	0.49	206	2.0	0	0	0.005	>2.9

Characteristic diagram

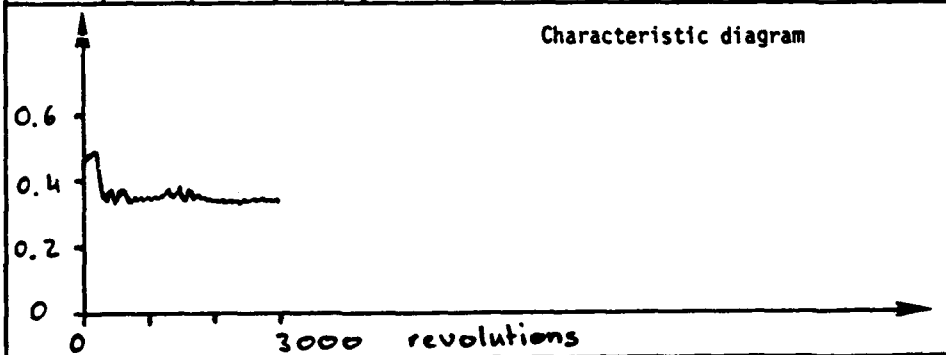

CHARACTERISTICS OF PARTNERS

	Geometry	Substrat	Layer (s)	Surface
a	disc 107	AISI 440C/TiO_2 polished		polished
b	ball	AISI 52.100	–	polished

FURTHER INFORMATIONS

Supplier:

Running-in: revolutions

for a ☐ b ☐

For the other partner see data sheet Nr.

APPENDIX AA

B.G. Bovard, S. Chiao, and H. Angus Macleod, "Deposition of titanium Oxide Films of Controlled Stoichiometries ," Final Report, U. of Arizona Optical Sciences Center; Tucson, AZ, Hughes P.O. M9-315734-KKD

Deposition of Titanium Oxide Films of Controlled Stoichiometries

Final report

February 9th, 1990

Bertrand G. Bovard, Shuchung Chiao, and H. Angus Macleod

Optical Sciences Center
University of Arizona
Tucson AZ 85721

Abstract

The deposition of thin titanium oxide films of controlled oxygen to titanium ratios ranging from 1.6 to 2.0, is demonstrated. The films are grown by reactive electron beam evaporation. Chemical composition is established by Rutherford Backscattering Spectrometry.

1. Purpose of the project

The purpose of this project was to establish whether the oxygen to titanium ratio of thin titanium oxide films grown by reactive evaporation could be controlled by a proper choice of deposition parameters. Five sets of one micron thick films of five different oxygen to titanium ratios in the 1.6 to 2.0 range had to be deposited on fused silica triboflats.

2. Approach

Because of its high refractive index, its transparency in the visible and near infrared range,[1] its chemical resistance, and its good mechanical properties, titanium dioxide is a very widely used material for optical coatings. It is often used in quarterwave stacks where it plays the role of the high refractive index material while silicon dioxide is the low refractive index material. The typical thickness of the titanium dioxide layer is around 50 to 100 nm depending on the wavelength of interest. These attractive properties are balanced by a large sensitivity of the material to deposition and annealing conditions. Very well known in the optical thin films community this problem was the purpose of a panel discussion at the 1986 Annual Optical Society of America Meeting where various groups and companies in the whole World were invited to present their results on the growth and characterization of thin films of titanium dioxide. Refractive indices and extinction coefficients were found to cover a very wide range of values. Inhomogeneity, the variation of the refractive index between the substrate/film interface and the air/film interface, was also shown to vary from sample to sample. This suggests that a very large range of stable microstructures can be achieved by these different processes making it very difficult to transpose deposition conditions from one laboratory to another.

A variety of processes exists and are currently used for the deposition of titanium oxide films. They include reactive evaporation,[2] ion-assisted deposition,[3] low-voltage reactive ion plating,[4] radio frequency sputtering,[5] dual ion-beam sputtering,[6] chemical vapor deposition,[7] and sol-gel techniques. The most widely used in the optical thin films industry is probably reactive evaporation, the evaporation in an oxygen background of a material that can be any oxide from pure titanium to TiO_2 itself. Since oxygen is provided to the film during its growth, intermediate oxides such as TiO, Ti_2O_3, Ti_3O_5 are very satisfactory.[2]

Our laboratory is equipped to grow thin films of titanium dioxide by reactive evaporation, ion-assisted deposition, and rf-sputtering. The process used in this study was reactive evaporation.

The reactive evaporation of titanium dioxide films for optical applications has been largely investigated. It relies on the choice of three main parameters: the deposition rate, the substrate temperature, and the oxygen partial pressure in the deposition chamber. Their proper choice determines whether the films are opaque, or transparent and proper for optical applications. In particular oxygen deficiency produces films of high absorption and poor optical interest.

In this work the interest is not defined by the optical properties but rather by the mechanical properties of the material. The focus of the fabrication process is on the ability to produce films of various stoichiometries ranging from 1.6 to 2.0 (oxygen to titanium ratio). The approach is the tuning of this ratio by an appropriate choice of the oxygen partial pressure. The starting material was Ti_2O_3 with an oxygen to titanium ratio of 1.5 close to the minimum value of 1.6. Supply of extra oxygen was expected to increase this ratio from 1.6 to the upper value of 2.0. The elemental analysis necessary to establish the corresponding oxygen to titanium ratio was performed by Rutherford backscattering spectrometry[8] in the Physics Department of the University of Arizona.

3. Experimental description

The films were deposited in a Balzers 760 box-coater equipped with a Cryo-pump (base vacuum 5×10^{-7} mbar) and a large number of accessories including two electron guns, two resistive sources, a substrate rotator, a direct optical monitoring system in reflection and transmission, a quartz-crystal deposition rate controller (closed loop), two additional deposition rate monitoring systems (open loop), a temperature regulation system with substrate heaters and thermocouple for chamber temperature measurements, a pressure regulation system for reactive evaporation, a 12-cm Kaufman ion source for reactive or non-reactive ion-assisted deposition, a Faraday cup for ion current density measurements, and a quadrupole mass spectrometer for residual gas analysis. The equipment relevant to this study was limited to one electron beam gun, the quartz-crystal deposition rate controller, the chamber temperature controller, and the pressure regulating equipment. The deposition system is also equipped to

allow the growth of 4 independent samples in a single vacuum. A set of masks has been designed so films can be grown one at a time on 4 different substrates without venting the system. This feature is very useful in investigations of process parameters.

As was already stated, the starting material was Ti_2O_3 evaporated from a molybdenum liner by an electron beam gun. The deposition rate was fixed at 0.4 nm/sec based on previous experience with titanium oxide films, length of deposition, and stability of the melt. The choice of the two other parameters: temperature and oxygen partial pressure was based on the measurement of the oxygen to titanium ratio by elemental analysis using Rutherford Backscattering Spectrometry (RBS). To achieve an optimum accuracy with this technique, the films should be grown on substrates that are lighter than the material to be analyzed. Since oxygen is present in the films of interest, carbon substrates have to be used. A second requirement of RBS is the use of film thicknesses such that the peaks produced by the backscattering of the alpha particles by the various elements present in the coating do not overlap. The overlap of the oxygen peaks on the carbon substrate peak had to be avoided and it is the reason why 100 nm thick films were produced for the first part of this project.

Since the films final thicknesses were 1 μm , supplementary deposition runs had to be performed to produce the thicker samples. The success of our project depended therefore on three assumptions: the process had to be repeatable i. e. the same process parameters would produce the same oxygen to titanium ratio, the films compositions should not be affected by the thickness of the films i. e. the film composition would not vary with time during the growth, and finally the film composition should not be affected by the choice of the substrate. The first assumption was the only one checked in this feasability study and the results are presented in the results section. This work determined the choice of the chamber temperature at 200°C. The oxygen partial pressure was then tuned to produce films with oxygen to titanium ratios in the proper range.

4. Results

4. 1. Study of the repeatability: optical properties and chemical composition

The repeatability study was designed to help us establish whether the chemical composition could be controlled in a satisfactory way. The deposition chamber is

equipped with a temperature controller that keeps chamber temperature constant when the heat load is negligible. Since there is no mechanism to cool the chamber, a heat load such as the radiation emitted by a molten pool of refractory oxide produces a temperature increase that is difficult to minimize. The first series of depositions were performed in the same residual vacuum in sequence without waiting for the system to cool between deposition of successive layers. The optical properties and oxygen to titanium ratios are presented in figure 1. The elemental analysis showed that the oxygen to titanium ratio was not affected by these variations the way the optical properties were. This observation suggested that ambient temperature are not a good choice for the substrate temperature because it cannot be guaranteed during deposition and second that the optical properties are extremely sensitive to temperature while the oxygen to titanium ratio is not. Another interesting feature was the finding that titanium oxide could be absorbing although the oxygen to titanium ratio was 2. These facts are not all understood at this stage and they deserve further investigation. Clearly there is a microstructural parameter that can be upset when substrate temperatures are varied and this parameter is not the oxygen to titanium ratio. To prevent the possibly negative effect of this unknown parameter we decided to add the optical properties to our list of repeatability criteria. Repeatability was achieved when the chamber was allowed to cool between successive depositions (figure 2). At 200°C the optical properties were also found repeatable (figure 3) and this temperature was preferred over the lower substrate temperature for the continuation of the project since temperature stability was easier to guarantee.

Table 1 presents a list of samples, deposition conditions, and oxygen to titanium ratios. The repeatability of the oxygen to titanium ratio is ±0.02 while the uncertainty is also ±0.02. These values are very satisfactory and show that provided chemical composition is not a function of substrate and thickness, process parameters determined to produce a particular composition in 0.1 μm thick films will produce the same composition in thicker films.

4. 2. Influence of the oxygen partial pressure

The influence of the oxygen partial pressure on the final properties of the films was the key to the success of this project. RBS showed that the oxygen to titanium ratio can be tuned by the proper choice of the oxygen partial pressure (figure 4). A similar result was obtained optically (figures 5 and 6). The low values of oxygen partial pressure yielded very opaque films while the higher values yielded more transparent films. An interesting feature is the position of the absorption edge. At low values of oxygen pressure the edge is located more to the blue side of the spectrum than at higher values. Since all films have been grown to have the same thicknesses it is safe to state that this difference is probably related to an actual property of the material rather than a thickness effect. This feature cannot be discussed any further because of the lack of appropriate measurements but it is now receiving more attention.

5. Deposition of the samples

The parameters needed for the deposition of films of various stoichiometries being established with RBS another set of deposition runs had to be performed to obtain thicker films. This task was less successful than the first one. The large thicknesses of 1 μm led to cracking and they had to be reduced. Attempts at 0.5 μm were unsuccessful. It is only at 0.25 μm that mechanical integrity could finally be achieved. The reasons for this mechanical failure are not clear and would deserve further investigation. The failure mode was characteristic of tensile cracking. The stress in thin films is usually decomposed into three components: the intrinsic stress due to the growth mechanism away for the thermodynamical equilibrium conditions, the thermal stress due to the expansion coefficient mismatch between substrate and thin film material, and the external stress due to external forces such as an applied load. Most thin films grown by thermal evaporation are tensile while films produced by sputtering or ion-assisted deposition can be compressive. There are reports in the literature of tensile cracking in titanium dioxide films produced by reactive evaporation.[9,10] Cracking is also reported for 0.5 μm thick films produced by chemical vapor deposition.[7] The sensitivity of thin films to atmospheric moisture is largely documented in the literature. Thin films produced by thermal evaporation suffer from a columnar void structure. Moisture can be adsorbed in these voids modifying the optical and mechanical properties of the film. Moisture adsorption can be dissociative or not. In the case of silicon dioxide it is established that the polar nature of the water molecule can lead to the breaking of

strained Si-O-Si chains by the formation of (Si–O–H H–O–Si) groups that lead to the formation of a crack. Diffusion of water inside the crack can lead to further propagation.[11] Whether the titanium oxide films produced by reactive evaporation behave in a similar way is not established and the nature of water adsorption, dissociative or non-dissociative, by titanium dioxide seems to remain a topic of research.[12] In the investigation of other materials used for optical applications, workers have reported large changes in stress during exposure to atmosphere[13] leading to mechanical failure. These observations have encouraged the development of ion-assisted processes such as ion-assisted deposition, low voltage ion plating, an ion-beam sputtering. All these processes have been successful in eliminating the porosity problem common to all films but ion-assisted deposition remains the only process that allows control of the stress by proper choice of the growth parameters.[14] Cracking could also be due to a thermal coefficient mismatch between the fused silica substrate and the titanium oxide film. Finally a third possibility is the occurrence of a phase transformation. The transformations from amorphous to anatase and anatase to rutile involve an increase in density that can lead to an increase in tensile stress followed by cracking. Published results indicate that titanium oxide films produced at temperature around 200°C are amorphous.[2,6] A possible phase transformation to rutile or anatase after deposition during cooling is therefore unlikely and this could be checked by x-ray diffraction.

The study of the origin of cracking was beyond the scope of this project and would require in situ stress measurements to establish whether cracking occurred during growth (intrinsic stress), during cool down (thermal stress), or during exposure to atmosphere (adsorption of moisture). Without this investigation it is difficult to predict what should be done to avoid this failure and it is difficult to understand the mechanisms involved. Possible solutions include changes in substrate temperature, cooling speed, post-deposition bake, dry-nitrogen venting, use of a glow discharge prior to deposition, and use of ion-assisted deposition.

Rather than starting a full investigation of this phenomenon which would be beyond the possibilities of the resources allocated to this effort we decided to grow thinner films of 0.25 μm. This effort was successful and the samples were produced for delivery.

The final samples delivered to Hughes at the end of this project are:

- two sets of nominally 1 μm thick films of five different compositions in the 1.6 to 2.0 range (see table 2);

- two sets of nominally 0.25 μm thick films of five different compositions in the 1.6 to 2.0 range (see table 3).

6. Conclusion

Reactive evaporation can be used to grow thin films of titanium oxides with various oxygen to titanium ratios. The use of Rutherford backscattering spectrometry allowed us to determine which conditions were appropriate. The films obtained by this technique were very pure and no other element were detected. Hydrogen remained the only unknown since RBS is not sensitive to this element and this uncertainty can be lifted by nuclear reaction analysis. The mechanical properties seem very critical at this stage since cracking stopped us from delivering 1 μm thick samples. We are working on an in-situ stress measurement interferometer to establish the evolution of stress during growth, post-deposition bake, cool down, and exposure to atmosphere. This device will also enable us to study the effect of ion-assisted deposition on stress during growth.

The transformation of the amorphous films to crystalline rutile was not attempted in this project. The stability of the oxygen to titanium ratio at high temperatures and the mechanical integrity of the films are a concern if high temperatures have to be used during annealing. The possibility of promoting rutile growth during deposition could be investigated. Pulker reports that the use of pure titanium as a starting material with substrates at 350°C or TiO at 380°C leads to the formation of rutile exclusively.[2] With other oxides, substrate temperatures such as 700°C or higher are needed to observe the formation of rutile. Pulker adds that the oxidation of the solid phase TiO or of the condensing molecules always leads to the formation of anatase. The only starting material remaining stable from one deposition to another appears to be pure titanium: it produces only titanium species in the vapor phase and the residues in the crucible remain pure titanium. All other materials produce higher level oxides in their vapors and in their residues and thus favor the formation of anatase.

run	sample	P_{O_2} (X 10^{-6} mbar)	T_1 (°C)	T_2 (°C)	O/Ti	Notes
941	A	none	218	223	1.55±0.01	(*)
941	B	none	219	224	1.57±0.01	
941	C	none	213	220	1.57±0.01	
941	D	none	218	229	1.60±0.02	
942	A	none	40	71	1.61±0.02	
942	B	none	114	132	1.60±0.02	
942	C	none	95	116	1.60±0.02	
942	D	none	71	96	1.61±0.02	
943	A	80	216	222	1.96±0.02	
943	B	80	206	211	1.96±0.02	
943	C	80	223	238	1.99±0.02	
943	D	80	222	225	1.95±0.02	
944	A	80	54	82	2.05±0.02	
944	B	80	30	83	2.00±0.02	
944	C	80	106	129	1.99±0.02	
944	D	80	83	109	2.05±0.02	
945	A	80	42	65	N/A	
945	B	80	42	65	N/A	
945	C	80	41	65	N/A	
945	D	80	41	64	N/A	
948	A	200	206	210	N/A	50 nm thick
948	C	600	208	214	N/A	50 nm thick
948	D	800	212	216	N/A	50 nm thick
949	A	50	209	216	N/A	
949	B	20	204	221	N/A	
950	A	4	195	204	N/A	
950	B	6	194	209	N/A	
950	C	8	200	209	N/A	
951	A	4	203	210	1.74±0.02	(*)
951	B	8	202	211	1.79±0.02	(*)
951	C	20	201	211	1.91±0.02	(*)

Table 1: Evaluation of the repeatability of reactive evaporation.

run	sample	P_{O_2} (X 10^{-6} mbar)	T_1 (°C)	T_2 (°C)	O/Ti	Notes
952	A	500	195	205	2.04±0.02	
952	B	20	199	210	1.88±0.02	
952	C	8.5	196	208	1.85±0.02	
958		20	200	215	final sample	951 C
959		8	194	221	final sample	951 B
960		4	196	219	final sample	951 A
961		500	191	215	final sample	952 A
962		none	220	223	final sample	941

Table 1: Evaluation of the repeatability of reactive evaporation (continued)

Note: The (*) indicates that the set of deposition conditions was used in the final series of evaporation for the production of the 1 μm thick samples. T_1 and T_2 are starting and finishing temperature of the chamber.

Run A	O/Ti	Run B	P_{O_2}(mbar)
958	1.91±0.02	951c	2×10^{-5}
959	1.79±0.02	951b	8×10^{-6}
960	1.74±0.02	951a	4×10^{-6}
961	2.04±0.02	952a	5×10^{-4}
962	1.60±0.02	941d	none

Table 2: Deposition conditions of the 1 μm thick samples delivered to Hughes Aircraft at the completion of the project. "Run B" numbers correspond to the samples used for RBS while "run A" numbers correspond to the 1 μm thick samples. Deposition rates are 0.4 nm/second and chamber temperature is 200°C.

Run A	O/Ti	Run B	P_{O_2}(mbar)
1015	1.91±0.02	951c	2×10^{-5}
1016	1.79±0.02	951b	8×10^{-6}
1018	1.74±0.02	951a	4×10^{-6}
1014	2.04±0.02	952a	5×10^{-4}
1013	1.60±0.02	941d	none

Table 3: Deposition conditions and chemical compositions of the 0.25 μm thick samples. "Run B" numbers correspond to the samples used for RBS while "run A" numbers correspond to the 0.25 μm thick samples. Deposition rates are 0.4 nm/second and chamber temperature is 200°C.

References

1. D. C. Cronemeyer, "Electrical ond Optical Properties of Rutile Single Crystals," Phys. Rev. **87**, pp 876-886 (1952).

2. H. K. Pulker, G. Paesold, and E. Ritter, "Refractive indices of TiO_2 films produced by reactive evaporation of various titanium-oxide phases," Appl. Opt. **15**, pp 2986-2991 (1976).

3. P. J. Martin et al., "Ion-beam assisted deposition of optical films (A)," J. Opt. Soc. Am. **72**, pp 1733 (1982).

4. H. K. Pulker et al., "Properties of ion plated oxide films," J. Vac. Sci. Technol. A **3**, pp 2700-2701 (1985).

5. M. M. Yang, "Titanium-oxide films made by rf diode sputtering from a compound target," J. Appl. Phys. **62**, pp 1035-1041 (1987).

6. D. G. Howitt, and A. B. Harker, "The oriented growth of anatase in thin films of amorphous titania," J. Mater. Res. **2**, pp 201-210 (1987).

7. E. T. Fitzgibbons, K. J. Sladek, and W. H. Hartwig, "TiO_2 Films properties as a function of processing temperature," J. Electrochem. Soc. **119**, pp 735-739 (1972).

8. W. K. Chu, J. W. Mayer, and M. A. Nicolet, Backscattering Spectrometry, Academic Press, New York, 1976,

9. H. Sankur, and W. Gunning, "Sorbed water and intrinsic stress in composite TiO_2-SiO_2 films," J. Appl. Phys. **66**, pp 807-812 (1989).

10. W. Heitmann, "Properties of evaporated SiO2, SiOxNy, and TiO2, films," Applied Optics **10**, pp 2685-2689 (1971).

11. T. A. Michalske, and S. W. Freiman, "A Molecular Mechanism for Stress Corrosion in Vitreous Silica," J. Am. Ceram. Soc. **66**, pp 284-288 (1983).

12. S. Eriksen, P. D. Naylor, and R. G. Egdell, "The adsorption of water on $SrTiO_3$ and TiO_2: a reappraisal," Spectrochim. Acta **43A**, pp 1535-1538 (1987).

13. A. E. Ennos, "Stresses developed in optical film coatings," Appl. Opt. **5**, pp 51-61 (1966).

14. P. J. Martin, and R. P. Netterfield. "Optical Films Produced by Ion-Based Techniques," Progress in Optics, Ed. E. Wolf, Elsevier, New York, 1986, **23**, 113-182.

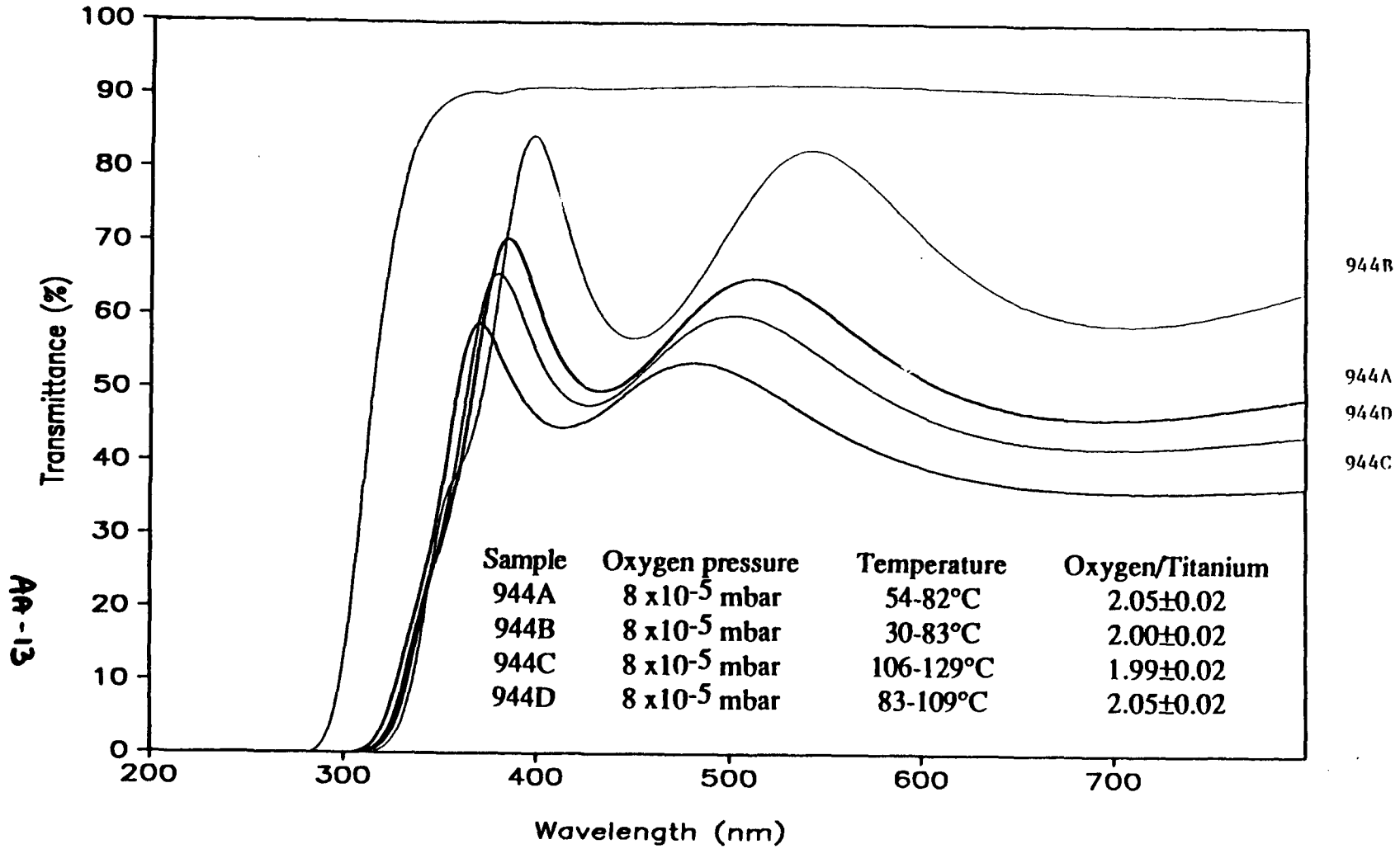

Figure 1: Transmission of four samples of titanium oxide deposited on glass in the same vacuum. $P(O_2)=8 \times 10^{-5}$ mbar, no heating and cooling. O/Ti is constant while the optical properties exhibit wide variations. RBS suggests the material is TiO_2 in disagreement with the optical properties.

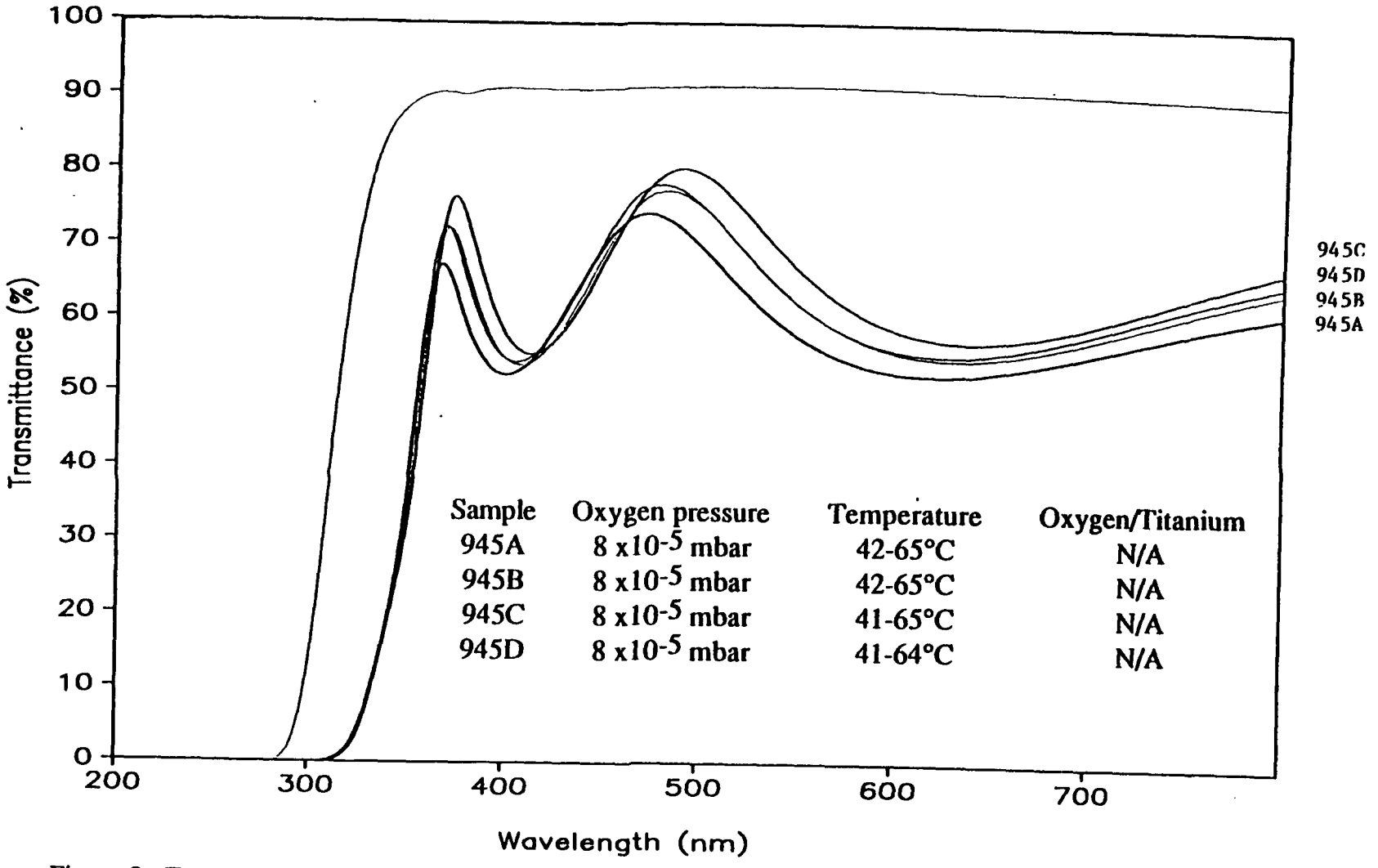

Figure 2: Transmission of four samples of titanium oxide deposited on glass in the same vacuum. $P(O_2)=8 \times 10^{-5}$ mbar, and the chamber was at room temperature. The chamber was cooled between each deposition so that starting temperature for all samples were the same.

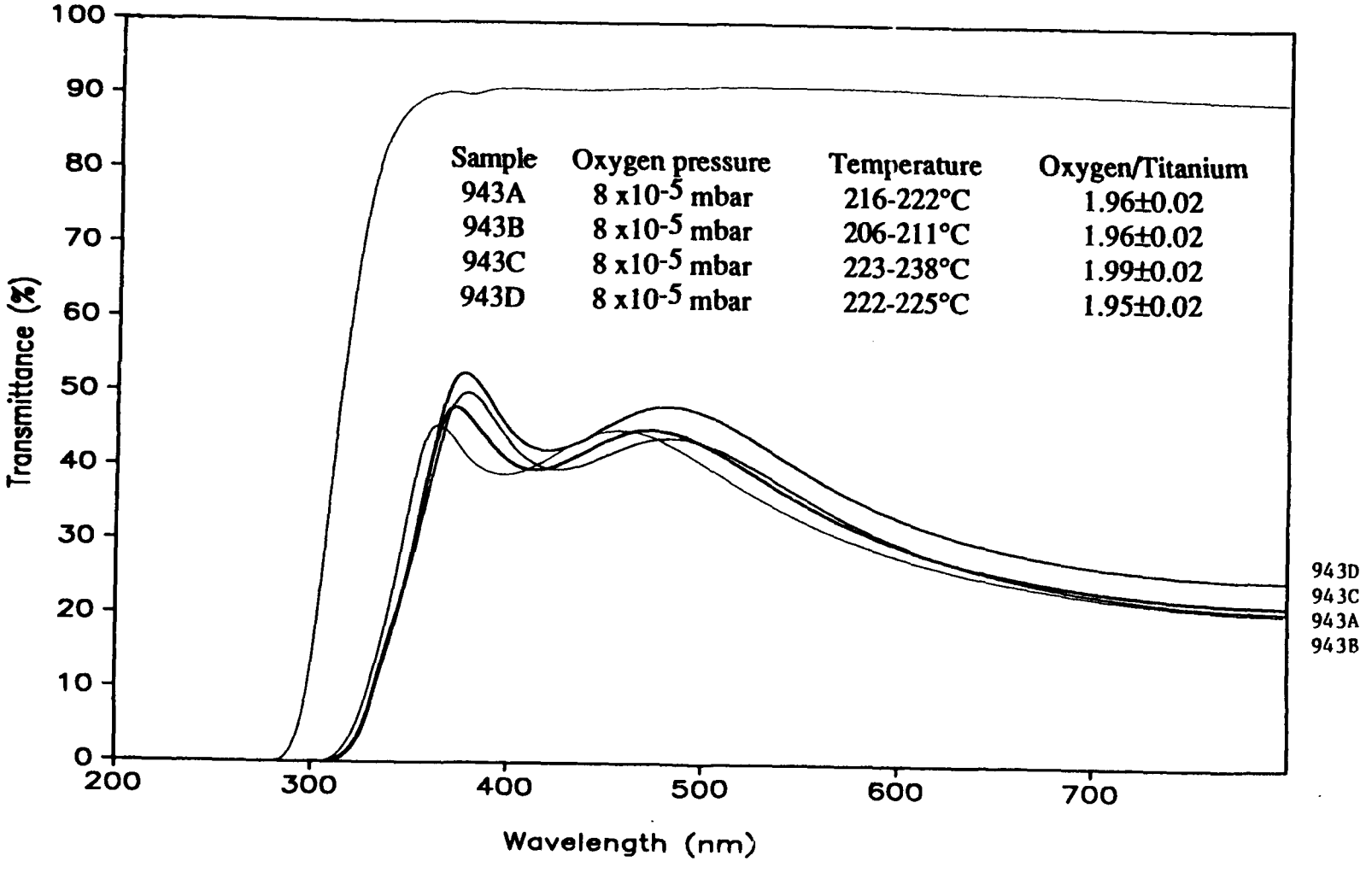

Figure 3: Transmission of 4 samples prepared at 200°C with P(O2)=8 x 10^{-5} mbar.

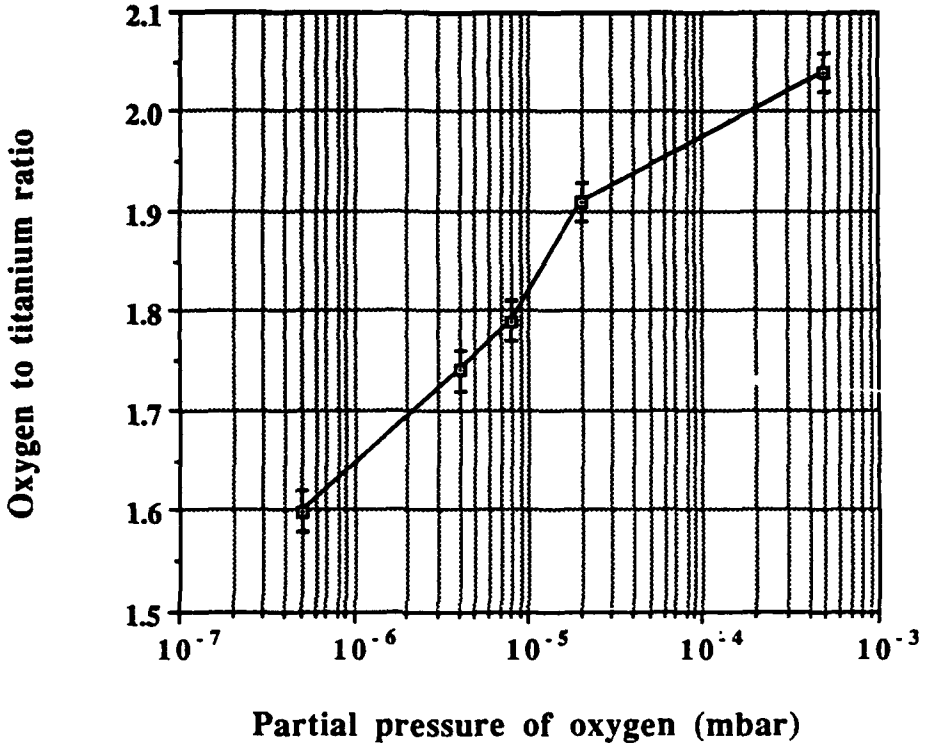

Figure 4: Oxygen to titanium ratio versus partial pressure of oxygen for the conditions chosen for the deposition of the final samples. Error bars do not include repeatability. No oxygen in the chamber is represented as 5.10^{-7} mbar.

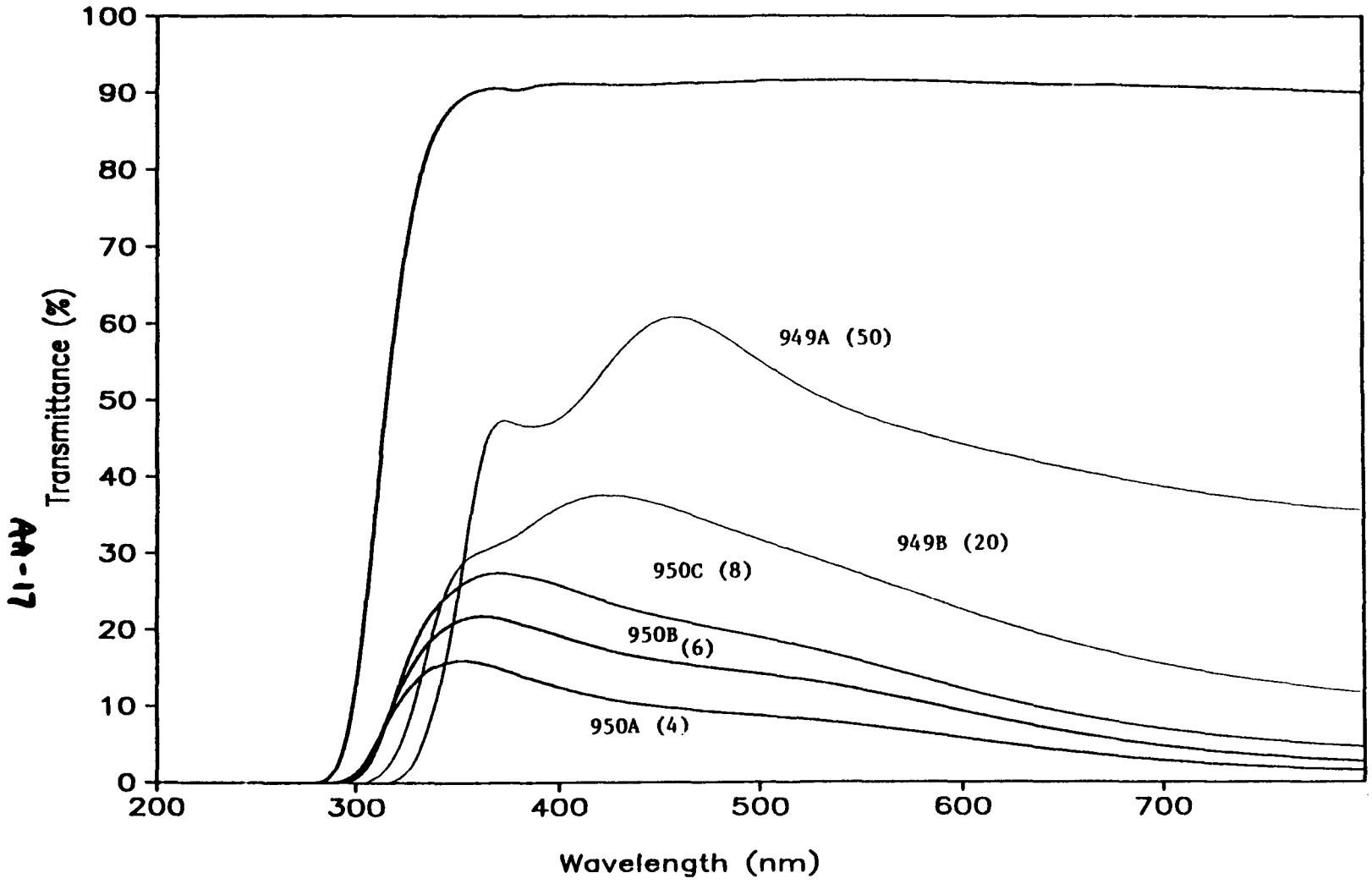

Figure 5: Influence of the oxygen partial pressure on the optical properties of titanium oxide films. Pressures are indicated between brackets (units of 10^{-6} mbar).

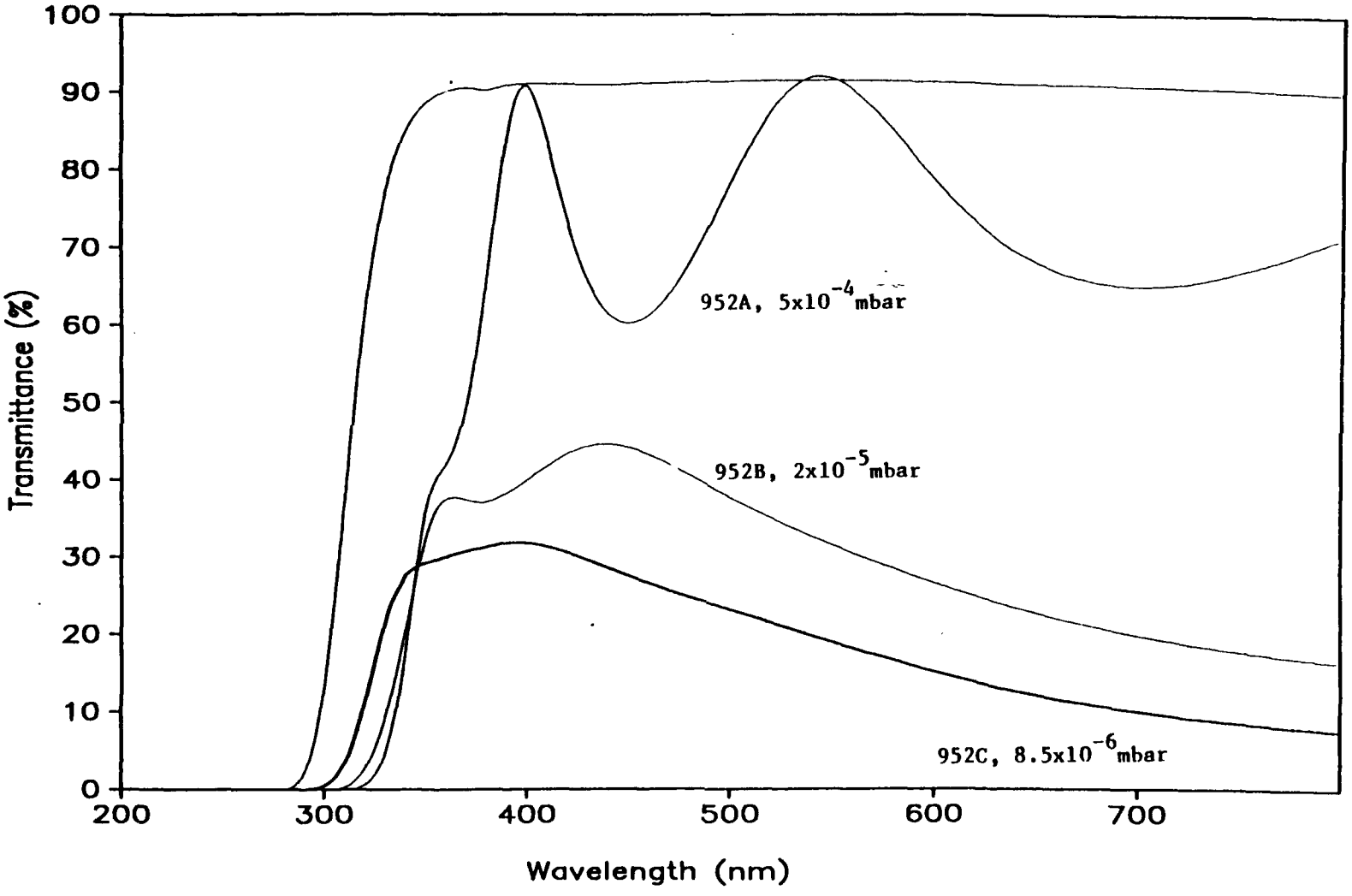

Figure 6: Transmission of three samples of titanium oxide deposited on glass in the same vacuum. The partial pressure of oxygen was varied and the chamber was nominally at 200°C. RBS indicates that the top curve corresponds to a superstoichiometric film with an oxygen to titanium ratio of 2.04. This ratio is 1.88 for 952B and 1.85 for 952C. Again the presence of hydrogen is possible.

APPENDIX BB

K.V. Ravi, et al. "Thin Film Diamond Deposition on Silicon Wafers for Tribological Testing," Final Report (Phase I), Crystallume, Palo Alto, CA, 29 December 1987, Hughes P.O. P9-519308-SLX

APPENDIX I

Thin Film Diamond Deposition on Silicon Wafers For Tribological Testing

Final Report

Submitted to:
Hughes Aircraft Corporation
Attention: Dr. Michael Gardos
By:
Crystallume
12/29/87

Telephone 415-494-0660

Crystallume
3180 Porter Drive, Suite 2 • Palo Alto, California 94304

Introduction

The objective of the research programme was to deposit good quality diamond films of thicknesses ranging from 1000 Å to 10,000Å over large area silicon substrates and characterize them. The films have been characterized with respect to factors such as structure, surface morphology and thickness and the wafers diced to the required dimensions prior to delivery to the prime contractor (Hughes) for tribological testing of the films.

This is the final report for the contract which will summarize the work done to date, review the results and discuss the findings. A concluding section will present some suggestions for further research whereby the superior mechanical properties of thin diamond films can be investigated for potential utility in a variety of applications.

Diamond Deposition

Diamond deposition is achieved by the plasma assisted decomposition of hydrocarbon gases in the presence of hydrogen. Plasma excitation is achieved by the use of DC techniques. Typical deposition conditions are as follows:

Deposition temperature	600- 800 °C
CH_4 volume %	0.3 to 1 %
H_2 volume %	99.7 to 99%
Flow rate	100 sccm

Substrates employed were <100> oriented polished silicon wafers and the deposition times were adjusted to achieve the desired film thickness.

Characterization

Extensive film characterization has been done with special reference to the bonding state of the film (sp^3 vs sp^2), the structure of the film with respect to grain size and morphology, the continuity of the film and the film thickness. Raman spectroscopy and scanning electron microscopy have been the predominant tools utilized in this work.

Crystallume
Telephone 415-494-0660
3180 Porter Drive, Suite 2 • Palo Alto, California 94304

Results and Discussion

The critical aspect of this research programme has been the development of an understanding of the nucleation and growth mechanisms at work in the deposition of very thin (<1 micron) diamond films deposited on silicon substrates. In particular the conditions that promote the nucleation of continuous films which also exhibit a predominance of the diamond phase have been sought. An additional important engineering variable that required significant development is the deposition of thin films over large areas of silicon with the objective of achieving uniform deposits over 4 in diameter silicon wafers. There has been no reported work on the deposition mechanisms of very thin diamond films and in particular the deposition of thin films over large areas.

Raman spectra and scanning electron micrographs of the films have been obtained as a function of position on 4 in diameter wafers. The key results from this work can be summarized as follows:

Optical observations of the surface of thin (<1 μ M) diamond films typically indicates the presence of two distinct regions in the films. These two regions are characterized by areas of the film that reflect light poorly and appear a dull grey in color and portions of the film that appear blue in color with less efficient light absorption. Several important variables govern the formation of these two phases of the material including the distribution of temperature, the plasma current density, and the active gases (methane and hydrogen) over the wafer surface. Extensive Raman spectroscopy and SEM analyses of these phases have been done and it has been determined that the grey, non reflecting region of the film is diamond, characterized by a granular surface structure and a sharp 1333 wavenumber peak in the Raman spectrum which is associated with sp^3 bonding of carbon.

Figures 1 and 2 show typical Raman spectra form these regions of the film. Although there exists some degree of sp^2 bonding in these films the fact that the sensitivity of the Raman technique is approximately 100 times greater to sp^2 bonding as compared to sp^3 bonding indicates that these films are predominantly diamond and should have the attendant physical properties including tribological properties. Adjacent to the Raman spectra are shown typical scanning electron micrographs of regions of the films that exhibit Raman spectra with a predominance of sp^3 bonding.There are no apparent voids in the film and the thicknesses in these regions also tend to be on the high side. The structure is

Crystallume
Telephone 415-494-0660
3180 Porter Drive, Suite 2 • Palo Alto, California 94304

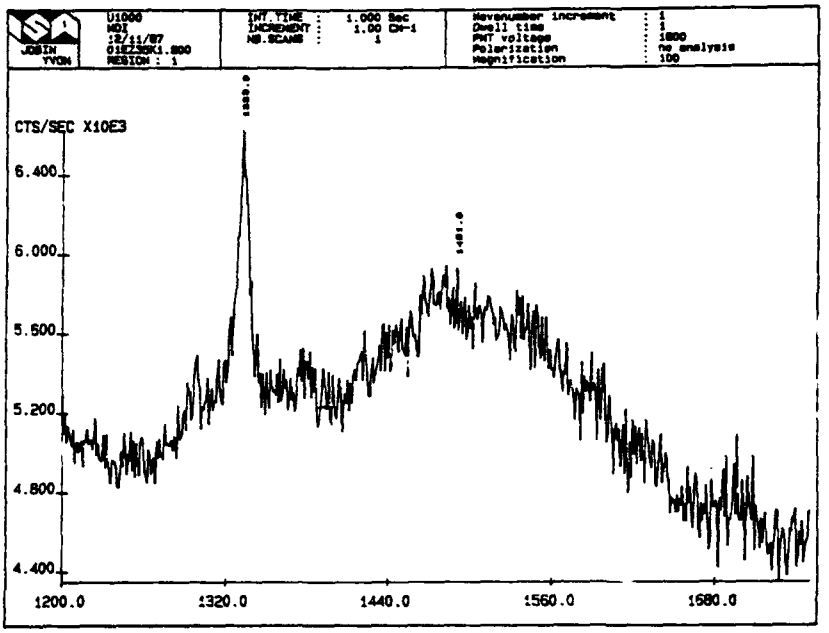

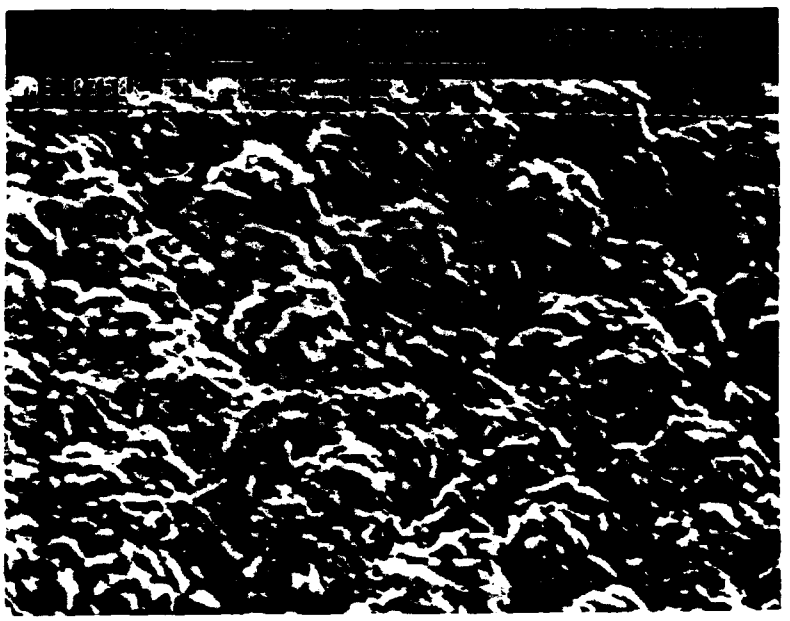

Figure.1 Raman spectrum and corresponding surface structure, as observed in a scanning electron microscope, of thin (<1 μ m) diamond film deposited on a 4 in diameter silicon wafer. The Raman spectrum shows the typical sharp peak at 1330 wave numbers. The broad peak centered around 1500 wavenumbers indicates the presence of small percentages of sp^2 bonded phase in the film. The SEM image shows the surface structure of such a film. The continuous film is characterized by rounded grains with some degree of facetting within them.

Crystallume
Telephone 415-494-0660
3180 Porter Drive, Suite 2 • Palo Alto, California 94304

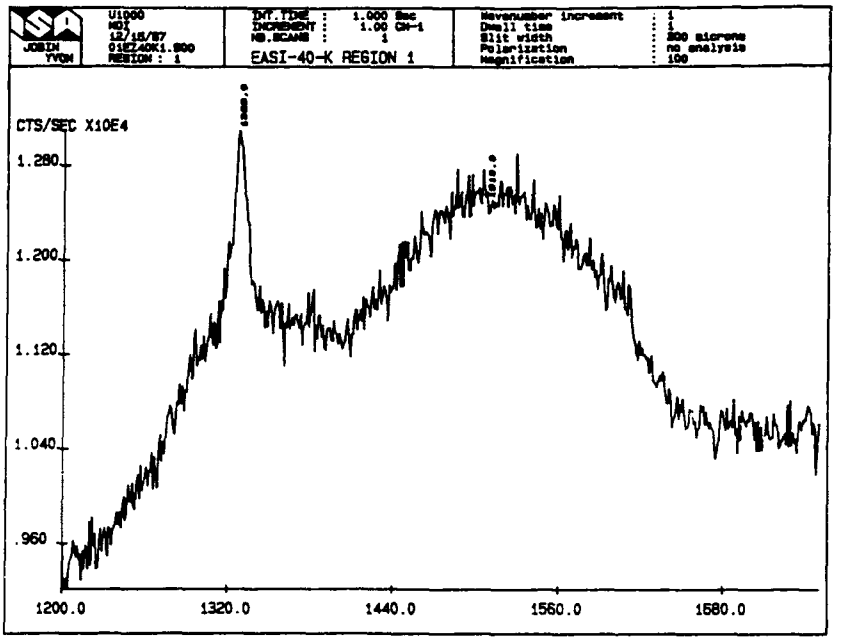

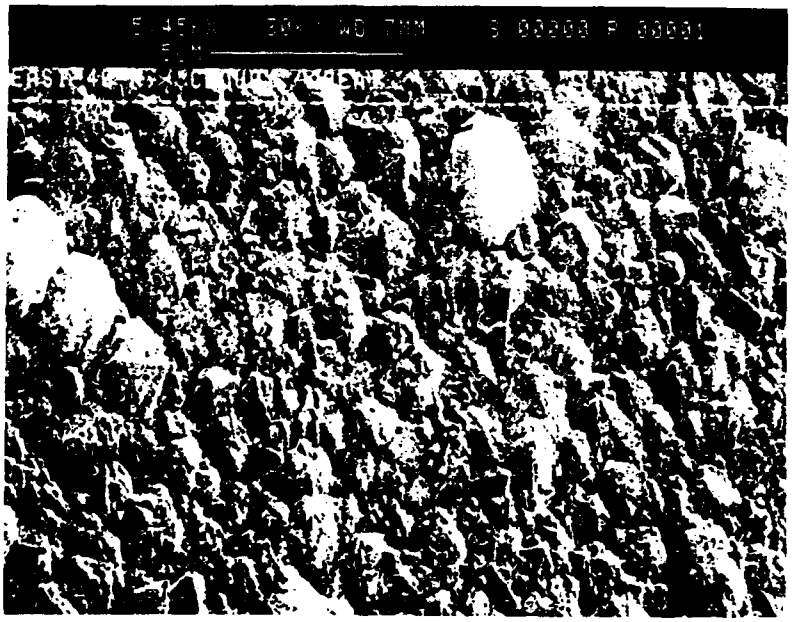

Figure. 2 Raman spectrum and SEM image of diamond film showing the strong signal due to diamond and the continuous crystallites comprising the film.

Crystallume
Telephone 415-494-0660
3180 Porter Drive, Suite 2 • Palo Alto, California 94304

generally in the form of crystallites completely covering the surface of the silicon. These crystallites can assume at least two morphologies, a sharply facetted structure reminiscent of a {111} surface orientation and a rounded structure which has been termed the cauliflower structure. Figure 3 shows examples of these two structures. It has been shown that the surface orientation of the crystallites is a function of the methane to the hydrogen concentration in the active gas mix. The fact that both types of structures can occur on different regions of a large wafer suggests that a variation of the CH_4/H_2 ratio can result over the diameter of a 4 in wafer. It has not been established whether other factors such as the local current density or temperature also have an influence on the surface morphology of the crystallites.

The growth of very thin films (1000 Å) which are contiguous has not been possible to date. Regions of a wafer that exhibit very thin or discontinuous films appear a dark blue in color and are also characterized by very poorly defined Raman signals. Figure 4 is a Raman spectrum of a thin film. The spectrum has no discernable structure to it and is characterized by a very noisy signal without any peaks that stand out. Such a structure is characteristic of discontinuous films where the size of the individual grains or crystallites are smaller than the diameter of the laser spot in the Raman spectroscope (5 microns), with the grains not coalesced into a continuous film. The corresponding scanning electron micrograph of a discontinuous film is also shown in figure 4. A significant aspect of the current research programme has been the development of equipment and processes which promote the formation of continuous diamond films rather than the discontinuous structure shown in figure 4 .

In order to enhance nucleation to promote the formation of a large density of very small grains which would subsequently coalesce into thin, continuous films, a two stage deposition process has been tested. In this approach the density of nuclei is increased by the use of a higher methane concentration in the gas mix during the early stages of the deposition process followed by a reduction in the methane concentration for completing film deposition. The expectation is a more contiguous film with fewer voids and pinholes. In general the films have been found to be more continuous with the use of a two step process, but the quality of the Raman signal is found to be degraded with the use of higher methane concentrations. It has generally been observed that the Raman signal is improved as the methane concentration in the gas mix is reduced. Even in the case of an initial high methane concentration for promoting a high nucleation rate, the concentration of the methane in the gas phase for the subsequent stages of the deposition process is found to

Crystallume
Telephone 415-494-0660
1180 Porter Drive, Suite 2 • Palo Alto, California 94304

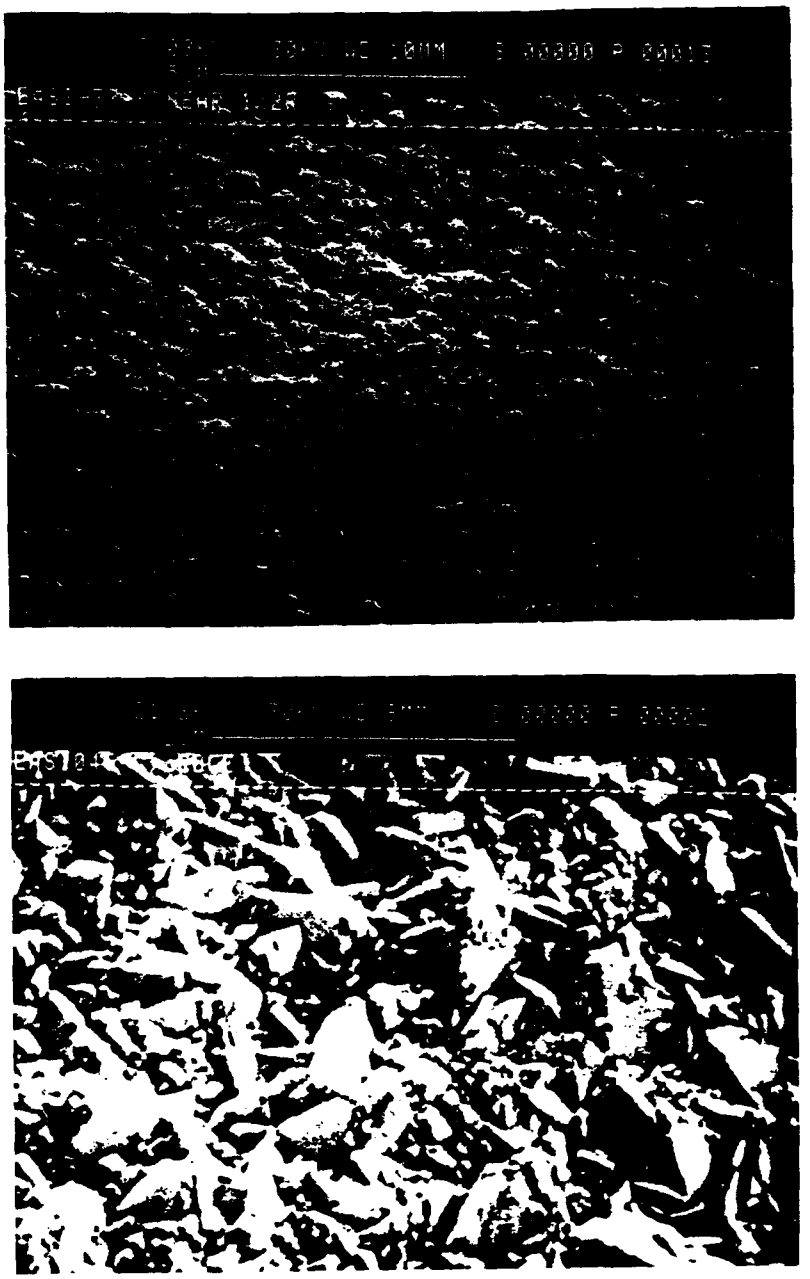

Figure. 3 Scanning electron micrographs showing the surface structure of PECVD diamond films deposited on silicon.The surface morphology is found to be a function of deposition conditions (temperature, gas chemistry, plasma conditions etc.). Top micrograph shows rounded, relatively smooth grains with a roughly octahedral morphology. Bottom micrograph shows a sharply facetted surface with a roughly {111} surface orientation of the grains.

Telephone 415-494-0660

3180 Porter Drive, Suite 2 • Palo Alto, California 94304

influence the Raman signal. The use of a lower (0.3%) methane concentration promotes diamond bonding whereas a higher (0.5%) methane concentration promotes graphitic bonding. A comparison of the Raman spectra of films deposited using a two stage process with an initial 1 % methane concentration for the nucleation stage followed by a longer deposition at a lower methane concentration is shown in figure 5. The lower methane concentration promotes sp^3 bonding whereas the higher methane concentration shows a predominance of sp^2 bonding.

The other aspect of this programme that has a bearing on the commercial viability of the CVD diamond deposition process is the uniformity characteristics of the films over large deposition areas. Figure 6 is a plot of film uniformity on a 4 in silicon wafer. The nominal thickness of this film is 0.8 microns with a thickness variation of + or - 10% across a 4 in wafer. The average grain size of the film is also plotted as a function of position indicating a very tight distribution of the grain size of about 1.25 microns.

Table 1 below summarises the relevant data for the 6 silicon wafers with diamond deposited on them.

Sample	Methane Concentration	Deposition Time (Hr)	Comments
20 K	0.3 %	110 hr	Reasonably good RamanSpectra, Spectrum quality is position dependant
36 I	0.3 %	100 hr	Poor Raman quality, high sp^2 bond content
35 K	1%	16 hr	
	0.3 %	48 hr	Good Raman spectra
40 K	0.3 %	72 hr	Good Raman spectra
41 K	0.3 %	52 hr	Good Raman spectra
51 K	1 %	16 hr	
	0.5 %	45 hr	Poor Raman spectra, high sp^2 bond content, Spectrtum similar to DLC

Telephone 415-494-0660

Crystallume

3180 Porter Drive, Suite 2 • Palo Alto, California 94304

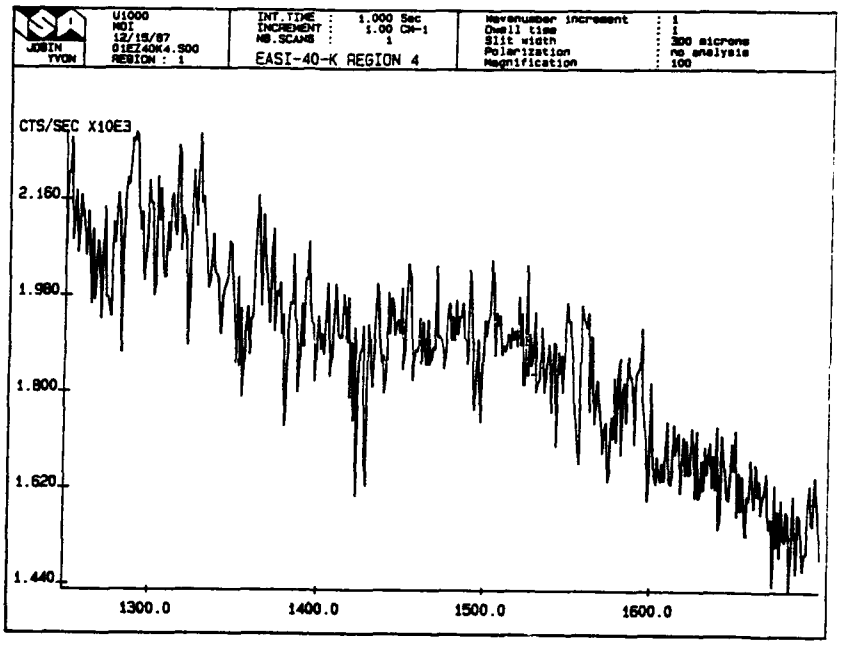

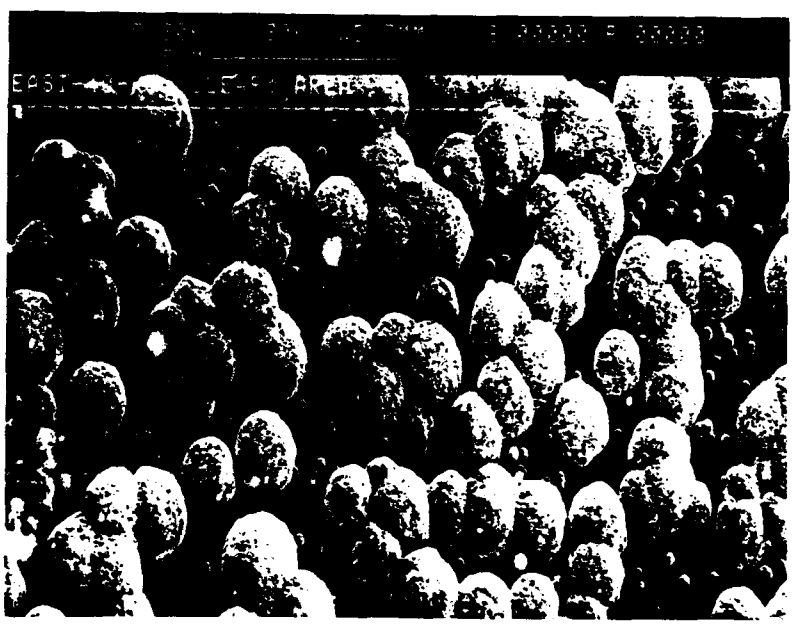

Figure 4. Raman spectrum and corresponding SEM image of a thin diamond film (< 3000 Å) deposited on a silicon surface. No distinct Raman peaks are observed since the film is not continuous being composed of isolated crystallites, approximately 2 μ m in diameter.

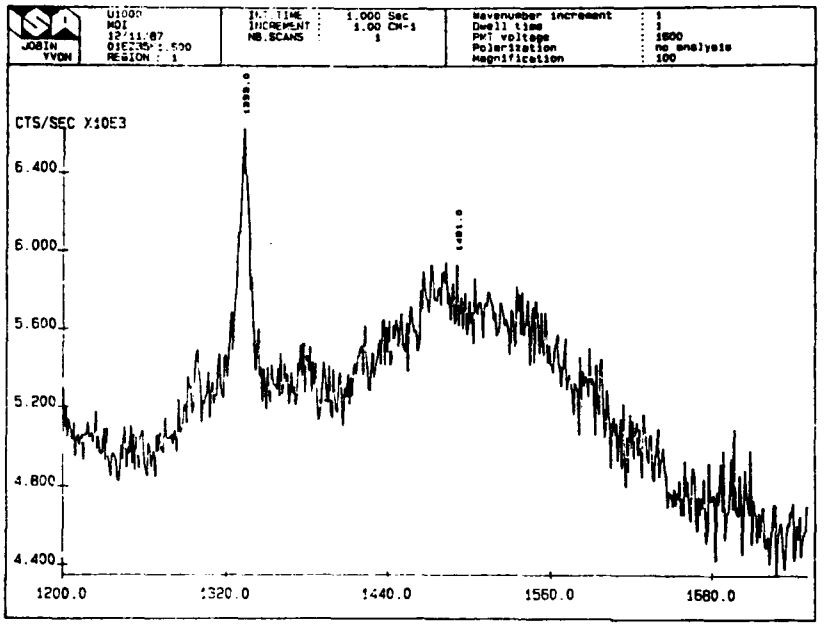

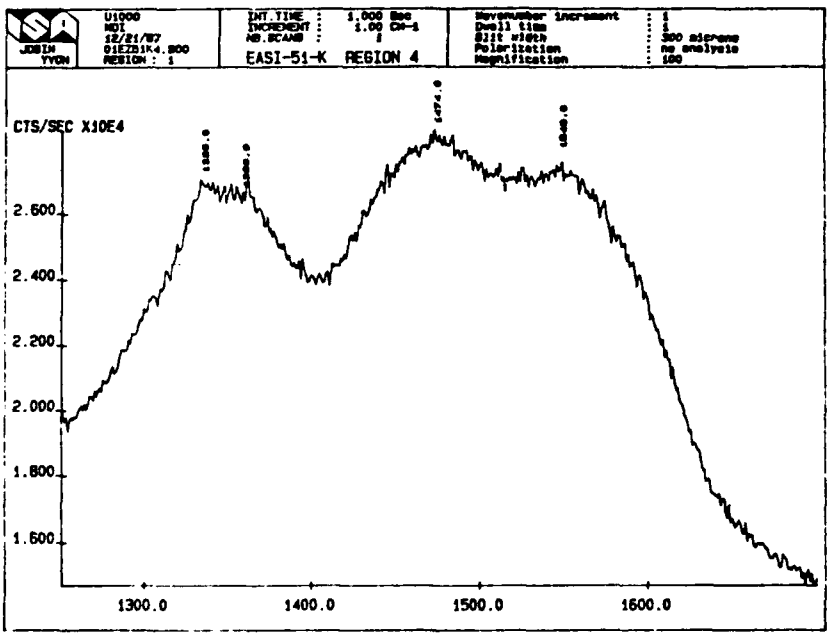

Figure. 5 Comparison of Raman spectra of diamond films deposited using two different concentrations of methane gas in the ambient. The lower methane concentration (0.3 % methane in hydrogen) results in a distinct Raman signal due to diamond bonding in the film (top spectrum) whereas higher methane concentration (0.5 %) results in a Raman signal that is more characteristic of diamond like carbon films with a significant sp^2 bond component (bottom spectrum). There are other variables such as the plasma current density which could have an influenced the structure of the films.

Crystallume
Telephone 415-494-0660
3100 Porter Drive, Suite 2 • Palo Alto, California 94304

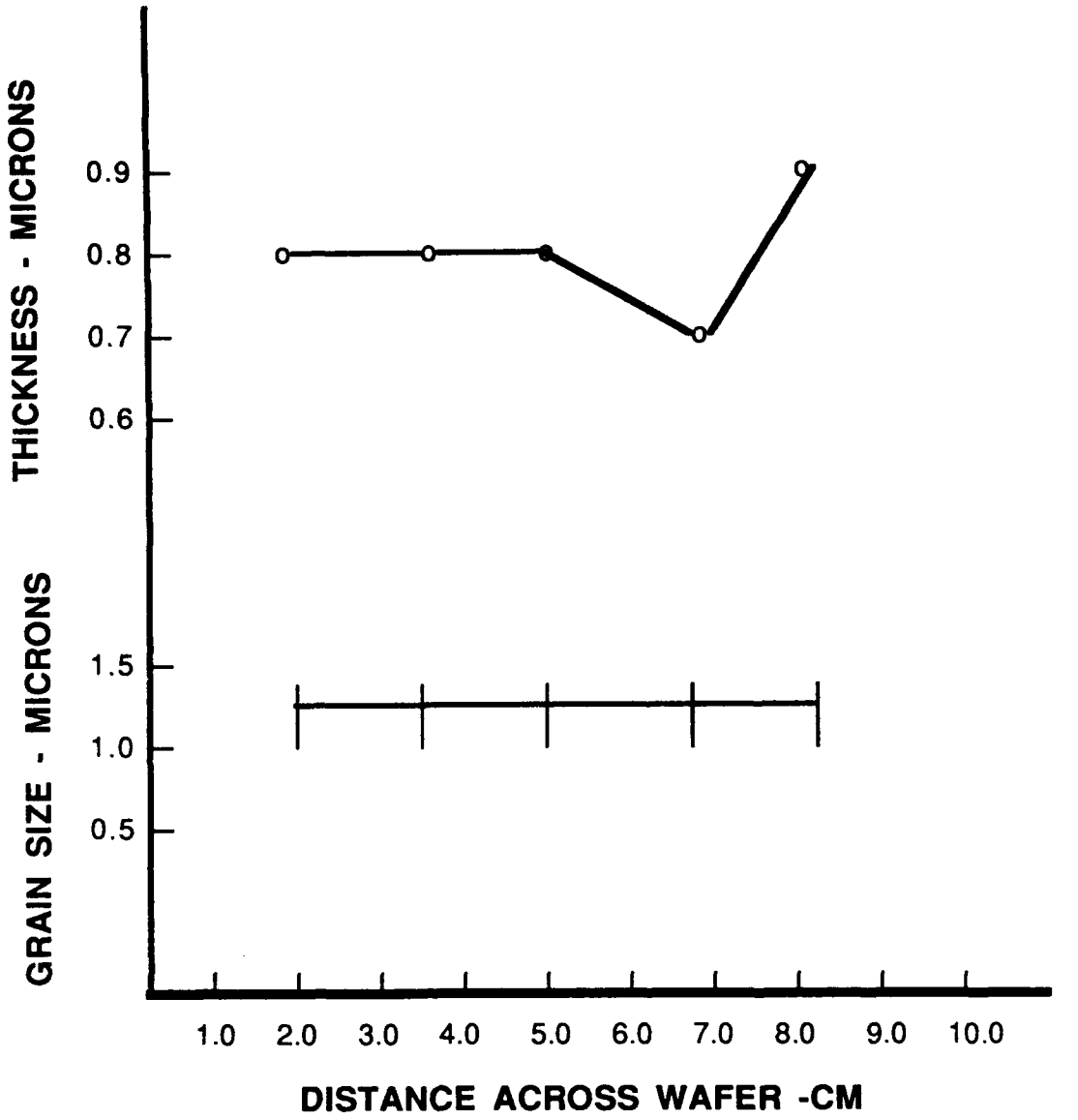

Figure. 6 Uniformity characteristics of diamond films depositesd on silicon substrates. A thickness uniformity variation of about 10 % is indicated with a very uniform distribution of the grain size over the surface of a 4 in diameter substrate.

Crystallume
Telephone 415-494-0660
1180 Porter Drive, Suite 2 • Palo Alto, California 94304

Conclusions

The work performed to generate thin, continuous films of diamond on silicon wafers to determine the tribological properties of the films has resulted in the following findings:

* The growth of very thin diamond films using plasma enhanced CVD techniques is very strongly dependant upon the nucleation and growth conditions that are operative in this process. Films of thicknesses < 1000 Å are difficult to grow under the current process conditions and utilizing current equipment designs. However, based on the work performed in this phase of the contract a variety of equipment and process improvements can be suggested which provide the opportunity for the growth of very thin (< 1000Å) films of diamond.

* Diamond films of thicknesses > 5000 Å can be grown in a fairly routine fashion. Such films are characterized by good Raman spectra and are contiguous and continuous over large areas. The quality of the films as determined by Raman spectroscopy is a strong function of the methane to hydrogen ratio with a high hydrogen supersaturation promoting diamond bonding in the films. Variations of the structure, including the relative ratios of the sp^3 and sp^2 bonded phases can occur over the surface of a wafer. Further development is required to enhance structural uniformity of thin diamond films deposited on large areas.

* An important technology development activity that has resulted in part from this work is the development of processes and equipment for the deposition of diamond films over substrate areas as large as 4 in in diameter. This is believed to be the largest area over which diamond films are deposited routinely today. The only other reported work on large area deposition has been on 3 in diameter substrates. It is clear that the commercialization of the diamond deposition technology and the utility of diamond films in industrial applications requires the development of large area deposition technology.

* An understanding of the nucleation and growth characteristics of diamond films is beginning to emerge in part as a result of this work

Crystallume
Telephone 415-494-0660
3180 Porter Drive, Suite 2 • Palo Alto, California 94304

Recommendations for future research

The present research programme has generated significant information which suggests a variety of new technical developments that warrant attention. Some of the recommendations for further work in this area include the following:

* The growth of very thin (<1000Å) films of diamond that are contiguous and pinhole free is of obvious interest in a variety of potential uses of diamond films. Based on the present work several new avenues are available for investigating the technology of the growth of very thin diamond films.

* The present work has been confined to the deposition of diamond films on silicon substrates. There is obvious interest in the deposition of diamond films on other materials including metals and ceramics. Depositing diamond on these materials would be of particular interest in hard coating and tribological uses. In this context one of the key technologies that needs investigation is the adhesion characteristics of diamond films to metals, semiconductors and ceramics. Work done at Crystallume has shown that adhesion between diamond films and a variety of substrates is a function, among other things, of the carbide forming nature of the substrate. Excellent adhesion between diamond and carbide formers such as molybdenum, titanium, silicon etc. has been achieved whereas the adhesion between the diamond film and non carbide formers such as copper, silver, and germanium is poor. The use of intermediate layers and adhesion promoters is of interest in this context.

* Tribological properties are expected to be a function of the surface structure and morphology of the diamond films. In this regard modification of the structure and the orientation of the crystallites in thin diamond films is possible by modifying the plasma deposition conditions. Further resaearch in this area can identify the mechanisms and processes relating process conditions to structure. A change in the orientation from a predominance of a {111} surface orientation to a predominance of a {100} surface orientation with changes in the methane to hydrogen ratio in the gas has been demonstrated. The mechanical and tribological properties of films of the two orientations would be clearly of interest. Extending this train of thought further, the properties of single crystal films of diamond in terms of their tribological behavior are of interest. There has been some limited

Telephone 415-494-0660
Crystallume
3180 Porter Drive, Suite 2 • Palo Alto, California 94304

success in the growth of heteroepitaxial single crystal films of diamond on nickel substrates. Crystallume has developed concepts for heteroepitaxial growth of diamond on lattice matched substrates such as nickel and copper. The mechanical properties of such single crystal (or large grained polycrystalline) films are of interest. A research effort relating PECVD process variables to diamond film structure and their tribological properties is recommended.

Appendix

Enclosed with this report are diced samples of diamond coated silicon chips from four 4 in diameter wafers. Maps of the wafers are attached along with the data on surface structure and Raman spectroscopy. The data summarized in table 1 above should be a guide to the expected tribological behavior of the samples from the different wafers.

Crystallume
Telephone 415-494-0660
3180 Porter Drive, Suite 2 • Palo Alto, California 94304

Wafer maps indicating position at which Raman spectroscopy and SEM analyses were performed.

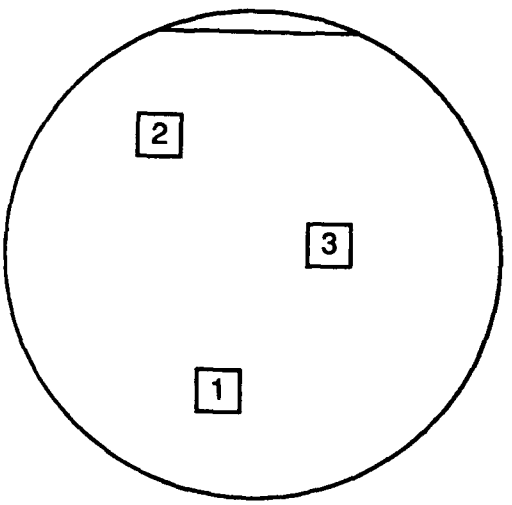

Sample 35 K

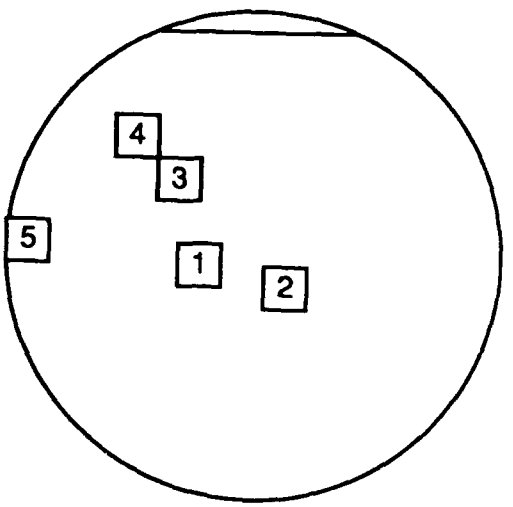

Sample 40 K

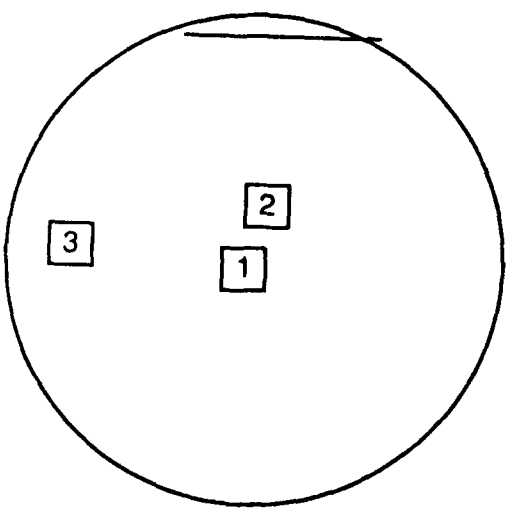

Sample 41 K

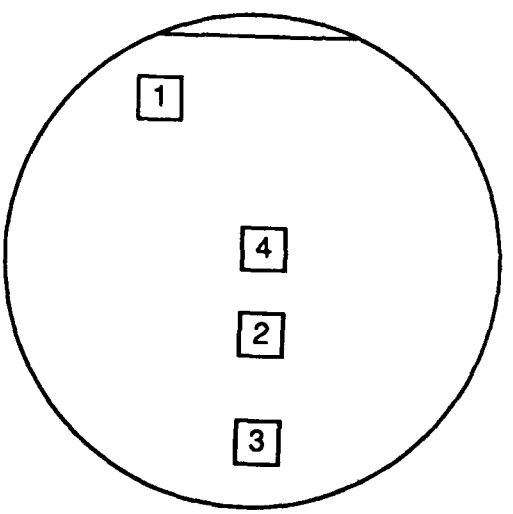

Sample 51 K

35-K

Telephone 415-494-0660

Crystallume

3180 Porter Drive, Suite 2 • Palo Alto, California 94304

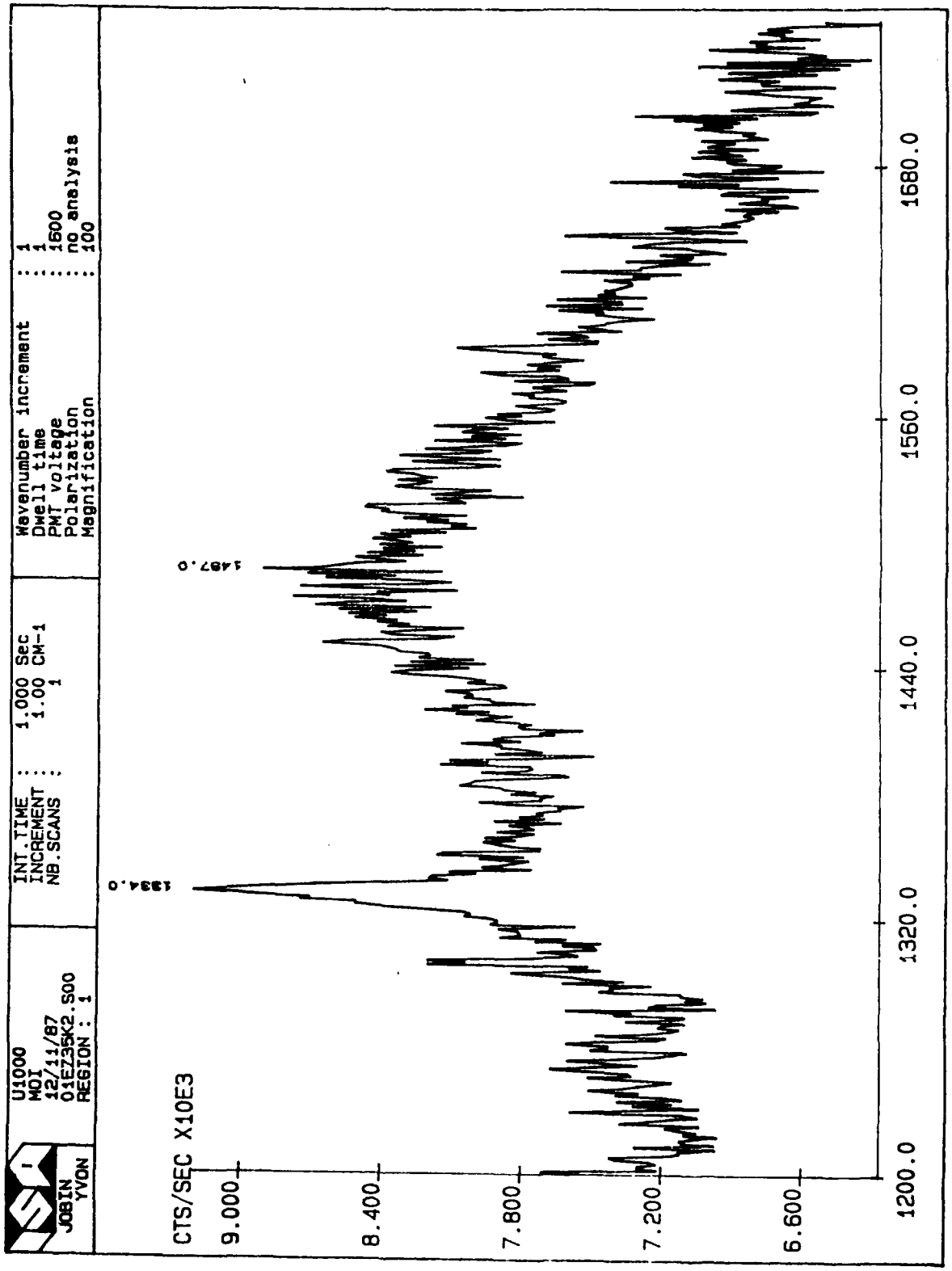

JOBIN YVON	U1000 DA 10/26/87 01E035K2.S00 REGION : 1	INT.TIME : INCREMENT : NB.SCANS :	1.000 Sec 1.00 CM-1 1	Laser wavelength Laser power Slits Microscope objective Polarization	: 514.532 nm : 50 mw : 300 um : 50X : Half wave plate

EAST-35-K AREA TWO

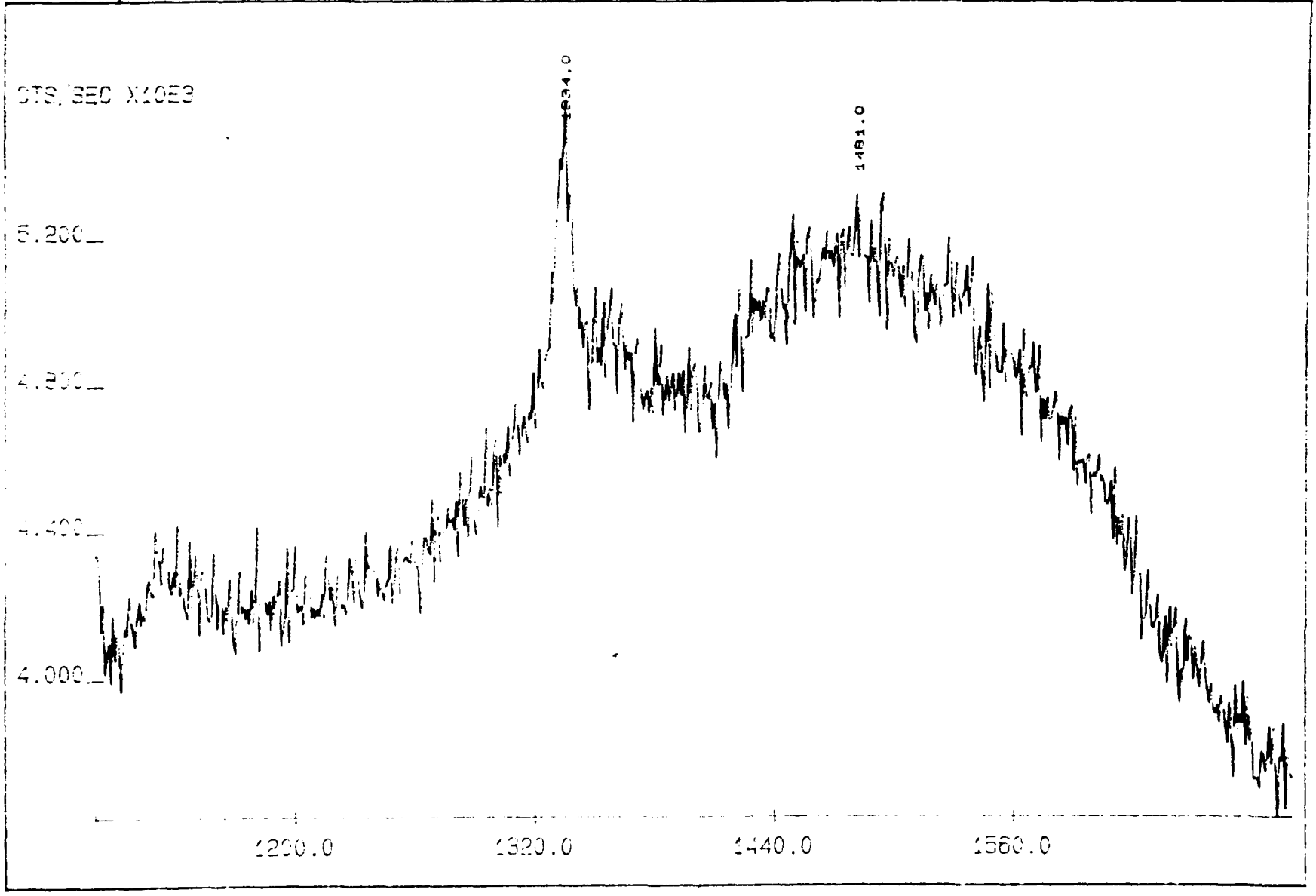

BB18

JOBIN YVON

U1000
DA
10/26/87
01E235R3.S00
REGION : 1

INT.TIME : 1.000 Sec
INCREMENT : 1.00 CM-1
NB.SCANS : 1

EAST-35-K AREA 3

Laser wavelength : 514.532 nm
Laser power : 50 mw
Slits : 300 um
Microscope objective : 50X
Polarization : Half wave plate

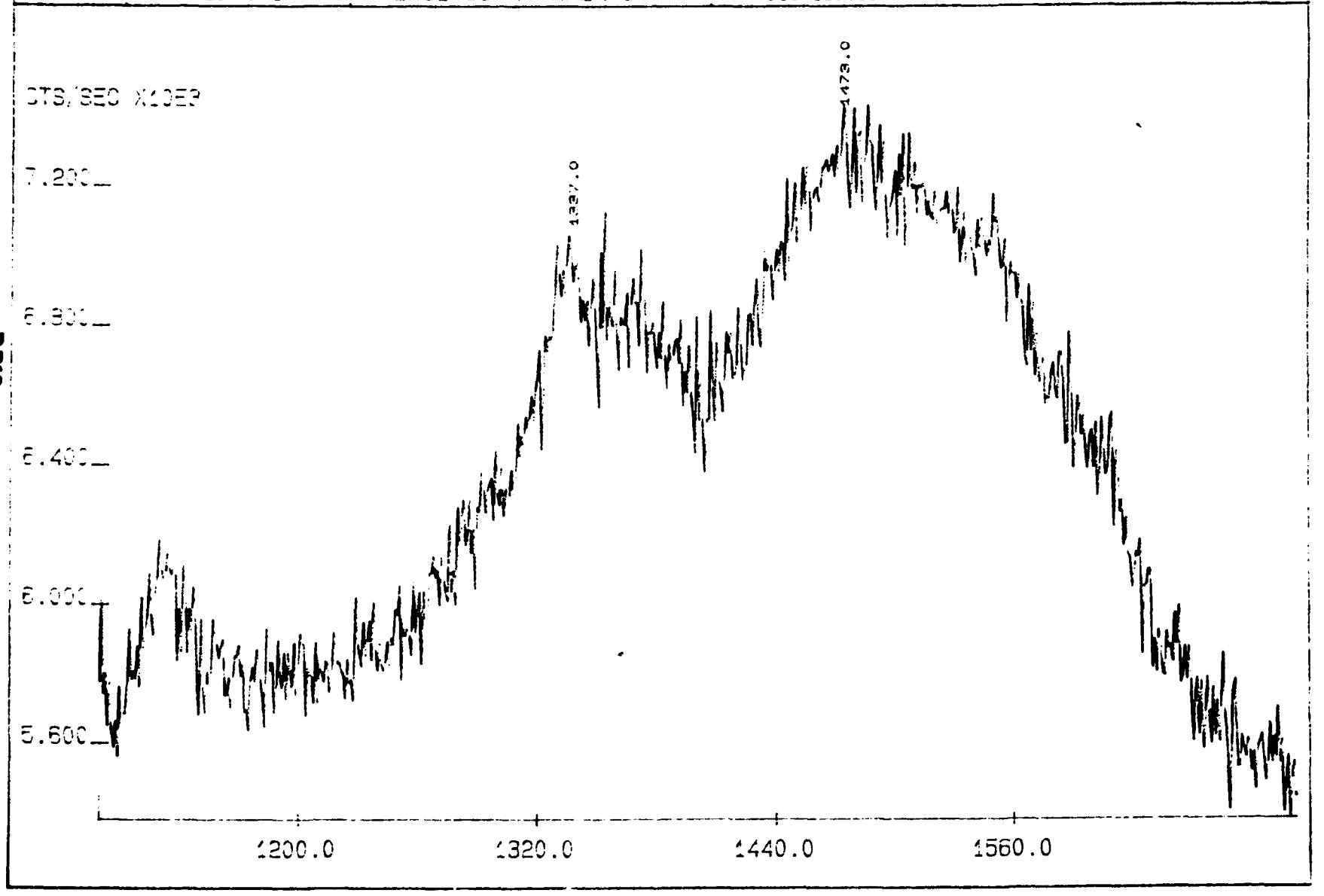

B19

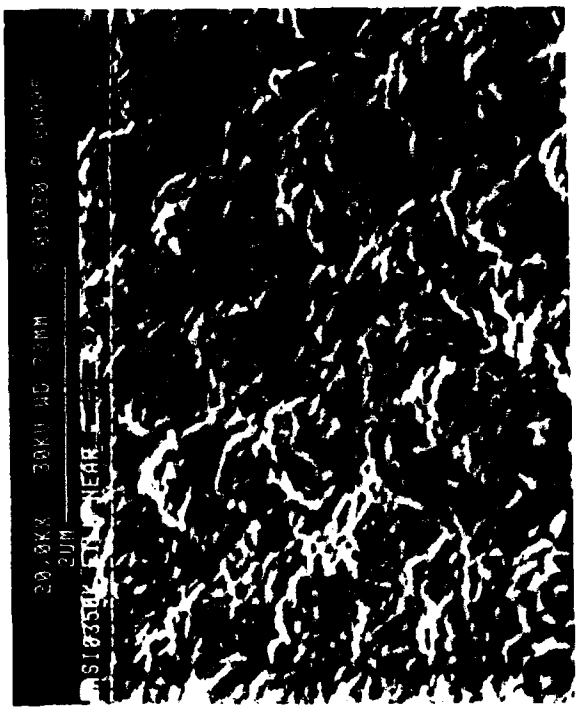

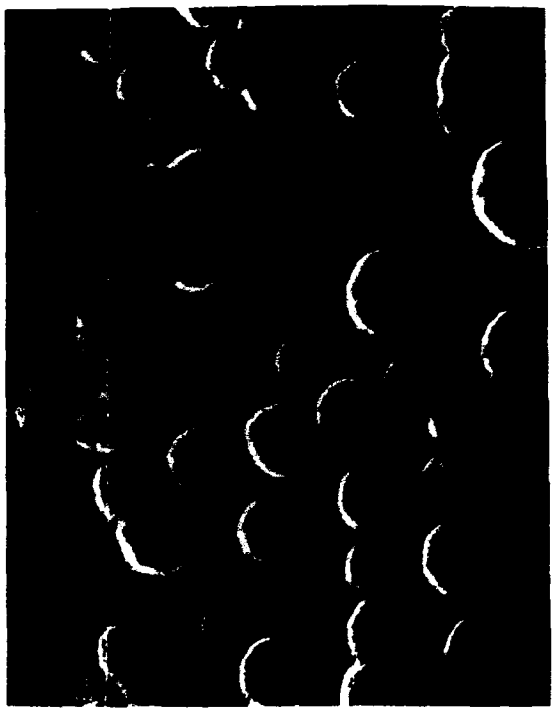

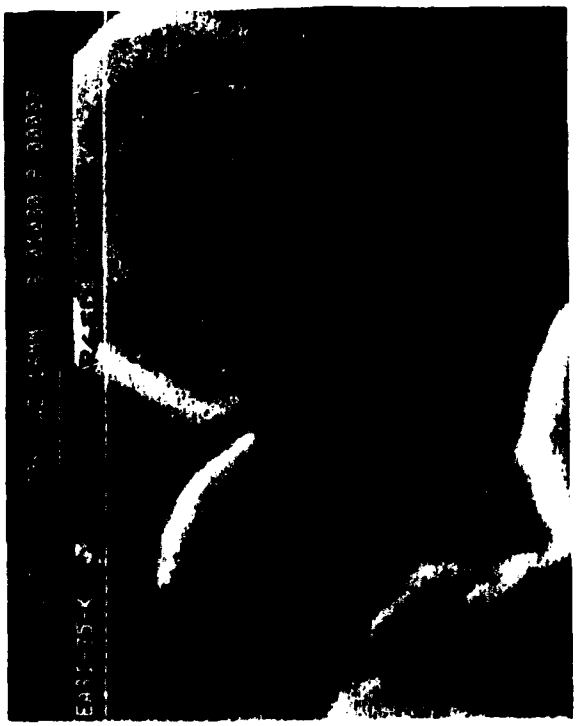

BB20

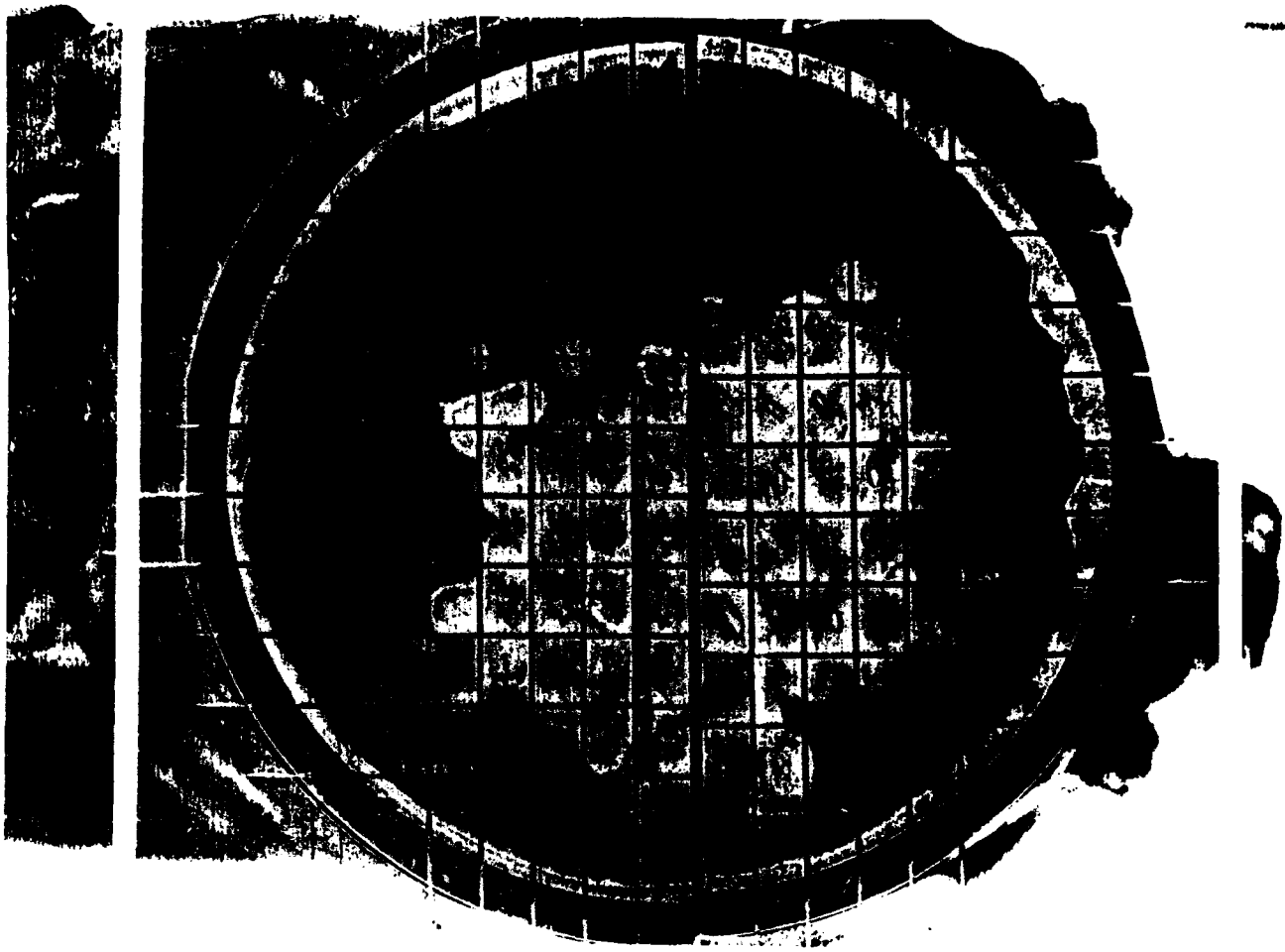

EASI·40K.

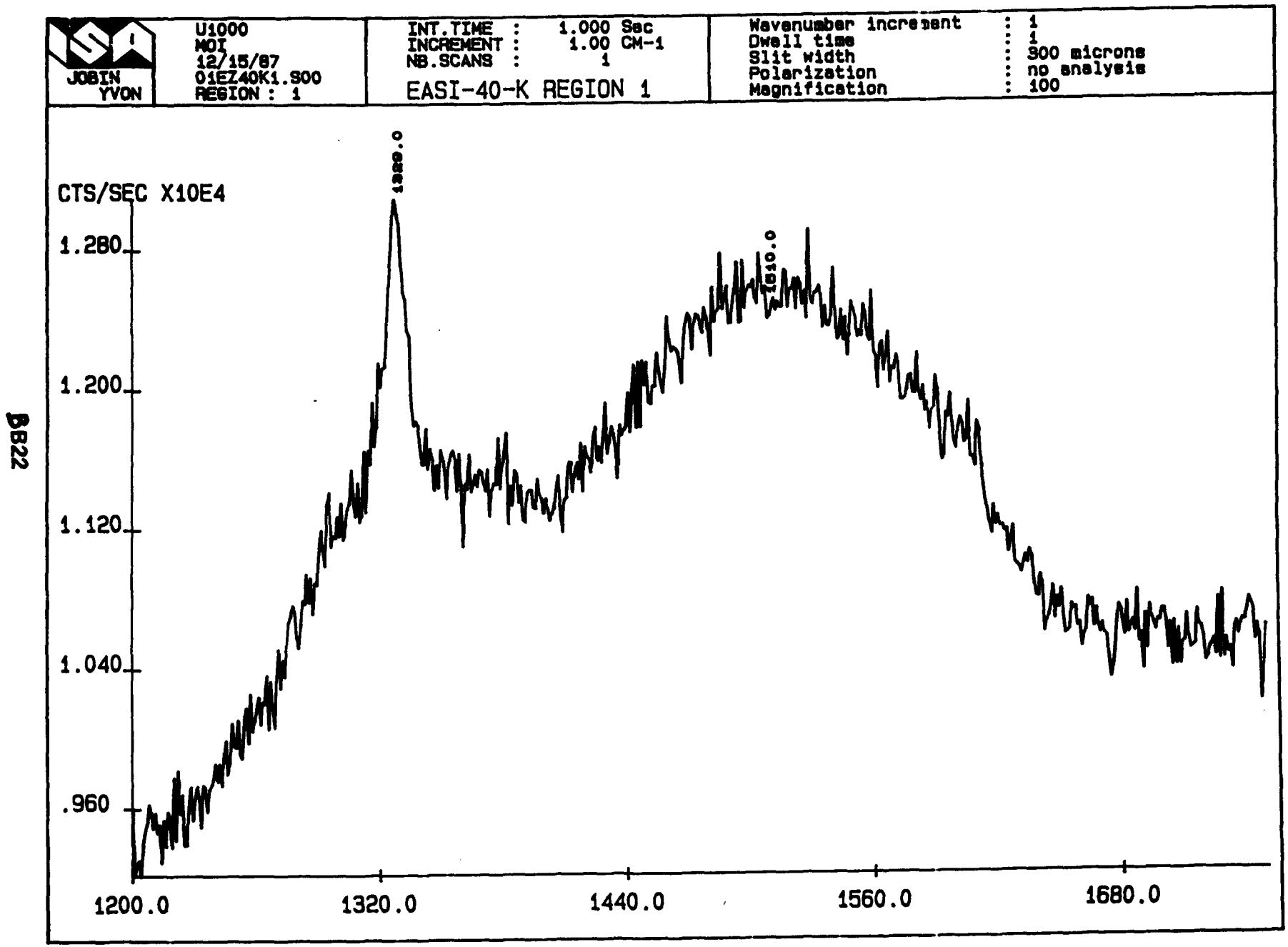
JOBIN YVON
U1000
MOI
12/15/87
01EZ40K1.S00
REGION : 1
INT.TIME : 1.000 Sec
INCREMENT : 1.00 CM-1
NB.SCANS : 1
EASI-40-K REGION 1
Wavenumber increment : 1
Dwell time : 1
Slit width : 300 microns
Polarization : no analysis
Magnification : 100
CTS/SEC X10E4
1.280
1.200
1.120
1.040
.960
1200.0
1320.0
1440.0
1560.0
1680.0
1380.0
1510.0
BB22

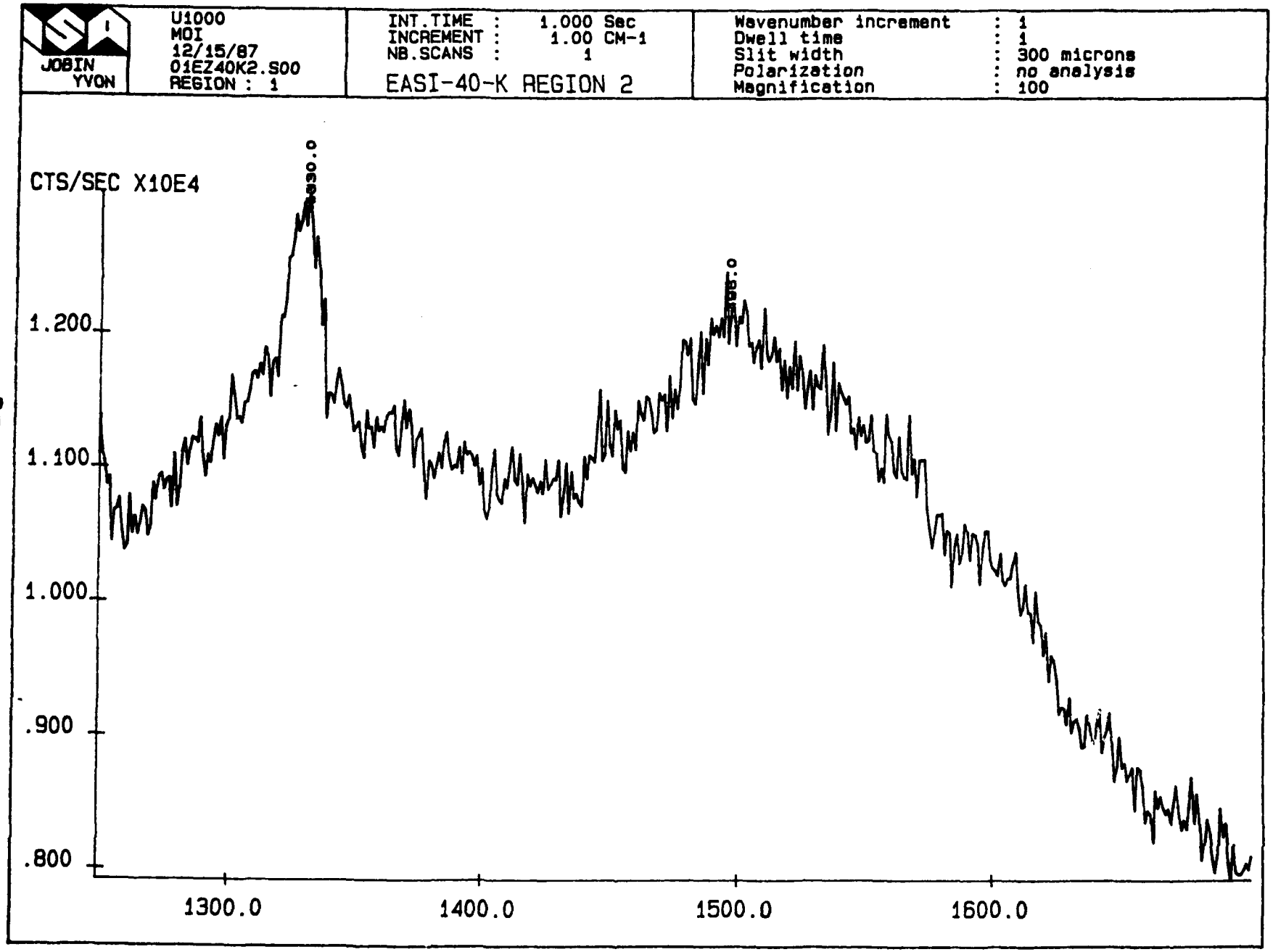
JOBIN YVON
U1000
MOI
12/15/87
01EZ40K2.S00
REGION : 1
INT.TIME : 1.000 Sec
INCREMENT : 1.00 CM-1
NB.SCANS : 1
EASI-40-K REGION 2
Wavenumber increment : 1
Dwell time : 1
Slit width : 300 microns
Polarization : no analysis
Magnification : 100
CTS/SEC X10E4
1.200
1.100
1.000
.900
.800
1300.0
1400.0
1500.0
1600.0
B23

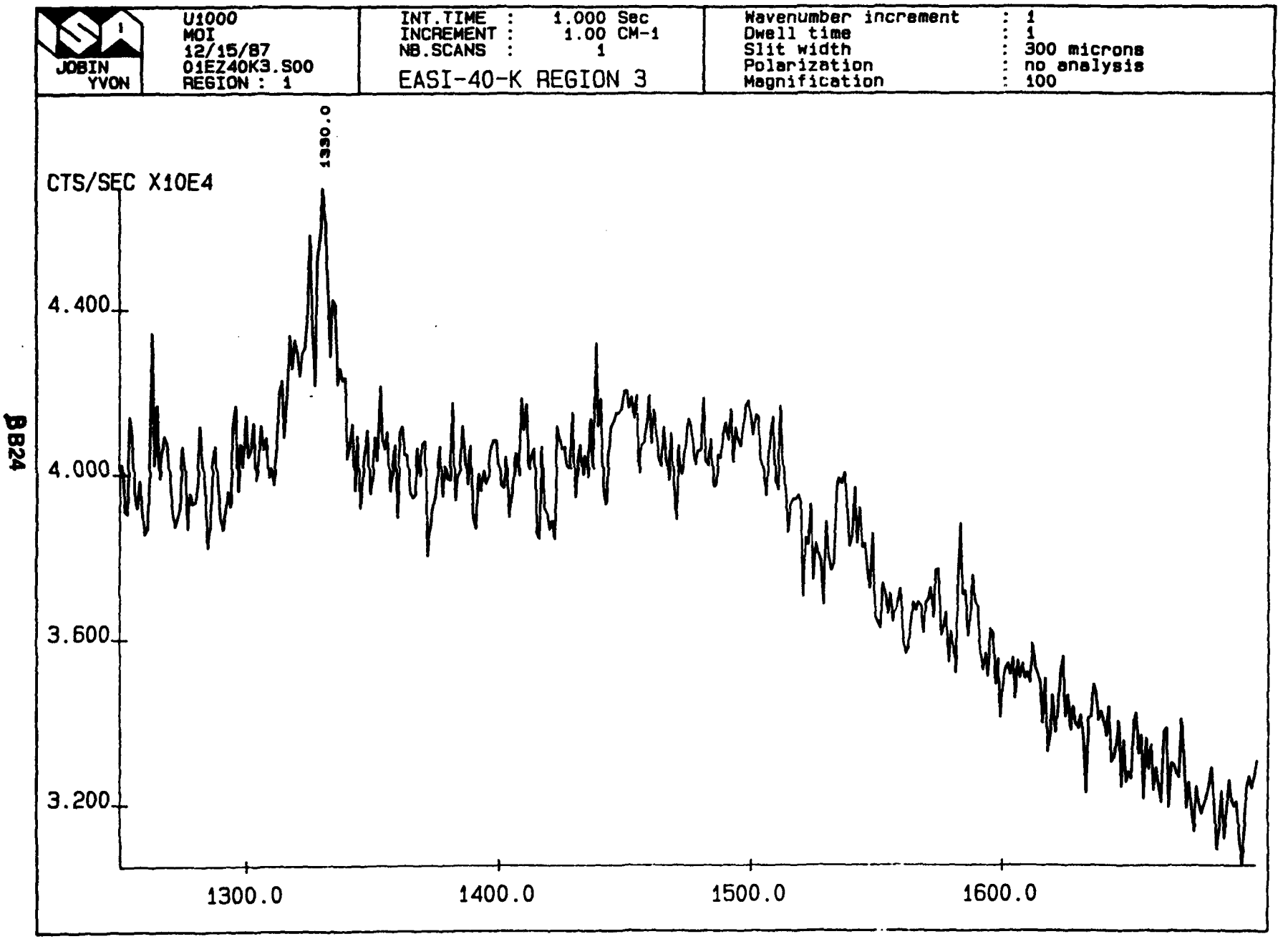
JOBIN YVON
U1000
MOI
12/15/87
01EZ40K3.S00
REGION : 1
INT.TIME : 1.000 Sec
INCREMENT : 1.00 CM-1
NB.SCANS : 1
EASI-40-K REGION 3
Wavenumber increment : 1
Dwell time : 1
Slit width : 300 microns
Polarization : no analysis
Magnification : 100
1330.0
CTS/SEC X10E4
4.400
4.000
3.600
3.200
BB24
1300.0
1400.0
1500.0
1600.0

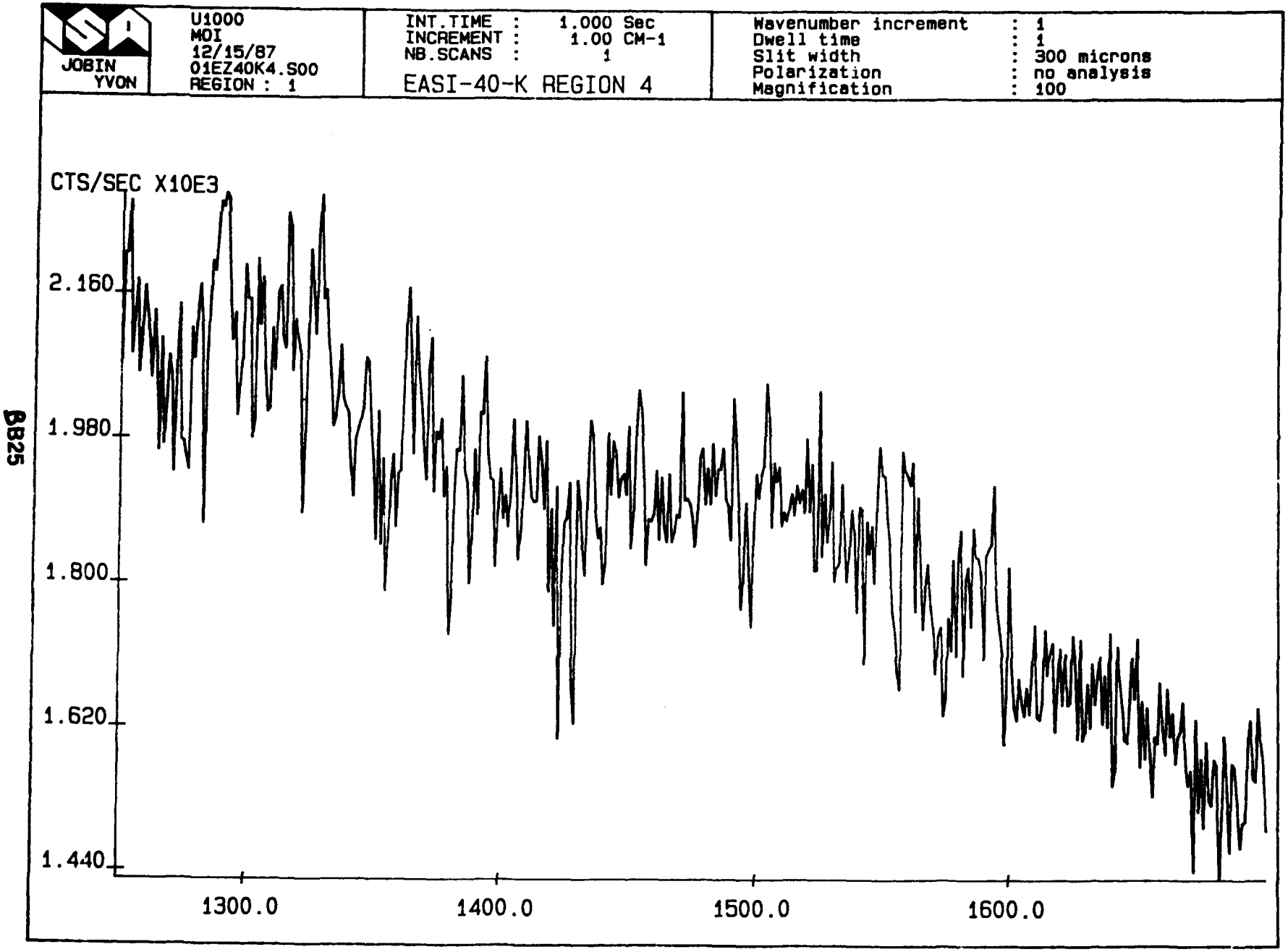
JOBIN YVON
U1000
MOI
12/15/87
01EZ40K4.S00
REGION : 1
INT.TIME : 1.000 Sec
INCREMENT : 1.00 CM-1
NB.SCANS : 1
EASI-40-K REGION 4
Wavenumber increment : 1
Dwell time : 1
Slit width : 300 microns
Polarization : no analysis
Magnification : 100
CTS/SEC X10E3
2.160
1.980
1.800
1.620
1.440
B825
1300.0
1400.0
1500.0
1600.0

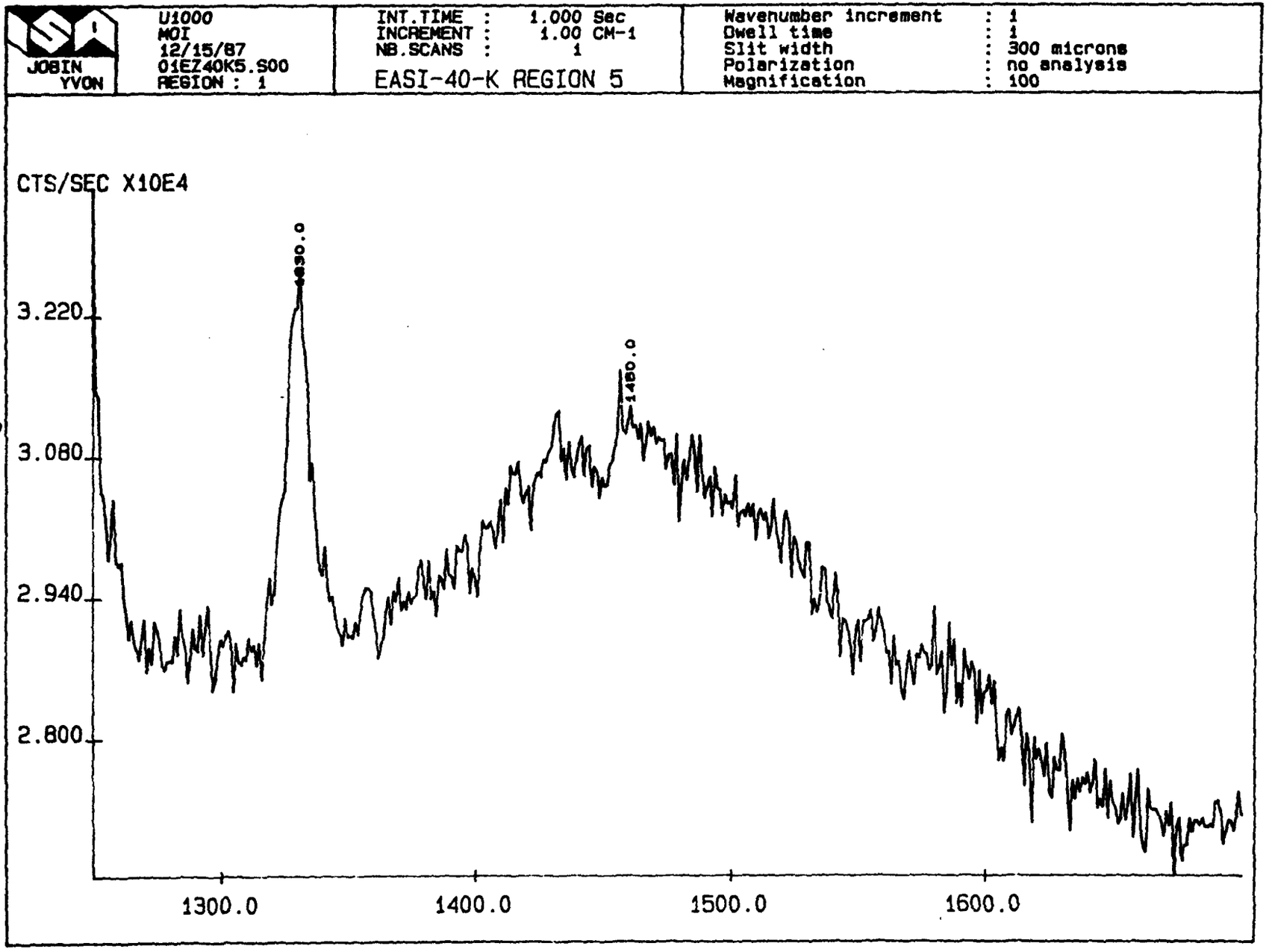
JOBIN YVON
U1000
MOI
12/15/87
01EZ40K5.S00
REGION : 1
INT.TIME : 1.000 Sec
INCREMENT : 1.00 CM-1
NB.SCANS : 1
EASI-40-K REGION 5
Wavenumber increment : 1
Dwell time : 1
Slit width : 300 microns
Polarization : no analysis
Magnification : 100
CTS/SEC X10E4
3.220
3.080
2.940
2.800
1630.0
1480.0
1300.0
1400.0
1500.0
1600.0
9826

ALL SHOTS HAVE DISTORTION IN Y-AXIS. X-AXIS MEASUREMENTS ARE OKAY

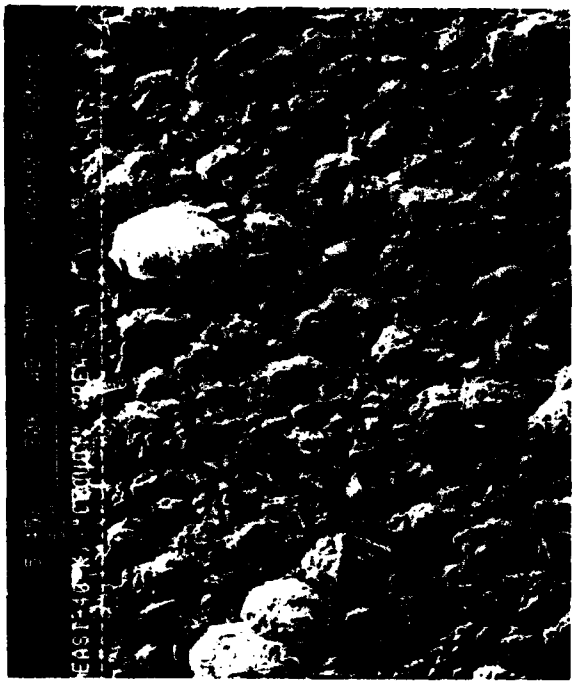

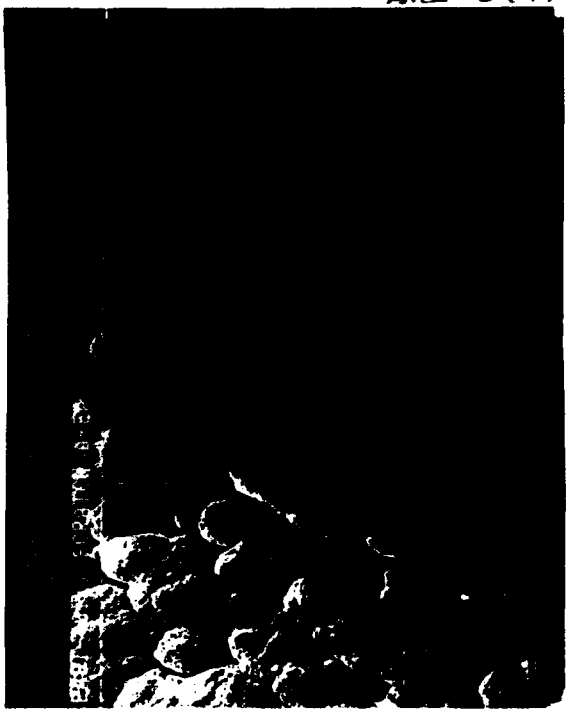

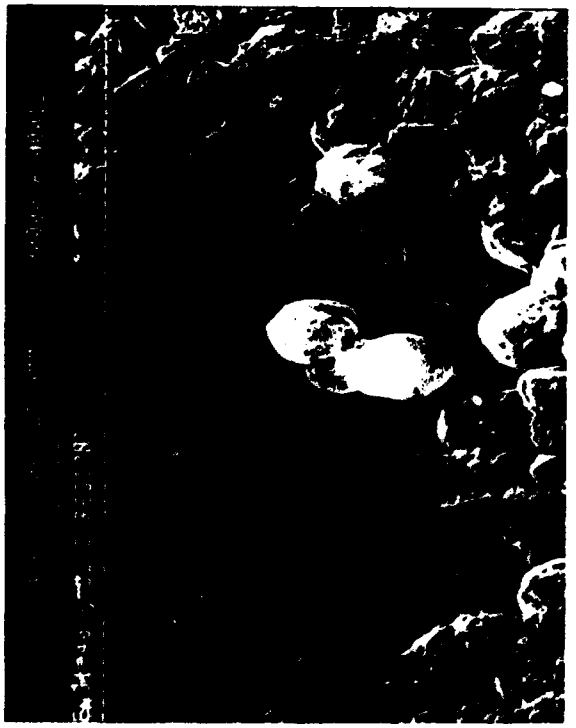

BB27

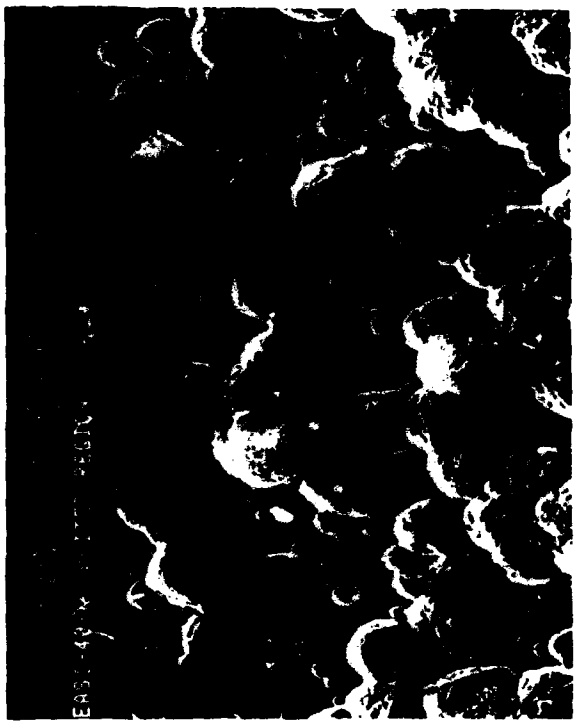

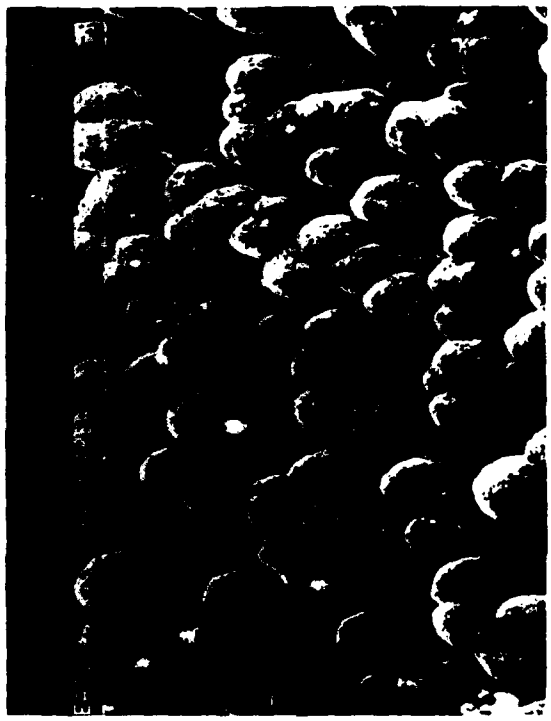

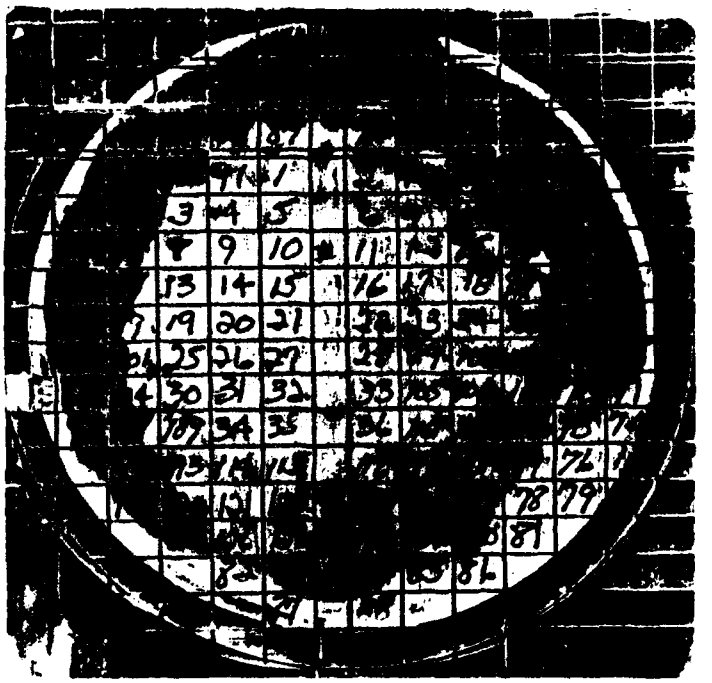

EASI-41K-

Area,1 - 1 - 36
Area,2 - 37 - 88
Area,3 - 89 - 130

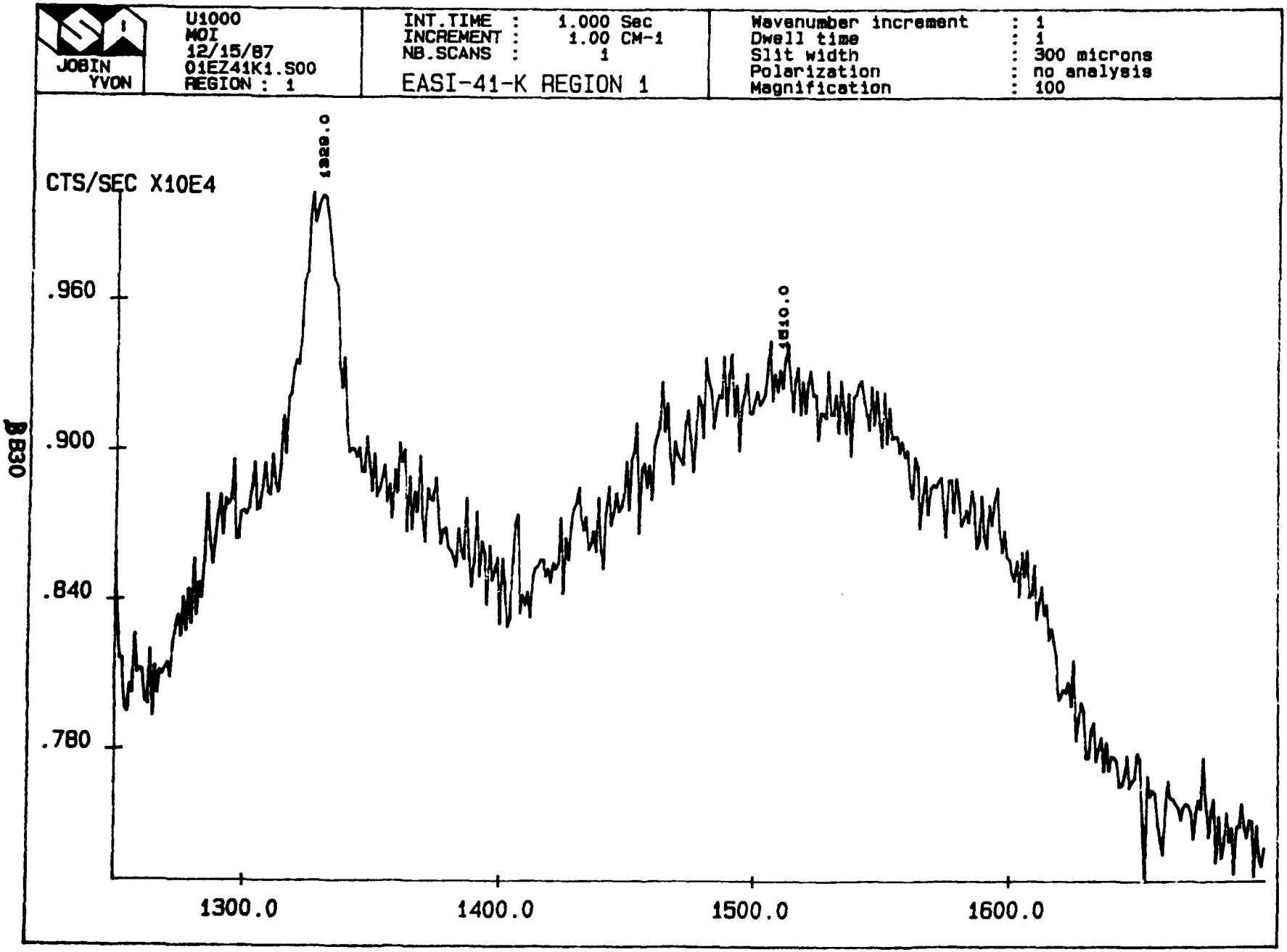
JOBIN YVON
U1000
MOI
12/15/87
01EZ41K1.S00
REGION : 1
INT.TIME : 1.000 Sec
INCREMENT : 1.00 CM-1
NB.SCANS : 1
EASI-41-K REGION 1
Wavenumber increment : 1
Dwell time : 1
Slit width : 300 microns
Polarization : no analysis
Magnification : 100
CTS/SEC X10E4
.960
.900
.840
.780
1328.0
1510.0
1300.0
1400.0
1500.0
1600.0

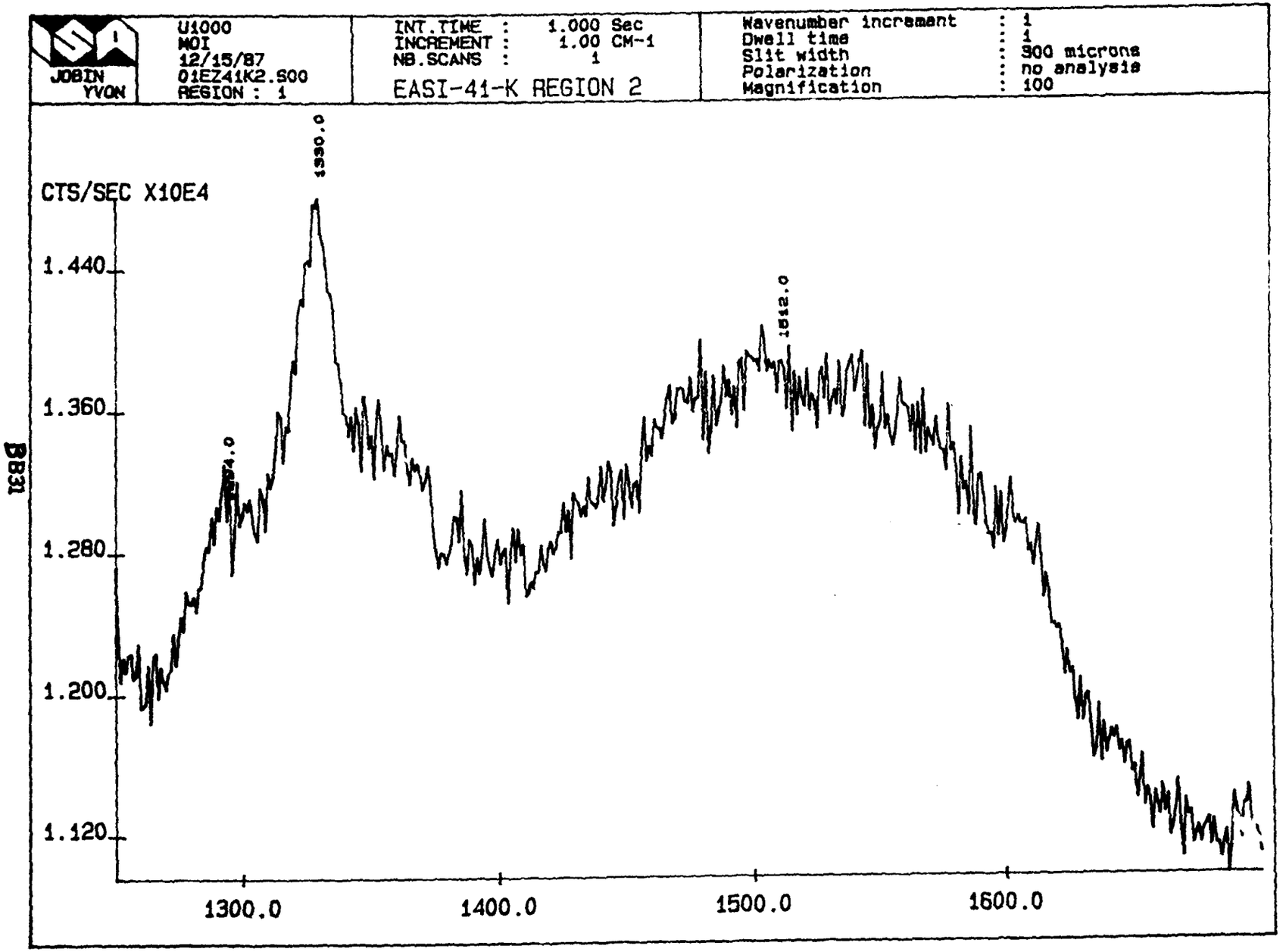
JOBIN YVON
U1000
MOI
12/15/87
01EZ41K2.S00
REGION : 1
INT.TIME : 1.000 Sec
INCREMENT : 1.00 CM-1
NB.SCANS : 1
EASI-41-K REGION 2
Wavenumber increment : 1
Dwell time : 1
Slit width : 300 microns
Polarization : no analysis
Magnification : 100
CTS/SEC X10E4
1.440
1.360
1.280
1.200
1.120
1330.0
1512.0
1300.0
1400.0
1500.0
1600.0
BB31

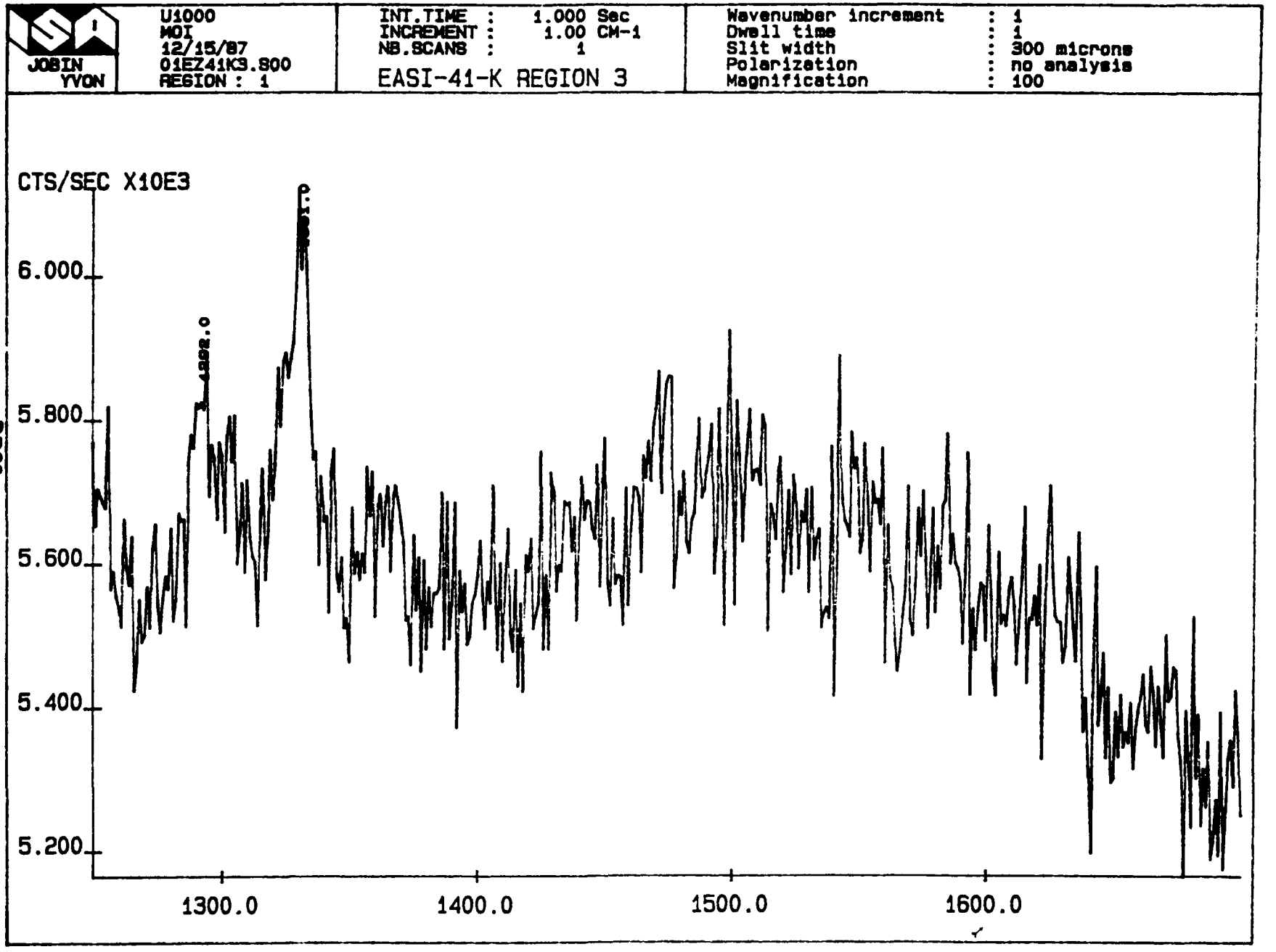
JOBIN YVON
U1000
MOI
12/15/87
01EZ41K3.800
REGION : 1
INT.TIME : 1.000 Sec
INCREMENT : 1.00 CM-1
NB.SCANS : 1
EASI-41-K REGION 3
Wavenumber increment : 1
Dwell time : 1
Slit width : 300 microns
Polarization : no analysis
Magnification : 100
CTS/SEC X10E3
6.000
5.800
5.600
5.400
5.200
BB32
1392.0
1300.0
1400.0
1500.0
1600.0

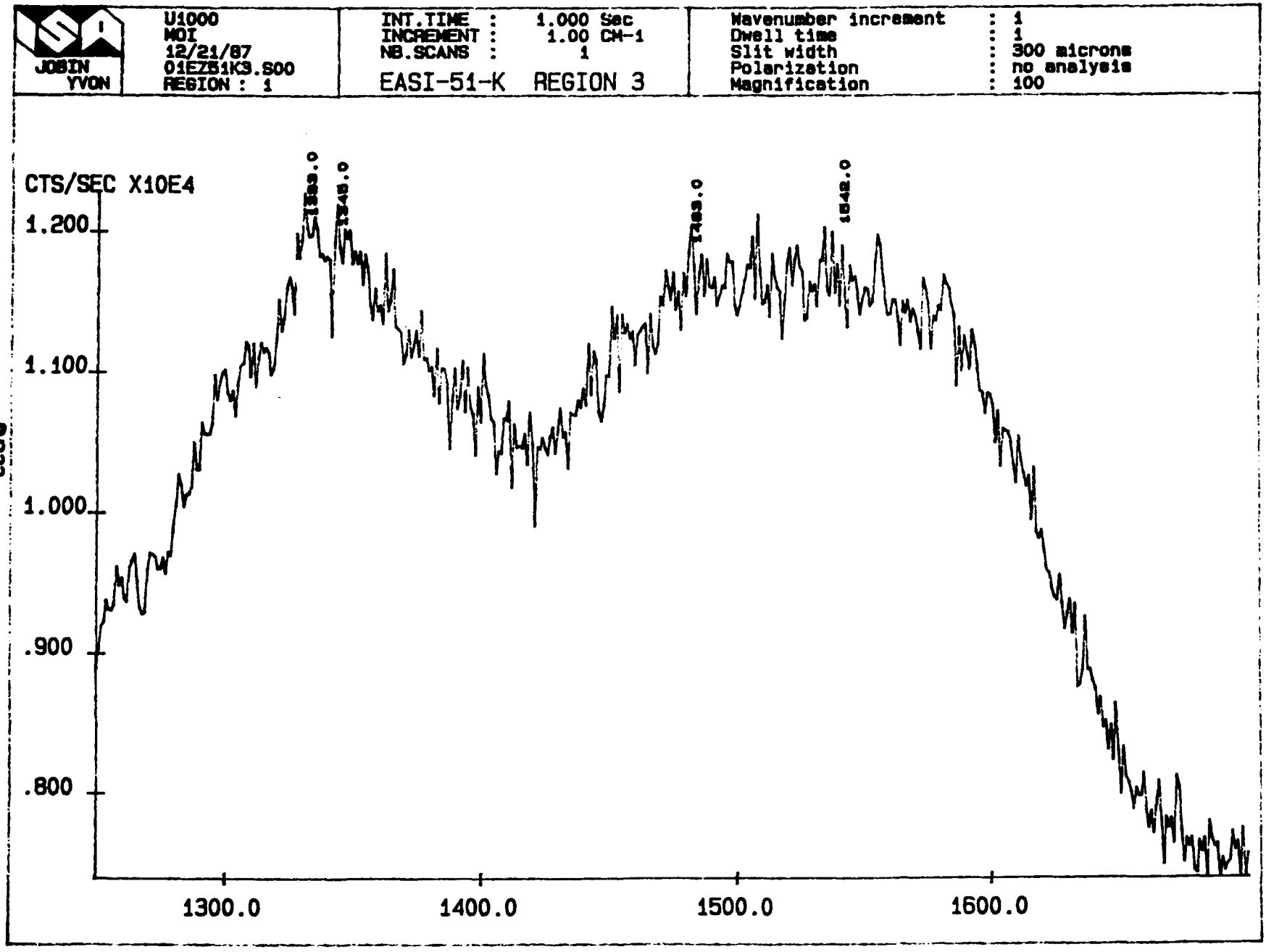
JOBIN
YVON
U1000
MOI
12/21/87
01EZ51K3.S00
REGION : 1
INT.TIME : 1.000 Sec
INCREMENT : 1.00 CM-1
NB.SCANS : 1
EASI-51-K REGION 3
Wavenumber increment : 1
Dwell time : 1
Slit width : 300 microns
Polarization : no analysis
Magnification : 100
CTS/SEC X10E4
1.200
1.100
1.000
.900
.800
1300.0
1400.0
1500.0
1600.0
1548.0
1543.0
1542.0
BB33

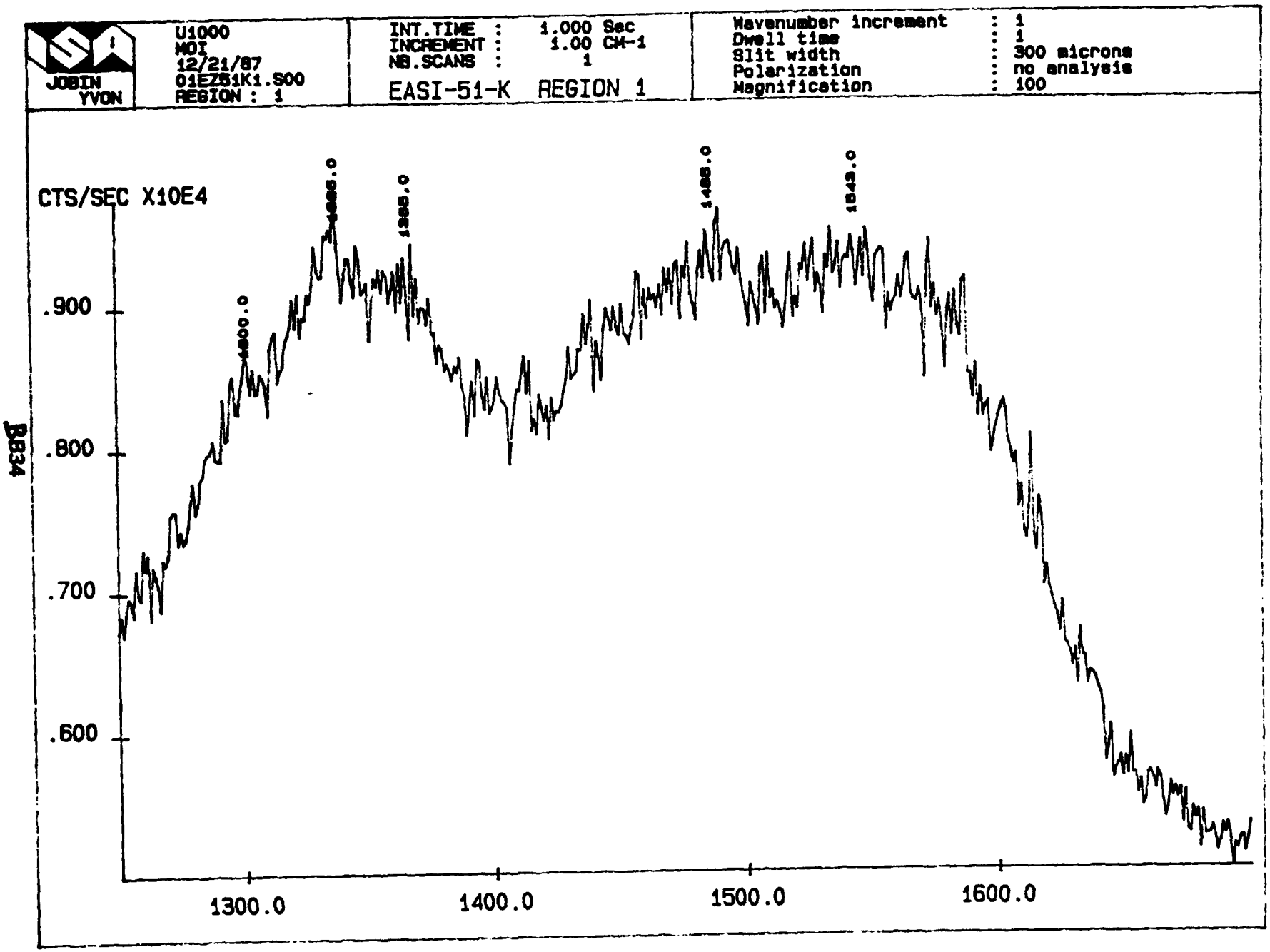
U1000
MOI
12/21/87
01EZ51K1.S00
REGION : 1
JOBIN
YVON
INT.TIME : 1.000 Sec
INCREMENT : 1.00 CM-1
NB.SCANS : 1
EASI-51-K REGION 1
Wavenumber increment : 1
Dwell time : 1
Slit width : 300 microns
Polarization : no analysis
Magnification : 100
CTS/SEC X10E4
.900
.800
.700
.600
1300.0
1400.0
1500.0
1600.0
1400.0
1395.0
1488.0
1543.0
B834

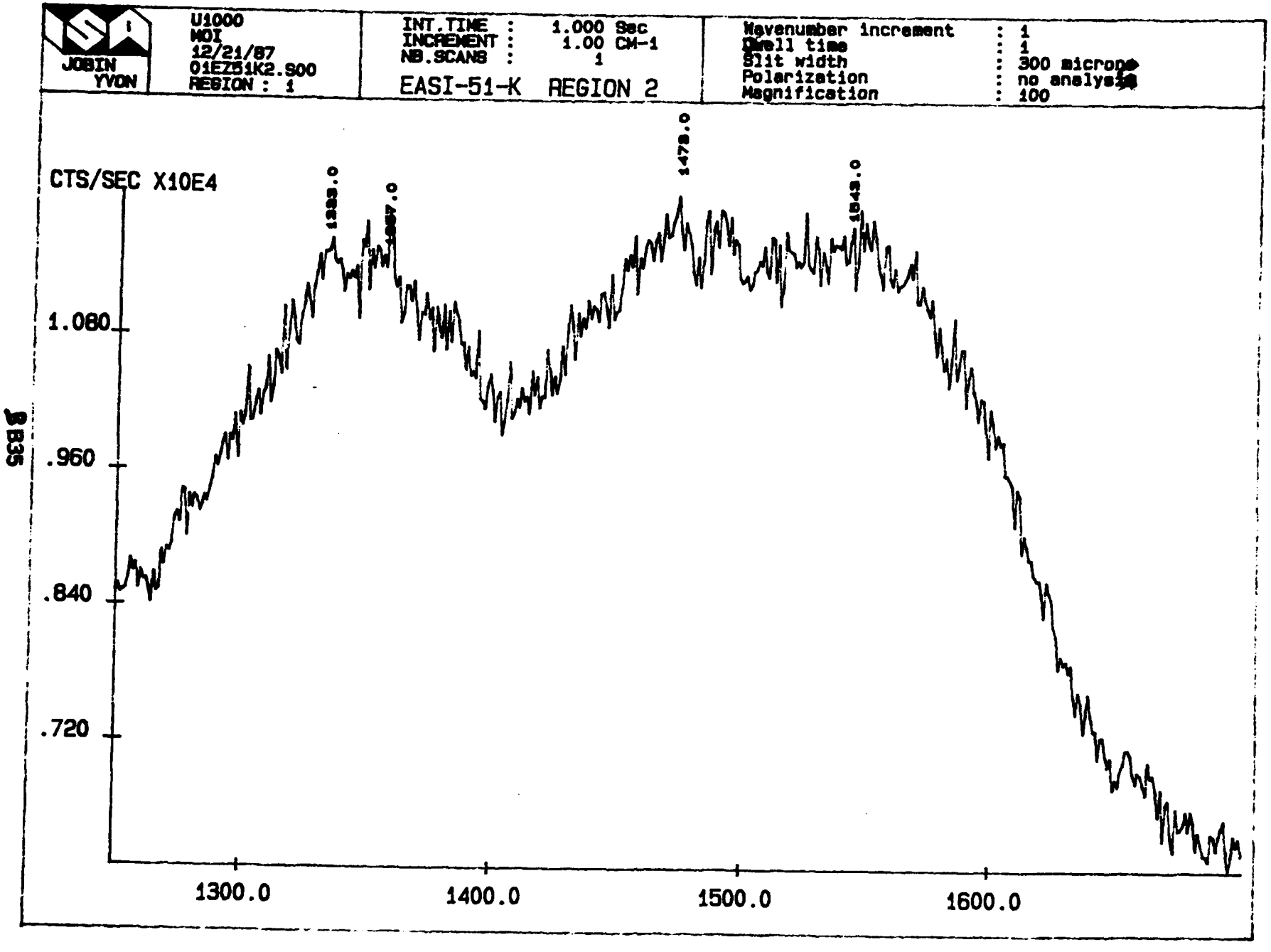
JOBIN YVON
U1000
MOI
12/21/87
01EZ51K2.S00
REGION : 1
INT.TIME : 1.000 Sec
INCREMENT : 1.00 CM-1
NB.SCANS : 1
EASI-51-K REGION 2
Wavenumber increment : 1
Dwell time : 1
Slit width : 300 microns
Polarization : no analysis
Magnification : 100
CTS/SEC X10E4
1.080
.960
.840
.720
1300.0
1400.0
1500.0
1600.0
1293.0
1357.0
1478.0
1543.0

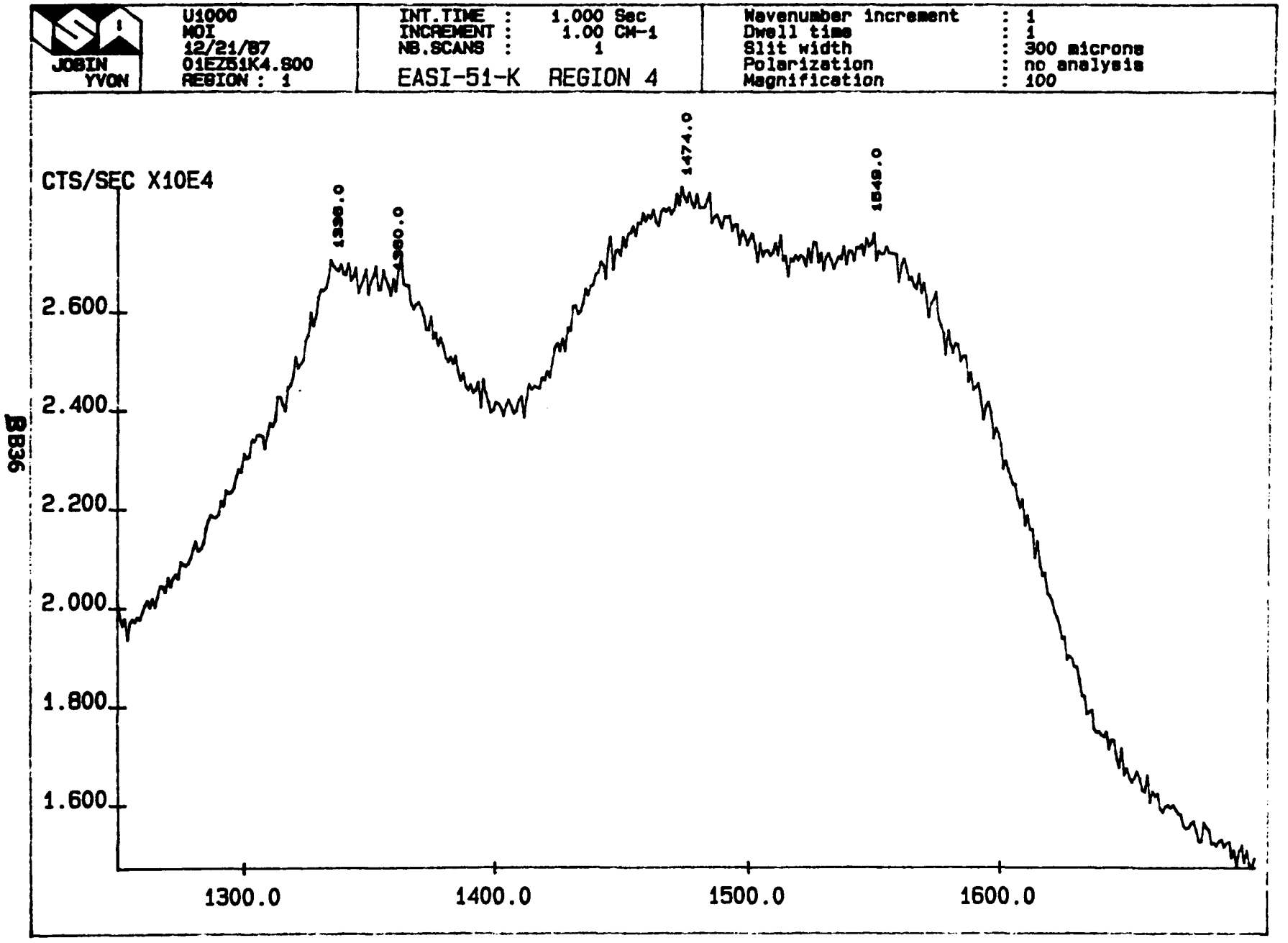
U1000
MOI
12/21/87
01EZ51K4.S00
REGION : 1
JOBIN
YVON
INT.TIME : 1.000 Sec
INCREMENT : 1.00 CM-1
NB.SCANS : 1
EASI-51-K REGION 4
Wavenumber increment : 1
Dwell time : 1
Slit width : 300 microns
Polarization : no analysis
Magnification : 100
CTS/SEC X10E4
BB36
1338.0
1380.0
1474.0
1548.0
2.600
2.400
2.200
2.000
1.800
1.600
1300.0
1400.0
1500.0
1600.0

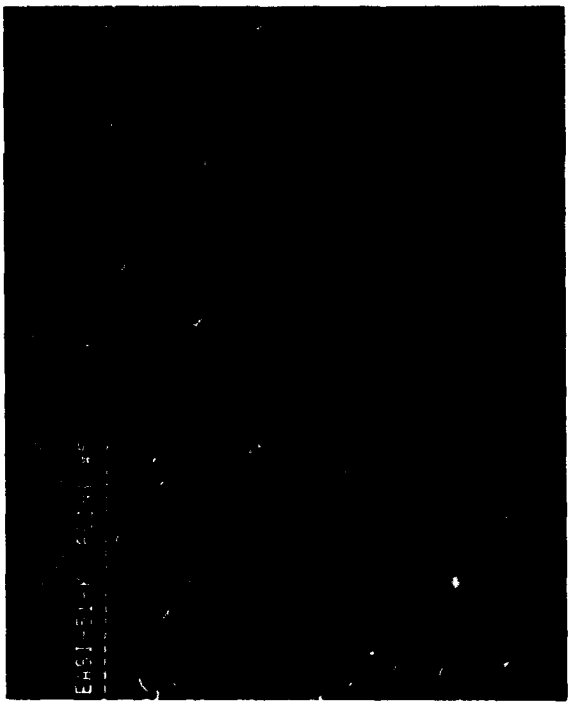

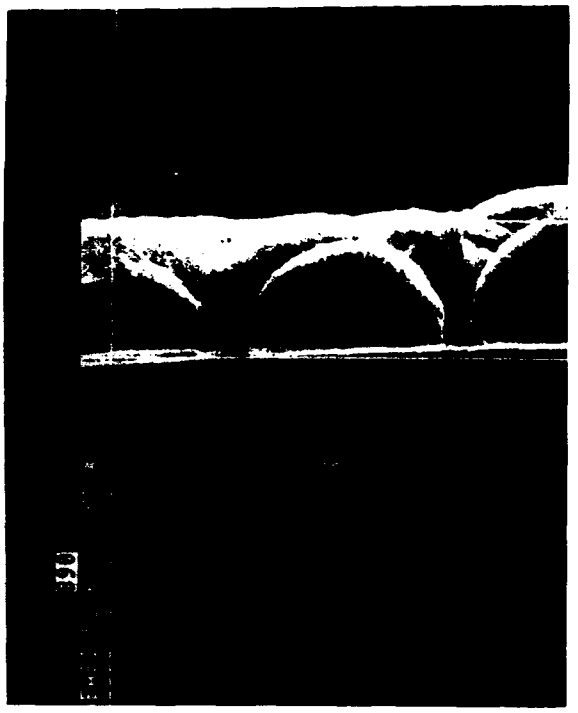

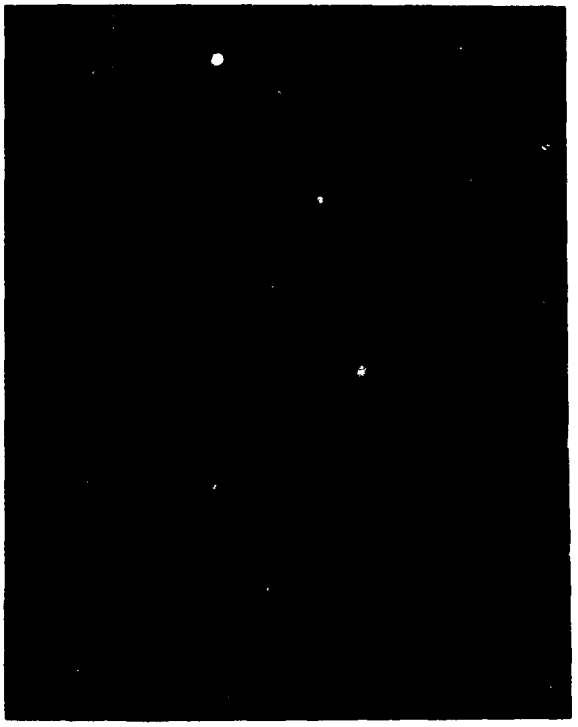

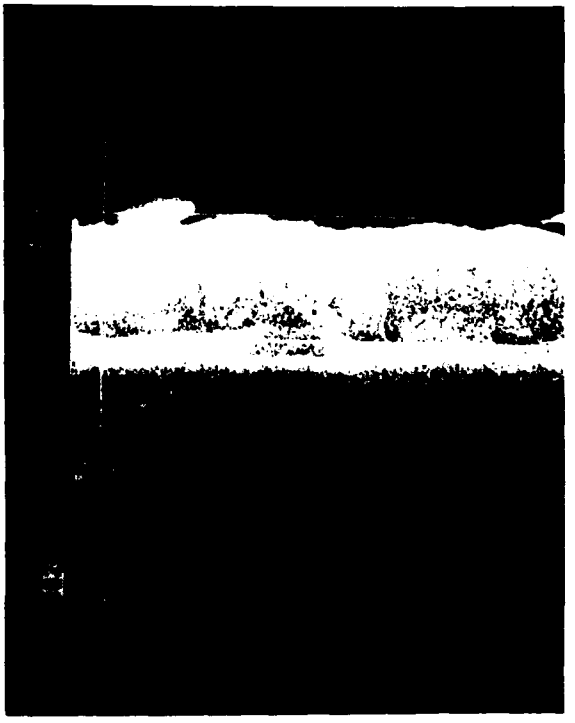

BB37

APPENDIX CC

L.S. Plano, S. Yokota, and K.V. Ravi, "Thin Film Diamond Deposition on Sapphire and Silicon Carbide for Tribological Testing, Crystallume, Menlo Park, CA, 30 June 1988, Hughes P.O. P9-519308-SLX

APPENDIX II

Thin Film Diamond Deposition on Sapphire and Silicon Carbide For Tribological Testing

L.S.Plano, S.Yokota and K.V.Ravi
Crystallume
125 Constitution Drive, Menlo Park, CA 94025

Submitted to:

Hughes Aircraft Corporation

Attention: Dr. Mike Gardos

6/30/88

Sample Shipment

Diamond on Sapphire

Sample #

P-1-Q-9

9-S-4

9-S-5

9-S-6

Diamond on Silicon Carbide

13-Y-7 - 3 Triboflats

13-Y-6 - 1 Triboflat

3-I-10 - 3 Tribopins

13-Y-6 - 1 Tribopin

Diamond on Single Crystal Silicon Carbide

3-I-10 - 4 single crystal silicon carbide Triboflats

Introduction

Plasma enhanced CVD diamond thin films have been deposited on single crystal sapphire and single and polycrystalline silicon carbide with the objective of providing thin continuous, adherent films of diamond for friction and wear tests. The details of the experimental procedures and the results are discussed here.

Diamond deposition on single crystal Sapphire

4 inch diameter wafers of polished single crystal sapphire were used as substrates for diamond deposition. From earlier work performed at Crystallume it has been established that adhesion of diamond films to sapphire is generally quite poor in the absence of adhesion promoting intermediate layers. Adhesion of diamond is found to be a function of the carbide forming nature of the substrate. Strong carbide formers such as the refractory metals and silicon and titanium are found to adhere strongly to diamond films whereas weak carbide formers such as copper, silver, and oxides such as sapphire, silica adhere poorly to diamond. As a result the ability to promote adhesion between non carbide formers and diamond is based upon the incorporation of carbide forming interlayers in the structure. In the present work thin (250 Å) films of titanium were sputtered on the sapphire wafers prior to diamond deposition. The presence of the titanium film also assists surface conductivity of the wafers which is required in the DC biased systems used for diamond synthesis.

The following experimental conditions were used for diamond deposition:

Methane volume %	0.3 to 0.5
Hydrogen volume %	99.7 to 99.5
Deposition temperature	550 and 725º C

The 550 ºC temperature was chosen in order to determine if diamond bonding can be promoted at temperatures below 600 ºC. The films were characterized by Raman spectroscopy and scanning electron microscopy. The methane to hydrogen ratio was varied since it has been shown to strongly influence the nature of the bonding between carbon atoms, a low methane concentration promoting sp^3 bonding. The relationship between

methane concentration and the ratio of sp^3 to sp^2 bonded carbon in diamond films is shown in figure below. The sp^3/sp^2 ratio is obtained from the ratio of the relevant peak heights from Raman spectra of the films.

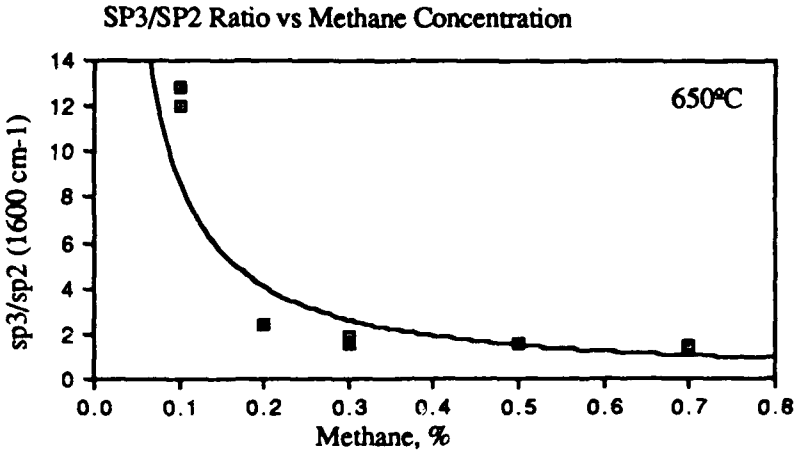

The specific process conditions utilized to deposit diamond films on titanium coated sapphire wafers are as follows:

Sample #	CH_4 concentration (volume %)	Film thickness	Deposition Temperature
P-1-Q-9	0.5 %	3000 Å	725 ºC
9-S-4	0.3 %	7500 Å	725 ºC
9-S-5	0.5 %	7000 Å	550 ºC
9-S-6	0.5 %	2000 Å	550 ºC

The high temperature deposition with the higher methane concentration resulted in the best film in terms of film continuity and uniformity. Figure 1 shows typical scanning electron micrographs and a Raman spectrum from diamond film deposited on titanium coated sapphire (Sample # P-1-Q-9). The Raman spectrum indicates diamond bonding in the film by the presence of a sharp peak at 1337 wavenumbers. However the film also

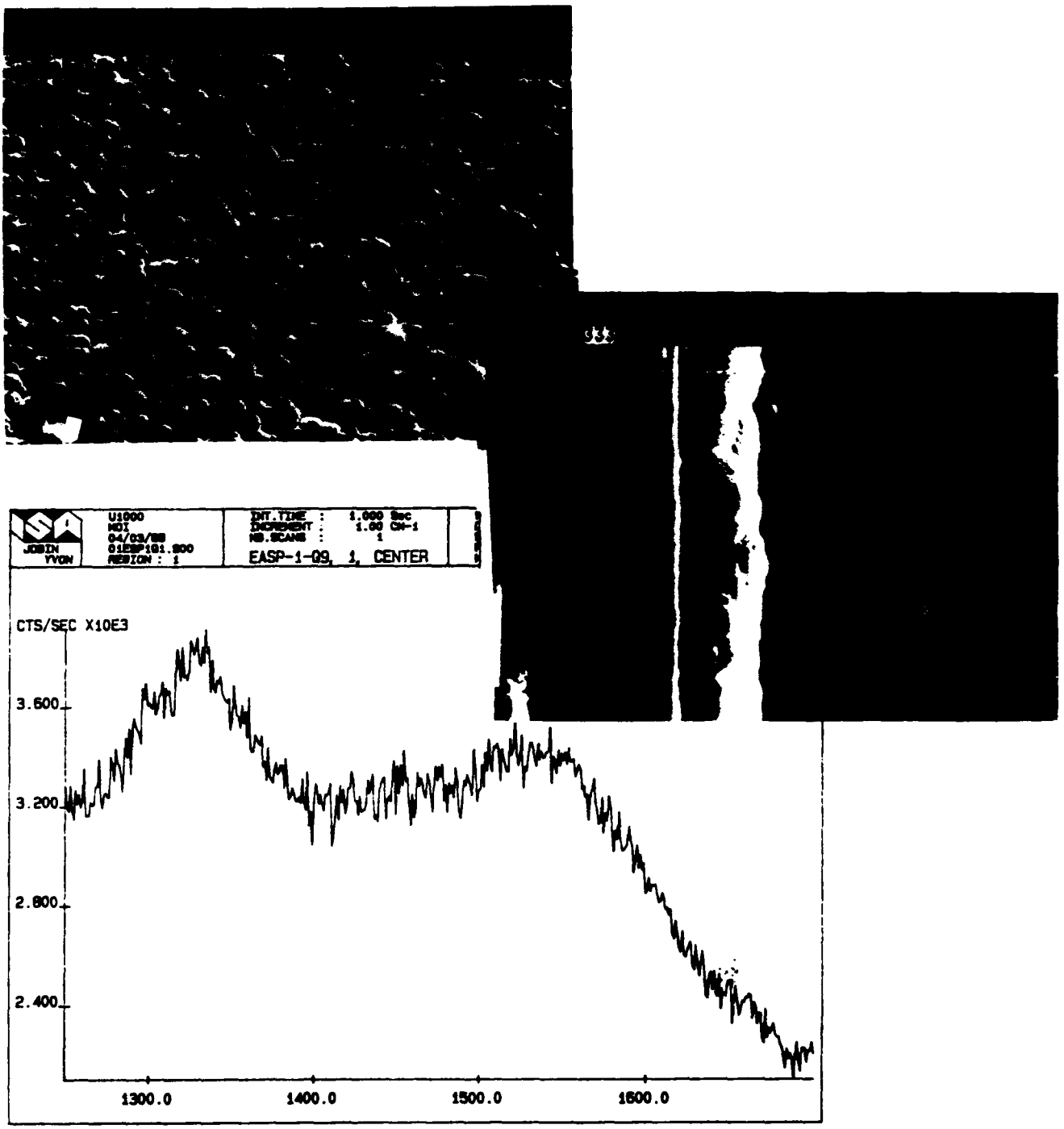

Figure 1. Scanning electron micrographs (plane view and cross sectional view) and Raman spectrum of diamond film on sapphire. The sapphire has been coated with a thin (~ 250 Å) film of titanium to promote adhesion.. (Sample # P-1-Q-9)

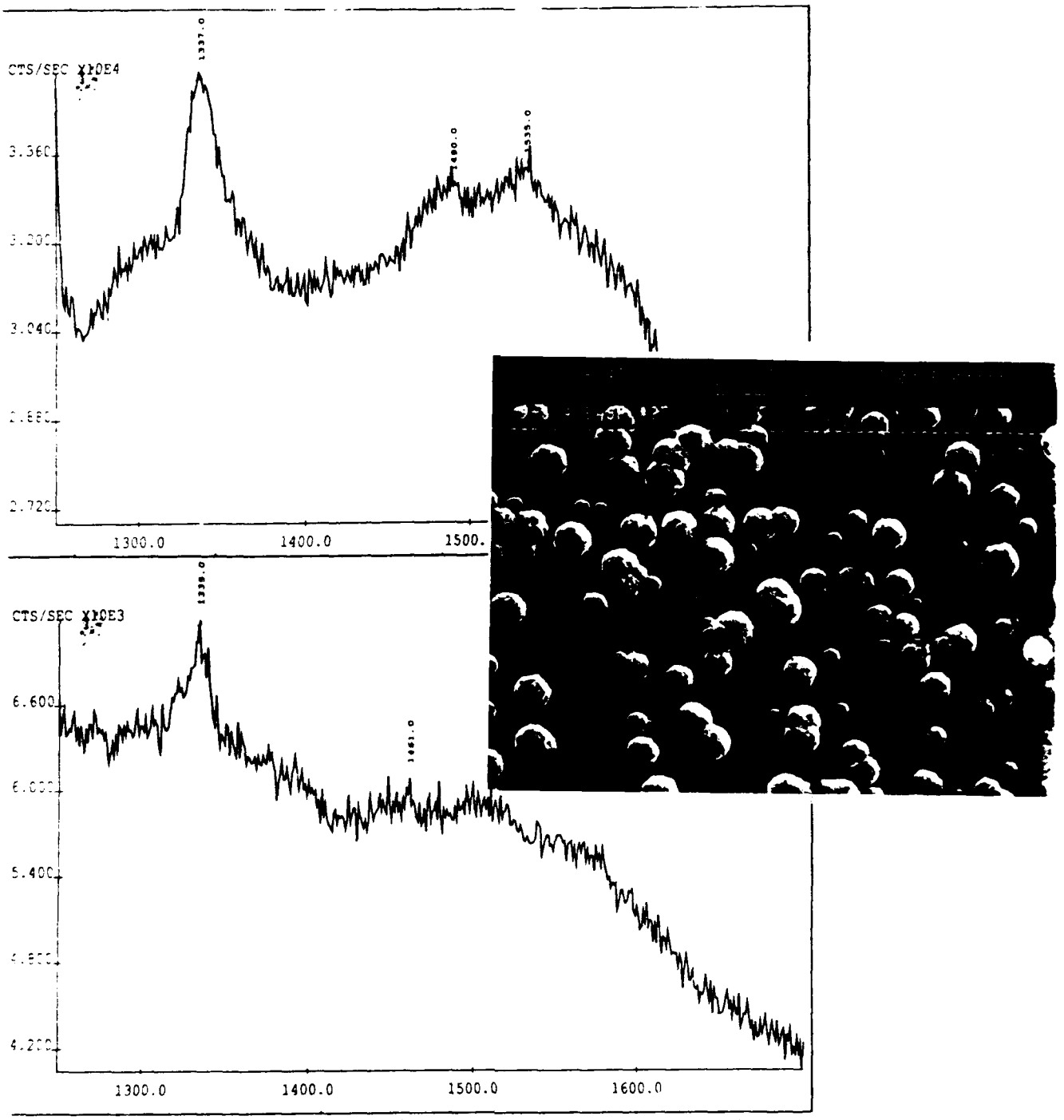

Figure 2. SEM micrograph and Raman spectra from diamond deposited on titanium coated sapphire utilizing a reduced methane concentration in the gas mix. The nucleation density is much reduced and discrete crystallites of diamond result. As expected the quality of the diamond is improved as evidenced by the increased spharpness and magnitude of the Raman peak at ~ 1335 wave numbers.

contains sp^2 bonded carbon as indicated by the presence of the broad peak centered around 1500 wavenumbers.

Reducing the methane concentration to enhance the sp^3 content of the film had the effect of reducing the nucleation density of diamond and the result is found to be a discontinuous film composed of discrete crystallites of diamond as shown in figure 2. The corresponding Raman spectra show the expected improvement in film quality with a sharper peak at ~1335 wave numbers as compared to the corresponding peak observed in figure 1.

The initial attempts at low temperature deposition on titanium coated sapphire have not been successful. Figure 3 shows the surface structure and a Raman spectrum of a film deposited at 550 °C. No Raman signal has been observed from this film. The lack of a distinct Raman signal may be related to the possible amorphous nature of the film or due to insufficient film thickness. However the film thickness has been estimated to be 7000 Å using an alpha step apparatus. The surface structure of the film, as observed in an SEM, is featureless suggesting an amorphous nature. A thinner film deposited at the same temperature displayed similar structural characteristics (Figure 4).

Concluding comments - Diamond on Sapphire

Diamond deposition on sapphire substrates has been achieved by using an adhesion promoting intermediate layer which is a carbide former. The phase mix in the diamond film on titanium coated sapphire follows the expected pattern with the concentration of sp^3 bonded carbon being high when the methane concentration is kept low. However when the methane concentration is kept low the nucleation density is reduced and the resulting films are discontinuous. In these series of experiments attempts have not been made to promote the initial nucleation of diamond by utilizing a high methane to hydrogen ratio followed by the deposition of a higher quality of diamond using a reduced concentration of methane. Further work is recommended whereby nucleation is promoted by the use of such a two stage deposition process. This approach has been successfully applied to the deposition of high quality thin films of diamond on silicon.

The results of low temperature diamond deposition on titanium coated sapphire have been inconclusive. Further work is needed to better understand the mechanisms at work in the synthesis of low temperature diamond films by plasma CVD.

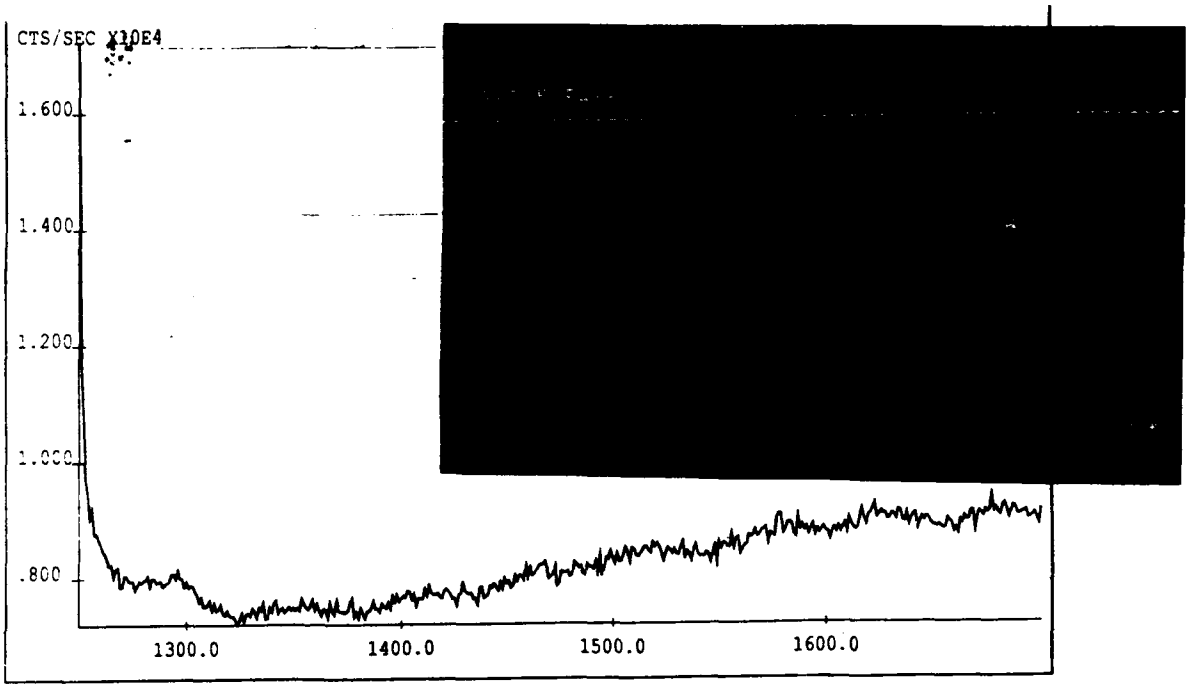

Figure 3. Scanning electron micrograph and Raman spectrum of diamond on titanium coated sapphire. Diamond deposition was achieved at 550 ºC

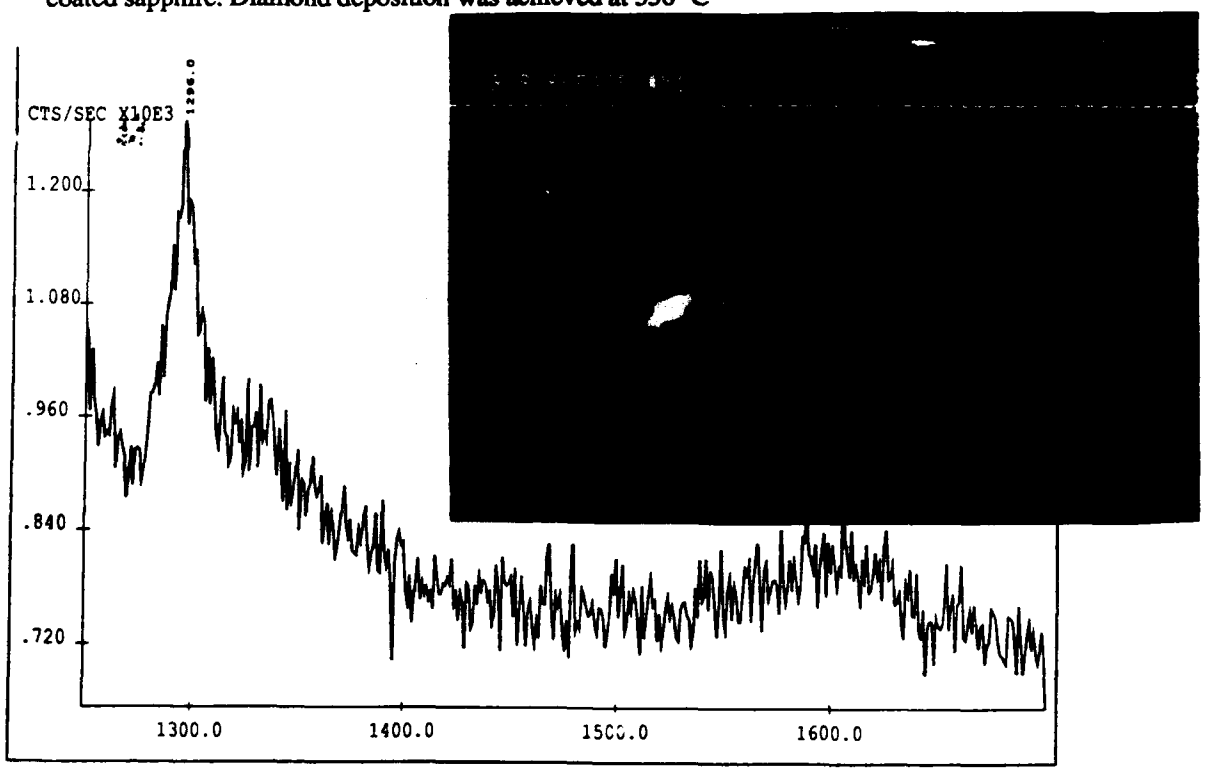

Figure 4. SEM image and Raman spectrum of thin diamond film on sapphire deposited at 550 ºC. In both figure 3 and 4 no distinct Raman peaks are observed in the Raman spectrum.

Diamond deposition on Silicon Carbide

The following table indicates the substrates and the process conditions employed for diamond deposition on silicon carbide :

Material	Surface treatment	Methane concentration	Film Thickness
Polycrystalline silicon carbide triboflats	Selected samples were etched in HF and HNO_3	0.3%	Typically 1 - 2 μM
Polycrystalline silicon carbide tribopins	"	"	"
CVD single crystal silicon carbide on single crystal silicon	"	"	"

• The silicon carbide triboflats and the tribopins in HIP and canned HIP conditions were obtained from Hughes (Mike Gardos).

• The single crystal silicon carbide on silicon wafer was obtained from North Carolina State University (Professor Bob Davis) and the wafer was fabricated by Fujitsu. The wafer was diced into the dimensions required for the SEM tribotester at Hughes.

The results of diamond deposition on silicon carbide are as follows:

Polycrystalline Silicon Carbide Triboflats

Figure 5 shows scanning electron micrographs of diamond films deposited on silicon carbide triboflats. The structure of the films is composed of facetted crystallites ~ 1 μM in diameter with the structure being essentially independent of the substrate preparation treatment. Both the HIP and the canned HIP specimens show similar structure and etching

the substrate with HF and HNO_3 solutions prior to diamond deposition appeared to have no effect. The thickness of the diamond films is estimated to be 1 μM although it has not been possible to obtain precise thickness information due to the lack of a clean interface that can be observed in the SEM.

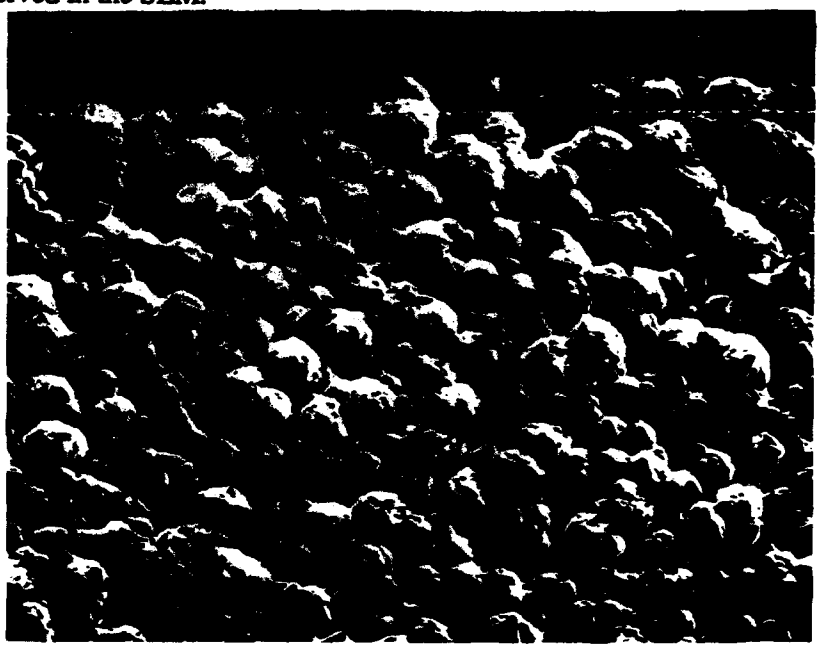

Figure 5. Typical example of surface structure of polycrystalline diamond on polycrystalline silicon carbide.

Polycrystalline Silicon Carbide Tribopins

The silicon carbide tribopins ~ 1 cm in length were diamond coated using a specially configured diamond reactor with a capability of depositing diamond films on non flat substrates. An important issue in this context is the ability to deposit diamond films uniformly over the tool. The uniformity characteristics of the film on the tool are shown in the series of scanning electron micrographs in figure 6. The structure of the film is observed to be very uniform over the entire coated surface of the pin with a tendency for some enhanced degree of facetting at the tip of the pin. It is also to be noted that the grain size of the diamond film in the early stages of nucleation is significantly smaller than the grain size of the silicon carbide substrate. This is evident from the micrograph of the transition region between the coated and the uncoated regions of the pin shown in figure 6. The grain size of the silicon carbide particles are in the several microns range while the diamond crystallites appear to be < 0.5 μM in size. This suggests that nucleation of

diamond on silicon carbide is not promoted by grain boundaries in the carbide but that nucleation is inragranular.

Figure 7 is a Raman spectrum of the diamond film on the tribopin. As in the case of the triboflats the quality of the diamond is found to be excellent.

Single Crystal Silicon Carbide

Diamond deposition on single crystal silicon carbide (CVD on single crystal silicon) was accomplished using the same process conditions as employed for diamond deposition on polycrystalline silicon carbide. The results however were found to be quite different. The barrier to diamond nucleation appears to be significantly higher on the single crystal surface. Figure 8 shows the typical surface structure of diamond film on single crystal silicon carbide. Widely separated crystallites are observed, the structure being very similar to that observed on single crystal sapphire (Figure 2). To enhance nucleation density the gas pressure in the diamond reactor was increased resulting in a higher nucleation density as shown in the bottom micrograph in figure 8. However continuous thin films of diamond have not been achieved to date on single crystal silicon carbide. Comparing the structure in Figure 8 to that of diamond film on silicon carbide (Figure 5) indicates that a significantly higher nucleation density is achievable on polycrystalline silicon carbide leading to continuous, thin films of diamond.

The dependance of nucleation density on gas pressure has also been observed on silicon carbide triboflats, although continuous films have been observed at gas pressure levels at which discrete particles are still observed on single crystal silicon carbide. Figure 9 shows an example of the gas pressure dependance of diamond nucleation on silicon carbide triboflats. The two gas pressure levels utilized to obtain the two structures were identical to that use to achieve the structures on single crystal silicon carbide shown in figure 8.

A phenomenon that has been often reported in the case of nucleation of diamond films on single crystal silicon surfaces has also been noted in the case of single crystal silicon carbide. The presence of any surface damage in the form of scratches often results in profuse nucleation of diamond in the vicinity of the scratch. Figure 10 shows an example in the case of single crystal silicon carbide. The surface scratches are observed to function as local nucleation sites for diamond crystallites.

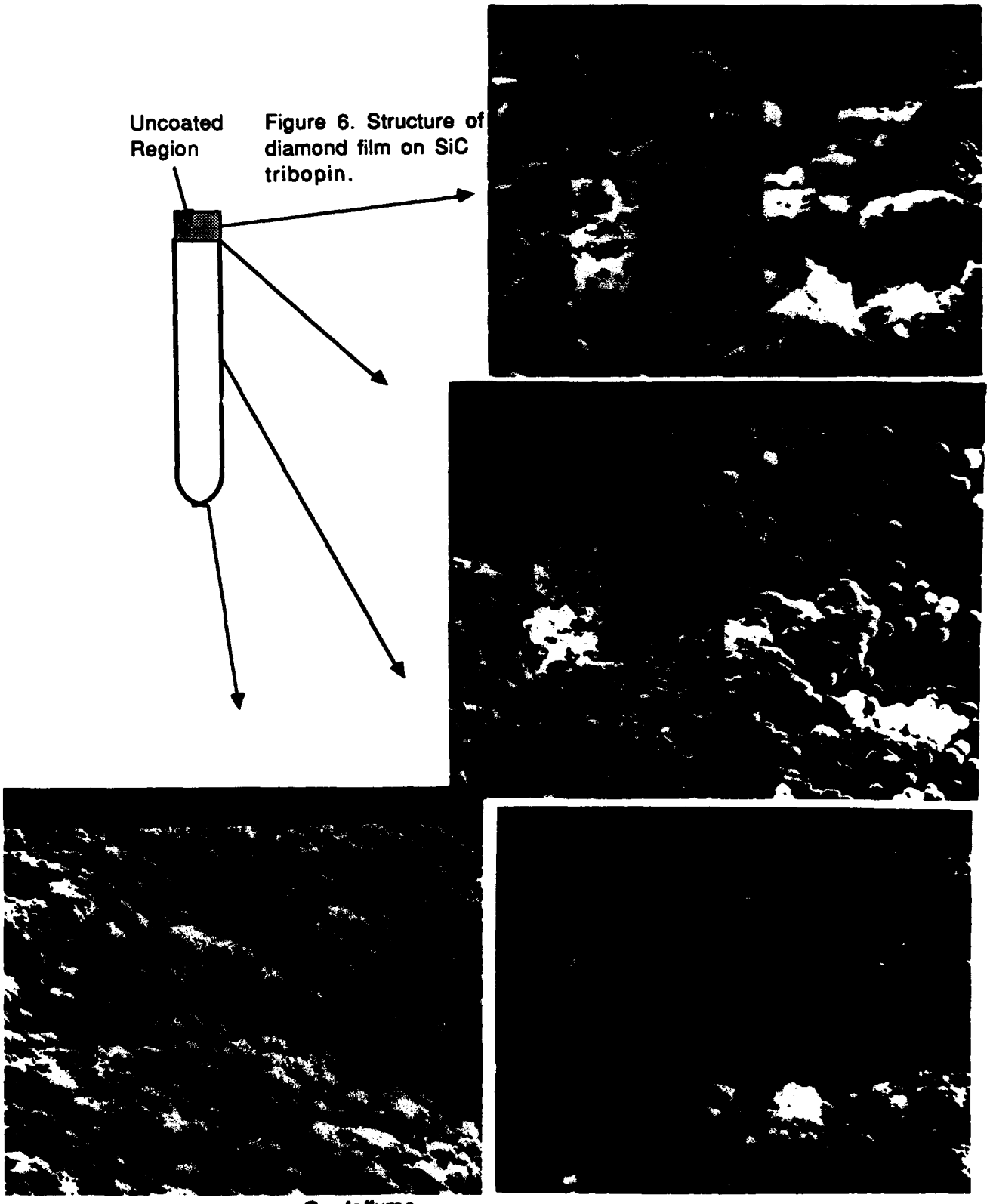

Figure 6. Structure of diamond film on SiC tribopin.

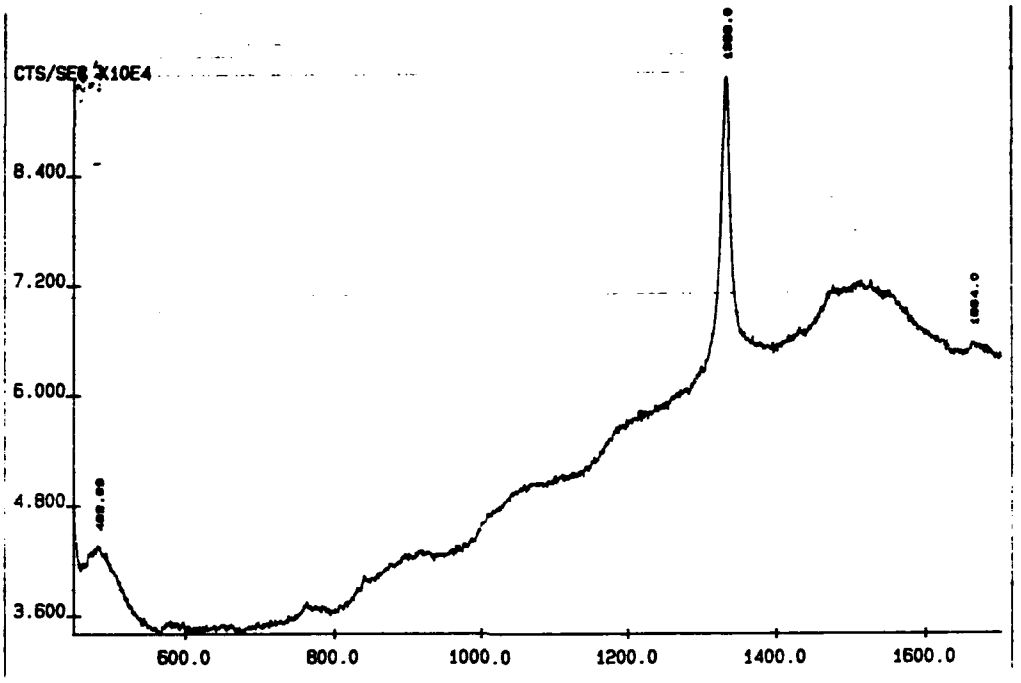

Figure 7. Raman spectrum of diamond film on silicon carbide tribopin

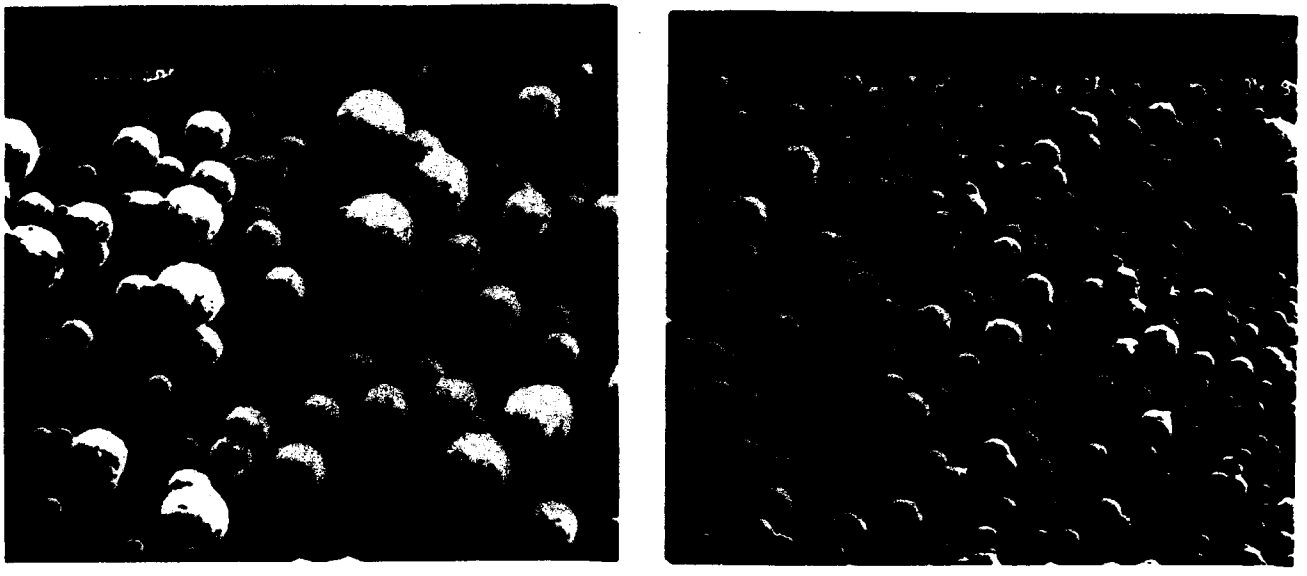

Figure 8. Structure of diamond crystallites on single crystal silicon carbide. Structure on the left was achieved utilizing the same diamond deposition conditions as was used to deposit diamond films on polycrystalline SiC triboflats (Figure5). The structure on the right was achieved by increasing the gas pressure in the reactor to enhance nucleation rate.

Figure.9 Gas pressure dependance of nucleation density of diamond on polycrystalline silicon carbide. Low gas pressure on the left.

Figure 10. Scanning electron micrograph of a diamond film on a single crystal silicon carbide surface showing the effect of a surface scratch on the nucleation of diamond crystallines. The low magfnification micrograph on the left shows the region of scratches on the surface. The higher magnification display on the right shows profuse nucleation at the site of the scratches.

Conclusions

The present work has been directed at the deposition of thin, continuous, high quality diamond films on materials of interest in the tribological and optical fields. Diamond deposition on sapphire single crystals and silicon carbide single and polycrystals as well as on silicon carbide tribopins has been achieved. The key results and some implications of the work are as follows:

- Diamond films of high quality as represented by the high content of sp^3 bonded carbon can be readily deposited on materials as disparate as sapphire and silicon carbide.

- The quality of the film with respect to the diamond to the graphite ratio is found to be a function of the methane to the hydrogen ratio in the plasma gas mix, as has previously been demonstrated.

- Film quality is also observed to be a function of the substrate on which the diamond is deposited with silicon carbide surfaces yielding high quality films. Titanium coated sapphire single crystal substrates have to date only resulted in films containing a mixture of diamond and graphite.

- In general, diamond deposition on sapphire has not been a very well controllable process. Further work is needed to better understand the nature of the interface between diamond films and oxides such as aluminum oxide and titanium oxide. It is speculated that the thin titanium layer utilized to promote bonding between the diamond and the sapphire may be oxidized and as such the oxide of titanium may be playing a part in influencing nucleation, the phase mix and adhesion in the diamond titanium system. The use of higher density plasmas as achievable in, for example, microwave enhanced CVD may be needed to promote bonding between diamond and oxides.

- The results of diamond deposition on silicon carbide have been excellent. Diamond deposition on polycrystalline silicon carbide yields high quality, continuous films.

• Diamond films deposited on single crystal silicon carbide, under the conditions utilized in these experiments, have been found to be discontinuous.

• The nucleation of diamond films on both single crystal and polycrystalline silicon carbide has been found to be a function of the gas pressure. Continuous films of diamond are more readily achieved on polycrystalline silicon carbide while for the pressure ranges utilized in these experiments continuous films of diamond have not been achieved on single crystal silicon carbide. There is a larger barrier to nucleation on single crystal silicon carbide than on polycrystalline silicon carbide.

• Diamond deposition on silicon carbide tribopins has been readily achieved by the use of a specially configured diamond reactor. The uniformity of the diamond film in terms of thickness, grain size, structure and morphology has been found to be very good over the entire surface of the three dimensional tribopin. This result indicates that the plasma CVD approach exhibits good throwing power permitting uniform coverage of complex shapes. This is an important result in the use of CVD diamond technology in conjunction with complex shaped components and hardware such as tools, lenses, mirrors, bearings etc. which can benefit from the superior tribological, mechanical, chemical, thermal and radiation resistance properties of diamond films.

An important outcome of this work is the development of technology for the deposition of thin, continuous, high quality diamond films on a variety of substrates. Thin films ($\leq 2\ \mu M$) are required for tribological applications since thicker films tend to suffer from excessive residual stress and can less easily accomodate interfacial stresses generated due to differences in thermal expansion coefficients between the diamond and various substrates of interest. The ability to deposite thin films in a controllable manner is dependant upon an undersatnding of nucleation and growth mechanisms at work in diamond film synthesis.

APPENDIX DD

L.S. Plano, S. Yokota, and K.V. Ravi, "Thin Film Diamond Deposition on Silicon Carbide," Crystallume, Menlo Park, CA, 12 September 1988

Thin Film Diamond Deposition on Silicon Carbide

L.S.Plano, S.Yokota and K.V.Ravi
Crystallume
125 Constitution Drive, Menlo Park, CA. 94025

Submitted to:

Hughes Aircraft Corporation
Attention: Dr. Mike Gardos
9/12/88

Introduction

The objective of this final phase of the Crystallume subcontract with Hughes Aircraft was to deposit thick diamond films on a variety of silicon carbide substrates, characterize the films and deliver coated parts. The substrates used are tabulated below.

Substrate	Comments
Single crystal β–SiC on single crystal silicon .	Thin diamond films have been difficult to nucleate on single crystal SiC. Thick film growth has been found to be effective.
Sintered α- Silicon Carbide triboflats	Triboflats previously coated with thin (1-2 μM) diamond films were returned to Crystallume for depositing thick diamond films on the reverse side of the flats. One etched and one unetched HIP sample, respectively, were subjected to thick film deposition.
3 in. diameter, ~ 0.5 in thick, graphite fiber reinforced glass matrix composite billet (HAC-GLAS-13-2) coated with polished, polycrystalline β-SiC.	β-SiC film on the billet was extremely non uniform and discolored.
Single crystal silicon troboflat for thickness calibration	Following diamond deposition the silicon sample was cut in half for accurate film thickness measurement.

Diamond deposition conditions were chosen to ensure maximum nucleation density in the early stages of the process and the achievement of high quality for the majority of the film. The reactor design had to be modified to accommodate the variety of samples of different sizes. In order to conserve space in the reactor the small tribo flats, the single

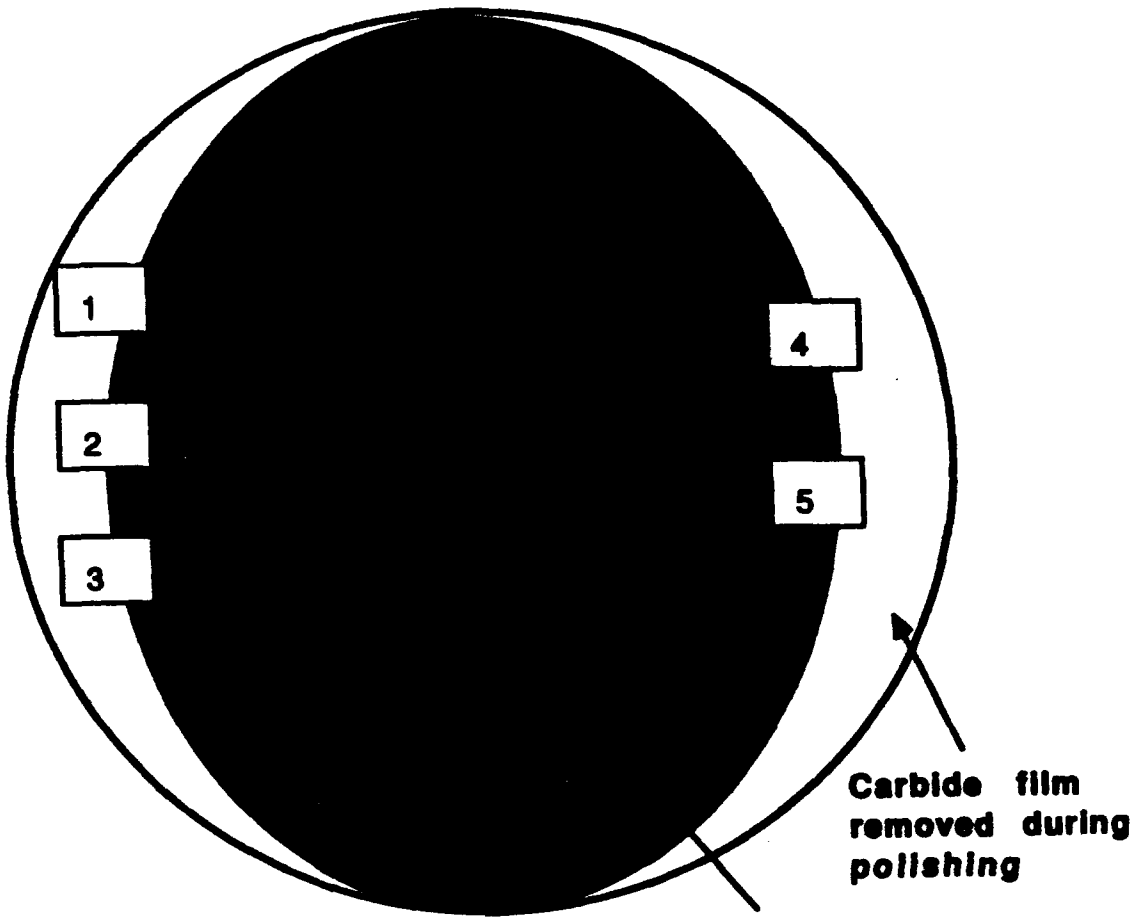

1. SiC Tribo Flat - Etched HIP
2. Single crystal SiC on silicon
3. Single crystal silicon thickness monitor
4. SiC Tribo Flat - Unetched HIP
5. Single crystal silicon thickness monitor

Figure 1. Sketch of the distribution of the various SiC and silicon specimens in the diamond deposition reactor

crystal SiC and silicon samples were placed on the graphite/glass matrix composite towards the periphery of the billet. This region was chosen since the polished SiC film on the billet had been removed at the edges of the billet. Figure 1 shows a schematic of the sample distribution in the reactor.

The results of the depositions were analyzed using scanning electron microscopy and Raman spectroscopy. The details of the analysis are as follows:

Diamond deposition on single crystal β-SiC on single crystal silicon

In figure 2 are shown scanning electron micrographs and Raman spectrum from the diamond film deposited on single crystal β-silicon carbide. Unlike the case with thin diamond film on single crystal silicon carbide the film is found to be continuous with a highly facetted structure. Based on the silicon calibration sample the thickness of the diamond film is estimated to be 8 to 10 μM. The Raman spectrum indicates a strong 1332 peak due to Sp^3 bonding. There is a small peak at 1538 cm-1 which is usually indicative of some degree of Sp^2 bonding in the film. This is very likely due to the Sp^2 contaminated nucleation layer deposited at the start of the deposition process.

Diamond deposition on polycrystalline α-SiC triboflats

Figures 3 and 4 show scanning electron micrographs and Raman spectra of diamond films deposited on α-SiC triboflats. The film thickness is estimated at 8 -10 μM. The structure is very well developed with sharply facetted crystallites with a predominantly {111} morphology. Occasional locally increased growth rates are observed in the unetched HIP specimen whose origins are not currently understood. The Raman spectra attest to the high quality of the films deposited. In this case as well the deposition process consisted in an initial nucleating promoting initial layer which can contribute to the observed 1546 wavenumber peak due to Sp^2 bonded carbon.

Diamond deposition on Graphite fiber/glass matrix composite billet.

In spite of the non uniform nature of the silicon carbide coating on the composite billet there were no major problems encountered in the diamond deposition process. However some volatile contaminant was found to evolve from the billet and coat the inner walls of the reactor with an orange colored film. The cracks in the carbide film appeared to

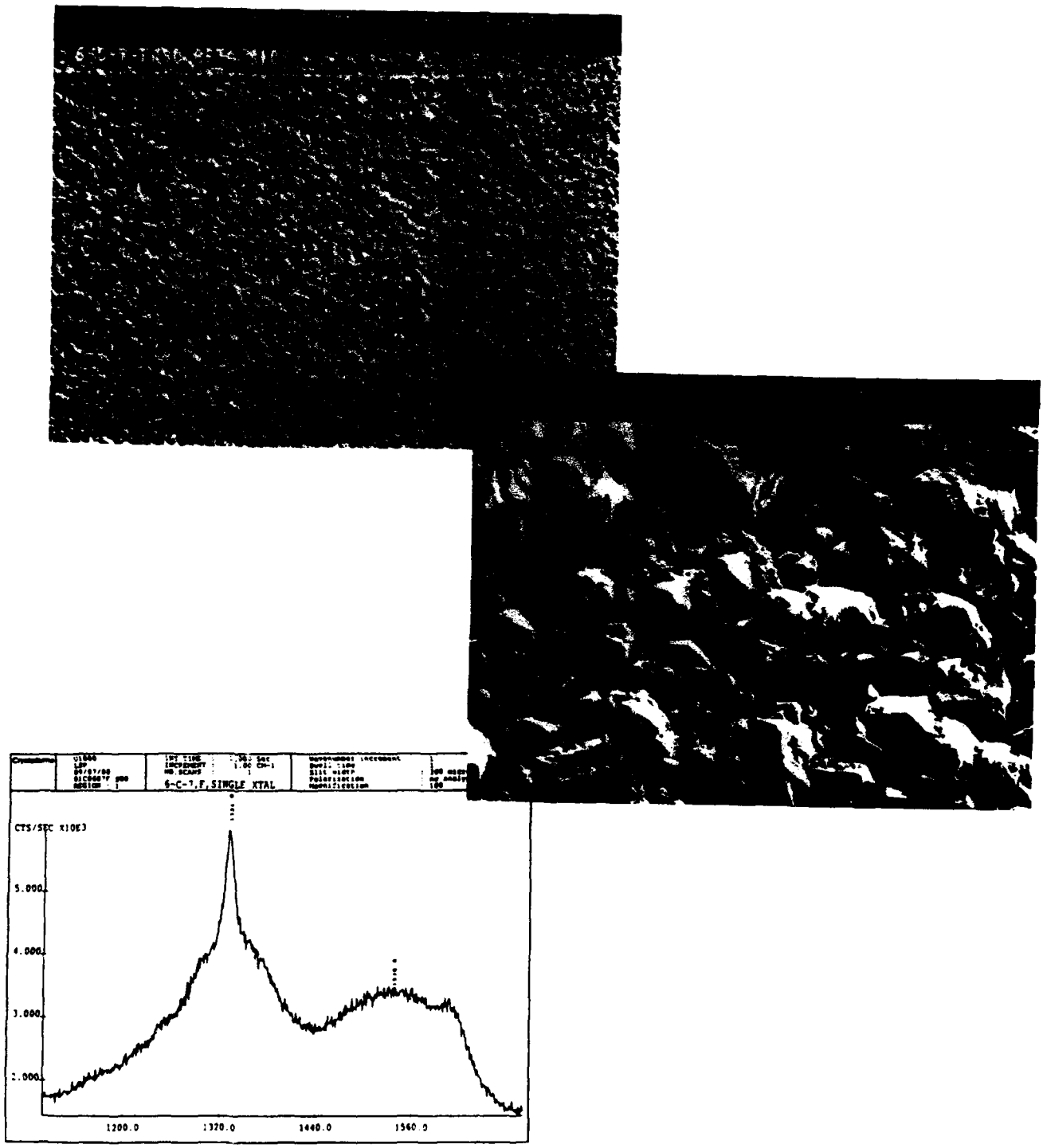

Figure 2. Scanning electron micrographs and Raman spectra of a thick diamond film deposited on single crystal β-Silicon Carbide

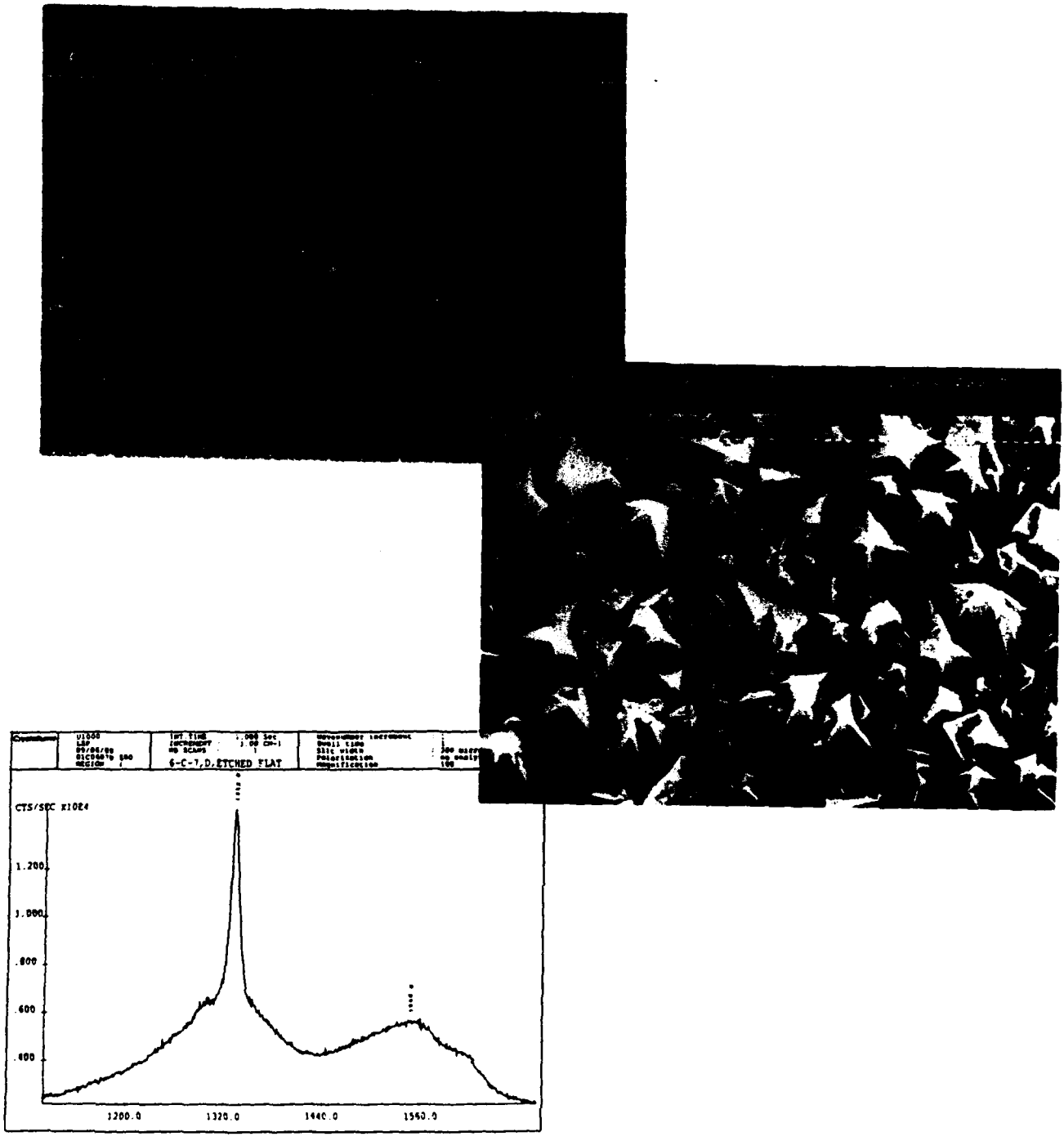

Figure 3. SEM images and Raman spectrum of diamond film deposited on an α-SiC triboflat (Etched HIP)

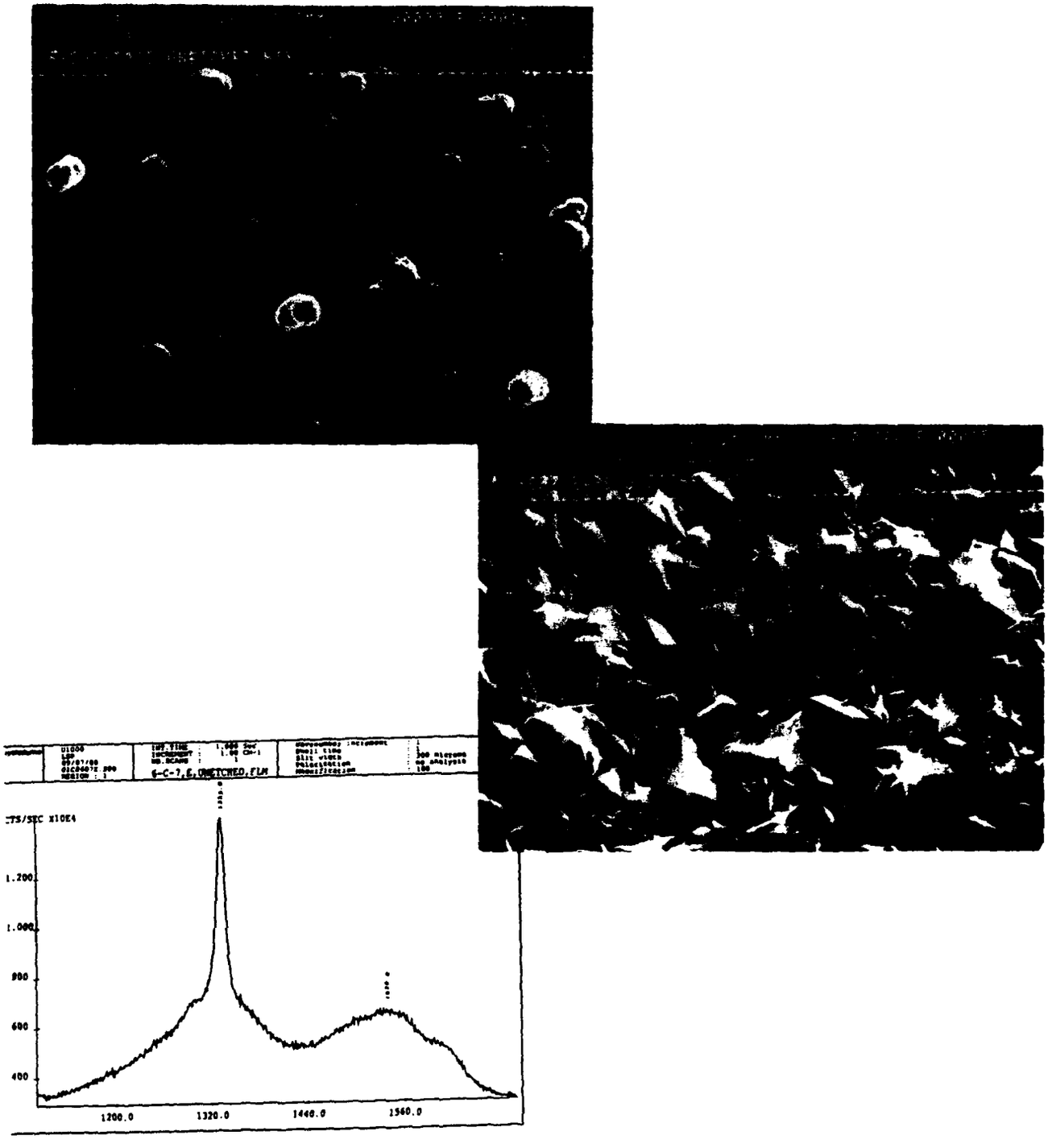

Figure 4. SEM micrographs and Raman spectrum of diamond film on an α-SiC triboflat (Unetched HIP)

be effectively covered up by the deposited diamond film although the traces of the cracks are still evident around the periphery of the sample. Figure 5 shows the cracks in the silicon carbide shown after diamond deposition. The higher magnification image shows the highly facetted crystalline diamond film.

Figure 5. SEM images of diamond coated composite billet showing the cracks in the SiC film being covered by the diamond film.

The diamond film was observed to be uniformly deposited over the region of the billet covered with silicon carbide. Figures 6 and 7 show SEM micrographs and Raman spectra at several locations on the 3 in. billet. The structure is found to quite uniform with occasional regions where local acceleration of the growth rate appears to have occurred.

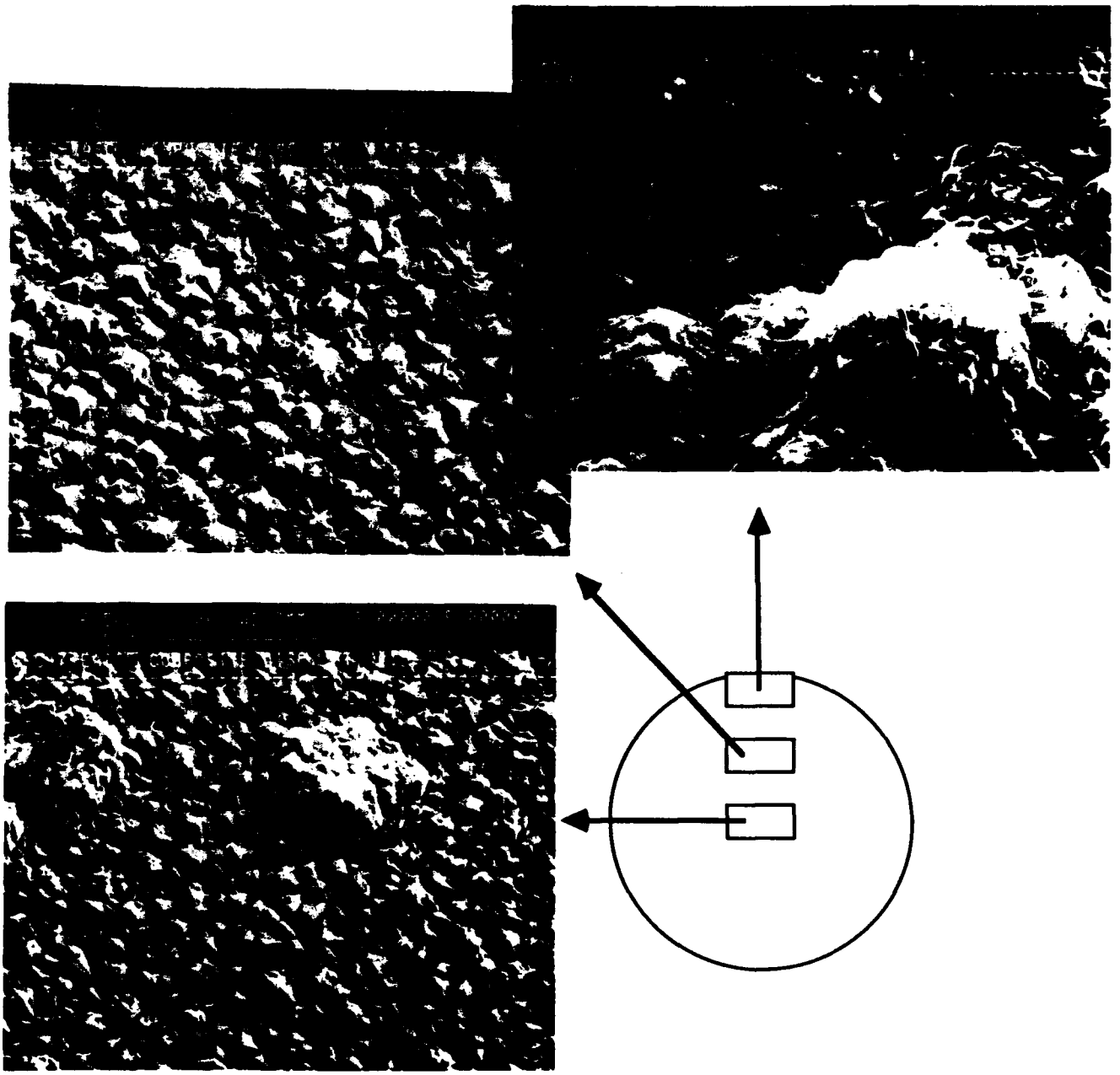

Figure 6. Surface structure of the diamond film at several regions on the graphite fiber/ glass composite billet.

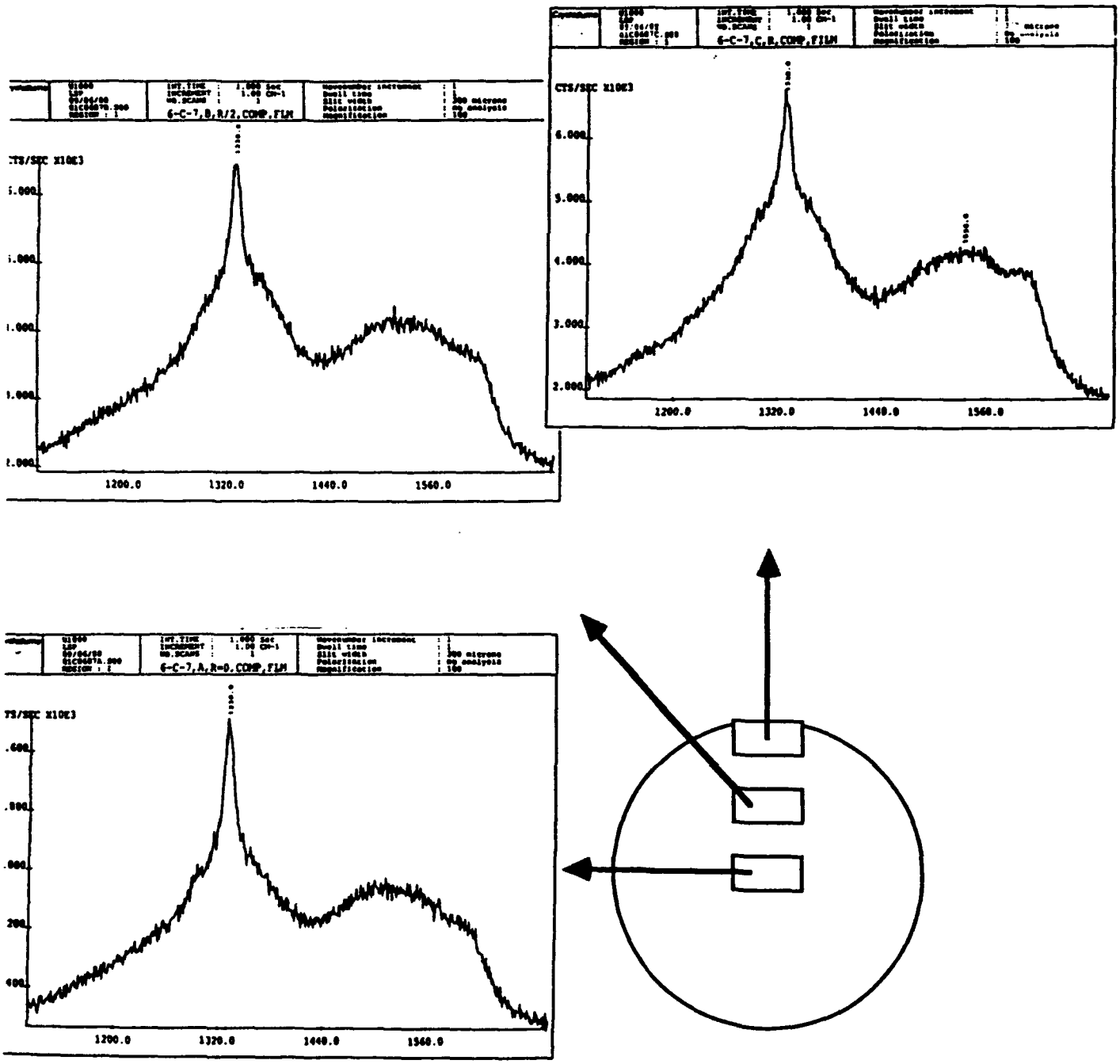

Figure 7. Raman spectra of diamond film at several regions on the graphite fiber/glass composite billet. These spectra correspond to the SEM micrographs shown in figure 6.

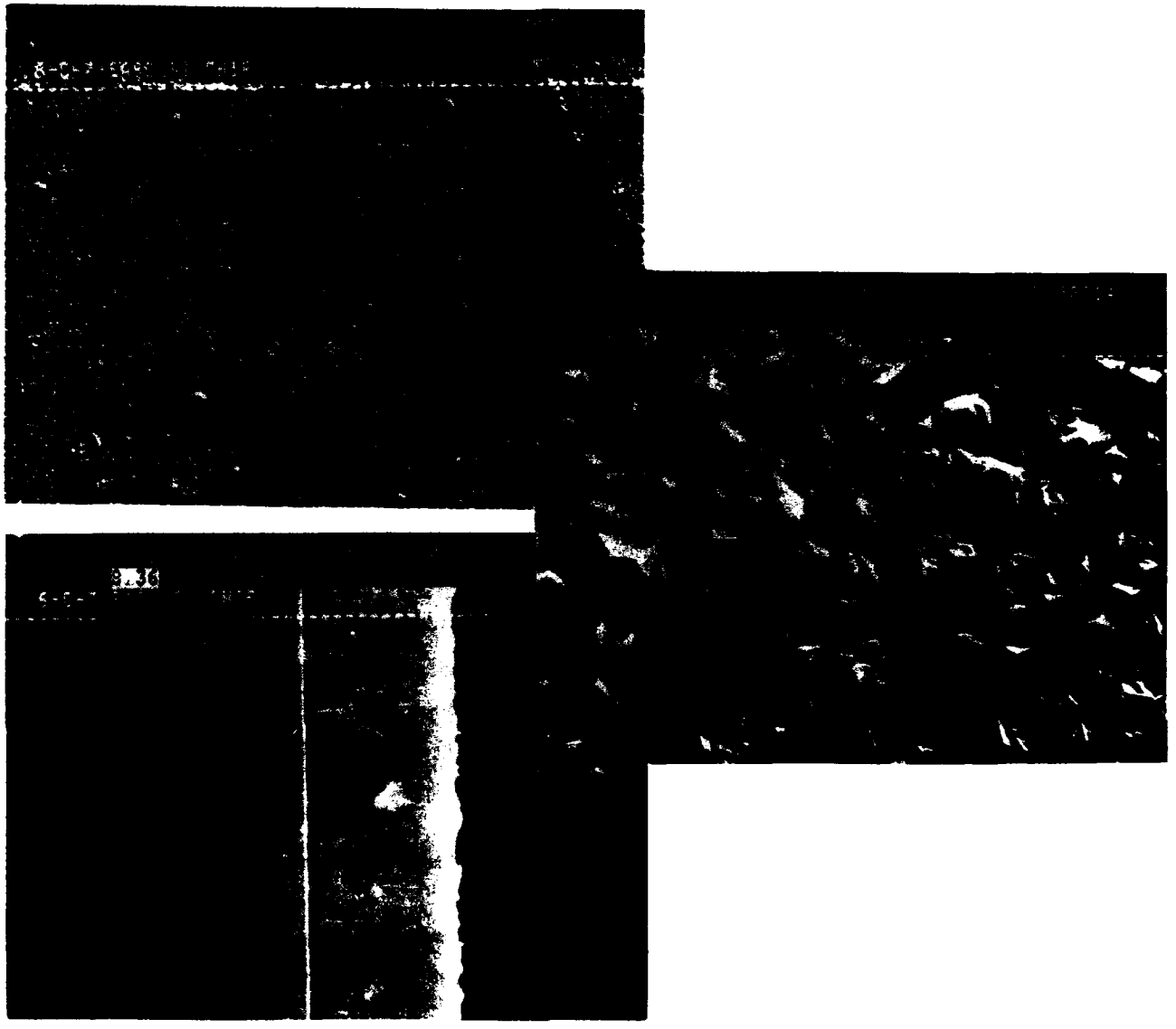

Figure 8. Surface and cross sectional structure of diamond film on single crystal silicon used as a thickness monitor. The film thickness is ~ 9 microns.

The phase relationships (Sp^3 to Sp^2 ratio) in the diamond films is found to be quite constant over the entire deposition area as shown in figure 6.

Diamond deposition on single crystal Silicon

Single crystal triboflats were used for obtaining an accurate measure of the film thickness. Ths silicon samples were cut following diamond deposition to create a clean

interface to permit thickness measurement using the SEM. Although the initial nucleation rate of diamond on silicon is likely to be different from that on silicon carbide the subsequent growth rates, once the initial nucleation event is complete, are likely to be substrate independent. Based on our work on the influence of the substrate material on the nucleation of diamond, the nucleation rate on polycrystalline SiC is found to be higher than on single crystal silicon. Consequently the measured thickness of the diamond film on silicon is at worst an under estimate of the film thickness on SiC. Figure 8 shows the surface structure and the cross section of diamond film on silicon. From this analysis the film is found to be ~9 microns thick. Consequently the thickness of the diamond film on silicon carbide is estimated to be 8 to 10 microns.

Conclusions

Thick diamond film deposition on a variety of silicon carbide samples has been achieved. Using an approach developed at Crystallume for promoting diamond film nucleation, films of thicknesses of 8 to 10 microns have been grown on single crystal SiC, polycrystalline SiC and silicon carbide coated graphite fiber/glass matrix composite billet. In general the structure of the films appear to be independent of the type of SiC substrate utilized. The surface roughness of the diamond film is found to be ~ 1 μM (peak to valley ratio) suggesting that polishing 1 to 2 microns of the top layer should result in a smooth diamond surface.

Other areas of research that this work has pointed to include the following:

• Achieve a more detailed understanding of the nucleation mechanisms at work in the deposition of diamond films on commercially important materials such as SiC.

• Develop the technology for enhancing the growth rate of diamond films in order to commercialize products which require thick diamond films.

• Develop production equipment for the large volume deposition of diamond films for commercial applications in tribology.

APPENDIX EE

R.W. Seibold, Hughes technical letter to Dr. K.V. Ravi of Crystallume, with data package on surface evaluation of HAC-GLAS disc prior to diamond coating, 8 August 1988

HUGHES

ELECTRO-OPTICAL & DATA SYSTEMS GROUP

August 8, 1988

Dr. K. V. Ravi
Director of Research and Development
Crystallume
125 Constitution Drive
Menlo Park, CA 94025

Dear Dr. Ravi:

Under separate cover, we are shipping you a graphite fiber reinforced glass matrix composite billet, designated HAC-GLAS-13-2, for diamond coating at Crystallume. The sides and one of the flat surfaces of this billet are pre-coated with β-SiC. I understand that your plans are to deposit the diamond coating onto the flat surface covered with the β-SiC undercoat. Please note that the β-SiC coating on this flat surface is severely cracked and crazed, and that areas near two opposite edges of this face are devoid of the β-SiC coating, for reasons discussed below. Optical and mechanical characteristics of the diamond coating may be affected by this irregular morphology of the β-SiC undercoat. We recommend that the diamond coating be deposited to a thickness, say 10 - 15 μm, that will provide optimum optical properties while allowing sufficient thickness for subsequent polishing operations. We also recommend that a method to directly measure the deposit thickness be employed, independent of estimates based on deposition time alone. Mike Gardos has informed me that this coating experiment will be incorporated into the Statement-of-Work under your subcontract from him.

HAC-GLAS billet 13-2 was fabricated about four years ago under a Hughes IR&D project. This early billet is far from optimum but is being provided for this experiment because (1) it is available, and (2) the diamond deposit is expected to adhere well to the polished β-SiC coating. This billet has high porosity (~6%) and contains some discontinuous graphite fibers oriented on their sides at the polished surfaces. Both of these characteristics can produce pits in the polished surface. Present HAC-GLAS materials have

neither of these drawbacks. Composition and properties of this billet are summarized in Attachment 1, excerpted from a Hughes report. Note that current HAC-GLAS billets have essentially zero porosity, >100 $W/m^{o}C$ thermal conductivity, and coefficient of thermal expansion approaching zero.

An explanation of the operations that led to bowing of the billet and concomitant cracking of the β-SiC coating is provided in paragraph 4.6 of Attachment 1. A set of photomicrographs documenting and mapping the crack pattern is provided in Attachment 2. As mentioned above, portions of this flat surface are devoid of SiC (near two opposite edges). The bowed geometry of this face caused the SiC coating to be polished completely away from these two areas, which are marked T (top) and B (bottom). It is seen in the micrographs that the SiC has a "dry lake bed" crack structure. Many small white patches, where pieces of the SiC are completely removed, can be seen. Because bowing of the billet occurred prior to the final polishing operation, a reasonable assumption can be made that the SiC thickness is greater near the billet center than near the edges. After the final polishing operation, the billet was immersed in boiling hexane for one hour to remove polishing waxes and other contaminants.

The dimensions, weight, and density of billet 13-2 are:

- Thickness (in.): 0.544, 0.543, 0.543; average 0.543
- Diameter (in.): 3.072, 3.068, 3.065; average 3.068
- Weight (g): 140.97
- Bulk density (g/cm^{3}): 2.137

After diamond coating, the billet should be returned to the undersigned for inspection. I then plan to ship it to Mr. Claud Martin, U.S. Army SDC, for polishing experiments, optical characterization and thermal cycling, as well as hardness and adhesion tests. Please also return the micrograph portfolio, which should accompany the billet when it is shipped to Mr. Martin. An additional copy of the micrographs can be made available.

Please contact me at (213)616-6183 if further information is needed. I am looking forward to hearing about your progress in this endeavor.

Sincerely,

R. W. Seibold

Robert W. Seibold
Project Manager
Mail Station E1/F150

Enclosures

CC: Mr. Claud Martin, USASDC
Mr. Lamoyne Cochran, USASDC
Mr. Ruben Cortez, DOE
Dr. Larry Fehrenbacher, TA&T
Mr. David McMahon, TBE
Mr. Michael Gardos, Hughes

ATTACHMENT 1

EXCERPTS FROM:

FINAL REPORT, HAC-GLAS-100

JANUARY 1988

PREPARED BY:
J. O. GIBSON

ATTACHMENT 2

MICROGRAPHS DOCUMENTING AND MAPPING CRACK PATTERN IN SILICON CARBIDE COATING ON SURFACE OF HAC-GLAS BILLET 13-2

AUGUST 1988

PREPARED BY:
B. W. BULLER

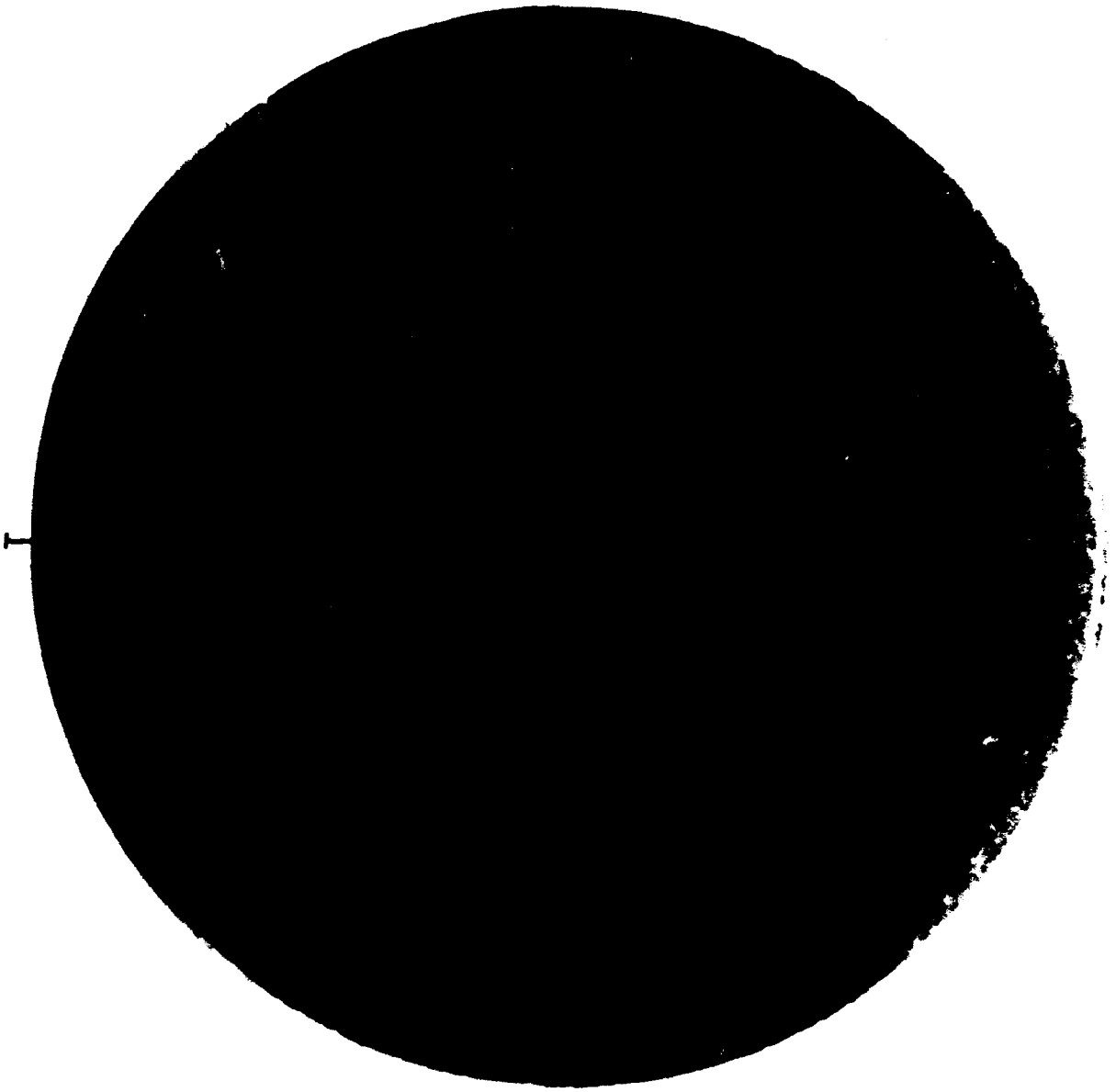

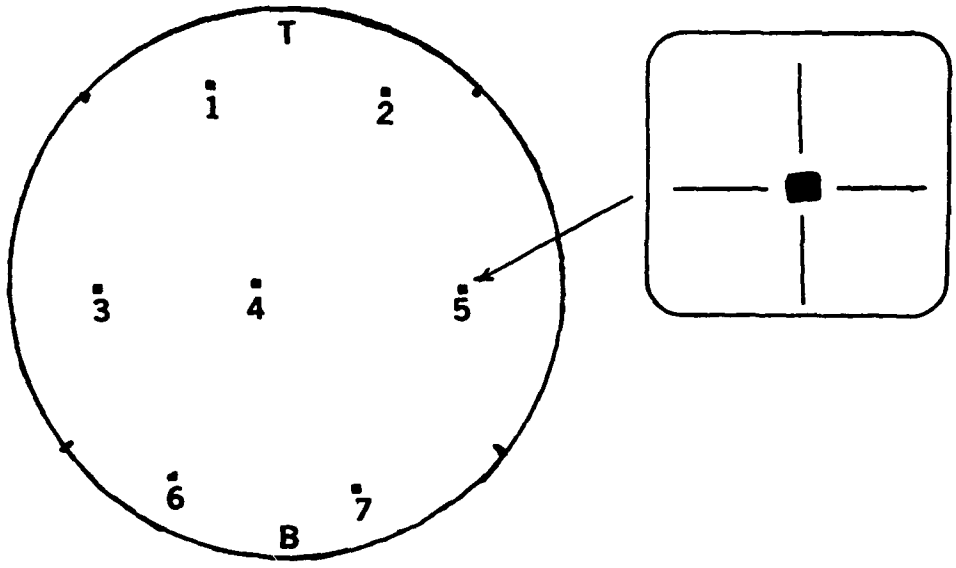

USE OVERLAY MAP TO LOCATE PHOTO FIELD

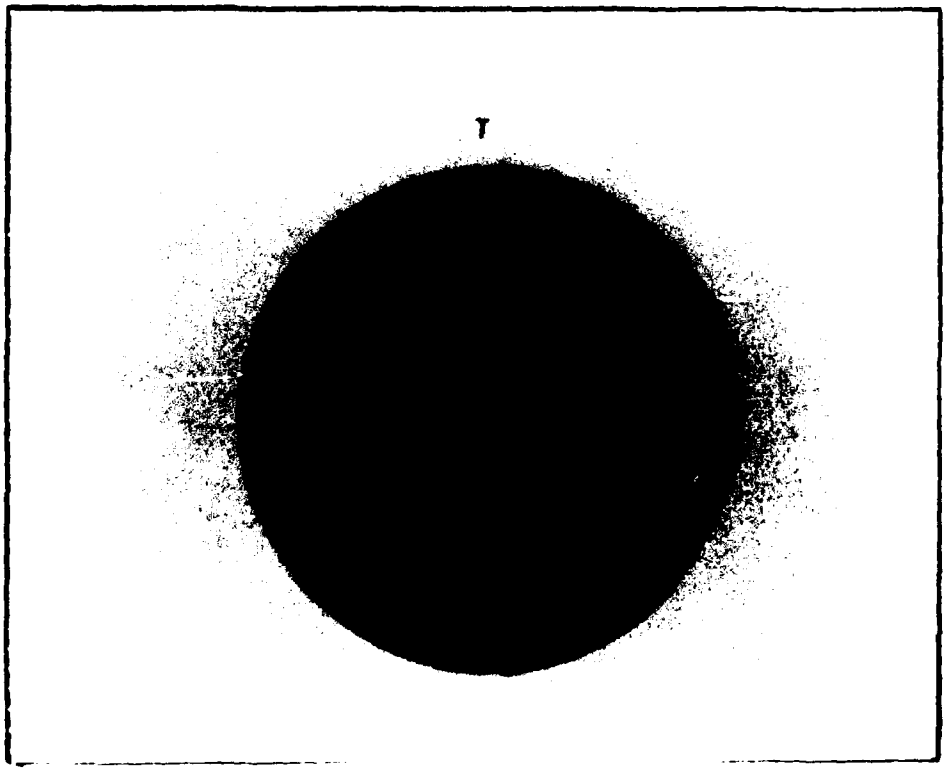

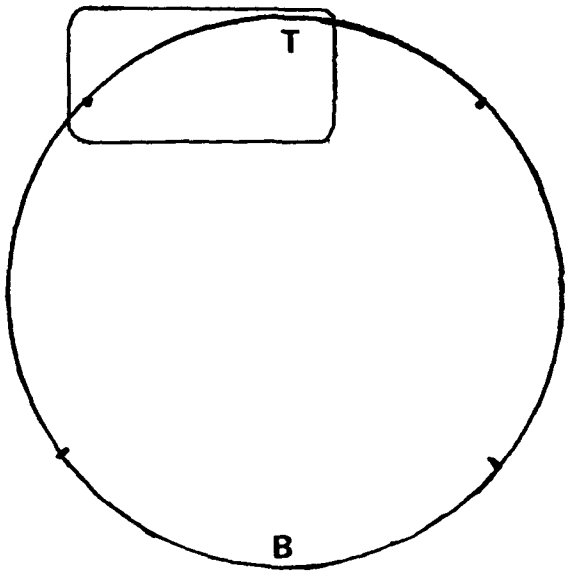

LOC. 1A MAG. 3.9×

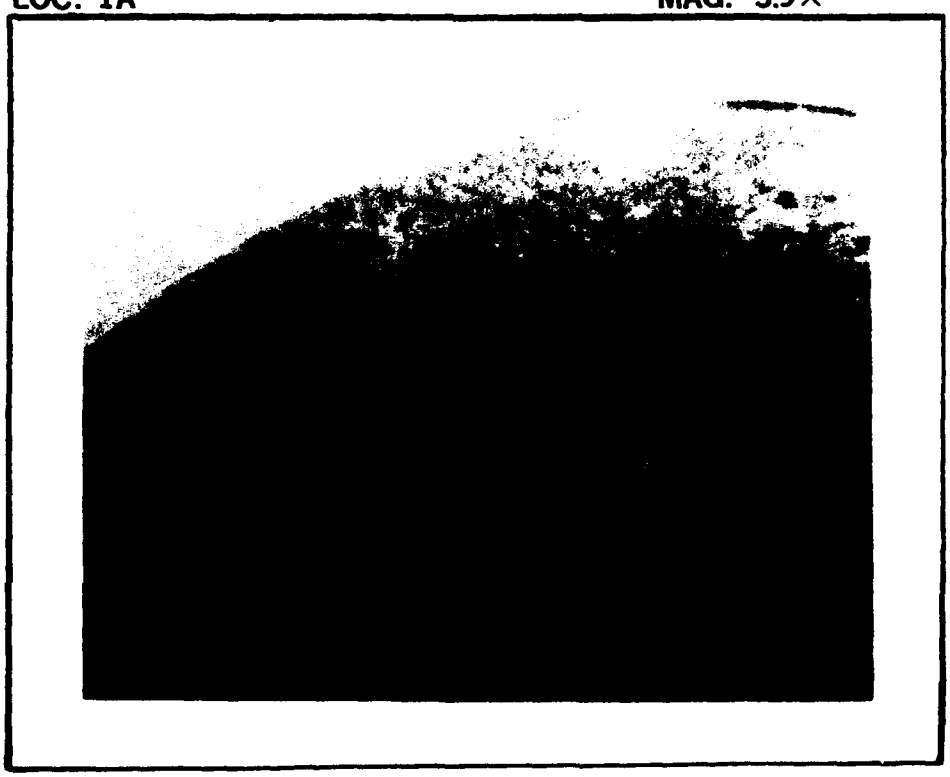

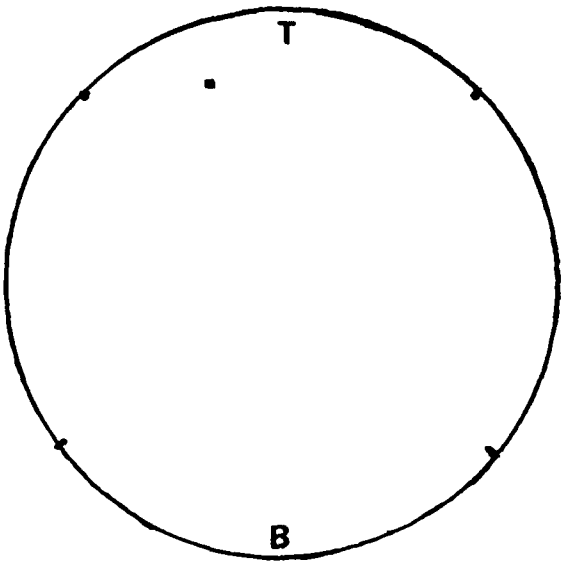

LOC. 1B MAG. 50×

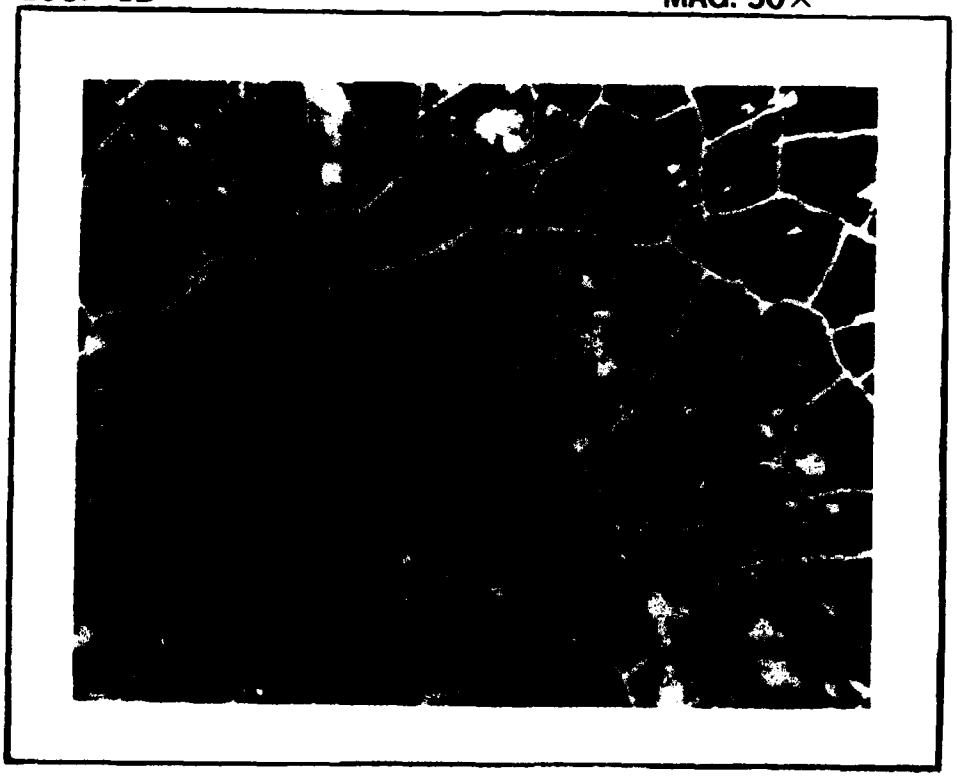

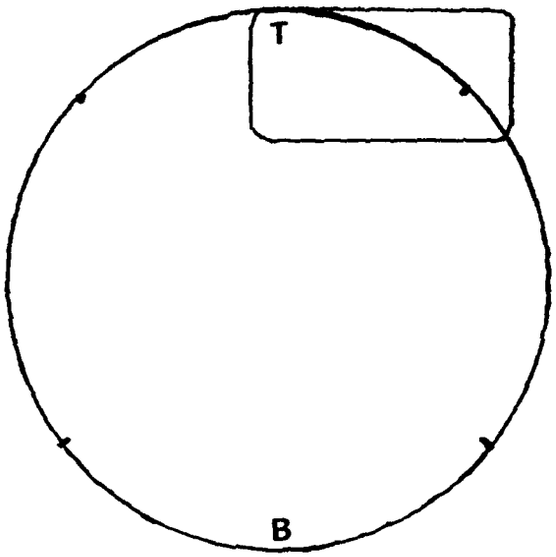

LOC. 2A MAG. 3.9×

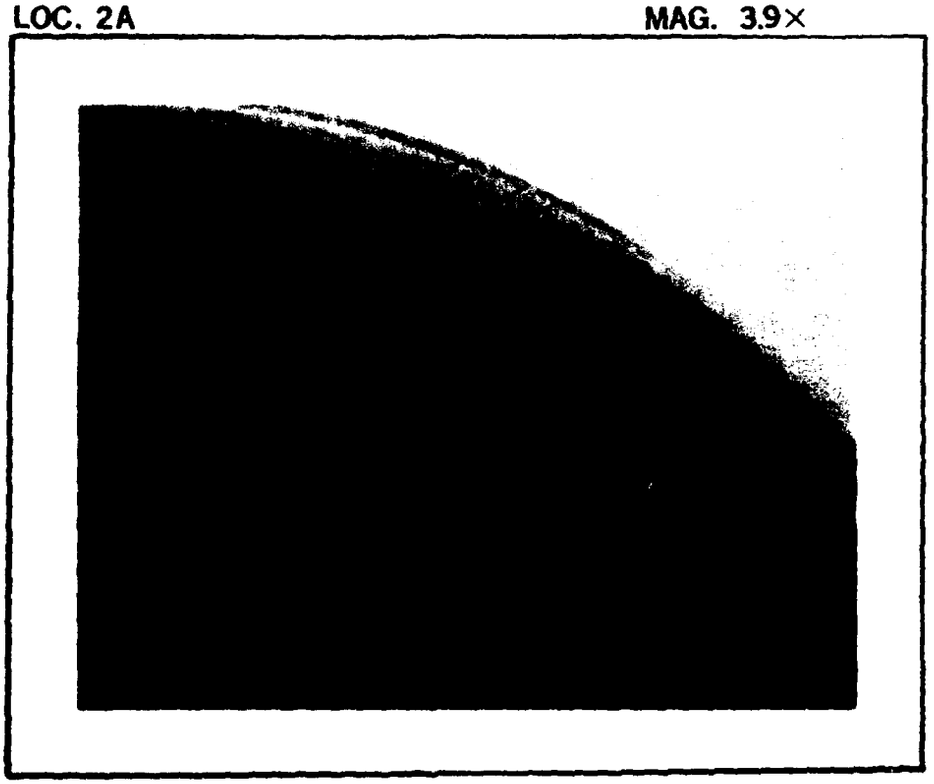

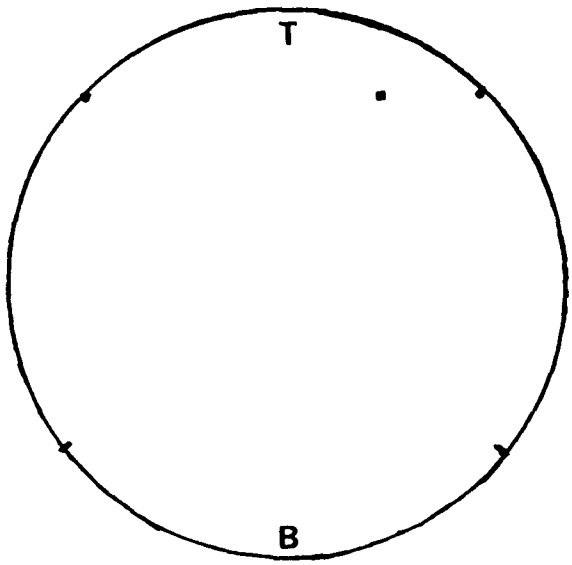

LOC. 2B

MAG. 50×

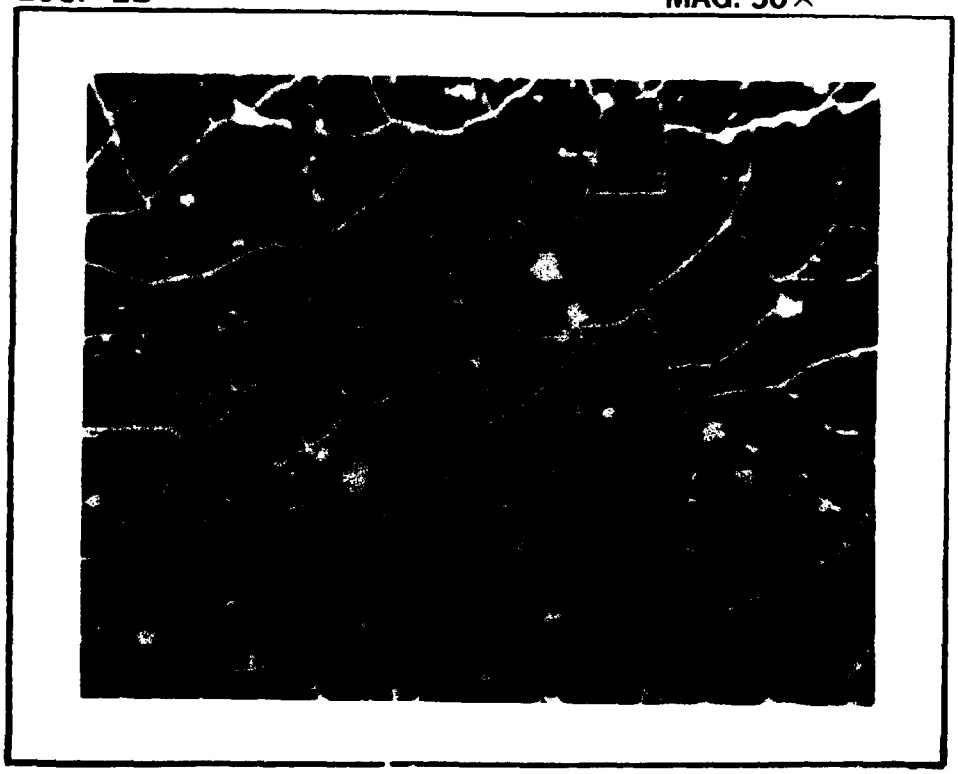

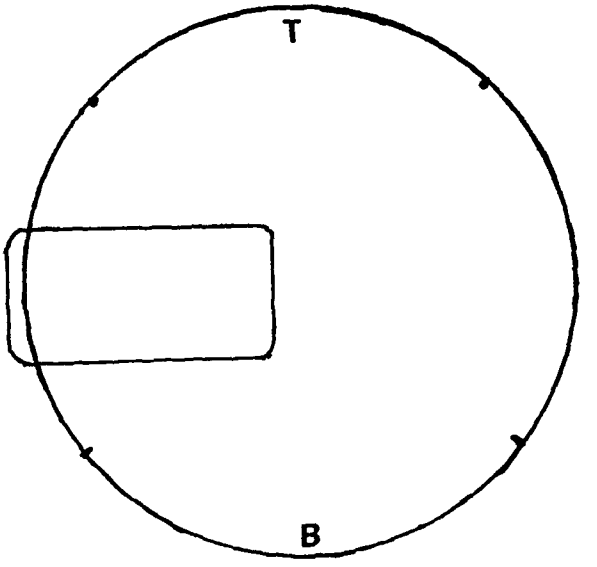

LOC. 3A MAG. 3.9×

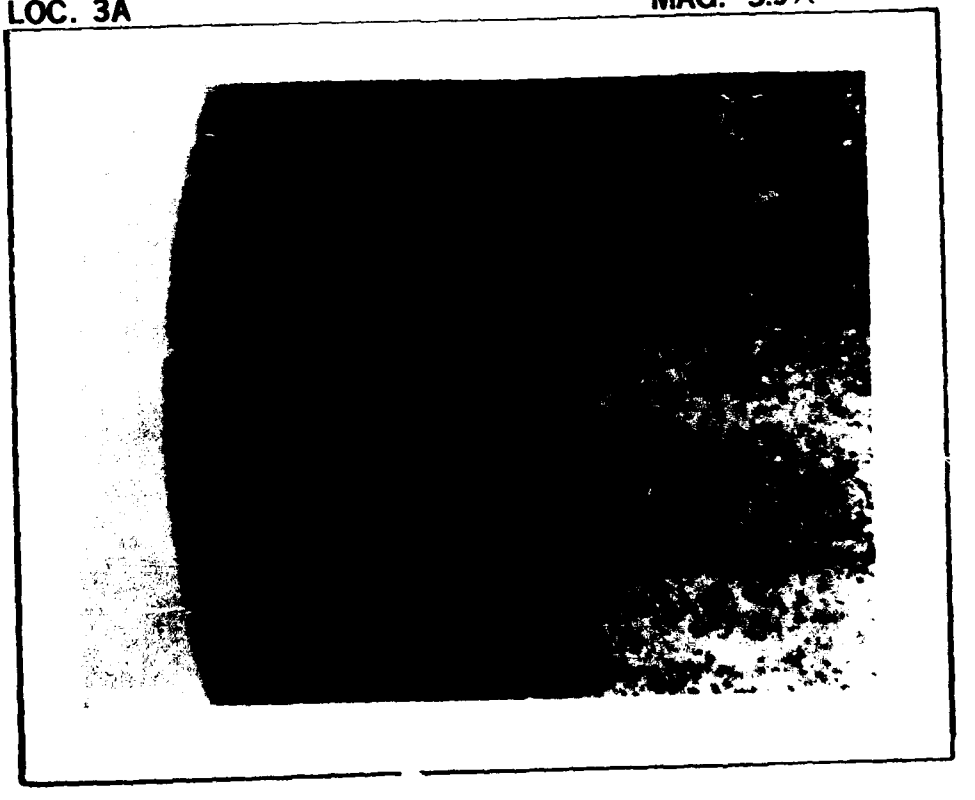

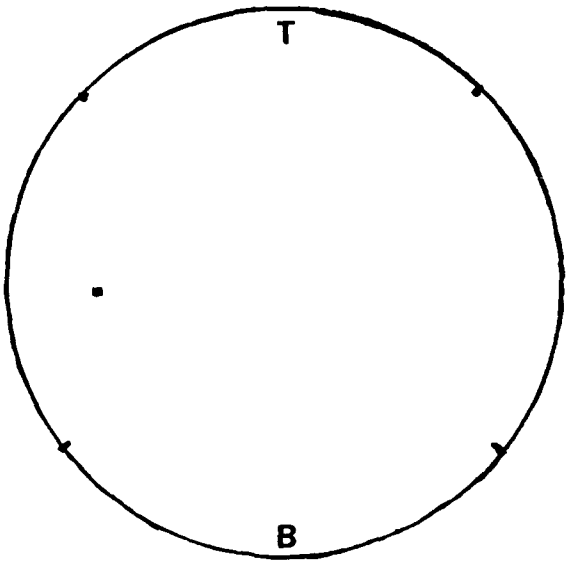

LOC. 3B MAG. 50×

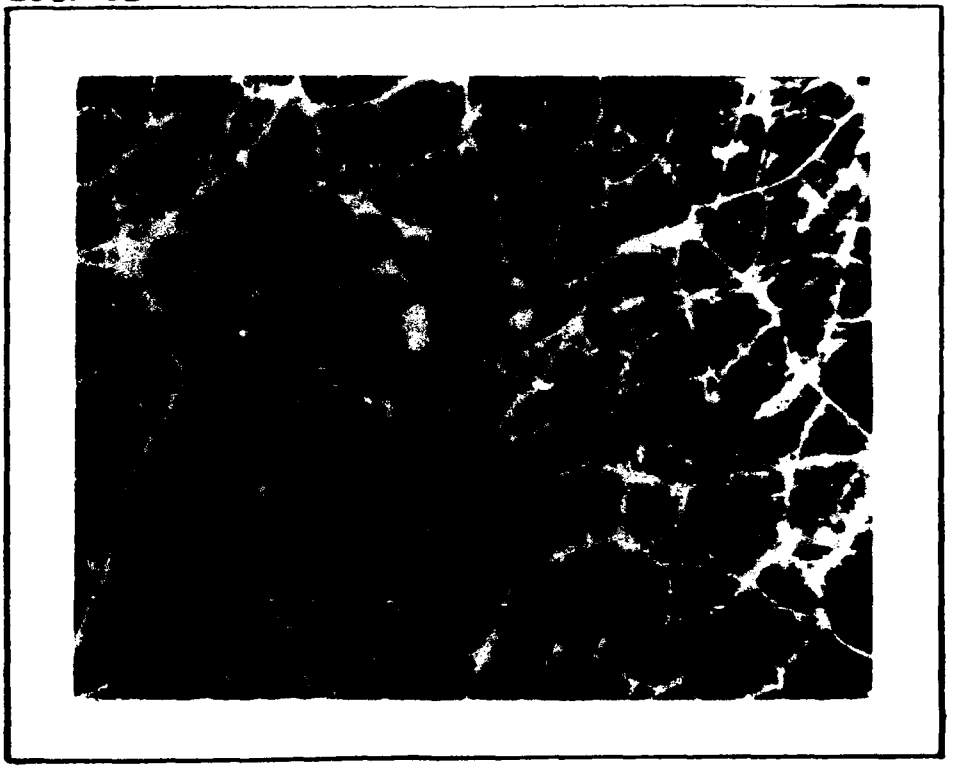

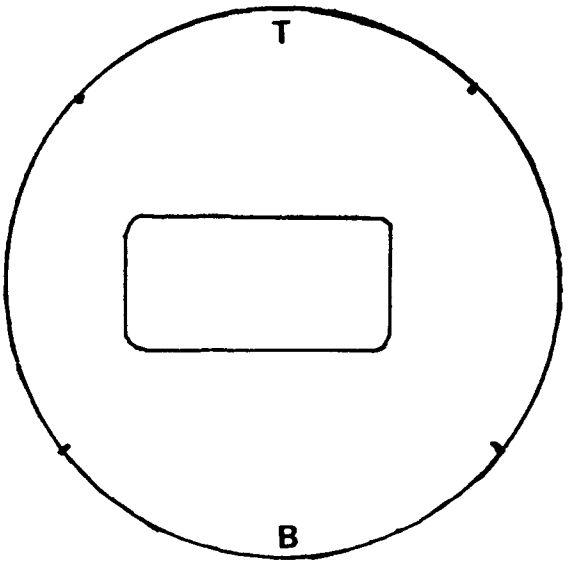

LOC. 4A MAG. 3.9×

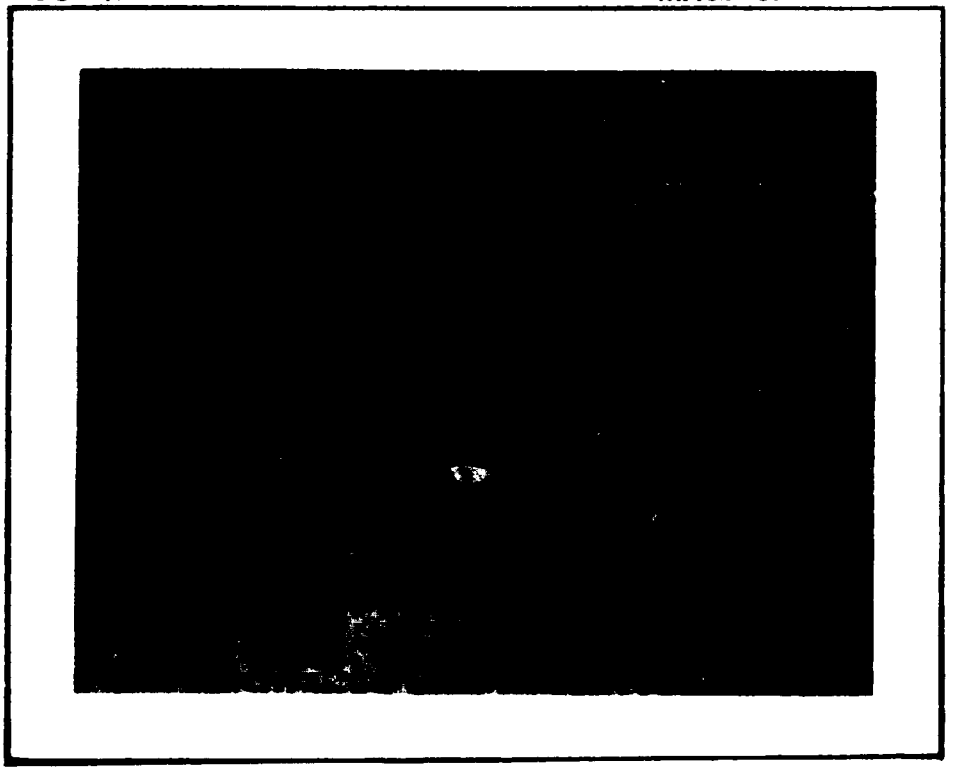

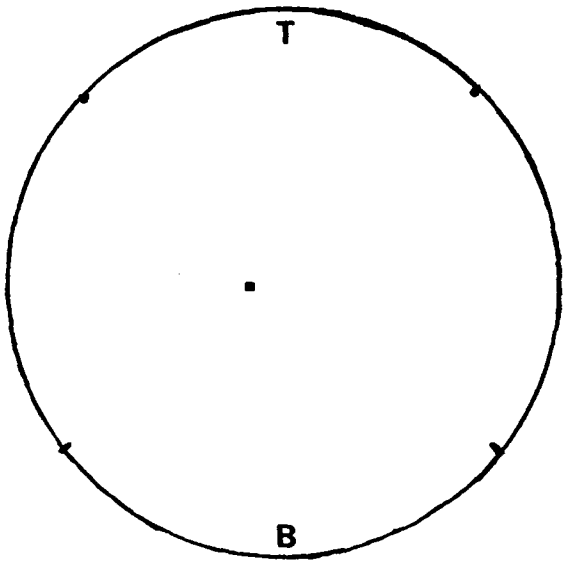

LOC. 4B MAG. 50×

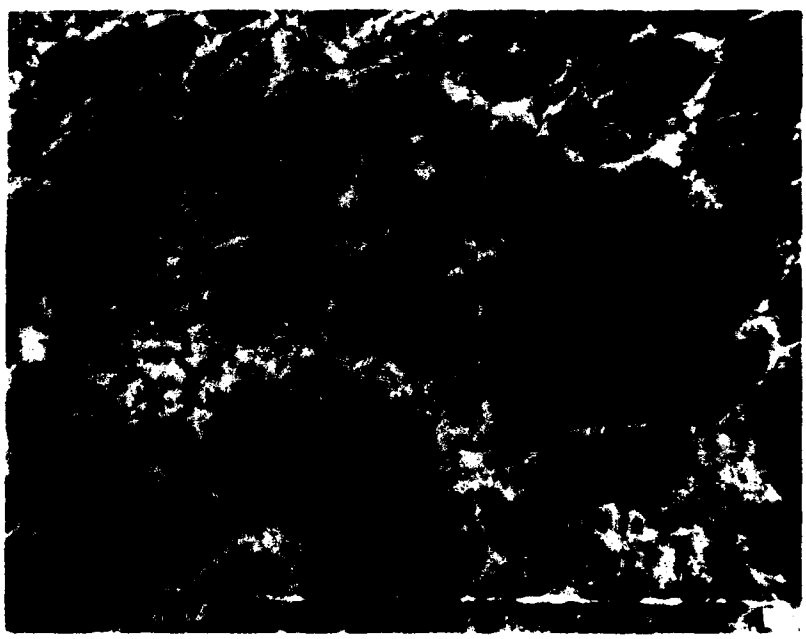

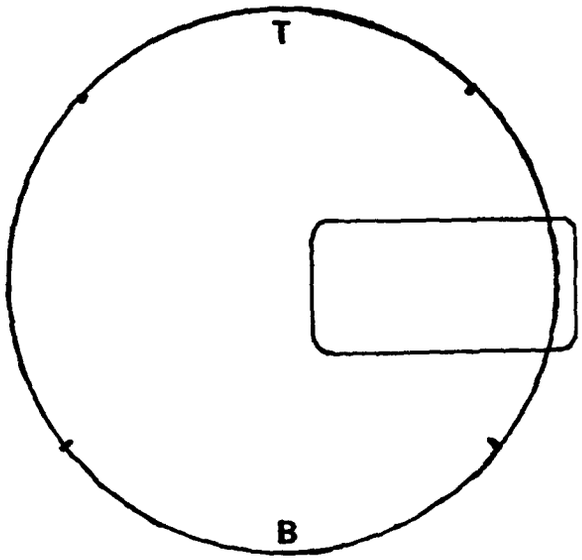

LOC. 5A MAG. 3.9×

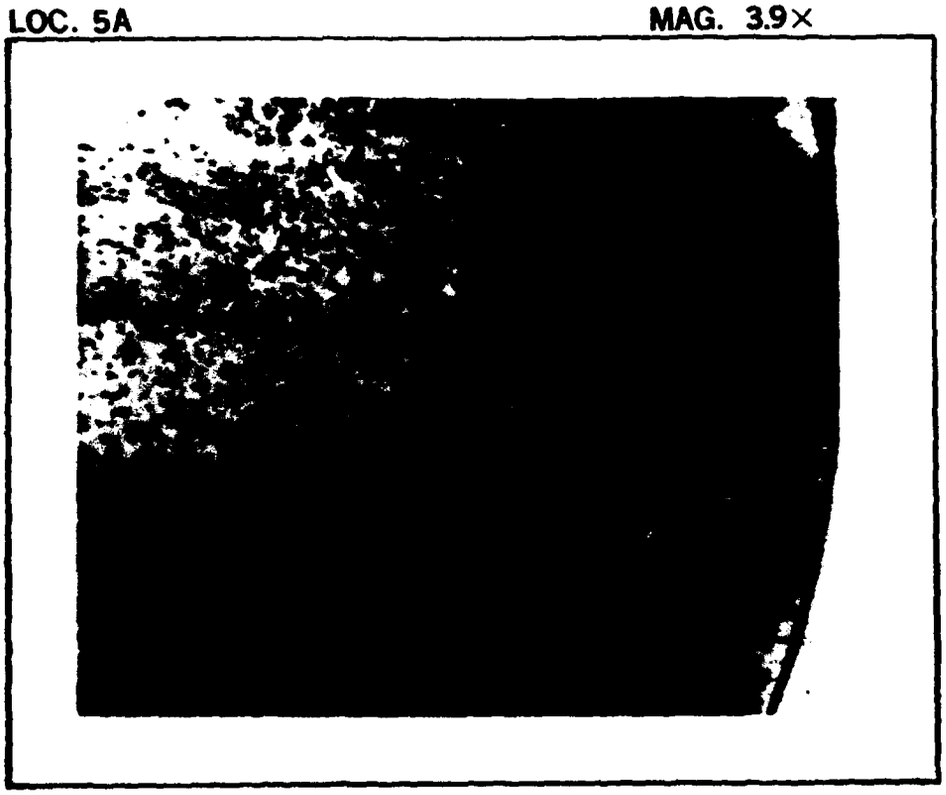

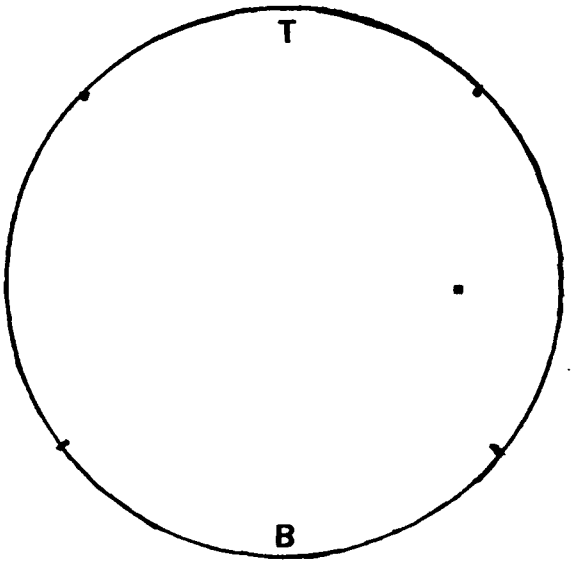

LOC. 5B MAG. 50×

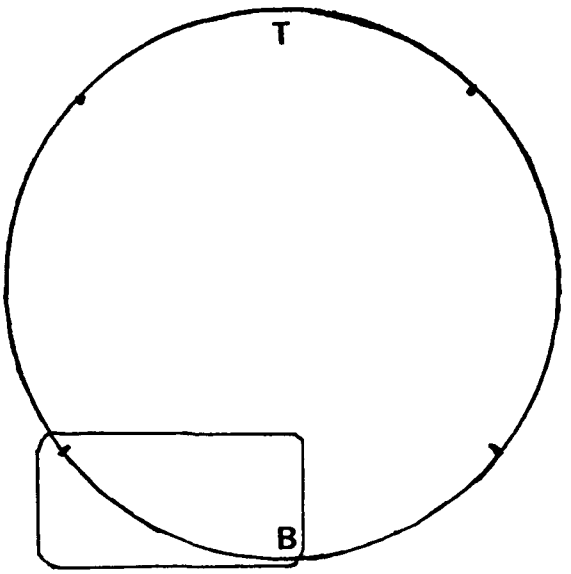

LOC. 6A MAG. 3.9×

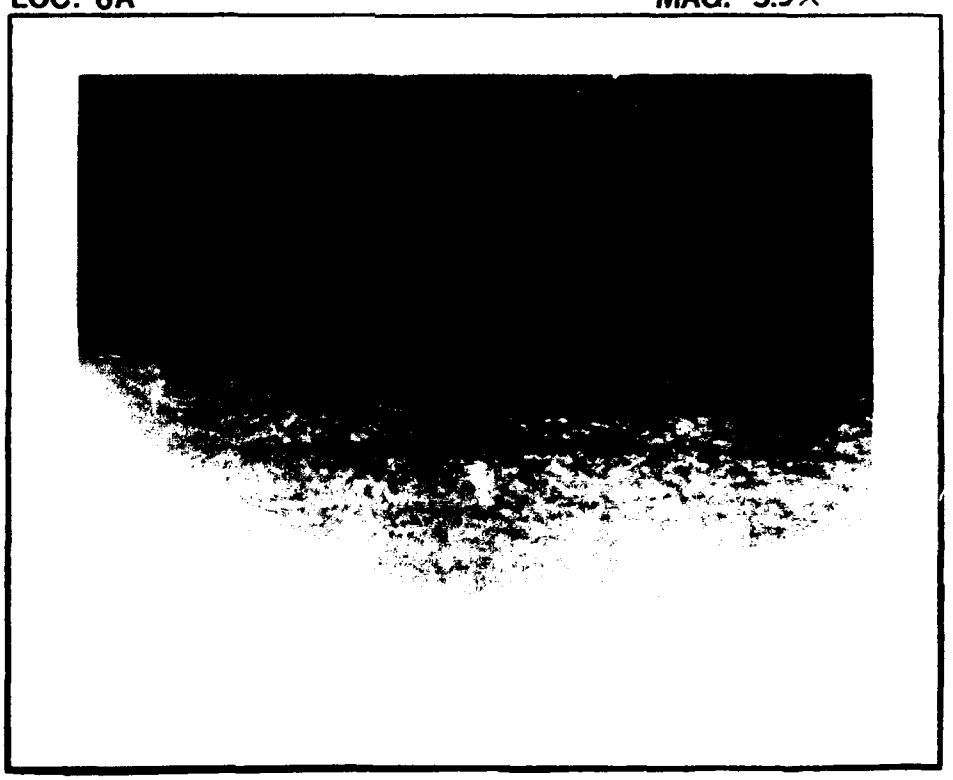

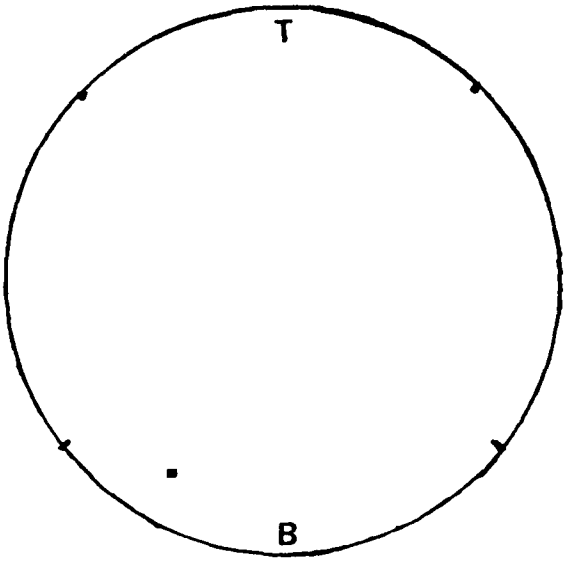

LOC. 6B MAG. 50×

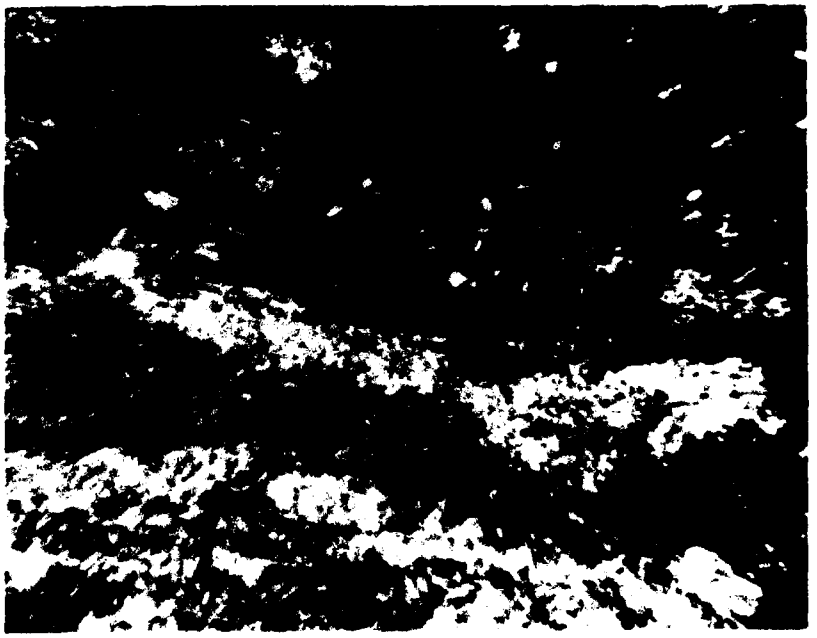

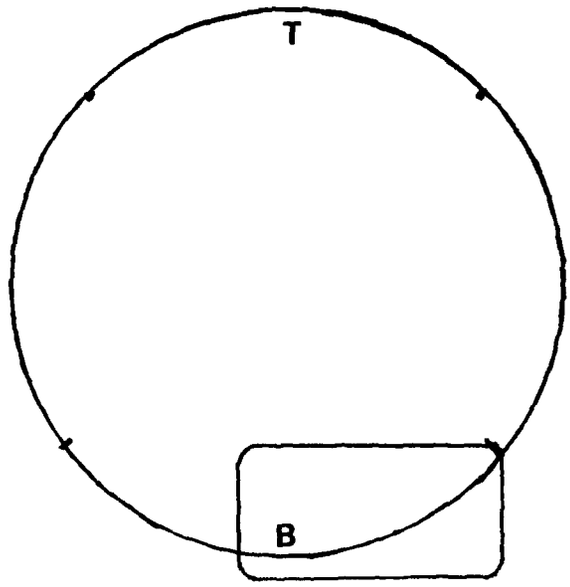

LOC. 7A MAG. 3.9×

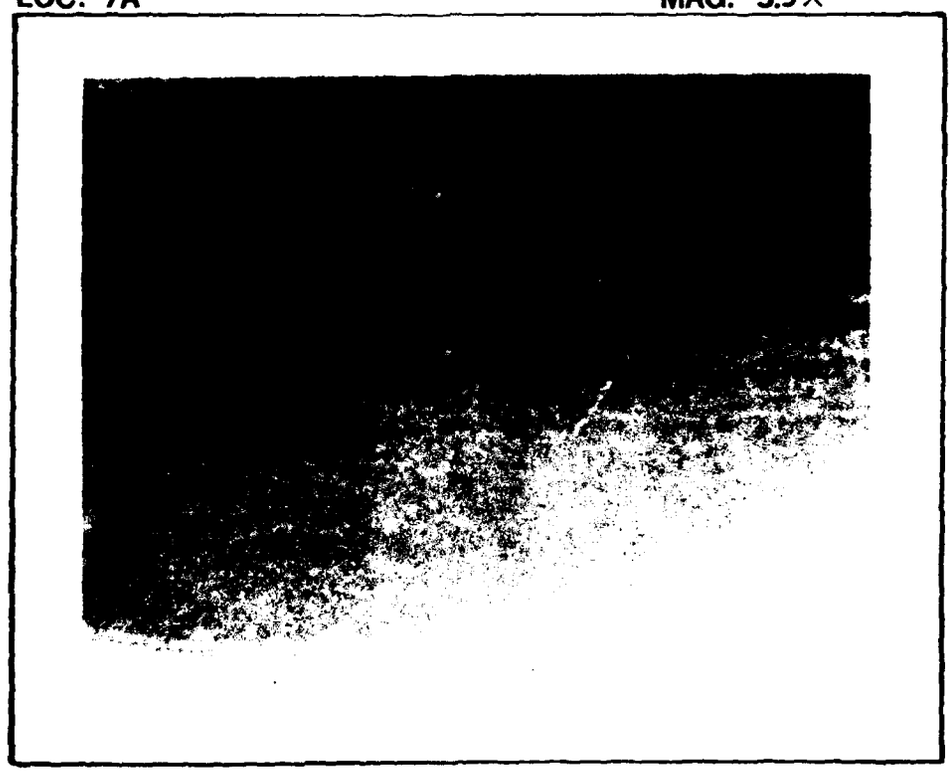

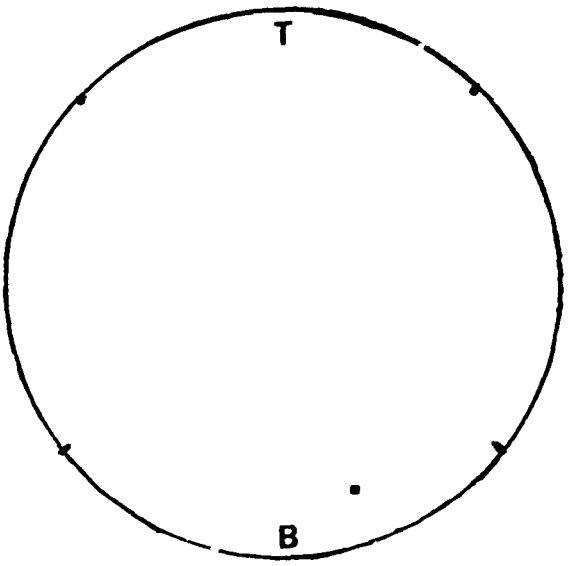

LOC. 7B MAG. 50×

APPENDIX FF

B.L. Soriano, and B. Buller, "HAC-GLAS 13-2 Optical Diamond Coating – Characterization and Polishing," Hughes Technical Internal Correspondence No. 7621.12/13, 21 February 1989

DISTRIBUTION

D. I. BASIULIS	EO	E01	F150
J. O. GIBSON	EO	E01	F150
R. L. HENDRIX	EO	E01	D109
E. B. HOLST	EO	E01	F150
R. E. HOOVER	EO	E01	F150
L. C. LIPP	EO	E01	F150
A. B. NASELOW	EO	E01	F150
R. W. SEIBOLD	EO	E01	F150
T. B. STANFORD	EO	E01	F150

INTERDEPARTMENTAL CORRESPONDENCE

HUGHES AIRCRAFT COMPANY

TO	M. N. Gardos	DATE	23 March 1989
ORG	76-21-00 C Distribution	REF	7621.12/13
SUBJECT	HAC-GLAS 13-2 Optical Diamond Coating - Characterization and Polishing	FROM	B. L. Soriano/ B. W. Buller
		ORG	76-21-12
		BLDG	E1 MAIL STA F150
		LOC	EO PHONE 70692

KEYWORDS: Diamond Film, Characterization

INTRODUCTION

A considerable research effort has been devoted to the chemical vapor deposition (CVD) synthesis of polycrystalline diamond thin films due to their unique properties. These properties include unsurpassed hardness, abrasion resistance, optical transparency over a wide range of wavelengths, high thermal conductivity, and chemical and thermal stability. Potential applications for these films include wear resistant tooling, high temperature semiconductors (with the proper doping), heat sinks, optical coatings and wear and abrasion resistant coatings for a variety of uses [1]. Attempts to synthesize diamond crystals and films have been made by a number of different CVD techniques and the structure of the various films range from amorphous carbon to graphitic to diamond.

The work described in this report has focused on the characterization of polycrystalline CVD diamond films deposited on various substrates by a DC plasma technique. The substrates consisted of one 3 inch diameter advanced ceramic composite substrate, two 5x7x2 mm polycrystalline α-SiC triboflats, one β-SiC coated silicon single crystal triboflat and two single crystal silicon thickness monitors. The triboflats are friction and wear specimens for SEM tribometry. The deposition was performed by Crystallume, Menlo Park, CA.

89-C CS FEB 72

The films were evaluated to determine if they were sufficiently adherent and uniform to withstand polishing and if they could yield a high final surface finish. A comprehensive characterization of the diamond films was performed by employing a number of analytical methods. These methods included optical mapping, SEM photomicrography, Raman spectroscopy and surface profilometry. Because of its unique nature as a substrate material and its large diameter, the characterization of HAC-GLAS-13-2 substrate surface required a more extensive analysis than that of the much smaller triboflats and thickness monitors. Since similar work had been performed previously for both α- and β-SiC triboflats, the majority of the work reported here focused on the characterization of the mirror's surface after diamond deposition, but before polishing. The characterization of the diamond coated substrate surface after polishing will be presented under separate cover.

The comprehensive information derived from these various examination techniques was employed to:

1) Judge the quality and adhesion of the diamond films on the various substrates to determine if these films can be polished (a) without delamination, and (b) to sufficiently high finishes using conventional (diamond-on-diamond) polishing techniques;

2) Enhance the fundamental understanding necessary to develop the optimum substrate/film combinations for superior adhesion, film structure, morphology and growth characteristics;

3) Provide feedback to Crystallume so they can further optimize their deposition variables and techniques.

DEPOSITION OF THIN POLYCRYSTALLINE DIAMOND FILMS

The object of this endeavor was to have Crystallume deposit thick diamond films on a number of different substrates. These films find use in both optical and tribological applications. Based on their previous work, Crystallume chose those deposition variables which produce the highest quality films in terms of diamond (sp^3) bonding, nucleation density and growth characteristics. The diamond films were deposited by a DC plasma-enhanced chemical vapor deposition process (PECVD). To conserve reactor usage and space, the triboflats and thickness controls were placed on the outer region of the substrate blank. Because the DC plasma-based deposition method typically yields the highest quality film but has a slow growth rate, the total deposition time was approximately 14 days for the substrate blank, β-SiC coated silicon triboflat and the two thickness controls. The polycrystalline α-SiC triboflats were removed from the chamber after only half the deposition time for unknown reasons. Additionally, Crystallume reported that a thin brown film formed on the chamber walls during the process. It is believed that it originated from volatile species emanating from the substrate blank; however, Crystallume performed no chemical analysis on this residue.

HAC-GLAS-13-2

BACKGROUND

The advanced ceramic composite blank, designated as HAC-GLAS-13-2, was developed for use as a low expansion, highly thermally conductive composite material [2]. Because this composite consists of a hard glass-ceramic matrix and a softer highly graphitic fiber, it is inherently difficult to polish a uniformly high surface finish. Therefore, one of the primary design considerations was to find or develop a highly abrasion

resistant optical coating which would provide the necessary thermal properties (high conductivity and low expansion) while lending itself to polishing to the required surface finish. Optical specifications require a final surface roughness in the range of 10 to 25 Å RMS[2]. Diamond films have exceptional promise for this application provided that the proper deposition and polishing techniques can be developed.

The substrate employed here was fabricated under a Hughes IR&D program. The fabrication process included sintering and subsequently hot-pressing the substrate blank constituents, then polishing to a surface finish of about 200 Å RMS. The polished blank was then coated with a 38 μm thick layer of CVD β-SiC and then polished a second time. Because the polishing rate of the first mirror face was too rapid, the β-SiC film was completely removed from that surface. Due to the high stress gradient that developed between the coated and uncoated surfaces, the blank (reinforced with Z-direction fibers only) bowed. As the consequence, the β-SiC on the opposite faced cracked and crazed extensively. Since the coated surface was no longer sufficiently flat (the top to bottom bow was worse than the left to right equivalent), the CVD β-SiC film was removed from the outer regions during polishing, exposing the composite underneath. Although this substrate blank, which was fabricated early in the IR&D program, was not the optimum choice in terms of thermal conductivity and its initial surface condition, it was used for this study because of its immediate availability. Furthermore, the diamond was expected to adhere well at least to the β-SiC coating covered portion, if not everywhere.

Characterization of the β-SiC coated surface was completed before polishing of the diamond film was attempted. Low magnification optical surface mapping of the HAC-GLAS-13-2 substrate blank was performed both before and after diamond deposition to

define those surface conditions which may have an effect on film characteristics. To determine the structure and morphology of the diamond films, Crystallume performed Raman spectroscopic analysis and SEM photomicrography before the samples were returned to Hughes. Upon receipt, we repeated the optical mapping for comparison with the pre-deposited surface. Additionally, energy dispersive x-ray spectroscopy (EDX) and additional SEM photomicrography was done to augment the information provided. Also, we re-examined the surface at various locations across the diameter to measure the surface roughness, film thickness and height variation across the diameter of the mirror blank.

OPTICAL MAPPING AND SEM MICROSCOPY

Optical Mapping Prior To Deposition

Before the substrate blank was sent to Crystallume for diamond deposition, the surface morphology was carefully mapped and recorded photographically in a series of over 20 optical photomicrographs. Figure 1 shows the substrate blank just before deposition. Both the β-SiC and bare composite regions are indicated. Additionally, this photograph shows surface discoloration in the center of the blank, attributed to entrapment of moisture or binder material under the essentially transparent CVD β-SiC film. Figure 2 indicates the various other types of surface defects found. As discussed previously, extensive cracking and crazing can be observed throughout the entire β-SiC coated surface region. Additionally, other surface irregularities such as chips and regions of exposed (bare) composite were photographed to determine their effect on the localized nucleation and growth of the diamond film. A complete set of our optical photographs was sent with the substrate blank to Crystallume for their review.

Optical and SEM Mapping After Deposition

Figure 3 shows the surface after the deposition of the thin polycrystalline diamond film. Several surface features and defects are readily observable even at the low magnification. The five areas where the triboflats and thickness monitors were located are readily observable and are indicated numerically in Figure 3. In addition to the five triboflat locations, other surface irregularities can be seen in this photograph. Two shadowed regions close to the perimeter indicate that the triboflats may have been moved (or changed positions inadvertently) during deposition, although no indication of this was reported in Crystallume's report. As mentioned above, the two α-SiC triboflats were in the chamber for the first half of the total deposition, then were removed for unexplicable reasons.

The nucleation and growth of the diamond were disturbed by the crack network and chips in the β-SiC. Figure 4 shows numerous chips throughout the diameter of the surface prior to the diamond deposition. A uniform coating covered the smaller irregularities; but, for the larger chip which extends into the substrate, the deposition was irregular within and around local areas of the chip. To determine the effect of the extensive cracking in the β-SiC film, a series of photomicrographs (see Figure 5) compare the pre- and post-diamond coated deposition surface condition. Figure 5 indicates that in the central region where the deposition characteristics are typically the best, the cracks were coated uniformly and the topography of the diamond surface is virtually crack-free. In the outer regions where the substrate surface was in poorer condition, the crack network was retained after deposition. Although the coating is more facetted and non-uniform in the regions where the composite was exposed, these protomicrographs show that diamond will nucleate and grow on the bare composite. Although we expected poorer film

characteristics in the regions where all of the CVD β-SiC interface film had been removed, we found that the diamond film was uniform and followed the topography of the composite surface. The SEM photomicrographs (Figure 6) indicate that the structure of the film is smoother and has a cauliflowered appearance in the central region and becomes rougher and more facetted in the outer peripheral regions. This finding is not in agreement with the average surface roughness traces which indicate that the surface is rougher in the central region.

Figure 7 shows a region of interfacial diamond film delamination where the cracks evidently extend from the substrate into the film. It is also apparent that the delamination perimeter followed the crack structure and boundaries. From this, we can conclude that the crack network in the β-SiC film affects both the interfacial and interfilm adhesion. Further examination of the crack structure in other locations shows that fracture is primarily intergranular in regions of cauliflowered morphology and transgranular in the facetted regions (Figure 6).

RAMAN SPECTROSCOPIC ANALYSIS

Basic Concepts

Raman spectroscopy is a powerful tool for the characterization of diamond and diamond-like carbon (DLC) films and has been studied by a number of authors for such uses (3-12). The reported Raman spectra vary depending on the film structure, but all are a combination of spectral peaks characteristic of amorphous carbon, graphitic and diamond structures. Common peaks for these films include the characteristic diamond (sp^3) line at 1332.5 cm^{-1} and the (sp^2) graphite peak near 1575 cm^{-1}. Both the diamond and graphite peak locations have been unambiguously identified, but may shift and broaden due to impurities or crystal defects. Other

peaks have been attributed to amorphous carbon, carbon-hydrogen bonding or regions where the major phase is not sufficient to provide a well-defined signal. Because the scattering efficiency is much higher for graphite than diamond (approximately 55 times)[8], the Raman spectrum is an especially sensitive method for determining the phase purity of the film. The ratio between the relative intensities of the diamond peak (1332.5 cm^{-1}) and the graphitic peak (1575 cm^{-1}) can lend qualitative information on the film purity with respect to concentrations of graphitic impurities. In addition, the full width at half maximum (FWHM) of the diamond peak can provide information on the crystal perfection. Natural diamond has a FWHM in the range of 2-2.5 cm^{-1}. Synthetic polycrystalline diamond typically has FWHM in the range of 7 to 10 cm^{-1} [8]. The line widths become narrower with increasing quality and crystal perfection of the films.

When the films are deposited on hard substrates, studies have shown the locations of the characteristic diamond and graphitic peak shifts. It has been suggested that this is due to interfacial stresses between the film and the substrate [3,4,12]. With further definition and clarification, this information may be valuable in predicting the adhesion of the films to their substrate, a very important consideration in practical applications.

Raman Spectra Of HAC-GLAS-13-2

Raman spectra were taken in three different locations across the diameter of the blank (see Figure 8). Each show a strong peak at 1330 cm^{-1} indicating a high degree of diamond sp^3 bonding. The shift in wavenumber from the characteristic 1332.5 cm^{-1} indicates a high degree of interfilm stresses and interfacial stresses between the substrate and the diamond film. The peak at 1538 cm^{-1} indicates the presence of either an interfacial sp^2 (graphitic) nucleation layer or other graphitic contamination. Since the

sampling depth of Raman probes at normal incidence can be as large as 10 to 20 μm, determination of the depth (location) of the sp^2 contaminant is not conclusive using this technique.

In the three locations where spectra were taken, the broad peak located at 1536 cm^{-1} (Figure 8) shifts and becomes slightly sharper towards the center of the substrate. This indicates that the structure of the carbon/graphitic phases change slightly. Because the peaks are broad and do not have well-defined peaks, the exact structure of the carbon cannot be identified. In addition, the characteristic diamond peak (1330 cm^{-1}) is sharpest in the spectra taken at the center of the mirror. With exception to these subtle differences, the peak intensities and locations are generally constant within the three areas measured.

SURFACE PROFILOMETRY

The coating thickness of the various samples was determined by a series of profilometric measurements. To determine the true film thickness on the substrate, Sloan Dektak surface traces were taken across the steps where the thickness monitors had been located during the deposition (Figure 9). These traces indicate that, at least in this localized region, the thickness ranged from 4 to 7 μm. Crystallume cross-sectioned one of the silicon thickness monitor flats and measured the film thickness by SEM photomicrography. They report that this thickness measurement is generally representative of all the films grown during a given deposition period because, after the initial nucleation, the growth rate becomes substrate-independent. The value that we measured by profilometry is lower than the thickness value that was determined by cross-sectioning one of the thickness monitors (9 μm).

The locations where the three triboflats (two α-SiC and one β-SiC coated Si) masked the substrate were measured to indirectly determine the film thickness on the flats themselves (Figure 10). These measurements indicate that the films were 4 to 5 μm. Table 1 summarizes the results of the surface profilometer measurements. Since Crystallume reported that the samples were in the deposition chamber only for half of the total deposition time, we would expect this value to be approximately half that of the substrate. The differences that arise between our values and those reported by Crystallume may be caused by the following:

1. Any shadowing effect around the 1 to 2 mm thick flat coupons would decrease the magnitude of the step between the coated and the uncoated regions (13). This would render our value lower than the true thickness in the regions where shadowing is a problem.

2. Because the thickness monitors are closer to the gas inlet than the mirror surface upon which they rested, their deposition rate may be greater than that of the mirror surface. The end-result may be that Crystallume's value is greater than the true substrate film thickness.

Prior to polishing the diamond film on the substrate, it was essential to establish the relative height variation across a diameter. If the height variation is greater than the thickness of the film at any location, portions of the film will be totally removed during polishing. Therefore, absolute magnitude of the height variation was measured using an unfiltered Taylor-Hobson profilometer trace (see Figure 11). Because of the bowed geometry, we expected the absolute magnitude to be different from side-to-side than from top-to-bottom. The results are summarized in Table 2. As expected, the relative height variation from top-to-bottom

(15 μm) was greater than the estimated thickness of the diamond film (4-9 μm).

Additionally, surface roughness measurements were performed across the diameter of the substrate's surface. The roughness trace indicated that the film is smoother in the outer regions and becomes rougher toward to center (Figure 12 shows representative profiles from the bottom, middle, and top of the trace). The average surface roughness is approximately 2500 Å. These results correlate with past work which indicates that the surface is more facetted in the regions of higher growth rate. For this particular deposition technique, the highest growth rate region is in the center and decreases by approximately ten percent in the outer regions. However, these results do not correspond with our visual (i.e., SEM) examination of the surfaces on these areas (Figure 6).

The most important result of these measurements was, again, the fact that the height variation was much larger than the thickness of the film. Therefore, uniform mechanical polishing of the surface was not viable and hand polishing of selected regions was our only option. Also, to achieve the necessary surface finish, the peak-to-valley ratio must be initially such that will allow the surface to be polished to 15 Å RMS. From our observations, this implies that a cauliflower diamond film morphology may be the best choice.

ENERGY DISPERSIVE X-RAY ANALYSIS

In addition to the chemical information derived from Raman spectroscopy, EDX (X-ray Dispersive Spectroscopy) was performed to determine if other contaminants were present. Additionally, EDX results for different locations on a specific substrate allow qualitative comparison of elemental content. The results of this analysis show that in the diamond film covering both the HAC-GLAS-13-2 blank and the silicon carbide samples, a uncharacteristically high level of silicon is present (Figure 13). We have not detected silicon impurities in any of our previous thick film deposition with either α- or β-SiC substrates. Since the sampling depth using EDX is on the order of 2 μm for this material, the presence of silicon is not a result of sampling in the substrate. A more probable explanation involves silicon transport from the lithium-aluminum-silicate substrate, incorporated by vapor transport into the actual diamond lattice structure[14]. Since the matrix of the composite is a silicate glass, it must have been the source of the silicon. Although the effects of this will show in the Raman Spectra, the peak location is much lower than the wavenumber range sampled.

CONCLUSIONS

The surface morphology of the CVD diamond film appears to be a function of the radial position on the substrate's surface. Toward the center of the mirror's surface, the morphology is more cauliflowered; toward the outer regions it becomes more facetted. In the regions where the bare composite was exposed, the surface morphology showed uneven growth rate and larger crystallites than the area that was fully coated with the β-SiC. Nucleation was good on both the β-SiC coated and the bare composite regions. The surface irregularities, chips, cracks, and other more minor defects affected the localized diamond nucleation and growth

characteristics. The indications are that the surface topography prior to deposition must meet or exceed the requirements of the final surface condition with respect to defect-free morphology. The relationship between substrate surface finish and diamond film growth characteristics and morphology are connected but not fully understood.

The adhesion of the film was compromised due to the cracked structure of the β-SiC substrate film. In the center of the substrate blank (where the growth characteristics seemed to be the best), the diamond coating uniformly covered the crack network and showed no visual evidence of localized disturbance. In the outer peripheral regions, the crack network propagated into the diamond film. At one location, the cracks in the diamond film merged and a large chip of the diamond film delaminated interfacially. It was visually evident that the perimeter of the delamination followed the network of the cracks in the β-SiC.

RECOMMENDATIONS

To develop the optimum diamond film characteristics in terms of defect free morphology, the substrate surface must meet or exceed the final substrate requirements prior to diamond deposition. Because of the size limitations of the present PECVD method, the size of the substrate surfaces must be kept to a minimum. The outer limit of the diameter at this time is four inches. The variation in film thickness is 10% even for the best possible set of conditions and deposition variables.

The substrate material, its processing, and coating must be developed with several considerations in mind. In addition to the inherent requirements necessary for the substrate , the substrate surface must be suitably treated to provide the optimum nucleation and growth conditions. The deposition variables must

produce the best quality films in terms of morphology, (i.e., whether facetted or cauliflowered, crystallite (grain) size, and chemical structure. It is apparent that many of these characteristics can not be fully controlled at this time. Additionally, the need for ever-larger substrate demands further studies as to the possibility of reliable scale-up of the present CVD technique and apparatus.

B. L. Soriano, Member of the
Technical Staff

B. W. Buller,
Developmental Engineer Specialist

Approved By:

M. N. Gardos, Chief Scientist
Materials Technology Laboratory

Attachment

SUBSTRATE	DIAMOND FILM THICKNESS (um)	MEASUREMENT METHOD
HAC GLAS-13-2	4.2	α -STEP*
α-SIC Triboflat	4.1	α -STEP
α-SiC coated single crystal Si	5.1	α -STEP
Thickness monitor (Single crystal Si)	4.3 7.0 4.26**	α -STEP
Thickness monitor (Single crystal Si)	9.0***	Cross-sectioning

Table 1. Summary of the diamond film thicknesses as deposited on the various substrates and the corresponding measurement technique used.

TRACE DIRECTION	HEIGHT VARIATION ACROSS DIAMETER
Bottom to Top	600.8 uin (15.2 um)
Right to Left	168.7 uin (4.3 um)

Table 2. Summary of surface height variation as a result of bowing of the HAC GLAS 13-2 composite.

* α-Step was measured using a profilometry trace across the diamond coated region and the region masked by the small flats.
** Three measurements were performed.
*** Crystallume performed cross-sectional thickness measurements.

HUGHES

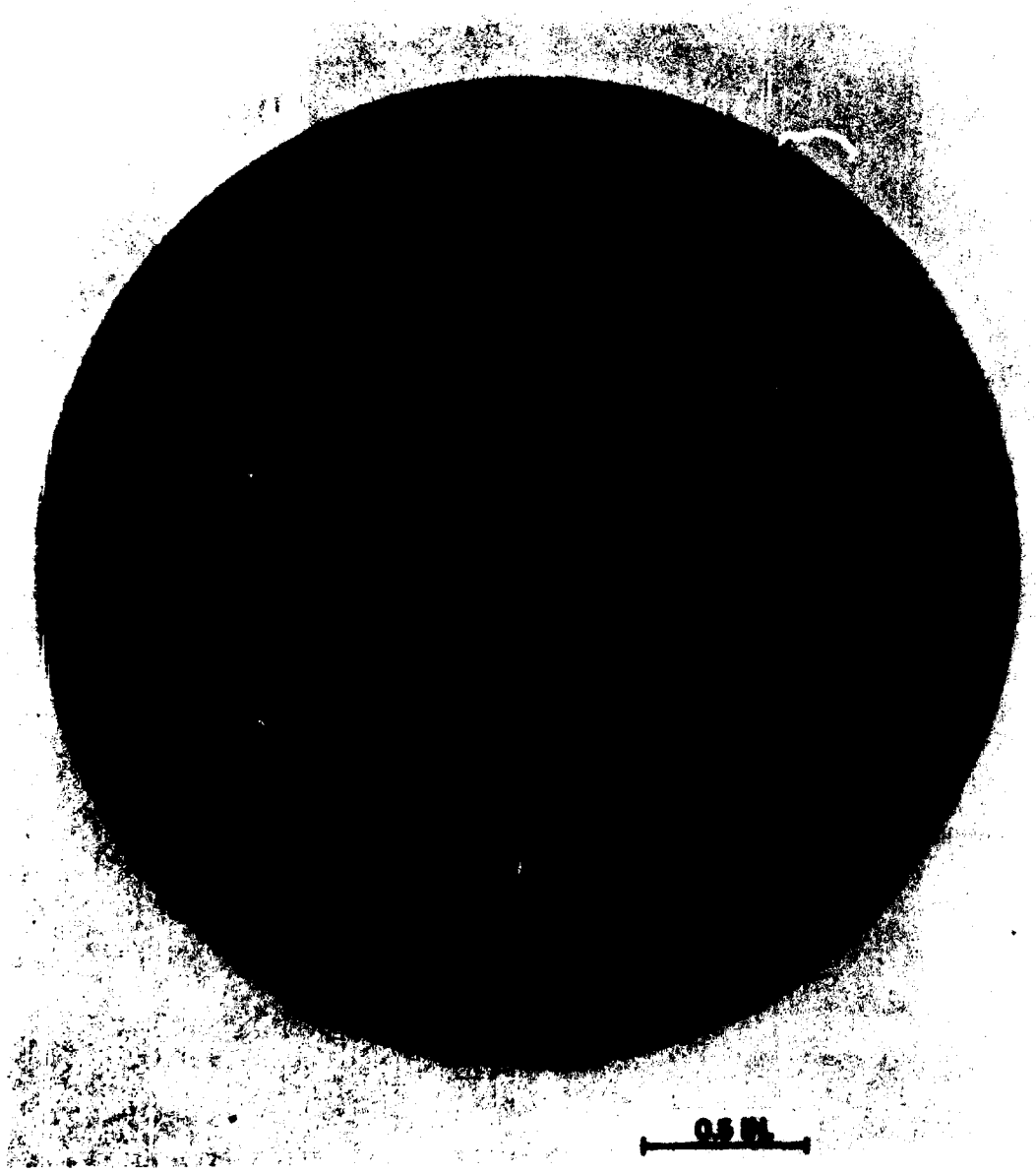

Figure 1. HAC-GLAS 13-2: β-SiC coated ceramic composite substrate.

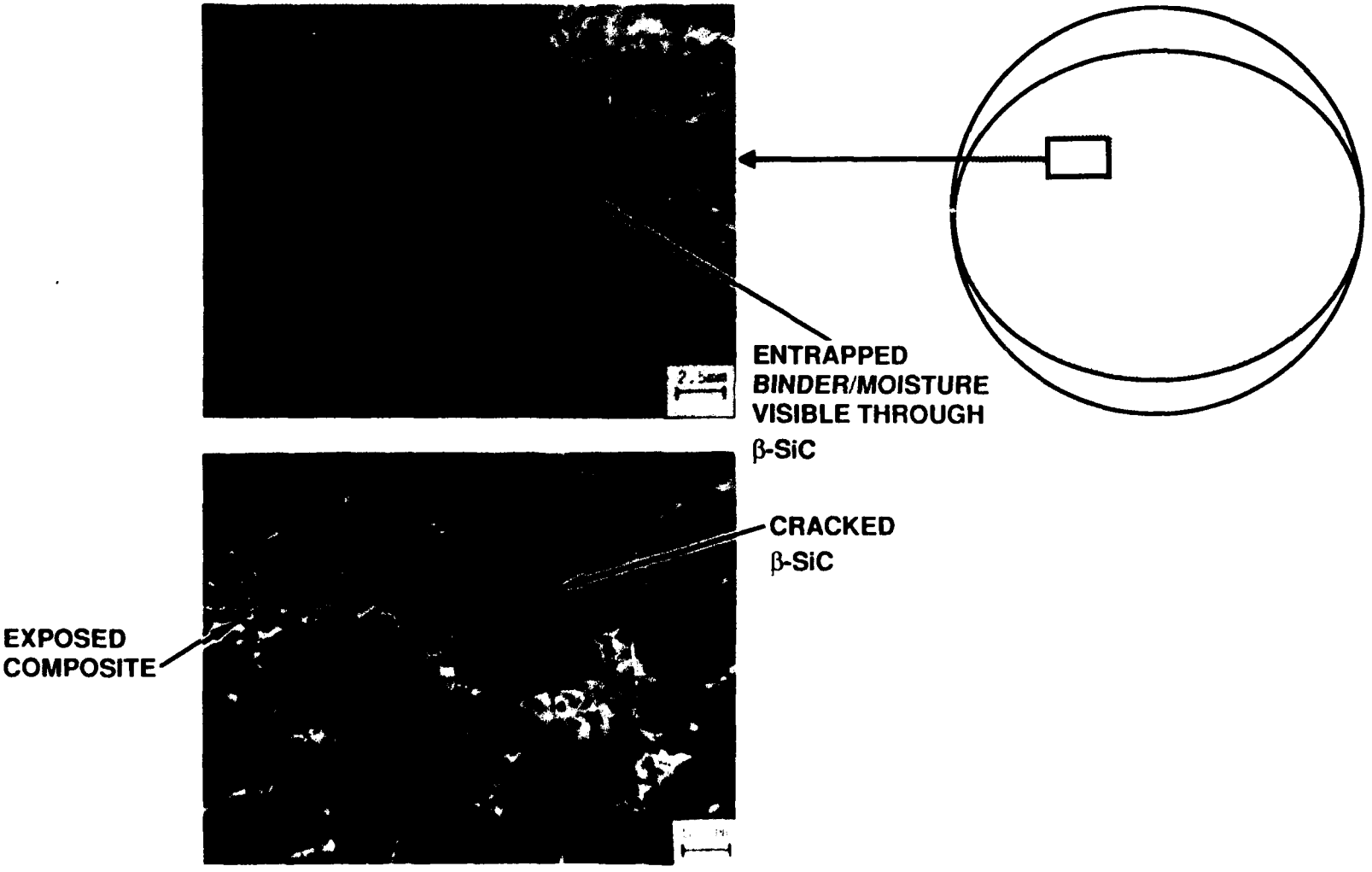

Figure 2. HAC-GLAS 13-2: β-SiC coated ceramic composite substrate.

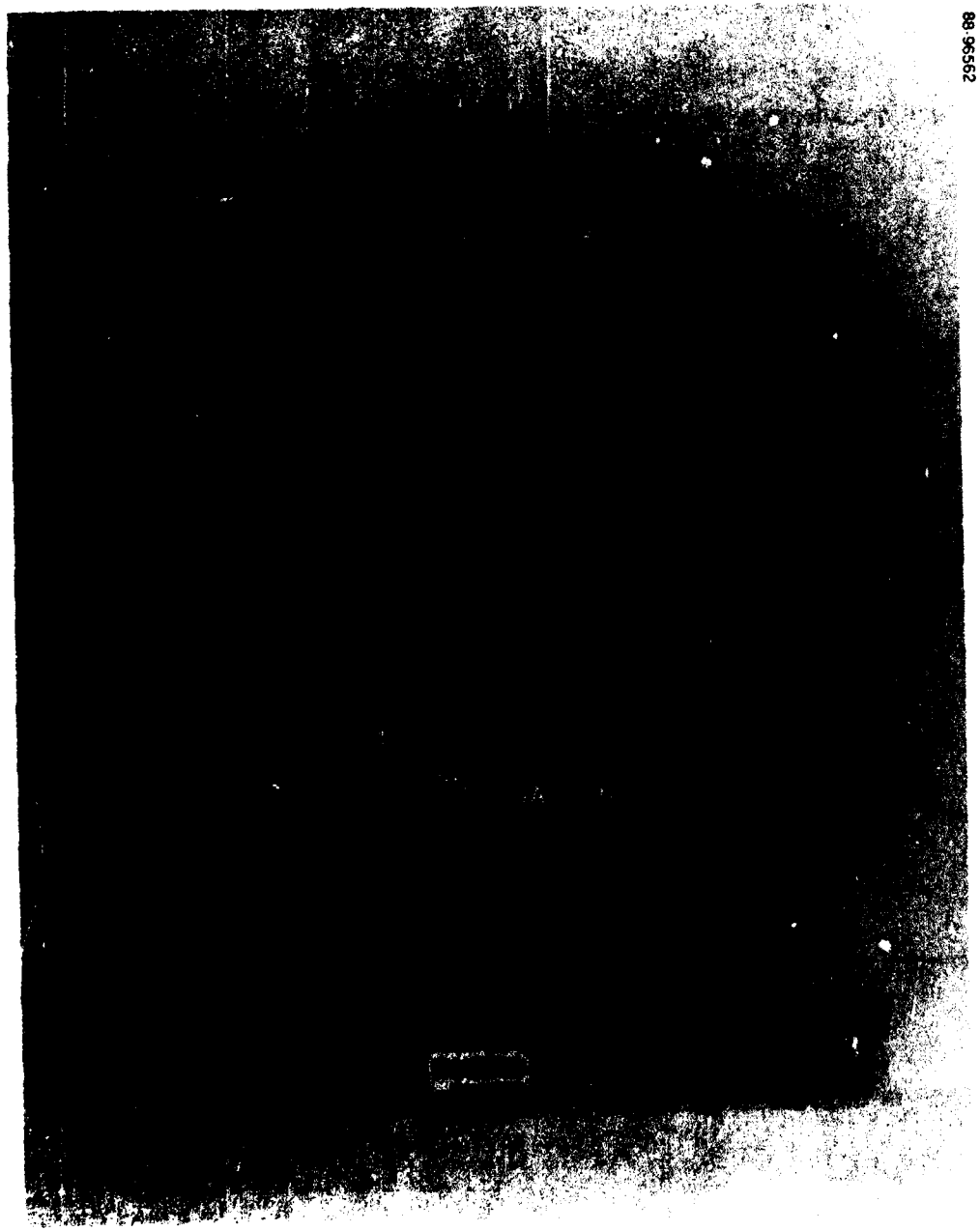

88-96562

HUGHES

Figure 3. HAC-GLAS 13-2: diamond coated ceramic composite (CVD β-SiC coated substrate).

1,2: α-SiC triboflats.
4,5: Single crystal Si thickness monitors.
6: β-SiC coated single crystal Si triboflat.

(Refer to figures 9 and 10)

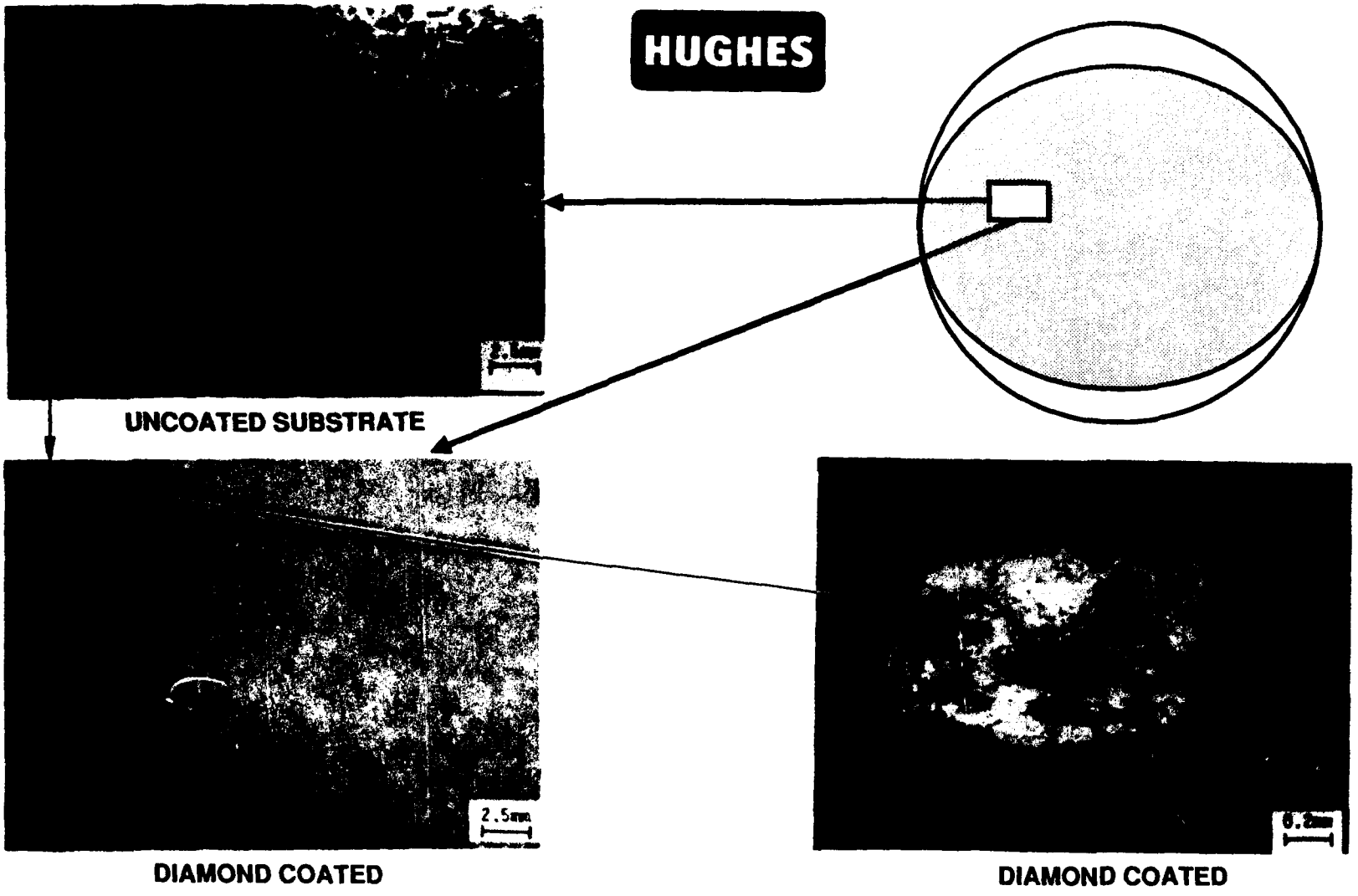

Figure 4. HAC-GLAS 13-2: Effect of macroscopic substrate defect (chip) on localized diamond film growth.

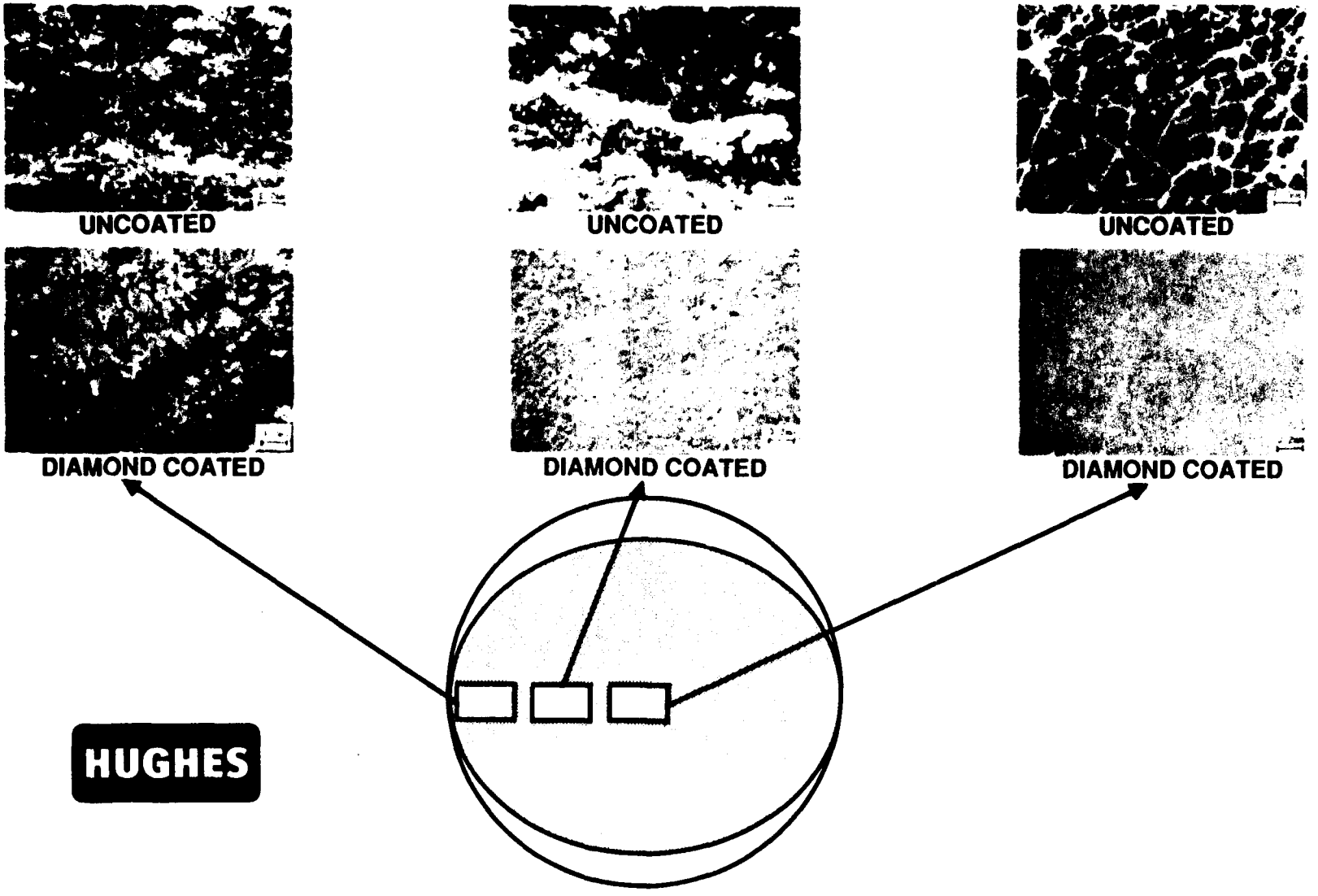

Figure 5. HAC-GLAS 13-2: Substrate and diamond coating surface morphology as a function of radial position.

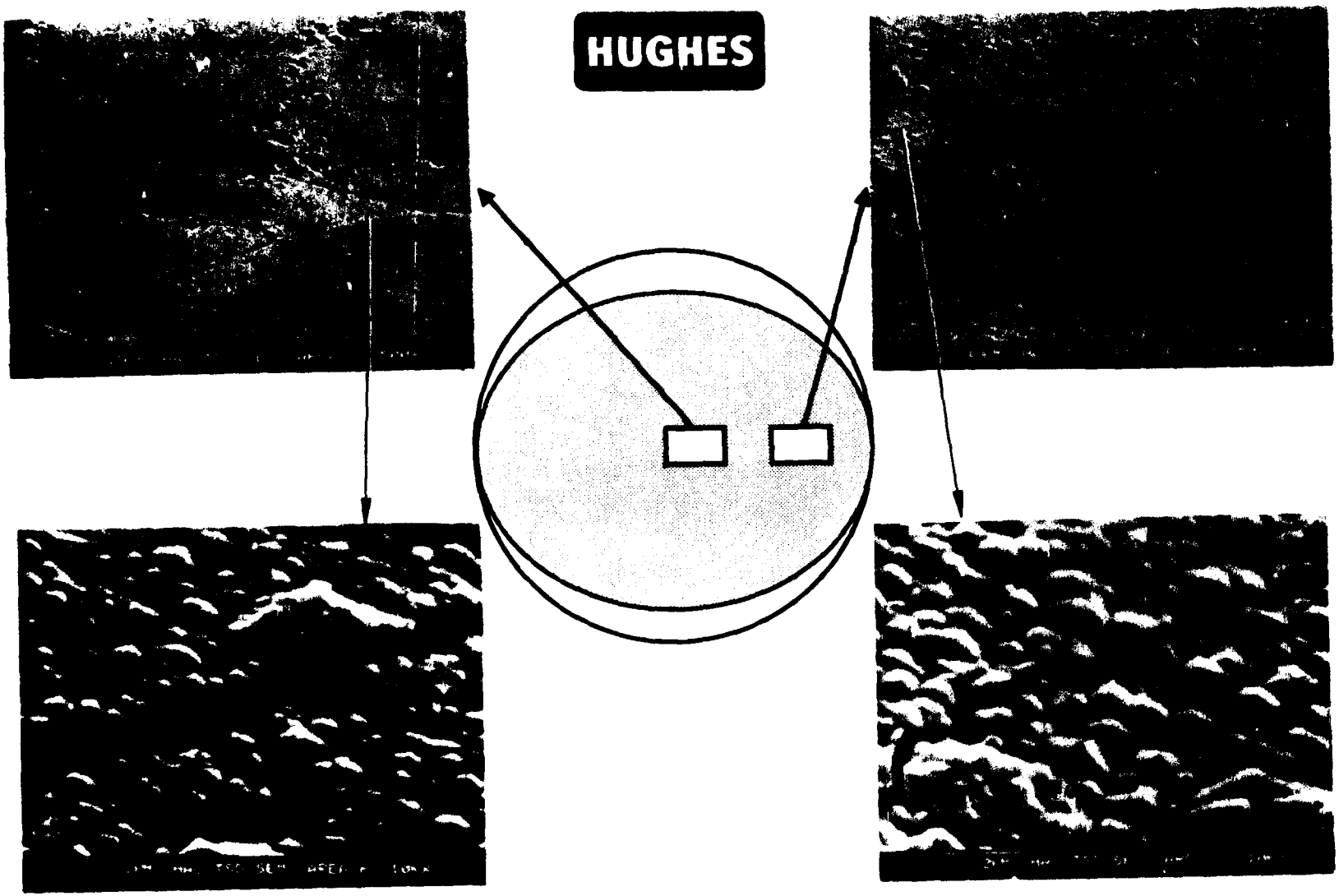

Figure 6. HAC-GLAS 13-2: diamond film morphology as a function of radial position.

HUGHES

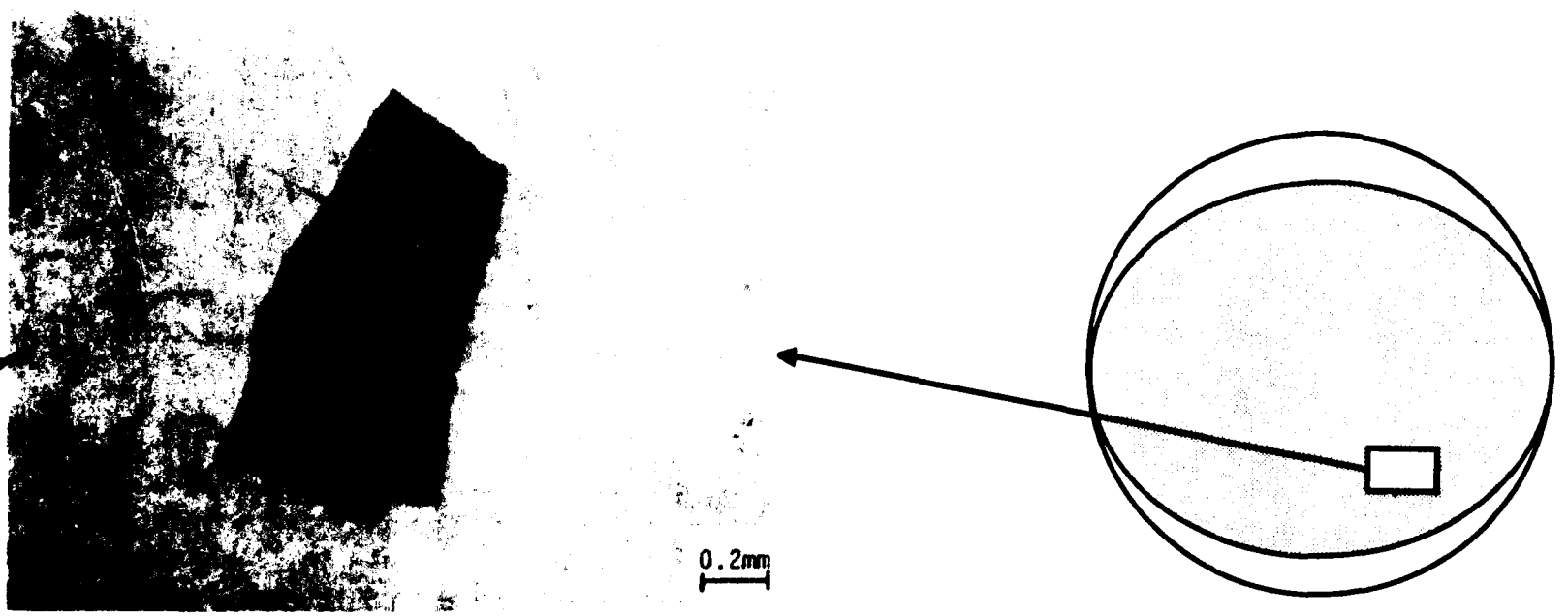

FF - 23

Figure 7. HAC-GLAS 13-2: Diamond film delamination resulting from cracks in the CVD β-SiC which extend into the diamond film.

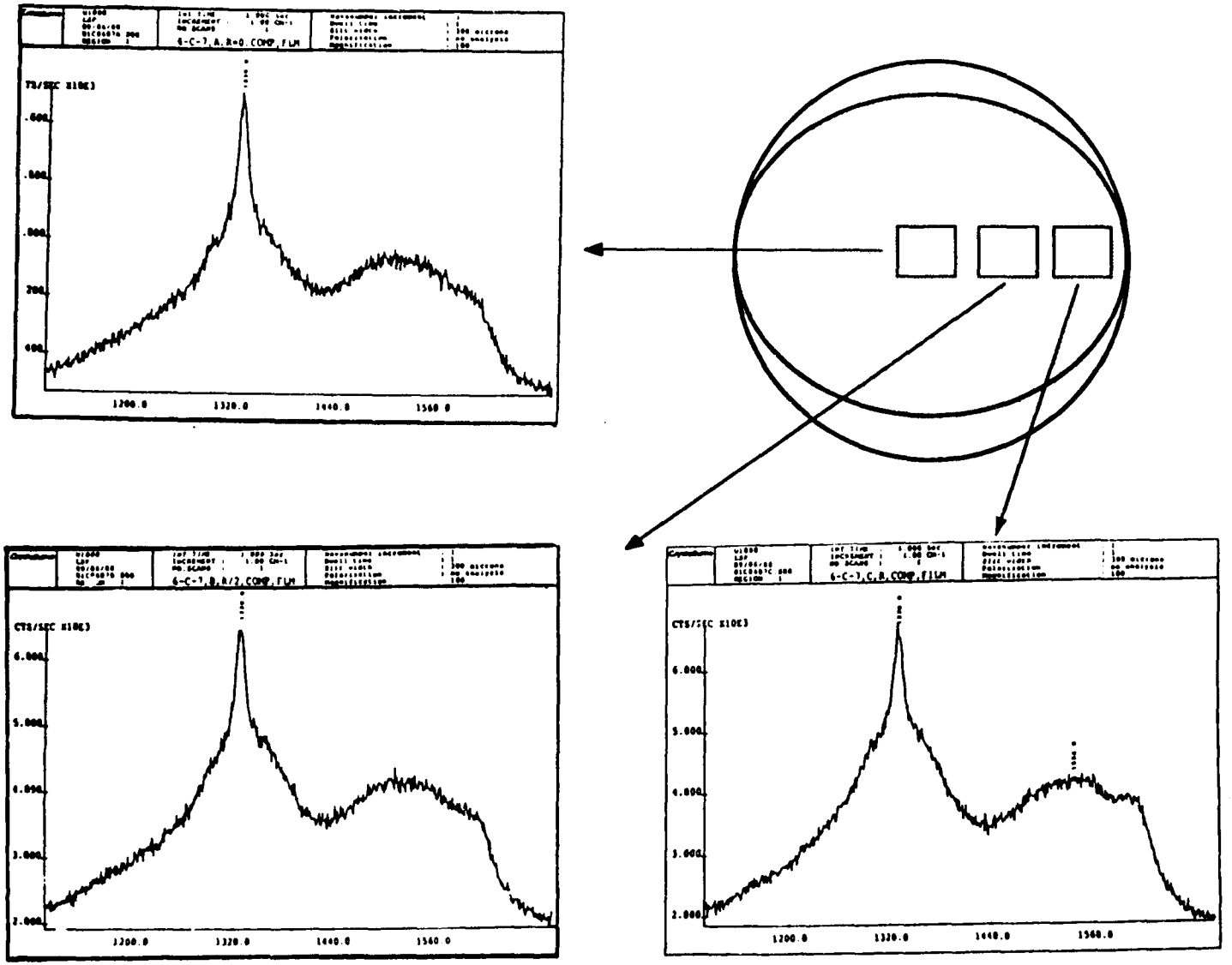

Figure 8. HAC GLAS 13-2: Raman spectra of diamond film indicating a high degree of sp^3 (1330 cm^{-1}) diamond bonding.

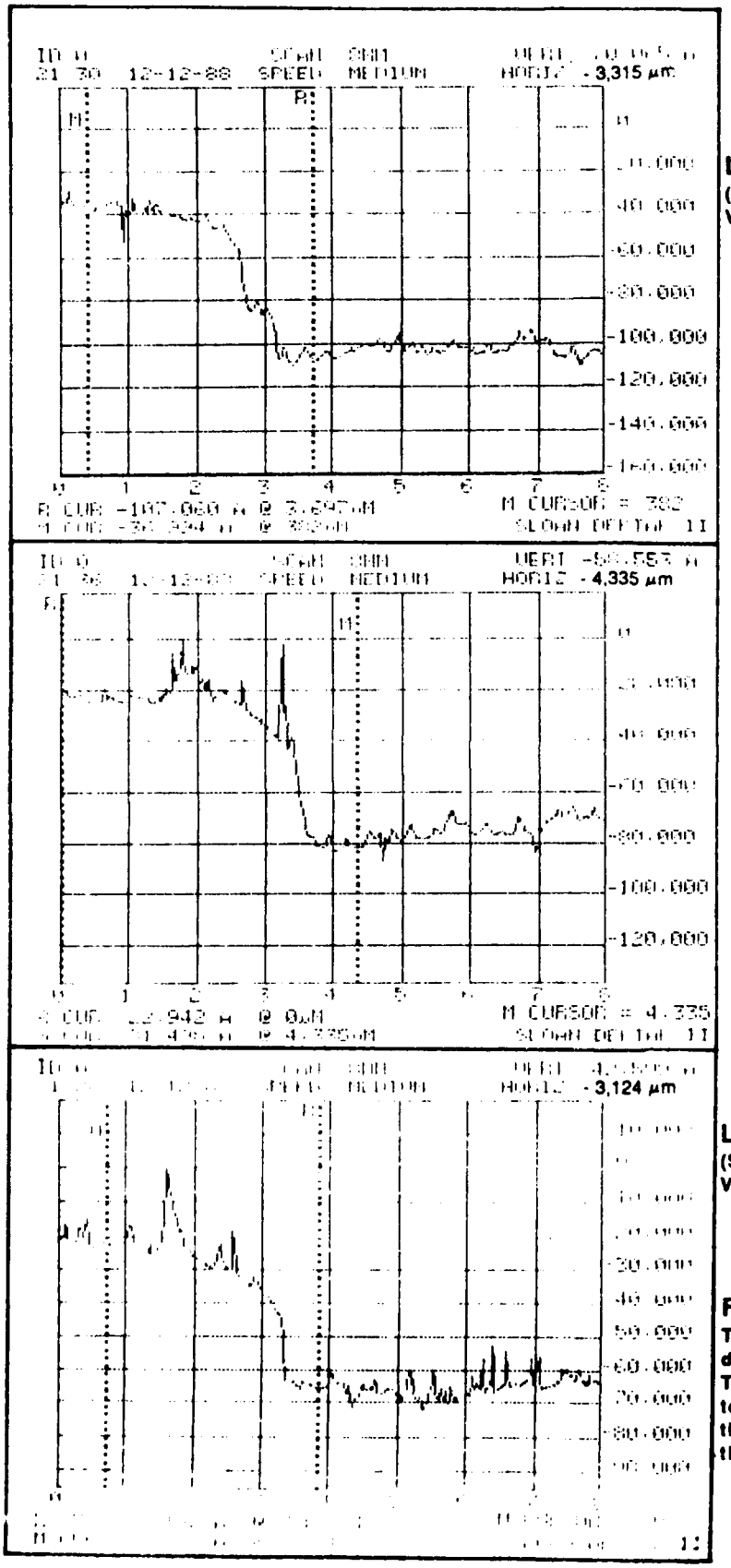

LOCATION 5A *
(SINGLE CRYSTAL Si THICKNESS MONITOR)
VERTICAL STEP: 70,065Å≈7.01 µm

LOCATION 5B
VERTICAL STEP: 42,599Å≈4.26 µm

LOCATION 4
(SINGLE CRYSTAL Si THICKNESS MONITOR)
VERTICAL STEP: 51,400Å≈5.14 µm

FIGURE 9
True film thickness of the HAC GLAS-13-2 diamond film measured by profilometry. The magnitude of the steps also corresponds to the film thickness of the coated thickness monitors which were placed in these locations.

* Refer to Figure 3 for location descriptions.

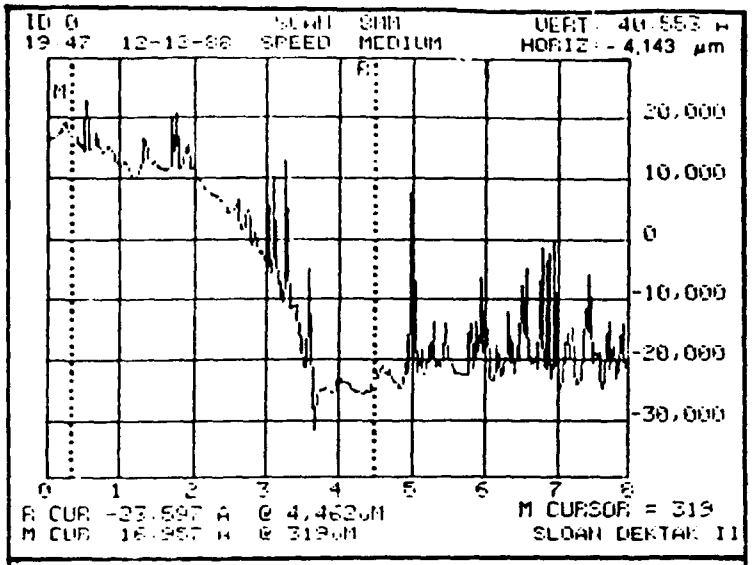

LOCATION 1 *
(SIC TRIBOFLAT)
VERTICAL STEP: 40,553Å=4.05 µm

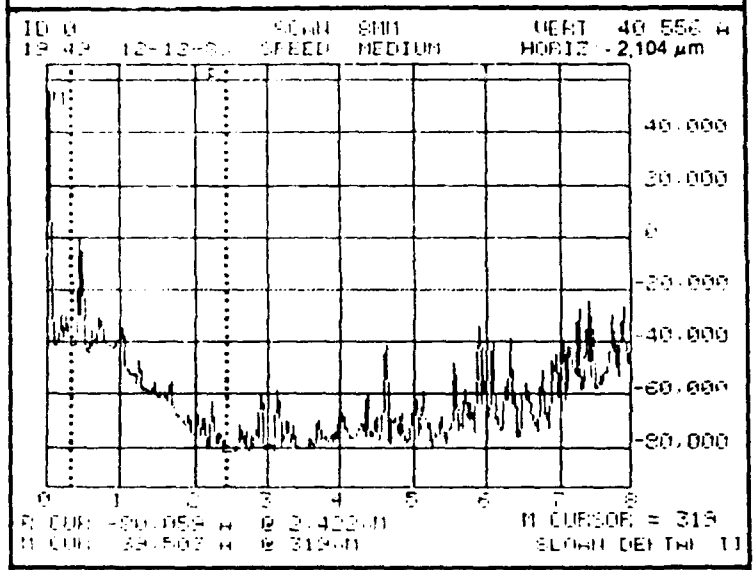

LOCATION 2
(SiC TRIBOFLAT)
VERTICAL STEP: 40,556Å=4.05 µm

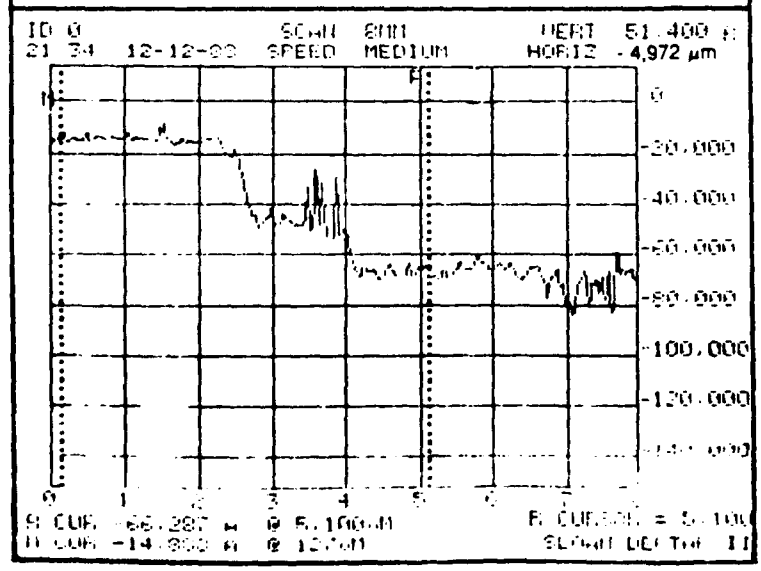

LOCATION 6
(β-SiC ON SINGLE CRYSTAL Si)
VERTICAL STEP: 42,599Å=4.26 µm

FIGURE 10
Height variations of HAC GLAS-13-2 diamond film thickness measured by profilometry. The magnitude of the step corresponds to the film thickness of the coated samples which were placed in these locations.

* refer to Figure 3 for location descriptions.

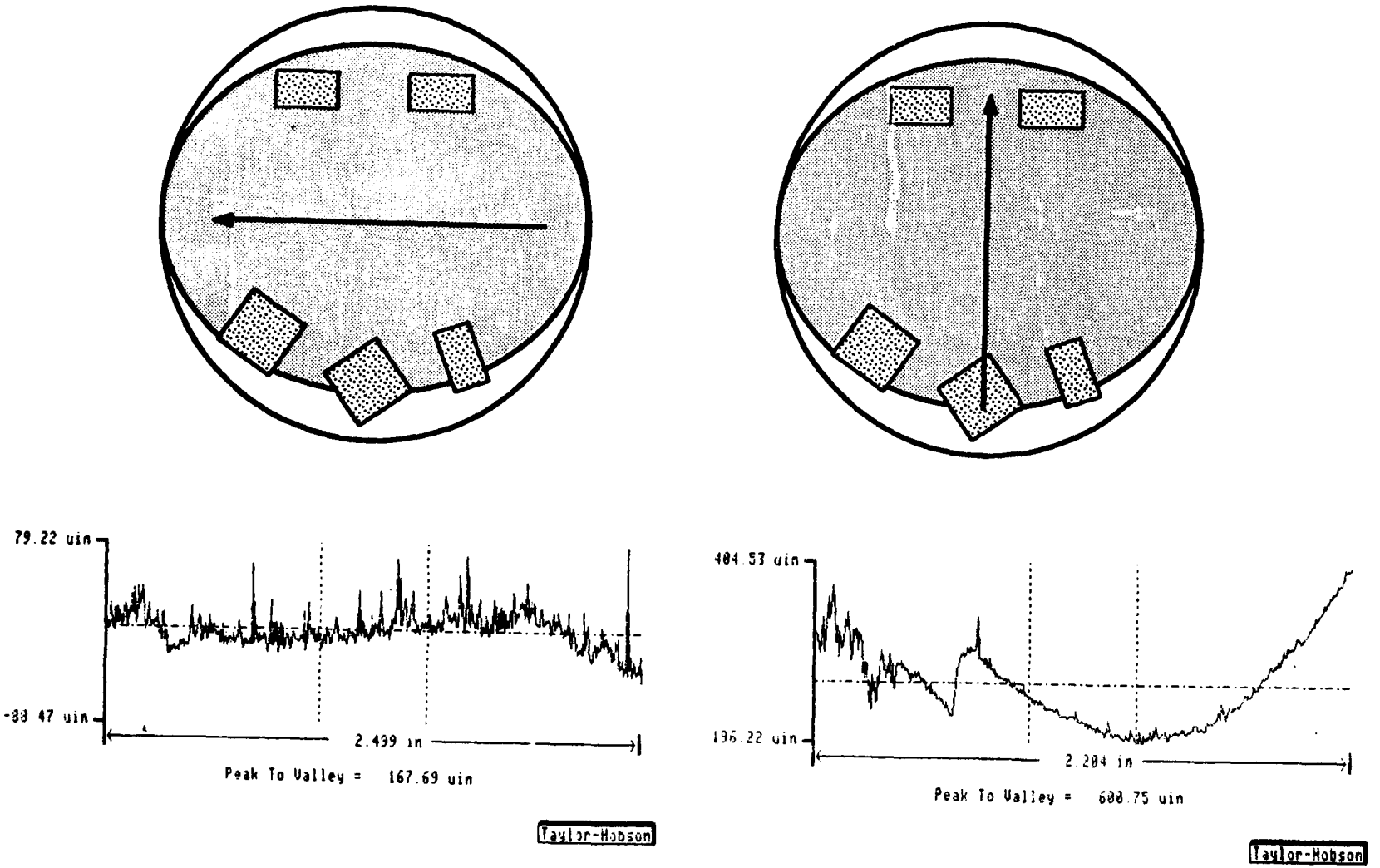

Figure 11. HAC GLAS 13-2: Taylor-Hobson profilometry profiles (unfiltered) showing surface height variation as a result of bowing. Arrows indicate trace direction.

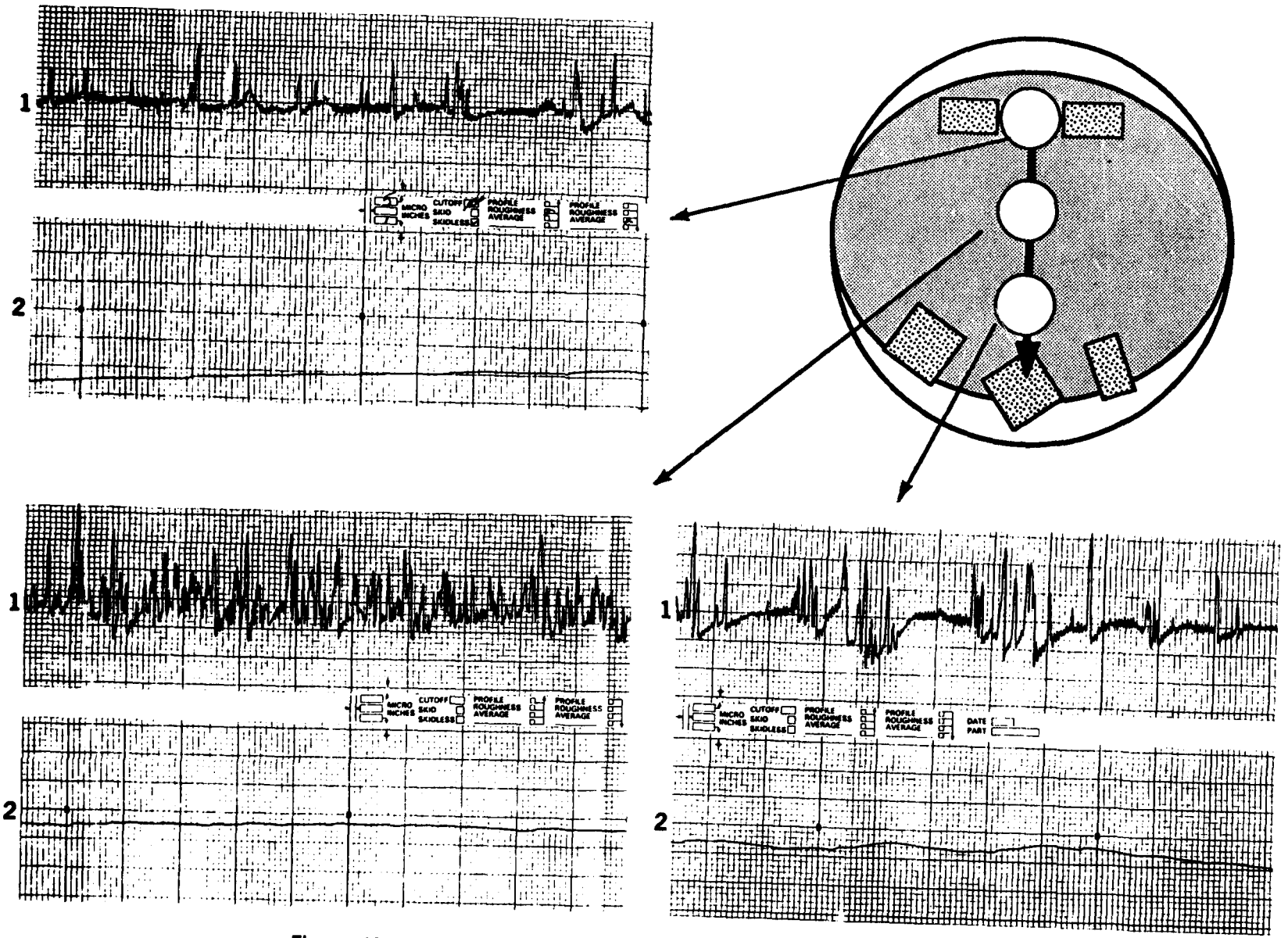

Figure 12. HAC GLAS 13-2: Surface roughness profiles of the diamond film in three locations. (1) RMS Roughness (5μin/div.) and (2) Ave. roughness (1μin/div) are presented for each location. (Clevite Surfanalyzer)

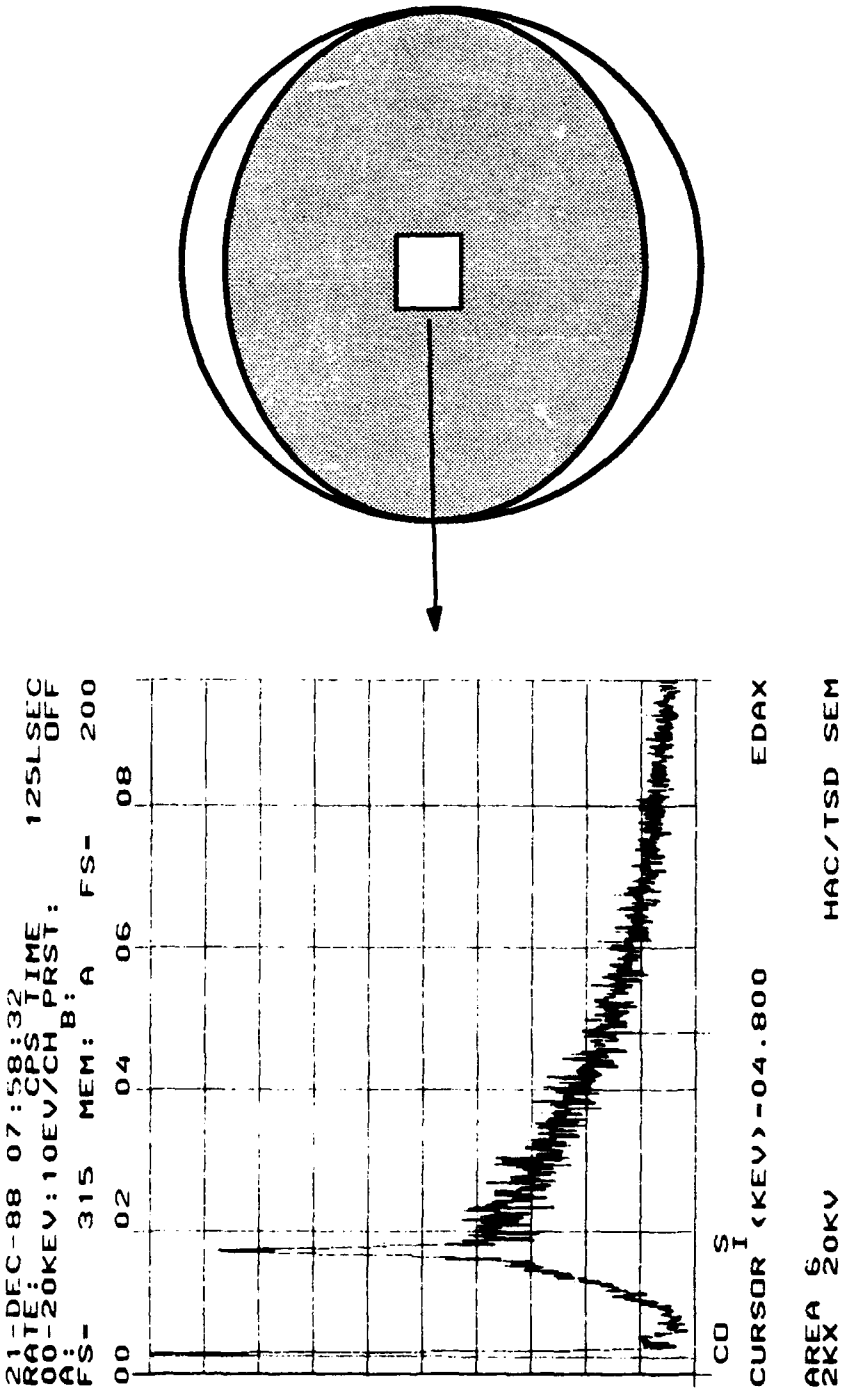

Figure 13. HAC GLAS 13-2: Energy dispersive x-ray (EDX) spectrum of diamond film indicating Si impurity.

REFERENCES

1. Matsumoto, S., Y. Sato and M. Kamo, "Vapor Deposition of Diamond Particles from Methane," Japanese Journal of Applied Physics, Part 2 Letters, Vol 21, No. 4, April 4, 1982, pp. 1183-1185.

2. Seibold, R. W. et al., Technical Status Reports, DOE Contract DE-AC03-87SF17126, 1988-1989.

3. Ramsteiner, M., J. Wagner, C. Wild and P. Koidl, "Raman Scattering of Amorphous Carbon/Semiconductor Interface Layers," Solid State Communications, Vol. 67, No. 1, pp. 15-18, 1988.

4. Matsumoto, S., Y. Sato, M. Tsutsumi and N. Setaka, "Growth of diamond particles from methane-hydrogen gas," Journal of Materials Science 17 (1982), pp. 3106-3112.

5. Beeman, D., J. Silverman, R. Lynds and M. Anderson, "Modeling Studies of Amorphous Carbon," Physical Review B, Vol. 30, No. 2, July 1948, pp. 870-875.

6. Tuinstra, F. and J. Koenig, "Raman Spectra of Graphite," The Journal of Chemical Physics, Vol. 53, No. 3, August 1970, pp. 1126-1131.

7. Yoshikawa, M., G. Katagire, H. Ishida and A. Ishitani, "Raman Spectra of Diamond-Like Amorphous carbon Films," Solid State Communications, Vol. 66, No. 11, pp 1177-1180, 1988.

8. Miyasoto, T., Y. Kawakami, T. Kaoano and A. Hiraki, "Preparation of sp3-Rich Amorphous Carbon Film by Hydrogen Gas Reactive RF-Sputtering of Graphite, and Its Properties," Japanese Journal of Applied Physics, Vol. 23, No. 4, April 1984, pp L234-L237.

9. Yarbrough, W.A. and R. Roy, "Nanocomposite Diamond Films by Hot Filament Assisted CVD," Diamond and Diamond-Like Materials Synthesis, MRS Symposium, April 5-9, 1988, p33.

10. Knight, D., W.R. Drawl, A. Badzian, T. Badzian and W. White, "Characterization of Crystallinity and Stress State of Diamond Films by Raman Spectroscopy, "Diamond and Diamond-Like Materials Synthesis, MRS Symposium, April 5-9, 1988, p.73.

11. Hartnett, T., A. Badzian and K. Spear, "Characterization of Diamond Deposition in a Microwave Plasma, "Diamond and Diamond-Like Materials Synthesis, MRS Symposium, April 5-9, 1988, p. 103.

12. Spitsyn, B., L. Bouilov and B. Derjaguin, "Vapor Growth of Diamond on Diamond and Other Surfaces," Journal of Crystal Growth 52 (1981) pp. 219-226.

13. Gardos, M. N., "Quality Control of Sputtered MoS_2 Films," Lubrication Engineering, 32, 1976.

14. Telecon between Dr. K. Ravi (Crystallume) and B. L. Soriano (Hughes Aircraft Co.), Dec 21, 1988.

APPENDIX GG

M.N. Gardos, "Graphite Fiber Reinforced glass-Ceramic Composite Materials – Program Summary and Status Report"

and

B.L. Soriano, "HAC-GLAS 13-2 Substrate Diamond Coating Characterization and Polishing;" viewgraph handouts of presentations given at the Diamond Initiative Planning Meeting, U. of Arizona Optical Sciences Center, Tucson, AZ, 23 Feb 1989

*Pages GG2 through GG14 are deleted because of ITAR regulations (see below)

WARNING

INFORMATION SUBJECT TO EXPORT CONTROL LAWS

This document may contain information subject to the International Traffic in Arms Regulation (ITAR) or the Export Administration Regulation (EAR) of 1979. This information may not be exported, released, or disclosed to foreign nationals outside the United States without first complying with the export license requirements of the International Traffic in Arms Regulation (ITAR) and/or the Export Administration Regulation (EAR). A violation of the ITAR or EAR may be subject to a penalty of up to 10 years imprisonment and a fine of $100,000 under 22 U.S.C. 2778 or Section 2410 of the Export Administration Act of 1979. Include this notice with any reproduced portion of this document.

GRAPHITE FIBER REINFORCED GLASS-CERAMIC MATERIALS

PROGRAM SUMMARY AND STATUS REPORT

PRESENTED AT
DIAMOND INITIATIVE PLANNING MEETING
TUCSON, ARIZONA

23 FEBRUARY 1989

HUGHES

HUGHES
AIRCRAFT COMPANY

G4-2

HAC GLAS 13-2 COMPOSITE MATERIAL: DIAMOND COATING CHARACTERIZATION AND POLISHING

BONNIE SORIANO

PRESENTED AT
DIAMOND INITIATIVE PLANNING MEETING
TUCSON, ARIZONA
2/23/89

HAC GLAS 13-2 DIAMOND FILM OVERVIEW

HUGHES AIRCRAFT COMPANY

- HAC GLAS 13-2 SUBSTRATE SURFACE CONDITION
- OPTICAL AND SEM MAPPING OF DIAMOND COATING
- CHARACTERIZATION TECHNIQUES AND RESULTS
- CONCLUSIONS
- RECOMMENDATIONS

HAC GLAS 13-2 COMPOSITE SUBSTRATE SCHEMATIC

HUGHES AIRCRAFT COMPANY

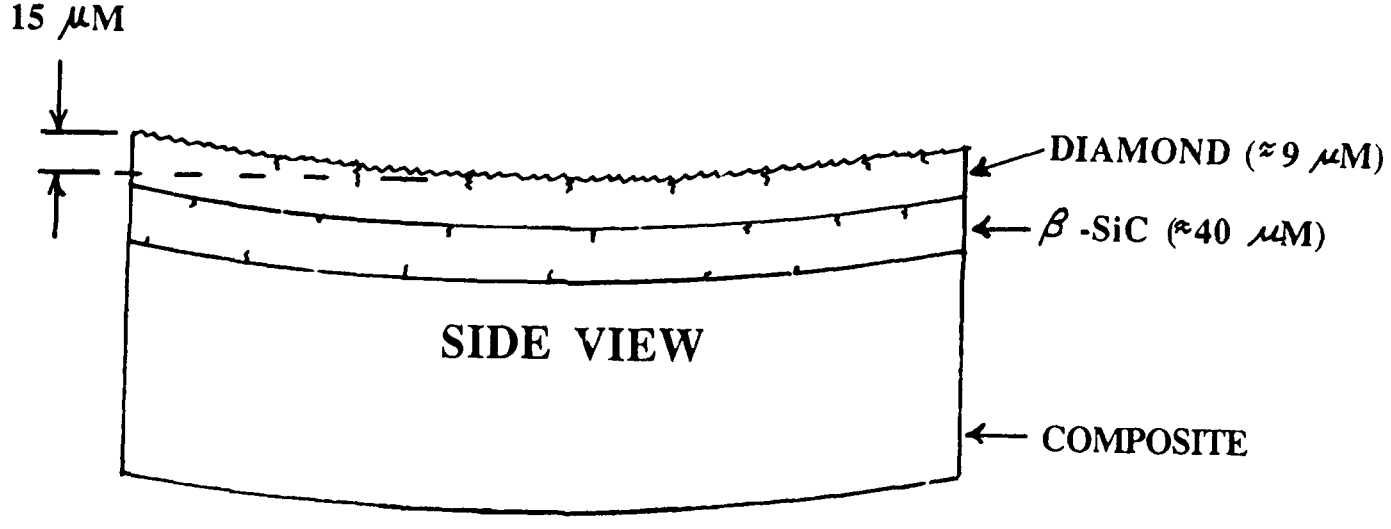

HAC GLAS 13-2 COMPOSITE SCHEMATIC
(NOT TO SCALE)

HAC GLAS-13-2 DIAMOND FILM
DIAMOND FILM CHARACTERIZATION TECNIQUES

HUGHES AIRCRAFT COMPANY

METHOD	INFORMATION
OPTICAL/SEM	MORPHOLOGY/MACROSCOPIC DEFECTS
RAMAN SPECTROSCOPY	SP^3/SP^2 FILM PURITY INTERFILM STRESSES
EDX	ELEMENTAL IMPURITIES
PROFILOMETRY	ROUGHNESS/ FILM THICKNESS SURFACE HEIGHT VARIATION

HAC GLAS 13-2 DIAMOND FILM CONCLUSIONS

HUGHES AIRCRAFT COMPANY

- DIAMOND FILM CHARACTERISTICS
  - * STRUCTURE: CAULIFLOWERED (CENTER) --> TO FACETTED (EDGE)
  - * GOOD (SP^3) QUALITY
  - * HIGH FILM STRESSES SUSPECTED
  - * HIGH SILICON IMPURITY CONTENT
  - * FILM THICKNESS BETWEEN 4 TO 9 μM

GG-6

- *DIAMOND GROWTH CHARACTERISTICS DEPEND ON*
  - * MACROSCOPIC SUBSTRATE DEFECTS (CRACKS, CHIPS)
  - * SUBSTRATE MATERIAL
  - * SUBSTRATE SIZE (POSITION IN CHAMBER)

- EXTREME HEIGHT VARIATION ACROSS DIAMETER OF BILLET
  - * RESULT OF BOWED SUBSTRATE
  - * DIFFICULT TO POLISH

HAC GLAS 13-2 DIAMOND FILM GENERAL RECOMMENDATIONS (SUBSTRATE PREP.)

HUGHES AIRCRAFT COMPANY

- DEPOSITION TEMPERATURES = 700 TO 900 DEG C
  * THERMAL MISMATCHES---> HIGH STRESSES (CRACKING)

- DIAM0ND FILM THICKNESS VARIES 10 % - 4 IN. DIA. (AT BEST)
  * SMALLER SUBSTRATES ARE DESIRABLE

- PEAK TO VALLEY RATIO OF DIAMOND FILM
  * 15 TO 25 Å RMS POLISHED SURFACE ??

HAC GLAS 13-2 DIAMOND FILM
DIAMOND FILM CHARACTERIZATION
-OPTICAL & SEM

HUGHES AIRCRAFT COMPANY

- CHIPS IN CVD β-SiC EFFECT LOCALIZED NUCLEATION AND GROWTH

- CRACKS IN CVD β-SiC EXTEND INTO *DIAMOND FILM-------> DELAMINATION*

- STRUCTURE RANGES FROM CAULIFLOWERED (CENTER) TO HIGHLY FACETTED (EDGES)

- HIGH FILM STRESSES RESULT IN <u>INTERGRANULAR</u> AND <u>TRANSGRANULAR</u> FRACTURE

- *DIAMOND GROWS ON BOTH CVD β-SiC AND BARE COMPOSITE*
  * NUCLEATES READILY ON GRAPHITE FIBERS

HAC GLAS 13-2 DIAMOND FILM DIAMOND CHARACTERIZATION -RAMAN SPECTROSCOPY

HUGHES AIRCRAFT COMPANY

- STRONG DIAMOND PEAK AT 1330 CM^{-1}

- SHIFT FROM 1332 TO 1330 CM^{-1}
  * INDICATES HIGH INTERFILM STRESSES

- SP^3/SP^2 RATIO GOOD
  * RATIO CONSISTANT IN ALL REGIONS TESTED
  * SLIGHT SHIFT IN AMORPHOUS/GRAPHITIC REGION

HAC GLAS 13-2 DIAMOND FILM
DIAMOND CHARACTERIZATION
-RAMAN SPECTROSCOPY

HUGHES

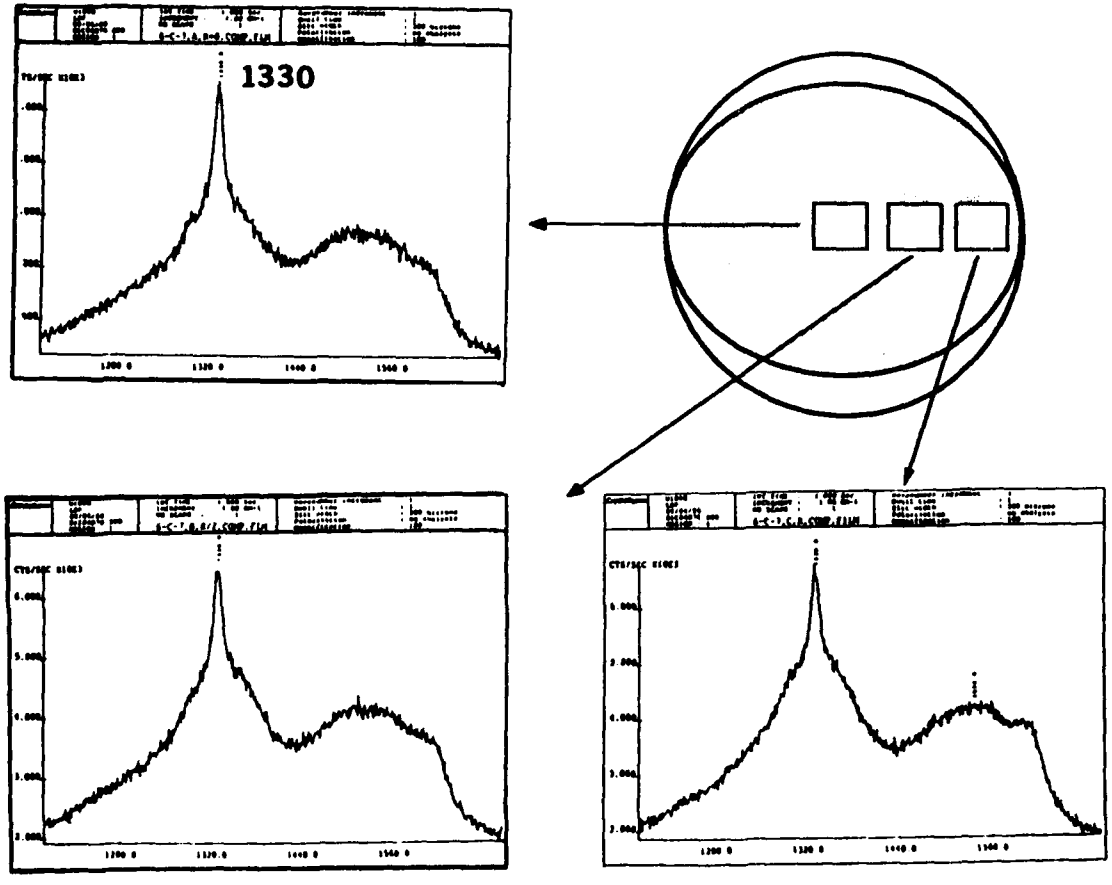

RAMAN SPECTRA OF DIAMOND FILM (CRYSTALLUME)

HAC GLAS 13-2 DIAMOND FILM
DIAMOND CHARACTERIZATION-EDX

HUGHES
AIRCRAFT COMPANY

- HIGH SILICON CONTENT OF DIAMOND TRIBOFLATS AND HAC GLAS
  * POSSIBLE SILICON TRANSPORT FROM COMPOSITE SUBSTRATE

- NO SILICON CONTENT IN DIAMOND ON α/β–SiC (PREVIOUS RUNS)

- OTHER IMPURITY CONTENT NOT DETECTABLE BY EDX

CQ-11

HAC GLAS 13-2 DIAMOND FILM
DIAMOND CHARACTERIZATION-EDX

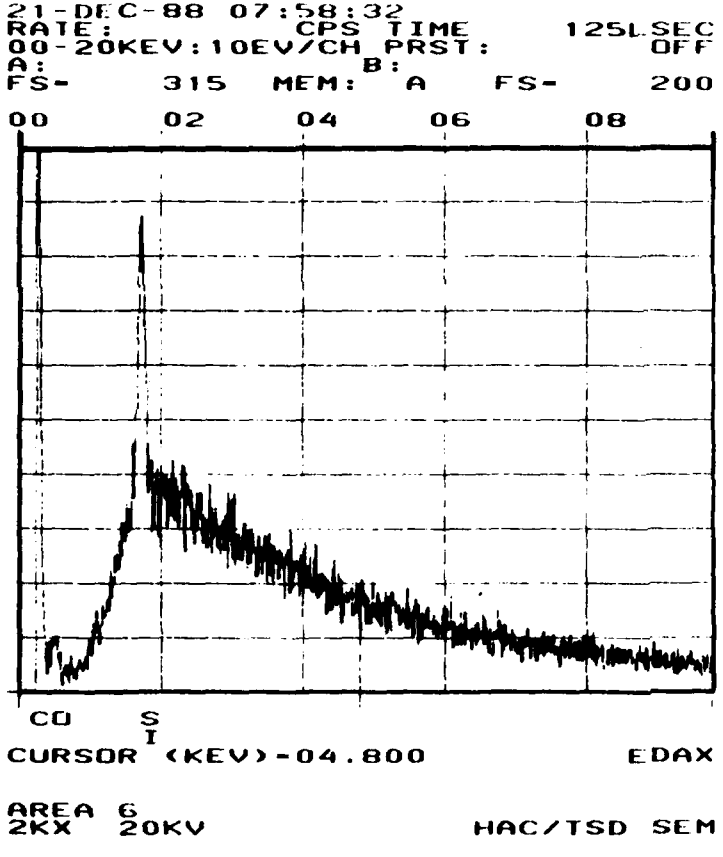

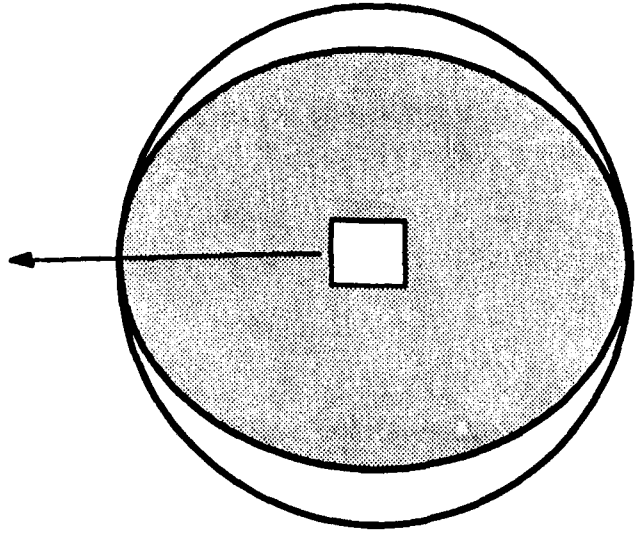

GA-12

HAC GLAS 13-2 DIAMOND FILM DIAMOND CHARACTERIZATION -PROFILOMETRY

HUGHES AIRCRAFT COMPANY

- **FILM THICKNESS VARIATIONS OBSERVED**
  - * PROFILOMETRY STEPS = 4μM (HUGHES) (SHADOWING EFFECT)
  - * CROSS-SECTIONED SI CHIP = 9μM (CRYSTALLUME) (THICKER SAMPLE--CLOSER TO GAS INLET)
- **SURFACE HEIGHT VARIATIONS (SUBSTRATE IS BOWED)**
  - * RIGHT TO LEFT 4.3 μM
  - * BOTTOM TO TOP 15 μM
- **SURFACE ROUGHNESS (AVE, RMS)**
  - * TOP TO BOTTOM = 2,500 Å

HAC GLAS 13-2 DIAMOND FILM DIAMOND CHARACTERIZATION -PROFILOMETRY

HUGHES AIRCRAFT COMPANY

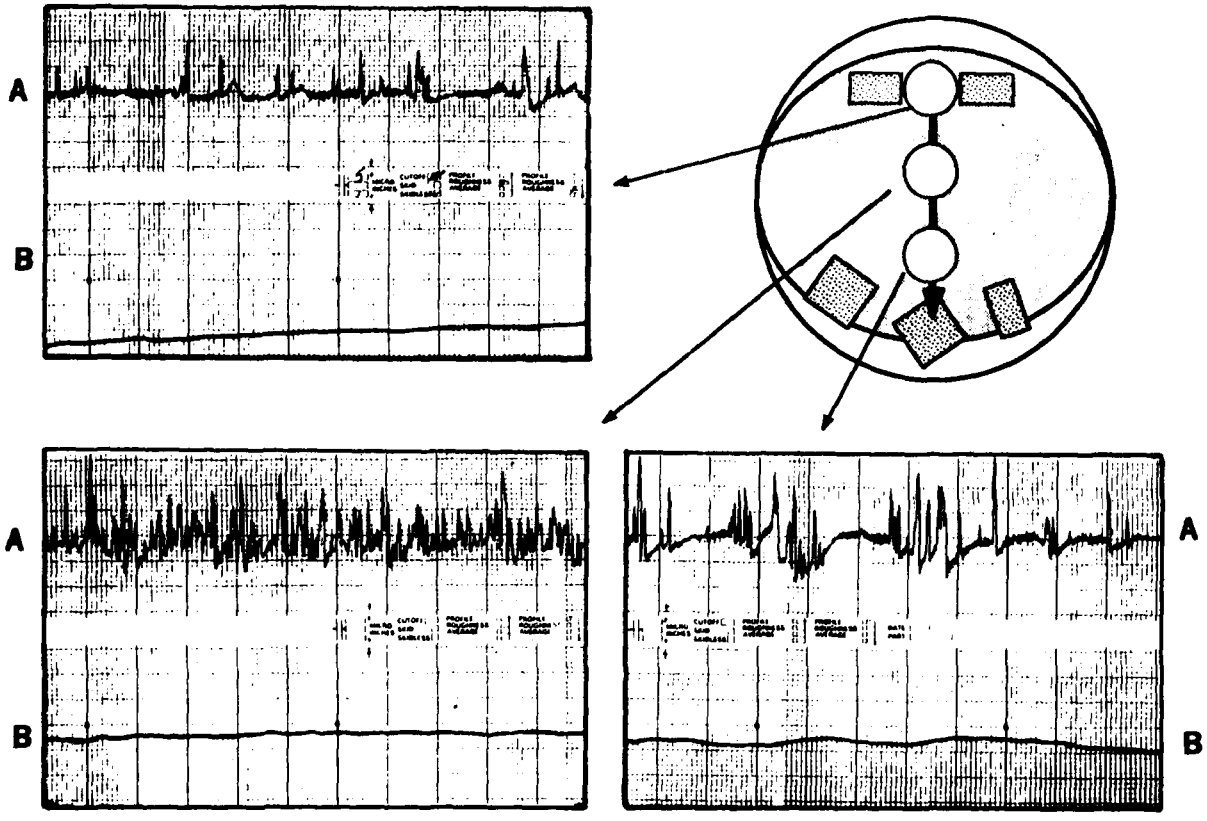

RMS SURFACE ROUGHNESS

a) 5 μIN. PER DIV. RMS ROUGHNESS

b) 1 μIN. PER DIV. AVE. RMS ROUGHNESS

HAC GLAS 13-2 DIAMOND FILM
DIAMOND CHARACTERIZATION
-PROFILOMETRY

HUGHES
AIRCRAFT COMPANY

GQ-15

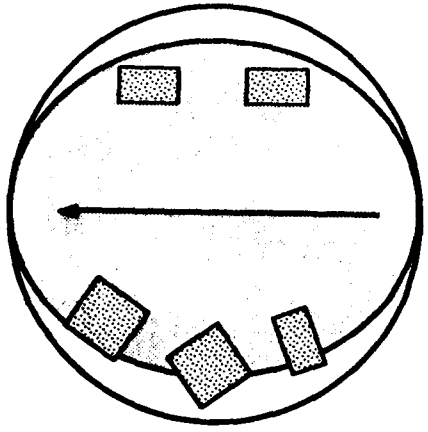

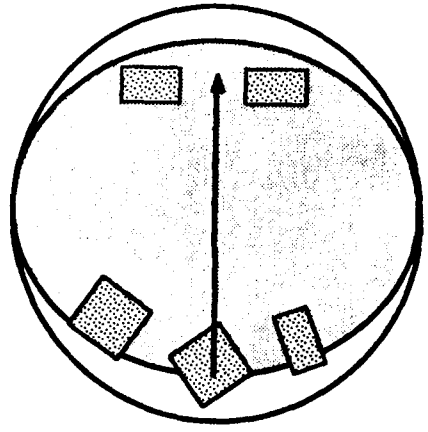

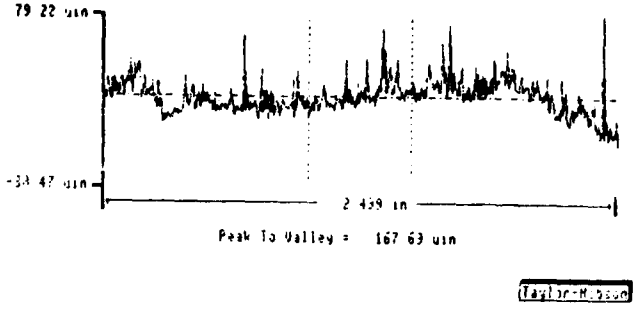

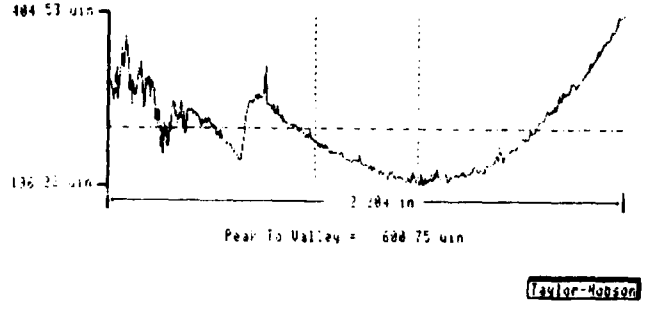

UNFILTERED PROFILOMETER TRACES
INDICATING SURFACE HEIGHT VARIATION (BOWING)

HAC GLAS 13-2 DIAMOND FILM DIAMOND CHARACTERIZATION -PROFILOMETRY

HUGHES AIRCRAFT COMPANY

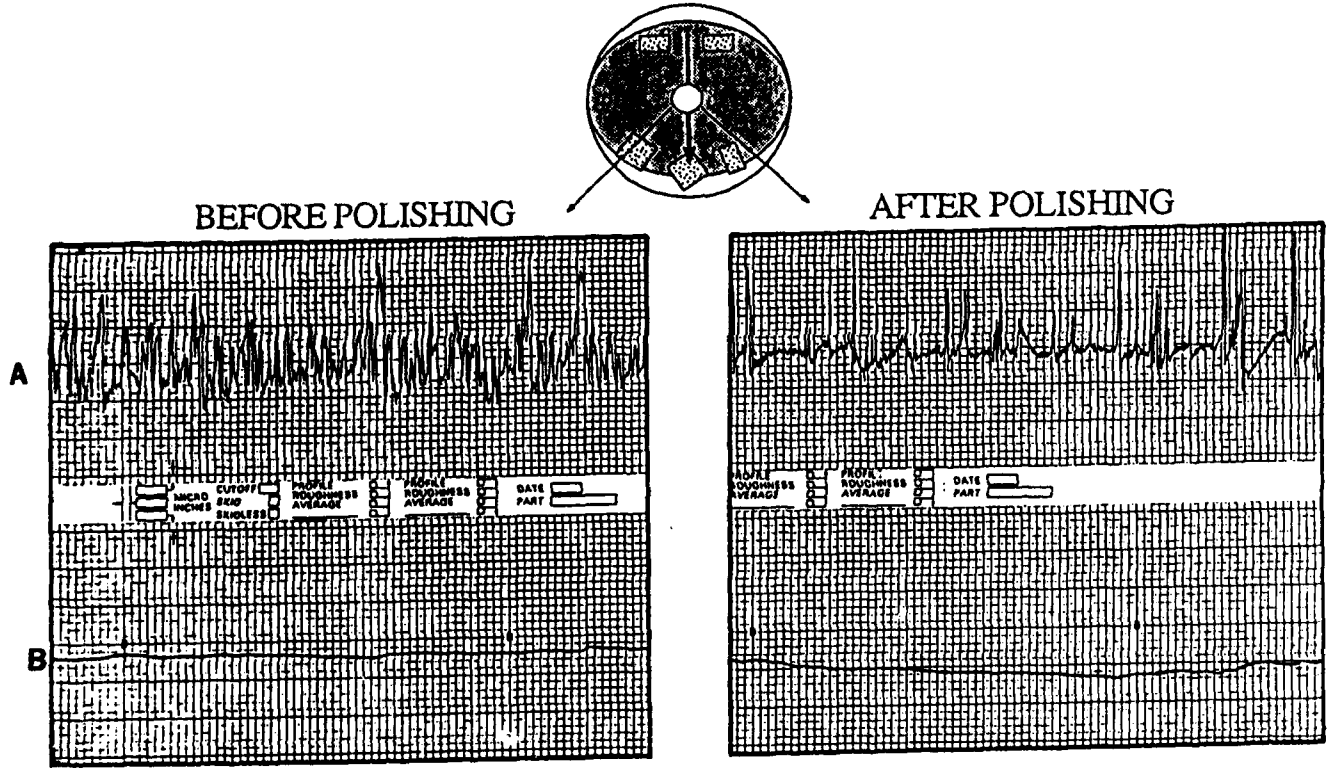

GG-16

RMS SURFACE ROUGHNESS

a) 5 μIN. PER DIV. RMS ROUGHNESS

b) 1 μIN. PER DIV. AVE. RMS ROUGHNESS

APPENDIX HH

P.G. Magallanes, "Crystallume Diamond Films—Analysis by FTIR," Hughes Analytical Chemistry Laboratory Memo, Materials Science Dept. (Div. 76), Hughes Aircraft Co., El Segundo, CA, 18 December 1988

and

P.G. Magallanes, "Wide Wavelength Spectrum of Diamond Film "Hughes Analytical Chemistry Laboratory Memo, Materials Science Dept. (Div. 76), Hughes Aircraft Co., El Segundo, CA 02 March 1989

MATERIALS SCIENCE DEPARTMENT

ANALYTICAL CHEMISTRY LABORATORY

* REPORT *

TO:	SOURCE CODE	LOC	BLDG	M/S	PHONE
Mike Gardos	76-21-01	EO	E1	F150	616-9890

FROM:	SOURCE CODE	LOC	BLDG	M/S	PHONE
Phil Magallanes	76-21-11	EO	E1	F150	616-6069

SUBJECT: Crystallume Diamond Films -- Analysis by FTIR

DATE: 18 Dec 1988

Two free-standing diamond thin films on silicon surrounds were studied to determine if organic contamination was present.

The study was performed using a model FTS-40 Fourier Transform Infrared (FTIR) Spectrometer (BIO-RAD, Digilab) with an IR-PLAN optical/FTIR microscope (Spectra-tech). The IR-PLAN microscope uses a 15X reflecting Cassegrainian objective. A 10X Cassegrainian is used as a condenser for the beam as it passes through the sample. The FTS-40 was set at 8 wavenumber resolution for optimum signal to noise. A wide open aperture in the microscope resulted in an 800 micron diameter field of view.

The two diamond films were quite different in appearance. One appeared to be quite clear and transparent. The other appeared to be quite hazy and nearly opaque. Neither sample was marked. The outside of the plastic package was labeled

EASI-51-N
-15,
-16.

Clearly, the numbers 15 and 16 refer to sample numbers. In this report, the samples will simply be referred to as "clear" and "hazy."

First, the clear film was examined with a wide open aperture. A single beam spectrum was obtained which was ratioed against an open background. Two broad absorptions appeared: a major peak at 808 wavenumbers and a moderate shoulder at about 1010 wavenumbers. The other weak absorptions appeared to be left over from the water vapor mismatch between the sample and the backgound. No absorptions could be attributed to organic material since no evidence of C-H, C-O, or C-F bonds were present.

The hazy film was also examined with a wide open aperture and ratioed against an open background. The resulting infrared spectrum appeared similar to the spectrum of the clear film. Again, no organic absorptions were detected.

Finally, a small (40 X 30 micron) blue spot which appeared on the clear film was examined with an appropriately apertured beam. A few small broad peaks appeared in the spectrum, but unfortunately, none could be attributed to organic material.

Even though the hazy film appeared to be quite opaque, it was quite transparent to the infrared beam. The height of the interferogram for the wide open beam measured 5.90 volts. The interferograms for the hazy sample and the clear sample measured 4.55 and 4.64 volts respectively showing little differences in infrared transparency.

CONCLUSION

An optical/FTIR microscope was used to examine two diamond thin films by transmission. No evidence of organic contamination was found on either film.

Philip G. Magallanes

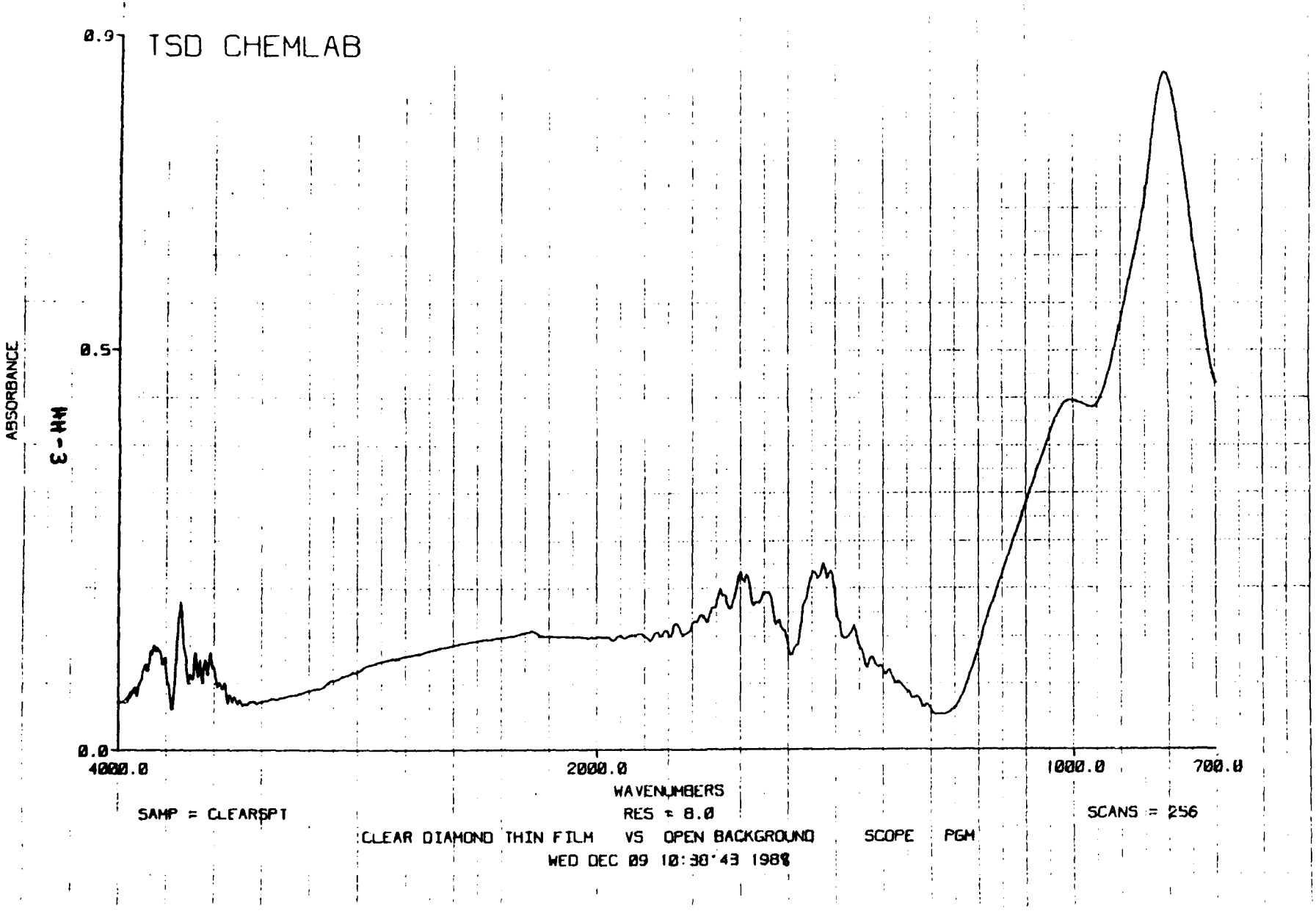
TSD CHEMLAB
0.9
0.5
0.0
ABSORBANCE
E-MM
4000.0
2000.0
1000.0
700.0
WAVENUMBERS
SAMP = CLEARSPT
RES = 8.0
SCANS = 256
CLEAR DIAMOND THIN FILM VS OPEN BACKGROUND SCOPE PGM
WED DEC 09 10:38:43 1988

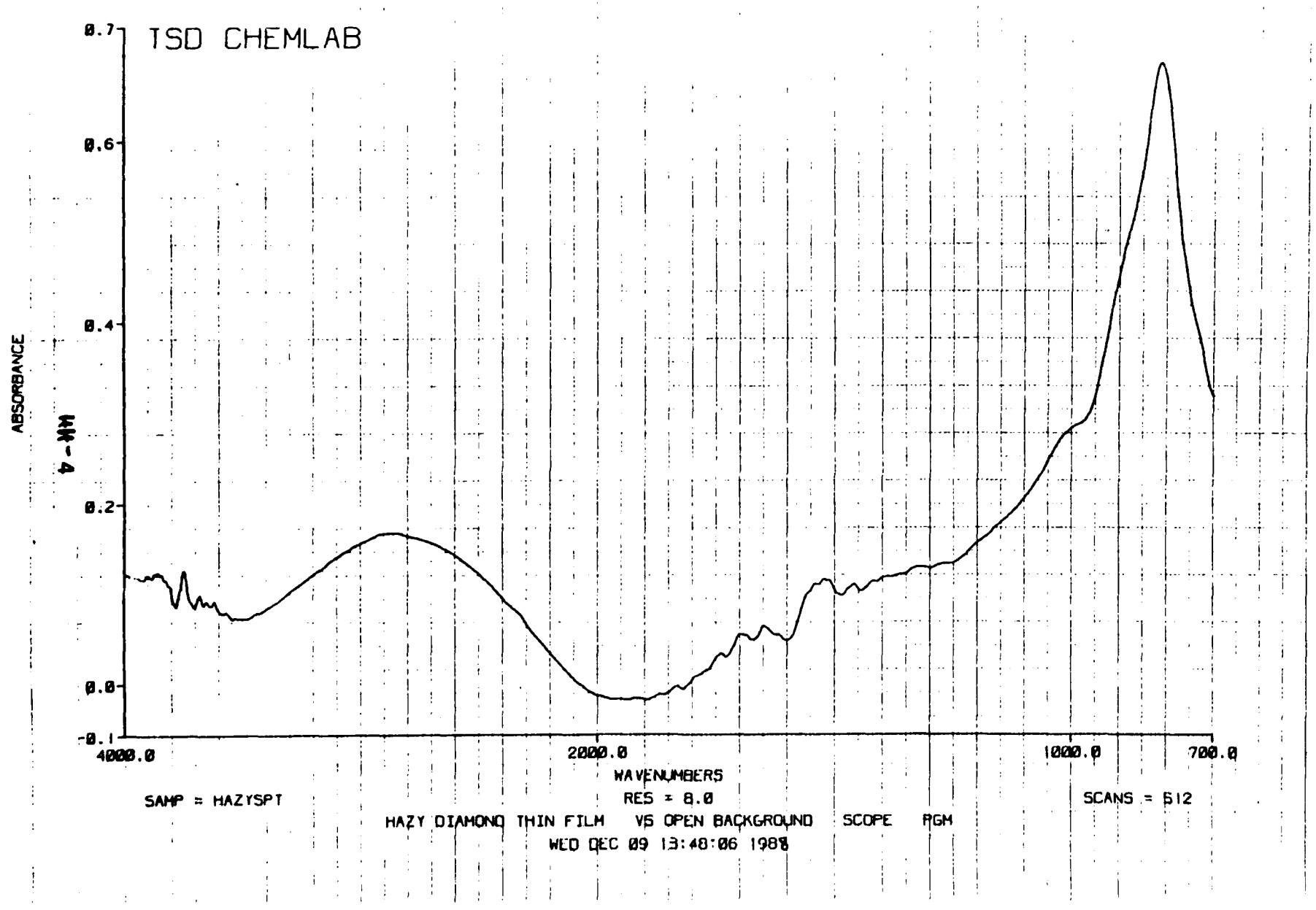
TSD CHEMLAB
0.7
0.6
0.4
0.2
0.0
-0.1
ABSORBANCE
4000.0
2000.0
1000.0
700.0
WAVENUMBERS
SAMP = HAZYSPT
RES = 8.0
SCANS = 512
HAZY DIAMOND THIN FILM VS OPEN BACKGROUND SCOPE PGM
WED DEC 09 13:48:06 1988

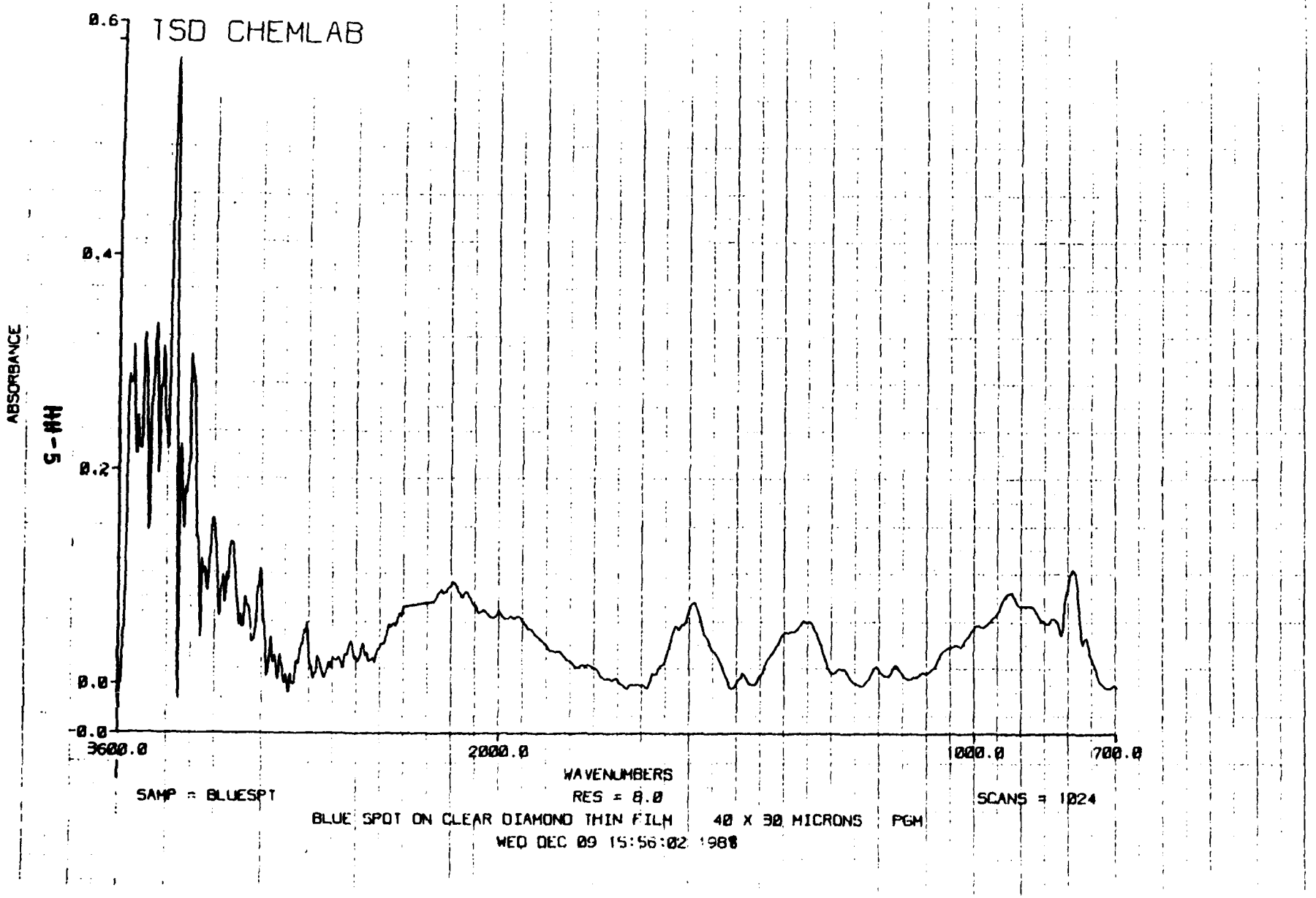
TSD CHEMLAB
0.6
0.4
0.2
0.0
-0.0
ABSORBANCE
HW-5
3600.0
2000.0
1000.0
700.0
WAVENUMBERS
SAMP = BLUESPT
RES = 8.0
SCANS = 1024
BLUE SPOT ON CLEAR DIAMOND THIN FILM 40 X 30 MICRONS PGM
WED DEC 09 15:56:02 1988

MATERIALS SCIENCE DEPARTMENT
ANALYTICAL CHEMISTRY LABORATORY

REPORT

	NAME	SOURCE	LOC	BLD	M/S	EXT
TO:	Mike Gardos	76-21-01	EO	E1	F150	616-9890
FROM:	P.G. Magallanes	76-21-10	EO	E1	F150	616-6069

SUBJECT: Wide Wavelength Spectrum of Diamond Film DATE 3-02-89

The spectrum of the thick diamond film (6-8 microns) made by Crystallume was obtained in the ultra-violet, the visible, portions of the near-infrared, and the middle infrared.

The UV/VIS/NIR spectrum was obtained with a CARY 2300 spectrophotometer. The slit height was set to 1/3. Approximately 80% of the beam energy was available to the sample which is more than enough to produce a spectrum with good signal to noise.

The middle infrared spectrum was obtained with a DIGILAB FTS-40 spectrometer. Two volts of signal strength were available out of a possible ten. Again, this is more than adequate energy. The spectral range was extended to 22 microns. Plots were obtained in both absorbance and percent transmittance. Spectra were taken with both the dull side and the shiny side facing the beam. There was no discernible difference between the two spectra.

Philip G. Magallanes

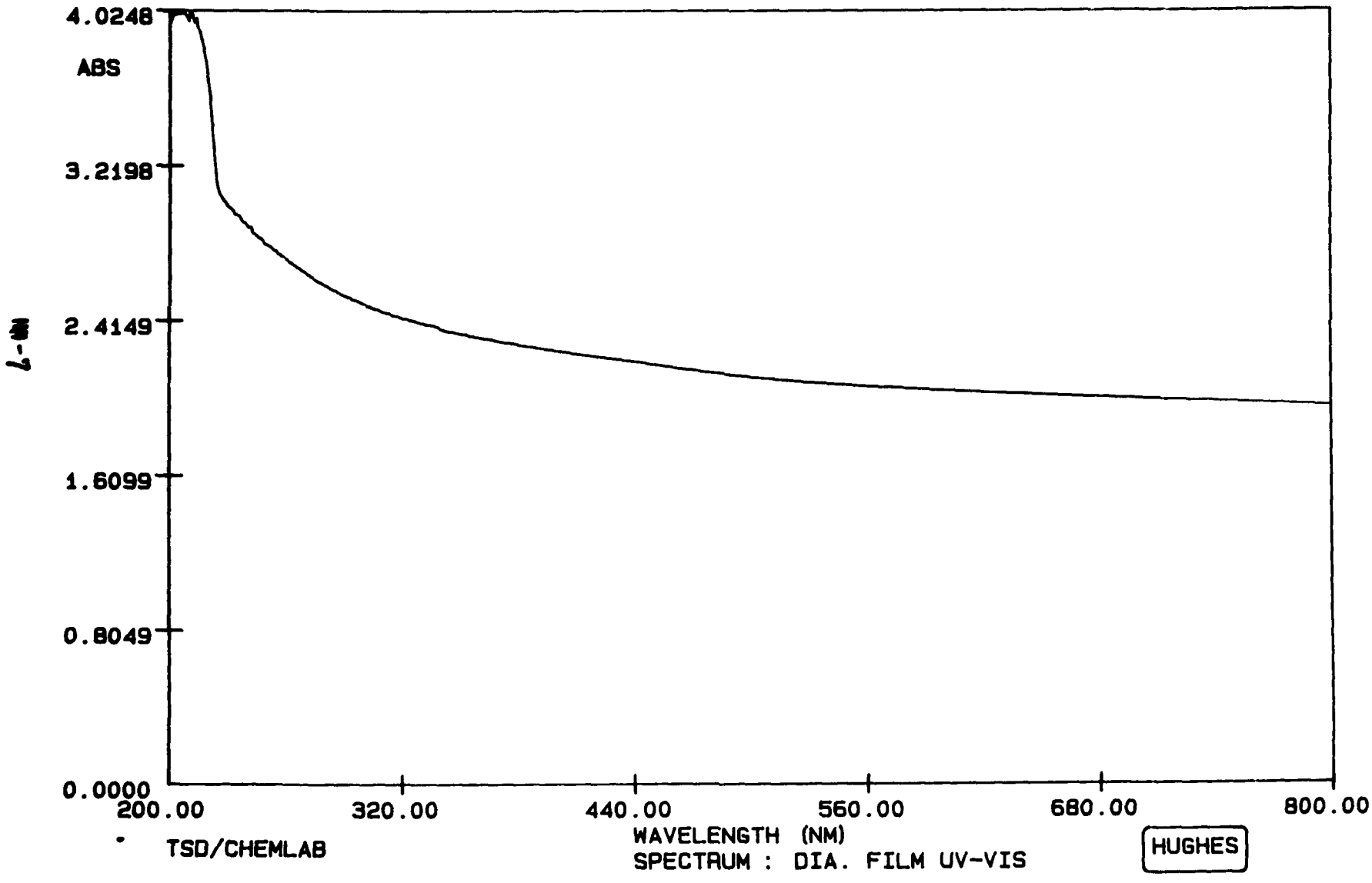
4.0248
ABS
3.2198
2.4149
1.6099
0.8049
0.0000
200.00
320.00
440.00
560.00
680.00
800.00
WAVELENGTH (NM)
TSD/CHEMLAB
SPECTRUM : DIA. FILM UV-VIS
HUGHES

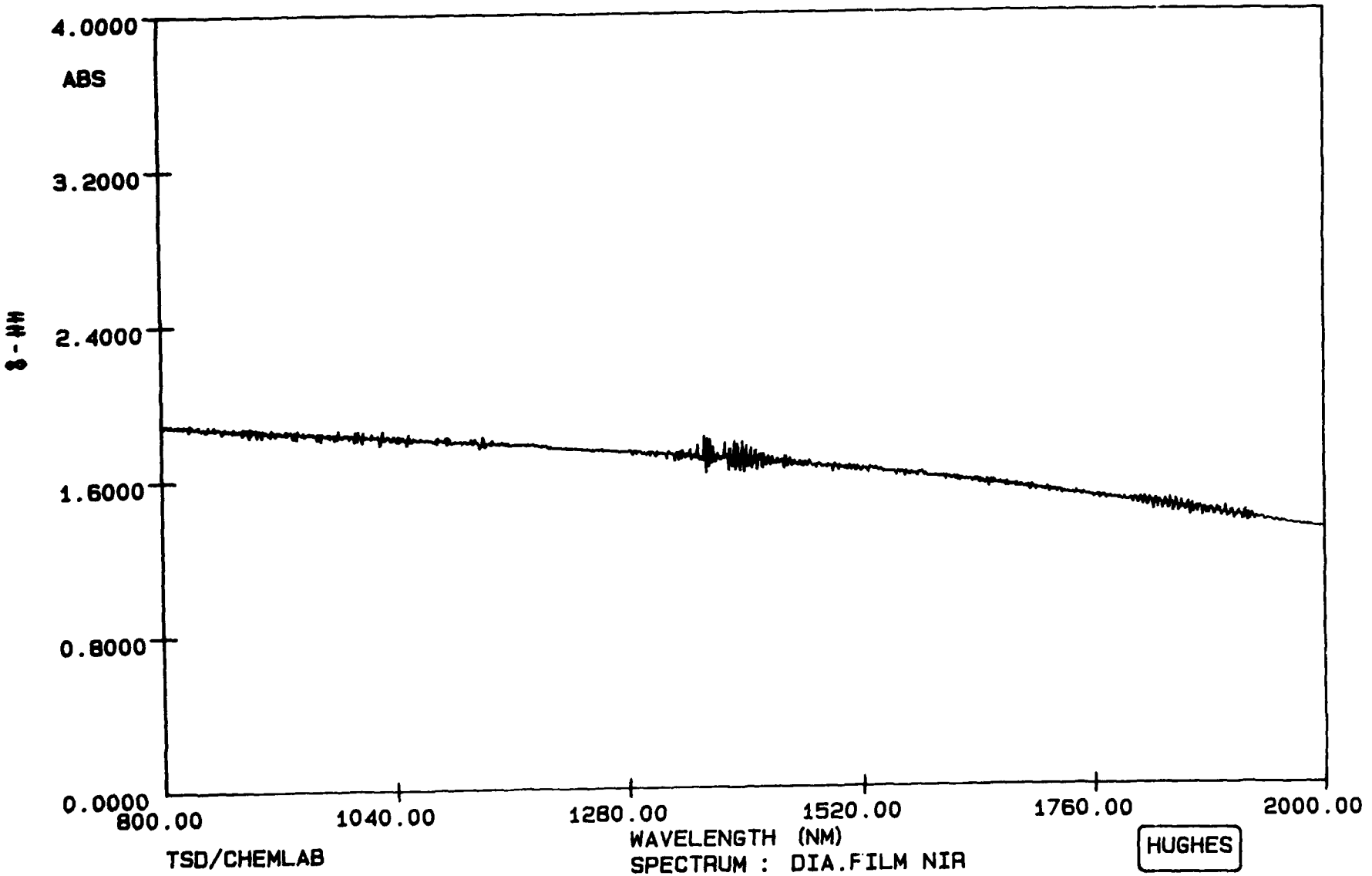
4.0000
ABS
3.2000
2.4000
1.6000
0.8000
0.0000
800.00
1040.00
1280.00
1520.00
1760.00
2000.00
WAVELENGTH (NM)
TSD/CHEMLAB
SPECTRUM : DIA.FILM NIR
HUGHES

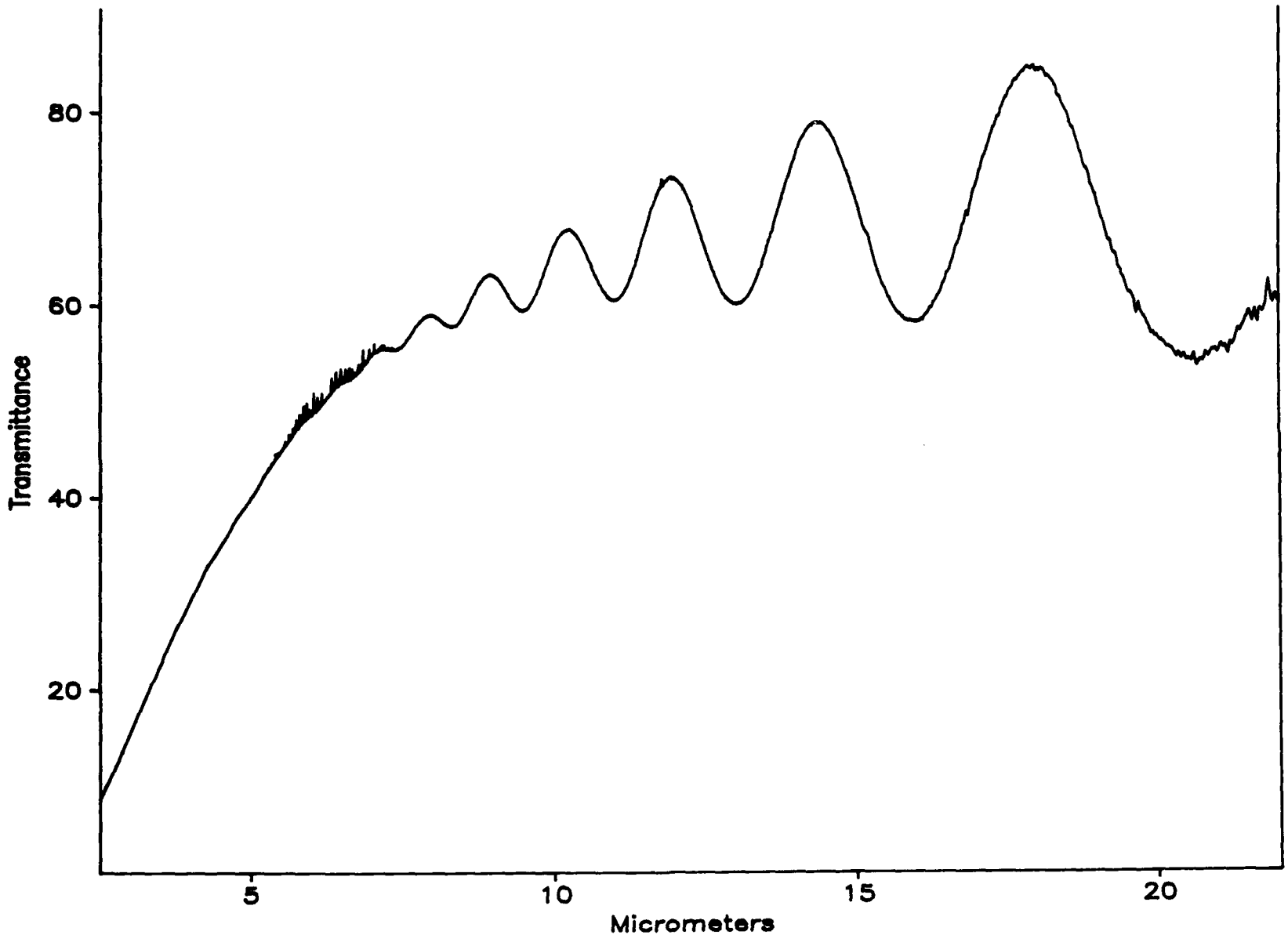

SHINYDIA Res= 1.0 cm−1 03/02/89

Shiny Side of Diamond Film from Crystallume, 6−8 microns thick

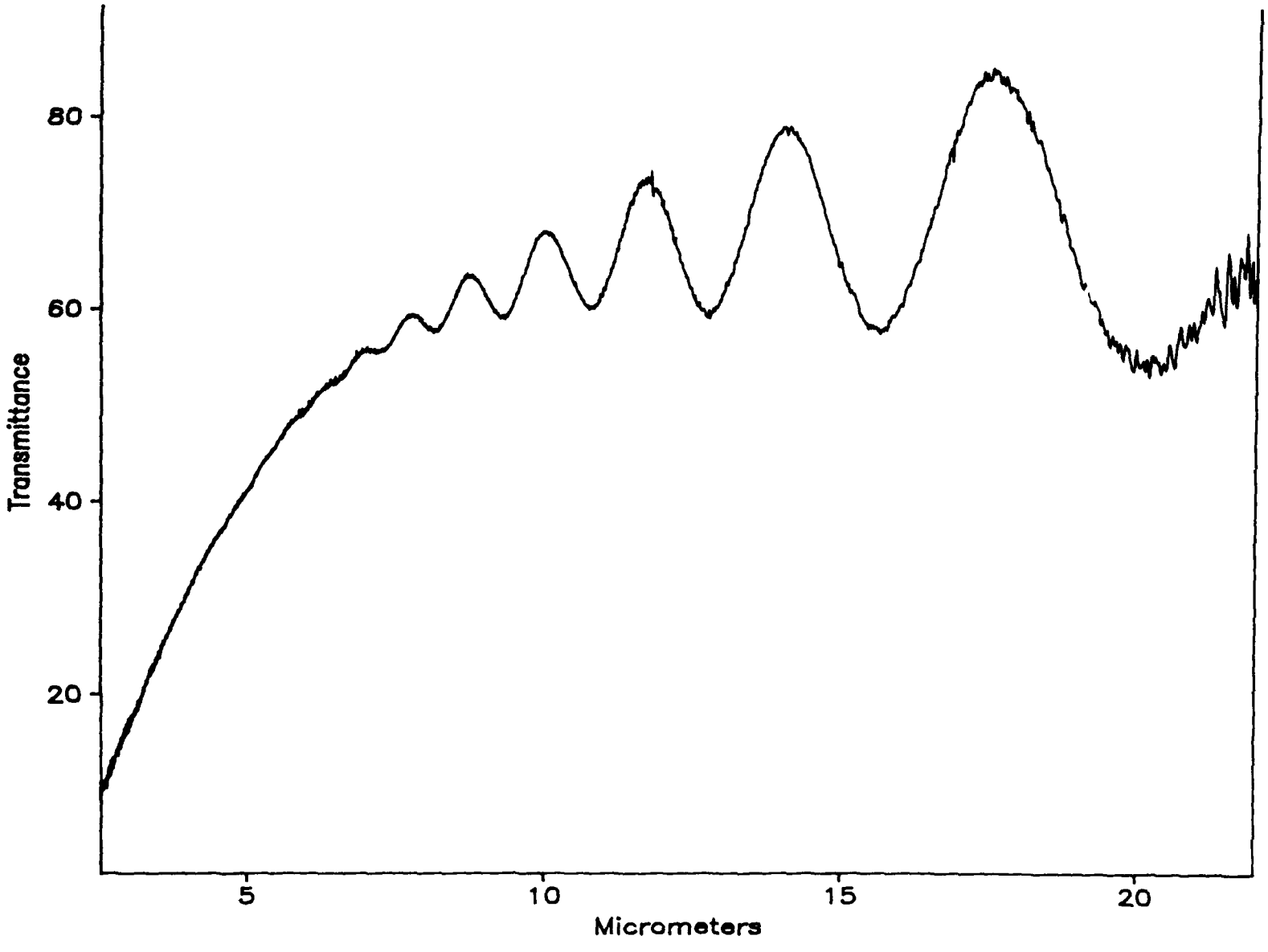

dullda Res= 1.0 cm−1 03/02/89

Dull side of Diamond Film from Crystallume, 6−8 microns thick

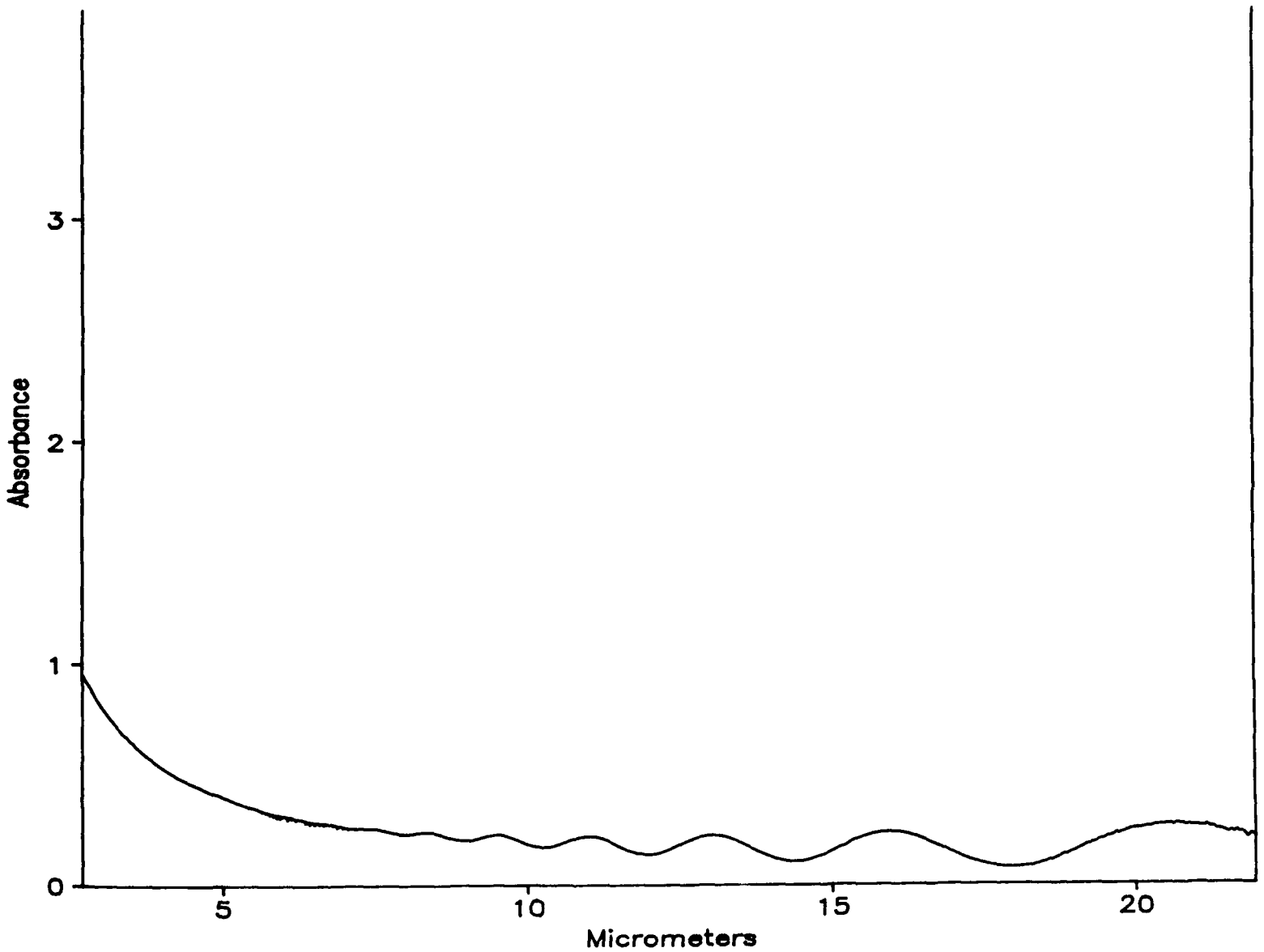

SHINYDIA Res= 1.0 cm−1 03/02/89

Shiny Side of Diamond Film from Crystallume, 6−8 microns thick

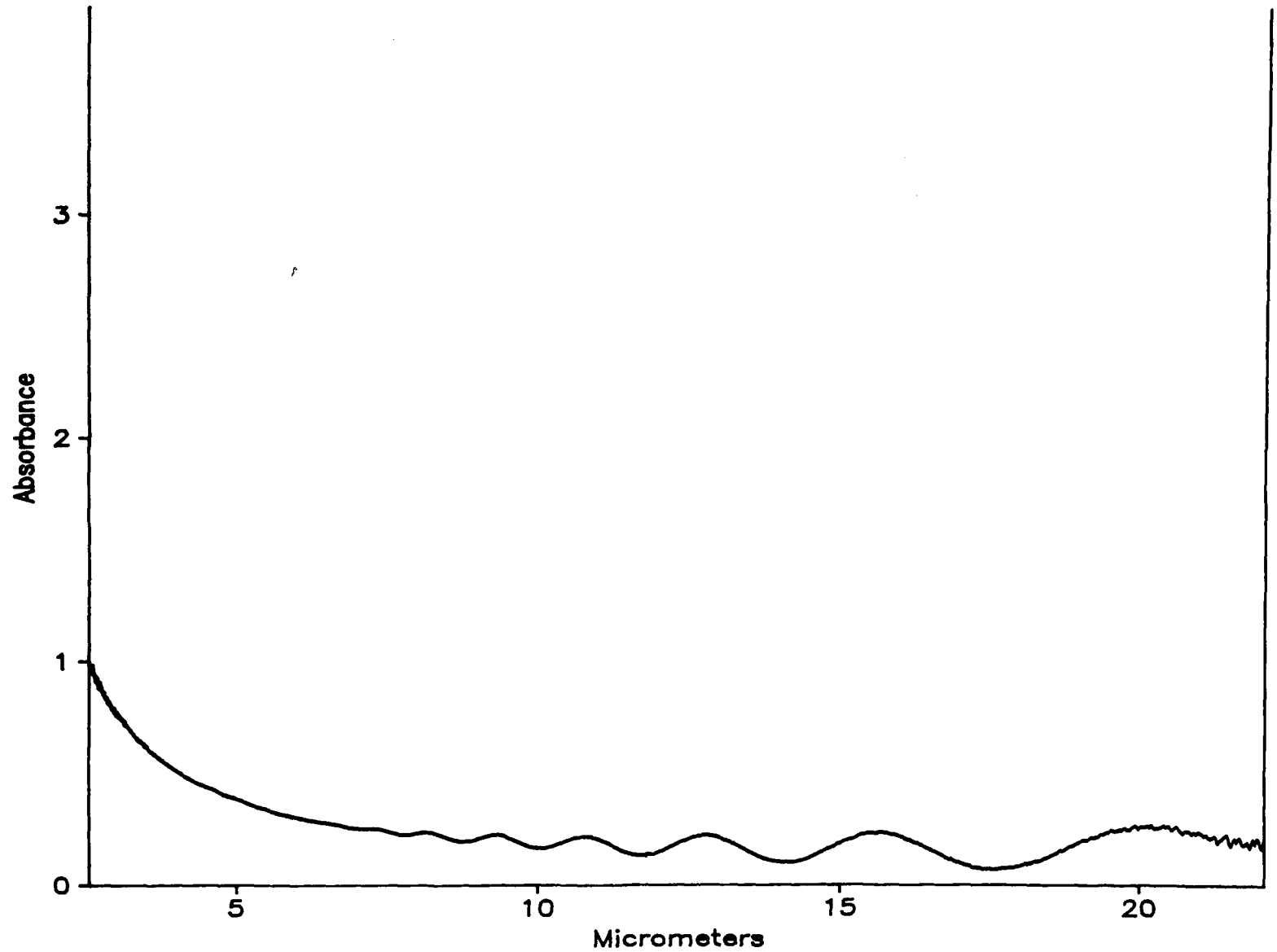

dullda Res= 1.0 cm−1 03/02/89

Dull side of Diamond Film from Crystallume, 6−8 microns thick

APPENDIX II

J.L. Margrave, R.H. Hauge, and R.B. Badachhape, "Oxidation and Fluorination Studies of Diamond," Program Report, Rice University, Houston, TX, 24 November 1987, Hughes P.O., S9-261816-Z7H

Oxidation and Fluorination Studies of Diamond

J. L. Margrave, R. H. Hauge, R. B. Badachhape

and Donald Patterson

Work Reported Through October 31, 1987

Surface oxidations and fluorinations of diamond powders have been conducted to determine optimum temperature ranges for reactions, optimum flow rates for reactions and also to test different experimental techniques for characterizing surface reaction products. Thus, we have utilized microbalance methods for measuring actual weight gains in fluorination and different infrared spectroscopic techniques for detecting surface reaction products.

A. Direct Fluorination of Diamond Powders

Direct exposures of diamond powdered samples to pure fluorine at various temperatures, times and pressures show minimal weight changes even up to 850^{0}C. Previous work with large diamond crystals showed weight changes at 950^{0}C and up to 1100^{0}C. Bulk IR spectra did not indicate C-F bonding.

It appears (and is explained in Part B) that initial exposure of diamonds to fluorine creates a thin protective "FluoroFilm" which then does not undergo further reaction up to 850^{0}C. Although not detected here, the DRIFTS spectra below give definitive evidence for the existence of a protective "FluoroFilm" on the "Dia-Fluor" crystals.

B. DRIFTS Studies of Oxidized and Fluorinated Diamond Powders

Preliminary studies of the effects of fluorination and oxidation on the surfaces of diamond powder (diameter less than 0.5 μ, supplied by Industrial Diamond Powders, Inc.) have been carried out using Diffuse Reflectance Infrared Fourier Transform Spectroscopy (DRIFTS). Untreated diamond powder was used as supplied and reacted with F_2 and/or O_2 (Air Products) in a specially designed flow apparatus. The F_2 and O_2 were passed over the diamond at a flow rate of 5 cc/min at a variety of temperatures (range: 20°C - 194°C) and times (range: 4.5 hrs. - 24.5 hrs.). DRIFTS spectra were collected using 3% sample in dried 99+% KBr (Aldrich) and were processed by use of the Kubelka Munk function.

The spectra of unreacted diamond powder showed significant peaks at ca. 3500 cm^{-1} (very broad) and 1265 cm^{-1} (medium) which indicate the presence of OH and COC groups, respectively, on the surface. Another broad peak at ca. 1750 cm^{-1} points to the presence of C=O groups. Upon oxidation of the diamond (O2 at 184 C for 4.5 hrs.), the peak at 1265 cm^{-1} was enhanced, the OH peak was decreased, and the carbonyl peak was unchanged. Passing F_2 over either the untreated diamond or the oxygenated diamond at 191°C for 4.5 hrs eliminated the OH and COC peaks associated with oxygen and gave rise to new peaks at 1330 and 1084 cm^{-1} (a CF_2 symmetrical stretch and C-F stretch for bond order less than 1, respectively). An intense broad peak centered at 740 cm^{-1} was also noted which may be due to bridging fluorines on the diamond surface or to M-F stretches caused by metal oxide impurities in the powder. The C=O stretch was shifted to 1844 cm^{-1} indicating the presence of neighboring fluorines to the carbonyl species.

Some of the fluorinated diamond powder was further subjected to oxygen at 191°C for 4.5 hrs. The IR spectrum obtained from this sample showed

virtually no change from the previously fluorinated diamond spectrum. There was no evidence of a recurrence of the OH or COC peaks; however, there was a slight shift to 1825 cm^{-1} for the carbonyl peak. It is apparent that the F_2 treatment of the diamond has made the diamond fairly stable against further oxidation.

In temperature and time of fluorination studies on the diamond powder, it was found that fluorine was reacting with the diamond at ambient temperatures in 4.5 hrs. The peaks associated with O_2 (i.e., the OH and COC peaks) could be totally eliminated by passing F_2 over the diamond at 20°C for 24 hrs. In the longer fluorination, the species showing the greatest growth was that associated with the 740 cm^{-1} peak. Obviously, the species related to this peak needs to be better characterized.

Conclusions

1. Both O_2 and F_2 reactions with diamond surfaces are extensive in the 20-194°C temperature range as shown by DRIFTS studies.
2. Passing F_2 over untreated or oxygenated diamond at 191°C eliminates OH and COC peaks and gives rise to new C-F characteristic peaks. The carbonyl peak is not eliminated but is significantly shifted.
3. Once a diamond sample has been fluorinated, e.g., at 191°C, the surface is inert with respect to further oxidation.

Future Plans

1. Surface fluorination/oxidation studies at higher temperatures will be conducted on diamond powders.
2. Similar fluorination/oxidation studies will be conducted on diamond slabs and the surfaces evaluated using ATR, ESCR and Auger techniques.

3. The stabilities of "fluorodiamonds" in oxidizing atmospheres will be established over a range of temperatures.

11/24/87